Biodiesel production from used cooking oil using novel solid acid catalysts

Jabbar Lashkeri Ismail Agha Gardy

Submitted in accordance with the requirements for the degree of

Doctor of Philosophy

The University of Leeds

School of Chemical and Process Engineering

March 2017

Declaration

The candidate confirms that the work submitted is his own, except where work which has formed part of jointly authored publications has been included. The candidate confirms that appropriate credit has been given within the thesis where reference has been made to the work of others.

o The work in Chapter Four of the thesis has appeared in publication as follows:

   Gardy, J., A. Hassanpour, X. Lai, M.H. Ahmed, and M. Rehan. *Biodiesel production from used cooking oil using a novel surface functionalised TiO_2 catalyst.* Applied Catalysis B: Environmental, **2017**. 207: p. 297-310. http://dx.doi.org/10.1016/j.apcatb.2017.01.080.

I can confirm that this work has been completely done by myself including writing up the manuscript, apart for the supervision role and/or accessing to some of the analytical instruments.

o The work in Chapter Five of the thesis has appeared in publication as follows:

   Gardy, J., A. Hassanpour, X. Lai, and M.H. Ahmed, *Synthesis of $Ti(SO_4)O$ solid acid catalyst and its application for biodiesel production from used cooking oil.* Applied Catalysis A: General, **2016**. 527: p. 81–95. http://dx.doi.org/10.1016/j.apcata.2016.08.031.

I can confirm that this work has been completely done by myself including writing up the manuscript, apart for the supervision role and/or accessing to some of the analytical instruments.

This copy has been supplied on the understanding that it is copyright material and that no quotation from the thesis may be published without proper acknowledgement.

© 2017 The University of Leeds and Jabbar Lashkeri Ismail Agha Gardy.

The right of Jabbar Lashkeri Ismail Agha Gardy to be identified as Author of this work has been asserted by him in accordance with the Copyright, Designs and Patents Act 1988.

Acknowledgment

Special thanks to my supervisors Dr Ali Hassanpour and Dr Xiaojun Lai for their advice, outstanding supervisions, valuable suggestions, continuous supports, discussions, guidance and criticisms during the entire period of my PhD.

I would like to thank the Ministry of Higher Education and Scientific Research in Kurdistan Regional Government for the scholarship funding by the Human Capacity Development Program. I am also extremely grateful for School of Chemical and Process Engineering at the University of Leeds for providing me with all the facilities to carry out my research.

I would like to take this opportunity to thank Professor Adam Lee (external examiner) and Associate Professor Hu Li (internal examiner) for their very helpful feedbacks, suggestions and comments.

I gratefully acknowledge Professor Frans Muller and Dr Bao Nguyen for their valuable feedbacks and suggestions during my 1st year transfer viva and 2nd year exam, respectively.

I lack the words to thank Dr Adriane Cunliffe, Mrs Suzanne Patel, Dr Faye Esat, Mrs Karine Alves Thorne, Mr Stuart Micklethwaite, Dr Michael Ward, Mr Neil Smith, Mr Simon Lloyd, Dr Tim Comyn, Mr Robert Harris, Dr Zabeada Aslam, Dr Ben Douglas, Miss Sara Dona and all the technicians at the University of Leeds for their advice as well as practical help.

I am very much thankful to Professor Karen Wilson and Professor Adam Lee from the University of Aston for their valuable feedbacks in few occasions (ISACS17: Challenges in Chemical Renewable Energy in Brazil and iPRD meeting in Leeds) as well as for accessing me to their labs at the European Bioenergy Research Institute (EBRI). I further wish to express my special thanks to Dr Amin Osatiashtiani at the EBRI for spending his valuable time to carry out DRIFTs and TPD-MS experiments for some of the samples. Great acknowledgment is given to Dr Mukhtar Ahmed from the University of Ulster who helped in obtaining the XPS data for few samples. Special thanks is given to Dr Oscar Céspedes for his kind help with using the VSM facility at the School of Physics and Astronomy in the University of Leeds.

I would like to offer special thanks all the members in Dr Ali Hassanpour's group, in particular Miss Mozhdeh Mehrabi, Mr Amin Farshchi, Dr Joseph Ghaffari, Dr Faiz Mahdi and Mr Mo

Behjani, for their friendship, geniality, kindness and valuable feedbacks during all the group meetings.

I must not forget to thank members of Professor Kevin Roberts and Professor Mojtaba Ghadiri's groups for their friendship and possible help in difficult times.

Heartfelt thanks goes to all other PhD students and PDRA whom I worked with during my research at the University of Leeds, in particular Dr Rodrigo Gu, Mr Zhongliang Hu, Dr Mohamed Manga, Dr Alejandro Lopez, and Dr Sergio Segado, for their great atmosphere and many years of friendship.

I am much indebted to all my friends who directly or indirectly played a role in the completion of this work that I forgot to mention their names.

Last but not least, I would like to record my deepest gratitude to my family for their belief in everything I try to succeed in and motivation from the beginning to the end of this project. This thesis would not have been possible without their help and support.

Dedication

This thesis is dedicated to my loving parents for their infinite support, supervisors and all friends for their constant supports and encouragements.

Conference and seminar activities

- *J. Gardy*, A. Hassanpour, X. Lai "*Waste to sustainable biodiesel fuel over novel solid acid catalysts*" *poster presentation* on **13th March 2017** to STEM for BRITAIN 2017 at the House of Commons in the Engineering Sciences Session, Attlee Suite, Portcullis House, SW1A 0AA London, UK.

- *J. Gardy*, A. Hassanpour, X. Lai, M. Ahmed, M Rehan "*Effect of surface grafting and impregnation of TiO$_2$-NPs on the esterification/transesterification processes of used cooking oil*" *poster presentation* on **25th November 2016** to the Material Chemistry-Division Poster Symposium, Royal Society of Chemistry (RSC) at Burlington House, W1J 0BA London, UK.

- *J. Gardy*, A. Hassanpour, X. Lai, M. Ahmed "*A novel green solid acid catalyst for biodiesel production from used cooking oil*" *poster presentation* on **6th-9th June 2016** to the European Biomass Conference and Exhibition (EUBCE) 2016, RAI Amsterdam Exhibition and Convention Centre Europaplein, 1078 GZ Amsterdam, The Netherlands.

- A. Hassanpour, *J. Gardy*, X. Lai "*Biodiesel production from used cooking oil using novel solid acid catalysts*" *oral presentation* on **28th October 2015** to the *iPRD* Industrial Club Meeting, School of Chemistry, University of Leeds, Weetwood Hall Conference Centre, LS16 5PS, Leeds, UK.

- *J. Gardy*, A. Hassanpour, X. Lai "*Transesterification of locally sourced used cooking oil using a novel catalyst*" *flash and poster presentation* on **8th-11th September 2015** to the Challenges in Chemical Renewable Energy (ISACS17), Hotel Othon Palace, Rio de Janeiro, Brazil.

- *J. Gardy*, A. Hassanpour, X. Lai, M. Ahmed "*Surface functionalization of TiO$_2$ nanoparticle and its application for biodiesel production from locally sourced used cooking oil*" *oral Presentation* on **15th-17th June 2015** to the International Nanotech & Nanoscience conference and Exhibition (Nanotech France 2015), Pôle Universitaire Léonard de Vinci- "La Défense" Business district, Paris, France.

- *Jabbar Gardy*, Ali Hassanpour, Xiaojun Lai, Adrian Cunliffe, Mohammad Rehan "*The influence of blending process on the quality of rapeseed oil-used cooking oil biodiesels*" *oral Presentation* on **07th-08th May 2014** to the International Conference on Environment and

Renewable Energy (ICERE 2014), Cité Internationale Universitaire de Paris, 17 Boulevard Jourdan, Paris, France.

- *Jabbar Gardy*, Chika *Wosu*, Ali Hassanpour, Xiaojun Lai, Mohammad Rehan "*The effect of process parameters on the production of biodiesel from various feedstocks*" **poster presentation** on **11th-13th March 2014** to the International Bioenergy Conference 2014, Manchester Central Convention Complex, Manchester, UK.

Abstract

Damage to the environment as a consequence of exploration, production, imminent depletion, use of fossil fuels and concerns over climate change (increasing lifecycle greenhouse gas emissions), has increased the need for a more eco-friendly, renewable and sustainable source of energy. The level of biodiesel production has been increasing over the last twenty years, reflecting a rapid rise in demand due to its availability, renewability, lower gas emissions, non-toxicity, and its biodegradability. The impact of CO_2 emissions on climate change, worldwide industrialisation, countries not having oilfields and need for a strategic and alternative source of energy have also driven an ever increasing demand. Biodiesel is mainly produced in industry by the transesterification process of triglycerides with low molecular weight alcohols using homogenous acid or base catalysts. However, the biodiesel industry faces some significant challenges; (i) high cost of biodiesel feedstock and (ii) the cost of biodiesel processing, including separation, purification and the neutralisation of by-products. These issues can be resolved with catalysts that are highly tolerant to moisture and free fatty acid (FFA) in feedstock oils. Solid acid catalysts have shown promise as catalysts in the simultaneous esterification and transesterification to overcome these issues.

Here, lab-scale biodiesel production from simultaneous esterification and transesterification of used cooking oil (UCO) over different developed novel solid acid catalysts has been investigated. The synthesised catalysts, including $TiO_2/PrSO_3H$, $Ti(SO_4)O$ and $SO_4^{2-}/Fe-Al-TiO_2$, were characterised via XRD, SEM, TEM, TEM-EDS, EDS-mapping, FT-IR, DRIFT-pyridine, TPD-MS with n-propylamine, TGA/FT-IR, CHNS analysis, DSC, TGA, N_2 porosimetry, VSM and XPS. The effect of different process parameters on the fatty acid methyl ester (FAME) yield over different catalysts was also studied, including the effect of reaction temperature, mole ratio of methanol to UCO, time of esterification/transesterification, and amount of catalyst to UCO loading in order to achieve the optimum process conditions to obtain the highest FAME yield. Furthermore, a significant aim was to design a highly active, low cost, stable, easy recoverable, FFA tolerant and highly re-usable solid acid catalyst for biodiesel fuel production. It was found that $SO_4^{2-}/Fe-Al-TiO_2$ performs well under optimum conditions of 2.5 h of reaction time, 3 wt% of synthesised magnetic catalyst to UCO ratio, 10:1 methanol to UCO mole ratio and 90 °C reaction temperature for simulations esterification and transesterification processes. A massive

improvement in catalytic stability, easy recovery (using external magnetic field), high tolerance to FFA and water have been achieved via the introduction of alumina and iron oxides to the catalyst support. The synthesised biodiesels from UCO over different solid acid catalyst processes were analysed in accordance to ASTM D6475 and EN14214 standard methods to determine characteristic fuel properties such as kinematic viscosity, density, flash point, FAME content, LAME content, and acid number.

Keywords

Table of contents

List of tables

List of figures

Nomenclature

List of abbreviations

Abbreviation	Description
Al-TiO$_2$	Alumina coated titania
ASTM	American Society for Testing and Materials
b/d	Barrels per day
B/L	Brønsted to Lewis acid sites ratio
BE	Binding energy
BET	Brunauer, Emmett and Teller
BIS	1,2,4-Butanetriol internal standard-1
BJH	Barrett-Joyner-Halenda
C%	Conversion%
CNF	Carbon nano-fiber
CNT	Carbon nano-tube
CP	Cloud point
D$_p$	Mean pore size
DRIFTS	Diffuse reflectance infrared Fourier transform spectroscopy
DSC	Differential scanning calorimetry
EDS	Energy-dispersive X-ray spectroscopy
EELs	Electron energy loss spectroscopy
EIA	Energy Information Administration
EtOH	Ethanol
EU	European Union
FAEE	Fatty acid ethyl ester
FAME	Fatty acid methyl ester
Fe-Al-TiO$_2$	Iron oxide coated Al-TiO$_2$
FFA	Free fatty acid
FT-IR	Fourier transform infrared spectroscopy
FWHM	Full width a half maximum intensity
GC-FID	Gas chromatography-flame ionization detector
GC-MS	Gas chromatography-Mass spectrometry
GHG	Greenhouse gas
H	Applied magnetic field
H$_0$	Hammett indicator
HAADF	High-angle annular dark field
hkl	Crystal planes (miller indices)
HPAs	12-Tungstophosphoric acid
HPDW	High purity deionised water
HR-TEM	High resolution transmission electron microscopy
HSA	High surface area
HTlc	Hydrotalcite-like compounds
ICP-MS	Inductively coupled plasma mass spectrometry
IUPAC	International Union for Pure and Applied Chemistry

Abbreviation	Description
JCPDS-ICDD	Joint Committee on Powder Diffraction-International Centre for Diffraction Data
LAME	Linolenic acid methyl ester
LDH	Double layered hydroxides
M	Magnetic field
Max	Maximiums
MeOH	Methanol
meq	Milliequivalent
Min	Minimums
M-O	Metal oxygen bond
M-O-M	Metal-oxygen-metal bond
MPTMS	(3-Mercaptopropyl)trimethoxysilane
MSTFA	N-Methyl-N-(trimethylsilyl) trifluoro acetamide
N.R.	Not reported
NH_3-TPD	Ammonia-temperature programmed desorption
NMR	Nuclear magnetic resonance
NPs	Nanoparticles
NRC	Not recyclable catalyst
P/P_0	Relative pressure
Pa	Pascal
PD	Petro-diesel
ppb	Parts part billion
ppm	Parts per million
RPM	Revolution per minutes
SAED	Selected area electron diffraction
SBA-15	Santa barbara amorphous-15
SCA	Supercritical alcohol
SCM	Supercritical methanol
SE	Secondary electrons
SEM	Scanning electron microscope
Sp.gr	Specific gravity
SSA	Specific surface area
STD	Standard
STEM	Scanning transmission electron microscopy
t/y	Tons per year
TAG	Triacylglycerols
TEM	Transmission electron microscopy
TEOS	Tetraethyl orthosilicate
TG	Triglycerides
TGA	Thermogravimetric analysis
TGA/FT-IR	Thermogravimetric analysis/Fourier transform infrared spectroscopy
THF	Tetrahydrofuran
TIS	1,2,3-Tricaproylglycerol (tricaprin) internal standrd-2
TPD	Temperature programmed desorption

Abbreviation	Description
TPD-MS	Temperature programmed desorption-Mass spectroscopy
UCO	Used cooking oil
UK	United Kingdom
US	United States
UV	Ultra violet
V_p	Total pore volume
VSM	Vibrating sample magnetometer
WCO	Waste cooking oil
XPS	X-ray photoelectron spectroscopy
XRD	X-ray diffraction
Y%	Yield%
ZSM-5	Zeolite socony mobil–5

List of Roman letters

Roman letter	Description
eV	Electron volt
g	Grams
h	Hour
J	Joules
Kg	Kilograms
kPa	Kilopascal
kV	Kilovolt
L	Litres
m	Metres
M	Molar
mg	Milligram
min	Minutes
mL	Millilitres
mmol	Millimole
nm	Nanometre
ºC	Degrees celsius
s	Seconds
T	Temperature
t	Time
w/w	Weight per weight percentage

List of Greek characters

Greek character	Description
Å	Angstrom
α	Alpha

β	Beta
γ	Shear rate
Δ	Delta
η	Dynamic viscosity
θ	Theta
λ	Wavelength
μ	Micro
ρ	Density
σ	Shear stress

List of symbols

Symbol	Description
$C_{14:0}$	Myristic acid
$C_{16:0}$	Palmitic acid
$C_{16:1}$	Palmitoleic acid
$C_{18:0}$	Stearic acid
$C_{18:1}$	Oleic acid
$C_{18:2}$	Linoleic acid
$C_{18:3}$	Linolenic acid
$C_{20:0}$	Arachidic acid
$C_{20:1}$	Gadoleic acid
$C_{21:0}$	Eicosadienoic acid
$C_{22:0}$	Behenic acid
$C_{22:1}$	Erucic acid
$C_{24:0}$	Lignoceric acid
$C_{24:1}$	Nervonic acid

Chapter 1

Introduction

1.1   **Background of research**

1.2   **Scope of work**

1.3   **Thesis layout**

This chapter is an introduction to the research project and includes a background to the work undertaken and the research question provides an outline of the challenges with objectives of the biodiesel industry. It also provides information on the overall structure of the thesis.

CHAPTER ONE

1. Introduction

1.1 Research background

Renewable fuel production has been a topic of research for more than a century and is expected to continue due to depletion of fossil fuel and increasing environmental concerns over their consumption, including rising CO_2 emissions [1]. According to the international energy report by the U.S. Energy Information Administration (EIA) in 2016, total world energy use is expected to increase by more than half over the next three decades, driven by global industrial and transportation growth [2].
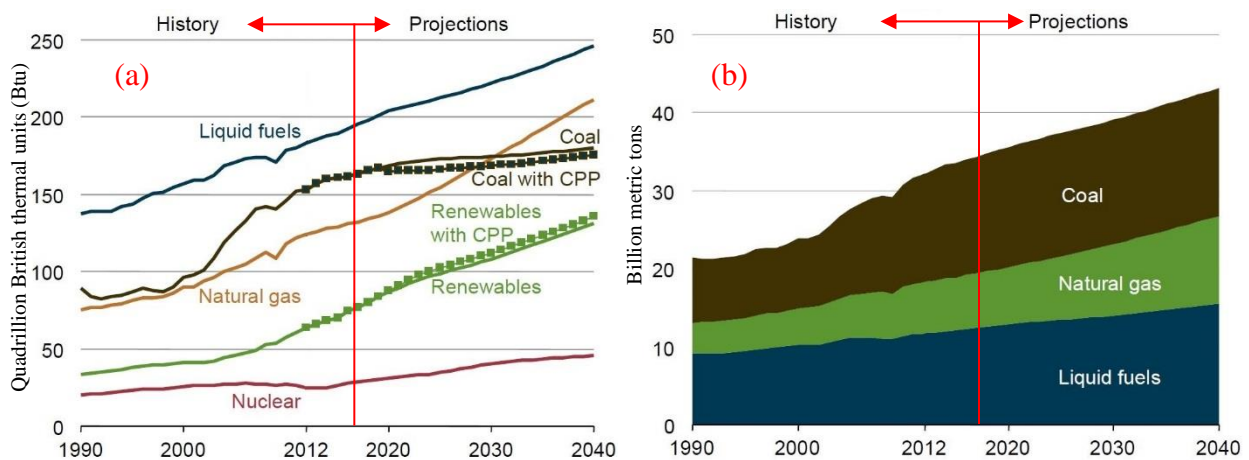
Figure 1.1 Total world energy consumption by energy source from 1990 to 2040 (a) and world energy-related carbon dioxide emissions by fuel type from 1990 to 2040 (b) [2]

For example, world liquid fuel use in 2012 was 90,000,000 barrels per day (b/d) with the figure expected to rise to 100,000,000 b/d in 2020 and to 121,000,000 b/d in 2040. As a result, CO_2 emissions, especially from fossil fuel consumption, will increase, as is projected in Figure 1.1 (b). The consequence of this could be global temperature increases (global warming). If temperatures

increase by more than 2 ℃, it is estimated the cost will be hundreds of millions of humans lives and other species lost [3]. Therefore, the world's fastest-growing energy source over the next three decades is going to be renewables, as seen in Figure 1.1 (a). This relates to renewable energy use increasing by an average 2.6% per year between 2012 and 2040. Atabani et al. [3] also reported that the use of renewable fuels as a share of overall fuel usage is expected to have grown by 4% between 2007 and 2035 with an accompanying reduction of the crude oil use from 35% to 30% (see Figure 1.2).
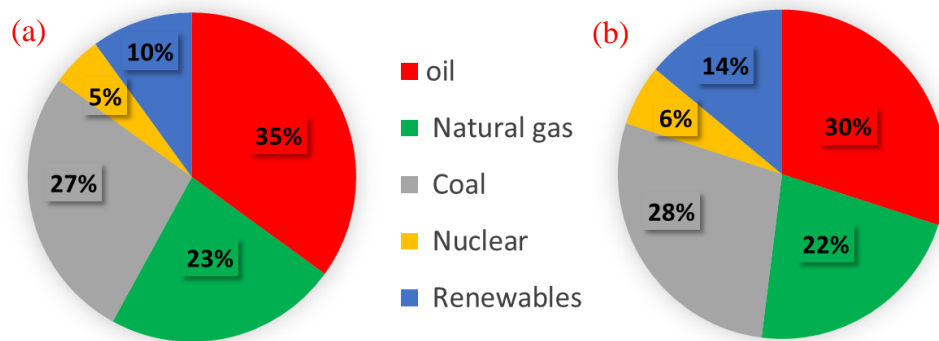
Figure 1.2 The world energy use by fuel in (a) 2007 and (b) 2035

Many researchers have investigated the possibility of partially/totally replacing crude oil and its derivatives with an alternative fuel. In 1893, Rudolf Diesel invented the use of peanut oil in a model diesel engine. This marked the beginning of the use of vegetable oils in diesel engines as opposed to petro-diesel. However, it has been highlighted that vegetable oils could not be used effectively in engines due to high viscosity, low volatility, and cold flow behaviours [4]. This led to exploration to try to overcome these problems, leading to the concept of biodiesel in 1980s. Research continues extensively with a view to producing a source of renewable and sustainable energy to meet global demand and supply [5-7]. Biodiesel is, according to the worldwide definition, an alkyl ester of long chain fatty acid made from vegetable oils or animal fats with low molecular weight of alcohol in the presence or absence of catalysts as shown in Figure 1.3 [5, 8]. The selection of feedstock is based on variables such as local availability, cost, government support and its performance as a fuel [9]. A variety of edible and non-edible oil feedstocks have been identified to produce biodiesel. These include virgin oil, such as rapeseed oil, soybean oil, sunflower oil, palm oil, mustard oil, jojoba oil, tung oil, rubber oil, cotton seed oil, neem oil, nahor oil, karanja oil, jatropha oil, pongamia oil and rice bran oils [10-12].
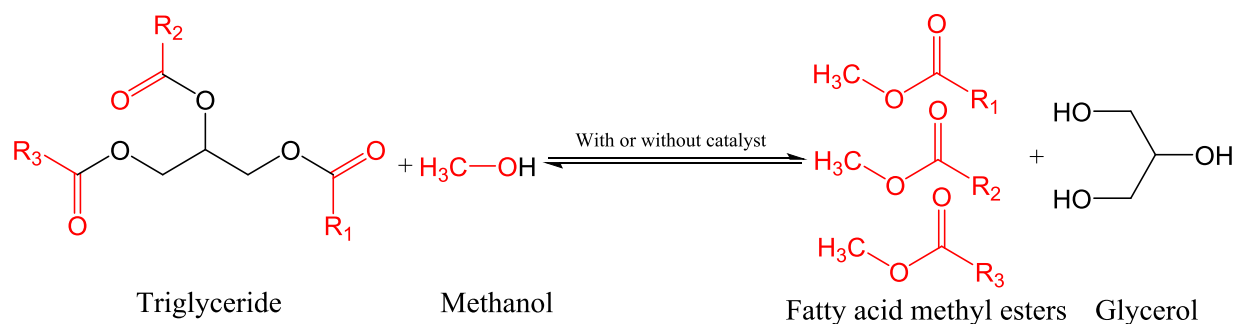
Figure 1.3 Biodiesel production from TG with methanol

Oils from tallow, lard, yellow grease, chicken fat and by-products of fatty acids from fish oil and flaxseed oils are also used [8, 13, 14]. However, edible oils compete with the food market which increases the cost of the biodiesel and exacerbates deforestation in some countries. Moreover, the transesterification process for many types of animal fats is difficult due to the high amounts of saturated FFAs which present problems regarding the use of biodiesel fuel in cold weather. Furthermore, the statistic reports show that the level of production and consumption of vegetable oils worldwide are almost the same rate as shown in Figure 1.4.
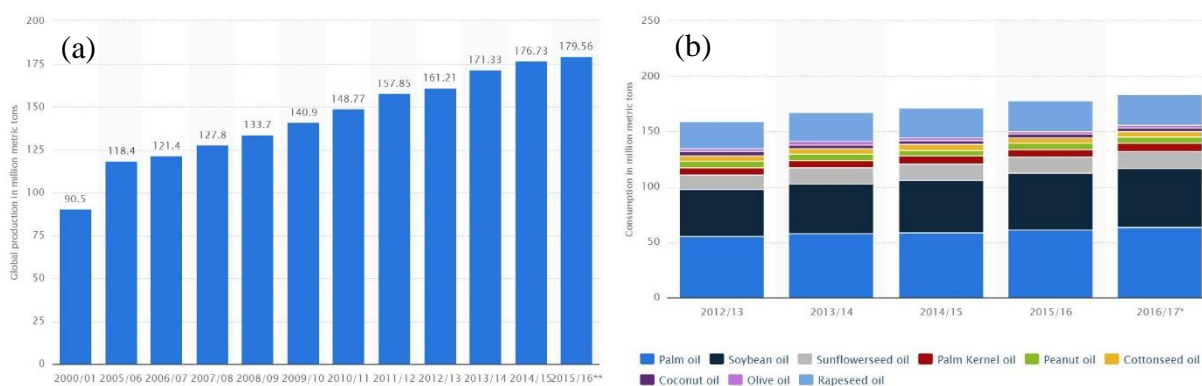
Figure 1.4 (a) Production and (b) consumption of vegetable oils worldwide [15]

In order to overcome such demerits, many researchers have shown interest in the use of non-edible oil feedstock [8, 16, 17]. Oils from waste cooking oil (WCO), (micro)algae and jatropha seeds have been the subject of many research studies in recent years with a view to providing good yields and low prices [13, 18-25]. The production of biodiesel (fatty acid methyl ester, FAME) around the world, using different feedstocks, is shown in the Figure 1.5. It can be observed from the figures that the choice of feedstock depends mainly on climate, local soil conditions and availability. This means that options vary between different regions of the world. For instance, palm oil is

predominant in Malaysia due to soil conditions there; soybean oil is predominant in the United States due to weather conditions, as well as utility value [26, 27].
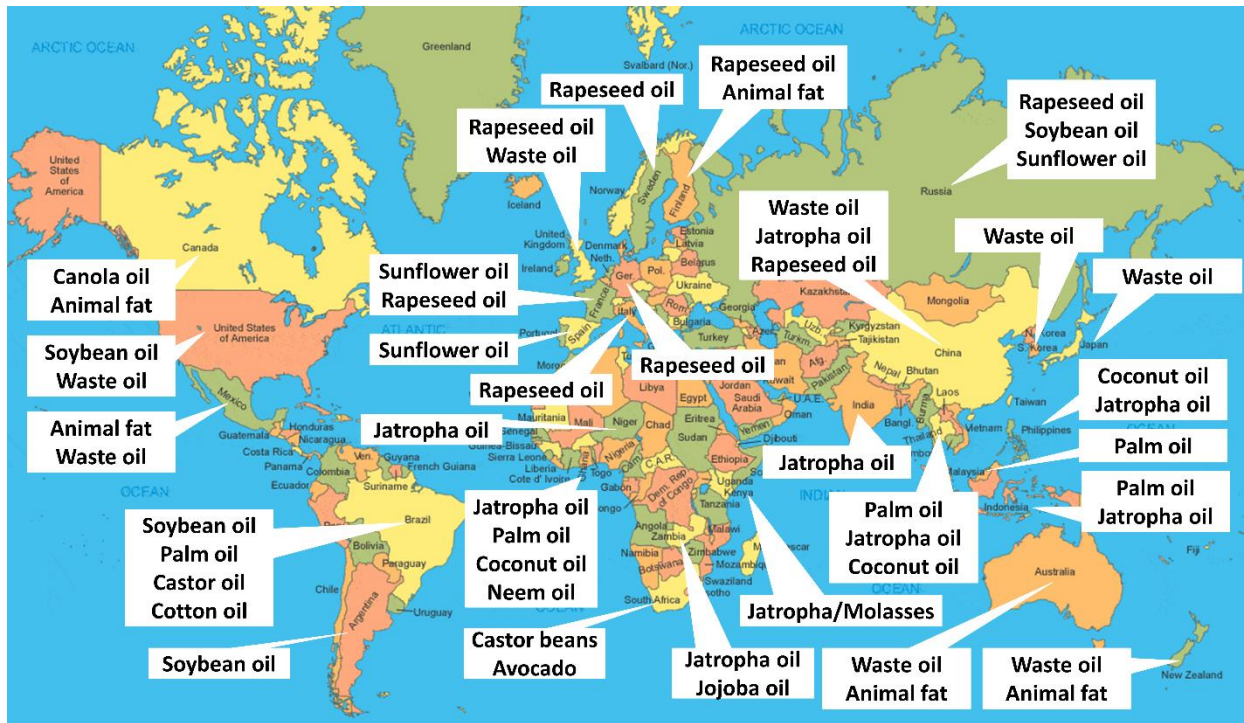
Figure 1.5 Production of biodiesel around the world

Table 1.1 Statistics of biodiesel production in some EU countries

EU countries	Production capacities per year/per x10^3 tonnes						
	2006	2007	2008	2009	2010	2011	2012
Germany	2662	2890	2819	2539	2861	2800	4968
Spain	99	168	207	859	925	604	4391
Netherlands	18	85	101	323	368	370	2517
France	743	872	1815	1959	1910	1559	2456
Italy	447	363	595	737	706	479	2310
Poland	116	80	275	332	370	363	884
Greece	42	100	107	29	33	78	812
Belgium	25	166	277	416	435	472	770
UK	192	150	192	137	145	218	574
Austria	123	267	213	310	289	226	535

The biodiesel production of the top ten European Union countries (based on 330 working days per year/per plant) was increased between 2006 and 2012 as can be seen in Table 1.1 [28]. In all EU countries, renewable energy targets are set at a minimum of 20% by the end of 2020 [29]. This is

mainly due to the advantages of biodiesel over petro-diesel fuel which are: availability, renewability, higher cetane number, environmental friendliness (fewer toxic pollutants), less greenhouse gas (GHG) emissions (reduces GHG up to 78%), lower sulfur content, high flash point, lower aromatic content, better lubricity and higher biodegradability [8]. Despite numerous advantages of biodiesel, there are some disadvantages which include low oxidative stability, high viscosity; a slight increase in NO_x emissions, the clogging of engines and difficulty for use in low-temperature operations [30-32].

The choice of raw materials for biodiesel production can greatly affect the price and quality of the produced fuel. For instance, the life cycle of biodiesel production from waste/used cooking oil (WCO/UCO) feedstocks, see Figure 1.6, significantly helps to commercialise the fuel due to its lower cost (2.5-3.5 times) than virgin vegetable oils as well as its general availability [33]. Also, it does not compete with food crop production and boasts better viscosity properties than virgin oil without affecting fuel quality [34]. This makes UCO (unconventional raw materials) good candidates for biodiesel production in terms of efficient use of feedstocks and reducing the potential serious environmental issues linked to the disposal of the waste oils. However, there are issues with direct use of UCO as feedstocks for biodiesel production due to it may contains FFA and water as impurities.
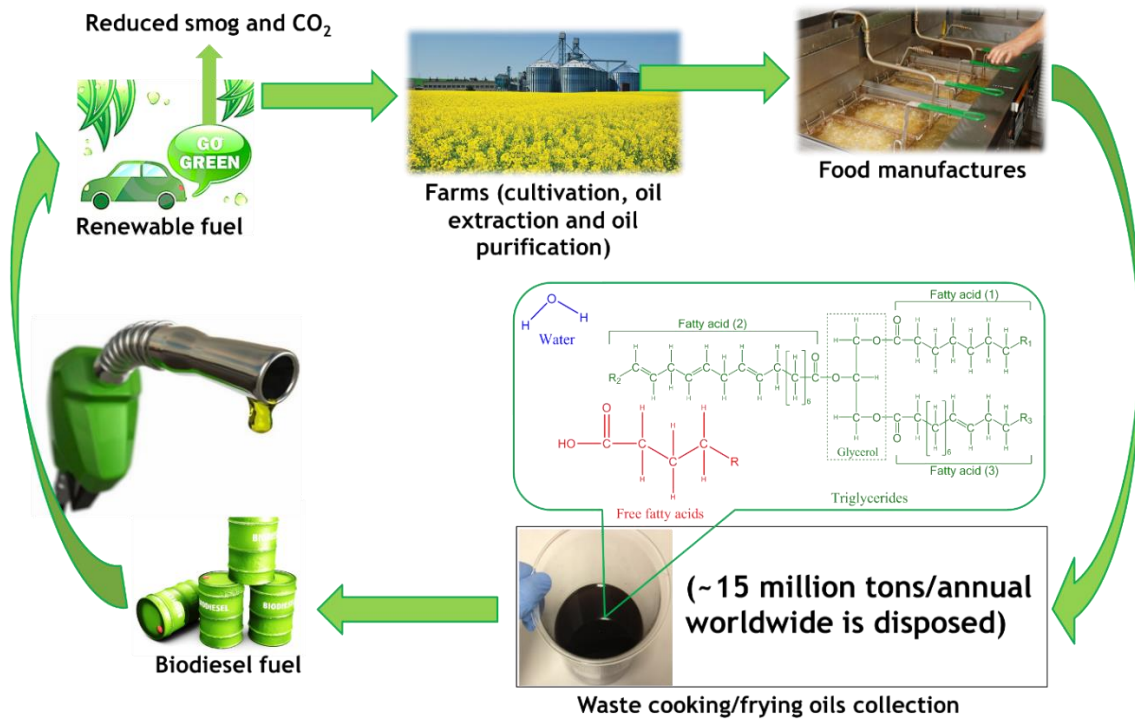
Figure 1.6 Life cycle of biodiesel production from vegetable oils

There are generally four main ways to produce fuel from vegetable oils (edible and non-edible oils), animal fats, (micro)algae or waste oil [35]. These are: microemulsion process, pyrolysis, direct use/blending of raw oils, and transesterification [36, 37]. The transesterification process, consists of three consecutive reversible reactions, has been mainly highlighted for biodiesel production among other approaches. The summary of classification for transesterification (alcoholysis) is presented in Figure 1.7.
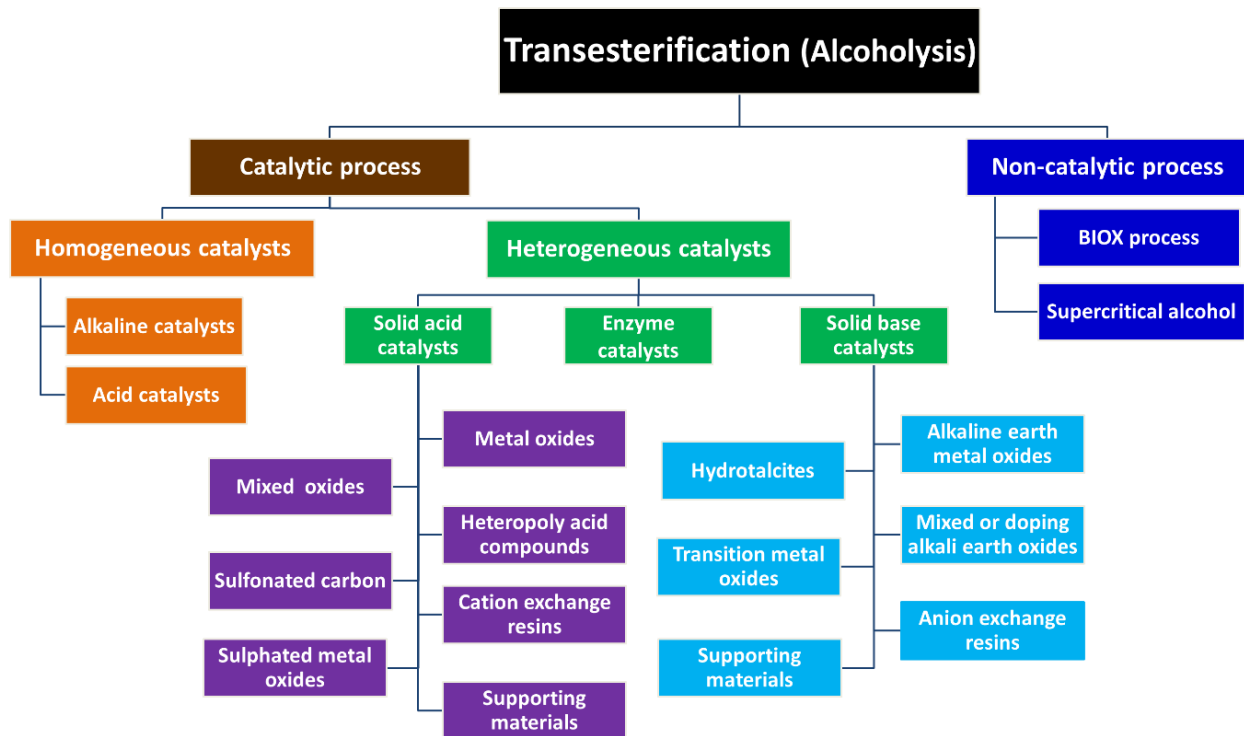
Figure 1.7 Classification of transesterification processes for biodiesel production

The transesterification can be a catalytic or a non-catalytic process. However, non-catalytic processes have more drawbacks than advantages. The catalytic transesterification process is more commonly adopted for biodiesel production from different feedstocks, including cheap feedstocks, due to simplicity and low cost. Cheap feedstock, e.g. WCO/UCO, contains more than 1.0 % of FFA and 0.5 % of water which means the homogenous alkali catalysed transesterification process is not desirable due to the formation of soap (fatty acid salts), hydrolysis of the product, aqueous quenching which demands large volumes of water, the need for neutralisation steps, difficulties in separation (formation of stable emulsion) and the decreasing reactivity of the catalyst [38-40].

Homogenous acid catalysts are an appropriate option for catalysing these materials to form biodiesel; however, they cannot be recovered, they demand costly fuel purification processes and they are very corrosive [36, 41, 42]. Enzyme catalysts are very expensive in industrial-scale production and are, therefore, not favourable for biodiesel production. Solid acid and base catalysts have been recently used for transesterification processes and have shown good catalytic activities due to their reusability, higher stability, high surface area, non-toxicity and the simplicity of purification. Solid acid catalysts have the added advantages of being more tolerant to high amounts of FFAs and also being able to simultaneously esterify FFAs and transesterify TG in cheap feedstocks (eg. WCO/UCO). These discoveries promise possibility of a continuous production for the biodiesel industry process.

According to the literature, nanomaterials have fascinating and unique properties for usage in various industrial fields. Titanium dioxide (TiO_2) nanoparticles (NPs) are among the most widely studied for their use in photocatalysis, gas sensors, medicine, catalyst support, pigments, cosmetics and solar cells [43-52]. This is due mainly to their favourable properties, including acidity, wide band gap, high surface area, low cost, and easy availability [as ilmenite ore ($FeTiO_3$), leucoxene ore, sphene (titanite: $CaTiSiO_5$) and the binary metal oxides]. Their other advantages are better redox selectivity, good mechanical and chemical stability, high reactivity, low toxicity, and high reusability [53, 54]. TiO_2 NPs occur naturally in three main crystallographic phases, these being anatase, rutile, and brookite based on the arrangements of TiO_6 octahedral units (see Figure 1.8) [47, 51, 55-59], however the most commonly used, because of its high photocatalytic activity, is a mixture of anatase and rutile phases of TiO_2 [60]. Rutile is the thermodynamically most stable TiO_2 phase but brookite and anatase exist in metastable phases [60]. When the particle size of TiO_2 goes below 14 nm, anatase phase is the most stable form in the bulk TiO_2 [59].

(a)   (b)   (c)
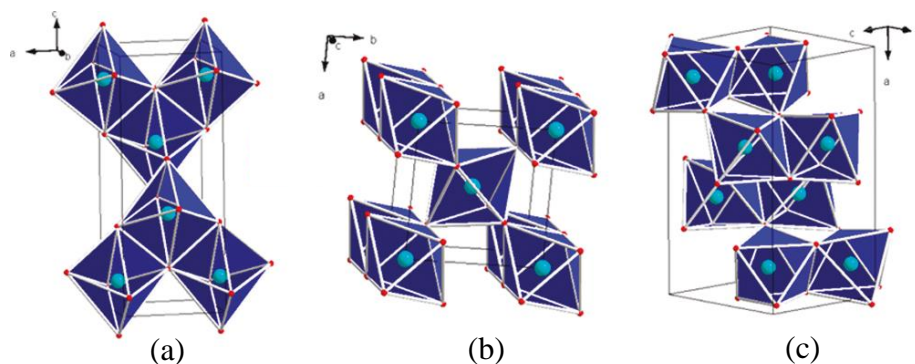
Figure 1.8 A 3D representation of the arrangement of TiO_6 octahedra in rutile (a), anatase (b) and brookite phases [56]. [Ti^{4+}] atoms in are pool blue; [O^{2-}] atoms in are red.

When anatase and brookite phases are heated up to above 550 and 750 °C, respectively, they slowly convert to rutile phase [61-63]. The basic crystal structure properties of TiO_2 polymorphs is given in Table 1.2 [64-67].

Table 1.2 Crystallographic structure properties of TiO_2 polymorphs

Properties	Rutile	Anatase	Brookite
Crystal structure	Tetragonal	Tetragonal	Orthorhombic
Lattice constants (Å)	a = b = 4.584 $c = 2.953$	$a = b = 3.782$ c = 9.502	$a = 5.436$ $b = 9.166$ $c = 5.135$
Space group	$P\frac{42}{m}$ nm	$l\frac{41}{a}$ md	Pbca
Molecule/cell	2	4	8
Volume/molecule ($Å^3$)	31.21360	34.061	32.172
Density (g/cm^3)	4.13	3.79	3.99
Ti–O bond length (Å)	1.949 (4) 1.980 (2)	1.937(4) 1.965(2)	1.87~2.04
O–Ti–O bond angle	81.2° 90.0°	77.7° 92.6°	77.0°~105°
Band gap (eV)	2.98	3.05	3.26

Three generations of TiO_2 polymorphs have been reported in the literature which are: pure TiO_2 (1st generation), metal doped TiO_2 (2nd generation) and non-metal doped TiO_2 (3rd generation) [68]. Several methods have been used in the preparation of titania (1st, 2nd and 3rd generations), including hydrothermal treatment [47, 69, 70], sol-gel process [71-73], solvothermal [74, 75], chemical vapour deposition [76], microemulsion [77], co-precipitation [78], and wet impregnation [79]. Because of their multiple potential applications, straightforward recoverability and excellent properties, a wide range of recent studies on synthetic routes have been undertaken to fabricate surface modified/impregnation NPs in order to increase their surface acidity/basicity [80-85]. This is of particular significance in relation to catalysts for biodiesel production involving the use of cheap raw materials containing free fatty acids (FFAs). The acid catalysts can facilitate simultaneous esterification of FFAs and transesterification of triglycerides without soap formation [86, 87]. Sulphated doped TiO_2 is a good example of a solid super-acidic catalyst which is also used in the petrochemical industry and petroleum refining process [88, 89] and showed better performances as compared to other sulphated metal oxides. This is due to the acid strength of the TiO_2 particles which further enhances with loading of SO_4^{2-} groups on the surface of TiO_2 [90]. Many recent studies have reported that the super acidity of sulphated titanium dioxide catalysts

could be based on Lewis acid and Brønsted acid sites, and the formation of Brønsted acid sites are possibly due to the higher content of sulphate groups in the catalyst [88, 91, 92]. The presence of Brønsted acid sites in acid catalysts is significantly important for the catalytic activity [93-95]. Some researchers have reported that the addition of sulphate ions to metal oxides enhances the acidic properties, catalytic activity, high selectivity, and causes less deactivation of the catalyst [96-100]. The use of inexpensive feedstock, such as UCO in this project, for biodiesel fuel production [101], helping to reduce environmental pollution while cutting production cost [3, 102, 103]. The yield and quality of biodiesel can be highly affected by the surface area, surface acidity/basicity, and particle size of the catalysts used in the esterification and/or transesterification processes [97]. This has encouraged the development of novel recyclable solid acid catalysts to replace conventional corrosive homogeneous acid catalysts [102, 104]. The latter can corrode reactors and requires further washing with neutralisation steps for their removal from the biodiesel and its by-products [105]. There have been numerous recent studies into the development of different classes of solid acid catalysts but, with regard to biodiesel production from cheap feedstocks containing FFAs, water and other impurities, they still suffer from deactivation, a leaching of acid sites, mass transfer (diffusion) limitation, and side reaction (poisoning) problems. Therefore, the design or development of new efficient, cheap, and stable solid acid catalysts are needed to obtain biodiesel with potential usage in a continuous system.

1.2 Scope of work

The single question underlying this research thesis is as follows:

Can we design/develop stable solid acid catalysts based on commercial TiO₂ NPs for biodiesel production from used cooking oil collected from a single restaurant?

The answer to the above question is delivered through the following core aims:

1- To develop a solid acid catalyst based on surface functionalisation of commercially available TiO$_2$ nanoparticles.

2- To design a solid super acid catalyst based on sulphate [SO_4^{2-}] groups impregnation of commercially available TiO$_2$ nanoparticles.

3- To engineer a super magnetic solid super acid catalyst based on commercially available TiO$_2$ nanoparticles which can be easily separated from the product.

4- To characterise all above catalysts using different analytical instruments.

5- To look at the activity of differently prepared acid based catalysts on used cooking oil.

6- To assess the reusability of spent catalysts on used cooking oil.

7- To analyse obtained biodiesel from simultaneous esterification and transesterification over different engineered solid acid catalysts in accordance with ASTM and EN standard specification methods in order to determine the physicochemical properties of the product fuels.

The general work plan of the research project and how the objectives are fulfilled is shown in Figure 1.9.
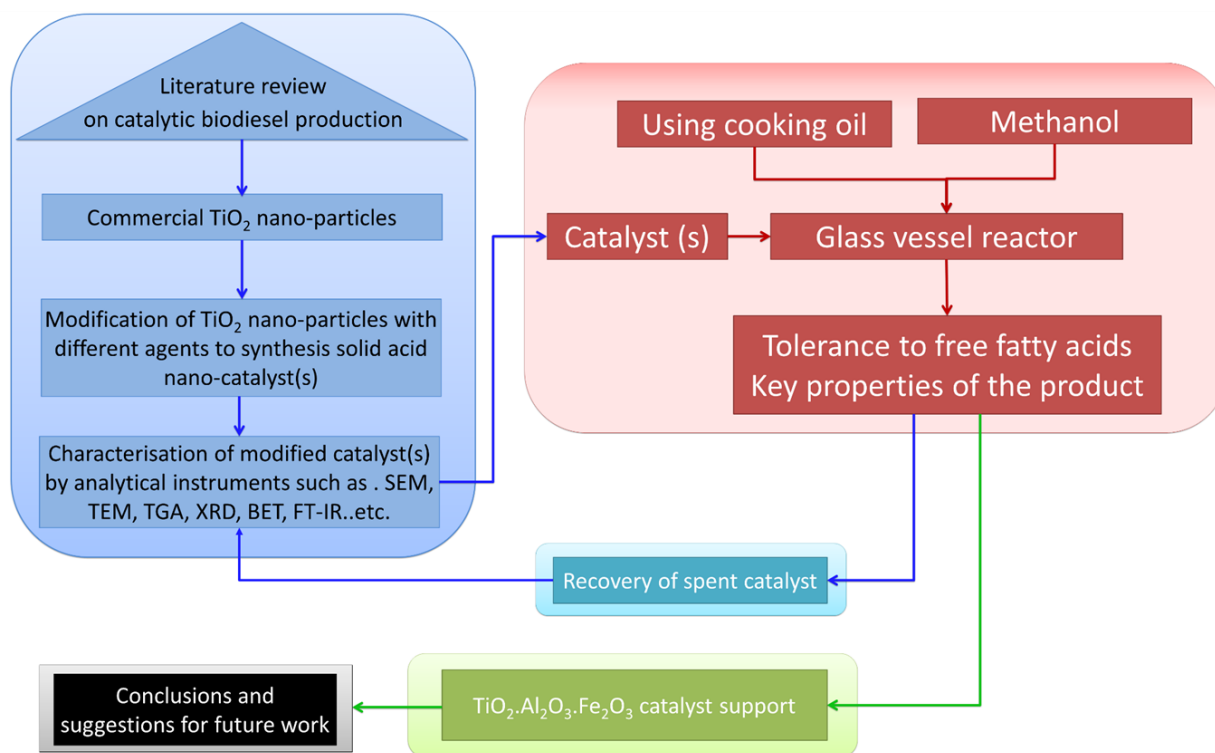
Figure 1.9 Schematic diagram of the work plan

1.3 Thesis layout

The structure of this PhD thesis is divided into eight chapters as follows:

Chapter 1 presents an overall background of biodiesel fuel preparation using different technologies that highlight the associated advantages and disadvantages of each method and prompt the research question for this PhD project.

Chapter 2 provides the literature review on all topics that are relevant to the biodiesel fuel, including biodiesel sources, chemical composition of biodiesel fuel, and biodiesel. Subsequently, a detailed review on the fundamental knowledge of biodiesel process technologies is presented.

Chapter 3 gives detailed information about the materials and experimental methods used throughout this study. The detailed catalyst preparations and characterisations, using different analytical techniques, are provided. Application of solid acid catalysts in the biodiesel production from used cooking oil is presented. The methodologies for quantification of FAME from obtained biodiesels and physicochemical analysis of obtained biodiesel fuels under investigation are discussed.

Chapter 4 gives a background of titania and detailed synthesis of surface modification of titania nanoparticles using 1,3-propane sulfone to obtain $TiO_2/PrSO_3H$ solid acid catalyst. The characterisations of synthesised catalyst, using FT-IR, N_2 porosimetry, XRD, SEM, TEM, TEM-EDS, EDS-mapping, XPS, CHNS analysis, TGA, TGA-FTIR, DRIFTs, TPD-MS, and DSC, are presented. Detailed process parameters on the simultaneous esterification and transesterification of used cooking oil are discussed. Finally, the physicochemical properties, i.e. flash point, FFA%, FAME%, density at 15.5 °C, and kinematic viscosity at 40 °C, of obtained biodiesel over $TiO_2/PrSO_3H$ solid acid catalyst is provided.

Chapter 5 begins with an introduction of sulphated titania and the effect of sulphate groups on the acidity of titania is presented. The detailed characterisations of synthesised titanium sulphate oxide or titanium oxy-sulphate [$Ti(SO_4)O$], using FT-IR, N_2 porosimetry, XRD, SEM, TEM, TEM-EDS, EDS-mapping, XPS, TGA, TGA/FT-IR, TPD-MS, and DRIFTs, is given. The catalyst performed in simultaneous esterification and transesterification of used cooking oil. The effect of different process parameters is discussed in detail. Finally, the physicochemical properties, i.e. flash point, FFA%, FAME%, density at 15.5 °C, and kinematic viscosity at 40 °C, of synthesised biodiesel over $Ti(SO_4)O$ is presented.

Chapter 6 begins with a background of the magnetic sulphated titania oxide catalyst and present challenges with the current deactivation of solid acid catalysts during removal stage. The characteristics of $SO_4^{2-}/Fe.Al.TiO_2$ solid acid catalyst are presented. Characterisation methods selected for this solid acid catalyst, including, FT-IR, XRD, N_2 porosimetry, SEM, TEM, TEM-EDS, EDS-mapping, XPS, TGA, VSM, TPD-MS, and DRIFTs are described in details. The performance of $SO_4^{2-}/Fe.Al.TiO_2$ catalyst in the simultaneous esterification and transesterification

of used cooking oil are given. Finally, the physicochemical properties, i.e. flash point, FFA%, FAME%, density at 15.5 ºC, and kinematic viscosity at 40 ºC, of prepared biodiesel over SO_4^{2-}/Fe.Al.TiO$_2$ are discussed.

Chapter 7 reviews a detailed summary on the overall results of the entire project. This chapter also provides recommendations of future work to expand on this project findings.

Chapter 2

Literature Review

This chapter presents a detailed review of literature on topics relevant to the study of biodiesel production. Its focus is mainly on reviews of process technologies.

CHAPTER TWO

2. Literature review

2.1 Source of biodiesel

A wide range of sources are available globally for biodiesel production, including around 350 oil-bearing crops. The feedstock requirements are mainly low production costs and large-scale production. The availability of these feedstocks usually depends on regional conditions, agricultural practices, and geographical locations. As shown in Figure 2.1, it is observed that 75% of the overall biodiesel production cost arises from choice of feedstock [3, 26, 106, 107]. It is worth mentioning that planting, harvesting technologies, seed, pesticides and transportation costs of vegetable oils have highly impact on the feedstock costs for the production of biodiesel. For example, rapeseed, palm, sunflower and soybeans are considered to be the first generation feedstocks for biodiesel production but diverting these crops to extract oils and amount of land required to grow crops in a large-scale could bring imbalance to the global food markets and food security [108]. This is why selecting the right raw material is the first and most important decision in industrial biodiesel production.
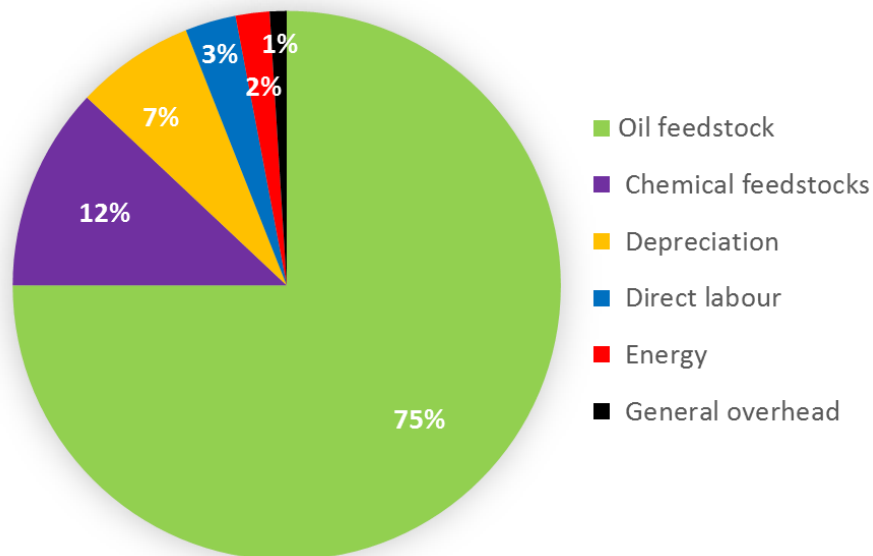
Figure 2.1 General cost breakdown for production of biodiesel

According to the literature, the main current potential feedstock categories around the world are edible vegetable oil, non-edible vegetable oil, waste or recycled oil and animal fats [3, 35].

Over the years, biodiesel formed from virgin vegetable oils was found to be not commercially economical due to raw material cost. Moreover, vegetable oils have high viscosity which has led to poor atomization of the fuel causing deposits and the coking of injectors, combustion chamber and valves of engines, therefore it cannot be used directly as a fuel. A variety of vegetable oils is used in the production process of biodiesel, which showed better engine performance and reduced emissions at a cheaper price [109, 110].

Biodiesel is an alternative fuel obtained from catalytic/non-catalytic conversion of renewable resources with alcohol. The final ester product is referred to as a mixture of fatty acid methyl ester (FAME) when methanol is used as the alcohol. However, there are biodiesels produced as ethyl esters referred to as fatty acid ethyl ester (FAEE). These are more expensive as ethanol costs more compared to methanol in the general market. Other higher alcohols have also been used, such as 2-propanol and 1-butanol for the production of biodiesels [109, 111, 112].

A well-known method of producing biodiesel is by transesterification reaction as shown below [113-115].

| Triglyceride | Methanol | | Fatty acid methyl esters | Glycerol |
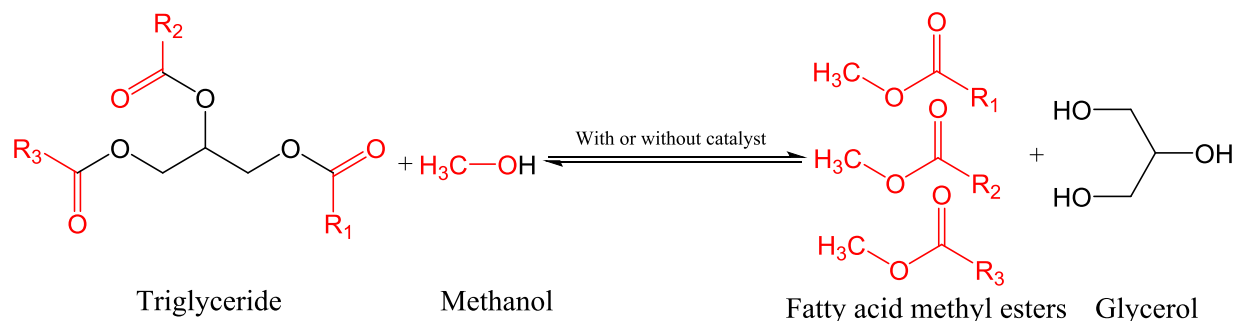
Figure 2.2 Formation of fatty acid methyl ester (biodiesel fuel)

The source used for biodiesel production has been an important parameter in calculating the cost of production and revenue. Biodiesel produced from virgin vegetable oils is 1.5 times costlier than petro-diesel. The main cost arises from the expense of the raw material utilised for production. Thus there are various sources which have been researched in recent years with a view to reducing biodiesel production costs [14]. The main sources utilised, apart from conventional vegetable oils (such as soybean, rapeseed, palm, and others), are soap nut (*Sapindusmukorossi*) seeds, pongamia, jojoba and Jatropha (*Jatrophacurcas L.)* seeds [116, 117]. In addition, waste cooking oil (WCO)

and waste animal fat are of great interest as cheap feedstocks for biodiesel production owing to high worldwide availability (estimated WCO in EU ~700,000 to 1,000,000 tons per year (t/y)) without competition with food markets, low cost and their environmentally friendly qualities [117]. Edible oils are more expensive than non-edible oils and as a result the latter have attracted increased attention worldwide as a topic of research. The non-edible oils are citrus reticulate seed oil, oil from different strains of algae, microalgae, fungi and the leguminous oilseed-bearing pongamia tree. Recent research in the US has identified tobacco seed as a source for biodiesel, mainly in North and South America [116, 118], where current yields are 15,000 t/y. Oils with high free fatty acid (FFA) content have also been one of the main raw material sources. These include rubber seed oil, tall oil (paper plant, in Turkey), mahua oil (found mostly in India) [34]. The neem tree, a multipurpose evergreen tree, is utilised for biodiesel production and has been shown to provide an increase in brake thermal efficiency of around 1.5% and improvement in exhaust emissions, especially reducing carbon monoxide and hydrocarbons [119]. Table 2.1 shows some feedstocks used for biodiesel production [120].

Table 2.1 Feedstocks used for the biodiesel production

Vegetable oils	Non-edible oils		Animal fats	Other sources
Soybeans	Almond	Abutilon muticum	Lard	Bacteria
Canola	Andiroba	Babassu	Tallow	Algae
Barley	Brassica carinata	B. napus	Poultry fat	Fungi
Rapeseed	Cynaracardunculus	Jatrophacurcas	Fish oil	Micro algae
Safflower	Camelina	Cumaru		Terpenes
Coconut	Jatropha nana	Jojoba oil		Latexes
Copra	Pongamiglabra	Laurel		Yellow grease
Cotton seed	Lesquerella fendleri	Mahua		(cooking oil)
Groundnut	Piqui	Palm		
Oat	Karang	Tobacco seed		
Rice	Rubber plant	Rice bran		
Sorghum	Sesame			
Wheat	Salmon oil			

The main issue with using virgin vegetable oils as biodiesel resources has been reported as being the amount of land required to grow the crops, which competes with food production. Therefore, one of the most currently viable options with a more affordable potential is the use of waste (used) oil [33]. It was reported that WCO is available in huge quantities from restaurants, the food processing industry and domestic households, making biodiesel production which uses WCO sources about 2.5 to 3.5 times cheaper than virgin vegetable oil use. For example, the amount of

WCO generated in China is approximately 1,000,000 to 2,500,000 t/y whilst in the United Kingdom figures are estimated at 65,000 to 80,000 t/y from commercial and food processing industries [121]. Such sources could provide an economic alternative to virgin vegetable oils and resolve associated environmental problems.

2.2 Chemical composition of biodiesel feedstock

Vegetable oils and animal fats are complex mixtures containing a wide range of triglycerides. Each triglyceride consists of three long chain fatty acid molecules linked to a molecule of glycerol. Triglycerides, which are the main property parameter of biodiesel production, can be saturated or unsaturated compounds. The number of carbon atoms, which usually range between 12 to 24, and the degree of unsaturation in the fatty acid chain are dependent on the source of triglyceride due to triglycerides from different oil and fat sources having different fatty acid compositions [122]. The raw material fatty acid profile has always had a major impact on the physicochemical properties of final biodiesel. As can be seen in table 2.2, vegetable oils and used oils are mainly composed of unsaturated long chain fatty acids. As a result of high unsaturated fatty acids, the corresponding biodiesel has poor oxidation stability and cetane numbers. However, the corresponding methyl esters have good cold weather performance.

Table 2.2 Summary of fatty acid profile of various vegetable oils

Fats/Oils	C16:0	C16:1	C18:0	C18:1	C18:2	C18:3	C20:0	C20:1	C22:0	C22:1	C24:0	References
Corn	12.	---	2.0	25	6.0	Trace	Trace	---	---	---	---	[123]
Rapeseed	3.0	---	1.0	64	22	8.0	---	---	---	---	---	
Rapeseed	3.5	---	0.9	64.1	22.3	8.2	---	---	---	---	---	[124]
Sunflower	7.3	---	1.9	13.6	77.2	0.0	---	---	---	---	---	
Soybean	13.9	0.3	2.1	23.2	56.2	4.3	---	---	---	---	---	
Used cooking oil	11.93	0.19	3.8	31.25	50.76	---	0.29	---	0.5	---	0.2	[122]
Used frying oil	20.4	4.6	4.8	52.9	13.5	0.8	0.12	0.84	0.03	0.07	0.04	[125]
Rapeseed	---	3.49	0.85	64.4	22.30	8.23	---	---	---	---	---	
Sunflower	---	6.08	3.26	16.93	73.73	0.0	---	---	---	---	---	[126, 127]
Soybean	---	11.75	3.15	23.26	55.53	6.31	---	---	---	---	---	
Corn	---	11.67	1.85	25.16	60.60	0.48	0.24	---	---	---	---	

2.3 Biodiesel properties

The properties of biodiesel have been extensively studied by many researchers in order to understand their performance [5, 128]. The comparison of different properties for biodiesel (B100) are based on the most common standards around the globe, which are the American Society of Testing and Materials [129] and the European Standard [130] and are summarised in table 2.3. The produced biodiesel from any reaction has to be processed and purified to meet these standards in order to ensure better engine performance. The biodiesel standards of some of the other countries are given as: China (GB/T 20828-2007), Germany (DIN V 51606) [131] and India (IS 15607) [132]. This is due to the physicochemical properties of biodiesel fuels differing from place to place, depending on their nature, feedstock resources, and production processes.

Table 2.3 Standards specification of biodiesel fuel according to ASTM D6751 and EN 14214

Property		Unit	Limits	
			ASTM D6751	EN14214
Flash point (closed cup)		ºC	93 min	101 min
Kinematic viscosity at 40 ºC		mm^2/s	1.9-6.0	3.5-5.0
Cetane number		---	47 min	51 min
Sulphated ash		% mass	0.02 max	0.02 max
FAME content		% mass	---	96.5 min
Acid number		mg KOH/g	0.8 max	0.5 max
Density at 15 ºC		Kg/m^3	---	860-900
Oxidation stability at 110 ºC		h	3.0 min	6.0 min
Carbon residue	ASTM D6751	% mass	0.05 max	---
	EN14214		---	0.3 max
Copper strip corrosion (3h at 50 ºC)		Rating	No.3	Class 1
Iodine value		g I$_2$/100 g	---	120 max
Distillation temperature at 90% recovered		ºC	360 max	---
Sulfur content	S 15 grade	ppm	15 max	---
	S 500 grade		500 max	---
Sulfur content		ppm	---	10 max
Water and sediment		% vol.	0.05 max	---
Water content		ppm	---	500 max
Total contamination		ppm	---	24 max
Cloud point		ºC	---	---
Methanol content		% mass	---	0.2 max
Linolenic acid methyl ester		% mass	---	12 max
Polyunsaturated (≥4 double bonds) methyl ester		% mass	---	1 max
Free glycerine content		% mass	0.02 max	---
Total glycerine content		% mass	0.24 max	0.25 max
Monoglyceride content		% mass	---	0.8 max
Diglyceride content		% mass	---	0.2 max
Triglyceride content		% mass	---	0.2 max
Group I metals (Sodium/Potassium), combined		µg/g	5.0 max	5.0 max
Group II metals (Calcium/Magnesium), combined		µg/g	5.0 max	5.0 max
Phosphorous content		ppm	10 max	4.0 max

2.4 Process technologies for fuel production

There are different technologies that have been reported as being feasible for fuel production, including microemulsion, pyrolysis, blending process, and transesterification. The following section reviews all these methods.

2.4.1 Microemulsion

Microemulsion is defined as a stable colloidal dispersion of optically isotropic fluid microstructure. The formed microemulsion droplet from two normally immiscible liquids and one and more ionic, or more ionic amphiphiles, has diameters ranging from 1.0 to 150 nm [116]. Due to the high latent heats of vaporisation of the alcohol solvents used in this method, the high viscosity problem and coking problems of vegetable oils are reduced because of cooling of the combustion chamber [133]. Microemulsion has been prepared by mixing 52.7% of soybean oil, 13.3% of methanol, 33.3% octan-2-ol and 1.0% of cetane improver [120]. Koh and Mohd. Ghazi [5] have reported a study for microemulsions of aqueous ethanol in soybean oil to produce biofuel. This method does not chemically alter the raw material and uses short chain alcohols such as methanol, ethanol, butanol and hexanol [6]. However, this method is not recommended for long-term use in diesel engines without further modifications to develop a stable biodiesel fuel.

2.4.2 Pyrolysis

Pyrolysis is a thermochemical decomposition process by which one organic substance (raw material) is converted into another in the presence of a catalyst or direct thermal cracking under anaerobic conditions (absence of oxygen) with the simultaneous change of chemical composition and physical phase. Pyrolysis has been carried out on vegetable oils and animal fats along with natural fatty acids and their methyl esters. Pyrolysis of triglycerides produces a variety of hydrocarbons (including paraffins, olefins, alkadienes and aromatics), ketones, esters, acrolein and carboxylic acids. Pyrolysed products from vegetable oils contain low enough levels of sulfur, copper corrosion values and water content to be acceptable but the carbon residues, high acidity, poor stability, high oxygen content, ash content, and pour point of this process was unacceptable [116, 134-136]. There has also been literature published stating that pyrolysis of vegetable oils or animal fats can be divided into non-catalytic (direct thermal cracking) and catalytic process

(catalytic cracking). The most common method for pyrolysis of vegetable oils is catalytic cracking which can be grouped into four types: molecular sieve catalysts (HZSM-5 catalyst is the most popular and effective); activated alumina catalysts; transition metal catalysts and sodium carbonate [137].

The pyrolysis process has been mainly investigated with non-edible vegetable oils such as karanja, babassu, jatropha curcas, copra, mahua, tung and castor oil to reduce costs associated with edible vegetable oils [116]. Figure 2.3 shows the reaction mechanism for the thermal decomposition of vegetable oils.
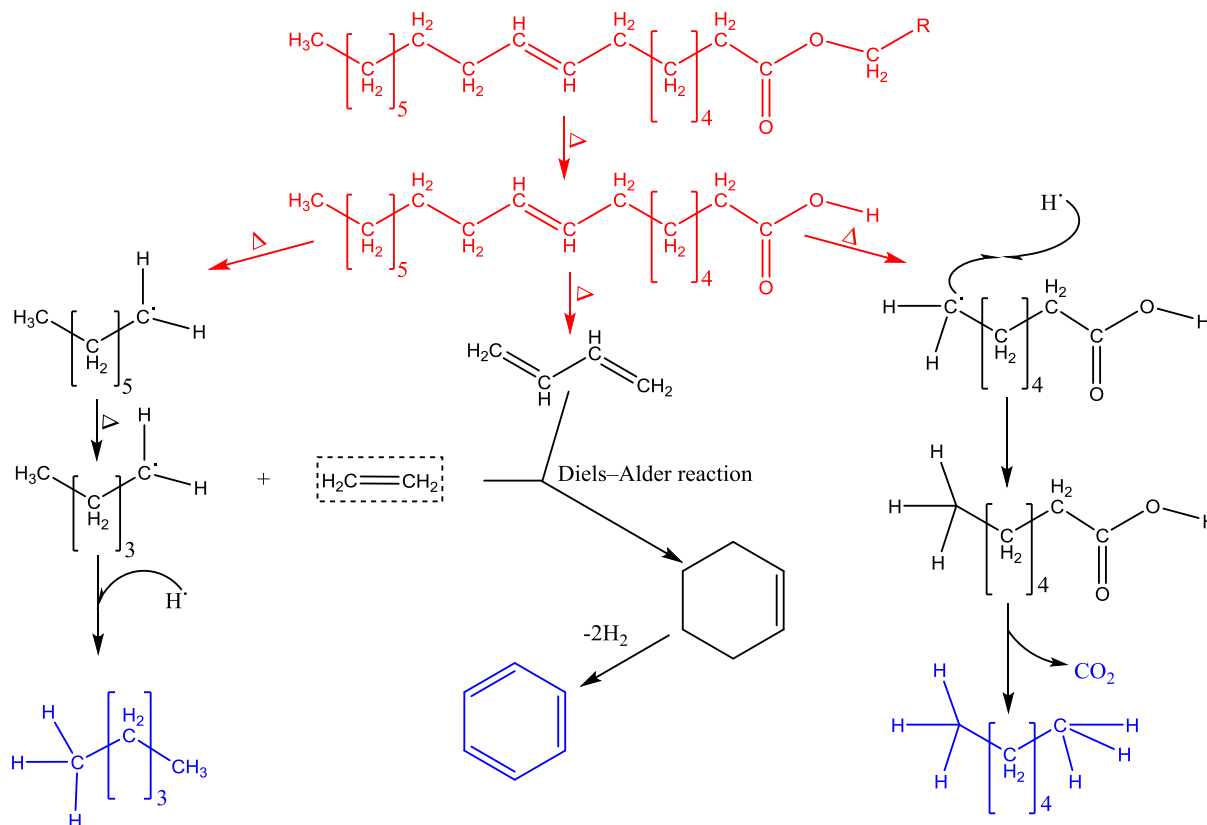
Figure 2.3 Mechanism of thermal decomposition of triglycerides

The advantages of this method over transesterification include less waste, infrastructure compatibility, lower processing costs, a similarity in fuel composition to diesel fuel and the advantage of raw material flexibility [120, 137]. However, this method is also not recommended for long-term use in diesel engines due to pyrolised oil contains lots of oxygenated compounds

(such as alcohols, phenols, aldehydes, ketones and carboxylic acids), high acidity (typically low pH=2.5-3) and poor thermal stability over time (aging) [136, 138].

As an example, Ito et al. [139] produced biodiesel from waste animal fats using the pyrolysis method. Fatty acids were generated using this method by cleavage of the ester bond while the triacylglycerols that were formed decomposed at 360-390 $^{\circ}$C. The light-oil hydrocarbons were formed by decarboxylation of the fatty acids with an increase in the retention time and the reaction temperature to 420 $^{\circ}$C. The decarboxylation reaction was improved by using a palladium supported catalyst supported on activated carbon (Pd/C) and the hydrocarbon product was obtained in high yield at 85 wt%. In comparison to the transesterification method, pyrolysis yield was higher with an improvement of about -5 $^{\circ}$C in the pseudo-cold filter plugging point.

Maher and Bressler [137] have reported the study of pyrolysis of used cooking oil at temperatures of 400 $^{\circ}$C and 420 $^{\circ}$C, for approximately 180 mins, to produce high concentrations of liquid hydrocarbons with direct thermal cracking. Catalytic cracking has also been investigated using, mainly, transition metal catalysts, activated alumina and molecular sieve catalysts (zeolites, H-ZSM-5) for pyrolytic conversion of the triglycerides. The reaction under atmospheric pressure, at temperatures between 400 $^{\circ}$C and 420 $^{\circ}$C, of sunflower oil, produced 96.6% conversion of the oil and 33% yield of hydrocarbon with the use of different amounts of HZSM-5.

2.4.3 Direct use or dilution (blending)

The direct use of vegetable oils for running diesel engines results in high viscosity, high FFA content, engine knocking, engine wear, plugging and gumming of filters, lines and injectors due to oxidation, polymerization during storage and combustion, carbon deposits on piston and head of engine, low volatility and lubricating oil thickening due to polymerisation [119, 133, 140]. A blending of vegetable oil with petro-diesel has been successfully carried out by different researchers to improve the performance of the diesel engine and reduce the viscosity. In 1982, research showed that using a blend of 95% filtered used cooking oil and 5% diesel resulted in better performance than the pure 100% vegetable oil by decreasing the viscosity [5, 133]. A research on 25/75 parts of high oleic sunflower oil/diesel fuel blend reported a kinematic viscosity of 4.92 cSt at 40 $^{\circ}$C, which has passed the 200 h Engine Manufacturers' Association test [5]. Another research on castor oil biodiesel (B100) and its blend (B10) indicated an increase in the lubricity and decreased viscosity (from 15.17 mm^{2}s^{-1} to 3.621 mm^{2}s^{-1}) [141].

2.4.4 Transesterification process

The transesterification of vegetable oils or animal fats is an equilibrium reaction which ensures the lowering of the viscosity and enhancement of other physicochemical properties by separating fatty acids from their glycerol backbone to form fatty acid methyl ester (FAME) and by-product (glycerol). The transesterification reaction, also called alcoholysis, involves the use of alcohol and ester causing a displacement reaction of the alcohol to form the FAME, also known as biodiesel, in the presence of a catalyst and the release of glycerol [112]. Transesterification transforms the triglyceride molecules (90-98% of the oil), which are long and branched, into smaller esters that have similar physical properties to those of petro-diesel oils. In this process, a greater amount of alcohol was used to push the reaction equilibrium forward and produce a more desired biodiesel product [6]. The transesterification of triglyceride with alcohol, as shown in Figure 2.4, involves various intermediate reversible consecutive reaction steps. The first step is the conversion of the triglyceride to diglyceride and this to monoglyceride followed by the formation of glycerol − all the reactions in the presence of a catalyst [6]. There has been various research in recent years working on the various catalysts utilised for this reaction and their modifications to improve the quality of the biodiesel produced [6, 8, 112]. However, the catalysed reaction was initiated by Dufek et al. [142] involving primarily acid-catalysed esterification reaction. They reported the transesterification of 9(10)-carboxystearic acid and its mono- and di-methyl esters.
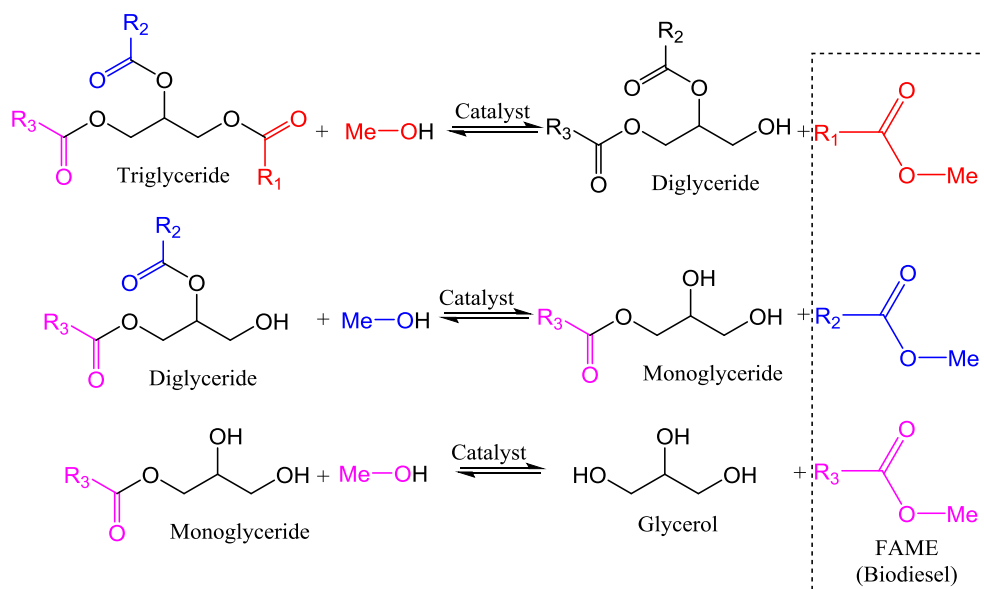
Figure 2.4 Three consecutive and reversible reactions of transesterification

23

2.4.4.1 Homogenous catalysed transesterification

Many homogenous catalysts have been studied to observe different reactions, including esterification, ester hydrolysis, transesterification etc. In homogenous catalysis reaction the catalyst is normally in the same phase as the reactant. The homogenous catalysts can be divided into two categories which are homogenous acid and base catalysts. The most commonly homogenous catalysts used for transesterification reaction are alkalis (NaOH, KOH, NaOCH$_3$ and KOCH$_3$) [143]. Gerpen [144] has reported that when free fatty acids (FFAs) are present in the oil or fat feedstock, the alkali catalyst reacts to form soap and water in the initial step. In his research, he has utilised an acid catalyst, sulfuric acid, as a pre-treatment process to remove the saponification process by esterification of the FFAs to methyl esters. This is then transesterified with alkali catalyst to form FAME (biodiesel).

The kinetics of both acid- and alkali-catalysed reactions have been extensively studied in order to find the rate of the reaction and it has been reported that the acid-catalysed transesterification process is much slower than alkali catalysis [145-150]. This is due to alkali-catalysed reactions commonly require lower transition states (TS$_1$ = triglyceride $\rightarrow$ diglyceride; TS$_2$ = diglyceride $\rightarrow$ monoglyceride; TS$_3$ = monoglyceride $\rightarrow$ glycerol + biodiesel). The alkoxide ion directly acts as strong nucleophile, which is ultimately responsible for the observed differences in activity, to attack the carbonyl group. In acid-catalysed reactions, the key step is the protonation of oxygen from the carbonyl group. This in turn increases the electrophilicity of the carbon atom and making it more susceptible to nucleophilic attack [151]. However, the use of alkali catalysts are limited only for raw materials with low impurities (<1% FFA and 0.5% water) [148]. The fuel production processes using homogenous catalysis are presented in brief here.

2.4.4.1.1 Acid-catalysed transesterification

Acid catalysed reaction is an esterification reaction using various acids such as sulfuric acid [H$_2$SO$_4$], phosphoric acid [H$_3$(PO)$_4$], hydrochloric acid [HCl], boron trifluoride [BF$_3$] and organic sulfonic acids [R-SO$_3$H] [152, 153]. Several studies reported that the use of homogenous acid catalysts is more suitable with raw materials that have high FFAs and water content compared to base catalysts [145, 154]. The reaction mechanism of acid-catalysed transesterification of vegetable oils is shown in Figure 2.5. Protonation of the triglyceride occurs as the first step,

followed by a nucleophilic attack of the alcohol to form unstable tetrahedral intermediate. Finally, the FAME is formed by the breakdown of the intermediate [151, 152, 155].

Step (1): Protonation of the carbonyl group by the acid catalyst

Step (2): Nucleophilic attack of the alcohol, forming a tetrahedral intermediate

Step (3): Proton migration and breakdown of the intermediate
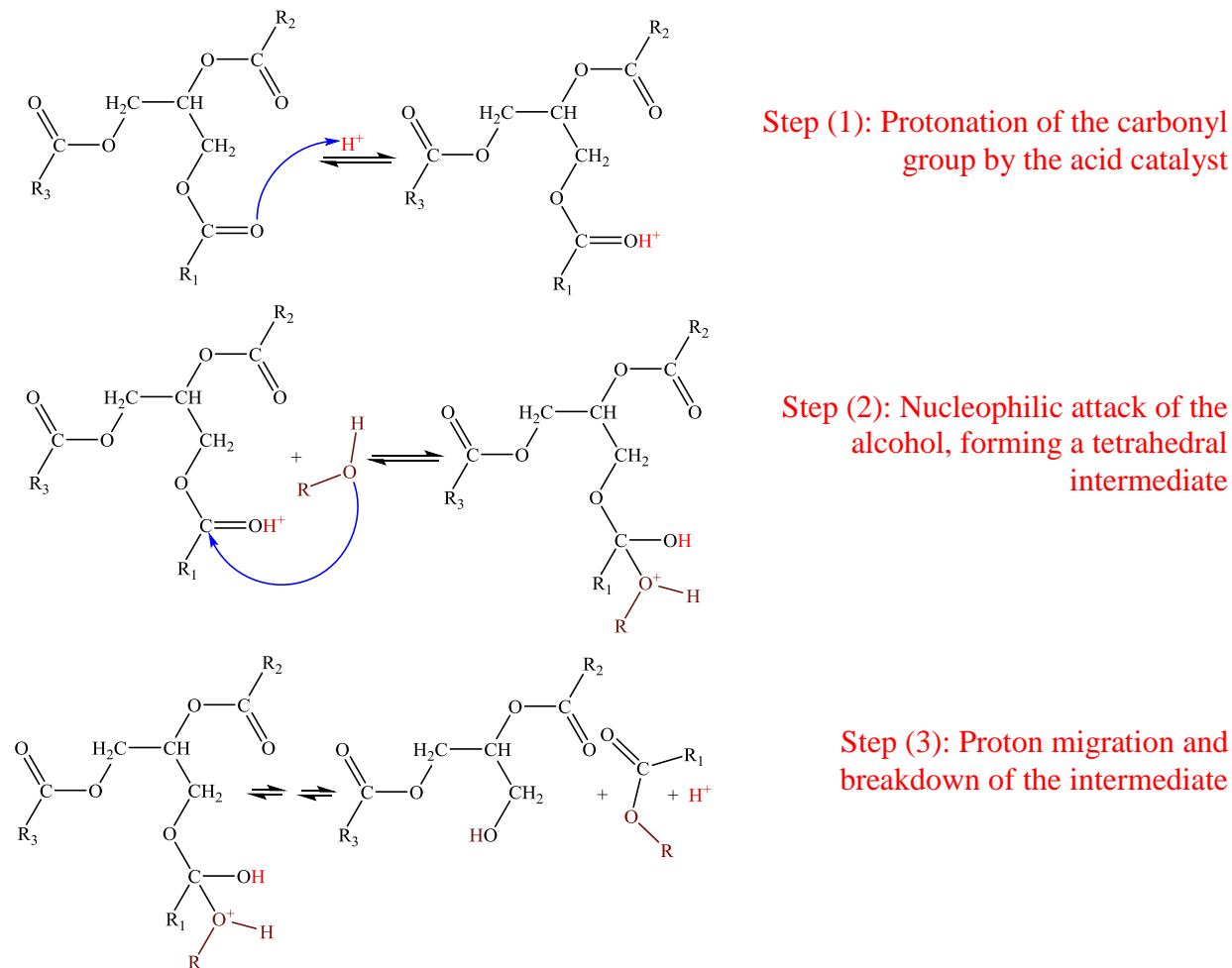
Figure 2.5 Mechanism of acid-catalysed transesterification of vegetable oils

Math et al. [156] reported that the rate of esterification of FFAs is relatively very fast compared to transesterification of TG which is very slow. Nevertheless, the formation of water (by-product) during the esterification of FFAs is the main issue for using acid catalyst as it might stop the reaction before completion. The acid catalysed method is commonly utilised for oils which contain more than 3% of FFA such as jatropha, used frying oil (or waste cooking oil), soybean oil etc. [157, 158]. A study by Al-Widyan and Al-Shyoukh reported the acid catalysis of waste cooking oil to form biodiesel [157]. Their research noted an optimum amount of 50:1 molar ratio of methanol to oil, a 1.3:1 molar ratio of sulfuric acid to waste oil, reaction temperature of 80 ^{o}C and a pressure of 170-180 kPa, which produced a 97% conversion of oil to FAME within 240 min.

The acid is usually removed by a cheap process using quicklime (calcium oxide) which absorbs the water produced [158]. In order to avoid the formation of emulsions with methanol during the washing step, hexane extraction is employed - a process used for acid catalysis which becomes a liquid-liquid extraction, especially for FAME.

Acid catalysis is generally a two-step process as shown in Figure 2.6 [159]. The first step is the reaction of FFA/TGA with alcohol in the presence of acid catalysts and the second step utilises the ester from first step produced, with a lower acid value, to transesterify with methanol in the presence of alkali (sodium or potassium hydroxide) catalyst to from FAME (biodiesel fuel).
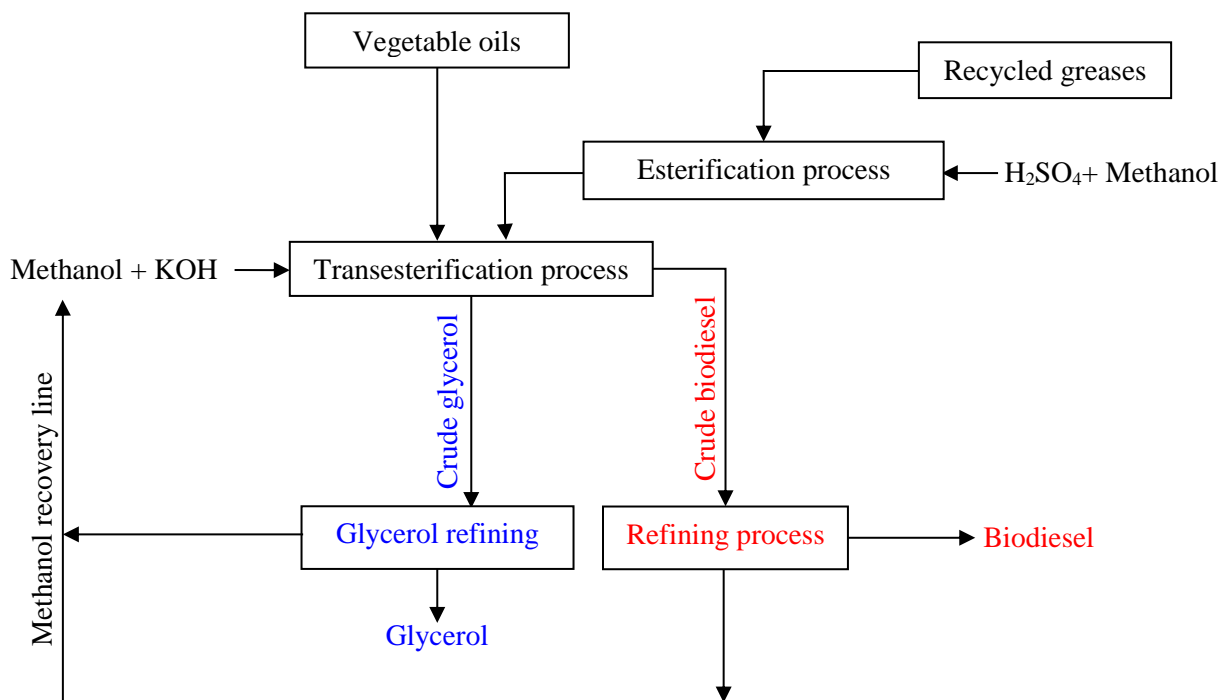
Figure 2.6 Esterification and transesterification processes

However, transesterification by acid catalysis is much slower than alkali catalysis [5] and the use of acidic catalyst requires costly equipment to resist acid corrosion, which adds costs to the expenses of biodiesel production process [160, 161]. In some cases, it has been reported that using a higher concentration of acid catalyst, such as sulphuric acid, for the transesterification process could lead to the formation of ether from the dehydration of alcohol and burn some of the oil (reduce the FAME yield) when a high temperature and high concentration of acid are employed [162, 163].

2.4.4.1.2 Alkali-catalysed transesterification

Many studies have reported that the more common approach in the production of biodiesel from pure vegetable oils is the alkali-catalysed transesterification process. Ma and Hanna [161] reported that the most effective alkali catalysts for the transesterification process are KOH, NaOH, $KOCH_3$, and $NaOCH_3$. Several researchers found that the alkali metal methoxide (methoxide salts) have higher catalytic activities for transesterification reaction compared to the hydroxides [164, 165]. However, the presence of more than 0.5 wt % of FFA content in the feedstocks enhances soap formation, producing a low yield of biodiesel and complicating by-product separation [5]. The other difficulty of using this kind of catalyst for biodiesel production is the formation of low FAME yield when the raw material contains above 0.06 wt% of water [117]. This is due to alkaline catalysts having high sensitivity to FFAs and moisture in raw materials. Thus pre-treatment of the FFA feedstock was required for an effective alkali-catalysed transesterification reaction. It has also been observed that potassium carbonate gives high yields of biodiesel in concentration of 2.0 or 3.0 mol% with less soap formation. As has been delineated so far, the presence of water causes a reduction in the yields of produced biodiesel and consumes more catalyst during the process [5]. A study by Encinar and co-workers [166] investigated the transesterification of soybean seed oil over NaOH, KOH, $NaOCH_3$ and $KOCH_3$ catalysts and ethanol to form biodiesel. They found that transesterification catalysed by KOH gives higher yield compared to the other catalysts due to the formation of KOC_2H_5 which is a stronger base than $KOCH_3$.

Fukuda et al. [145] reported that sodium methoxide produced similar conversion and yield of biodiesel (98% yield) as that from the hydroxide but required the use of half the amount of catalyst under reaction conditions of 70 ^{o}C and 6:1 molar ratio of methanol to soybean oil.

Saydut et al. [167] experimented with the use of a non-conventional vegetable oil as feedstock - sesame seed oil - and reported promising yields of biodiesel of 74% under the optimum conditions of 6:1 molar ratio of alcohol to oil, 0.5% of sodium hydroxide, reaction time of 2.0 h and a temperature of 60 ^{o}C. Sesame oil, which contains compounds called lignans, increases the oxidation stability and reduces the heating value of the product. This oxidation property makes its usage more appealing.

The stoichiometry of the reaction as shown in Figure 2.4 indicates that 3.0 moles of fatty esters and 1.0 mole of glycerol are formed from 3.0 moles of alcohol and 1.0 mole of triglyceride. The optimum molar ratio in alkali-catalysed reaction was found to be 6:1 for obtaining higher than

98% of methyl ester yields [158]. The reaction mechanism for the alkali catalysed transesterification reaction, as shown in Figure 2.7, indicates three steps. The first step is deprotonation of alcohol with alkali catalyst to produce strongly basic with highly catalytic active species (CH_3-O^-) followed by nucleophilic attachment of methoxide ion on the carbonyl carbon atom of the triglyceride molecule to form a tetrahedral intermediate. The last step includes the rearrangement of the tetrahedral intermediate into FAME and a diglyceride [120, 151, 152, 168].
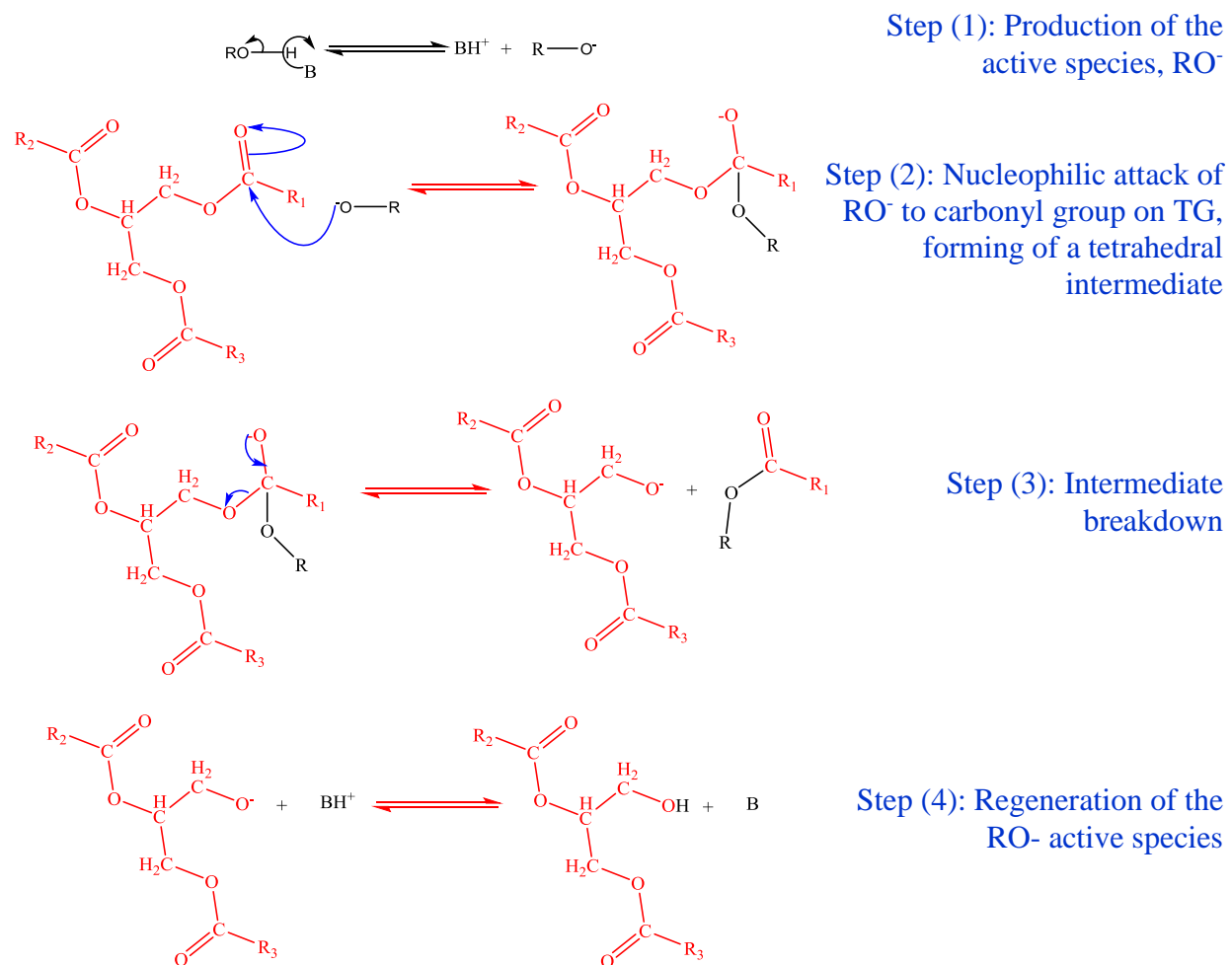
Figure 2.7 Mechanism of the alkali-catalysed transesterification of vegetable oils

The effect of various parameters on the alkali catalysed transesterification process, which was reported by different researchers, is summarized in Table 2.4. It can be observed that using inexpensive alkali-catalysed transesterification can achieve high yield of FAME with low temperature in a short time. However, this catalytic process is recommended only for raw materials

with a low FFA (less than 1 wt%) and moisture content. In addition, the removal and recycling of this kind of catalyst from the product and by-product is relatively difficult due to its solubility. Therefore, the design of a new catalyst to replace the homogenous catalyst is required.

Table 2.4 Summary of optimization alkali-catalysed alcoholysis process

Oil/fat feedstock	Methanol to oil ratio	Catalyst Type	wt%	RPM	t/Min	T/ºC	Y%	References
Used frying oil	7:1	NaOH	1.1	600	20	60	94.6	[125]
Used frying oil	9:1	NaOH	0.72	---	45	65	92.05	[169]
Waste cooking oil	6:1	NaOH	1.0	---	90	50	89.9*	[170]
Jatropha curcas	5:1	KOH	0.55	---	24	60	>99.0	[171]
Safflower	6:1	NaOCH$_3$	1.0	600		60	98	[172]
Rapeseed	6:1	KOH	1.0	600	120	65	95-96	[173]
Sunflower	6:1	NaOH	1.0	600	120	60	97.1	[174]
Sunflower	4.5:1	NaOH	0.43	---	2.5^a	40	99	[175]

* Conversion % reported instead of yield%. ^{a} 1130/Down flow Liquid Contactor Reactor used as a reactor in this work.

2.4.4.2 Enzyme catalysed transesterification

The biocatalytic transesterification process is more advantageous than the acid- and alkali-catalysed transesterification as there is no saponification problem during washing or purification process and no neutralisation issues. The reaction also utilises mild conditions and can be used for feedstocks with high FFA content [159]. Singh and Singh [120] have reported the production of various biodegradable esters and polyesters using lipase as a catalyst. Transesterification of rapeseed oil using *Candida rugosa* lipase powder with 2-ethyl-1-hexanol was carried out and an attainment of 97% conversion of esters was reported. Prior to this, research was conducted on ethanolysis of fish oil and grease using *Candida Antarctica* and *Pseudomonas cepacia*, respectively to exceed 80% yields [145, 159]. Fukuda et al. [145] have also reported that primary alcohols used for the lipase catalysis process, to form alkyl esters, give nearly 96% conversion, whereas secondary alcohols give between 61 and 84% conversion with or without solvent. Research studies on methanolysis using extracellular lipase *C. Antarctica* lipase (Novozym 435) have shown conversion of more than 95%. General lipase-catalysed process is shown in Figure 2.8.

The lipase catalysis has also been carried out on soybean oil, linseed oil and rapeseed oil by using mostly lipozymes. In a technical review paper by [159], rapeseed oil was converted to biodiesel in the presence of 5% Novozym 435 as catalyst, in 24 h with methanol/oil molar ratio of 3:1 at 40 ^{o}C giving a conversion of 76% (extracellular lipase catalysis).
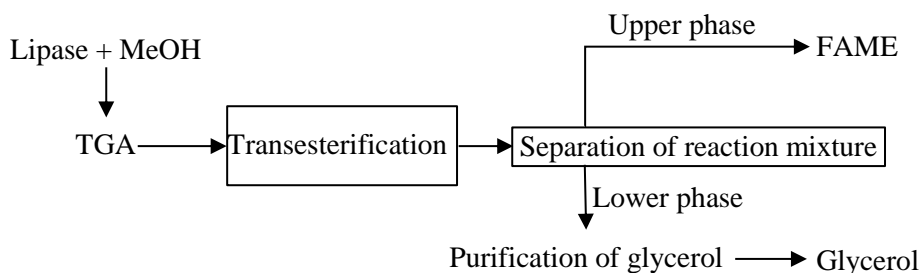
Figure 2.8 Biodiesel production using lipase- catalysis processes

In a review paper by Fukuda and co-workers [145], a whole cell lipase, *Rhizopusoryzae* immobilised on biomass support particles was utilised to produce biodiesel from Jatropha oil and Novozym 435. This was also called the intracellular method. The researchers reported that Jatropha oil is catalysed more efficiently than Novozym 435 with the yield of biodiesel being 80% after 60 h using 4% catalyst in the presence of 5% added water, methanol to oil ratio of 1:1 and reaction temperature of 30 ^{o}C.

A recent research of immobilised lipase catalysed transesterification on cotton seed oil with methanol has produced a green biodiesel, meeting international specifications with 90% purified product yield. The optimum conditions for this reaction were oil to methanol molar ratio of 1:15, water content of 5.0% (w/w of oil) and an enzyme amount of 1.0% (w/w of oil). The reaction mixture was incubated at 37 ^{o}C for 10 h to complete the reaction. It also showed that emission characteristics improved with biodiesel-diesel blends such as B10 and B20 with increased brake thermal efficiency for diesel engines, brake fuel consumption and exhaust gas temperature. Hence, the use of this fuel as an efficient environmentally friendly bio-additive for diesel engines provides scope for further research in commercial applications [176]. The conditions used for the enzymatic transesterification processes for various feedstocks are shown with their resulting yields or conversions by different researchers in Table 2.5. It can be concluded that enzymatic catalysts can completely convert FFAs in the waste oils to fatty acid methyl esters [145]. However, enzyme catalysis has demerits in its production costs being higher (high cost of enzyme catalysts), reaction

time longer and the limited reuse and regeneration of the catalyst. The biodiesel yields obtained from this process have also been reported as being unfavourable compared to the alkali-catalysed reaction, making it less economical [5, 159].

Table 2.5 Enzymatic transesterification reactions using various types of lipases

Feedstock	MeOH to oil ratio	Enzyme		t/hr	RPM	T/^{o}C	C % Y %	References
		Type	amount					
Soybean	3.4:1	Rhizomucormiehei (Lipozyme IM-77)	0.9 BAUN[*]	6.3	200	36.5	92.2 C	[177]
Waste frying oil	3.8:1	Novozym 435	15 wt%	12.0	200	44.5	100 Y	[178]
Sunflower	4.5:1	Pseudomonas fluorescens (Amano AK)	10 wt%	48.0	200	40	>90 C	[179]
Rapeseed oil	4:1	Combined Lipozyme TL IM and Novozym 435	3 to 1 wt%	12.0	130	35	95 Y	[180]

[*] BAUN: Batch Acidolysis Units NOVO.

2.4.4.3 Supercritical alcohol process

This process is a recent non-catalytic transesterification approach at high temperature and pressure that is more tolerant to FFAs and water in the raw material, allowing reaction times to be very short. Saka and Kusdiana [181] studied a process of forming biodiesel without the use of any catalyst compared to the conventional catalysed transesterification reactions mentioned earlier. In their research, they have reported that preheating to a temperature of 350 ^{o}C, at a pressure of around 18-20 MPa and treatment for 240 seconds in supercritical methanol (SCM), rapeseed oil was converted to methyl esters with a 95% yield. The kinetics of the reaction in supercritical state was observed to be towards a higher conversion of rapeseed oil to methyl esters due to the increased solvation of the oil by the hydrophobic nature of the supercritical methanol forming a single oil/alcohol phase. The optimum conditions for this supercritical alcohol process was found to be 350 ^{o}C and a molar ratio of methanol to oil of 42:1.

Used cooking oils also showed higher methyl ester conversion rates using the supercritical methanol process, as the FFAs and TG present in virgin oils could be converted to methyl esters efficiently in this medium [159]. Moreover, there is no need for any purification process of the products as the reaction is non-catalytic and more environmentally friendly. The SCM process is carried out in a high-pressure reactor or autoclave [127]. This has been investigated using

continuous and batch process to reduce the cost of production of the biodiesel, which is an issue considered in detail later. The transesterification by SCM process is shown in Figure 2.9 [182].
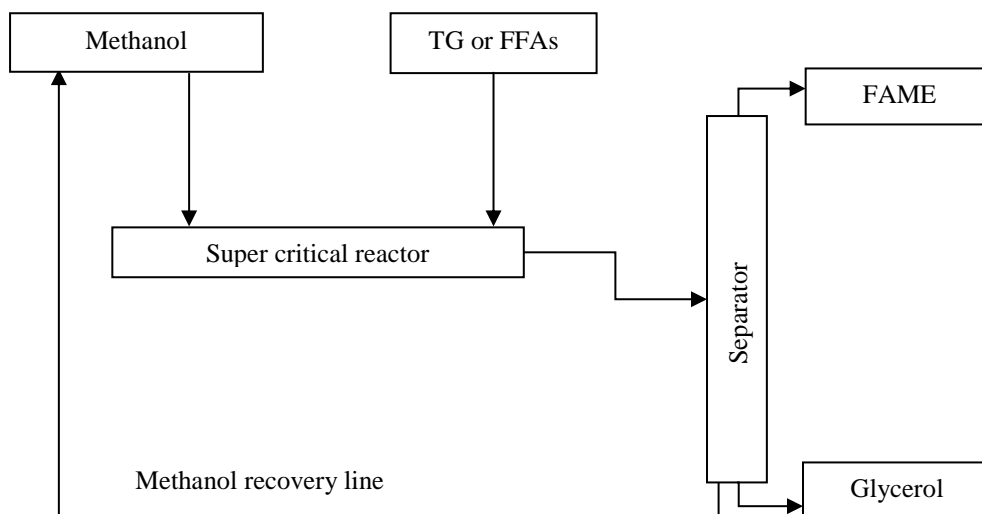
Figure 2.9 Supercritical transesterification process

It can be observed from table 2.6 that a large excess of alcohol is required to push the equilibrium reaction forward, an observation reported by different researchers. The other disadvantage of this method is the use of high temperature and pressures – 350 ^{o}C and 45 MPa, respectively, increasing the cost of industrial biodiesel production. Therefore, more research work needs to be done to improve this technology in terms of economic and technologically viability.

Table 2.6 Summary of SCA transesterification process for various feedstocks

Oil/fat feedstock	Alcohol to oil ratio	t/Min	T/^{o}C	P/MPa	Type of reactor	Y % C %	References
Rapeseed	42:1	4.0	350	45	5 mL Inconel-625	99.0 Y	[181]
Sunflower	40:1	40	350	20	8 mL stainless steel	>96 C	[183]
Soybean	40:1	25	310	35	75 mL tube	>77 Y	[184]
Jatropha	43:1	4.0	320	8.4	3.7 L stainless steel	100 Y	[185]
WCO	41:1	30	287	---	---	99.6 Y	[186]
Chicken fat	9:1	6.0	400	30	8 m long tubular	99 C	[187]
Palm	40:1	16	372	5-25	12 mL stainless steel-super Duplex	81.5 Y	[188]

2.4.4.4 BIOX process

The BIOX process is an innovative, continuous co-solvent process for the production of biodiesel without the use of a catalyst from raw materials with high FFAs. It was developed by Professor David Boocock in 1996. The transesterification reaction is known to be a slow process requiring 30 min to a few hours. The reactants used are immiscible, which lengthens the process due to mass transfer limitations [189]. In order to increase the rate of the reaction, inert co-solvents have been recently utilised at ambient temperature and pressure, taking 5-10 min to complete the reaction of triglyceride conversion to esters without any residues either on the biodiesel phase or the glycerol phase [8, 144]. Tetrahydrofuran (THF) is commonly used as a co-solvent in this process to help in forming a homogenous phase for the mixture, facilitating the transesterification reaction and reducing significantly the reaction time. Other co-solvents used in this process are methyl tertiary butyl ether [144], hexane and diethyl ether [189]. These solvents increase the solubility and thus improve the mass transfer rate between the oil and the methanol phase reducing the reaction time [189]. Fig 2.10 shows the typical BIOX process using the co-solvent [156, 182].
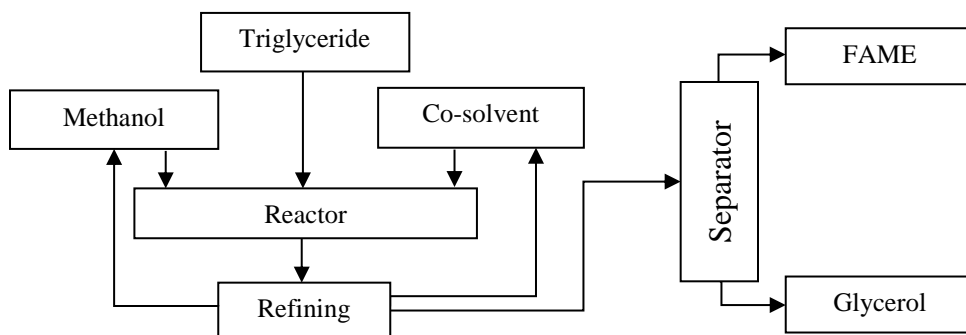
Figure 2.10 BIOX co-solvent transesterification process

The demerit of this method is that the used co-solvent must be completely removed from the product phases in order to be free of any hazard and toxicity. Moreover, since the boiling point of the co-solvents (such as THF) is very close to methanol, the excess alcohol remaining in this process is difficult to recover [8]. Additionally, similar to one-phase butanolysis, single-phase methanolysis initially exhibits a rapid formation of the ester in this process which then drastically slows it down [190].

2.4.4.5 In *situ* transesterification process

This process was developed by Harrington and D'Arcy Evans in 1985 for converting oil to biodiesel by transesterification of its acylglycerols. In this process, the oil within the seed is directly added to the huge amount of methanol at room temperature and pressure, in which the catalyst has been dissolved already. For higher efficiency, requiring less alcohol, during in situ reaction, the oilseeds (such as soybean or sunflower oil) need to be dried before the reaction starts. After heating for 1-5 h, crude biodiesel appears which is washed, dried over anhydrous sodium sulphate and then filtered for final production. The conversion is around 98% which conforms to the ASTM standard.

Table 2.7 Summary of optimum condition for in situ transesterification process

Feedstocks	MeOH to oil ratio	Catalyst		t	T/ºC	Y % C%	References
		Type	amount				
Soybean	281:1	H_2SO_4	0.75wt%	3 h	65	96 Y	[191]
Sunflower seeds	300:1	H_2SO_4	0.7wt%	4 h	64.5	51.6 Y	[192]
Sunflower[*]	476:1	NaOH	2.0wt%	40 min	60	96 Y	[193]
Cotton seed[**]	135:1	NaOH	0.1 M	3 h	40	98 C	[194]
Jatropha curcas[***]	300:1	H_2SO_4	15wt%	24 h	60	99.8 Y	[20]
Marine microalgae	300:1	NaOH	1.0wt%	11 h	60	17.1 Y	[195]

[*]Ultra-sonication with low frequency or mechanical stirred with 600RPMis used in this work.   [**]Petroleum ether is used as a co-solvent.
[***]n-Hexane is used a co-solvent.

This method eliminates the need for the isolation and refining of the oilseed lipid used, thereby reducing production costs and the lengthy times of the pre-extraction procedure in other processes, degumming and increasing the yield of the biodiesel production. However, the disadvantage of this process is not being able to use cheaper feedstock - waste cooking oils and animal fats [8]. Table 2.7 summarises the optimum conditions for the in situ alcoholysis process observed by different researchers. Evident from the table, is that all researchers have used large amounts of methanol to overcome substantial mass transfer resistance in order for the reaction to proceed at an appreciable rate and obtain reasonable conversion. The rate of reaction falling with an increase in the particle size of seed is further evidence of the need to use a large quantity of alcohol in this process [191].

2.4.4.6 Ultrasound assisted transesterification

One of the recent practical and economical approaches added to the catalogue of transesterification methods for production of high quality biodiesel is the ultrasound method of using a sound frequency higher than human ear response. Using the ultrasound method, the rate of reaction, mole ratio and the yield is seen to increase with less energy consumption than with the conventional mechanical stirring method.
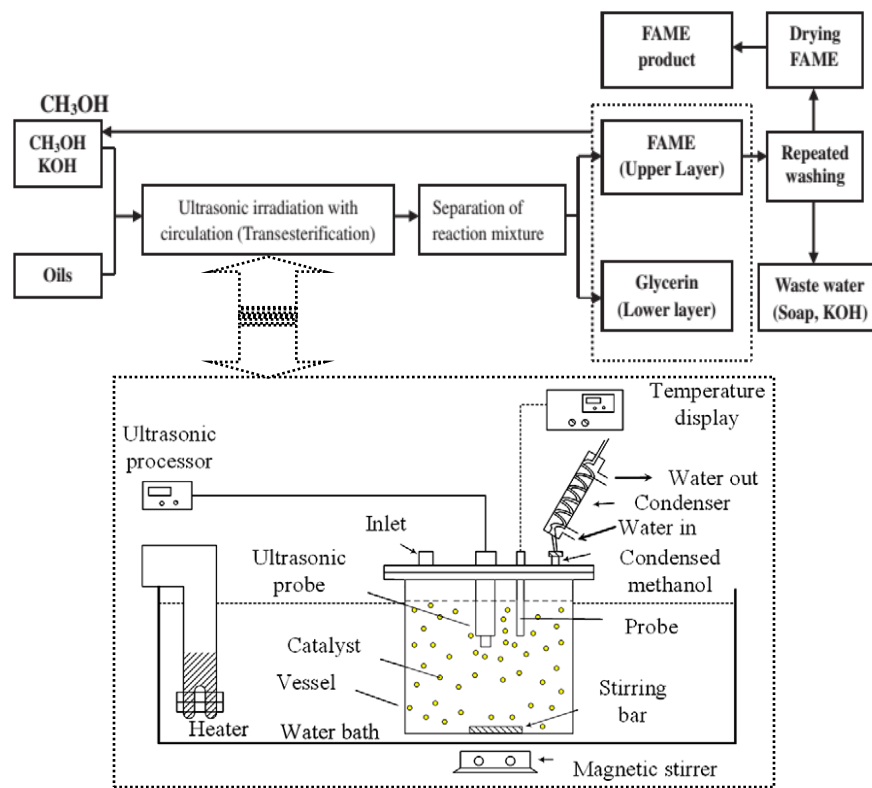
Figure 2.11 Ultrasonic assisted alkali-catalysed transesterification process [196]

Deng and co-workers [197] have investigated the production of biodiesel from *Jatropha curcas* oil using KOH as a catalyst in a two-step process of acid-esterification followed by ultrasonification assisted alkali-transesterification to avoid soap formation. This process produced a yield of 96.4% with different methanol: oil ratios ranging from 16 to 48 vol.% and 4 vol.% sulfuric acid in the first step using the ultrasonic reactor and then sodium hydroxide (0.8-1.6 wt.%) for methanol: oil 24 vol.% in the second step. They have found that the two-step process is effective and time-saving for biodiesel production from Jatropha oil and the properties for produced biodiesel was close to that reported in the ASTM standard for biodiesel [197]. Another study using

waste cooking oil by this method produced 85% conversion at 45 $^\circ$C reaction temperature, 1 wt% catalyst concentration and molar ratio of methanol to oil ranging from 4:1 to 7:1, and 200 W power [198]. A flow chart of the ultrasonic irradiation process in the presence of a base catalyst for biodiesel production is shown in Figures 2.11 [196, 199]. A summary of some ultrasound assisted alkali transesterification processes by different researchers is given in Table 2.8.

Table 2.8 Summing up of optimum condition for ultrasound method

Feedstocks	Alcohol to oil ratio	Catalyst		t	T/$^\circ$C	Ultra sound reactor	Y % C%	References
		Type	wt%					
Coconut oil	6 EtOH:1	KOH	0.75	7 min	60	UP200S, 200W	≥98 Y	[200]
Soybean oil	9 MeOH:1	NaOH	0.2	30 min	29	USC40, 4870W	100 Y	[201]
Waste cooking oil	4 MeOH:1	KOH	1.0	55 sec	25	Horn, 1kW	93.8 Y	[202]
Canola oil*	5 MeOH:1	KOH	0.7	50 min	70	Horn,1kW	>99 C	[203]

*Reduced pressure is used in this work.

2.4.4.7 Microwave assisted transesterification

Microwave use has increased in recent years in domestic households since its advent in 1954. Microwaves can heat matter faster and easier rather than conventional ovens as they have a frequency of irradiation with wavelength of 0.01 to 1 m (300 MHz to 300 GHz) [199].
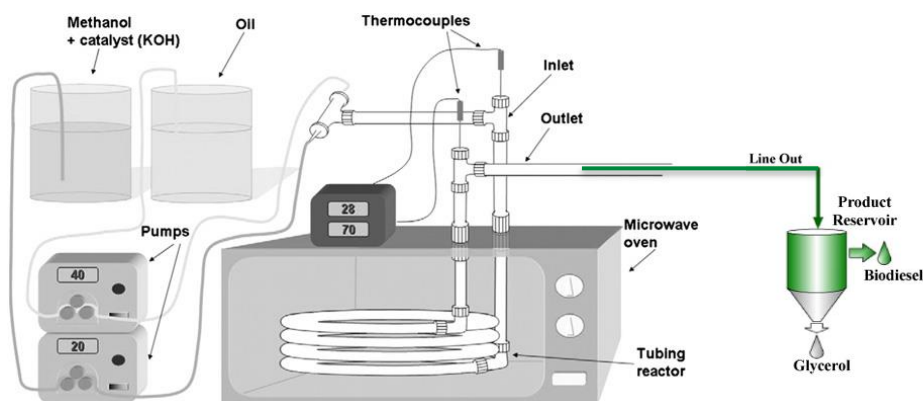
Figure 2.12 Microwave-assisted transesterification process [204]

Microwaves have been reported to accelerate chemical reaction rates and obtain higher yields in the production of biodiesel. Recently, Motasemi and Ani [204] have reported that microwave irradiation, utilised for biodiesel production from rice bran oil, reduced the reaction time to 30

seconds with optimum conditions of 1.0 wt% of sodium hydroxide as the catalyst and 9:1 molar ratio of ethanol to oil to produce 94% yield of biodiesel. A microwave assisted technique for biodiesel production is depicted in Figure 2.12. A modified ultrasound method in combination with microwave is a recent trial method, which has shown promising results with a 97% FAME yield. For instance, in a recent household-microwave method for continuous synthesis of biodiesel from waste frying palm oil using Teflon tubing and 1.0% catalyst, 1:12 molar ratio and residence time of 30 seconds, 97% conversion was obtained [205].

The summary of the optimum condition for the microwave heated alkali-catalysed transesterification process by different researchers is shown in Table 2.9. It can be seen clearly that microwave irradiation reduced the reaction time more than 10 times compared with the conventional method. They have also reported that the raw materials with high free fatty acid can be converted to high yield biodiesel with high purity. However, it would need more catalyst to neutralise the FFA [206]. This technique opens the way for industry to develop this method for large scale FAME production especially for feedstocks with high FFA contents.

Table 2.9 Summing up of optimum condition for microwave method

Feedstocks	Alcohol to oil ratio	Catalyst		t	T/ºC	Type of microwave	Y % C%	References
		Type	wt%					
Waste frying oil	12 EtOH:1	NaOH	3.0	30 Sec	78	Household, 75 kW	>97 C	[207]
Waste cooking oil	9 MeOH:1	KOH	2.0	6.0 Min	80	Domestic, 800W	92 Y	[208]
Rapeseed oil	6 MeOH:1	KOH	1.0	5.0 Min	50	S model, 1200W	93.7 C	[209]
Rapeseed oil	6 MeOH:1	NaOH	1.0	3.0 Min	40		92.2 C	

2.4.4.8 Heterogenous catalysed transesterification

Heterogeneous catalysts have been recently used in different commercially available industrial applications. The current technology process for biodiesel production over homogenous catalysts (sodium hydroxide, potassium hydroxide, sodium methoxide, potassium methoxide, sulphuric acid, etc.) has many disadvantages and limitations, including hazards, corrosion, separation from products/by-products, high sensitivity to water and FFA impurities in feedstocks, soap formation, requiring aqueous quench and neutralisation process steps. Therefore, the design/development of suitable heterogeneous catalysts for the production of biodiesel from different cheap feedstocks is

required for simultaneous esterify of FFAs and transesterify of TG in cheap feedstocks. Hence, this has been the subject of intensive industrial and academic research [40, 87, 210-214]. Heterogeneous catalysts are generally divided into solid base and solid acid catalysts.

2.4.4.8.1   Solid base catalysed transesterification

Solid base catalysts show higher catalytic activities than solid acid catalysts for high purity raw material containing very low FFAs [40, 215]; however, they have shown low stability [151]. A range of solid base catalysts have been widely examined for their catalytic activities in the literature for the production of biodiesel from different feedstocks. Some of these have shown good catalytic performance, including alkaline earth oxides [216, 217], alkali metal doped alkali earth oxides [218], hydrotalcites [219-222], and supported alkali metals or alkaline earth oxides [223-226].

The most widely used alkali earth metal oxides for transesterification reaction are calcium oxide (CaO) [217, 227-231], strontium oxide (SrO) [232-234] and magnesium oxide (MgO) [97, 235, 236]. CaO is the most studied and promising catalyst among all alkaline earth single metal oxides for biodiesel production due to its availability, high basic strength, its lesser environmental impact, its lower cost and long catalyst lifetime [235, 237, 238].

In general the catalytic activity of alkaline earth oxides for the transesterification process depends on their basicity strength and the origin of the basicity strength is believed to appear as ion pairs $[M^{2+}\text{-}O^{2-}]$ in coordination environments [239]. This basicity can arise in different ways, including cationic defect site in the lattice and surface terminations as shown in Figure 2.13 [215].
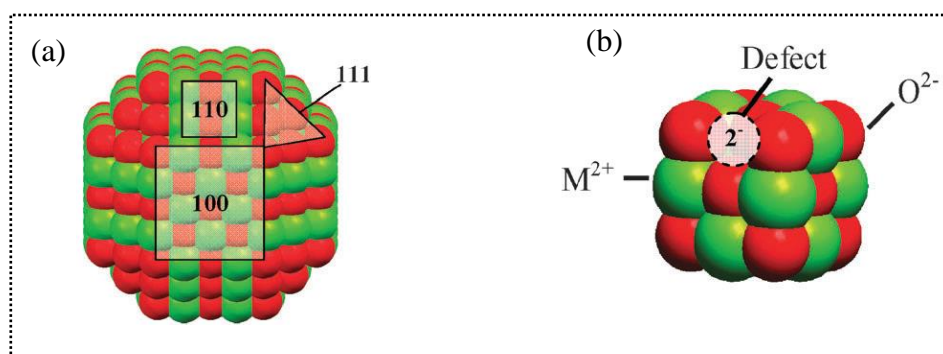
Figure 2.13 Origin of basicity in an alkaline earth oxides (a) crystal facet termination on the surface crystal and (b) defects in lattice [215]

Liu and et al. [231] investigated the influence of water on the catalytic activity of CaO and found that the use of an appreciate water level (up to 2.8%) in the transesterification reaction medium enhanced the catalyst activity of CaO, improving FAME yield. This is because the O^{2-} attracts proton from the water to form hydroxide anion on the surface of the catalyst, according to the reaction mechanism below (see Figure 2.14). However, the addition of water more than 2.8% into methanol could result in saponification due to hydrolysis of FAME under basic condition (OH^-) to form FFAs.
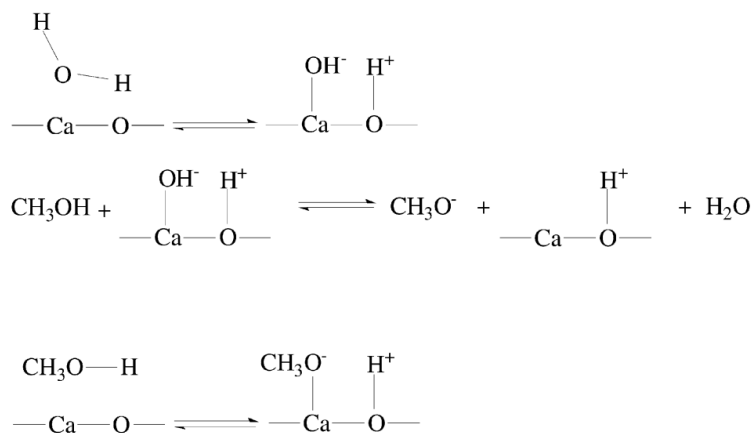
Figure 2.14 Mechanism of H^+ abstraction from water by the surface of CaO [231]

The catalytic activity of CaO with different particle size was also evaluated by Zhao and co-workers [216] for transesterification of canola oil with methanol in a batch reactor at optimum conditions of 65 °C using a methanol to oil ratio of 9:1 and 600 rpm stirring speed. The biodiesel yield over nano-particle CaO was nearly 81%.
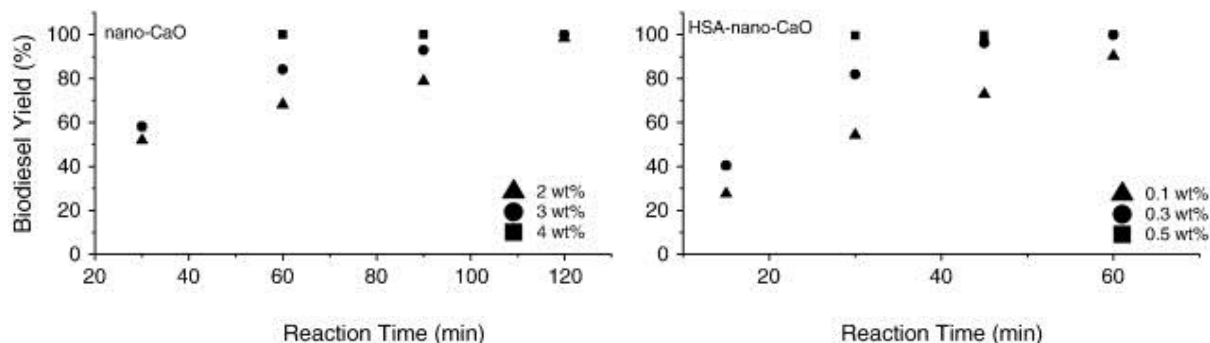
Figure 2.15 Effect of catalyst loading on biodiesel yield [216]

As a comparison, it was reported that the CaO with average particle size 27.3 nm and a high surface area (HSA-nano-CaO) of 89.25 m^2/g shows higher activity compared to that with average particle

size 37.3 nm and a lower surface area of 22.25 m^2/g under fixed reaction temperature and molar ratio using 0.3 wt% of HSA-nano-CaO in comparison to 4.0 wt% for nano-CaO, to reach 100% of biodiesel yield, reducing the time of reaction to half as shown in figure 2.15. They have also reported the effect of reusability of catalysts on the fatty acid methyl ester yield, which slightly dropped after 12 cycles. Another work by Venkat Reddy et al. [230] examined the effect of CaO nano-crystalline on the soybean oil transesterification at room temperature for 24 h with 1.3 wt% catalyst and 1:27 mole ratio of oil to methanol in order to obtain >99% conversion. The also noted that the deactivation of the catalyst after 8 cycles might be due to the impurities of CaO.

More recently, Kouzu and Hidaka [237] reported the catalytic activity of CaO at low concentration ratio corresponding to calcium methoxide (Ca-OMe) or the surface of CaO as an initial active sites catalyses the transesterification reaction as illustrated in Figure 2.16. Veljković et al. [240] studied the kinetic of calcined CaO at 500 °C for transesterification process of biodiesel production from sunflower. The reaction was performed using 6:1 mole ratio of methanol to oil, 2 h reaction time, 1 wt% catalyst and 60 °C to achieve 98% of FAME yield. Moreover, they noted that the rate of reaction at the beginning of transesterification process depends on a rate mass transfer of the reactants and this became faster with an active surface of CaO catalyst.
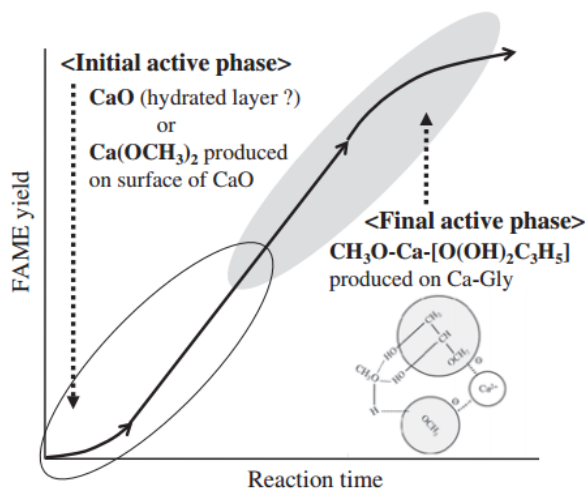
Figure 2.16 Transesterification reaction showing the variation in active phase of CaO at low concentration ratio with methanol [237]

MgO and SrO have also shown good catalytic activity in the transesterification process to produce biodiesel from different feedstocks. Verziu and co-workers [236] obtained around 80% of FAME

yield with MgO as the catalyst under optimum reaction conditions of 1:4 of rapeseed oil to methanol, 70 $^\circ$C reaction temperature, 2 h of reaction time with 300 mg of catalyst. They also found that the catalyst can be re-used without any reactivation/regeneration after recycling from the reaction. Wang and Yang Liu [241] earlier reported the use of MgO catalyst for biodiesel production from soybean oil with supercritical/subcritical methanol at optimum conditions of 1000 RPM, 3 wt% nano-MgO, 260 $^\circ$C, 30 MPa, 10 min of reaction time with 36:1 mole ratio of methanol to oil to convert 100% of soybean oil. Liu et al. [232] studied the transesterification of soybean oil over SrO with strong basicity H_0=26.5 and BET surface area of 1.05 m^2/g. $SrCO_3$ being used as a promising solid base precursor for synthesising of SrO at 1200 $^\circ$C for 5 h. The reaction was carried out at 65 $^\circ$C, 3 wt% catalyst, 12:1 mole ratio of methanol to oil and 30 min of reaction time. They also reported that the catalyst can be re-used for 10 cycles with a slight decrease in biodiesel yield. The mechanism of the reaction over SrO also revealed that the catalytically active phase was the surface of SrO catalyst to form CH_3O^-. Several other alkaline earth metal and transition metal oxides have been investigated for transesterification reaction to synthesise biodiesel, including zirconium oxide (ZrO_2) (Jitputti et al., 2006) and zinc oxide (ZnO) [38, 242]. It was found that ZnO can catalyse crude palm kernel oil and crude coconut oil to produce 86.1 and 77.5% FAME yield, respectively, whilst 64.5 and 49.3% of FAME yield could be achieved using 3 wt% of ZrO_2 catalyst with crude palm kernel oil and crude coconut oil, respectively, being raw materials.

Many other mixed metal oxides, supported alkali and alkali earth oxides, have been reported in biodiesel production in literature. It has been investigated that doping of lithium ion (Li^+) with MgO using chemical vapour deposition increases the surface basicity [243]. Montero and co-workers [218] assessed the effect of caesium (Cs) impregnated to MgO on the structure and basicity in the tributyrin transesterification reaction. It was found that the Cs doping MgO (CsNanoMgO-C) catalyst enhanced the rate of tributyrin transesterification (100% conversion within 3 h) but the surface of the CsNanoMgO-C catalyst deactivated after one cycle. There were a number of reasons reported for this, including leaching of Cs, the large agglomeration post-transesterification, surface reconstruction, and sintering of spent catalyst. Taufiq-Yap et al. [244] described newly mixed metal oxides for catalysing the transesterification of non-edible Jatropha curcas oil to biodiesel. The binary catalyst demonstrated good activity with optimum conditions of 25:1 methanol to oil molar ratio, 3 h reaction time, 120 $\circ$C reaction temperature and 3 wt% catalyst loading for a various Ca/Mg atomic ratio to form a FAME yield in the range of 70 to 90%.

They found that the catalytic activity after five consecutive runs without any treatment was slightly reduced. This reduction was due to the dissolution of bulk CaO in the methanol or the unstable CaO phase being dragged out by FFAs in the raw material to form organosol (calcium soap) which competed with the FAME yield and created difficulties for FAME separation from the by-product. It has been reported, however, that the surface of the mixed oxides (MgO:CaO) resist the deactivation by CO_2 [245].

Alonso and co-workers [246] studied the effect of different lithium loading on CaO and the activation temperature of Li-doped CaO catalyst in the transesterification of food-grade sunflower oil to form biodiesel. They found that 4.5 wt% of Li loading was needed to promote the catalytic activity of CaO for biodiesel production whilst the activation temperature of Li-doped CaO catalyst required a temperature above the melting point of lithium nitrate (Li precursor). Likewise, Watkins et al. [211] examined the influence of lithium contents in the range of 0.26–4.0 wt% onto the CaO catalyst for glyceryl tributyrate transesterification. They reported that the basic strength of Li-doped CaO samples have a $17.2 > pK_{BH^+} > 15$ whilst for the bulk CaO has $10 > pK_{BH^+} > 8$. CaO catalyst showed poor catalytic activity for transesterification reaction with only 2.5% conversion for 20 min whilst loading 1.23 wt% of Li on CaO increased the conversion to 100% within the same period of time.

Kawashima et al. [247] examined the combination of different types of metal oxides on the transesterification of rapeseed oil with a 6:1 mole ratio of methanol to oil at 60 °C to form 90% of FAME yield using $CaTiO_3$, $CaZrO_3$, $CaMnO_3$, $Ca_2Fe_2O_5$ and $CaO-CeO_2$ catalysts. They found that the calcium-containing catalysts showed high catalytic activities for transesterification reaction. Macedo and co-workers [248] studied the transesterification of soybean oil over $ZnO-Al_2O_3$ and $SnO-Al_2O_3$ catalysts at optimum conditions of 4 h of reaction time, 5 wt% catalyst and 60 °C reaction temperature to obtain 80% of FAME yield.

Good results in the transesterification reaction were obtained over hydrotalcite catalysts in the literature. Therefore, there is more interests for such catalysts in biodiesel production because of their surface area and basicity. Hydrotalcite-like compounds (HTlc) are a class of inorganic naturally occurring materials called as layered double hydroxides with the general formula in equation 2.1 [249];

$$[M(II)_{1-x} \cdot M(III)_x \cdot (OH)_2]^{x+} \cdot [(A^{n-})x_{/n}]^{x-} \cdot mS \qquad \text{Equation 2.1}$$
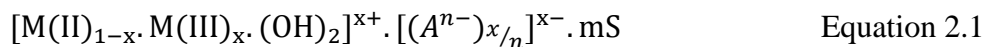
Where, mS is the number of molecules of solvent (generally solvent is water); A^{n-} charge balanced by interlayer anions (CO_3^{2-}, SO_4^{2-}, NO_3^-, Cl^-, organic anions, etc.) as shown in Figure 2.17; M(II) may be divalent ions (Zn, Ni, Co, Mg, Mn, etc.); M(III) may be trivalent ions (Al, Cr, Fe, V, Co, etc.); x is equal to mole ratio of M(II)/[M(II)+M(III)].
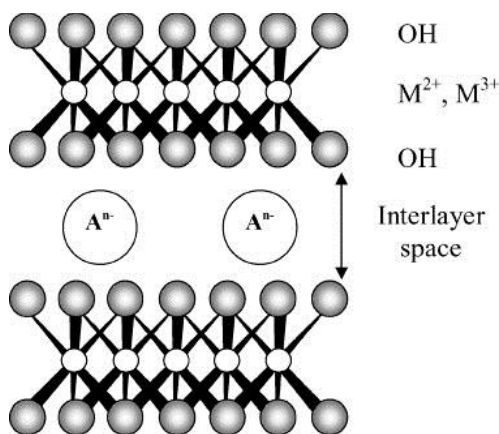
Figure 2.17 General layered structure of HTlc [219]

The best known HTlc is the calcined Mg-Al [220, 221, 250-252]. Cantrell and co-workers [219] synthesised a series of HTlc with compositions over the range x = 0.25–0.55 and tested glyceryl tributyrate for biodiesel production. They found that the rise in the mole ratio of Mg to Al in the precursor hydrotalcite enhanced the basicity of the obtained HTlc. The rate of tributyrate conversion also increased with an increase of Mg content in the bulk Al_2O_3 (see Figure 2.18) whilst pure Al_2O_3 was completely inactive.
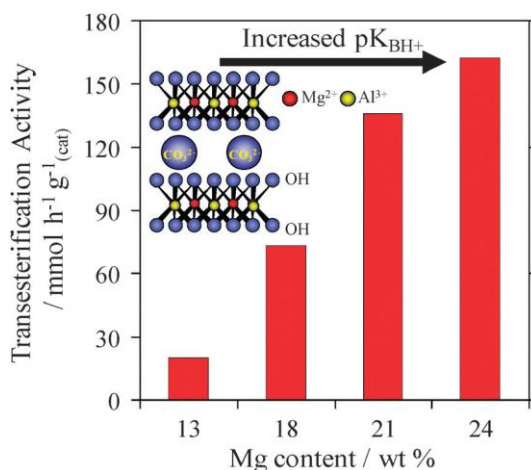
Figure 2.18 Mg-Al performance in the biodiesel transesterification reaction [215]

Liu et al. [253] examined the Mg-Al catalyst for transesterification of poultry lipids to obtain biodiesel. They reported that calcination at optimum temperature (500-550 $^{\circ}$C) for Mg-Al catalyst could lead to better thermal stability with higher basicity, in order to produce a 67% FAME yield at optimum reaction condition of 60 $^{\circ}$C, 15:1 methanol to oil mole ratio, 9 h reaction time, and 7.5 wt% of Mg-Al catalyst with 3:1 ratio of Mg to Al. Debecker and co-workers [254] reported the HTlc had good ion exchange capacity to reconstruct back (retro-topotactical transformation or memory effect) after calcination if put in contact with an appreciate water. The preferable calcination temperature for HTlc is between 400 and 500 $^{\circ}$C for a prolonged time from 1 night to 48 h. Another study by Barakos et al. [255] evaluated Mg-Al catalyst in transesterification of cottonseed oil (43 wt% of FFAs with 3.5 wt% of water) and animal fat (45 w% of H_2O) with 1 wt% catalyst, 200 $^{\circ}$C, 6:1 methanol to oil mole ratio, and 3 h reaction time. They found the highest catalytic activity with 99% conversion of both feedstocks. The main benefits of this kind of catalyst are their high catalytic activity, their economical availability and their robustness in the presence of water and free fatty acids whilst the main drawback comes from their poor physical properties (i.e. low surface area and low porosity) and leaching of alkali metal residue (i.e. Na or K). It is worth mentioning that the complete removing of alkali residues from the HTlc catalyst preparation via co-precipitation, using caustic pH regulators, is essential to avoid resulting interfere between homogenous (NaOH/Na_2CO_3 or KOH/Na_2CO_3 contributions to catalysis arising from leached Na or K) and heterogeneous (HTlc) catalytic transesterifications of TGA to form biodiesel [40, 213, 256]. This interfere of alkali residue has a significant effect on the catalytic activity and basicity of the HTlc catalyst [257] and consequent FAME contamination [258]. This problem has been overcome by using NH_4OH and $(NH_4)_2CO_3$ as alkali-free precipitation routes for the preparation of HTlc catalyst [219].

Over the past twenty years, a few studies have been carried out using ion-exchange resins and zeolite catalysts for transesterification reaction. Diaion PA308, Diaion PA306, Diaion PA306s and HPA 25 anion exchanges have been tested in the transesterification of triolein [259]. The anion exchange catalyst (Diaion PA306s), with small particle size and lower cross-linking, produces better catalytic activity (98.8% FAME yield) than cationic exchange resin catalyst. Zeolite-X is the most commonly used for transesterification to synthesise biodiesel. Lee et al. [260] reported that the Si/Al framework, amount of ion exchange cation to be introduced to the structure of zeolite and type of zeolite can change the acidity and basicity sites of synthesised zeolite catalyst. The

activated zeolites faujasite NaX at 500 °C have been tested in the transesterification reaction of soybean oil [261] under 120 °C for 24 h reaction time. It was reported that the 90% FAME yield was achieved and the catalyst re-used without any observed catalytic activity loss. According to their study, the ion-exchange with potassium was preferable for catalytic transesterification reaction in comparison with Cs ions due to the larger size of the later limiting the exchange capacity.

Literature suggested that supporting metal oxides as active sites on the surface of high surface materials enhances the thermal stability, minimising mass transfer for transesterification to liquid phase and increasing dispersion of active sites in the reaction medium [235]. Among materials reportedly used for catalyst supports are: alumina (Al_2O_3) [262, 263], titania (TiO_2) [264-266], zinc oxide (ZnO), silica (SiO_2) [267-269], and zirconia (ZrO_2) [270, 271].

Xie and co-workers [272] examined the catalytic efficiency of different K loading (15-45 wt% of KNO_3) onto Al_2O_3 support for transesterification of edible grade soybean oil to obtain biodiesel. They found that the basic strength in most of the cases was $15.0 < H_0 < 18.4$ and the active basic sites was K_2O species produced by thermal decomposition or Al-O-K groups formed. It was also noted that the basicity of K-supported Alumina was decreased when the materials calcined above 500 °C in parallel with the catalytic activity for transesterification of soybean oil. The optimum KNO_3 loading on alumina was 35 wt% with calcination temperature at 500 °C to reach maximum conversion (87%) under optimum conditions of 15:1 mole ratio of methanol to oil, 7 h reaction time, 6.5 wt% catalyst, 600 RPM with reaction temperature above boiling point of methanol. In another study, Kim et al. [273] evaluated the catalyst $Na/NaOH/\gamma$-Al_2O_3 prepared by sodium hydroxide being loaded on gamma alumina for transesterification of soybean oil. The reaction was carried out at 60 °C by 9:1 methanol to oil mole ratio with 5:1 n-hexane (co-solvent) to oil mole ratio under a mixing rate of 600 RPM for 2 h to obtain 94% of FAME yield. They also reported good catalytic activity related to the high basicity (H_0=37) of $Na/NaOH/\gamma$-Al_2O_3 catalyst. In a similar approach Ma co-workers [274] synthesised $K/KOH/\gamma$-Al_2O_3 for biodiesel production from rapeseed oil. The loading of KOH and K on γ-Al_2O_3 support was 20 wt% and 7.5 wt%, respectively. It was found that the FAME yield reached 84.2% after 1 h reaction run at 60 °C with 9:1 mole ratio of methanol to oil under a stirring rate of 270 *g* and 4 wt% of catalyst. Hammett indicator test shows such a catalyst has basic strength above H_0=37 indicating the catalyst is super basic. The catalytic activity of $K/KOH/\gamma$-Al_2O_3 was claimed to be a result of the ionisation of

potassium in the catalyst. However, leaching of sodium and potassium for Na/NaOH/γ-Al$_2$O$_3$ and K/KOH/γ-Al$_2$O$_3$ during the transesterification reaction were reported indicating both catalysts lacked stability.

Many other solid base catalysts have been tested in the transesterification of biodiesel from different raw materials (see Table 2.10) showing good catalytic activity, some even at low temperature. This provides a commercially viable way to decrease production costs for the biodiesel industry. However, the main problems encountered for commercial exploitation of such catalysts are: slow reaction rate (high basicity of alkaline earth oxides having low solubility in methanol) [269], catalyst leaching [40, 215, 236, 275], dissolution of catalyst in the reaction medium (solid-liquid-liquid phases) [276], unsuitability for feedstocks containing high FFAs [277] and some catalysts having a low activity, low porosity with low surface area [244]. Furthermore, it is difficult to create a catalyst possessing simultaneous qualities as a strong basic, high surface area, large pore size, cheaper and chemically stable. Therefore, more research need to be carried out to find cheap and more efficient catalysts for transesterification of raw materials containing FFAs by designing or developing suitable solid base catalysts.

Table 2.10 Summary of solid base catalysed esterification/transesterification process

Feedstock	MeOH to oil ratio	Catalyst Type	Amount	Time	Particle size,nm	T/ºC	Y % C %	Catalyst recycled	References
Soybean oil	9:1[b]	Na/NaOH/γ-Al$_2$O$_3$	20 wt%	2 h	*N.R.	60	94 C	**NRC	[273]
Soybean oil	25:1	CaO/MgO	5 wt%	3 h	24-68	120	90 Y	5	[244]
Soybean oil	15:1	Calcined LDH (Li–Al)	1 wt%	3 h	~25 nm	65	77.6-83.1 Y	1	[278]
Soybean oil	6:1	20-nano-MgO/TiO$_2$	0.1 wt%	1 h	*N.R.	225	95 C	**NRC	[279]
Soybean oil	20:1	KI/Mg-Al	5 wt%	8 h	*N.R.	70	>90 Y	**NRC	[280]
Ethyl butyrate[a]	4:1	MgO/CaO	62 mg	1 h	*N.R.	60	60 C	**NRC	[281]
Waste cooking oil	12:1	3.5-K-CaO	7.5 wt%	*N.R.	~40	65	98±2 Y	3	[282]
Waste cooking oil	50:1	MgO/TO$_2$	10 wt%	6 h	21.4 nm	170	91.6 Y	**NRC	[275]
Palm oil	30:1	Mg-Al-CO$_3$ (hydrotalcite)	7 wt%	6 h	Few μm	100	86.6	**NRC	[220]
Sunflower oil	4:1	CaO	1.4 wt%	2 h	22-34 nm	75	92 C	3	[217]
Sunflower oil	6:1	CaO	1 wt%	2 h	3-15 μm	60	98 Y	**NRC	[240]
Sunflower oil	1:4	MgO	300 mg	40 min	1-4.5	70	98 Y	7	[236]
Sunflower oil	6:1	16-nano-CaO/NaX	10 wt%	6 h	5-25	60	93.5 Y	**NRC	[283]
Sunflower oil	12:1	MgO/MgAl$_2$O$_4$	3 wt%	3 h	11 nm	110	95 C	2-6	[284]

Feedstock	MeOH to oil ratio	Catalyst Type	Amount	Time	Particle size,nm	T/ºC	Y % C %	Catalyst recycled	References
Canola oil	15:1	15-Kf/nano-γ-Al₂O₃	3 wt%	8 h	*N.R.	65	97.7±2.14 Y	3	[285]
Jatropha oil	12:1	1.75-Li/CaO	5 wt%	2 h	500	65	>99 C	**NRC	[223]
Triacetin	6:1	Fe/Mg-Al	1 wt%	40 min	*N.R.	60	100 C	**NRC	[286]

[a] Catalyst activated at 800ºC and a stirring rate of 1250 RPM was used. [b] n-Hexane used as co-solvent. * N.R: Not reported. **NRC: Not recyclable catalyst.

2.4.4.8.2 Solid acid catalysed transesterification

In the late 1930s, the Houdry process used solid acid catalysts in catalytic cracking [214]. Since then, a wide range of solid acid catalysts have been designed, developed and tested for their catalytic activities in different applications to replace homogenous catalysts. Their use eliminates drawbacks associated with liquid acid catalysts, such as corrosion, quenching steps, toxicity, environmental issues and non-reusability. Their potential in conventional biodiesel production from different feedstocks has, therefore, been the subject of recent studies [287-299]. Solid acid catalysts are generally less active, requiring more reaction time and higher temperature than solid base catalysts for transesterification reaction. However, solid acid catalysts are more stable and can be effectively used for simultaneous esterification and transesterification of feedstocks containing high FFAs and water [151, 300]. This advantage, has led to the recent development of a wide range of solid acid catalysts to obtain biodiesel from various feedstocks. They include zeolites [301], metal oxides and mixed metal oxides [289, 290], supported acids [302, 303], sulphated oxides [41, 304-307], heteropoly compounds [212, 308], sulfonated carbon [309-312] and cation exchange resin [313-315]. In simultaneous esterification and transesterification reactions, Brønsted acid (proton donation property) in solid catalysts is able to esterify FFAs whilst Lewis acid (electron pair acceptor property) is suitable for the transesterification reaction [316]. This indicates that the catalytic activity of solid acid catalysts depends on the accessibility of the reactant to the active sites (Brønsted and Lewis acids) in order to initiate reaction. Solid acid catalyst would also simplify and provide an economic way for pre-treating raw materials containing high FFAs [317]. Owing to the good catalytic properties of solid acid catalysts on refined and non-edible oils, there have been many studies exploring how to increase the concentration of active acid sites, minimise leaching of active acid sites and, reduce the diffusional limitations for producing cheap biodiesel [318, 319]. However, there are limited reports on developed solid acid catalysts for cheap and readily available feedstocks, such as used cooking oil,

without the need for pre-treatment [289]. This has prompted new research to design suitable catalysts for the esterification and transesterification processes.

The most common inorganic solid acid catalyst used for organic synthesis since the 1940s is zeolite [214] because the level of control for zeolite synthesis allows for different crystal structures, surface hydrophobicities, framework of Si/Al ratios, pore sizes, strength of acid sites, exchangeable cations present in their cavities, and their distribution. The ratio of Si/Al in zeolite catalysts, surface hydrophobicity and acid sites highly affect the yield of FAME and conversion of FFAs [320]. Some authors claim that the lowest Si/Al ratio in Al-MCM-41 catalyst gives maximum conversion in palmitic acid esterification reaction [301]. This is because a low Si/Al ratio increases the acidic strength; conversely, a high Si/Al ratio increases hydrophobicity of the zeolite catalyst. On the other hand, it has been found that the small pore size (see Figure 2.19) of zeolite catalysts limits the diffusion of the large molecules, i.e. TG, in the transesterification reaction due to TG access to the active sites being restricted [102]. As a result, the transesterification reaction is only on the external surface of crystals [321] and FFAs absorb inside the pore without mass transfer limitation [322]. Therefore, several studies have reported on the use of zeotypes (silicoaluminophosphates) and modified H-ZSM-5 with larger pores and channels enhancing catalytic activity and selectivity [323, 324].
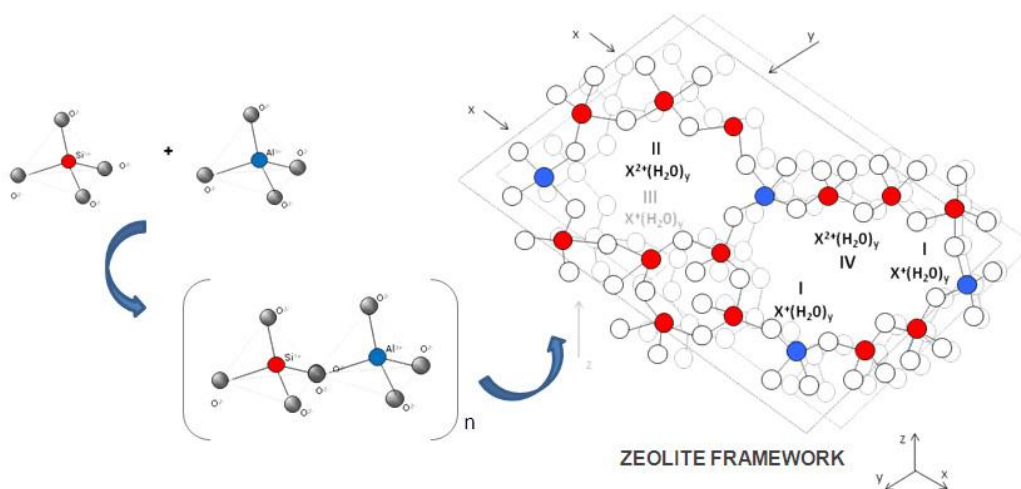
Figure 2.19 Three-dimensional framework zeolite-clinoptilolite structures [322]

Karmee et al. [242] examined the use of Hβ-zeolite, montmorillonite K-10 and ZnO for transesterification of pongamia pinnata oil to form biodiesel. The maximum conversions were

found to be 83, 59 and 47% on ZnO, Hβ-zeolite and montmorillonite K-10, respectively, at optimum conditions of 0.12 wt% catalyst to oil, 10:1 methanol to oil mole ratio, 120 $^\circ$C reaction temperature and 24 h reaction time. Another study by Shu and co-workers [325] reported the effect of β-zeolite with a high Si/Al ratio, containing an intersecting three-dimensional structure of 12-membered ring channels, in biodiesel production from soybean oil. They prepared the modified zeolite catalyst by ion-exchange method in suspension of β-zeolite in lithium nitrate. The conversion of TG was found to be 48.9% under optimum reaction conditions of 500 RPM stirring rate, 14.5:1 mole ratio of methanol to oil, 60 $^\circ$C reaction temperature, 4 h reaction time and 0.011 mass ratio of catalyst to oil loading. The modified zeolite showed higher stability and activity than β-zeolite. This was due to the availability of more external Brønsted acid sites being available for the reactants assigned to Si–OH–La groups and La–OH groups in the modified structure.

Several studies on the cation ion-exchange resin catalysts for the esterification and transesterification have been reported [315, 326-329]. López et al. [330] investigated the catalytic transesterification of triacetin over Nafion® SAC-13 (silica-supported Nafion) and Nafion® NR50 (unsupported Nafion). The schematic diagram of Nafion®SAC-13 (silica-supported Nafion) and Nafion®NR50 (unsupported Nafion) are shown in Figure 2.20. It was reported that for the Nafion®NR50 catalyst (with acid site density 1104±7 µmol/g) the catalytic activity is highly dependent on the accessibility of the reactant to the acid sites; for the Nafion®SAC-13 (with acid site density 144±7 µmol/g) accessibility of reactant molecules into the active sites was unrestricted.
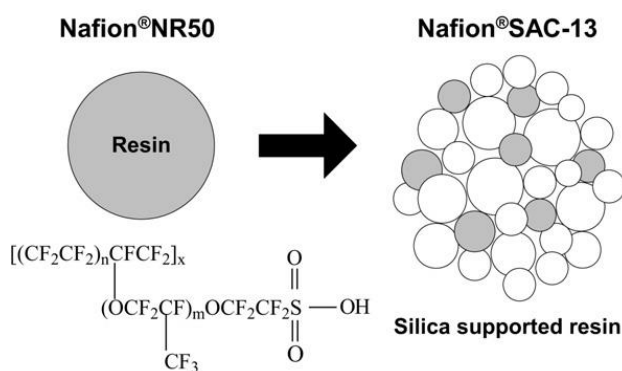
Figure 2.20 Nafion® diagram: m=1, 2 or 3, n = 6-7, and x∼1000 [330]

Most published works on the use of cation ion-exchange resin, which are composed on copolymers of styrene, divinyl-benzene and sulfonic acid groups, has found sulfonated cation exchange resin

for esterification and transesterification reaction to be more effective. For example, Amberlyst 15 and 31 was tested in the esterification of soybean oil/oleic acid. Kouzu et al. [331] reported that the catalytic activity of Amberlyst 31 was higher than Amberlyst 15. This was due to the swelling property (from small pore concerted to macro pores) in the case of Amberlyst 31, which increased the reactant molecules accessibility to the active sites which was sufficient for long chain molecules in TG.

The effect of impurities (i.e. metal ion, water, organic acid, etc.) on the catalytic activity of cation exchange resins Amberlyst A15 and Amberlyst BD20 in the biodiesel production from used cooking oil (UCO)/oleic acid have been investigated recently [315]. The Amberlyst A15 and Amberlyst BD20 resin catalysts have 4.7 and 4.8 meq H^+/g acidity, respectively. It was found the presence of water in feedstock caused deactivation of the resin catalysts because of the formation of ($-H_3O^+$-SO_3^-), but the effect of non-FFAs organic acid enhanced the activity of the resin catalyst on the esterification reaction. Fu et al. [315] believed the presence of Fe^{3+} at high concentration (50-100 ppm) resulting to form a complex ($-(SO_3)_3$-Fe) through cation exchange, as shown in Figure 2.21. The main explanation for this surprising result could be due to the experiment performed at high conversion to determine the changes and they were ignored the experimental error during their analysis. Therefore, the amount of Fe^{3+} impurity in the UCO/oleic acid feedstock did not cause any deactivation of the catalyst or affect on the FFA conversion.
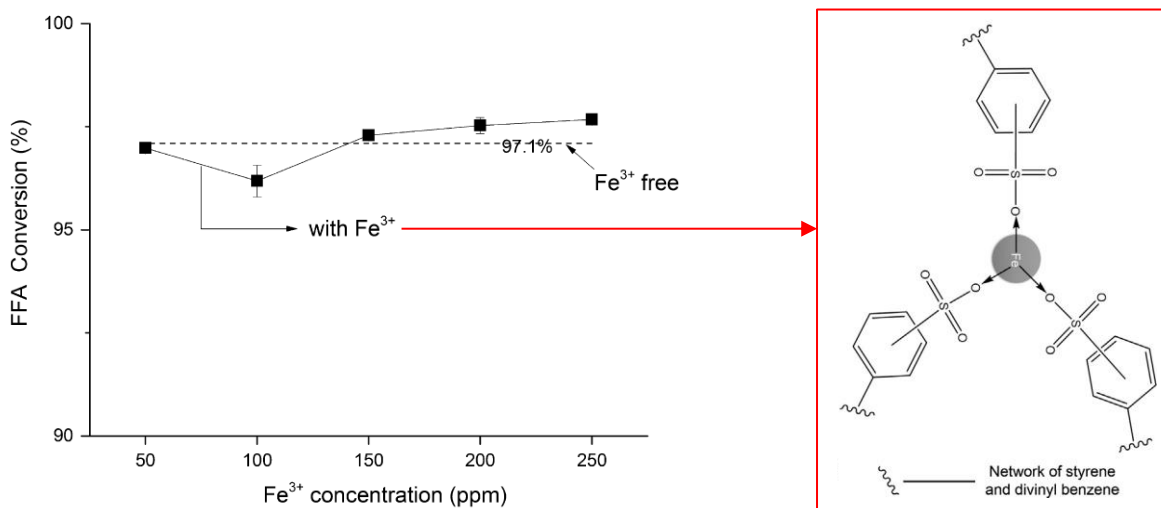
Figure 2.21 The effect of Fe^{3+} loading on the conversion of FFAs [315]

A recent study by Ma and co-workers [329] have investigated the kinetic and catalytic activity of modified cation-exchange resin (macroporous styrene) by $FeCl_3$ on the transesterification of

WCO. The synthesised catalyst shows good activity for FAME production. The FAME yield obtained was 92% under optimum condition of 10:1 methanol to oil mole ratio, 8 wt% of catalyst loading, 90 °C reaction temperature, and 2 h reaction time. The transesterification reaction of WCO over modified resin was a first order reaction controlled by the interfacial chemical reaction diffusion and the catalyst remained almost stable after 9 cycles, reducing FAME yield by 19%. dos Reis and co-workers [332] examined the catalytic activity and selectivity of various ion-exchange resins (Amberlyst 15, Amberlyst 31, Amberlyst 35, and Amberlyst 36) for the transesterification of soybean oil, corn oil, Babassu coconut oil, palm kernel oil and palm oil. They found that the suitability of ion-exchange resin for esterification and transesterification reactions depend mainly on the chain length of fatty acid compositions in biodiesel feedstocks. An increased number of carbon atoms in fatty acid chains resulted in lower conversion to methyl esters owing to the reactant molecules accessibility to the active. The shorter chain of fatty acid chains has better access to the active sites. The low thermal stability of the organic-based resin solid acid catalysts at high temperatures, the cost of catalyst resin and the accessibility of reactant molecules to the active sites inside micro-pores, are all disadvantages in using this type of catalyst for esterification and transesterification reactions.
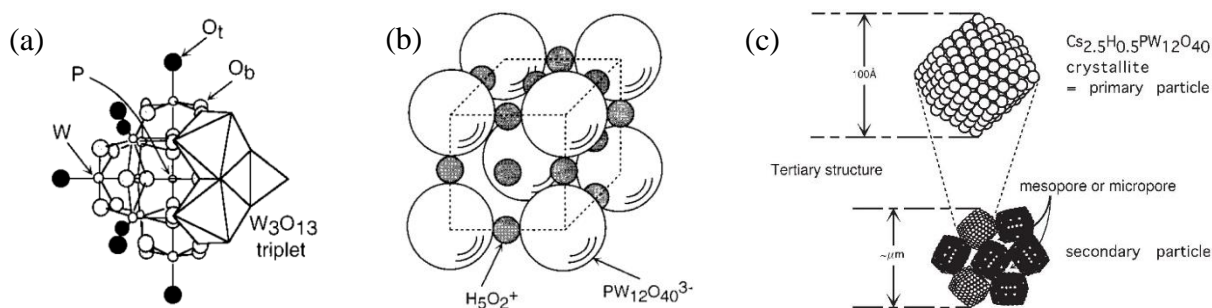
Figure 2.22 (a) Primary (Keggin structure, $PW_{12}O_{40}$), (b) secondary ($H_3PW_{12}O_{40}.6H_2O$) and (c) an example for tertiary ($Pt–Cs_{2.5}H_{0.5}PW_{12}O_{40}$) HPAs structures [333, 334].

Heteropolyacids (HPAs) have attracted a good deal of attention in their practical use for a wide variety of reactions as solid acid catalysts owing to their super acidity properties, easier separation and reusability. The HPAs have been classified into two categories: the primary and the secondary structures as shown in Figure 2.22; later the tertiary (hierarchic) structure of HPAs was recognised [333]. It has been reported that the parent HPAs are not suitable for biodiesel production due to

their low surface area, low number of accessible acidic sites and high solubility in the polar media [40, 102]. Therefore, this class of catalyst is not suitable for synthesis of biodiesel without modifications similar to homogenous acid catalyst.

Different strategies, including Cs^+, K^+, NH_4^+ and Ag^+ ion-exchanged Keggin HPAs; and supporting HPAs, have been used to overcome these limitations during esterification and transesterification reactions [104, 212, 308, 334-336].

Cao and co-workers [337] demonstrated the transesterification of waste frying oil (containing 15.56 wt% FFAs and 0.1 wt% moisture)/palmitic acid over $H_3PW_{12}O_{40}.6H_2O$ catalyst. The catalyst was prepared from heat treatment of $H_3PW_{12}O_{40}.3H_2O$ at 120 °C overnight in air. The catalyst exhibits high catalytic performance at optimum conditions of 65 °C reaction temperature, 70:1 methanol to oil ratio, 0.1 mmol catalyst loading, 300 RPM stirring rate and 14 h reaction time to form 87% of FAME yield for transesterification of frying oil and 97% FAME yield for esterification of palmitic acid.

Verhoef et al. [338] tested MCM-1 supported Keggin-type of HPAs (HPAs: $H_3PW_{12}O_{40}(PW_{12})$ and $H_4SiW_{12}O_{40}(SiW_{12})$) in two different reaction systems (1-propanol and hexanoic acid; acetic acid and 1-butanol) for esterification reaction. They reported that the synthesised catalysts were found to be active in comparison with HPAs due to the high proton sites dispersion of the HPAs. MCM-41 supported PW_{12} shows better catalytic activity than MCM-41 supported SiW_{12}. This is consistent with the difference in acidic strengths, as PW_{12} is slightly stronger than SiW_{12}. It was, however, found that the high dispersion of the HPA on MCM-1 was lost after one reaction cycle. The XRD results revealed the formation of new peaks corresponding to HPA crystals with 10 nm. The new crystals formed from the dissolution of HPAs in the reaction medium (FAME and water). The location of the large crystals confirmed by TEM on the external surface of MCM-41 explained the decrease in activity of the spent catalyst.

Narasimharao et al. [212] examined the effect of a monovalent (Cs^+) external layer on the structure of $Cs_xH_{3-x}PW_{12}O_{40}$ (x=0.9-3) for the esterification of palmitic acid and transesterification of glyceryl tributyrate. The Cs-exchanged HPAs had a remarkable effect on the solubility, average pore size and surface area of the parent HPAs catalyst. The preparation concept of $Cs_xH_{3-x}PW_{12}O_{40}$ and proposed structure of Cs-exchanged HPAs is shown in Figure 2.23. The surface area increased in line with an increase the Cs content from 1.0 m^2/g to 156.3 m^2/g whilst the surface acidity decreased. It was also reported that the catalytic activity increased with Cs content up to x=2.0-2.3

due to the variation of surface area and the total acid sites. A further increase of Cs content leads to a drop in catalytic activity. Low loading of Cs salts on HPAs showed slight dissolution of active sites (loss of Brønsted acid sites) whilst high loading of Cs salts (x=3) revealed the stability in hot methanol after 6 h. The $Cs_xH_{3-x}PW_{12}O_{40}$ (x=2.3) showed the greatest number of accessible surface acid sites with 100% conversion of the palmitic acid at optimum conditions of 6 h reaction time, 1.9 wt% of catalyst loading, 30:1 mole ratio of methanol to oil and 60 ℃ reaction temperature. The catalyst can be re-used for three consecutive cycles with negligible loss of activity and selectivity.
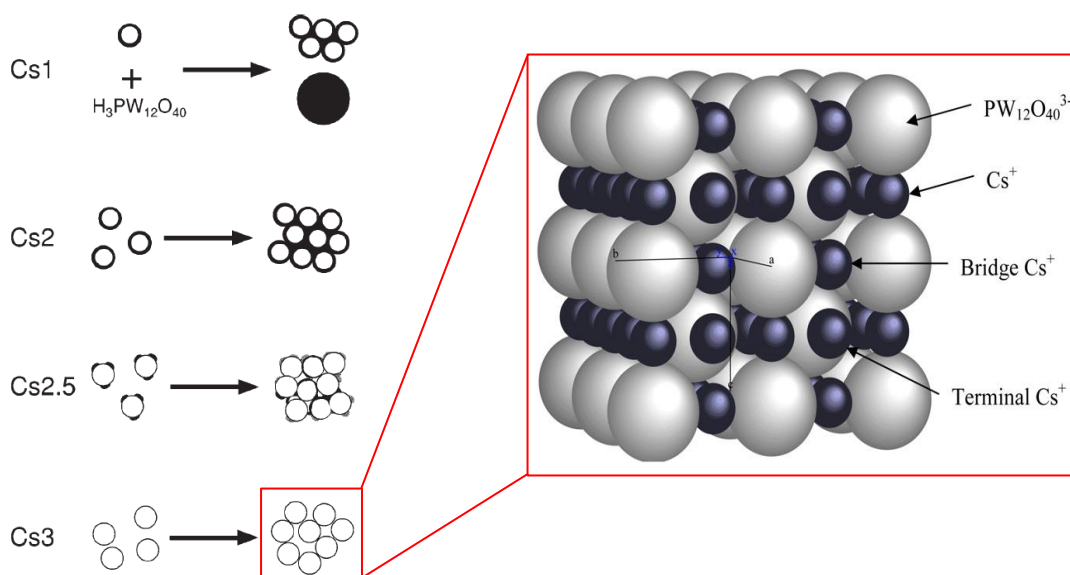
Figure 2.23 The preparation concept of $Cs_xH_{3-x}PW_{12}O_{40}$ and proposed crystal structure model of $Cs_3PW_{12}O_{40}$ [212, 334]

Zhao et al. [336] have recently reported a simple and straightforward route, as shown in Figure 2.24, to design a novel catalyst $(C_6H_{15}O_2N_2)HPW_{12}O_{40}$ with acidic-basic properties for the esterification of palmitic acid and transesterification of TG. The catalyst showed excellent activity with water tolerance and re-usability for up to 6 cycles with no leaching. The activity of the catalyst in the esterification reaction was related to the Brønsted acidity (3.6-4.15 mmol/g) whilst the higher acidity and basicity cooperation are involved in the transesterification reaction. There are a few drawbacks to this type of catalyst: the hydrophobicity of surface and open surroundings, which might block the active sites inside the pore structure; and the chemical stability (decomposition of lysine at 296 ℃).
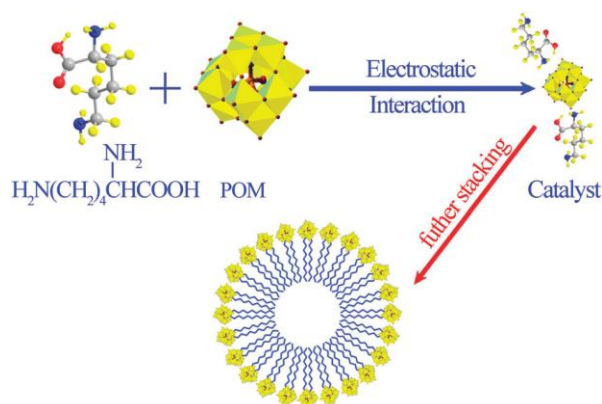
Figure 2.24 Schematic diagram of self-assembly of lysine and HPA to form bifunctional HPAs $[(C_6H_{15}O_2N_2)HPW_{12}O_{40}]$ catalyst [336]

Picolinic acid modified 12-tungstophosphoric acid (PA-HPAs) catalyst has been recently used for the esterification of oleic acid [104]. Based on the potentiometric titration with n-butylamine, the synthesised catalyst has an initial electrode potential (E_i) around 308-322 mV (very strong acid sites). The catalyst displayed a promising solid acid catalyst with 100% conversion of oleic acid at optimum condition of 10:1 mole ratio of methanol to oil, 5 h reaction time, 7 wt% of catalyst loading, and 80 °C. This is because of Brønsted acid sites and high amount of Lewis acid sites can activate the carbonyl group in oleic acid. The catalyst was reused for 4 consecutive cycles after washing with methanol and heat treatment at 110 °C.
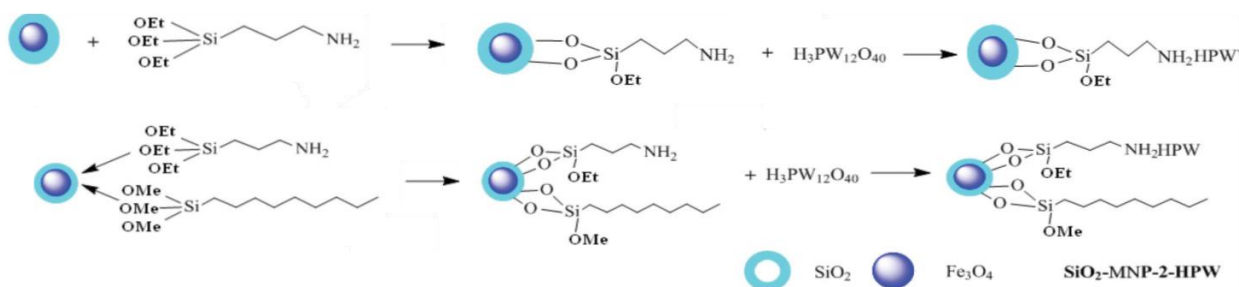
Figure 2.25 Schematic steps of SiO$_2$-MNP-1-HPW and SiO$_2$-MNP-2-HPW preparation [339]

Duan et al. [339] recently designed easily separable HPAs supported on magnetic nanoparticles (see Figure 2.25) with acid content 0.429-0.579 mmol/g for the esterification of palmitic acid. The catalyst exhibited good activity to give 90.2% of conversion with an optimum reaction

performance of 65 °C reaction temperature, 6:1 methanol to oil mole ratio, 8.2 wt% of catalyst loading, and 2 h reaction time. The catalyst was easily separated from the reaction using an external magnet without activity loss and could be used for 5 cycles of esterification. It was, conversely, found that the catalyst limited water tolerant and the structure of HPAs was destroyed after the addition of 1 wt% of water to the feedstock as a result of weak bonding between HPAs and the support magnetic nanoparticles.

Li and co-workers [308] found the double acid sites ($Zn_{1.2}H_{0.6}PW_{12}O_{40}$ nanotubes) catalyst perform effectively in the esterification of palmitic acid and transesterification of WCO containing 26.86 wt% of FFAs and 1 wt% of moisture. The study eliminated the need to treat WCO and afforded maximum conversion (>97.2%) at optimum conditions of 28:1 mole ratio of methanol to oil, 65 °C reaction temperature, 12 h reaction time and 2.5 wt% of catalyst loading. This was due to the synergistic effect of Brønsted and Lewis acid sites with the high surface area of synthesised $Zn_{1.2}H_{0.6}PW_{12}O_{40}$ nanotubes catalyst. The catalyst was re-used for 5 cycles with negligible loss of activity. Zhang et al. [340] also developed a water tolerant catalyst zirconium dodeca tungstophosphate $Zr_{0.7}H_{0.2}PW_{12}O_{40}$ nanotube (ZrHPW) with double acid sites for transesterification of WCO containing 26.89 wt% of FFA and 1 wt% of moisture. The synthesised ZrHPW catalyst has a high surface area of 256 m^2/g and displayed a remarkable enhancement in the activity (98.9% of conversion) in comparison with parent HPAs as catalyst under the optimum conditions of 20:1 mole ratio of methanol to oil, 65 °C reaction temperature, 2.1 wt of catalyst loading and 8 h reaction time. The high catalytic activity owes to the high acidity (double acidic sites inside and outside the channel tube) and dispersion of active sites on the high surface of the catalyst. The catalyst was reused for 6 cycles with a slight reduction of the conversion.

Several research efforts have been carried out on the use of metal oxide catalysts to obtain biodiesel. All in all this class of solid acid catalyst is not highly water tolerant and, in some cases, low thermal stability has been reported. Therefore, more research needs to be carried out to design better water resistant catalysts for esterification and transesterification reactions from cheap feedstocks.

Carbon based materials, including carbon nanofibers [341]; carbon nanotubes [310, 342, 343]; biochar [344]; amorphous carbon [345]; graphene oxide [299]; sugar [346, 347]; and waste [86, 295], have also grown in significance as solid acid catalysts in biodiesel production from different feedstocks. These types of catalyst are modified by sulfonic acid functional groups on the carbon

support as active sites. Stellwagen and co-workers [341] have developed a solid acid catalyst from the functionalisation of carbon nanofibers (CNF) by aryl sulfonic acid groups using selective diazonium coupling reaction for the transesterification of triolein. They found that the maximum total acid sites (sulfonic acid groups) load on the CNF could be 0.62 mmol/g with high reactant molecule accessibility to the $Ar-SO_3H$ sites. The catalytic performance of the $CNF-Ar-SO_3H$ catalyst reached 72% of methyl oleate yield after 4 h at 120 ^{o}C, 1:10 of triolein to methanol mole ratio, and 0.75 g of catalyst. The catalyst, after simple treatment, could be re-used for 4 cycles with slight deactivation based on the titration of acid sites result.

Sulfonic acid functionalised carbon nanotubes (CNT) have also been tested in biodiesel production from different feedstocks including cottonseed oil, palm fatty acid distillate, bio-oil, and trilaurin. Shuit et al. [342] have recently examined the effect of sulfonation routes, including in *situ* polymerisation of poly(sodium-4-styrene sulphonate); in *situ* polymerisation of acetic anhydride and sulfuric acid; thermal decomposition of ammonium sulphate; and thermal treatment with concentrated sulphuric acid, on the multi-walled CNT for the esterification of palm fatty acid distillate to form biodiesel. It was reported that the acid density sites of synthesised catalysts was between 0.016 and 0.061 mmol/g. The sulfonated multi-walled CNT through in *situ* polymerisation of 4-styrene sulfonate gave 93.4% of FAME yield after 3 h at 170 ^{o}C with 20:1 mole ratio of methanol to oil and 2 wt% of catalyst loading, due to the high acid density sites loading on the multi-walled CNT. Another example of sulfonation of multi-walled CNT by thermal treatment at 210 ^{o}C with concentrated sulphuric acid is reported by Shu and co-workers [348]. The synthesised catalyst had a high acid site $-SO_3H$ density (2.04 mmol/g) loading, surface area (41.27 m^2/g) and average pore size (43.90 nm). The large pore of catalyst allows better accessibility of the FFAs and TG for contact with active sites. The highest conversion of cottonseed oil was 89.9% under optimised reaction conditions of 240 ^{o}C, 1.5 wt% catalyst loading, 240 RPM mixing rate, 2 h reaction time, and 20:1 mole ratio of methanol to oil. The catalytic activity of the spent catalyst decreased after a few runs because of sulfonic acid leaching and the swelling effect of the catalyst. Guan et al. [310] have recently reported FAME yield of 97.8% from the transesterification of trilaurin in ethanol under reaction conditions of 150 ^{o}C reaction temperature, 3.7 wt% catalyst loading, 1:20 trilaurin to ethanol mass ratio, and 1 h reaction time. However, the spent catalyst lost around 13% of its activity after 1 h of reaction in the first re-used cycle. This was despite the loss of catalyst surface area and agglomeration of CNTs.

Amorphous carbon bearing SO_3H, COOH and OH groups as a solid acid catalyst was tested for its efficiency and stability for esterification of oleic acid [345]. The catalyst had a high acidity of $H_0=$-8 to -11 with low surface area (2 m^2/g). The low surface area was related to the large amount of hydrophilic groups into the bulk of the catalyst. The results exhibited high catalytic esterification activity of oleic acid with 99.5% conversion. Dehkhoda et al. [344] tested three types of sulfonated biochar as solid acid catalysts for transesterification of canola oil. The catalyst has been prepared via concentrated sulfuric acid and fuming sulfuric acid. The total acid site loading was found to be 36.3-83.4 μmol/g and all catalysts performed at 65 °C for 24 h, 5 wt% of catalyst loading with 15:1 methanol to oil mole ratio. The acidity of prepared catalysts attributed entirely to the Brønsted acid sites showed good catalytic activity for feedstocks containing low amount of FFAs.

Ji et al. [349] used an effective method to produce a water-tolerant solid acid catalyst as shown in Figure 2.26. Mahto and co-workers [299] have also demonstrated the suitability of single step sulfonation of graphene oxide as a solid acid catalyst for the esterification of oleic acid. The high surface area, ample amount of sulfonic acid groups, π-π stacking interaction and cavities between thin layers, facilitate adsorption of reactants of the solid acid catalyst to convert 97.6% of oleic acid after 4 h at 100 °C with 0.1972 mole of methanol in 2 mL of oil and 5 wt% of catalyst loading. The re-usability of the catalyst was found to decline in the first cycle because of the blockage of –SO_3H groups.
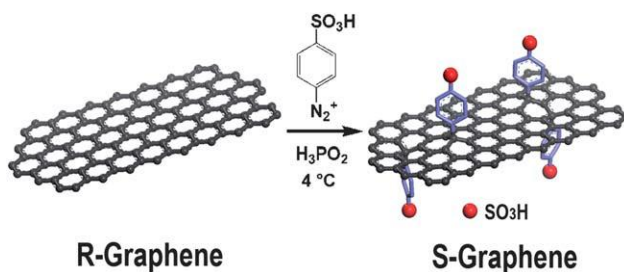
Figure 2.26 Preparation of sulphated graphene oxide [349]. Where R-graphene is reduced graphene oxide and S-graphene is sulfonated graphene oxide.

Another important group of carbon based catalysts used in biodiesel production is that formed from sugar. Fu et al. [346] have recently synthesised solid acid catalyst from β-cyclodexrins via incomplete hydrothermal carbonization followed by sulfonation process. The catalyst tested for simultaneous esterification and transesterification of triolein containing 50.2 wt% of oleic acid. The catalytic activity was found to reach 80% of FAME yield after 12 h reaction time at 85 °C

with 30:1 methanol to oil mole ratio and 5 wt % of catalyst. Recycling of spent catalyst showed a gradual decline in the conversion to 79% after six cycles. They found the main reason for the deactivation of the catalyst was restricted access of the active sites (hydrophobic groups of the polyaromatic carbon sheets by the formation of a water layer during the washing process or water as by-product from the reaction).

Sulfonated carbonaceous materials from waste of vegetable oil and microalgae residue have also been used as solid acid catalysts in biodiesel production. Fu et al. [295] have synthesised an inexpensive and stable solid catalyst with a high density of active sites (4.25 mmol/g) from microalgae residue via in *situ* hydrothermal carbonisation with sulfuric acid. The activity of the synthesised catalyst was tested for the esterification of oleic acid and transesterification of triolein. The catalyst displayed good stability after 6 cycles with high catalytic activity even though it has a low surface area of below 1 m^2/g. It was concluded that the highly catalytic activity attributed to the high density of acidic –SO$_3$H groups, the hydrophilic –COOH and –OH groups and strong affinity between the hydrophilic parts of the reactant molecules and the –OH groups bonded to carbon catalyst matrix. The same conclusion was extracted from the study of Shu et al. [86] who reported a way to prepare an inexpensive solid acid catalyst based on carbon from sulfonation of vegetable oil asphalt. The resulting catalyst was tested in the simultaneous esterification and transesterification of cottonseed oil containing 50% of oleic acid. They achieved 80.5 and 94.8 wt% of FFAs and TG conversions, respectively, when the catalyst performed in an autoclave under optimum conditions of 220 ^{o}C reaction temperature, 4.5 h reaction time, 0.2% of catalyst to oil mass ratio and 16.8 molar ratio of methanol to oil. The main drawbacks of this type of solid acid catalyst are deactivation, thermal instability, a large amounts of methanol to oil ratio, high temperature and long reaction time in most cases are required.

Clays have been extensively used for a long time as good solid acid candidates for different catalytic processes. This type of catalyst consists of layered SiO$_4$ tetrahedral (silicates or aluminosilicates) and MO$_6$ octahedral – where M is Fe^{2+}, Fe^{3+}, Mg^{2+}, Al^{3+}, etc. – form two-dimensional sheets as shown in Figure 2.27. Some types of clay, amorphous montmorillonite, have swelling effect properties with the addition of water penetrating the interlayer molecular spaces to produce Lewis protons [350]. However, some reports claimed that clays exhibit Brønsted and Lewis acidic properties as a result of the multivalent metal cations compositions. This mainly depends on the electronegativity of interlamellar exchangeable cations within the catalyst

framework [102, 351, 352]. Kanda et al. [353] have recently studied the esterification kinetic reaction for various fatty acids with different chain lengths and unsaturation over acidic montmorillonite K10 catalyst. This catalyst exhibits a high surface area (268.4 m^2/g) with a large number of Brønsted and Lewis acid sites (309 mV). The catalyst showed good catalytic activity for the esterification of short chain fatty acids with ethanol, but the great affinity towards impurities led to the deactivation of clay catalyst during the recycling process. The thermal stability limitation of clays caused a dramatic decrease of the surface area as a result of the layered structure of clays collapsing because of loss of water molecules. This is the main concern clays in biodiesel applications.
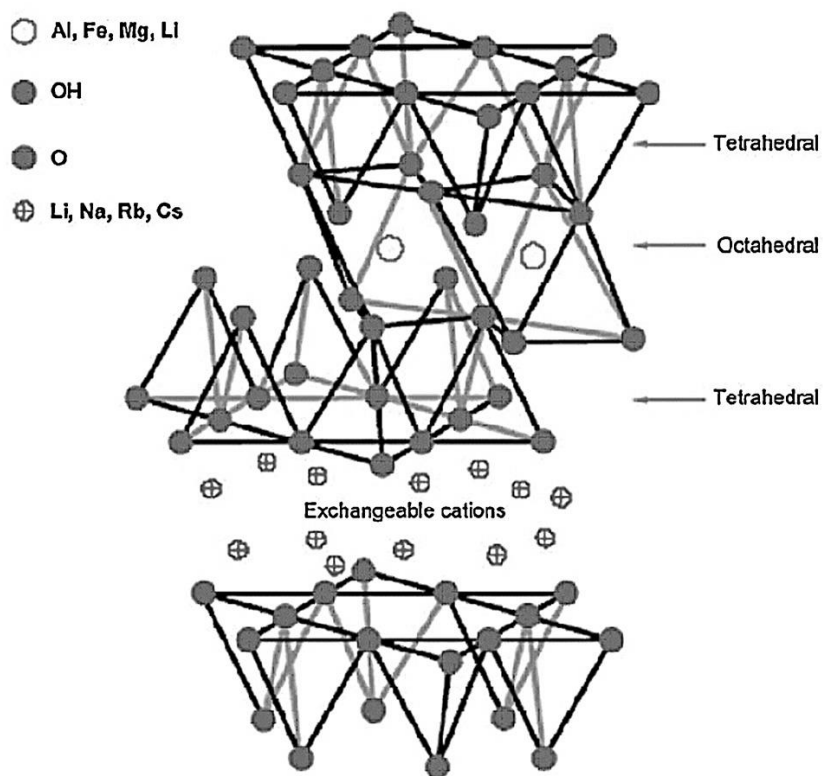
Figure 2.27 Two-dimensional structure of 2:1 layered silicate [102]

Another promising field in solid acid catalysis is the use of mixed oxides for esterification and transesterification reactions. Madhuvilakku and co-workers [354] have recently designed a mixed metal oxide (ZnO-TiO$_2$) catalyst for biodiesel production from palm oil. They reported that the synthesised mixed oxide catalyst did not form any specific structure with exhibiting good catalytic activity compared to ZnO catalyst. The mixed oxide (ZnO-TiO$_2$) catalyst displayed catalytic

activity at optimum reaction conditions of 60 °C reaction temperature, 5 h reaction time, 6:1 mole ratio of methanol to oil, and 200 mg catalyst loading to reach 92% of FAME yield and 98% of conversion. Jacobson et al. [289] reported the catalytic activity of zinc stearate/SiO$_2$, zinc ethanoate/SiO$_2$, 12-tungesten phosphoric acid/ZrO$_2$, MoO$_3$/ZrO$_2$, WO$_3$/ZrO$_2$, and WO$_3$/ZrO$_2$-Al$_2$O$_3$ solid acid catalysts for the simultaneous esterification and transesterification from waste cooking oil containing 15 wt% of FFAs. It was found that zinc stearate on the SiO$_2$ support catalyst was the most effective catalyst with 98% of FAME yield at optimum conditions of 18:1 methanol to oil mole ratio, 200 °C reaction temperature, 3 wt% of catalyst concentration, 600 RPM stirring rate and 600 psig pressure with nitrogen gas. Recycling tests of this catalyst revealed catalytic activity of this solid acid catalyst without deactivation after four consecutive runs.

The acidity of metal oxides can be much enhanced after modification with sulphate (SO_4^{2-}) groups and this has attracted academic and industrial interest since 1976. The common synthetic route for the preparation of sulphated metal oxide is: (step 1) preparation of sol-gel metal oxide; (step 2) introduction of sulphate ions by exposure the get with sulfuric acid, chlorosulfonic acid, or ammonium sulfate; and (step 3) calcination of the sulphated gel at high temperature. The structure of the solid super acidic catalyst is the combination of SO_4^{2-} groups with metal (metal oxide, binary mixed metal oxides or ternary metal oxides) oxide. The general structures for sulphated metal oxides are presented in Figure 2.28 [88].
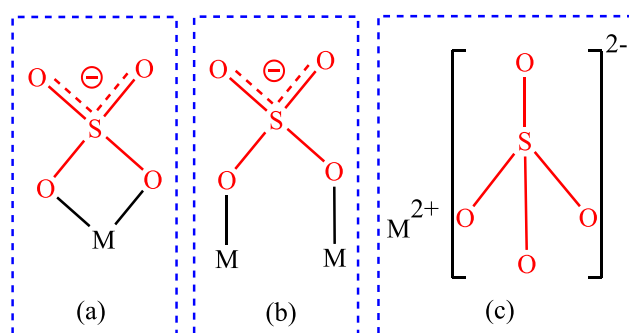
Figure 2.28 Sulphated metal oxide structure (a) coordinated (chelated), (b) coordinated (bridge), and (c) free sulphate (salt)

An examples of sulphated metal oxides, SO_4^{2-}/ZrO$_2$ [93, 95, 290, 355-358], SO_4^{2-}/SnO$_2$ [304, 359, 360], SO_4^{2-}/TiO$_2$ [88, 361-365], SrO/SO_4^{2-}-ZrO$_2$ [305], SO_4^{2-}/ZrO$_2$-TiO$_2$/La$^+$ [307, 366], SO_4^{2-}/SiO$_2$-TiO$_2$ [291, 294, 367-369], SO_4^{2-}/Nb$_2$O$_5$ [370], SO_4^{2-}/V$_2$O$_5$ [155], SO_4^{2-}/Fe$_2$O$_3$-TiO$_2$

[371-373], $S_2O_8^{2-}$/ZrO$_2$-TiO$_2$-Fe$_3$O$_4$ [374], SO_4^{2-}/ZrO$_2$-B$_2$O$_5$-Fe$_2$O$_3$ [375], and Fe$_2$O$_3$-MnO-SO_4^{2-}/ZrO$_2$ [101] have been acclaimed to be an interesting solid catalysts due to their exhibit as super acidic. Among these, sulphated zirconium oxide ($H_0 \geq$-14.52) and sulphated titanium oxide ($H_0 \leq$-14.52) are well-known effective solid super acidic catalysts in esterification and transesterification processes in the preparation of biodiesel fuel.

Lopez et al. [290] compared the catalytic activities of commercial sulphated zirconia with calcined amorphous mixed oxides at between 400 and 900 ^{o}C for the esterification of caprylic/palmitic acid and transesterification of tricaprylin. They found that sulphated zirconia was the most effective catalyst of those evaluated. The spent catalyst was regenerated by re-impregnation with sulfuric acid followed by calcination at 500 ^{o}C. It was reported that leaching of sulphate ions from the catalyst in the polar media was dependent on the percentage of sulphur loading, calcination temperature, reaction media and reaction temperature. Although leaching of sulphate ions in water as a by-product from esterification reaction form HSO$_4^-$ or H$_2$SO$_4$ which increases rate of reaction, it leads to interference of homogenous and heterogeneous catalytic activity, poisoning of active sites and pore blockage of the sulphated zirconia catalyst were occurred, which later affects the activity of the solid catalyst. The same finding has been drawn by other researchers [355, 376]. More recently, Raia et al. [356] have studied the activity of SO_4^{2-}/ZrO$_2$ catalyst in the simultaneous esterification and transesterification for Jatropha curcas L. oil containing 14.29% of FFAs with ethanol. The catalyst was prepared by impregnation method followed by calcination at 550 ^{o}C for 3 h. Despite the high acidity of catalysts, it showed low activity for esterification of FFAs and transesterification of TG in jatropha curcas L. oil after 8 h at 150 ^{o}C, 10 wt% of catalyst and 10:1 mole ratio of ethanol to oil with 800 RPM mixing rate. A possible mechanism of esterification and transesterification for non-edible oil is shown in Figure 2.29. The authors concluded that SO_4^{2-}/ZrO$_2$ catalyst was more effective in the esterification reaction rather than transesterification of TG. However, Garcia et al. [376] reported the preparation of zirconium oxide and the sulfonating process have a significant influence on the activity of prepared SO_4^{2-}/ZrO$_2$ catalysts.

Several studies have suggested different ways to overcome the stability of sulphate ions in the zirconia. Nayebzadeh et al. [305] enhanced the reusability and activity of sulphated zirconia catalyst in the esterification of oleic acid by doping the catalyst with SrO. The sulphated zirconia was prepared by solvent free method followed by calcination for 5 h at 500 ^{o}C. The authors

demonstrated that the loading of SrO from 15 to 25 % increased the conversion of oleic acid from 88.94 to 94.88% despite the low surface area of the catalysts (1.8-6.14 m^2/g).
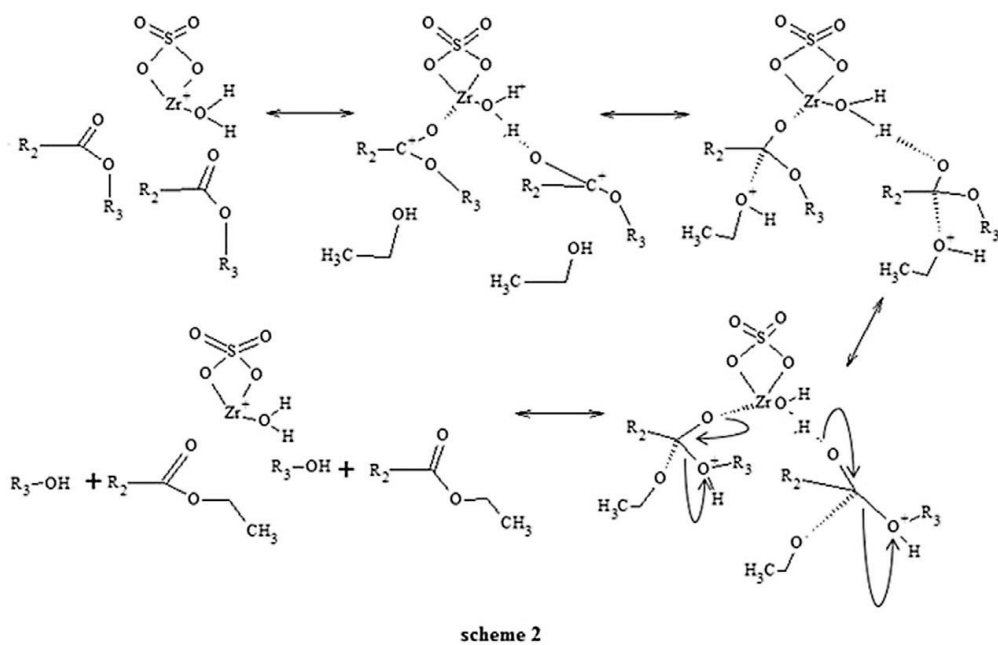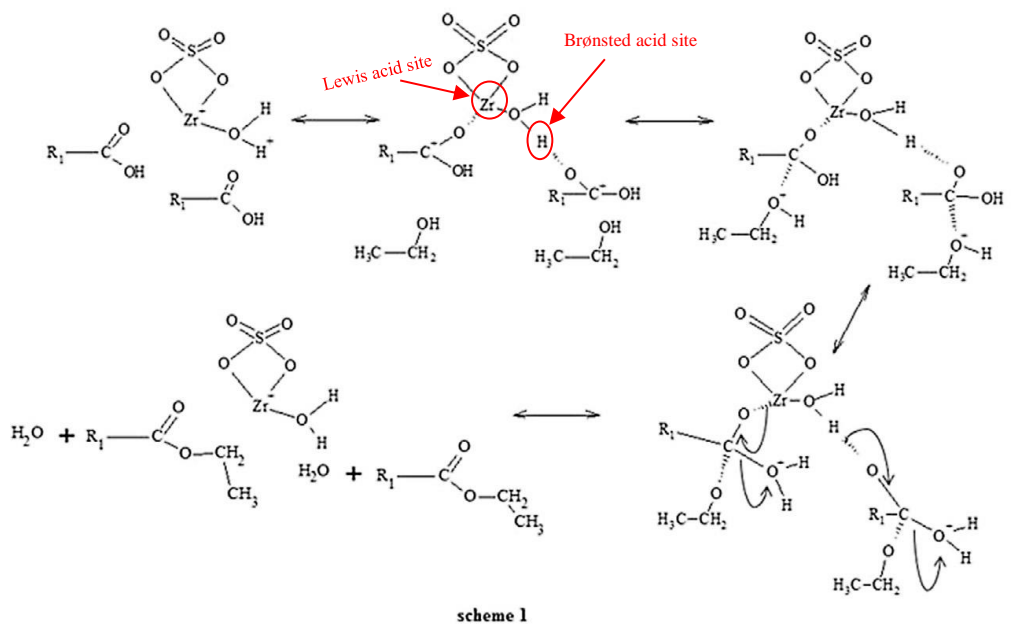
Figure 2.29 Proposed mechanism of esterification of FFAs (scheme 1) and transesterification of TG (scheme 2) reactions [356]

The reason for this was increase in acidity of the catalysts from 4.5 to 6.8 mmol NaOH/g and amphoteric property of zirconia with the addition of SrO. A further increase of SrO loading by 5%

leads to a decrease in conversion by 69.43%. This was explained by phase transformation of catalyst from tetragonal to monoclinic phase and decreasing the acidity of catalyst to 2.8 mmol NaOH/g. High loading (30%) of SrO on the SO_4^{2-}/ZrO$_2$ catalyst would cause the formation of a new phase (SrZrO$_3$) with 65.6% of monoclinic phase. The catalyst showed good stability for up to 5 cycles in the esterification of oleic acid system.

de Almeida and co-workers [362] studied the effect of different sulphate loading (5, 10 and 20%) on titania as the super acidic catalyst for the transesterification of soybean/Castrol oils. This catalyst was synthesised by single step sol-gel method and followed by calcination at 300 ºC for 4 h. The catalyst exhibited good thermal stability (400-700 ºC) with high surface area in the range of 193-266 m^2/g. However, the synthesised catalysts with 5 and 10% of sulphur loading were performed low catalytic activities. In the case of high loading (20%), almost no catalytic performance was reported [362]. It was also reported that the ratio of Brønsted to Lewis acid (I_B/I_L) was higher with lower loading (5%) of sulphate ions on the titania. This indicated the super acidic property by forming more Brønsted acid sites in the SO_4^{2-}/TiO$_2$ catalyst. The acidity of sulphated metal oxides increases with the presence of neighbouring strong Lewis acid sites and superior sulphate content. The strength of these Lewis acid sites is due to the inductive effect exerted by the sulfate on the metal cation, which becomes more electron deficient. The acidity also depend on the degree of hydration, preparation method and calcination temperature for the sulphated metal oxides. For example, low sulphur loading leads to form a bond chelating structure whilst high loading between metal and oxygen causes the formation of polynuclear sulfates with a higher proportion of Brønsted acid sites compared to Lewis sites as presented in Figure 2.30 [94].
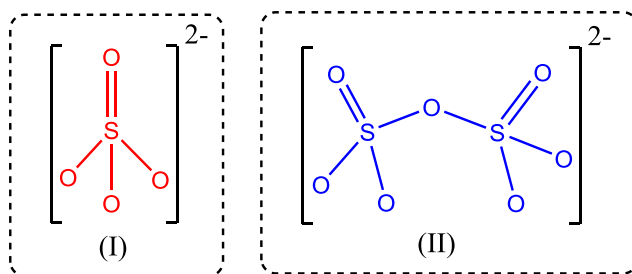
Figure 2.30 Structure of (I) low sulphur loading and (II) high sulphur loading on the metal oxides

According to the definition of Brønsted and Lewis acidity, a solid acid shows a tendency to donate a proton and to accept an electron pair, respectively. Whereas, super acidity is defined as an acid

whose acidic strength (acidity) is stronger than that of 100% of sulfuric acid which has a Hammett acidity function of -12 [377]. The acidic strength is normally determined by Hammett acidity function using organic indicators to study the catalytic activity of a proper model reaction [378]. Ropero-Vega and co-workers [364] compared the catalytic activity of SO_4^{2-}/TiO_2 catalyst synthesised using different sulfonating agents [(H_2SO_4 and $(NH_4)_2SO_4$] for esterification of oleic/linoleic acids with ethanol. All prepared catalysts were shown to have Brønsted and Lewis acid sites by the formation of pyridinium ions. The authors found the lowest effective catalyst was the one prepared with sulfuric acid precursors which had a low loading of sulphur. This acid strength was not enough to carry out the esterification of oleic/linoleic acids. Conversely, the SO_4^{2-}/TiO_2 catalyst synthesised with ammonium sulphate had higher Brønsted acidity, which led to the highest activity with 82.2% conversion after 3 h at 80 °C with 10:1 ethanol to FFA mole ratio and 2 wt% of catalyst loading. It was concluded that preparation and sulfonating methods are important for preparing sulphated titania for the esterification reaction. In a different study, Zhao et al. [365] have recently synthesised a high surface area sulphated nano-titania for esterification of acetic acid with n-butanol. The TiO_2 with exposed [101] support was prepared by a one-step hydrothermal method without any template followed by sulfonation using impregnation method and then calcination at 450 °C to form a super acidic catalyst. The authors postulated that this novel method allowed the synthesis of a mesoporous SO_4^{2-}/TiO_2 with sulphate content of 793.8 μmol/g. The XRD and Raman spectroscopy results for this catalyst showed no extra characteristic peaks corresponding to the sulphate groups. However, FT-IR showed an extra four peaks between 900 and 1230 cm^{-1} attributed to the bidentate sulphate ions coordinated to Ti^{4+}. The NH_3-TPD analysis showed two peaks in the range of 350-600 °C ammonia desorption profile and 650-800 °C formation of acid sites with super acidic nature which indicated the bidentate covalent nature of SO_4^{2-} linked to Ti^{4+}. The DRIFT-pyridine also detected the presence of both Brønsted and Lewis acid sites. The pyridine adsorbed onto Brønsted acid sites exhibited two bands at 1640 and 1539 cm^{-1} whilst the band at 1440 cm^{-1} was attributed to that coordinatively bound to Lewis acid sites. Optimal reaction conditions of 120 °C reaction temperature, 1.2 mole ratio of n-butanol to acetic acid, 0.18 g of catalyst loading, and 2.5 h reaction time, enabled a 92.2% of butyl acetate yield. The reusability of the catalyst was tested through four consecutive runs. After four catalytic runs a significant fall in the yield to 52.1% was evident. This was due to the adsorption of water on the surface of the catalyst and the deposit of butyl acetate molecules which inhibited the contact

between reactant molecules and the active sites. However, soaking of the spent catalyst in sulfuric acid followed by the calcination could help to regenerate activity.

Several other sulphated metal oxides have been tested in the esterification and transesterification processes for their activities and stabilities. Sulphated titania-silica nanomaterial has been used as a solid acid catalyst for the esterification of acetic acid with glycerine [367]. The catalyst was prepared by sol-gel method and then calcined at 500 $^{\circ}$C for 1 h. The sulphate ions were introduced to the TiO$_2$-SiO$_2$ support by impregnation method and followed by re-calcination at 400 $^{\circ}$C for 3 h. This catalyst (SO$_4^{2-}$/SiO$_2$-TiO$_2$) showed a high surface area 550 m^2/g and super acidity (H$_0$≤12.7). The super acidity corresponded to the nature of S=O from sulphate ions coordinated to the TiO$_2$-SiO$_2$. The catalyst exhibited good catalytic activity with 91.4% of conversion under mild conditions. The combination of TiO$_2$ and SiO$_2$ generated stronger acid sites compared to separate metal oxides. It was concluded that the catalytic activity depends on the percentage of TiO$_2$; sulphate loading; calcination temperature for the final gel; and interaction between sulphate ions and TiO$_2$ in the support. Embong and co-workers [368] have also synthesised the SO$_4^{2-}$/SiO$_2$-TiO$_2$ super acidic catalyst from a cheap and available silica source. The catalyst was tested for the transesterification of decanter cake and found to have good catalytic performance (91% of FAME yield after 5 h at 120 $^{\circ}$C with 15:1 mole ratio of methanol to oil and 13 wt% of catalyst to oil). In a different study similar activity reported for transesterification of waste soybean oil using the SO$_4^{2-}$/SiO$_2$-TiO$_2$ catalyst [294]. The authors reported that the catalyst showed good catalytic activity (93.8%) on the first run and then the catalytic activity drastically decreased to 21% of conversion. This was possibly due to the poisoning of the active site and leaching of sulphate ions. The TGA results revealed a weight loss of 20% from 140 to 380 $^{\circ}$C for fresh catalyst.

Other potential solid acid catalysts that have been investigated were sulphated trinary metal oxides to improve the stability and activity of the solid acid catalyst in cheap feedstocks. Li and co-workers [307] conducted a study on the performance of SO$_4^{2-}$/ZrO$_2$-TiO$_2$/La$^+$ in the esterification and transesterification of acid oil (~60% of FFAs). The support was prepared by precipitation method followed by sulphate ion impregnation. The conversion efficiency was found to be 97.8% under the conditions of the catalyst amount of 10 wt%, 80 $^{\circ}$C, 2 mL of methanol/g of oil, and 5 h. The catalyst was reused for five consecutive cycles without any treatment of the spent catalyst and enabled a conversion of 93.6%. The impregnation of lanthanum (La$^+$) to the ZrO$_2$-TiO$_2$ improved the catalytic activity and stability of sulphated zirconia-titania. This was due to loading of La$^+$

changing (i) the strength interaction of sulphate ions with zirconia-titania support and (ii) the chemical state of exterior atoms. However, loading of La^+ above 0.1 wt% would lead to a reduction of the number of SO_4^{2-} linked to the surface of ZrO_2-TiO_2 support.

Studies from several authors [101, 374, 375] showed that the catalytic activity of magnetic sulphated ternary metal oxides could be improved by fast separation of solid super acidic catalysts from the product and by-products. Guan and co-workers [375] proposed super magnetic sulphated ternary metal oxides as an alternative way for fast catalyst separation from the reaction and low energy consumption. The uniform and highly dispersed iron oxide nanoparticles were prepared by co-precipitation method followed by growing zirconia on the surface of iron oxide nanoparticles whilst the introduction of boron oxide into the solution was to inhibit the nucleation and grain growth of zirconia by delaying the phase transformation of zirconia from tetragonal to monoclinic. The catalyst has the potential to overcome the limitation for separating solid acid catalysts from the reaction products and by-products. The acidity of synthesised catalyst displayed stronger (H_0<-13.8) than 100% sulfuric acid (H_0=-12). The activity of this catalyst was tested at different calcination temperatures (400-900 ^oC) for the esterification of acetic acid with n-butanol. It was reported that a yield from 96.73 to 98.20% formed under optimum conditions of 100 ^oC reaction temperature, 4 h reaction time, 850 RPM mixing rate, and 1 atm nitrogen pressure.

Wu et al. [374] have recently designed a super magnetic polysulphated trinary metal oxides catalyst for the transesterification of cottonseeds with methyl acetate. The core was made from iron oxide and prepared by co-precipitation method. Titania and zirconia was introduced to the iron oxide core by another co-precipitation with different mole ratios of Zr/Ti/Fe, followed by impregnation of sulphate ions from $(NH_4)_2S_2O_8$. The final gel was calcined at 550, 650 and 750 ^oC for 3 h. The synthesised catalysts showed super acidity (155.3±0.9 − 598.6±1.3 µmol/g) with polysulphate ions coordinated to ZrO_2-TiO_2-Fe_3O_4 support. It was found that SO_4^{2-}/ZrO_2-TiO_2-Fe_3O_4 catalyst calcined at 550 ^oC enabling a FAME yield of 98.5% after 10.8 h at 50 ^oC with 21.3 wt% of catalyst and 13.8 mL of methyl acetate per g of seed. The effects were observed of different mole ratios of Zr/Ti and calcination temperatures on the sulphated trinary metal oxides in the transesterification reaction. The acidity of the catalyst increased with the addition of an appreciable amount of titania (3:1 mole ratio of Zr:Ti) into the catalyst texture due to the formation of Zr-O-Ti units during the calcination . This resulted into more sulphur species being adsorbed on the surface and inhibit the zirconia grain growth. As a result, the number of Lewis acid sites increased

which enhanced the catalytic activity of the catalyst. The catalyst was re-used for 8 cycles with a slight decrease in activity.

A bifunctional magnetic sulphated ternary metal oxide catalyst has recently been designed by Alhassan and co-workers [101]. The catalyst [Fe_2O_3-MnO-SO_4^{2-}/ZrO_2] was prepared via impregnation method followed by calcination at 600 $^{\circ}$C for 3 h. This catalyst performed good catalytic activity (96.5 ± 0.02 % of FAME yield) for transesterification of WCO under optimum conditions of 180 $^{\circ}$C reaction temperature, 20:1 mole ratio of methanol to oil, 3 wt% of catalyst loading, and 600 RPM stirring rate. Loss of catalytic activity occurred after 6 re-runs of the spent catalyst because of pore blockage and sulphur leaching. Therefore, the spent catalyst has to be re-impregnated with sulfuric acid followed by re-calcination of the gel. All in all, the catalytic activity of sulphated metal oxide depends mainly on the precursors, type of sulfonating agent, calcination temperature, amount of sulphate content, and crystallinity of the catalyst. However, low activity at lower temperatures, water sensitivity, leaching of active sites, low surface area, and poor porosity are the main drawbacks of sulphated metal oxides. Therefore, more research is needed to design a better catalyst for biodiesel production from cheap raw materials.

Mesoporous solid acid catalysts have attracted attention in the past 20 years in biodiesel production research because of their high surface area, large pore sizes and that their good accessibility lets reactants diffuse into the interior of the catalyst's acid sites (i.e. TG, long chain fatty acids, etc.) to the active sites. Since the discovery of porous materials in the early 1990s, different methods have been involved in the designing and development of such materials with excellent texture properties, i.e. pore size, stability, active sites, to improve their performance in various reactions. The pore size can range from 15 to 300 Å based on the synthesis way and interaction between precursor and template particles [379]. A wide range of mesoporous materials have been synthesised recently and according to IUPAC can be classified as ordered and non-ordered [380]. Among them, ordered mesoporous carbon and ordered mesoporous silicate have been mostly studied due to their high surface area, large pore volume, uniform pore-size distribution, controllable wall composition, good mass transfer properties and high thermal and mechanical stabilities. Their large pore sizes generally facilitate the reactant molecules, i.e. TG (5.8 nm), to penetrate into the pore channels and contact the active sites [381, 382]. Sol-gel, polymeric precursor, microwave and hydrothermal are some of the important synthetic processes for fabricating mesoporous materials [383]. Mesostructured solid acid catalysts can be prepared via

grafting methods (post-synthesis procedure) and co-condensation reactions (direct synthesis). Direct synthesis is the co-condensation process of siloxane (i.e. tetraethyl orthosilicate, TEOS; or tetramethyl orthosilicate, TMOS) and organosiloxane (i.e. mercaptopropyltrimethoxysilane, MPTMS) precursors in the presence of structure-agent template whilst post-synthesis is the surface modification process of silica with organic precursors (i.e. 3-mercaptopropyltrimethoxysilane, MPTMS) as shown in Figure 2.31. An example is propyl sulfonic acid modified mesostructured material as a solid acid catalyst prepared by post oxidation route [379].
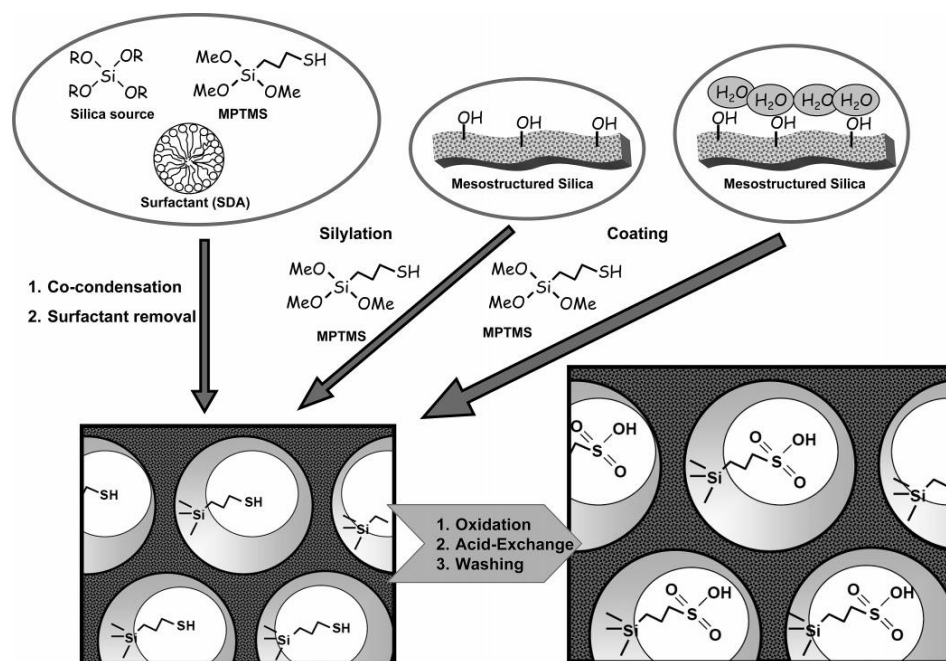
Figure 2.31 Mesostructured silica functionalised with propyl sulfonic acid (PrSO$_3$H) groups synthesised by post-oxidation of thiol groups [379]

Mbaraka et al. [381] synthesised uniform mesoporous SBA-15-PrSO$_3$H catalyst by co-condensation of TEOS and MPTMS in the presence of Pluronic P123 template followed by post-oxidation of mercaptopropyl groups with hydrogen peroxide (H$_2$O$_2$). This catalyst has a high surface area (920 m^2/g) with pore size of 48 Å and was effectively used for the esterification of FFAs in pre-treated beef tallow under optimum conditions of 120 ^{o}C, 20:1 methanol to FFAs mole ratio, and 30 min reaction time to reach 92% of conversion. Melero and co-workers [80] investigated the effect of different sulfonic acid incorporated with mesostructured SBA-15-type as solid acid catalysts in the transesterification of palm oil containing high FFAs. The sulfonic acid functionalised mesostructured SBA-15 were prepared by co-condensation of different silanes in

the case of propylsulfonic acids modified SBA-15 (SBA-15-PrSO₃H) and in arene sulfonic acids modified SBA-15 (SBA-15-ArSO₃H), but post-synthesis grafting was used for perfluorosulfonic acid modified SBA-15 (F-SBA-15-SO₃H). The synthesised catalysts (see Figure 2.32) showed high surface areas (404-712 m^2/g) with narrow pore diameters (8.2-9.6 nm) and acidity (0.28-1.17 meq/g). The SBA-15-PrSO₃H and SBA-15-ArSO₃H exhibited good thermal stabilities up to 350 ⁰C whilst perfluorosulfonic acid modified SBA-15 progressively decomposed after 250 ⁰C.
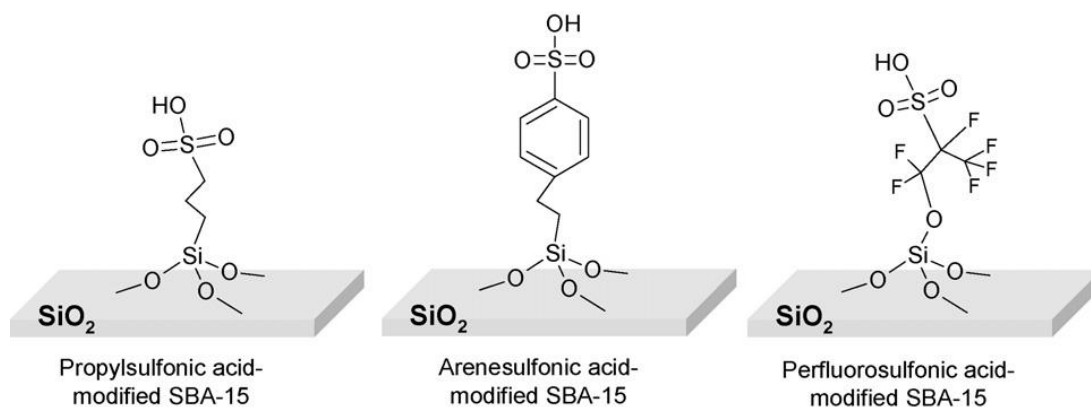
Figure 2.32 Sulfonic acid functionalised mesostructured SBA-15 catalysts [80]

The transesterification reaction was performed in a stainless-steel batch reactor (autoclave) at 150 ⁰C with 20:1 mole ratio of methanol to oil and 6 wt% of catalyst loading for 2 h, resulting in 70, 80 and 90% FAME yields over SBA-15-PrSO₃H, SBA-15-ArSO₃H and F-SBA-15-SO₃H, respectively. This was mainly dependent on the nature of the molecular environment of the sulfonic acid sites, i.e. the high electronegativity of fluorine atoms in the F-SBA-15-SO₃H giving higher acid strength than SBA-15-ArSO₃H and SBA-15-PrSO₃H. Likewise, the aromatic ring in SBA-15-ArSO₃H had higher acid strength than SBA-15-PrSO₃H due to the resonance effect of the ring (electron withdrawing environment leads to higher Brønsted acid sites). Thus, higher acid strength in the catalyst improved the catalytic performance of the catalyst. However, the spent F-SBA-15-SO₃H was deactivated after first the run compared to other mesoporous catalysts. This can be explained by the non-stability of Si-O-C bonds in polar media. The same explanation can be extracted from Zuo et al. [384] work when they studied the microwave-assisted transesterification process of soybean oil with 1-butanol over these catalysts. These authors also claimed that the catalytic activity of surface functionalised mesostructured SBA-15 was strongly dependent on the acid strength rather than amount of acid sites.

The hydrophobisation process was carried out to solve the issues in the relation with the interaction between reactant molecules, FAME and surface interaction of the silica catalyst (surface polarity issue) and provide a hydrophilicity-hydrophobicity balance for SBA-15-ArSO₃H catalyst in the transesterification process as shown in Figure 2.33 [80]. It was found that the catalytic activity increased by 10% even though the surface and pore size decreased after hydrophobisation (incorporating alkyl/aromatic groups directly into the silica framework). The spent catalyst, however, was reused for three consecutive cycles without any deactivation owing to the hydrophilicity-hydrophobicity balance.
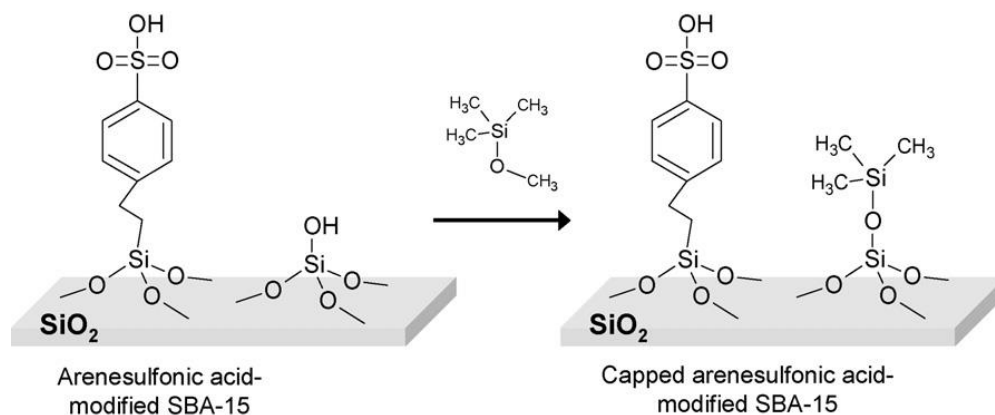
Figure 2.33 Hydrophobisation of SBA-15-ArSO₃H catalyst [80]

Sulfonated mesoporous materials are of particular interest for transesterification reactions because bulk reactants are too large (TG size=5.8 nm) to be incorporated into the small pore. Hence, Valle-Vigón and co-workers [385] reported a novel route for preparing highly functionalised mesoporous silica-carbon composites (uniform carbon layer ~30%) with large pore size (10-29 nm). The high surface area (590 m^2/g) catalyst was tested in the esterification of maleic anhydride, succinic acid, and oleic acid with ethanol. Steps for the synthesising procedure for the catalyst preparation are depicted in Figure 2.34. According to this study, it is important to have a large number of surface silanol groups to maximize the amount of carbonaceous deposited within the silica pores. The results revealed a high product yield formations over the use of this catalyst. However, the authors found that the sulfonation step caused the collapse of the total pore structure and the catalyst was suitable only at a reaction temperature below 150 ℃. According to their TGA results this was because of–SO₃H decomposition in the catalyst between 150 and 650 ℃. The same observation,

in terms of harsh conditions creating a destruction and degradation of structure uniformity, was reported by Wang et al. [386].
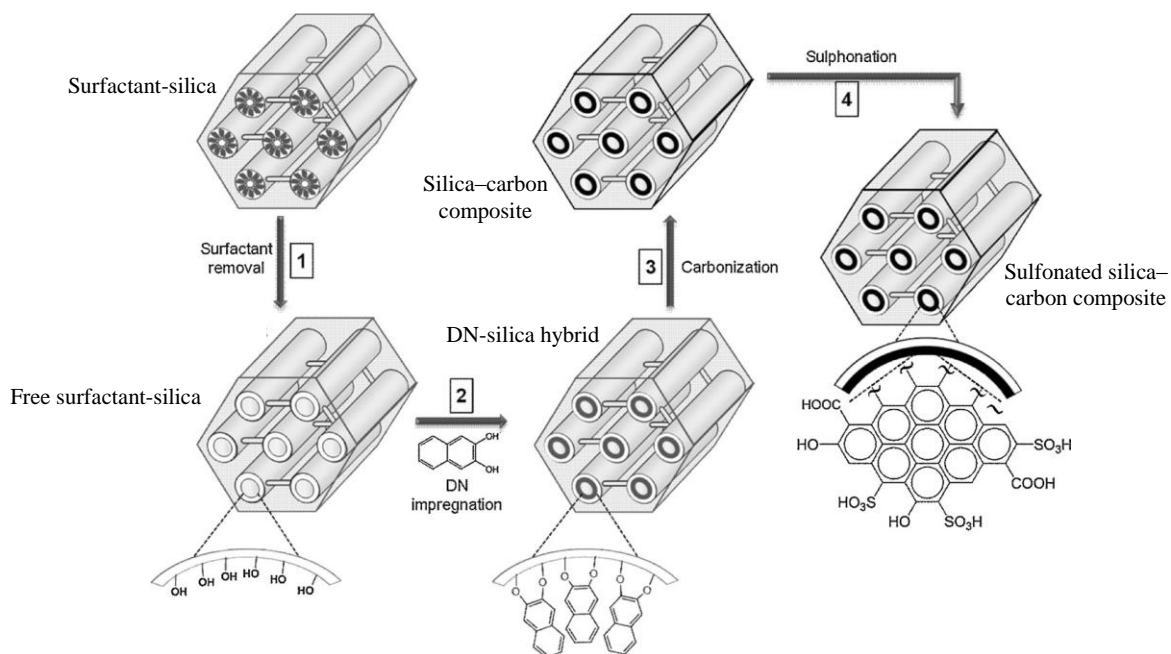
Figure 2.34 Schematic shows all four steps for the preparation of sulfonated silica-carbon composite [385]
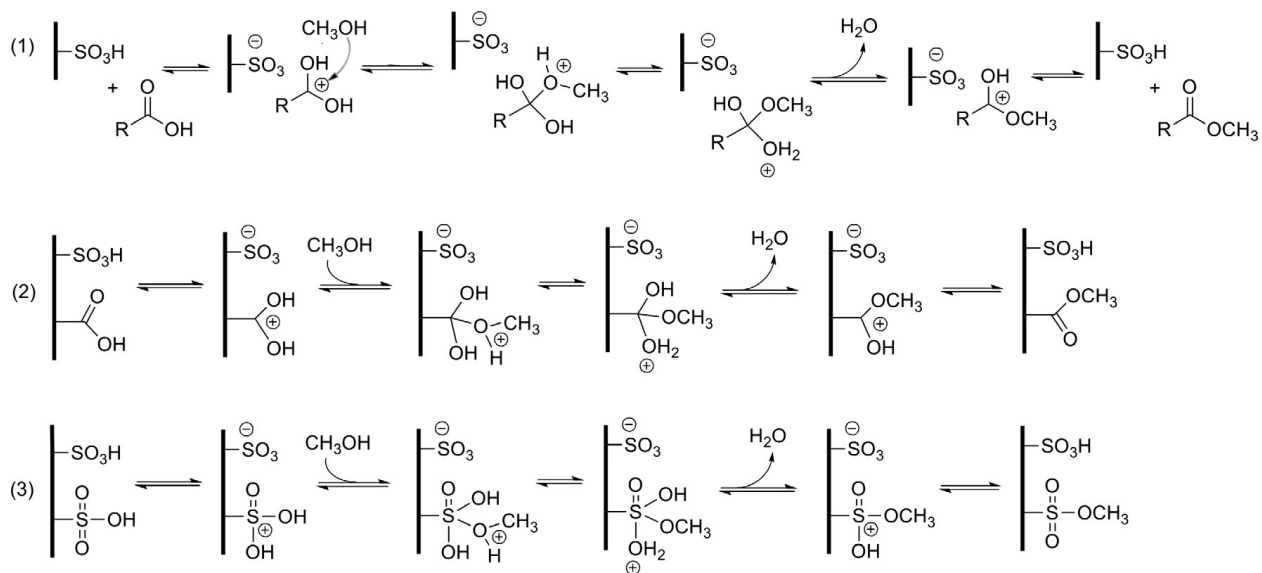
Figure 2.35 Proposed mechanism by [387] for the esterification reaction (1), the partial deactivation of the catalyst by side reactions (2) and (3).

A study on the deactivation of materials bearing -SO₃H, -OH, and -COOH catalysing the esterification reaction has been reported by Fraile et al. [387]. The authors found that the high surface acid density of -SO₃H, -OH, and -COOH on the catalyst also esterified as a side reaction according to the NMR results for recovered catalyst. The proposed mechanism for the esterification reaction and side reaction for partial deactivation of catalyst is shown in Figure 2.35. The creative exploration of solid acid catalyst has also resulted in the discovery of super acidic mesoporous materials [41, 357, 388, 389]. Yi et al. [389] have recently tested the catalytic activity of SO_4^{2-} /Zr-SBA-15 for biodiesel production and observed 95.2% of FAME yield in the transesterification with 6:1 mole ratio of waste cooking oil to methanol, 3 wt% catalyst loading at 160 °C within 3 h reaction time and the catalyst also recycled for six runs. Soltani et al. [297] have recently examined the surface modification of mesoporous ZnO material by sulfuric acid to form a solid acid catalyst for biodiesel production from the esterification of palm fatty acid distillate containing 90% of FFAs. The mesoporous ZnO catalyst was synthesised via hydrothermal treatment followed by the post-sulfonation treatment to introduce the sulfonic acid groups as shown in Figure 2.36.
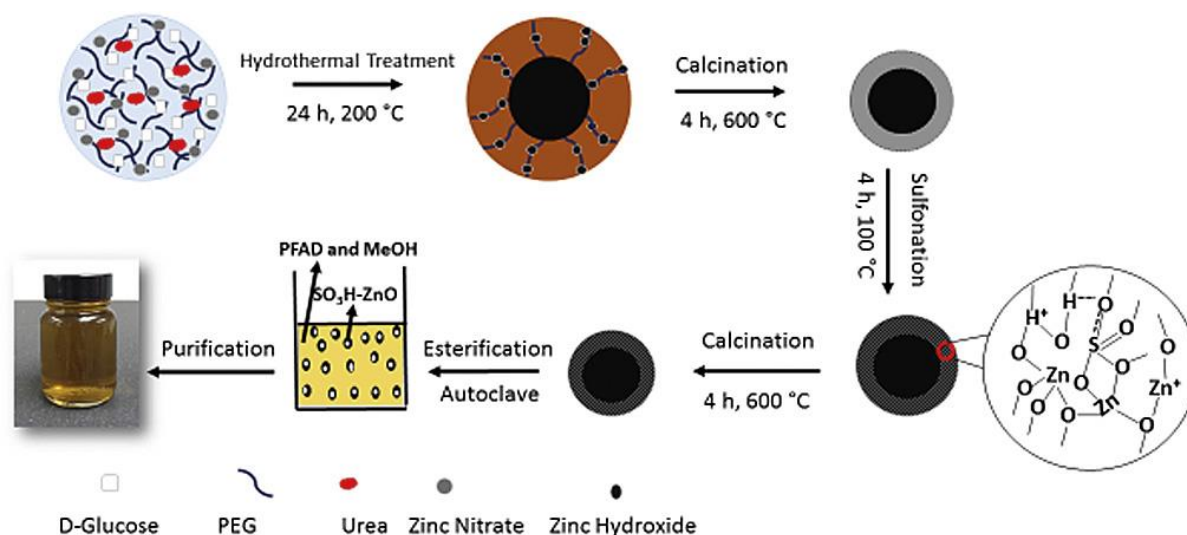
Figure 2.36 Biodiesel production using sulfonated mesoporous ZnO [297]

The catalyst showed high surface area (305.62 m²/g) with average pore size of 3.16 nm and high acid density (1.72 mmol/g). The reaction was performed using 9:1 methanol to oil mole ratio, 2 wt% of catalyst amount, 120 °C, 1.5 h reaction time to reach 95.6% of yield. This catalyst exhibited good activity in acid-catalysed esterification of palm fatty acid distillate with methanol and a high

stability for spent catalyst up to 5 cycles followed by loss of active sites in run 8. The activity of the catalyst was mainly related to the acid strength of acid sites.
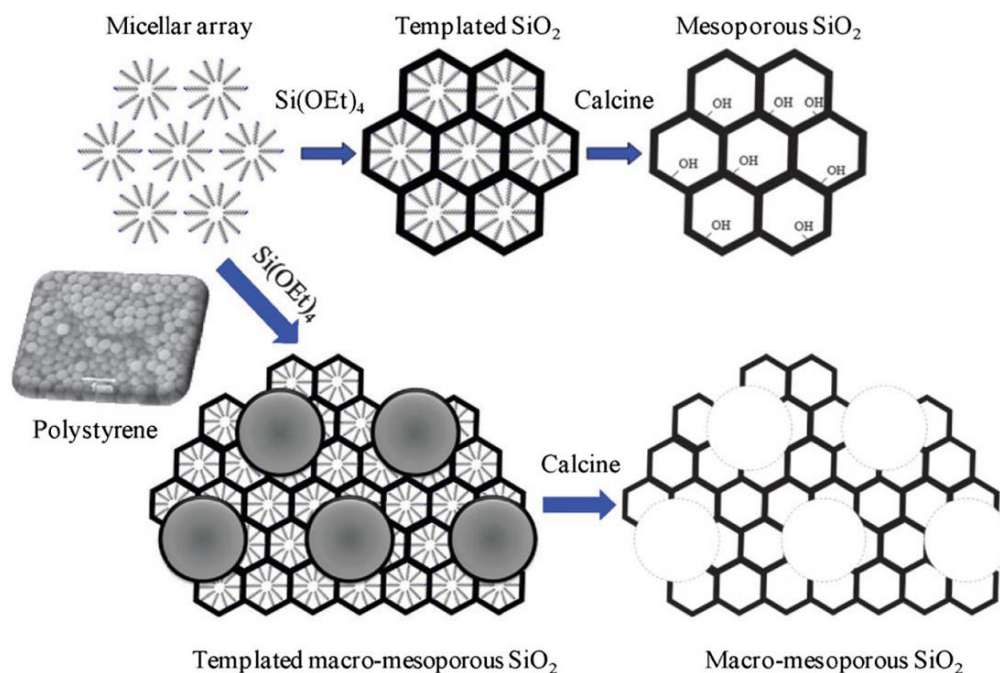
Figure 2.37 Protocol for hierarchical meso-macroporous silicas preparation [105]

Dacquin et al. [390] reported a novel study focused on the pore-expansion up to 14 nm with hexagonal symmetry of SBA-15-PrSO$_3$H catalyst for esterification of palmitic acid and transesterification of triolein and tricaprylin. The pore expansion led to a decrease of the surface area, but it accelerated the initial rate of reactant molecules to active sites in both reactions. This indicated that the reactant molecules have good accessibility to contact with sulfonic acid sites and as a result of that the catalytic activity increased by >3 times in both reactions. It was concluded that the catalytic activity was greatly dependent on the pore dimensions or texture properties.

Another remarkable hierarchical meso-macroporous solid acid catalysts via dual-templating routes employing liquid crystalline surfactants (soft template) and a good dispersion of polystyrene beads (hard template) has been designed by Dhainaut et al. [293] for the esterification of long chain palmitic acid and transesterification of Tricaprylin. The –SO$_3$H grafting groups in the catalyst were obtained by post-synthesis from 3-mercaptopropyl trimethoxysilane followed by post-oxidation with H$_2$O$_2$. These catalysts showed very high surface area (938-976 m^2/g) and large pore sizes (34.6-98.2 nm). The preliminary results for macro-mesoporous SBA-15-PrSO$_3$H catalyst has been

proven to be successful in increasing the catalytic activity toward the esterification/transesterification reactions by 2 fold in comparison with SBA-15-PrSO₃H catalyst. The authors explained that the rapid increase in initial rates of esterification/transesterification reactions was a result of the presence of large channels (macro-pore) enhancing the mass transfer for the bulky reactant molecules into the active sites which are located within the mesoporous in the pore network solid acid catalyst. The proposed steps, as shown in Figure 2.37, for the meso-macroporous silicas catalyst preparation is reported by Lee [105] in a comprehensive review paper. Despite numerous good results, aforementioned and also summarised in Table 2.11, solid acid catalysts for esterification and transesterification reactions are still far from being perfect in order to be used for industrial biodiesel applications. Major barriers are instability, deactivation, side reactions of active sites, water resistance, mass transfer limitation, long reaction time and high temperature, particularly for cheap feedstocks such as WCO.

Table 2.11 Summary of solid acid catalysed esterification/transesterification process

Feedstock	MeOH/EtOH to oil ratio	Catalyst Type	Amount, wt%	Time	Particle size, nm	T/ºC	Y % C %	Catalyst recycled	References
Croton megalocarpus oil	9:1	2%-WO₃/silica mesoporous-macroporous	4.5	45 min	3.18	70	96 Y	*NR	[303]
Non-edible oil	30:1	PD-En-SO₃H	4	4 h	*NR	100	>85 Y	4	[391]
Waste cooking oil	15:1	SO_4^{2-}/SnO₂SiO₂	3	3 h	*NR	150	92.3 Y	*NR	[304]
Used oil	9:1	SO_4^{2-}-ZrO₂/MCM-41***	5	30 min	1-30	60	96.9 C	5	[392]
Used cooking oil	9:1	SO_4^{2-}/SiO₂-TiO₂	3	4 h	10.8	200	90 Y	4	[291]
Used vegetable oil	40:1***	Cs₂.₅H₀.₅PW₁₂O₄₀	3	1 h	10	260	92 Y	**NR	[393]
Trilaurin	20:1	Sulfonated MWCNT	3.7	20 min	*NR	170	~90 C	**NR	[310]
Palm oil	20:1	Sulfonated-graphene oxide	10	14 h	*NR	100	>98 Y	4	[394]
Palm kernel oil	6:1	SO_4^{2-}/ZrO₂	1	1 h	*NR	200	90.3 Y	*NR	[38]
Palm datty acid distillate	20:1	Amberlyst 15	30	6 h	*NR	60	>95	15	[395]
Lauric acid	3:1	H₃PW₁₂O₄₀/Ta₂O₅	3	3 h	*NR	78	70	*NR	[396]
Jatropha curcas L. oil	9.88:1	SO_4^{2-}-ZrO₂/Al₂O₃	0.5	4 h	*NR	150	90.32 Y	*NR	[397]
Sunflower oil	12:1	SO_4^{2-}-ZrO₂/MCM-41	14.6	2 h	*NR	200	91.5 Y	*NR	[398]

*NR: Not Reported; **NR: Not Recovered; ***Super critical methanol

2.5 Summary of literature review

Biodiesel is considered to be an environmentally friendly fuel, non-toxic and biodegradable source of energy and is usually made by the transesterification of TG with low molecular weight of alcohol. Generally, around 90% of biodiesel is produced in the industrial transesterification process by homogeneous base catalysts from vegetable oil with methanol. However, the use of virgin vegetable oil poses dilemmas, in particular that of food versus fuel. The biodiesel industry faces feedstock and high cost problems. As a consequence different feedstocks and technologies have been used in attempts to reduce the cost of fuel and commercialise production in developing and developed countries. Some non-edible oils, such as jatropha oil, microalgae oil and waste/used cooking oil are considered to offer promising future feedstocks. Nonetheless, these feedstocks contain high quantities of FFA (>1 wt%), moisture (>0.5 wt%) and other impurities that form soap (fatty acid salt), aqueous quenching and difficulties of separation while transesterified via homogenous base catalysts. Homogenous acid catalysts are an appropriate option for catalysing these materials to form biodiesel; however, they cannot be recovered, they demand costly fuel purification processes and they are very corrosive. Heterogeneous catalysts have recently attracted interest as alternative catalysts for biodiesel production from cheap feedstocks and shown promising for easy separation of product and by-products from the catalyst. This allows the catalyst reusability and reduction of waste which have an environmental impact too. Heterogeneous base catalysts exhibit higher activity than heterogeneous acid catalysts, but they are unable to esterify high amounts of FFAs of cheap feedstocks. Therefore, solid acid catalysts have beneficial for simultaneous esterification and transesterification of cheap feedstocks containing high FFAs. Solid acid catalysts, then, have been extensively studied as offering the biodiesel industry an alternative to homogenous catalysts in simultaneous esterification and transesterifion in cheap feedstocks under mild conditions. Their advantage over other catalysts are (1) they are less sensitive to raw materials that contain high amount of FFAs; (2) they provide simultaneous esterification of FFAs and transesterification of TG; (3) they eliminate the aqueous quenching step; (4) they are easily separable from the reaction media; and (5) they can be regenerated while recycling the catalyst. A wide range of inorganic, organic and polymeric solid acid catalysts have been recently explored with a view to biodiesel production using cheap feedstock oils but there are some issues that remain and still need to be resolved. Low reactivity, small pore sizes, low stabilities, long reaction times as well as high reaction temperatures are the main challenges of using solid acid catalysts in

industrial applications. Furthermore, some solid acid catalysts suffer from a low concentration of acid sites, high amount of catalyst, deactivation, leaching of acid sites, mass transfer (diffusion) limitation, and side reaction (poisoning) problems. It is also important to mention that calcination at high temperature of sulfonated solid acid catalysts destroys catalyst templates, reduces their activities as well as making the process energy intensive. Surface functionalisation of solid acids is an effective route to introducing some crucial functional groups on the internal or external surface but it reduces the surface area and porosity of the solid acid catalyst. Therefore, development is needed to prevent deactivation of catalyst sites and produce efficient, cheap, durable, and stable solid acid catalysts to overcome current problems associated with biodiesel production.

Chapter 3

Experimental work

This chapter provides an overview of the project's experimental work. The obtained materials and preparation of solid acid catalysts are also described. The methodology of biodiesel production from used cooking oil over synthesised novel solid acid catalysts and the detailed analysis methods of synthesised biodiesel fuels are presented.

3. Experimental work

3.1 Introduction

In this chapter, we present the detailed methodologies employed for solid acid catalyst preparation throughout this work. The experimental set up for simultaneous esterification and transesterification of used cooking oil (UCO) to obtain biodiesel are also discussed in detail. The synthesised solid acid catalysts studied were characterised using different techniques. Finally, the materials, including catalyst precursors, and the detailed characterisation methodologies for obtaining biodiesels from different catalytic processes based on ASTM and EU standards are reported.

3.2 Synthesis of solid acid catalysts

3.2.1 TiO_2/$PrSO_3H$ catalyst

This work is focused on the surface functionalisation of the mixed phase (anatase and rutile) titania as catalyst support (TiO_2 NPs, Product number 718467-100G from Sigma-Aldrich, CAS number 13463-67-7). The properties of titania are listed in Table 3.1.

Table 3.1 Summary of TiO_2 manufacture product specifications

Test	Specification
Appearance (Colour)	White
Appearance (Form)	Powder
Surface area (BET)	35 - 65 m^2/g
pH	3.5 - 4.5
HCl content	≤ 0.30 %
Purity using ICP	$\geq 99.5\%$ Based on trace metals analysis
Mp	1850 °C
Primary particle size (TEM)	21 nm
Density	4.26 g/mL at 25 °C

TiO$_2$ NPs occurs naturally in three main different crystallographic phases which are anatase, rutile, and brookite as discussed in Chapter One. Anatase has a higher photocatalytic activity then a rutile phase but is thermodynamically less stable [399]. It has been also reported that mixed phases of titania exhibit enhanced photocatalytic activity properties relative to single-phase titania [60] and that is why we have chosen as a catalyst support in this work. The surface charge of TiO$_2$ NPs is pH dependent. Therefore, we pre-treated the mixed phase (anatase and rutile) TiO$_2$ NPs with an aqueous solution of ammonium hydroxide to reduce agglomeration and increase the receptor sites ($TiO_2 + nOH^- \longrightarrow TiO_2(OH)n^{n-}$) on the surface of titania support [400]. 6 g of TiO$_2$ NPs was added slowly into 50 mL of 0.5 M ammonium hydroxide solution at room temperature. The suspension was then sonicated for 30 min. The resultant was transferred into a centrifuge tube for washing with double deionised water and oven-dried at 80 °C for 4 h. Typically, 1 g of the dried powder was charged into a three necked glass flask at ambient temperature and then 20 mL suspension solutions of 0.1 M 1,3-propane sulfone in dry toluene was added dropwise. The resultant suspension was slowly stirred under reflux for 72 h at 120 °C. The synthesised TiO$_2$/propyl sulfonic acid powders were cooled to room temperature. Thereafter, the synthesised catalyst was separated from the solution using a centrifuge and washed off several times with fresh toluene to remove remaining unreacted 1,3-propane sulfone. The resulting precipitate sample was dried overnight at 80 °C then denoted as sample TiO$_2$/PrSO$_3$H.

3.2.2 Ti(SO$_4$)O catalyst

The titanium sulphate oxide or titanium oxysulphate catalyst was prepared using the following procedure: 17.16 mmol of chlorosulfonic acid was added dropwise using a glass syringe at room temperature into a round-bottom flask containing 5.0 g of TiO$_2$ NPs. The resulting mixture was then heated on an automatic hotplate-magnetic stirrer at 120 °C using an agitation rate of 500 RPM, to prevent generation of hydrogen and chloride gases in the flask. The flask containing the produced gel solution was connected with a reflux condenser using tap water to condense the remaining reagent for 2 h at the constant stirring rate. The resulting gel solution aged quiescently at room temperature for 2 h and then dried in an oven at 110 °C overnight. The resultant catalyst was crushed and grinded by pestle mortar, and then the grinded powders were washed thoroughly with 1:1 ratio of acetone to n-hexane in order to remove any remaining residues on the surface. Finally, the

obtained fine powder was dried in an oven at 110 °C to remove any moisture on the surface of the catalyst and the sample was labelled as Ti(SO$_4$)O.

3.2.3 Sulphated/Fe-Al-TiO$_2$ catalyst

3.2.3.1 Synthesis of alumina doped TiO$_2$ NPs

0.1 M of aluminium iso-propoxide was dispersed in a round bottom flask containing 50 mL of ethanol. Subsequently, 1 g of commercial TiO$_2$ NPs was added to the solution and the resulting solution was stirred at 250 RPM for 10 min with the addition of 5 mL of ammonium hydroxide. The suspension solution was refluxed at 80 °C under vigorous stirring at 250 RPM until the light-yellowish gel was formed. The solvent was then evaporated by ageing the solution quiescently at room temperature for 24 h and the obtained gel was washed several times with 1:1 ratio of ethanol to deionised water. Finally, the impregnated TiO$_2$ precipitates were oven-dried overnight at 100 °C followed by calcination statically in air at 400 °C for 5 h and then powder denoted as Al-TiO$_2$.

3.2.3.2 Synthesis of iron oxide coated Al-TiO$_2$

A core-shell structured super magnetic solid acid catalyst was prepared via co-precipitation of Fe^{2+} and Fe^{3+} under alkaline condition to form reddish-brown to black Fe$_3$O$_4$ NPs (

$$Fe^{2+} + 2Fe^{3+} + 8OH^- \longrightarrow Fe_3O_4 + 4H_2O$$ [401, 402]) depositions on the surface of Al-TiO$_2$ NPs in order to be simply and efficiently removed from reaction mixtures with an external magnetic field. 0.15 M of ferric chloride hexahydrate and 0.1 M of ferrous chloride tetrahydrate were separately dissolved in 50 mL of 1:1 ratio of ethanol and double deionised water using an ultrasonic bath until they became clear solutions. The obtained solutions were added dropwise into a three-necked round bottom flask containing 2 g of pre-suspended Al-TiO$_2$ NPs in 50 mL of ethanol and 10 mL of ethylene glycol. Meanwhile, a few millilitres of concentrated ammonium hydroxide were injected into the reaction mixture with continuous mixing of the solution until the pH reached between 9 and 10. The resulting mixture was then heated at 75 °C under reflux and N$_2$ atmosphere and vigorously stirred at 250 RPM for 2 h followed by ageing for 12 h. The obtained gel was separated from the mixture solution using an external magnetic field and thoroughly rinsed several times with

1:1 ratio of ethanol to double deionised water until the chloride ion in the discarded solution could not be detected. The collected dark-reddish precipitate gel was then oven-dried overnight at 80 °C. Finally, the dried powder was calcined at 400°C for 4 h to inhibit the anatase to rutile phase transformation [60] and achieve hematite phase. Finally, the resulting powder labelled as Fe-Al-TiO$_2$.

3.2.3.3 Chlorosulfonic acid functionalised Fe-Al-TiO$_2$ support

1 g of calcined Fe-Al-TiO$_2$ powder was dispersed in 50 mL of dry toluene using an ultrasonic bath. The suspended solution was cooled in an ice bath and stirred gently followed by the injection of 2 mL of chlorosulfonic acid at 0.1 mL/min and slow stirring. Thereafter, the resulting solution was refluxed at 60 °C for 2 h under N$_2$ atmosphere, followed by separation of the dark-reddish gel from the solution using a magnet. The gel was thoroughly washed few times with fresh toluene. The synthesised magnetic solid acid gel was oven-dried overnight at 80 °C and calcined at 400 °C for 4 h. Finally, the collected powder was denoted as $SO_4^=$/Fe-Al-TiO$_2$.

3.3 Catalyst characterisations

Detailed descriptions are presented of the different analytical techniques used to characterise TiO$_2$ NPs, synthesised solid acid catalysts and re-used solid acid catalysts with the theory behind their working principles also being discussed.

3.3.1 X-ray diffraction (XRD)

XRD is a rapid technique used for the determination of crystal structure (atomic arrangement of a material), phase identification, miller indices (hkl, to identify different planes of atoms), inter planar spacing, crystalline size and the shape of molecules. X-rays, which are highly energetic electromagnetic radiations with wave length of the order of 1 Å (=1x10^{-10} m) lying between ultraviolet and gamma rays in the electromagnetic spectrum, were discovered by German physicist Rontgen in 1895 [403]. Powder XRD, which involves the scattering of incident X-ray photons from electrons bound to atoms and can be used to fingerprint crystal structures, was discovered by Herren Friederich, Knipping and Von Laue in 1912 and later developed by Bragg [404].
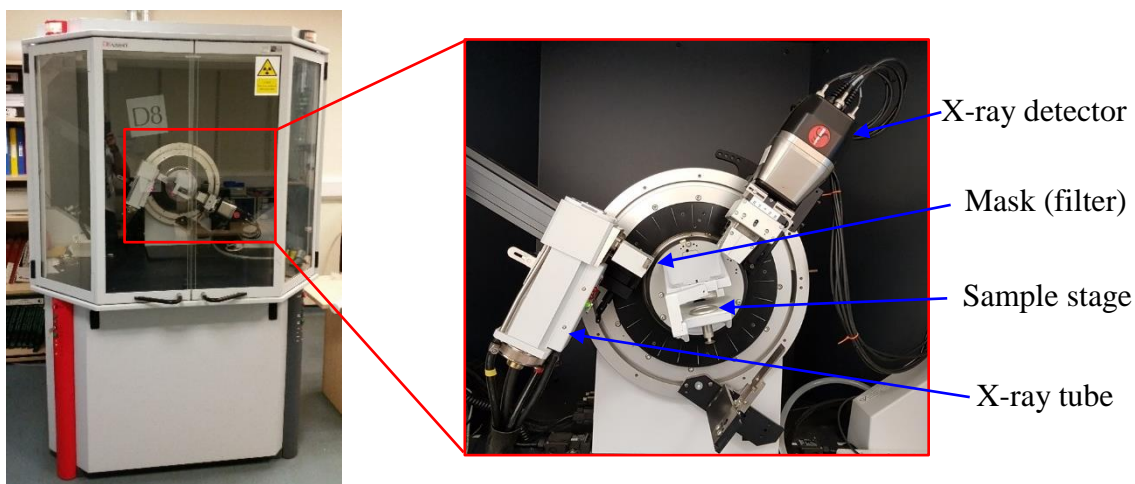
Figure 3.1 Bruker Powder D8 advance X-ray diffractometer

An X-ray tube, a sample holder, and an X-ray detector are the main three elements for X-ray diffractometers as shown in Figure 3.1. The X-rays are normally generated by the inner shell transitions of complex atoms or the deceleration of electrons [403]. Thereafter, the polychromatic X-ray radiations filtered to produce monochromatic radiation and collimated to concentrate then directed towards the sample on the sample holder. Some of the monochromatic beam can be diffracted by atoms in crystal and the rest either absorbed by crystal or transmitted through crystal. The interaction of the incident X-rays with the crystalline materials satisfy Bragg's Law (Equation 3.1), constructive interference occurs and a peak in intensity occurs. A detector then records and converts the signals to a count rate. Bragg's law can be used to derive lattice spacings within crystal lattices in crystalline samples.

$$n\lambda = 2d_{hkl}sin\theta \qquad\qquad \text{Equation 3.1}$$

Where n is an integer (always get the first order maxima for which n=1), d_{hkl} is the inter planar spacing (lattice spacing) generating the diffraction, λ is a wavelength of the Cu Kα radiation, and θ is the angle between the beam incident ray and the normal to the reflecting lattice plane. But for reflection angles, the distance between scatters must be equal to an integer multiplied by the X-ray wavelength. Figure 3.2 shows the Brag's X-ray diffraction.

In this work, the XRD patterns of the TiO_2 NPs, synthesised solid acid catalysts and reused one were obtained using XRD Philips X'Pert and/or Bruker D8 X-ray diffraction fitted with a LynxEye detector, using CuKα (λ=1.54 Å) radiation source operating at 40 kV and 40 mA, calibrated against

a Si standard. Each sample was scanned twice from 2θ angle ranging 10º to 70º with step size 0.0495º at 1 second per step (fast scan run) and 35 seconds per step (slow scan overnight run).
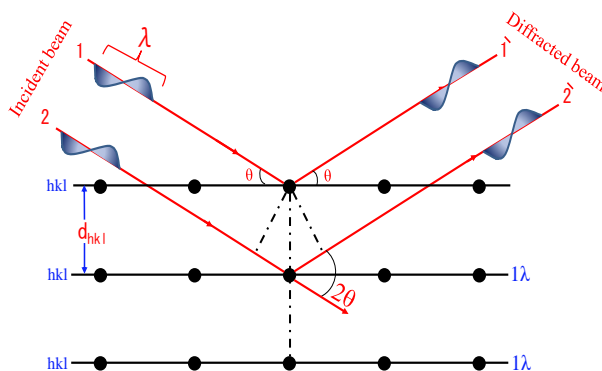
Figure 3.2 Schematic representing Bragg's Law
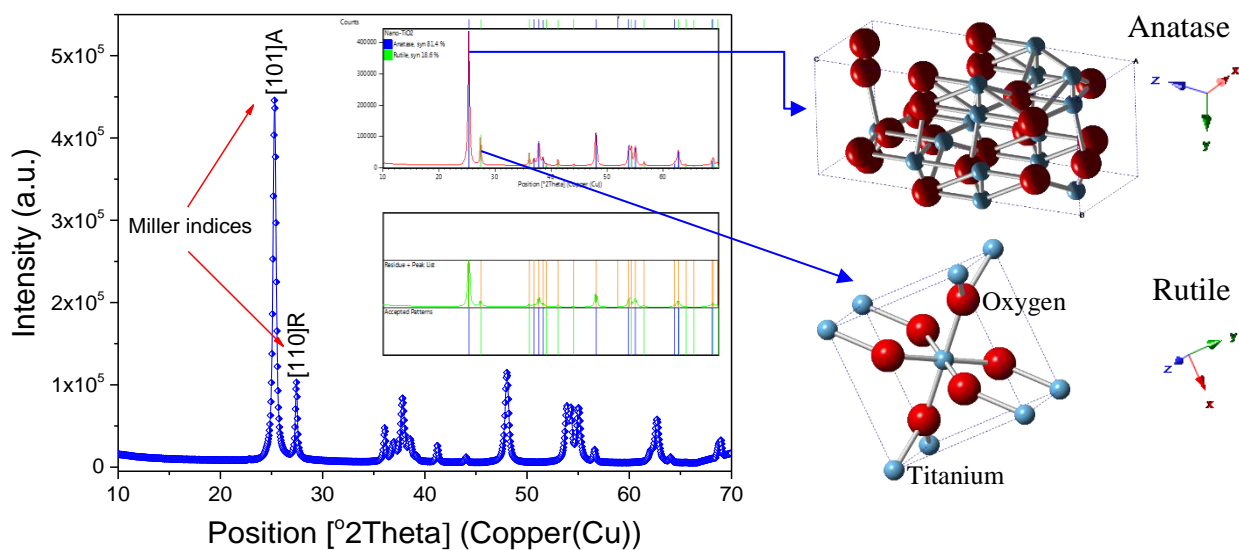
Figure 3.3 Powder XRD pattern of TiO_2 NPs showing crystal structures of anatase and rutile

The obtained raw files from the XRD instrument were analysed using PANalytical's High Score PLUS software. The process matched the results derived from the diffraction with known patterns for different compounds available in the database of the Joint Committee on Powder Diffraction-International Centre for Diffraction Data (JCPDS-ICDD) to confirm the diffraction peaks, purity of samples, and phase identifications. The powder XRD of commercial TiO_2 NPs can be seen in Figure 3.3. Thereafter, the Rietveld Refinement method was used to quantify the phase and peak

fitting in each catalyst sample [405]. Finally, the average crystallite sizes of samples were calculated by selecting few peaks using Debye-Scherrer's equation (Equation 3.2).

$$Crystallite\ size\ (D) = k\lambda/\beta cos\theta \qquad \text{Equation 3.2}$$

Where k is a shape factor of the particles (k=0.9), λ is a wavelength of the CuKα radiation, θ is the incident angle of the X-rays, and β is the full width at half maxima of the diffraction peaks (FWHM, see Figure 3.4).
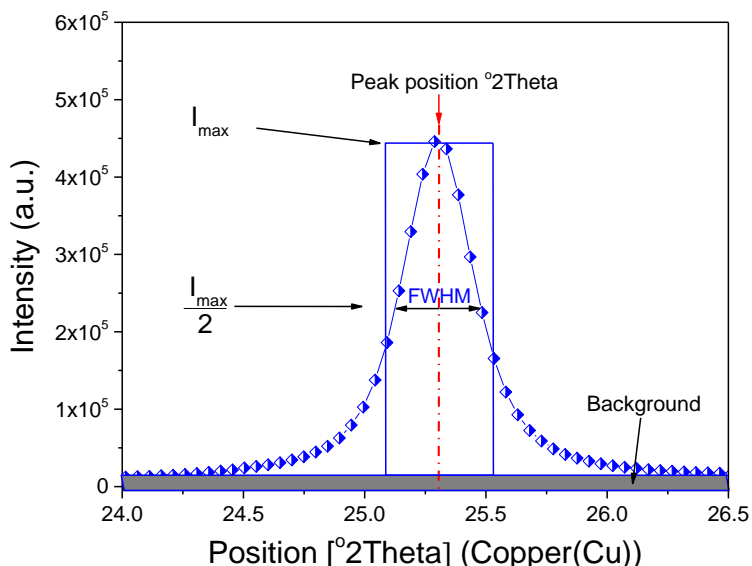
Figure 3.4 Determination of FWHM for TiO$_2$ NPs

Table 3.2 shows the inter-planer spacing values and calculated crystallite sizes of the [101] peak for anatase and [110] peak for rutile from the commercial TiO$_2$ NPs used in this project:

Table 3.2 Summarises the *d*-spacing and crystallite sizes of TiO$_2$ for main peaks (A and R)

XRD peak	°2θ	θ$_r$ (radians) = [°2θ/2]	FWHM	FWHM (radians)	*d*-spacing, Å = λ/[2*cos θ$_r$]	D, nm
[101] A	25.30	0.22	0.39	0.0068	3.52	20.87
[110] R	27.43	0.24	0.33	0.0569	3.24	25.08

3.3.2 Fourier transform infrared (FT-IR) spectroscopy

Infrared (IR) generally refers to any electromagnetic radiation within the wavelength region of 0.7 µm to 1000 µm (near-IR: 14000-4000 cm^{-1} changes in vibrational and rotational levels, overtone region and some low energy electron transitions; mid-IR: 4000-400 cm^{-1} changes in fundamental

vibrational levels of most molecules; and far-IR: 400-20 cm^{-1} changes in rotational energy level), though chemists are mostly interested in the vibrational portion of the region between 2.5 μm and 25 μm (mid-IR: 4000-400 cm^{-1}) for chemical analysis [406]. This technique can be used for qualitative and quantitative analysis because an IR spectrum provides a fingerprint of each absorbed functional group in the sample, which corresponded to the frequencies of vibrations between the bonds of atoms making up the material. The most typically expressed unit for radiation in the vibrational IR are wavenumbers, which are directed proportional to the energy. Although IR is extensively used for qualitative analysis in organic chemistry, band intensities are generally assigned to the concentration of absorbing species and path length of the light through the Beer-Lambert Law as shown in equation 3.3 [407].

$$A_\lambda = \log\frac{1}{T_\lambda} = \log\frac{I_o}{I} = \mathcal{E}_\lambda bc \qquad \text{Equation 3.3}$$

Where A_λ is absorbance at a given wavelength (relative amount of light absorbed by sample solution); $\mathcal{E}_\lambda$ is the molar absorptivity at a given wavelength (L/mole.cm); b is the path length in cm (typically is 1 cm for the distance light travels through the chemical species); and c is the molar concentration of chemical species in sample solution (mole/L). In transmittance mode is expressed as:

$$T_\lambda = \frac{I}{I_o} = e^{-\mathcal{E}_\lambda bc} \qquad \text{Equation 3.4}$$

Where T_λ is a transmittance at a given wavelength (relative amount of light passing through a sample solution); I is the intensity of transmitted light; I_o is the incident radiation.
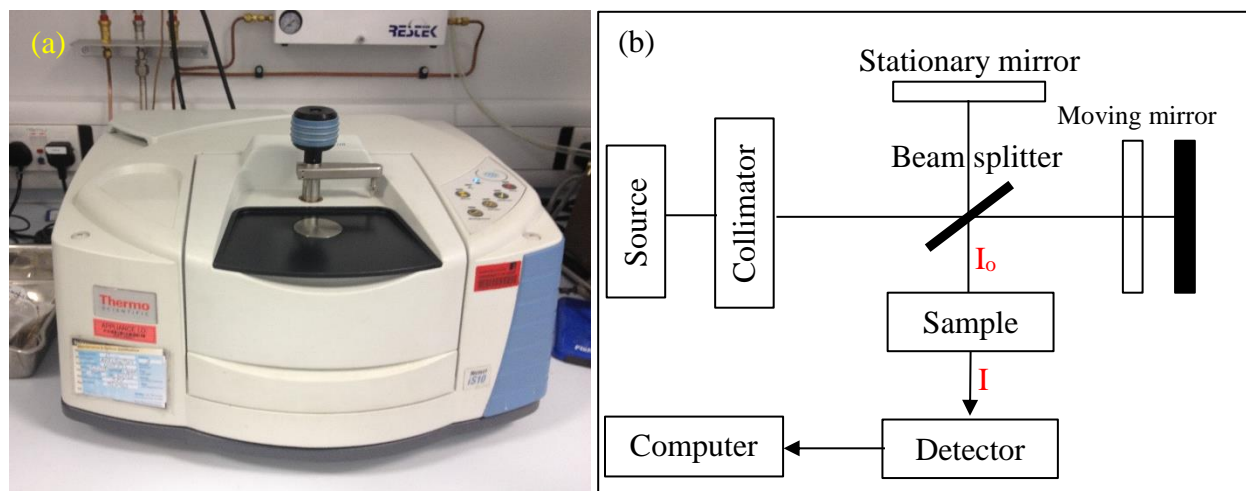
Figure 3.5 FT-IR instrument (a) and schematic diagram of a Michelson interferometer (b)

The FT-IR spectroscopy is an easy and rapid technique used to provide information about the vibration and rotation of chemical bonding and molecular structures. When the source of energy generates IR radiation which passes the sample via interferogram, the output information pattern is a plot of intensity verses time which is a complex signal as shown in Figure 3.5. A Fourier transform (FT), mathematical operation technique, then separates the individual frequencies from the interferogram to produce a single spectrum and reaches the detector. This technique can be used to identify the functional groups in organic and certain inorganic molecules because each different material is a unique combination of atoms. When a molecule in the sample absorbs infrared radiation at selected frequencies, chemical bonds vibrate at characteristic frequencies that match their vibration modes which produces a spectrum that can be used to identify functional groups and compounds [408, 409]. However, in general molecules can only interact with light and lead to infrared absorption when they are met all the following requirements (selection rule):

- The frequency of the IR radiation must be identical to the frequency of the vibration.
- The dipole of the molecule must change during vibration.
- The direction of the dipole change must be the same as the direction of the electric field vector.
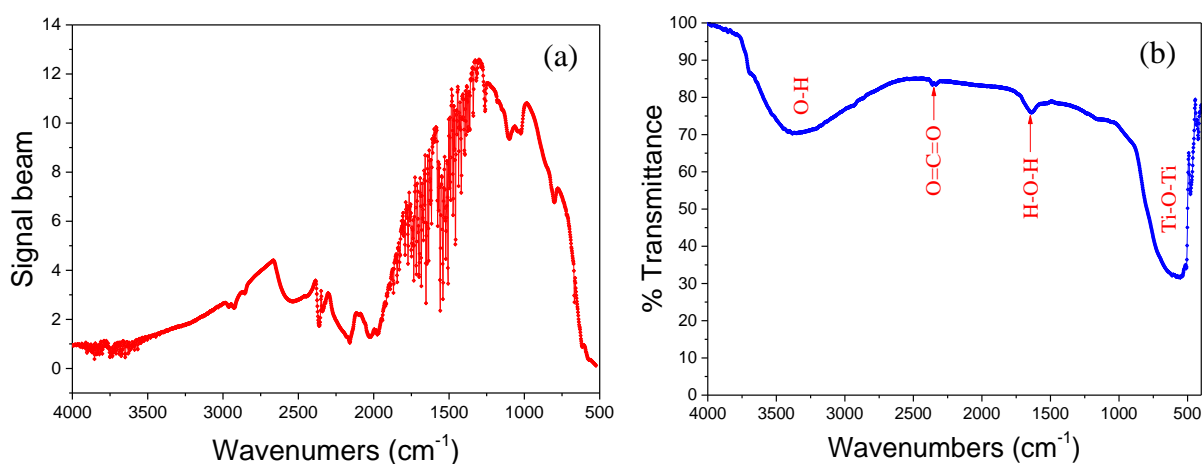
Figure 3.6 FT-IR spectra of (a) background and (b) TiO$_2$ NPs

In this work, FT-IR spectra of all catalysts were recorded at room temperature using a Nicolet iS10 FT-IR spectrometer equipped with a deuterated triglycine sulfate (DTGS) diamond detector to investigate the chemical vibrational modes in each catalyst sample, as shown in Figure 3.6. A minimum of 36 scans was performed at the average signal of infrared with a resolution 4 cm^{-1} in the ranges of 400 cm^{-1} to 4000 cm^{-1}. At the beginning of each experiment, a spectrum of the

background was recorded (see Figure 3.6a) which consists of the IR-active atmospheric gases including CO_2 and moisture in air. A few crystals of TiO_2 NPs sample were then placed into the beams and spectrum was taken. Afterwards the OMNIC™ FT-IR Software automatically subtracted the background from the TiO_2 NPs spectrum and the output is shown in Figure 3.6b.

3.3.3 Scanning electron microscopy (SEM)

SEM is a type of electron microscope that scatters electrons onto a target surface and produces an image allowing the examination of the morphologies (size and shape) of all samples (organic and inorganic materials) from nano to micron scale. The idea of SEM floated in 1927 by H. Stizing, but H. Knoll was developed the first image [410]. The lens system, electron gun, electron collector, visual and recording cathode ray tubes and electronics associated with them, are the main components of the instrument [411].
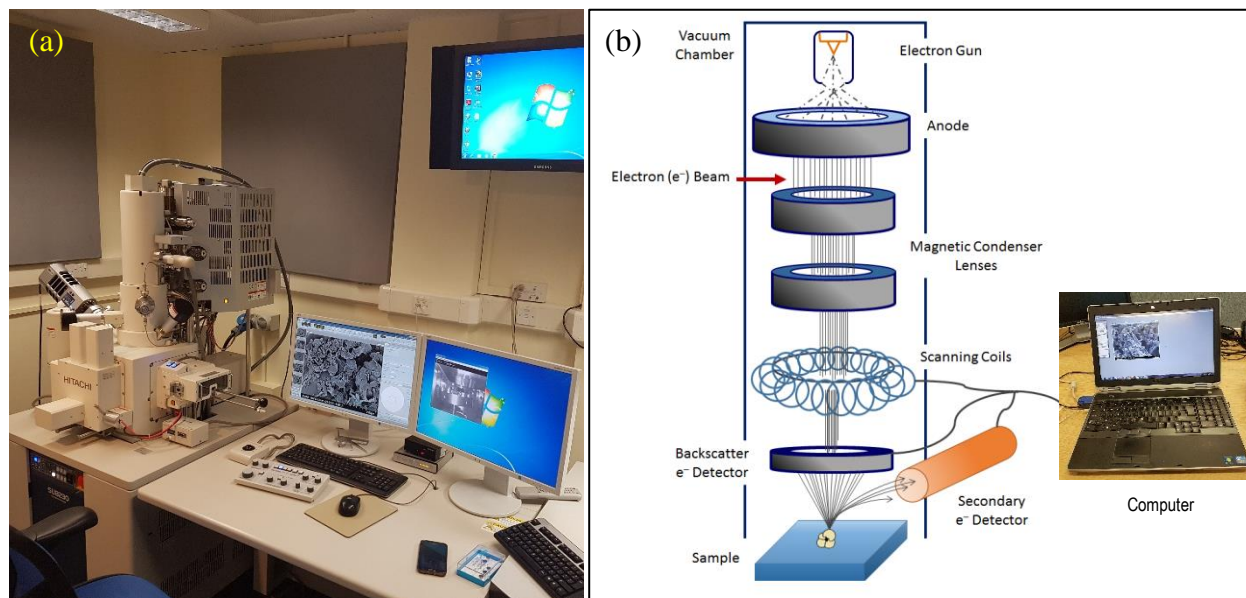
Figure 3.7 (a) SEM instrument and (b) a schematic diagram of an SEM [412]

The principle of SEM is that the surface of the solid sample is bombarded with electrons via an electron gun [413]. The electron gun located at the top of the microscope generates an electron beam. The beam travels down a vacuum zone and passes through electromagnetic lenses. The electrons hit the sample, resulting in energy loss as characteristic X-rays, backscattered, secondary electrons and some other photons of various energies [411]. The ejected signals (secondary

electrons, backscattered and X-rays) from the sample are collected by detectors thereafter convert them into a signal to produce a final image as shown in Figure 3.7. The magnification and resolution of SEM depend mainly on the working distance between the detector and the sample.
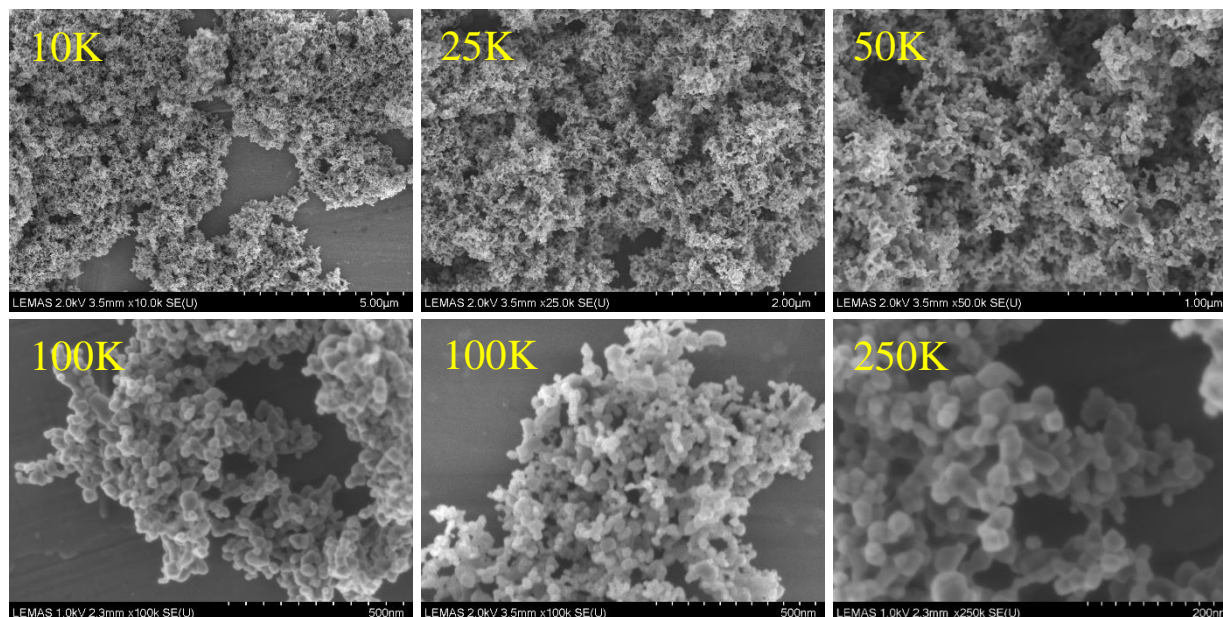
Figure 3.8 SEM micrograph images for TiO$_2$ NPs at different magnifications

In this work, the particle size, morphology and surface structure of the powder samples were studied using a high performance cold field emission scanning electron microscope (CFE-SEM, SU8230 Hitachi) operating between 1 kV and 20 kV in secondary electron (SE) imaging mode. The sample was prepared by adding a small amount of powder into 2 mL of methanol and keeping it in an ultrasonic bath for 10 min. One drop of this suspension was then put on the SEM sample holder (aluminium stubs) and placed in a zone SEM cleaner in order to remove any contaminants using UV radiation/Ozone at 1 Pascal for 10 min. Images were taken at different magnifications (see Figure 3.8 for TiO$_2$ NPs) using Gatan Digital Micrograph Software.

3.3.4 Transmission electron microscopy (TEM)

TEM is a type of an electron microscopy where a beam of electrons is transmitted through an ultra-thin sample dispersed on the TEM grid. The interaction of the electron beam through the sample forms 2D images. The degree of interaction (diffraction) between beam and sample depends on the variation in thickness, atomic mass and density of the sample. TEMs are capable of imaging at

a significantly shorter than both visible and X-ray radiation and enhanced to an atomic level under high resolution TEM [414].
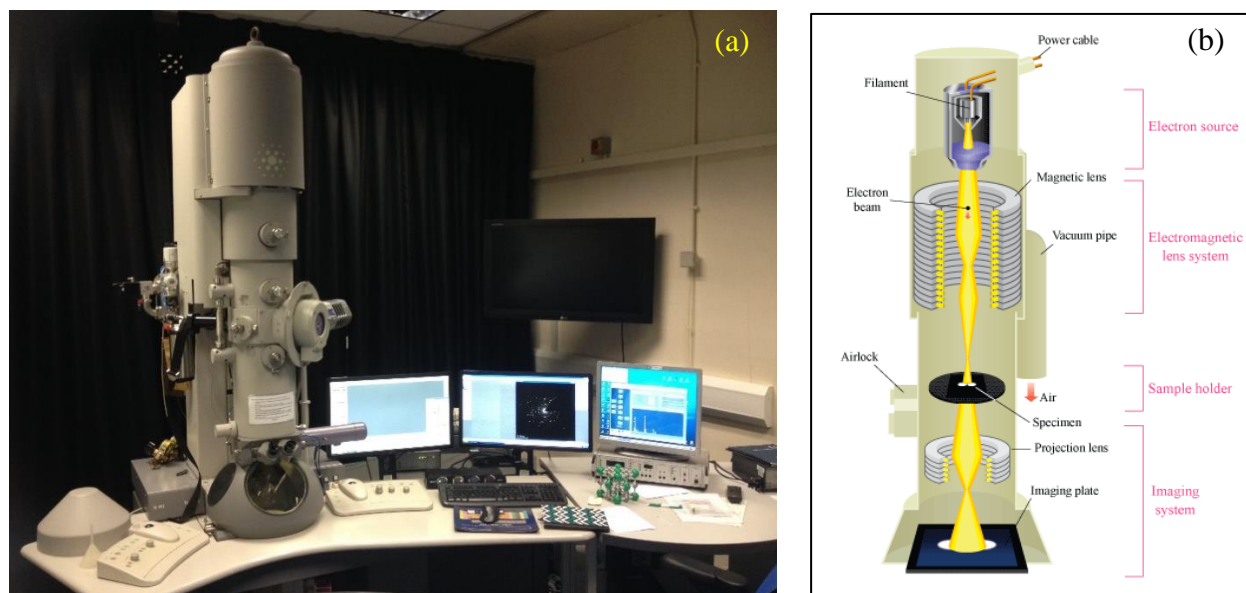
Figure 3.9 (a) TEM instrument and (b) a schematic diagram of a TEM layout [415]

Figure 3.9 illustrating a Tecani TEM instrument (a) and schematic outline of a TEM column (b). In general, TEM consists of electron source, electromagnetic lens system, sample holder (single tilt or double tilt), and imaging system [415, 416]. An electron gun (tungsten filament) emits a beam of high velocity electrons when being heated using sufficient voltage of between 100 and 300 kV. The beam is then accelerated towards the sample by the electromagnetic lens and transmits through the sample. The magnetic lens system can be used for re-focusing the electrons after they pass through the sample or for enlarging the image (high magnification) for projecting onto the TEM screen. The column is under a high vacuum while analysing samples in order for the electrons to travel long distances.

In this work, TEM images were taken on a FEI Tecnai TF20 FEG operated at 200 kV and/or a FEI Titan Themis Cubed 300 operated at 300 kV. The object was the investigation the particle size distribution, morphology at high resolution (HR-TEM), composition using energy dispersive X-ray spectroscopy (EDS), inter-planer spacing from diffraction of electrons (selected area electron diffraction, SAED), location of elements (TEM-mapping), and the surface and internal structure properties of catalysts. The catalyst sample was prepared by suspending a small amount of powder

sample in acetone, followed by ultra-sonication for 10 min. One drop of this suspension was put on a carbon-coated copper/gold grid for TEM analysis.
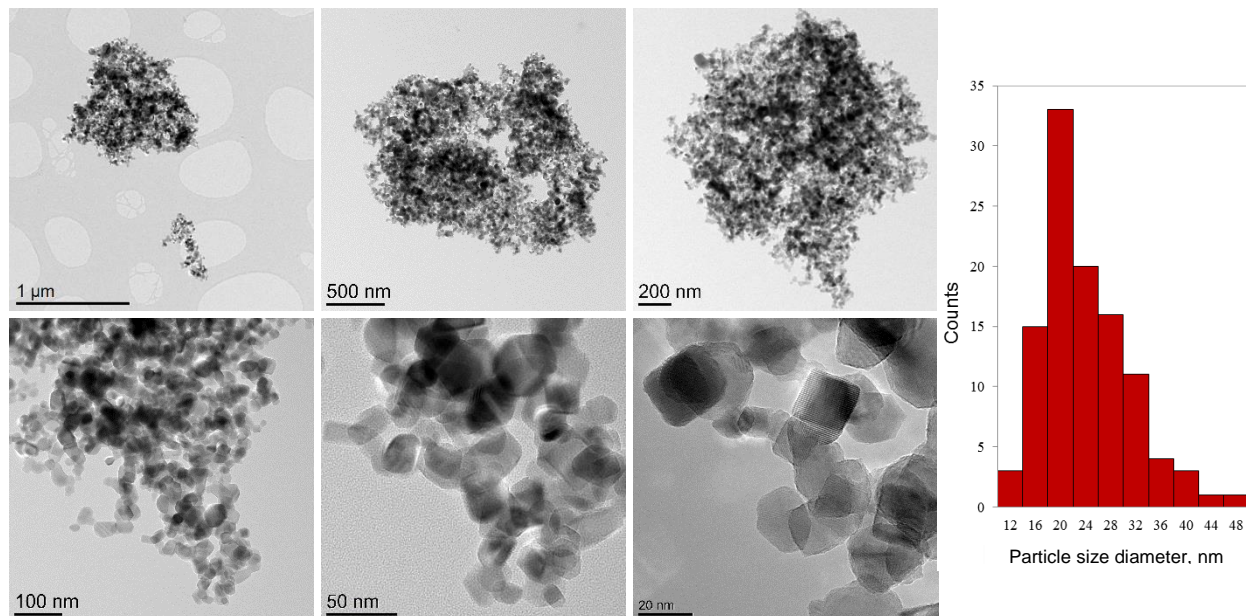
Figure 3.10 TEM images at different magnifications showing the morphologies and particle size distributions of commercial TiO_2 NPs used in this work
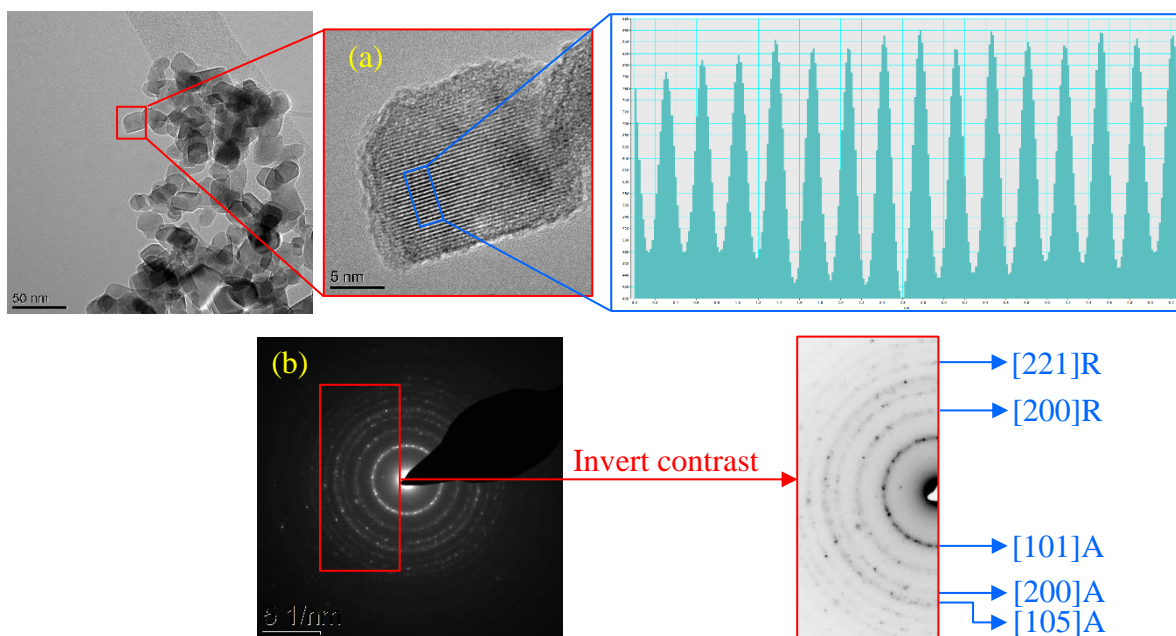
Figure 3.11 (a) HR-TEM image showing fringes and (b) SAED for TiO_2 NPs

The location of the elements and elemental compositions of the prepared catalyst sample were identified using the TEM fitted with a high-angle annular dark field (HAADF) detector operated at an accelerating voltage of 200 kV/300 kV and equipped with an energy dispersive X-ray spectroscopy (EDS, Oxford INCA 350). Further analysis of average size and d-spacing was carried out using Gatan Digital Micrograph software. Figure 3.10 shows an example of TEM images were taken on a Tecani microscope at different magnifications and particle size distributions as per 108 particles in different TEM images for TiO_2 NPs. The lattice planes were also determined from SAED pattern and a high resolution TEM image as shown in Figure 3.11. A detailed analysis and discussion will be given in the following chapters.

3.3.5 Nitrogen adsorption-desorption isotherm

When a gas is in contact with the surface of solid material, molecules of the gas stick that surface. The adsorption processes can be classified into physisorption (van der Waals forces, dipole-dipole interaction, etc.) and chemisorption (covalent bond) based on the interaction strength as shown in Figure 3.12 [417, 418].
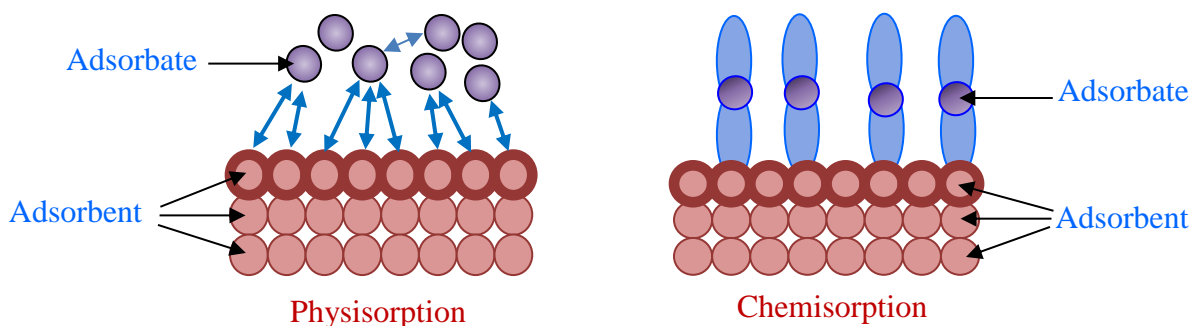
Figure 3.12 Physisorption and chemisorption of gas molecules on the surface of solid material

However, the adsorption isotherm (physisorption) is the most common form used to determine the surface area and porosity of solid materials - defined as the measurement of the quantity of gas adsorbed over a range of partial pressure at constant temperature [419]. Chemisorption involves the chemical bonding between the adsorbent and adsorbate at high temperature and above the critical pressure of adsorbate, which is mainly used to determine the surface area for active metals [418]. Figure 3.13 (a) shows the surface analyser instrument that we used. Figure 3.13 (b) illustrates four stages during the sorption isotherms of gas molecules on the solid surface with increasing the relative pressure from 0.05 to 1. During the first stage the adsorption of gas

molecules on the surface of the solid sample occur, the more energetic sites on the surface of the sample are occupied by gas molecules at low gas pressure then the gas molecules cover the surface of sample to form a monolayer when the gas pressure is increased as shown in stage 2 [420]. According to the Langmuir theory [421], the surface area of material can be determined from the amount of adsorbed gas molecules that are required to make a homogenous monolayer on the surface of a solid sample. The Langmuir's model (main assumptions) explains by assuming (1) adsorbate will adsorb only at active surface sites; (2) each of these active sites can accommodate one molecule (adsorption saturates at monolayer coverage only); (3) the surface is energetically homogenous (the surface is uniform and all sites are equivalent); and (4) there are no interactions between adsorbed molecules and adsorbed molecules immobile [418].
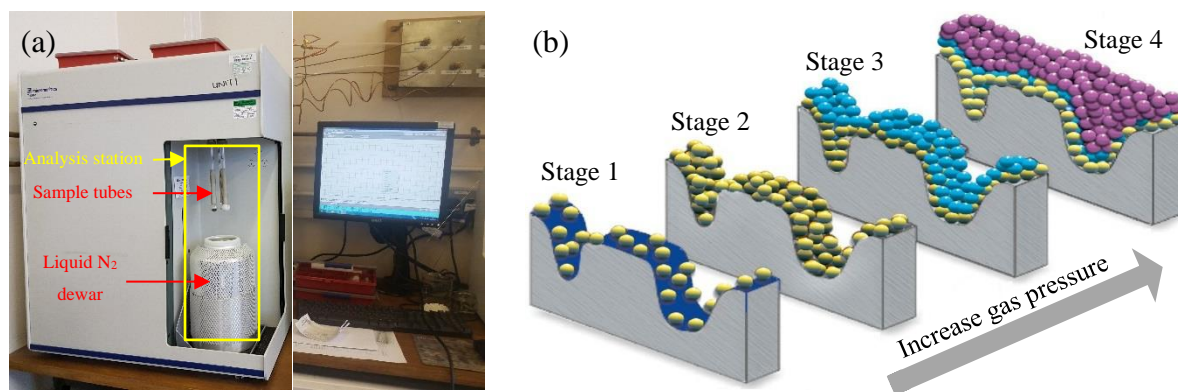
Figure 3.13 (a) Micromeritics TriStar 3000 surface analyser instrument and (b) how molecules of gas absorb on the surface of solid materials [420]

A further increase in gas pressure leads to multilayers of gas on the surface, filling smaller pores in the solid sample as shown in stage 3. However, Langmuir's assumptions are not applicable for many materials (lack of linearity in the Langmuir plot and overestimated the surface area for the type II to type V isotherms) due to surface area measurements obtained from type I isotherms regardless whether physisorption or chemisorption is occurring. Therefore, Brunauer, Emmett and Teller (BET) developed Langmuir's assumption to accommodate multilayer formation via an additional parameter which is called C (molecules of gas physically adsorb on a solid surface in layers infinitely). According to BET theory [422], the total surface area of solid material can be calculated from the monolayer capacity according to equation 3.5:

$$\frac{1}{W[\frac{P_0}{P}-1]} = \frac{1}{W_m C} + \frac{C-1}{W_m C}\left(\frac{P}{P_0}\right) \qquad \text{Equation 3.5}$$

in which P is the equilibrium pressure, P_0 is the saturation, W is the quantity of adsorbed gas, W_m is the quantity of monolayer adsorbed gas, and C is the BET constant. This equation requires a linear plot between $1/W[(P_0/P)-1]$ and P/P_0. The relative pressure (P/P_0) for most solid material is restricted between the ranges of 0.05 and 0.35 [417, 418] as shown in Figure 3.14.
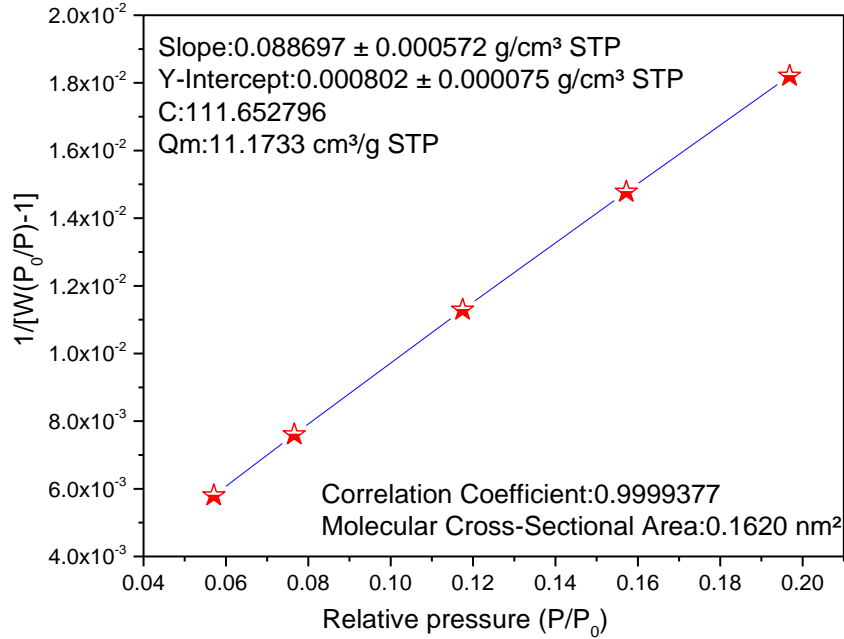
Figure 3.14 Typical BET plot for commercial TiO_2 NPs used in this work

The weight of absorbed monolayer gas molecules (Q_m or W_m) can be obtained from the slope and intercept as given in Equations 3.6 and 3.7;

$$s = \frac{C-1}{W_m C} \qquad \text{Equation 3.6}$$

$$i = \frac{1}{W_m C} \qquad \text{Equation 3.7}$$

$$c = 1 + \frac{s}{i} \qquad \text{Equation 3.8}$$

In which s is the slope obtained from the BET plot and i is the intercept. By combining equation 3.6 and 3.7 we could determine the adsorbed monolayer weight W_m as follows;

$$W_m = \frac{1}{s+i} \qquad \text{Equation 3.9}$$

The total surface area of the solid sample can be calculated using Equation 3.10;

$$S_t = \frac{W_m \, N \, A_{cs}}{M} \qquad \text{Equation 3.10}$$

Where M is the molecular weight of the adsorbate, A_{cs} is the molecular cross-sectional area, and N is Avogadro's number (6.023×10^{23} molecules/mole).

The specific surface area of the solid materials can be derived from S_t and the weight of the solid sample (W_s) according to equation 3.11:

$$S = \frac{S_t}{W_s} \qquad \text{Equation 3.11}$$

The particle size of solid materials can also be estimated from specific surface area (S) in m^2/g and density of the sample according to equation 3.12;

$$D_{particle}(nm) = \frac{6}{(\rho*S)} \qquad \text{Equation 3.12}$$

The final stage in Figure 3.13 (b) shows how gas molecules completely covered the surface of solid material and filled all the pores. This is the stage that can be used to calculate the porosity of solid materials. In general, solid materials can be classified into two categories: non-porous and porous. Figure 3.15 illustrates examples of non-porous and porous materials. Non-porous materials normally have low specific surface area with very low pore volumes whilst porous materials have a high specific surface area with large pore volumes.
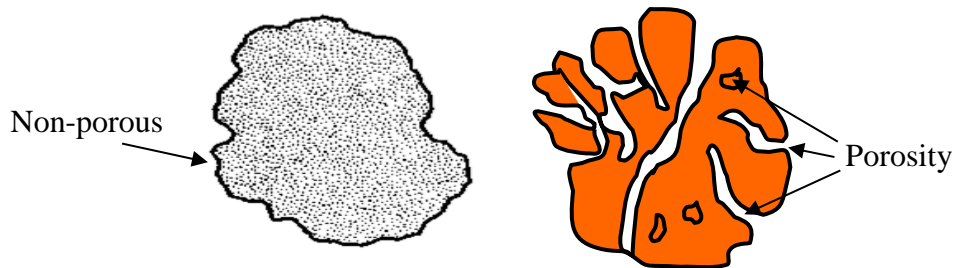
Figure 3.15 Non-porous and porous solid materials [423]

Porosity of solid materials can be used to perform specific functions based on their pore sizes. According to the International Union for Pure and Applied Chemistry (IUPAC), there are three types of porous materials: microporous (less than 2 nm); mesoporous (between 2nm and 50nm); and macroporous (bigger than 50 nm) [419, 424]. Total pore volume and pore size distribution are the most common techniques for describing porosity of solid material. There are several mathematical methods for determining the pore size distribution from sorption isotherms. Among them, Barrett-Joyner-Halenda (BJH) is the most popular one. It is based on the application of Kelvin's model (see equation 3.13) of pore filling [425].

$$\ln\left(\frac{P}{P_0}\right) = -\left(\frac{2\gamma v_m \cos\theta}{RTr_m}\right) \qquad \text{Equation 3.13}$$

Where (P/P_0) is a relative vapour pressure at which condensation occurs, θ is an adsorbate surface contact angle assumed to be zero for N_2, v_m is the molar volume of liquid nitrogen (34.7 cm^3/mole), γ is the surface tension of the liquid N_2 (8.85 ergs/cm^2 at 77 K), R is a real gas constant (8.314x10^7 ergs/degree/mole), T is a boiling point of N_2 (77 K), r_m is the mean radius of condensed gas meniscus [424].
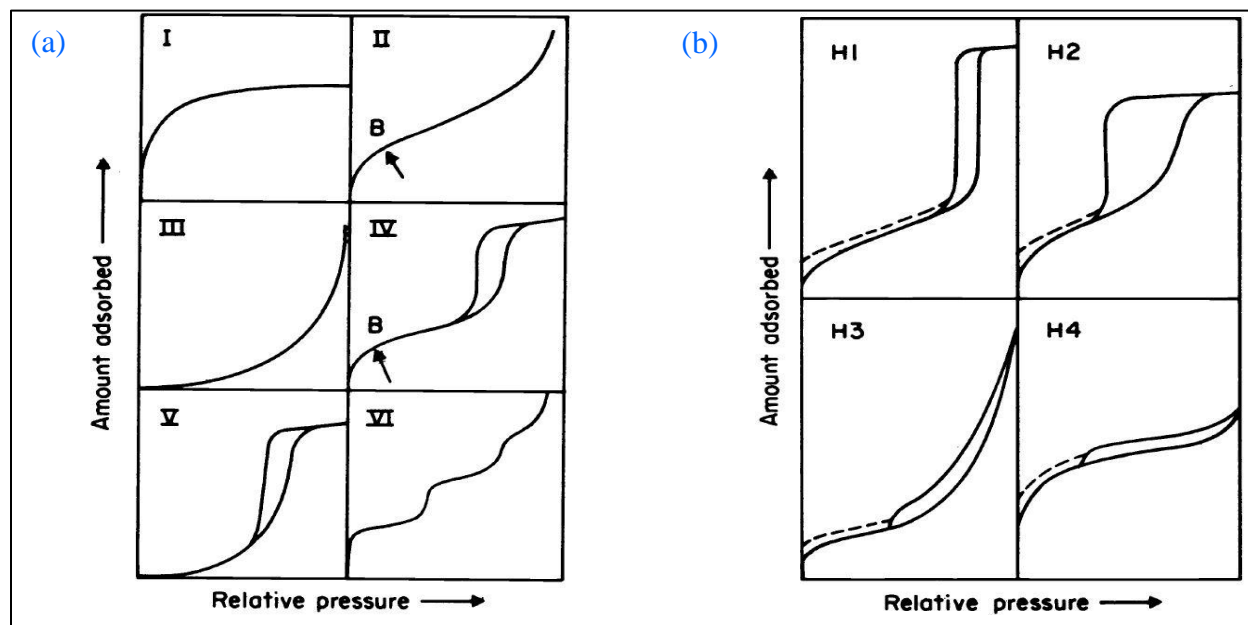
Figure 3.16 Classification of (a) adsorption isotherms and (b) hysteresis loops [419]

Throughout this work, nitrogen porosimetry was obtained according to the multipoint nitrogen adsorption (condensation-desorption (evaporation) method at 77.3 K using Micromeritics TriStar 3000 surface analyser. A desired amount of catalyst samples (about 0.5 to 1.0 g) were added to the glass tubes and the weight recorded. After the samples have been weighed, we put the glass tubes in a vacuum oven at 120 °C for 24 h under a vacuum of 10 mmHg for outgassing [424] in order to remove contaminates (if any) such as moisture and/or gases which may have been adsorbed to the surface of the samples. After degassing was complete, the sample tubes were re-weighted and attached to the surface analyser port unit. A dewar of liquid nitrogen was filled with liquid N_2 and all parameters set using TriStar 3000 software for analysis after which the isotherm was constructed point by point. Once the analysis was completed, MicroActive software was used for exporting all data. In order to calculate the BET surface area, the N_2 adsorption isotherms [$\Delta G_{ads.}$=RT(ln$P_{ads.}$-lnP_o)] data over the relative pressure range of 0.04-0.2 were used for all catalyst

samples; however, desorption isotherms [$\Delta G_{des.}=RT(\ln P_{des.}-\ln P_o)$] were used to calculate the average pore size and total pore volume for all samples using the BJH method. Since $P_{des.} < P_{ads.}$ it follows that $\Delta G_{des.} < \Delta G_{ads.}$. Therefore, the desorption value of relative pressure corresponds to the more stable adsorbate condition and that is why desorption isotherms should be used for pore-size analysis [418]. The obtained sorption isotherms and hysteresis were classified according to the IUPAC as shown in Figure 3.16 [419, 424]. Type I isotherm characterises microporous materials corresponding to a complete formation of monolayer having relatively small external surface area and strong interaction between the molecules of gas and solid materials. Type II isotherm describes adsorption on non-porous or macroporous materials with formation layer by layer. Adsorption (unrestricted monolayer-multilayer) progresses with increasing relative pressure until P/P_0 close to 1. Type III is a relatively rare isotherm having a monolayer adsorption with weak adsorbent-adsorbate interactions. Type IV isotherm corresponds to the consecutive adsorbate layer formation, having hysteresis loops. The initial region of Type IV is closely related to Type II. The hysteresis loop is usually associated with the filling at a relative high pressure during adsorption and then at lower pressure during desorption. Type V is an uncommon isotherm related to Type III, but it exhibits hysteresis loop. Type VI isotherm describes a stepwise multilayer adsorption on uniform nonporous materials.
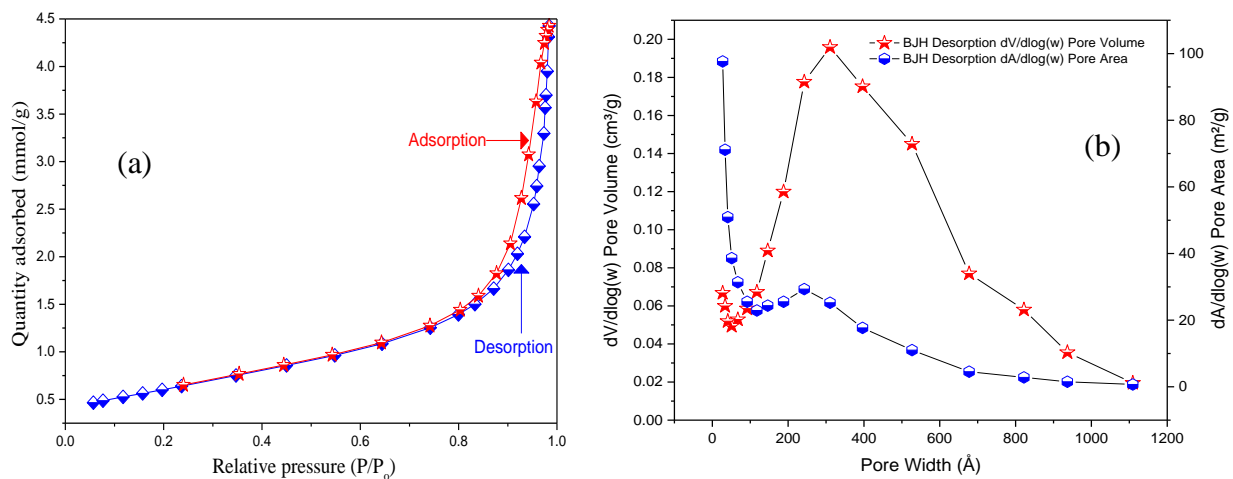
Figure 3.17 A typical nitrogen sorption isotherm (a) and total pore volume with mean pore size (b) for TiO_2 NPs

Hysteresis loops reveal information about the shape of the pores and are more common in mesoporous materials. Hysteresis loop one (H1) is a fairly narrow loop with near parallel

adsorption and desorption which is witnessed of uniform pore size for typical cylindrical pores, but hysteresis loop two (H2) is a broad with long and depicts a non-uniform ink-bottle pore shape. Hysteresis loops three (H3) and four (H4) produce slit shaped pores. H3 is normally produced by aggregate particles [418, 424, 425]. An example of nitrogen adsorption-desorption isotherm of commercial TiO_2 NPs used in this work is presented in Figure 3.17.

3.3.6 X-ray photoelectron spectroscopy (XPS)

XPS, also known as Electron Spectroscopy for Chemical Analysis (ESCA), is an essential technique for the analysis of external surface layers in solid material, providing information on the elemental composition, oxidation state, purity and chemical environmental of the solid materials by evaluating the electronic structure of atoms/ions [426]. This technique is based on Einstein's principle (E = *hv*) concerning the photoelectron spectroscopy. It was later developed by Kai Siegbahn and his research group at the University of Uppsala in the mid-1960s [427]. The surface of sample to be examined is irradiated by a mono-energetic soft X-ray photon beam, Mg Kα (*hv*=1253.6 eV) and Al Kα (*hv*=1486.6 eV) mainly used because of their low energies, *in vacuo.* They interact (absorption of incident X-rays) with the atoms in the surface region then eject a photoelectron by energy, leaving a core hole behind [428] as shown in Figure 3.18. This creates an excited ionic state, which later relaxes into the final ground state as outer electrons fill the core holes [429].
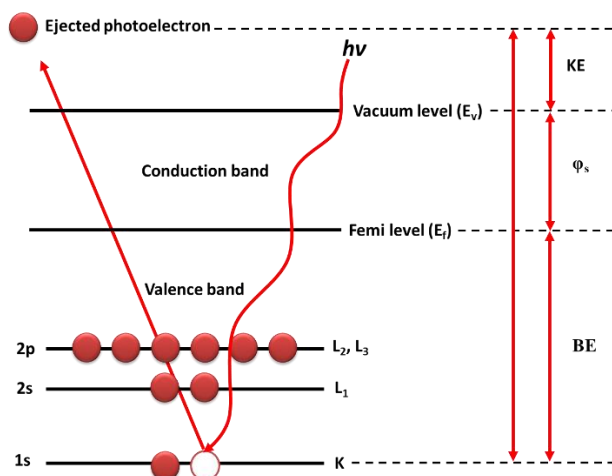
Figure 3.18 Schematic diagram of XPS process illustrating a photo-ionisation of an atom. (*hv* is an incident X-ray source (photon energy); BE is the electron binding energy; φ_s is the work function; KE is the photoelectron kinetic energy; E_f is the Fermi level; E_v is the vacuum level)

The kinetic energy distribution of the ejected photoelectron can be detected from the XPS (see Equation 3.14) which is characteristic of the elements and its environment.

$$KE = h\nu - BE - \varphi_s \qquad \text{Equation 3.14}$$

Where φ_s is the spectrometer work function; BE the electron binding energy; $h\nu$ the energy of the incoming photon (Planck's constant multiply by frequency); KE the photoelectron kinetic energy. The number of detected photoelectrons per energy interval versus their kinetic energy produces a unique XPS spectrum which is for the detected electrons originate only from the top few atomic layers. This is due to the short distance (1-3 nm) that a photoelectron can travel without losing energy by some sort of interactions, inelastic collisions, excitation of the sample and recombination within the material. This can reduce the number of escaping photoelectrons. However, the surface sensitivity can be enhanced by varying the tilt angle from $0°$ to maybe $90°$ at which electrons are detected from the surface. Therefore, the ejected photoelectrons from the surface can travel longer distance. The intensity of decay can be expressed by the following equation:

$$I_{(d)} = I_o e^{(-d/\lambda \cos\theta)} \qquad \text{Equation 3.15}$$

Where θ is the angle between the analyser and the surface normal (from $0°$ to $90°$), λ is the inelastic mean free path of an electron (IMFP), d is the depth, I_o is the intensity of the primary electron at depth per unit time and $I_{(d)}$ is the intensity of the same electron that reaches the surface. Quantification of the concentration of the elements in the surface can be also obtained from the areas or heights (intensities) of peaks because each element has a unique set of binding energies [430]. Finally, the oxidation states can be extracted from the peak positions. According to Koopmans' theorem, binding energy is the energy difference between the initial (atom with n electrons) and final states after the photoelectron has left the atom (n-1 electron/ion) in case relaxation of excited ionic state followed the photoemission to fill the core hole. All orbital levels (p, d and f), except the s orbital level, become split upon ionization giving rise to a doublet with the two final states due to spin-spin orbital splitting (j-j coupling) as given in equation 3.16;

$$j = l + m_s \qquad \text{Equation 3.16}$$

Where j is the total angular momentum; l is the orbital angular momentum (l=0, 1, 2, 3, etc. corresponding to s, p, d, f orbital levels); m_s is the magnetic field of spin ($m_s=\pm\frac{1}{2}$ for one unpaired electron) [426]. An example of wide scan spectrum and the spin-spin splitting of Ti 2p peak in TiO_2 NPs is shown in Figure 3.19 (b). The number of components fitted to an XPS spectrum depends on the number of environments that the electron being analysed is found in within the

sample. The observed peaks originating from photoemissions in Figure 3.19 (a) can be grouped into three groups which are: (1) from core levels, (2) from valance levels at low binding energy, and (3) from X-ray excited Anger emission.

In this work, the XPS was performed, at the University of Ulster, on a KRATOS XSAM 800 fitted with an energy analyser. The X-ray source employed was Al Kα X-ray source (monochromated radiation 1486 eV) generated from an aluminium anode operating at the emission voltage 15 keV and 5 mA. The base pressure within the spectrometer during examination was 6.5×10^{-10} bar to maintain an uncontaminated surface during data acquisition. The films of catalyst samples were prepared by dispersing a few milligrams of each sample in chloroform and methanol (3:1) then coating on the silicon wafer surface. The surfaces were exposed to near infrared light to evaporate the solvent to make a thin film. The CasaXPS and origin software were used for spectral fitting and binding energies charge correction to the C 1s peak at 285 eV to compensate for residual charging effects due to an increasing positive charge at the analyte surface. The peak intensities and peak positions from the XPS spectra were used to measure how much of a material is at the surface and the elemental/chemical composition of the sample, respectively.
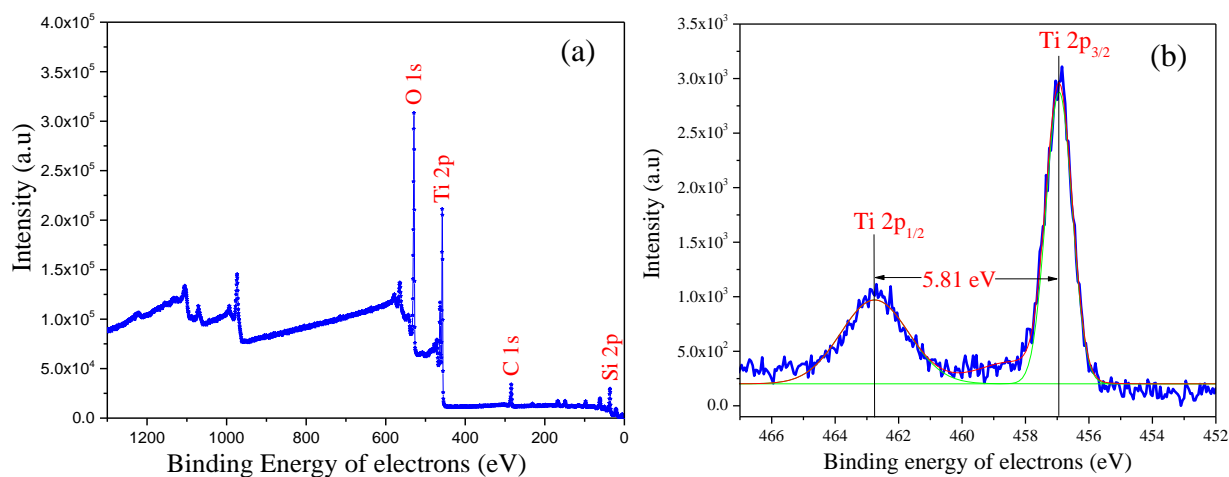
Figure 3.19 A survey spectrum (a) and high resolution of Ti 2P peak for TiO$_2$ NPs

3.3.7 Thermogravimetric analysis (TGA)

TGA is a method of thermal analysis in which microbalance monitors the weight changes of a sample as a function of time and temperature in a controlled atmosphere such as N$_2$ gas (inert). This technique can be used to characterise any materials (liquids or solids) that exhibit a weight

change (loss or gain) as a result of decomposition, dehydration, desorption, reduction and oxidation [431]. TGA was employed in this work to analyse the thermal stability of solid acid catalysts and to quantify volatile components in the catalyst samples. Figure 3.20 illustrates the schematic diagram of the TGA used, which consists of a balance control unit, mass flow controller unit, furnace, loading/unloading samples (pan), and a temperature programming facility connected with thermocouples.
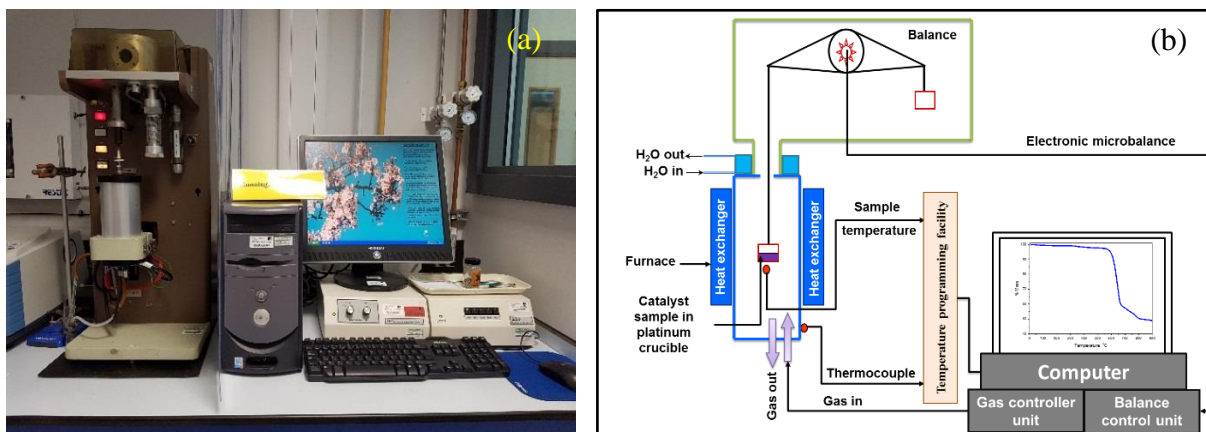
Figure 3.20 TGA instrument (a) and schematic diagram of the TGA (b)

The basic principle of this technique is that an empty platinum pan is tared then the sample loaded inside the pan. The pan with sample is positioned inside the furnace and heated under constant heating rate while mass changes are monitored via microbalance against time and temperature. The temperature of the system and sample is monitored accurately via thermocouples and the output data is plotted as mass of the sample with respect to time/temperature. The atmosphere in the sample chamber is normally purged with an inert gas to prevent oxidation or other reactions during the experiment. The weight loss or gain from the sample can be used to assess the thermal stability of the sample [431].

Throughout this work the thermal stability of catalysts was performed on a Mettler Toledo (TGA/DSC-2) star^e system and/or a Stanton Redcroft thermogravimetric analysis (TGA-TGH 1000). The system was programmed to heat up from 25 °C to 900 °C at 10 °C/min under nitrogen gas at 50 mL/min with a constant flow rate. STAR^e and TAS infinity PRO software were used to export the data for all catalysts. In order to analyse the evolved gases from the decomposition of samples in the TGA system [409], TGA/FT-IR was used in some cases. The thermal

decomposition of evolved gases was investigated using Stanton Redcroft thermogravimetric analysis (TGA-TGH 1000) connected via a transfer line to a Nicolet iS10 FT-IR spectrometer to confirm the decomposition of the catalyst via gas production, in particular loss of SO_x molecules and absorbed surface species as shown in Figure 3.21. The transfer line was kept at 170°C and the interface cell oven was maintained at 220 °C to prevent any condensation of evolved gases. (20±5) mg of sample was weighted in a 100 µL platinum crucible and placed in the TGA sample holder. The system was programmed to heat the catalyst samples from 25 °C to 900 °C at 10 °C per min under different purge gases, nitrogen and air separately at 30mL per min with a constant flow rate. The system was then held at 900 °C for 10 min before being cooled to room temperature using a water jacket circulator (Julabo F32).
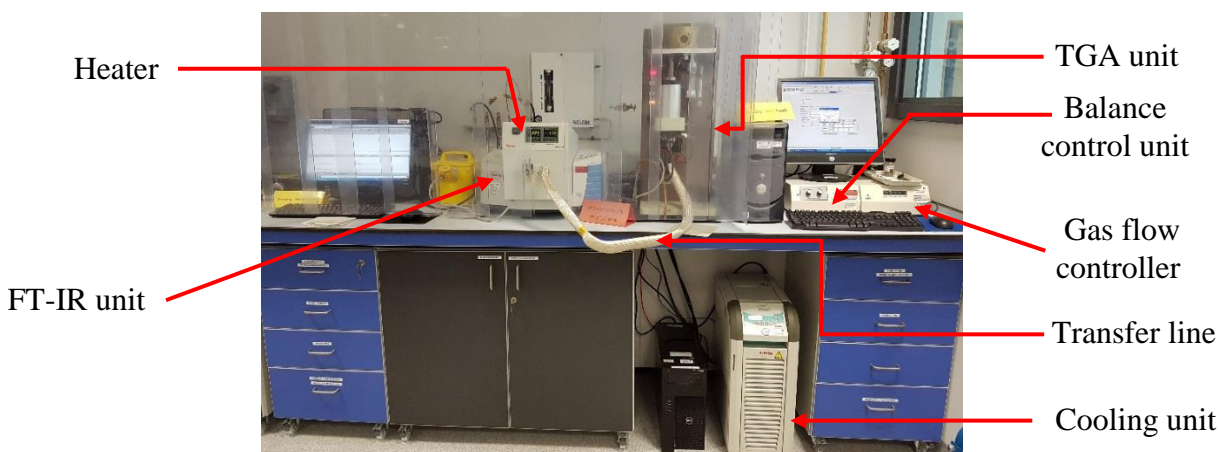
Figure 3.21 Photographic of the TGA/FT-IR system

3.3.8 CHNS analysis

CHNS analysis was used to quantify the percentage of elemental analysis for propyl sulfonic acid loading onto the surface of TiO_2 NPs. The principle of this technique is based on the Pregl-Dumas method. The elemental analyser (Thermo Scientific™ FLASH 2000 CHNS Analyzer) is calibrated using different standard components for each element (C, S). About 2-3 mg of sample was weighted into pressed silver capsules then the capsules with the sample were loaded into the CHNS analyser followed by complete sample combustion in pure oxygen at high temperature (furnace at 1000°C) using "flash combustion". The combustion products (H_2O, CO_2, SO_2) are removed from the combustion chamber using helium as an inert gas and they are separated using a

chromatographic column and are detected on the thermal conductivity detector (TCD) as an output signal. These signals are proportional to the concentration of the individual components in the mixture [432]. The EA 2400 Data Manager, which is SQL-based software, was used for data manipulating and exporting the results.

3.3.9 Diffuse reflectance infrared Fourier transform spectroscopy (DRIFTS)

DRIFTS, also known as "Kubelka–Munk " reflection, is an IR spectroscopy technique which was in this work as a surface sensitive infrared method to identify the types of acid sites on the surface of catalyst samples by recognising the adsorption bonds formed between the acid sites and a probe molecule [433, 434]. The measured intensity of the reflected light in a DRIFTS experiment depends upon the shape and size of the particles in the sample/KBr, crystallite orientation, sample homogeneity, analyte concentration and how they are packed together. The basic principle of this surface sensitive technique is that when an IR beam is focused onto the particles in a diluted sample with a non-absorbing matrix (eg. KBr powder to achieve low absorbance), the incident beam of the IR penetrates before being scattered and interacts with the particles (reflected from neighbouring particles) in the sample under controlled temperature and environment conditions or transmitted through particles [435]. The penetration depth of the beam (10 to 500 µm) depends on the reflective and adsorptive surface characteristics of the catalyst samples. The absorbed radiation are then diffusely reflected in different directions (see Figure 3.22) then directed by the mirror to the IR detector. It records as an interferogram signal which can be used to generate the spectrum of the sample. Finally, the ratio of Brønsted to Lewis acid sites can be determined from the spectrum based on the ring vibrational of absorbed pyridine (chemisorbed) in the range of 1400-1650 cm^{-1} [434, 436]. In diffuse reflectance spectroscopy, require the use of Kubelka–Munk function to provide the linear relation between the concentration of the sample and sample concentration [437].

Different molecular probe methods, including pyridine, CO, CH_3CN, NH_3, NO molecules, have been used to determine the strength of acid sites. Among them, pyridine has been preferred as an IR probe base molecule due to (1) being much more strongly absorbed than CH_3CN and carbon monoxide; (2) its more stability and selectivity in comparison with ammonia; and (3) being relatively more sensitive to the strength of Lewis acid sites than nitrogen monoxide molecules [438, 439].
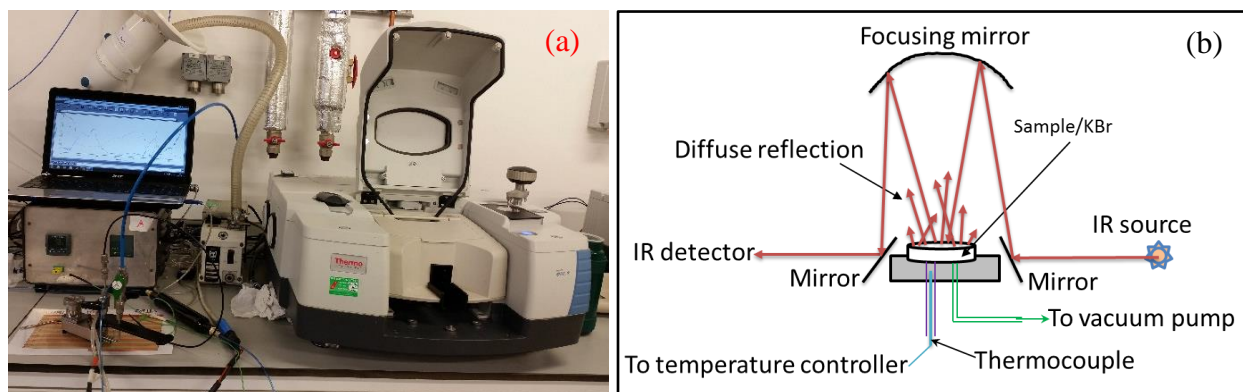
Figure 3.22 (a) DRIFTS instrument and (b) schematic diagram of a basic concepts of DRIFTS.
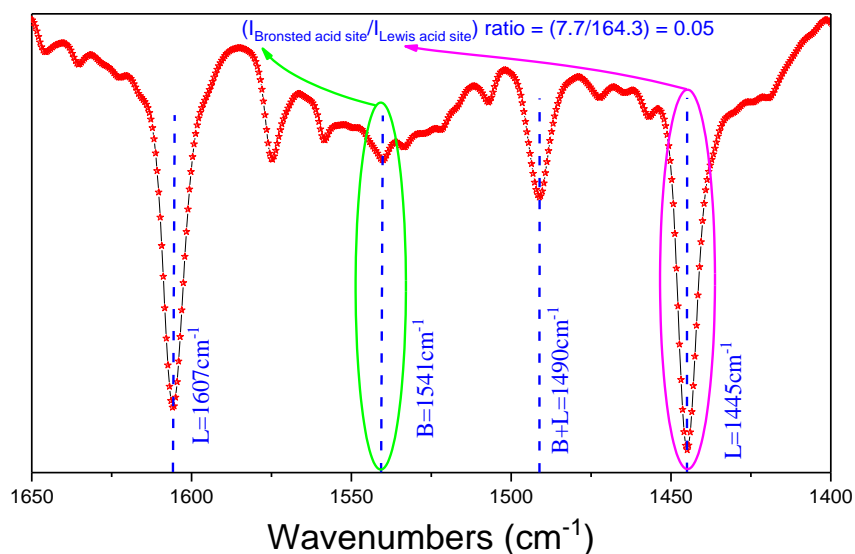
Figure 3.23 DRIFT spectrum illustrating the ring vibration of pyridine detected on the surface of TiO$_2$ NPs. The area under the Brønsted acid sites (1541 cm^{-1}) and Lewis acid sites (1445 cm^{-1}) absorption bands were measured and used to determine the ratio of Brønsted to Lewis.

In this work, the Brønsted to Lewis acid ratios were determined using a DRIFT spectroscopy pyridine technique at the European Bioenergy Research Institute (EBRI). Prior to DRIFTS analysis, 10 mg of catalyst samples were diluted with 500 mg of potassium bromide. *Ex situ* pyridine adsorption was carried out by wetting the samples with pyridine and the excess of pyridine removed in a vacuum oven at 100 °C overnight. Spectra were collected at 50 °C with a spectral resolution 4 cm^{-1} in the range of 650-4000 cm^{-1} with an environmental cell and smart collector accessory using a Thermo Scientific Nicolet iS50 FT-IR spectrometer with mercury cadmium telluride (MCT)

detector. The obtained spectrum was subtracted from the background and processed with the OMNIC^{TM} software. An example of DRIFT spectrum taken for TiO$_2$ NPs is presented in Figure 3.23.

3.3.10 Temperature programmed desorption (TPD)-Mass spectroscopy (MS)

Several different techniques including spectroscopic and thermo-chemical methods have been reported for characterisation of acid-base properties on catalyst surfaces [433, 434]. Among them, TPD is most widely used to extract information on the quantity and strength of sites of acidic and basic [440]. The amount and sites of acidic and basic information are crucial to understanding and predicting the performance of solid acid catalysts because the activity of solid acid catalysts depends on many factors including Brønsted-acid site densities on the surface of the catalysts. Many molecular probes, including ammonia (pK$_a$ = 9.24, proton affinity in gas phase = 857.7 kJ.mol^{-1}), ethylamine (pK$_a$ = 10.71, proton affinity in gas phase = 912 kJ.mol^{-1}), n-propylamine (pK$_a$ = 10.71, proton affinity in gas phase = 917.8 kJ.mol^{-1}), iso-propylamine (pK$_a$ = 10.63, proton affinity in gas phase = 923.8 kJ.mol^{-1}), tert-butylamine (pK$_a$ = 10.68, proton affinity in gas phase = 934.1 kJ.mol^{-1}) and pyridine (pK$_a$ = 5.19, proton affinity in gas phase = 922.2 kJ. mol^{-1}), have been used for measuring the quantity of acid sites on the surface of solid acid catalysts by neutralising the acid sites [441, 442]. Ammonia-TPD is a very common method for characterisation of site densities in solid acid catalysts due to the simplicity of the technique [181]. However, ammonia-TPD often overestimates the quantity of acid sites and sometime it cannot distinguish between Lewis and Brønsted-acid sites [181, 443]. Therefore, the most widely used reactive probes are the alkyl amines, including n-propylamine, iso-propylamine and t-butylamine. These alkyl amines are very reactive over acid sites at high temperatures to form ammonia and alkene via a reaction similar to the Hoffman elimination reaction [181, 444], as shown below:

$$HRNH_2 + ZOH \longrightarrow NRNH_3^+\text{-----}ZO^-$$
$$NRNH_3^+\text{-----}ZO^- \longrightarrow R + NH_3 + ZOH$$
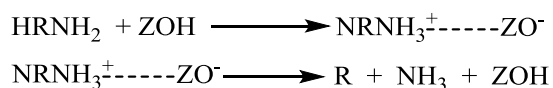
From the amount of n-propylamine mass loss for pure (without n-propylamine)/contaminated (n-propyl amine) catalysts during the TPD, total acidity of the catalyst was calculated and the nature of the acid sites were identified from the MS results. The weight loss stage for molecules associated with low temperature desorption could be probably due to a number of different types of species, including molecules which are hydrogen bonded to protonated amines at the Brønsted-acid sites;

molecules associated with Lewis acid sites and molecules associated with hydroxyl defects. However, the decomposed n-propylamine molecules to propene and ammonia can be detected at higher temperature (650 to 700 K). This desorption feature can be associated with protonated molecules at Brønsted-acid sites [444, 445].

In this work, the acid sites content of solid acid catalysts were performed by using n-propylamine as a probe for TPD-MS at the European Bioenergy Research Institute (EBRI). TPD alone cannot be used for identification of evolved gases [446]. Hence, TPD coupled with mass spectroscopy (MS) is used, at the EBRI, as an extremely sensitive technique for collecting complimentary information (chemical and structure) about the evolved traces of gaseous substance from the decomposition of solid acid catalysts (if any). The samples were separately saturated with n-propyl amine and then the excess of physisorbed n-propyl amine removed *in vacuo* at 30 °C overnight. TPD for pure (without n-propylamine) and contaminated (n-propyl amine) catalysts was performed on the TGA/DSC-2 (Mettler Toledo) connected with a mass spectroscopy (MS, ThermoStar [TM], Pfeiffer Vacuum) under flowing helium gas at 30 mL/min during heating at 10 °C/min from 40 - 800 °C. In order to gain insight into the decomposition process during the TPD for pure (without n-propylamine) and contaminated (n-propyl amine) catalysts, the process were on-line monitored by MS at m/e of 17 (ammonia), 30 (physisorbed n-propylamine), 32 (sulphur), 41 (propene), 49 (propylamine) and 64 (sulphur dioxide) amu. An example of TPD connected with a quadrupole MS for TiO_2 NPs is presented in Figure 3.24.
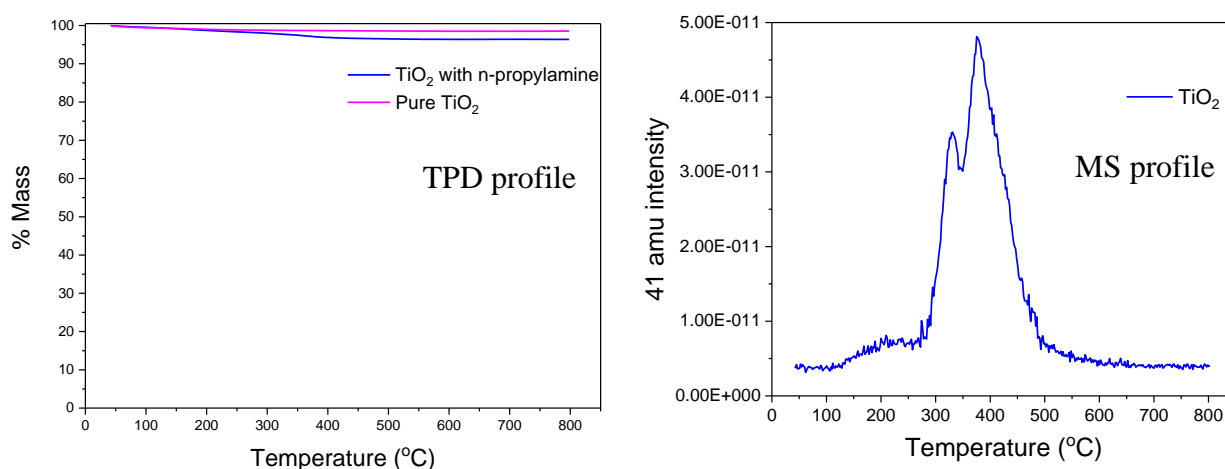
Figure 3.24 TPD-MS profile for irreversibly adsorbed n-propylamine molecules on the surface of TiO_2 catalyst.

3.3.11 Differential scanning calorimetry (DSC)

DSC is a type of thermal technique and was used in this work as a quick method to obtain information about the decomposition point of substances on the surface of the catalyst. The basic principle of this technique is in which the measured heat flow (mW, mJ/s) of the sample and reference as a function of the temperature or time when the material cooled, heated or held isothermally at constant temperature. The measured energy changes can be used to characterise the material for melting, phase transformation or measuring the glass transitions [431, 447, 448].
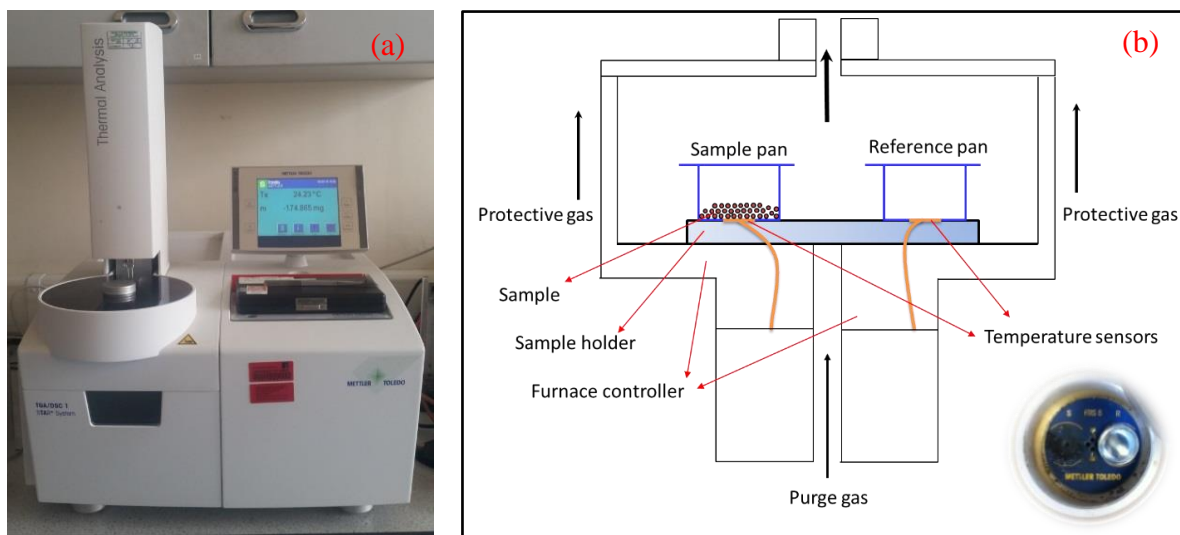
Figure 3.25 (a) TGA/DSC-1 instrument and (b) schematic principle of DSC

In this work the decomposition of propyl sulfonic acid on the surface of TiO_2 NPs was determined by differential scanning calorimetry (TGA/DSC-1, Mettler Toledo, UK) equipped with an intracooler system (Huber TC45) as a temperature controller unit as shown in Figure 3.25. About 5mg of catalyst sample was accurately weighed in a 40 µL sealed standard aluminium pan and the sample spread evenly on the bottom of the pan in order to ensure good thermal contact with the crucible. The pan was then sealed and placed in a DSC 1 sample chamber. The system was programmed to heat from 25°C to 500°C at 10°C/min under nitrogen gas at 50 mL/min with a constant flow rate. Mettler Star^e software was used for programming the system and data processing. Heat flow is equivalent to enthalpy changes as the DSC is at constant pressure;

$$\left(\frac{dq}{dt}\right) p = dH/dt \qquad\qquad \text{Equation 3.17}$$

106

Where dH/dt is the heat flow,

$$\Delta\left(\frac{dH}{dt}\right) = \left(\frac{dH}{dt}\right) sample - \left(\frac{dH}{dt}\right) reference \qquad \text{Equation 3.18}$$

The enthalpy of the melting (decomposition) is calculated by integration of the area of the DSC peak.

3.3.12 Vibrating sample magnetometer (VSM)

VSM was invented by Simon Foner in 1955 [449] and based on Faraday's Law of induction. It was used in this work to measure the magnetic property of catalysts. The principle of this technique is that a small amount of sample is loaded on a sample holder then placed inside a uniform external magnetic field (H) to magnetise the sample. The magnetic sample is sited between two pick-up coils, creating oscillatory motion as shown in Figure 3.26(b) [450]. The resulting magnetic flux will induce a voltage in the pick-up coils that is proportional to the sample's magnetisation. The output hysteresis curve of a sample displays magnetic moment (M in unit Am^2) as a function of H [451]. Materials can be classified into five categories based on their magnetic behaviours responding to the external magnetic field. These are (1) ferrimagnetic, (2) ferromagnetic, (3) anti-ferromagnetic, (4) paramagnetic, and (5) diamagnetic. The magnetisation of material in the cases of paramagnetic and diamagnetic (magnetically disordered) is lost when the external magnetic field (H) is removed. However, in the cases of ferromagnetic, ferromagnetic and anti-ferromagnetic, the external magnetic field only changes the volume of the magnetic domains wall and magnetisation rotation. The magnetised state of these materials can be retained even when the applied external magnetic field is removed [452].

In this work, the magnetic properties of catalyst samples were measured on a Maglab 9T Vibrating Sample Magnetometer (VSM, Oxford instruments). Around (10-15) mg of sample was weighted into gelatine capsules and loaded on the sample holder rod. The sample attached at the end of the sample holder is inserted between pick-ups coils which are in a helium flow cryostat that is driven sinusoidally. The centre of oscillation from the sample is positioned at the vertical centre of pick-up coils then off-set at the centre of the sample. The sample is then vibrated at 2 Tesla after the temperature is set at room temperature. This results in a change in magnetic flux via the coils that induce an electromagnetic field (EMF). The size of the EMF output is proportional to the M of catalyst samples.
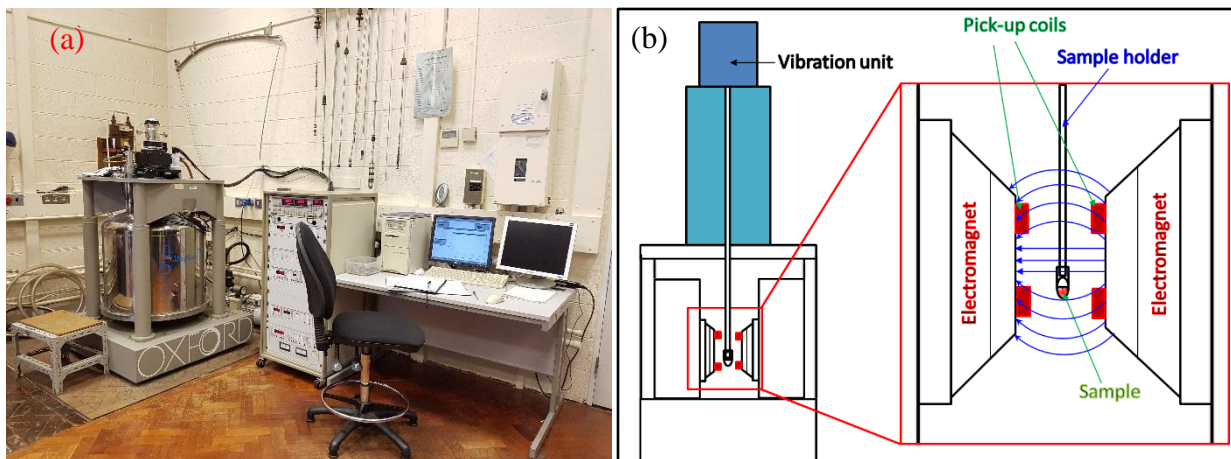
Figure 3.26 (a) A VSM instrument and (b) schematic diagram of the VSM instrument

3.4 Catalytic performances

3.4.1 Synthesis of biodiesel fuel

The simultaneous esterification and transesterification of UCO was performed in a 1 L glass batch reactor connected with an automatic temperature controller loop system (Ministat Huber 125 Pilot ONE Controller, UK) under a constant agitation rate at 600 using a digital mechanical stirrer (Eurostar digital IKA) and a reflux condenser using tap water to condense methanol vapour escaping from the reaction process, as shown in Figure 3.27.
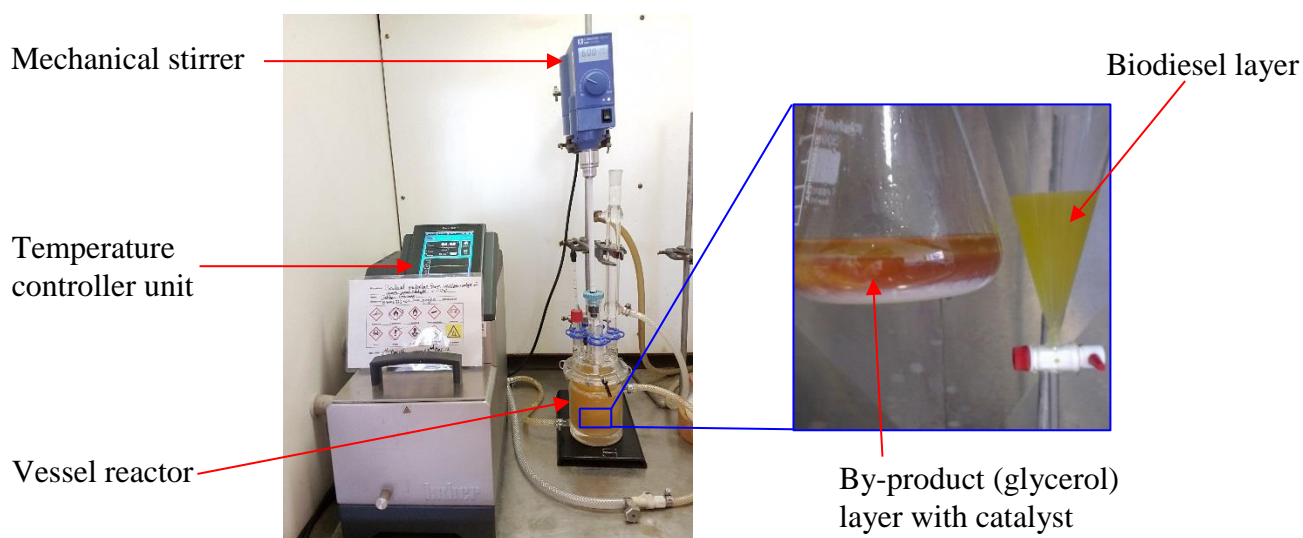
Figure 3.27 A lab-scale experimental set up for biodiesel production

Specified amounts of catalyst, pre-treated UCO and methanol were charged into the batch reactor. The three-phase mixture (solid-liquid-liquid) was agitated and heated to specified temperatures and times. The final reaction mixture was allowed to cool to ambient temperature then transferred into a separating funnel. The crude methyl ester was separated by gravity from the glycerol layer and catalyst. The crude biodiesel layer was then taken for further purification from any remaining catalyst and glycerol using a centrifuge at 9000 RPM for 10 minutes. The purified biodiesel was analysed using GC-MS and GC-FID in accordance to ASTM [129] and EU [130] standards in order to quantify the fatty acid methyl esters (FAME) in synthesised biodiesel.

In order to achieve an optimum process condition, all the process parameters were fixed except for one in turn being changed to obtain the maximum biodiesel yield using response surface methodology. The design variables were reaction time (hr), catalyst loading (wt%), methanol to oil mole ratio and reaction temperature ($^\circ$C) whilst the response factor variable was FAME yield (%). Each experiment was carried out three times and the average biodiesel yield was taken as the response variable FAME yield. For example, the optimum reaction temperature for biodiesel production over $TiO_2/PrSO_3H$ solid acid catalyst was determined by varying the duration reaction time at ½, 1, 2, 3, 4, 5, 6, 7, 8 and 9 h while keeping other parameters fixed at 1 wt% of catalyst loading to UCO, 6:1 methanol to UCO mole ratio, 65 $^\circ$C reaction temperature and 600 RPM agitation rate. This process was repeated for each of the other process parameters to achieve the optimum condition for biodiesel production from UCO. Finally, the effect of level of FFA (oleic acid) in the virgin oil feedstock (corn oil) on the biodiesel yield, as well as the catalyst activity and stability during the esterification/transesterification, were studied in detail under the obtained optimum condition for the production of biodiesel from UCO.

3.4.2 Biodiesel quality

Final product analysis of the transesterification process is an important factor in determining the quality of biodiesel fuel because of the potential presence of contaminants with FAME such as free and total glycerol, remained catalyst, unreacted methanol, and FFAs. In the literature, different analytical techniques have been applied for analysing biodiesel fuels, some of which are: thin layer chromatography [154]; gas chromatography [453-455]; thermo-gravimetric analysis [456]; high

performance liquid chromatography [457, 458]; nuclear magnetic resonance [459]; flow injection analysis [460] and near-IR spectroscopy [461, 462]. In this work, biodiesel products from different catalytic esterification and transesterification processes were analysed and quantified by gas chromatography equipped with a mass spectroscopy instrument (GC-MS) modified procedure of EN-14103 [463]. Figure 3.28 presents the Perkin Elmer Clarus GC-MS used to quantify individual FAMEs in biodiesel samples.
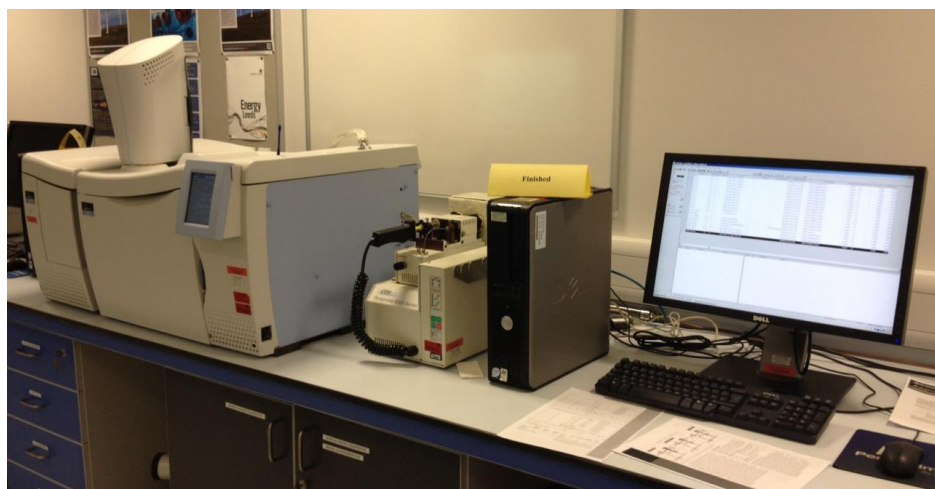
Figure 3.28 Gas chromatography-mass spectroscopy instrument

3.4.2.1 Preparation of sample and standard solution for GC-MS

In order for accurate quantification of FAME from obtained biodiesel, the method has optimised using a standard FAME mixture (between C_{14} and C_{24} neat fatty acid methyl ester). A standard solution was prepared in a volumetric flask by dissolving 50 mg accurately weighted internal standard (methyl heptadecanoate, $C_{17:0}$) with 100 mg of reference FAME mix in 10 mL of n-heptane. A 1.0 mL of the resulting solution was transferred into a 2.0 mL GC amber bottle and 0.5 µL was automatically injected to the GC instrument to calibrate the system for quantitative analysis. The amount of each FAME was calculated via relative response factor between any FAME and internal standard (methyl heptadecanoate). The detailed manufacturing analysis of reference FAME mix rapeseed oil determined by using a capillary GC-FID is given in Table 3.3. Figure 3.29 presents the resulting chromatogram showed the retention times and elution order of the FAME peaks. The total FAME and FAML were calculated using the integrated peak areas of the FAME identified in the calibration standard reference. In general, the FAMEs elute in order of increasing carbon number from $C_{14:0}$ to $C_{24:0}$.

Table 3.3 Summary of reference FAME mix rapeseed oil (supplier Sigma-Aldrich, catalogue number: O7756-1AMP, analytical GC standard, ampule of 100 mg)

Component Name	RT [min]	Purity [%]	Area [uV*sec]	Height [uV]	Area [%]	Norm. area [%]	Adjusted Amount
$C_{14:0}$	21.145	99.9	90041.64	23252.04	0.96	0.96	0.09
$C_{16:0}$	25.086	99.7	374240.4	65383.7	4.01	4.01	0.3742
$C_{18:0}$	29.133	99.9	281016	19504.7	3.01	3.01	0.281
$C_{18:1}$	30.349	99.9	5615525	331565.8	60.12	60.12	5.6155
$C_{18:2}$	31.769	99.9	1111213	147224.6	11.9	11.9	1.1112
$C_{20:0}$	32.509	99.9	284555.7	41752.7	3.05	3.05	0.2846
$C_{18:3}$	33.651	99.9	542398.4	77628.4	5.81	5.81	0.5424
$C_{22:0}$	36.028	99.8	286460.3	31184.5	3.07	3.07	0.2865
$C_{22:1}$	37.1	99.9	463471.3	56235.76	4.96	4.96	0.4635
$C_{24:0}$	39.586	99.9	291342.4	30667.55	3.12	3.12	0.2913
			9340264.67	824399.76	100	100	9.3403
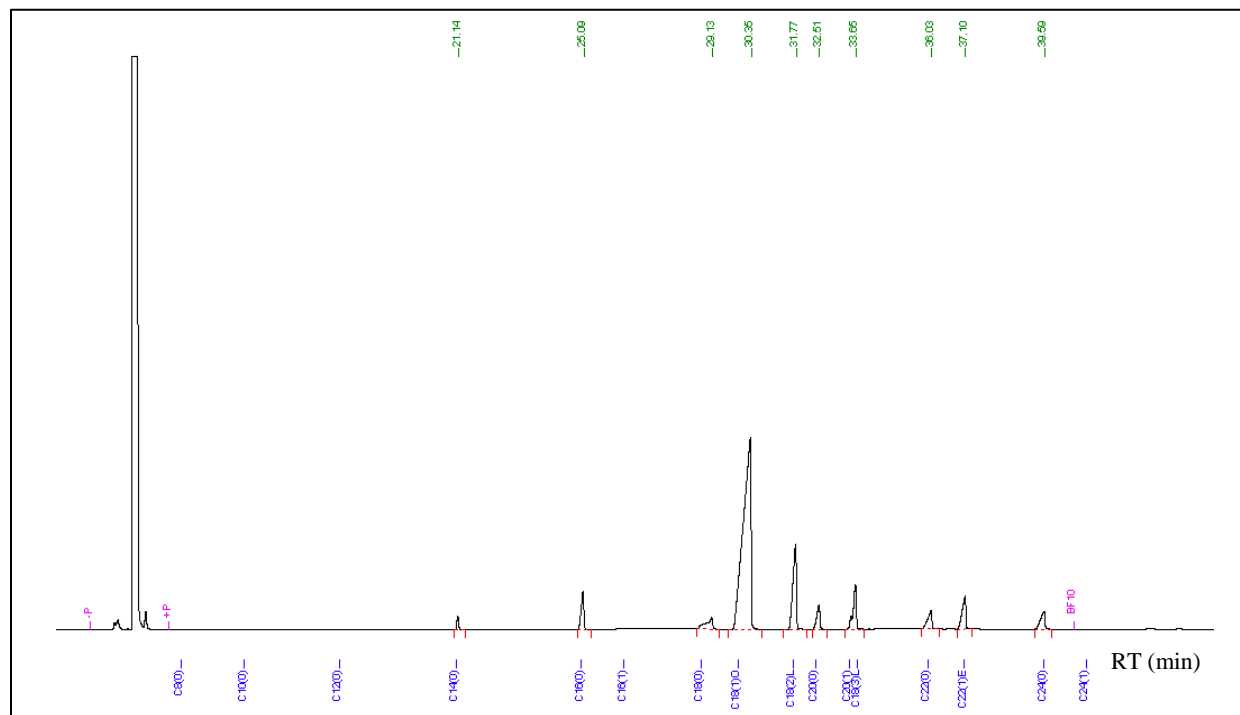
Figure 3.29 GC-FID chromatogram for FAME mix rapeseed oil standard

250±5 mg of biodiesel was weighted in a 7.5 mL sample vial. Then 5.0 mL of prepared fresh solution from 500 mg of internal standard dissolved and 50 mL of n-heptane were added. For FAME analysis, 1.0 mL of the above solution was transferred into 2.0 mL of GC automatic sampler vial for injection, followed by the instrument injecting automatically 0.5 μL of this solution into the GC instrument. This process was repeated for all synthesised biodiesel samples in order to identify the individual FAMEs in each sample. Turbo Mass^{TM} software was used for data processing and reporting. The method to calculate the percentage of total FAMEs (equation 3.19) and linolenic acid methyl ester (LAME, equation 3.20) has been reported elsewhere [463].

$$\text{Total FAME \%} = \frac{(\sum A) - A_{IS}}{A_{IS}} * \frac{C_{IS} * V_{IS}}{W} * 100 \qquad \text{Equation 3.19}$$

$$\text{Linolenic acid methyl ester \%} = \frac{A_L}{(\sum A) - A_{EI}} * 100 \qquad \text{Equation 3.20}$$

Where $\sum A$ =Total peak area of methyl esters

$\quad$ A_{EI} =Peak area of methyl heptadecanoate

$\quad$ C_{IS}= Methyl heptadecanoate concentration in mg/mL

$\quad$ A_L = Peak area of LAME

$\quad$ V_{IS}= Used volume of methyl heptadecanoate solution in mL

$\quad$ W= Mass of the sample in mg

3.4.2.2 Sample analysis by GC-MS

The GC-MS set-up conditions are summarised in Table 3.4. The FAME content of the synthesised biodiesel samples were quantified by Perkin Elmer Clarus gas chromatography (580S, GC), equipped with a mass spectroscopy (560S, MS) instrument.

Table 3.4 GC-MS instrumental conditions

Perkin Elmer Clarus 580S GC operational conditions in this experiment	
Column	Elite 5ms with dimension 30.0 m x 250 µm
Injection temperature	250
Carrier gas	Helium
Carrier gas flow	1.0 mL
Split ratio	2:1
Oven programme	Initial temp 60 °C for 0 min, ramp 10 °C/min to 200 °C, hold 10 min, ramp 10 °C/min to 270 °C, and at 270 °C hold 5 min
Total run time	36 min
Dilution	n-Heptane
Solvent delay	4.0 min
Injection volume	0.5 µL

Perkin Elmer Clarus 560S MS parameters	
Ionization source	EI +TIC
Electron energy	70 EV
Source temperature	180 ºC
Transfer line temperature	250 ºC
Scan range	50 to 600 Da

The chromatographic separation was achieved on an Elite 5 MS capillary column (30.0 m x 250 µm) and helium was used as a carrier gas at a constant flow rate of 1mL per minute. The initial oven temperature in the column was programmed at 60 ºC for 0 min then ramped to 200 ºC at 10 ºC/min. The temperature was held for 10 min at 200 ºC then increased to 270 ºC at 10 ºC/min. Finally, the temperature was held for 5 min to remove any remaining traces of sample residue. Biodiesel sample was injected in splitless mode with a split ratio of 2:1. The transfer line temperature and the injection temperature were kept at 250 ºC. GC-MS was operated in the 70 eV electron ionization mode with a collected scanning mass range of 50 to 600 Da.
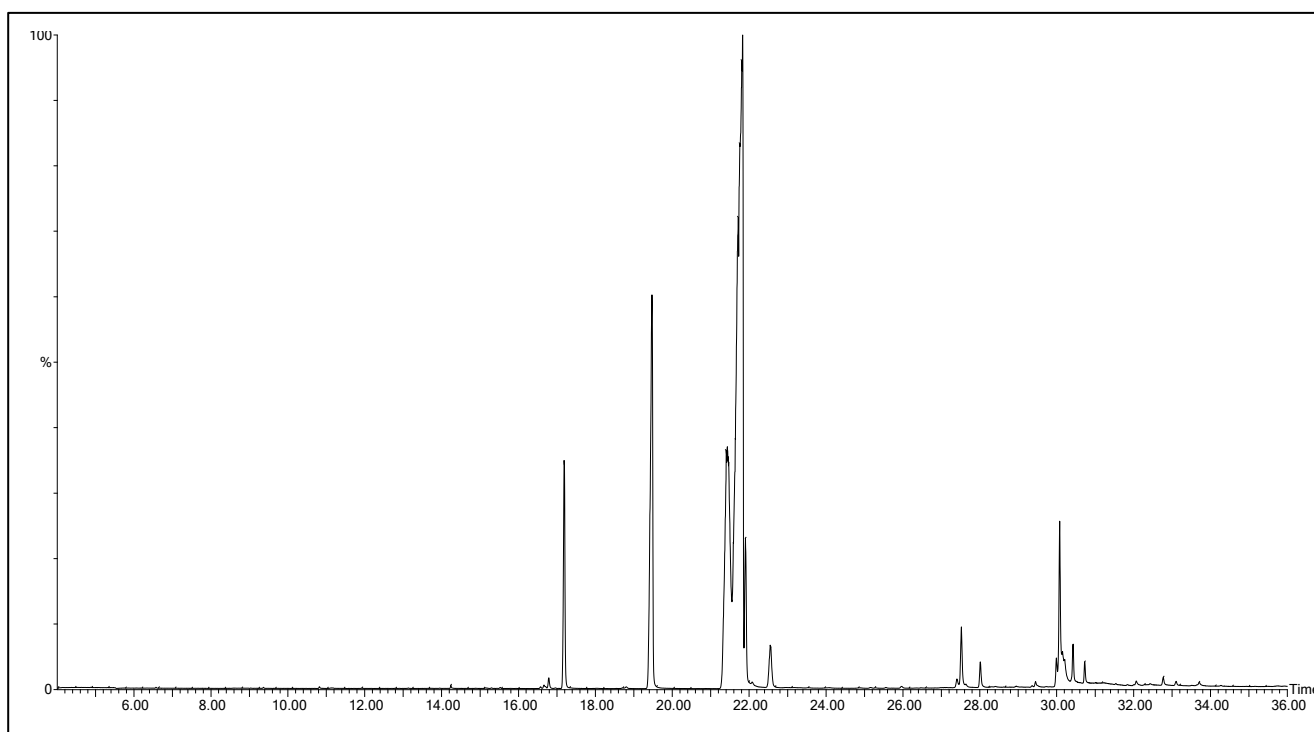
Figure 3.30 An example of GC-MS spectrum for obtained biodiesel fuel

Turbo Mass[TM] software was used for data processing and reporting by integration of peak areas on each chromatogram and direct comparison of individual FAMEs to the relative retention times of the reference FAMEs mix according to EN14103 [463] standard method. The reference response

factor was determined for each biodiesel using the recorded weight and area of the $C_{17:0}$ peak. The areas of the other FAME peaks in each sample was then calculated using the $C_{17:0}$ reference response factor and the recorded weight of the sample. The weight percent of FAML was then determined separately from the FAML peaks. An example of GC-MS spectrum for synthesised biodiesel is provided in Figure 3.30.

3.4.3 Free and total glycerine contents

Free glycerol, mono-, di-, and triglyceride were quantitatively determined in the synthesised biodiesel samples by gas chromatography-flame ionization detector (GC-FID) according to EN-14105 [464] standard method. Figure 3.31 shows the Perkin Elmer GC-FID (Clarus 560, UK) instrument used to determine the percentage of free and total glycerine contents.
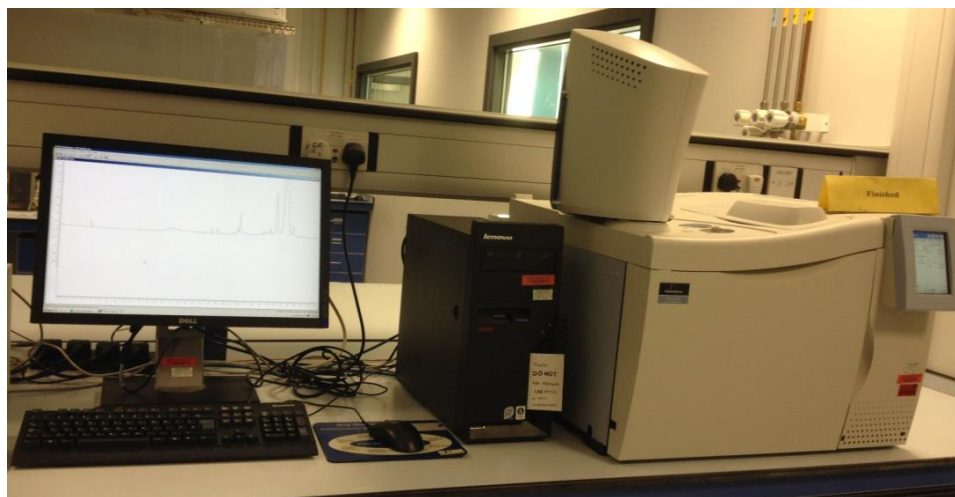
Figure 3.31 Gas chromatography-flame ionization detector instrument

3.4.3.1 Preparation of sample and calibrationstandards for GC-FID

Biodiesel sample preparation for the quantification of free glycerol, mono-, di-, and triglycerides by using GC-FID is a vital step. The free glycerol, mono-, di-, and triglycerides in biodiesel samples are polar and high boiling components, they must be derivatized in order to reduce their polarity (reduce their activity before injection into the GC) and improve the thermal stability (increase their volatility) of the molecule. The derivatization of biodiesel EN 14105 kits were done in accordance with the guideline procedure from Agilent Technologies. The composition of Agilent biodiesel EN 14105-1409 standard calibration kits is presented in Table 3.5.

Table 3.5 Summary of reference Agilent biodiesel EN 14105-1409 kits composition
(supplier Agilent Technology-SUPELCO)

	Neat material	Concentration [µg/mL]	Concentration [%]	Purity [%]
Standard solution 1 STD 1 (1x1 mL)	1,3-diolein	50	0.005	99.9
	Glycerol	5	0.0005	99.9
	Monoolein	250	0.025	99.9
	Triolein	50	0.005	99.9
	Butanetriol (internal standard 1)	80	0.008	97.5
	Tricaprin (internal standard 2)	800	0.08	99.9
	Anhydrous pyridine used as a solvent		99.88	99.9
	Neat material	**Concentration [µg/mL]**	**Concentration [%]**	**Purity [%]**
Standard solution 2 STD 2 (1x1 mL)	1,3-diolein	200	0.02	99.9
	Glycerol	20	0.002	99.9
	Monoolein	600	0.06	99.9
	Triolein	150	0.015	99.9
	Butanetriol (internal standard 1)	80	0.008	97.5
	Tricaprin (internal standard 2)	800	0.08	99.9
	Anhydrous pyridine used as a solvent		99.82	99.9
	Neat material	**Concentration [µg/mL]**	**Concentration [%]**	**Purity [%]**
Standard solution 3 STD 3 (1x1 mL)	1,3-diolein	350	0.035	99.9
	Glycerol	35	0.0035	99.9
	Monoolein	950	0.095	99.9
	Triolein	300	0.03	99.9
	Butanetriol (internal standard 1)	80	0.008	97.5
	Tricaprin (internal standard 2)	800	0.08	99.9
	Anhydrous pyridine used as a solvent		99.749	99.9
	Neat material	**Concentration [µg/mL]**	**Concentration [%]**	**Purity [%]**
Standard solution 4 STD 4 (1x1 mL)	1,3-diolein	500	0.05	99.9
	Glycerol	50	0.005	99.9
	Monoolein	1250	0.125	99.9
	Triolein	400	0.04	99.9
	Butanetriol (internal standard 1)	80	0.008	97.5
	Tricaprin (internal standard 2)	800	0.08	99.9
	Anhydrous pyridine used as a solvent		99.692	99.9

* According to the certificate of composition, the standard have been produced gravimetrically using ISO9001 quality procedures.

N-Methyl-N-(trimethylsilyl) trifluoro acetamide (MSTFA, derivatization reagent) was used for the derivatization of all reference standards (STD 1, STD 2, STD 3 and STD 4) and biodiesel samples. The reaction involves the replacement of active hydrogen of the groups by a trimethylsilyl group. The GC analysis of free glycerol, mono-, di-, triglycerides, internal standards (STD 1 and STD 2) identifies each analyte by its retention time (RT) and the RT is determined by the analysis of a known reference STD 1-4. Reference STD (1-4) are used to create a calibration curve, which relates FID response to weight percentage in the samples. The linear correlation coefficients (r^2) exceeded the specification of 0.9 for each STD curve. For biodiesel sample analysis, peak exact position for each group of components are identified using the relative retention times published in the EN 14105 standard method and the retention times for used STD (1-2). Following that, the calculation of all the peak areas for each group in every specified RT was automatically achieved using Clarus 560S software.

Each 1.0 mL ampoule from the set standard kits was transferred into 25 mL volumetric flasks labelled as STD 1, STD 2, STD 3 and STD 4. 100 μL of MSTFA reagent was added to each volumetric flask using 250 μL glass syringes, then securely sealed and shaken vigorously. The resulting derivatization reaction solutions were allowed to stand at ambient temperature for 15 min. Following derivatization, 8.0 mL of n-heptane was added to each flask. After proper mixing, 1.0 μL of individually prepared standard solution was injected into the GC-FID to create a calibration curve for all compounds [465].

Biodiesel monoglyceride kit (Agilent Monoglyceride EN 5190-1410 standard: check mix contained monopalmitin, monostearin and monoolein in pyridine) was derivatized in accordance with guideline procedures from Agilent Technologies. 200 μL of monoglyceride standard was accurately transferred to labelled 25 mL volumetric flask. A 250 μL glass syringe was used to add 100 μL of MSTFA into the flask, then securely sealed and shaken vigorously. After 15 min, 8.0 mL of n-heptane was added to the flask. For analysis, 1.0 μL of prepared solution was injected into the GC-FID. For biodiesel samples, 100±5 mg was accurately weighted in a 25 mL volumetric flask. Then 80 μL of (s)-1,2,4-Butanetriol (BIS, PerkinElmer CAS#42890-76-6, 98% purity, 997.449 μg/mL final concentration in pyridine verified by GC-MS), 100 μL of Tricaprin (TIS, PerkinElmer CAS#621-71-6, 98% purity, 8000 μg/mL final concentration in pyridine verified by GC-MS) and 200 μL of pyridine were added to the flask using microliter glass syringes. After securely sealing and shaking vigorously, the sample solution was allowed to stand at ambient

temperature for 15 min. 8.0 mL of n-heptane was added to the flask. For the analysis, 1.0 mL of aliquot was transferred into 2.0 mL of an auto sampler vial for injection, followed by the instrument being run to inject automatically 1.0 µL of this solution into the GC instrument. This analysis was repeated for all synthesised biodiesel samples over different solid acid catalysts. An example of calibration chromatogram from glycerol and glycerides analysis by GC-FID is depicted in Figure 3.32 (a) whilst the chromatogram for glycerol and glycerides in the synthesised biodiesel sample analysis by GC-FID is shown in Figure 3.32 (b).
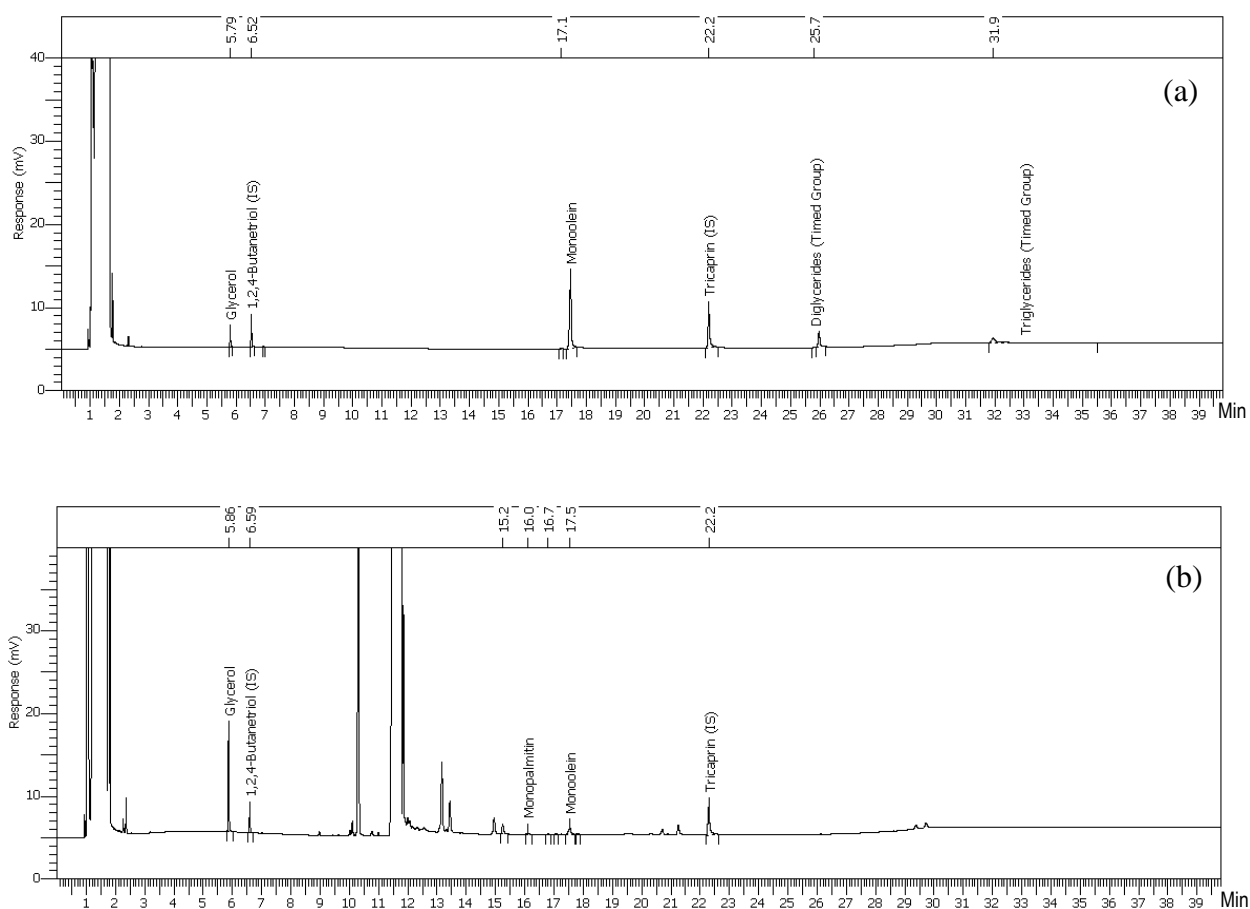
Figure 3.32 Chromatogram examples from glycerol and glycerides analysis in (a) biodiesel sample (b) calibration by GC/FID

3.4.3.2 Sample analysis by GC-FID

The GC-FID set-up conditions are summarised in Table 3.6. Clarus 560S software was used for identifying the areas of peaks of mono, di and triglycerides in the sample by direct comparison to the relative retention times of monoolein, diolein, and triolein in the standard.

Table 3.6 GC-FID operational conditions

Perkin Elmer Clarus 560S GC operational conditions	
Column	Cool on column 15.0 m x 0.32 mm, 0.1 µm
Carrier gas	Helium
Carrier gas flow	3.0 mL/min constant flow
Oven programme	Initial temp 50 ºC held 1 min, ramped to180 at 15 ºC/min, ramped to 230 ºC at 7 ºC/min, and ramped to 380 ºC at 30 ºC/min then hold for10 min
Total run time	36.0 min
Dilution	n-Heptane
Solvent delay	4.0 min
Injection volume	1.0 µL
Detector	FID at 380 ºC

The percentages of free and total glycerine were calculated based on EN-14105 [464] standard methods as follows:

For free glycerol determination:

$$\text{Glycerol, mass \%} = \frac{\left(a_g * \frac{A_g}{A_{BIS}} + b_s\right) * W_{BIS}}{W} * 100 \qquad \text{Equation 3.21}$$

Where: a_g: Slope of the calibration function; A_g: Peak area of glycerol; A_{BIS}: Peak area of BIS

b_g: Intercept of the calibration function; W_{BIS}: Weight of BIS; W: Weight of sample, mg

For total glycerine determination:

$$\text{Total glycerine, mass \%} = \text{Glycerol \%} + \text{Bound glycerine \%} \qquad \text{Equation 3.22}$$

The mass percentage of bound glycerine was calculated in accordance to the equation below:

$$\text{Bounded glycerine, mass \%} = \sum(Gl_M, Gl_D, Gl_T) \qquad \text{Equation 3.23}$$

Where: Gl_M=0.2591*Σ monoglyceride, mass%

Gl_D=0.1488*Σ diglyceride, mass%

Gl_T=0.1044*Σ triglyceride, mass%

While the mass percentage of mono-, di- and triglycerides in the sample determined by applying the following equation:

$$\text{Mono}-, \text{di} - \text{or triglycerideinsample, mass \%} = \frac{\left(a_{ol} * \frac{A_{gli}}{A_{TIS}} + b_{ol}\right) * W_{TIS}}{W} * 100 \qquad \text{Equation 3.24}$$

Where: a_{ol}: Slope of the calibration function for mono-, di- or triolein; A_{gli}: Peak area of mono-, di- or triolein; A_{TIS}: Peak area of TIS; b_{ol}: Intercept of the calibration function for mono-, di- or triolein; W_{TIS}: Weight of TIS; W: Weight of sample, mg

3.4.4 Inductively coupled plasma-mass spectroscopy (ICP-MS)

In this work, ICP-MS was used as an effective technique to determine the percentage of sulfur during solid acid catalyst leaching. Figure 3.33 depicts the Perkin Elmer Sciex ICP-MS (Elan DRC-e, UK) instrument equipped with an auto sampler used in this experiment to analyse the leaching of sulfur in biodiesel samples with detection limit at part per trillion.
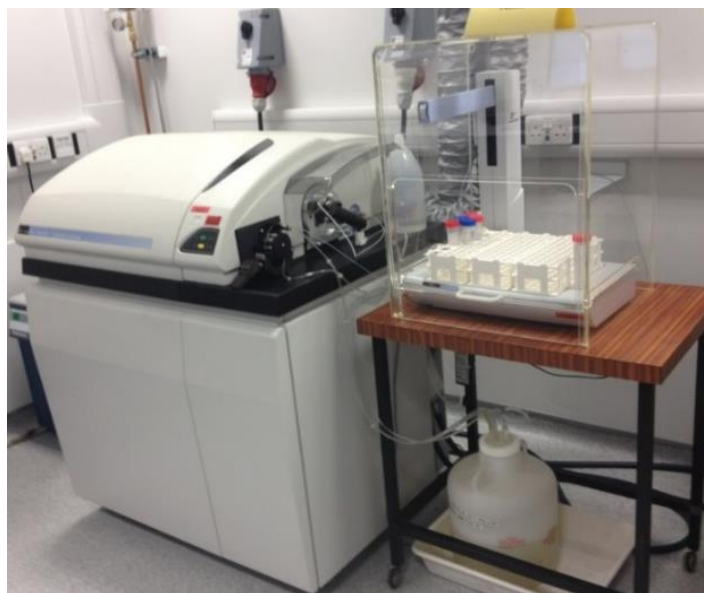
Figure 3.33 Inductively coupled plasma-mass spectroscopy instrument.

3.4.4.1 Sample preparation

The synthesised biodiesel sample was centrifuged to eliminate the remaining solid acid catalyst and glycerol and then a few millilitres was used for the catalyst leaching test. Digestion of biodiesel samples was performed on pressurised vessels HF100-multiwave 3000 (Anton Paar). Accurately weighted 175 ± 25 mg samples of biodiesel were transferred to the microwave reaction vessels. The reagent, about 7.0 mL of concentrated nitric acid, 1.0 mL of concentrated hydrochloric acid and 2.0 mL of hydrogen peroxide, were carefully added into the microwave reaction vessel and allowed to react for a couple of min. A seal forming tool to expand the seal vessels was used and the venting screws on each vessels were closed with a key. The microwave reaction vessels were inserted into the rotor according to their reference positions (from 1 to 8 positions). The rotor was then covered by the rotor lid and placed into the multiwave oven cavity. The multiwave door was locked and the oil digestion programmed according to the set-up summary in Table 3.7.

Table 3.7 Operational conditions for oil digestion on microwave 3000

Ph	Power	Hold	Fan
1	900	02.00	1.0
2	600	15.00	1.0
3	900	15.00	1.0
4	0.0	15.00	3.0
p-Rate:0.5 bar/s; IR:280ºC; p:80bar; Drive: Rot			

After the sample digestions finished, a supplied key was used to open the venting screw through the rotor lid in each vessel in order to release gases. The fan was turned on and a couple of minutes allowed to pass to remove any released gases. The rotor was transferred from the oven cavity to the fume hood and the rotor lid and the protective caps with seal vessels taken off. Dark-brown fumes appeared after opening the seals of the vessel tube as shown in Figure 3.34. 45 mL of high purity deionised water (HPDW) were used to rinse each vessel. The resulting solution was then transferred into a pre-weighted 50 mL centrifuge tube. The centrifuge tube was re-weighted to a weight of 50 g by adding HPDW. Approximately 10 mL of well-mixed resulting sample solutions were transferred into 10 mL centrifuge tubes for analysis.

Preparation and dilution of samples with reagents   Multiwave 3000 apparatus   Dilution of acid digested samples with HPDW
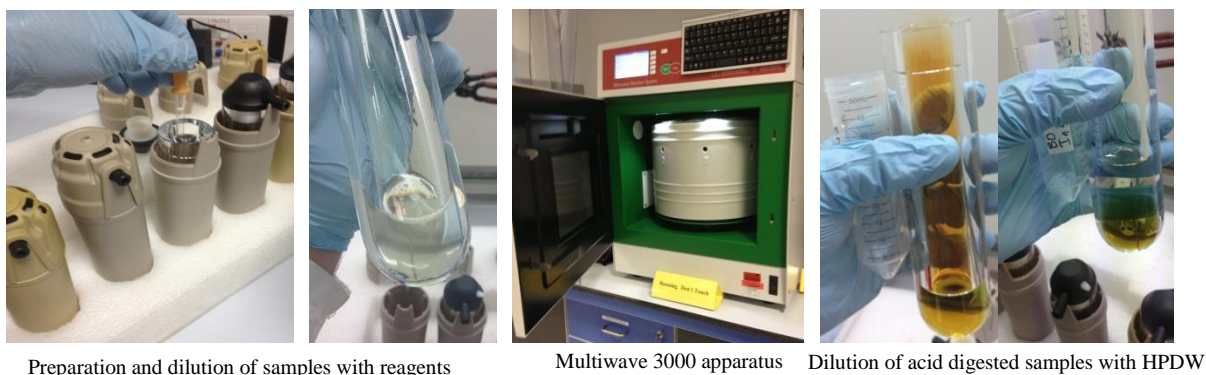
Figure 3.34 Microwave sample preparation steps

3.4.4.2 Sample analysis by ICP-MS

The operating conditions for ICP-MS used to analyse catalyst leaching in biodiesel samples are summarised in Table 3.8. After the instrument was calibrated with multi-element single calibration standard, the diluted acid digested sample solutions were nebulised into the ICP instrument. Elan software was used for data processing by comparing the signal intensities with standards to determine the concentration of sulfur in the sample solution. Blank then subtracted from the

concentration of each element in analytical solutions. Lastly, the concentrations of sulfur in the sample solution were corrected, based on the following equation:

$$\text{Trace sulfur concentration, ppb} = \frac{C}{W} * F \qquad\qquad \text{Equation 3.25}$$

Where: C: Concentration of sulfur in the solution, µg/L

F: Dilution factor

W: Weight of sample, mg

Table 3.8 Operational conditions for ICP-MS using the semi-quantitative scan mode

Parameters	Settings
Generator frequency	27 MHz
Torch inner diameter	2.5 mm
RP power	1.52 kW
Points per peak	2.0
Scans/replicates	20
Replicates/samples	5.0
Dwell time	25 ms
Nebulizer	Glass concentric
Carrier gas	0.88 L/min
Make up gas	0.27 L/min
Sample flow rate	0.5 mL/min
Cell gas flow rate	Argon, 4.6 mL/min
Spray chamber	Quartz cooled to 2 ºC

3.4.5 Viscosity

The viscosity of biodiesel fuel is indicated by the ability of biodiesel fuels to flow. Vegetable oils can be used as fuel for combustion engines, but their viscosity is much higher than usual petro-diesel. Therefore, viscosity is an important property of biodiesel since it affects the operation of fuel injection equipment, particularly at low temperatures when the increase in viscosity affects fuel fluidity [466]. High viscosity leads to poorer atomisation of the fuel spray and less effective operation of fuel injectors [467]. In this work, viscosities of biodiesels were measured on a Bohlin-Gemini 150 rotary rheometer (Malvern, UK). The selected settings of rheological analysis of biodiesel samples are summarised in Table 3.9. Once the settings were ready, 2.0 mL of biodiesel sample was placed, using a glass pipette, onto the base plate and allowed to sit in position as shown in Figure 3.35. The test run started and data with graphical output recorded using Bohlin software. The data analysis process was carried out by applying the Newtonian model from the Bohlin program in order to determine the dynamic viscosity of the biodiesel sample from the slope curve

of the shear stress versus the shear rate (see equation 3.26). The kinematic viscosity of biodiesel is obtained by dividing the dynamic viscosity at 40 ºC with its density at the same temperature.

$$\sigma = \eta \, \gamma \qquad\qquad \text{Equation 3.26}$$

Where: σ = Shear stress in Pa

η = Dynamic viscosity in Pa.s

γ = Shear rate in s

Table 3.9 Set up conditions for rotary rheometer

Parameters	Settings
Gap	500
Mooney	2.0 mL
Sweep time	120 sec
Temperature	40ºC
Max speed	30 rad/sec
Min shear stress	0.01 Pa
Max shear stress	5.0 Pa
Total test time	120 sec
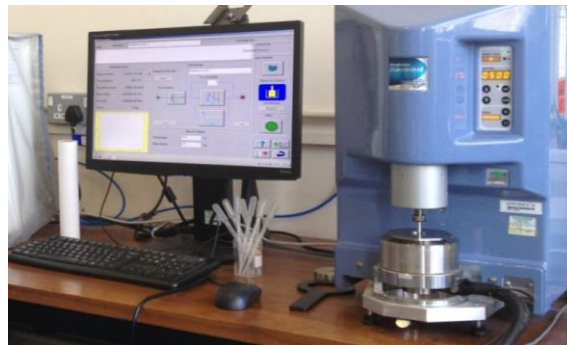
Figure 3.35 Set up of Bohlin-Gemini rotary rheometer.

3.4.6 Flash point

The flash point is a very important factor of biodiesel samples in considering safe storage, transportation and handling of fuels. It is defined as the lowest temperature at which the vapour of the fuel sample can flash for a short time under specified test conditions of test [468].

In this work, the flash point of biodiesel samples was measured by an auto ramp closed cup flash point tester (Setaflash series 3, England) equipped with a coolant block unit in order to assist cooling of the sample cup after each run. At room temperature, 2.0 mL of FAME sample was

manually injected, using a syringe, into the sample cup via the filter orifice. Once the sample was injected, the instrument was switched on and the expected flash point temperature set for the sample fuel by pressing and holding down the temperature button. The pilot and test jets lighted within no more than 4.0 mm diameter of jet flame as shown in Figure 3.36. During the ramp operation, the temperature increased at 1-2 ⁰C/min until the flash was captured automatically by the flash detector probe, which appears on the display screen. The detected flash point for the sample was recorded and the gas and instrument switched off. After each test, the sample cup was wiped clean and left open in order for the system to cool down quickly.

Figure 3.36 Setaflash closed cup equipment.

3.4.7 Water content

The presence of water in biodiesel fuel can have various consequences, including increased oxidation, low stability and reduced calorific value over a long period of storage. Therefore, determination of trace water content is a vital aspect of obtained biodiesel due to water becoming acidic and corroding engines and storage tanks. Sometimes, contaminated biodiesel with moisture at the bottom of the tank can form a sludge and slime because of the growth of microorganisms which can plug the filter during pumping [3].

In this work, trace moisture content in UCO and biodiesel samples was analysed by volumetric Karl Fischer titration (Mettler Toledo-V20, Germany). The lowest amount of moisture can be detected by this system up to 100 parts per million as described per manufacturer' manual. In general, this system works based on the following reaction:
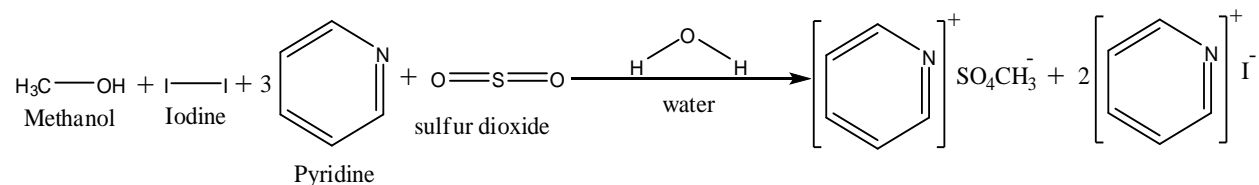
Before the test is run, the burette should be filled with Karl Fischer reagent (KFR), anhydrous methanol as a solvent added to the titration vessel, and then the double platinum-pin electrode immersed into the titration vessel. After standardisation of the instrument, the biodiesel sample weighted in a pre-weighted glass syringe with needle, was injected into the titration vessel. The syringe with the remaining UCO or biodiesel sample was reweighted after the addition and the difference noted in order to determine the exact weight of UCO or biodiesel delivered to the titration vessel. The obtained weight of UCO or biodiesel sample was entered on the titrator via touch screen. The titration process was commenced by pressing the start analysis button on the screen. After a few minutes, the result automatically appeared on the screen of the instrument. The result is calculated based on the following equations:

$$\text{Trace moisture in UCO or biodiesel sample}, \% = \frac{\text{Sample titer (mL)} * \text{WE}}{\text{Sample weight (mg)}} * 100 \qquad \text{Equation 3.27}$$

Where:

$$\text{Water equivalent of KFR (WE)}, \frac{\text{mg } H_2O}{\text{mL KFR}} = \frac{\text{Water weight (mg)}}{\text{Water titer (mL)}} \qquad \text{Equation 3.28}$$

3.4.8 Density

Density is of importance as it defines the mass of biodiesel per unit volume of biodiesel. The pycnometeric method was used as a precise procedure to determine the density of biodiesel samples at 15 °C. An empty, clean and dry 25 mL pycnometer was inserted into the prepared water bath at 15 °C and it remained in place for 15 minutes for the thermal equilibrium of the pycnometer to be established at the same temperature. After this period of time, the dry pycnometer was weighed and the weight recorded as w_1. 25 mL of biodiesel sample was introduced into the dried pycnometer. The pycnometer completely filled with biodiesel sample was transferred into a water bath at 15 °C. After thermal equilibrium of the pycnometer for 15 min at 15 °C, the pycnometer was removed and the volume corrected again with the same biodiesel sample due to the volume of liquid decreasing with temperature decrease of the liquid. Without delay, the outside of the pycnometer was cleaned, it was weighted and the weight recorded as w_2. The density of biodiesel samples were calculated based on the following equation:

$$\rho = \frac{W_2 - W_1}{v} \qquad \text{Equation 3.29}$$

Where: ρ= Density of biodiesel sample at 15 °C, g/mL

w_1= Weight of empty pycnometer at 15 °C, g

w_2= Weight of pycnometer with biodiesel sample at 15 °C, g

v= Volume of pycnometer, mL

3.4.9 Acid value and FFAs

The acid numbers of biodiesel samples, expressed as being the amount of KOH per one gram of sample and used to describe the FFAs content in biodiesel, were measured in accordance to the colour indicator titration method as prescribed in [469, 470]. Free fatty acid is one of the most crucial properties of biodiesel because biodiesel fuel containing high free fatty acid can cause diesel engine corrosion.

The experiment was performed by dissolving accurately 10.0 g of biodiesel sample in 100 mL of titration solvent (50 mL of toluene, 49.5 mL of propan-2-ol, 0.5 mL of deionised water) in an Erlenmeyer flask. After the mixture solution was vigorously shaken in order to dissolve the biodiesel sample, 5 drops of phenolphthalein indicator was added to the resulting single-phase solution. Without delay, the solution was titrated against 0.1 M of standardised alcoholic potassium hydroxide solution at room temperature. The endpoint was indicated by a change to the colour pink. The consumed volume of alcoholic potassium hydroxide was recorded. The experiment was repeated three times for each sample and the mean value used for calculation.

In order to determine the blank, 100 mL of fresh titration solvent with 5 drops of phenolphthalein indicator was titrated against 0.1 M of standardised alcoholic potassium hydroxide solution at room temperature. The volume of consumed alcoholic potassium hydroxide was recorded after the colour changed to pink. Finally, the acid value (see equation 3.30) and the percentage of free fatty acid (see equation 3.31) of biodiesel samples were calculated as follows:

$$\text{Acid value, mgKOH/g} = \frac{(V_{bs}-V_b)*C*56.11}{W} \qquad \text{Equation 3.30}$$

$$\text{Free fatty acid, \% } (\frac{g}{100g} \text{ expressed as oleic acid}) = \frac{(V_{bs}-V_b)*C*28.246}{W} \qquad \text{Equation 3.31}$$

Where: V_{bs}: Consumed volume of the titrate for biodiesel sample, mL

V_b: Consumed volume of the titrate for blank, mL

C: Exact concentration of standardised alcoholic potassium hydroxide solution, mole/l

W: Mass of biodiesel sample used, g

28.2246: Mwt of oleic acid (g/mole) divided by 10 (when the Mwt of oil is unknown)

56.11: Mwt of KOH (g/mole)

3.4.10 Cloud point (CP)

CP is a very important parameter for low-temperature applications of a fuel. Biodiesel is known to have a higher CP than petro-diesel. On cooling biodiesel below a certain temperature, crystals form due to clogging of the molecules [4]. These crystals cause the liquid to become cloudy, the "cloud point" being the temperature at which the cloud or first crystal starts to form. The lowest temperature at which the oil or any liquid flows is the pour point [471] and that occurs in a standard test filter at what is called the "cold filter plugging point" [4, 472, 473]. The CP is affected mainly by the fatty acid composition of biodiesel fuel [474]. Crystallisation occurring during cloud point occurs faster with long chain hydrocarbon (paraffinic) forming large clusters [475]. The clusters of crystals grow as a small wax crystal at the bottom of the test vessel in multiple directions from the bottom or as a ring of cloud along the bottom as the temperature decreases. The wax crystals continuously grow and agglomerate as the temperature decreases until they have precipitated as a large wax crystal which can cease to pour and cause blockage of the fuel filter system during injection in the engine.

In this work, different analytical techniques, including DSC and/or hot-stage microscopy (HSM) were used to detect the cloud point of synthesised biodiesels from different catalytic processes.

For the DSC experiment, the cloud point of the biodiesel sample was determined using the DSC-1 (Mettler Toledo, UK) equipped with an intracooler system (Huber TC45) as a temperature controller unit. 5 ± 2.5 mg of biodiesel sample was accurately weighted in a 40 µL sealed standard aluminium pan and placed in the DSC-1 sample chamber. The experiment was initiated by keeping the sealed sample pan at 50 $^{\circ}$C for 5 min in order to homogenise the sample should it contained any wax materials. The system was then cooled to -35 $^{\circ}$C at 3 $^{\circ}$C/minutes and held at that temperature for 5 min. The sealed sample pan was then heated to 50 $^{\circ}$C at 3 $^{\circ}$C/min and held at that temperature for 5 min. Nitrogen gas at 50 mL/min (constant flow rate) was used as a purge gas during all steps in this experiment. Mettler Star^{e} software was used for programming the system and data processing.

For HSM, the cloud point of the biodiesel sample was examined on the optical microscope (Olympus, Japan) with 10 and 40 x objectives fitted with Pixelink camera (PL-A662) and a hot-stage unit (EHEIM professional 3, Germany) to screen the crystal nucleation/growth in biodiesel sample during cooling as shown in Figure 3.37. The operation temperature specification of this microscope, based on the manual, was between -40 °C and 120 °C with controlling rate of 0.1 to

30 °C/min. A few drops of filtrated biodiesel sample were placed on the sample holder (glass slide) and the sample then heated up to 50 ºC at 25 ºC/min and held at 50 ºC for 5 min in order to dissolve any wax materials in the biodiesel sample. The system was then cooled to -40 ºC at 3 ºC/min and then held at each specified temperature stage for 5 min. Images were collected with a Pixelink camera (PL-A662, Canada) at 15 seconds intervals upon cooling. Linksys32 software was used for programming (temperature profile) and image processing.
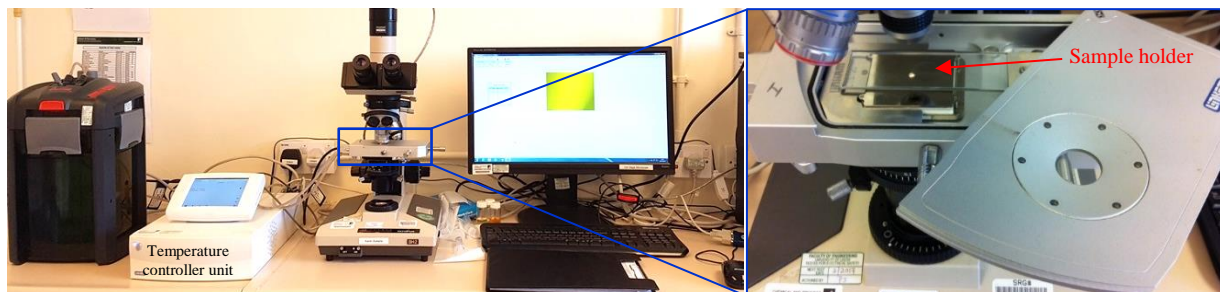
Figure 3.37 Hot-stage microscope instrument used for assessing the CP of biodiesel samples

3.4.11 Oxidation stability

The oxidation stability of obtained biodiesel samples over different solid acid catalysts were assessed on the Stanton Redcroft thermogravimetric analysis (TGA-TGH 1000) according to the published methods in the literature [476, 477]. 20±5 mg of biodiesel sample was accurately placed into a platinum pan. The temperature profile was set from 25 °C to 700 °C at heating rate of 10 °C/min under air gas at 50 mL/min with a constant flow rate.

3.5 List of materials used in this work

The sample of used cooking oil (UCO), which was provided by a single restaurant in Leeds, UK, was used as a cheap feedstock. The UCO were collected from Newroz restaurant after the virgin rapeseed/corn oil being used several times for frying fish and other deep frying foods. The reason for choosing this restaurant was due to no cost of the UCO feedstock collection and the restaurant obtained the virgin oil from one single supplier. The feedstock was pre-treated by filtration through filter paper, as shown in Figure 3.38, to remove impurities and heated to 100°C to minimise the moisture in the esterification/transesterification process.

Figure 3.38 Filtration steps of collected UCO from Newroz restaurant.

The physicochemical properties of commercial corn oil (as a virgin oil) and UCO were used as a feedstock for biodiesel productions are presented in Table 3.10.

Table 3.10 Characterisation of raw materials (UCO and commercial virgin oil)

	Parameters		Corn oil (virgin oil)	UCO
Fatty acid compositions	Myristic, %	$C_{14:0}$	0.1	0.1
	Palmitic, %	$C_{16:0}$	13.0	7.3
	Palmitoleic, %	$C_{16:1}$	0.1	0.3
	Stearic, %	$C_{18:0}$	5.0	2.5
	Oleic, %	$C_{18:1}$	23.47	61.09
	Linoleic, %	$C_{18:2}$	53.2	17.9
	Linolenic, %	$C_{18:3}$	2.63	5.21
	Arachidic, %	$C_{20:0}$	0.5	0.8
	Gadoleic, %	$C_{20:1}$	0.6	2.2
	Eicosadienoic, %	$C_{21:0}$	0.5	0.5
	Behenic, %	$C_{22:0}$	0.6	0.5
	Erucic, %	$C_{22:1}$	0.00	1.1
	Lignoceric, %	$C_{24:0}$	0.2	0.1
	Nervonic, %	$C_{24:1}$	0.00	0.3
Kinematic viscosity @ 40 ºC, mm^2/s			32.31	36.891
Water content, vol.%			0.06	0.14
Flash point, ºC			287	289
Acid value, mg KOH/g			0.6172	4.04
Free fatty acid, mass%			0.3107	2.034
Density @15 ºC, Kg/m^3			933.09	921

Throughout this work, all materials, including solvents, catalyst precursor, standards and other chemicals were used without further purifications and are listed in Table 3.11.

Table 3.11 List of chemicals, their purities and the suppliers

Material	Purity, %	Supplier
Oleic acid (CAS number: 112-80-1; cis-9-octadecanoic acid)	≥99	
Hydrochloric acid, HCl	37	Fluka Analytical
Nitric acid, HNO_3	96	
Aluminium iso-propoxide, $Al(O-i-Pr)_3$, granular	+98	Alfa Aesar
Chlorosulfonic acid, HSO_3Cl	99	
Titanium (IV) oxide nano-particles, TiO_2 NPs	99.5	
1,3-Propane sulfone	---	
Methanol, MeOH	≥99.9	
Ethanol	≥99.8	
Ethylene glycol, EG	99.8	
Ammonium hydroxide, NH_4OH	28-30	
Ferric chloride hexahydrate, $FeCl_3.6H_2O$	≥98	
Ferrous chloride tetrahydrate, $FeCl_2.4H_2O$	≥99.99	
Methyl heptadecanoate, Internal standard for GC (IS)	≥99.5	Sigma-Aldrich
FAME mix reference standard (C_{14} to C_{24}), for GC	99.9	
N-Methyl-N-(trimethylsilyl) trifluoro acetamide, for GC	≥98.5	
Pyridine anhydrous	99.8	
n-Heptane, for GC	≥99	
Acetone	99.9	
Toluene	99.8	
n-Hexane	99.5	
Hydrogen peroxide, H_2O_2	~30	
Propan-2-ol, IPA	99.7	
Sodium carbonate, Na_2CO_3	99.98	
Biodiesel EN 14105 kit, part № 5190-1409		Agilent Technologies (UK)
Biodiesel monoglyceride EN 14105 kit, part № 5190-1410		
Butanetriol internal standard, BIS	98	Perkin Elmer (UK)
Tricaprin internal standard, TIS	98	
Potassium hydroxide		Fischer Chemical
Phenolphthalein indicator		Acros Organics
Methyl orange indicator		

Chapter 4

TiO$_2$/PrSO$_3$H catalyst

An introduction is presented on titania nanoparticle surface functionalisation. The syntheses and characterisation of a novel mesoporous TiO$_2$/PrSO$_3$H solid acid catalyst are described in detail. The catalyst activity and stability of TiO$_2$/PrSO$_3$H during the esterification/transesterification of UCO are also discussed. Finally, a summary is presented on the processes employed to meet ASTM and EN standards of synthesised biodiesel.

CHAPTER FOUR

4. Synthesis, characterisation and application of TiO$_2$/PrSO$_3$H catalyst

4.1 Introduction

According to the literature, the surface modification of nanoparticles can create solid acid catalysts [478]. The surface modification can be carried out through different strategies such as chemical treatments, plasma treatment, ozonolysis, polymer grafting, encapsulation in a silica shell (silanization), ligand exchange technique, or capping agents (surfactants)/encapsulation in a surfactant corona [58, 155, 479, 480]. Modification of the surface of nanoparticles by integration of acidic functional groups (e.g. -SO$_3$H) to produce solid acid catalysts for different applications has been highlighted in the literature over recent years [82, 84, 102, 105, 379, 481-492]. This is because sulfonic acid functional groups on the surface of nanoparticles lead to the formation of porous materials with high accessibility to the active sites [493].

There are several recent works that describe the performance of such promising materials for biodiesel production [80, 103, 381, 384, 485, 494]. The surface modification of mesoporous materials, such as SBA-15, with organosilane sulfonic groups increases the hydrophobic character of the solid acid catalyst surface, resulting in high catalytic activity and selectivity towards glycerol in the esterification of FFAs [495]. Melero et al. [80] studied the use of sulfonic acid functionalised SBA-15 catalysts for biodiesel production from crude palm oil containing 5.6 wt% of FFAs. These catalysts show better catalytic activity compared to Ambertyst-36 and SiO$_2$-Tosic acid for transesterification reaction under optimised process conditions. Zuo and co-workers [384] have also reported a similar study, comparing catalytic activities for different functionalised SBA-15 catalysts with sulfonic acid organosilane groups for transesterification of soybean oil with 1-butanol. Their process was assisted by a microwave. The catalytic activity of sulfonic acid functionalised SAB-15 catalysts was significantly lower after the first run under optimised process

conditions. The catalytic deactivations were ascribed to the loss of acidity because of the instability of Si-O-C bonding from fluoro-sulfonic acid functionalised SBA-15 catalyst. In the cases of propyl sulfonic acid and arene sulfonic acid, however, the adsorption of polar impurities, caused pore blocking and/or was linked to access of the reactants to the active sites being hindered [80, 384, 496]. These types of catalysts are quite sensitive to the presence of impurities in raw materials, such as those found in recycled oil feedstocks [496]; also, low sulfonic acid site loadings on the surface of nanoparticles are hampered in the practical application of such catalysts [491]. There are, so far, no reports on the surface functionalisation of titania with 1,3-propyl sultone for direct-preparation of propyl-sulfonic acid grafting the surface of TiO_2 NPs and/or on the use of such material as a solid acid catalyst for biodiesel production.

Therefore, the aim of this chapter is to prepare a novel $TiO_2/PrSO_3H$ solid acid catalyst for the simultaneous esterification and transterification process in order to understand the impact of catalytic activity and reusability of such catalyst on biodiesel production from used cooking oil (UCO) as a cheap feedstock. The chemical structure, thermal stability, morphology, surface area, porosity and particle size of prepared solid acid catalysts have been characterised using different analytical techniques. Furthermore, the influence of different process parameters on the production of biodiesel were investigated. The catalyst activities and stabilities during the esterification/transesterification of UCO were also studied. Finally, the synthesised biodiesel from the catalytic esterification/transesterification processes was analysed in accordance to ASTM and EN standard methods.

4.2 Results and discussion

4.2.1 Catalyst characterisations

$TiO_2/PrSO_3H$ catalyst was prepared by the reaction of TiO_2 NPs support with an extremely reactive sulfoalkylating agent to increase the surface acidity of TiO_2 NPs. The concentration of propyl sulfonic acid groups attached on the surface of TiO_2 NPs mainly depends on the amount of available –O-H terminated adsorption sites. Such surface modification was formed through a ring opening reaction of 1,3-propane sultone with nucleophile cleaving the carbon-oxygen bond as shown in proposed Figure 4.1.
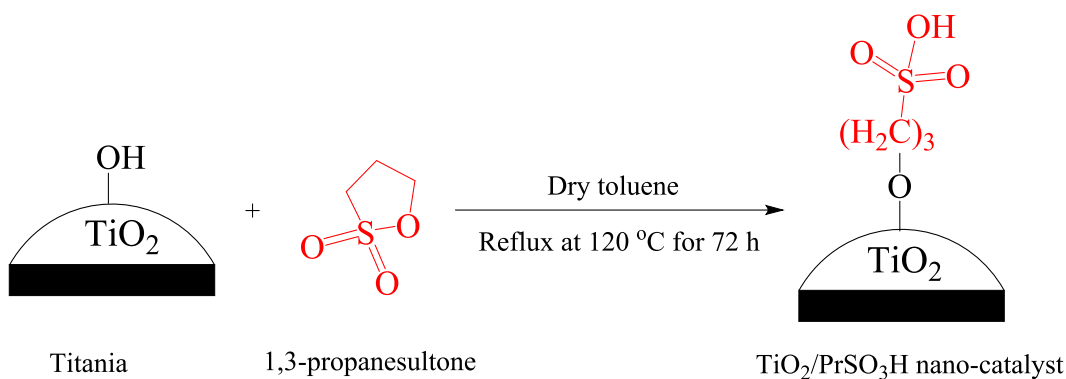
Figure 4.1 General proposed protocol for the synthesis of TiO$_2$/PrSO$_3$H catalyst

4.2.1.1 Crystal structure

Figure 4.2 illustrates that the surface grafting of TiO$_2$ with PrSO$_3$H groups resulted in the position shift of all diffraction peaks to slightly higher 2θ angles by 0.2° indicating the decrease of the unit-cell sizes.
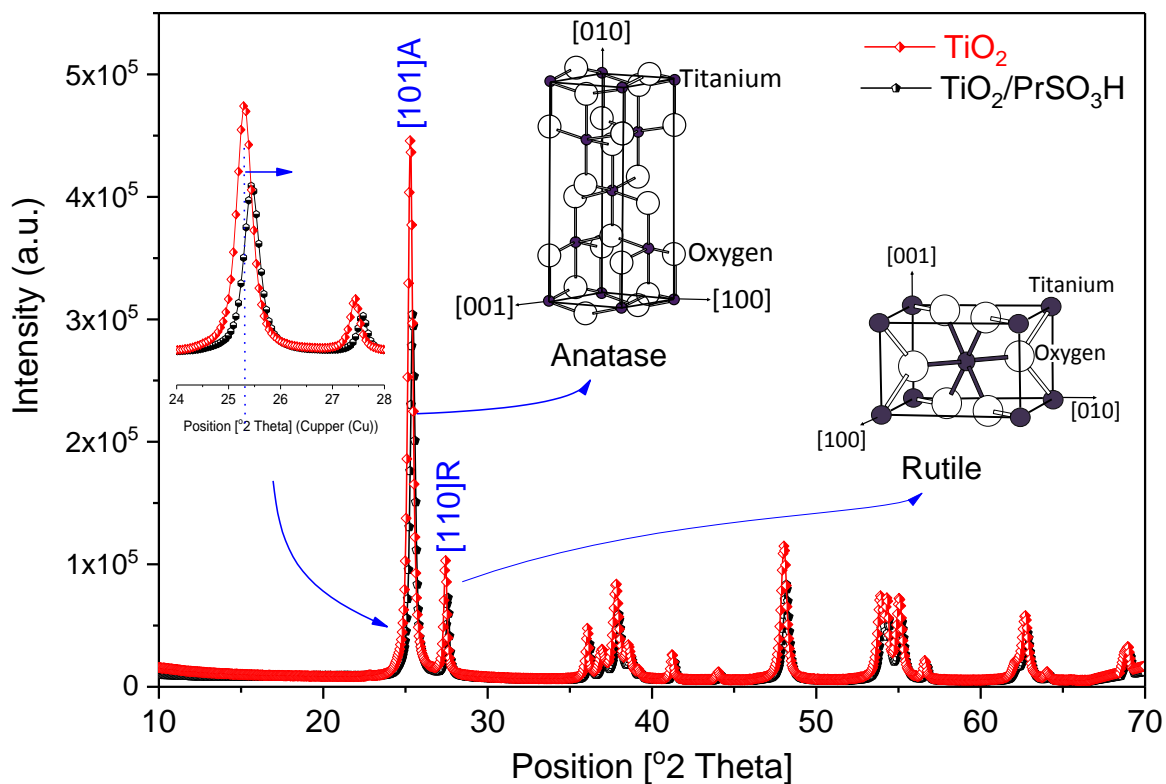
Figure 4.2 Powder XRD profiles for TiO$_2$ NPs and synthesised TiO$_2$/PrSO$_3$H catalyst at room temperature.

Moreover, a reduction of intensity in all reflections is observed for TiO$_2$/PrSO$_3$H as compared with the initial TiO$_2$ NPs. The XRD patterns of TiO$_2$ NPs have been indexed using JCPDS-ICDD and confirmed that all diffraction peaks matched with 81.6% of tetragonal anatase phase (04-014-5762, TiO$_2$) and 18.4% of tetragonal rutile phase (01-072-4815, TiO$_2$). The major diffraction peaks of TiO$_2$ NPs were observed at 2θ values of 25.30°, 36.95°, 37.80°, 38.56°, 48.03°, 53.89°, 55.06°, 62.11°, 62.69° and 68.76° assigned to the (101), (103), (004), (112), (200), (105), (211), (213), (204) and (116) reflections for the anatase structure of TiO$_2$, respectively. The rest of the diffraction peaks were observed at 2θ values of 27.43°, 36.07°, 39.18°, 41.23°, 44.04°, 54.31°, 56.62°, 62.75°, 64.04°, 65.50° and 68.99° corresponded to the (110), (101), (200), (111), (210), (211), (220), (002), (310), (221), (301) and (112) planes for the rutile structure of TiO$_2$, respectively. Furthermore, XRD Rietveld refinement quantitative phase analysis confirms that the raw material TiO$_2$ NPs were a mixture consisting of 18.4% rutile and 81.6% of anatase crystal phases.

In the case of TiO$_2$/PrSO$_3$H catalyst, the XRD patterns matched all the diffraction peaks with tetragonal anatase phase structure (JCPDS-ICDD: 01-084-1286) and tetragonal rutile phase structure (JCPDS-ICDD: 01-072-4817). However, no characteristic extra peak was observed for the PrSO$_3$H groups, which suggested that these groups were only grafted on the surface of TiO$_2$ NPs, rather than impregnating the main crystallographic structure as expected.

The detailed interlayer spacing values and calculated crystallite sizes of the [101] peak for anatase and [110] peak for rutile from the initial TiO$_2$ NPs and PrSO$_3$H surface functionalized TiO$_2$ NPs are summarised in Table 4.1.

Table 4.1 Comparison of *d*-spacing and crystallite sizes of TiO$_2$ and TiO$_2$/PrSO$_3$H

Sample	XRD peak	°2θ	FWHM	*d*-spacing, Å	D *, nm
TiO$_2$	[101] Anatase	25.30	0.39	3.52	20.87
	[110] Rutile	27.43	0.33	3.25	25.08
TiO$_2$/PrSO$_3$H	[101] Anatase	25.47	0.41	3.49	19.86
	[110] Rutile	27.52	0.33	3.25	25.08

*D: The crystallite size of the 100% relative intensities XRD main peaks for anatase and rutile phases

4.2.1.2 Surface analysis

4.2.1.2.1 FT-IR spectroscopy

Figure 4.3 illustrates the FT-IR spectra over the range 500–4000 cm^{-1}, corresponding to the TiO_2 support (in red) and TiO_2/PrSO$_3$H (in black) catalysts. The FT-IR spectrum for TiO_2/PrSO$_3$H catalyst shows several extra peaks compared to TiO_2 NPs spectrum. The broad band in the range of 500-626.4 cm^{-1} related to Ti-O stretching vibrations can be clearly observed in both spectra [497]. The appearance of a new strong peak at 1031 cm^{-1} assigned to the stretching vibration of S-O bond, whereas the band occurring at 1130 cm^{-1} corresponded to C-O stretching vibration [408].
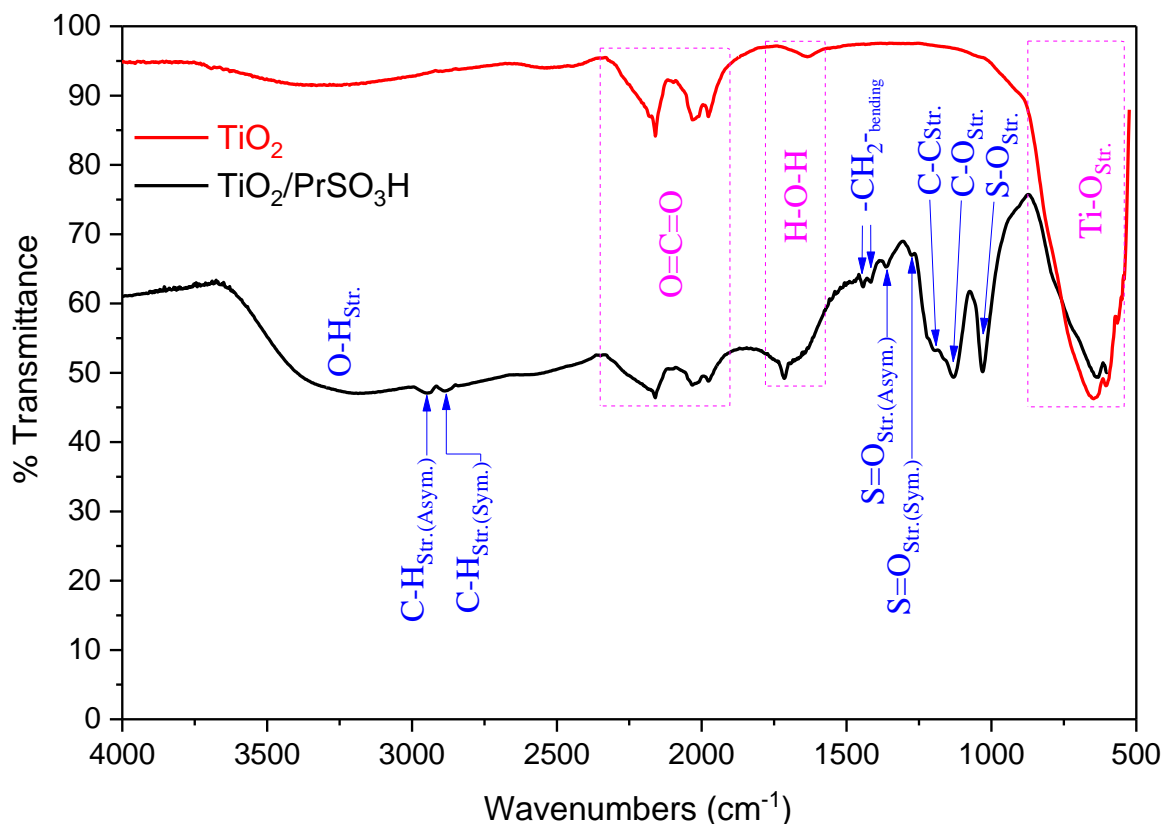
Figure 4.3 FT-IR spectra of TiO_2/PrSO$_3$H (in black) and TiO_2 (in red) catalysts showing nine extra peaks related to the surface modification of TiO_2 with PrSO$_3$H groups

Moreover, the existed band at 1198 cm^{-1} attributed to the C-C stretching vibration. The new extra two peaks appearing on the black spectrum at 1275 and 1362.5 cm^{-1} are considered to be a

fingerprint of the S=O symmetric and asymmetric stretching vibrations, respectively, for sulfonic acid group attachments on the surface of TiO_2 NPs [408]. Similarly, the new peaks located at 1416 and 1447 cm^{-1} are attributed to the methylene groups [–CH_2–] bending in $PrSO_3H$ functional groups [408]. The region below 3000 cm^{-1} clearly showed two distinct peaks at 2886 and 2946 cm^{1} that are likely to represent the C-H stretching vibrations, representing symmetric and asymmetric modes respectively, for the –CH_2– groups in $PrSO_3H$ functional groups [408, 498]. Furthermore, the weak absorption bands at 1640 cm^{-1} in TiO_2-NPs and 1712 cm^{-1} in $TiO_2/PrSO_3H$ belong to H-O-H symmetric vibration of the physisorbed water molecules on the surface. The region between 1975 and 2160 cm^{-1} clearly showed a few peaks related to the asymmetric stretching of CO_2 molecules adsorbed on the surface of the both $TiO_2/PrSO_3H$ and TiO_2 catalysts [499]. Additionally, the broad band at 3200-3500 cm^{-1} in $TiO_2/PrSO_3H$ catalyst assigned to O-H stretching vibration of sulfonic acid functional groups on the surface of TiO_2 NPs [408].

4.2.1.2.2 Electron microscopy

Surface morphological and structure features of the TiO_2 NPs and $TiO_2/PrSO_3H$ catalysts were examined at different magnification on the Hitachi CFE-SEM. It is clear from Figure 4.4 (a) that TiO_2 NPs have relatively uniform sized particles with unclear morphology and some agglomerates. $TiO_2/PrSO_3H$ catalyst [see Figure 4.4(b)], however, show non-uniform particle size distributions with some well-defined hexagonal and tetragonal shaped structures (SEM images @ 100K and 250K magnifications). This may suggest that the surface modification caused slight enlargement of the particle sizes of TiO_2 support as can be seen clearly in Figure 4.4 (b) @ 100K and 250K magnifications. Figure 4.5 shows the TEM images for TiO_2 catalyst support and $TiO_2/PrSO_3H$ solid acid catalyst. It is noticeable from TEM images [Figure 4.5 (a)] that most TiO_2 NPs have tetragonal or hexagonal morphologies whereas $TiO_2/PrSO_3H$ is agglomerated resulting in larger clusters owing to interaction between the head groups of $PrSO_3H$ on the surface of TiO_2 NPs [see Figure 4.5 (b)]. It is also important to mention that the enlarged particle sizes (red arrow) of as-synthesised $TiO_2/PrSO_3H$, observed in different TEM images, were due to the effects of surface grafting and crystallisation following Ostwald ripening. The TEM images also show a mixture of tetragonal/hexagonal morphologies of $TiO_2/PrSO_3H$ catalyst with good crystallinity. A similar case has been reported for surface modification of different particles using silanization method [489, 500].
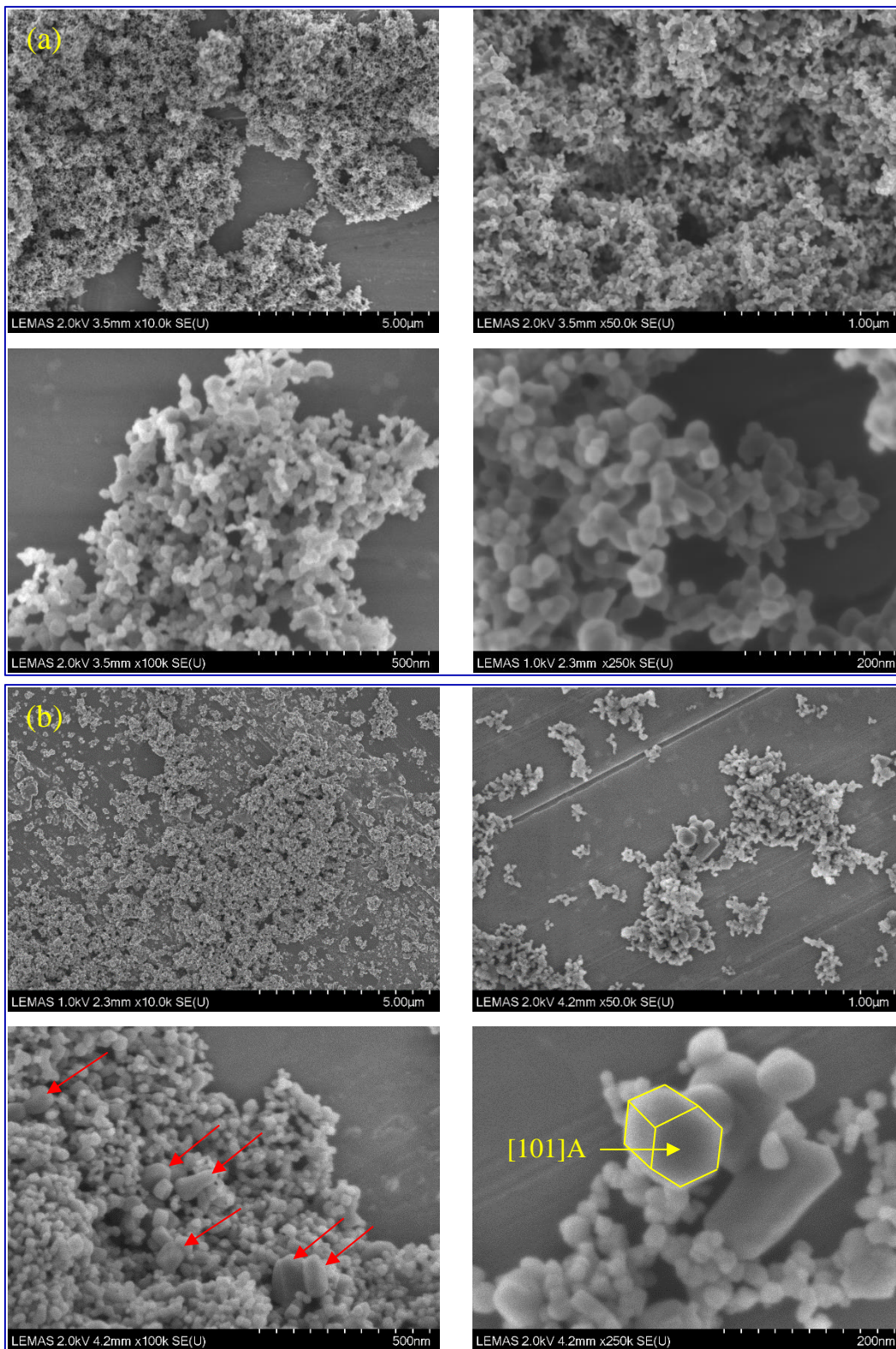
Figure 4.4 SEM images showing particle size and morphology distributions of TiO₂ catalyst support (a) and synthesised TiO₂/PrSO₃H catalyst (b)

It should be noted that the uniform and broad particle size distributions of prepared catalyst mainly depend on the initial TiO_2 NPs support with the grafting of propyl sulfonic acid into the surface of TiO_2 around the particle. The number based particle size distributions of $TiO_2/PrSO_3H$ were estimated from different TEM images and presented as histograms in Figure 4.6. These particles were found to have a size range of 8.2-42 nm with an average particle size of 23.1 nm; whereas, the average particle size of initial TiO_2 NP was 22.3 nm per 108 particles.
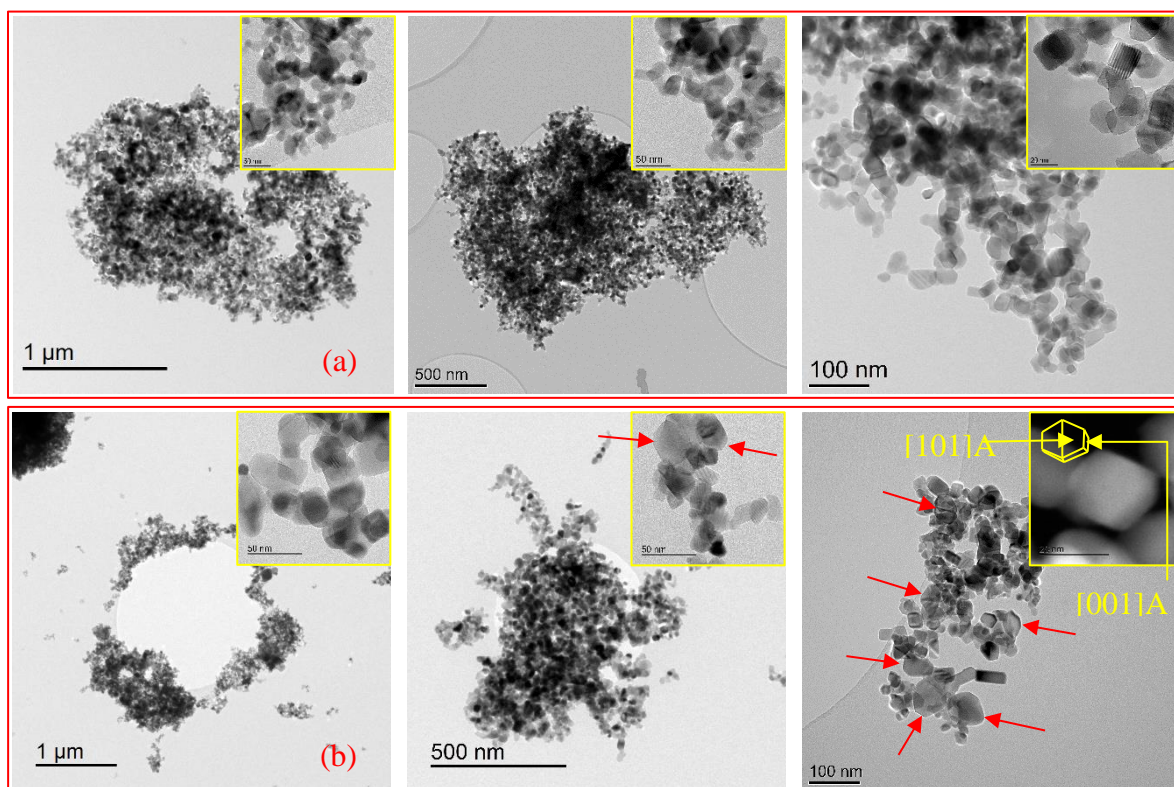
Figure 4.5 TEM images at different magnifications of TiO_2 catalyst support (a) and $TiO_2/PrSO_3H$ catalyst (b)

HR-TEM and SAED were conducted to investigate the particle morphologies for TiO_2 and $TiO_2/PrSO_3H$ catalysts as depicted in Figure 4.7. HR-TEM image confirms polycrystalline TiO_2 nanoparticles as shown in Figure 4.8 (a). The visible lattice fringes [Figure 4.7 (a)] with interplanar spacing of (3.54 Å, 3.52 Å, 3.52 Å) and 3.35 Å correspond to [101] and [112], respectively, lattice planes of TiO_2 according to JCPDS-ICDD file 04-014-5762. This was further confirmed by the SAED pattern of the TiO_2 NPs sample showing a set of diffused rings/spots poly-crystallinity corresponding to the [101], [112], [211], [310], [110], [200], [111], [202], [410], [221] and [202] lattice spacing of anatase TiO_2 crystal phase whilst the rest of rings/spots were assigned to the

[110], [200], [220] and [210], [110], [200], [111], [202], [410], [221] and [202] lattice spacing of rutile TiO$_2$ crystal phase, as shown in Figure 4.7 (b).
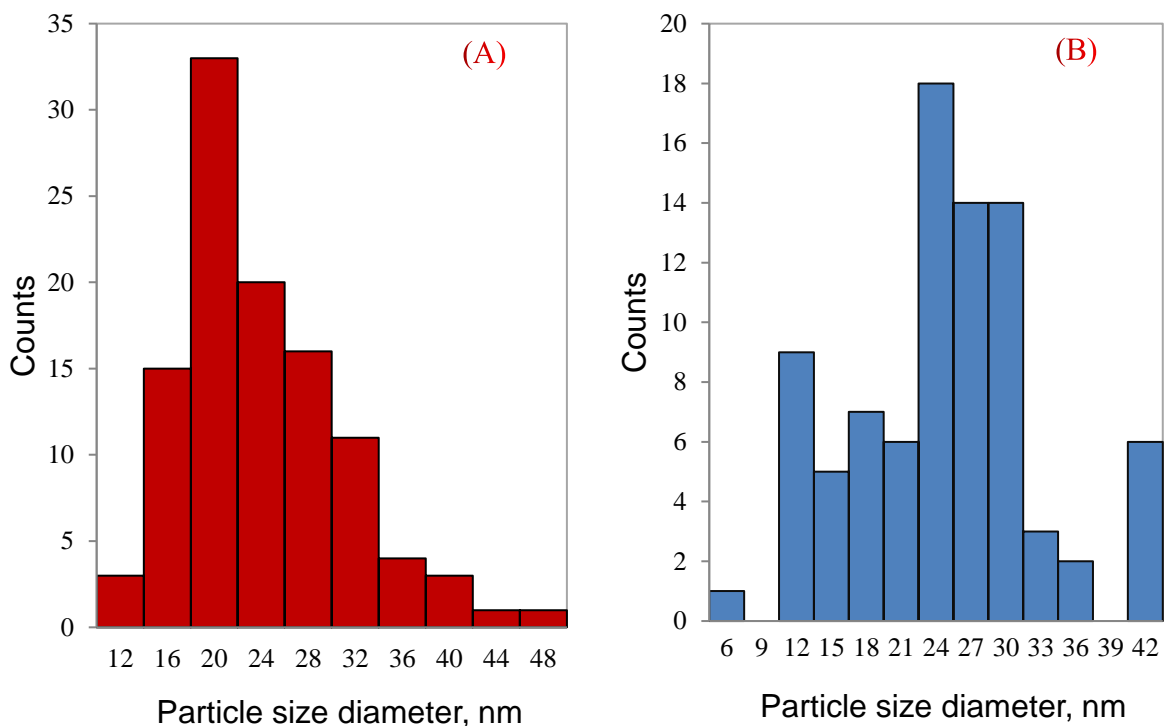
Figure 4.6 Particle size distributions for (a) TiO$_2$ and (b) TiO$_2$/PrSO$_3$H catalysts

In the case of TiO$_2$/PrSO$_3$H catalyst the HR-TEM images [Figure 4.7 (c)], there were two different kinds of lattice fringes observed, attributed to [101] interplanar spacing of anatase phase and [200] interplanar spacing of rutile phase with a tiny amorphous layer surrounding the surface of each particle. This indicates that [101] and [200] facets have more preferable planes in anatase and rutile crystal phases, respectively. Noticeably, the synthesised catalyst has good core crystallinity [inset in Figure 4.7 (c)] regardless of the presence of PrSO$_3$H groups on the surface. Furthermore, several obtained SAED patterns [see Figure 4.7 (d)] confirm the mixed phases of rutile and anatase with poly-crystallinities, in the TiO$_2$/PrSO$_3$H catalyst. In addition, the clear poly-crystallinity rings/spots correspond to the [101], [116], [004], [200], [220], [213], [216] and [204] lattice planes of anatase TiO$_2$ crystal phase in the TiO$_2$/PrSO$_3$H catalyst. The other poly-crystallinity rings/spots, on the other hand, were attributed to the [101], [210], [220], [310], [110], [200], [111], [202], [410], [221] and [202] lattice spacing of rutile TiO$_2$ crystal phase in TiO$_2$/PrSO$_3$H catalyst.
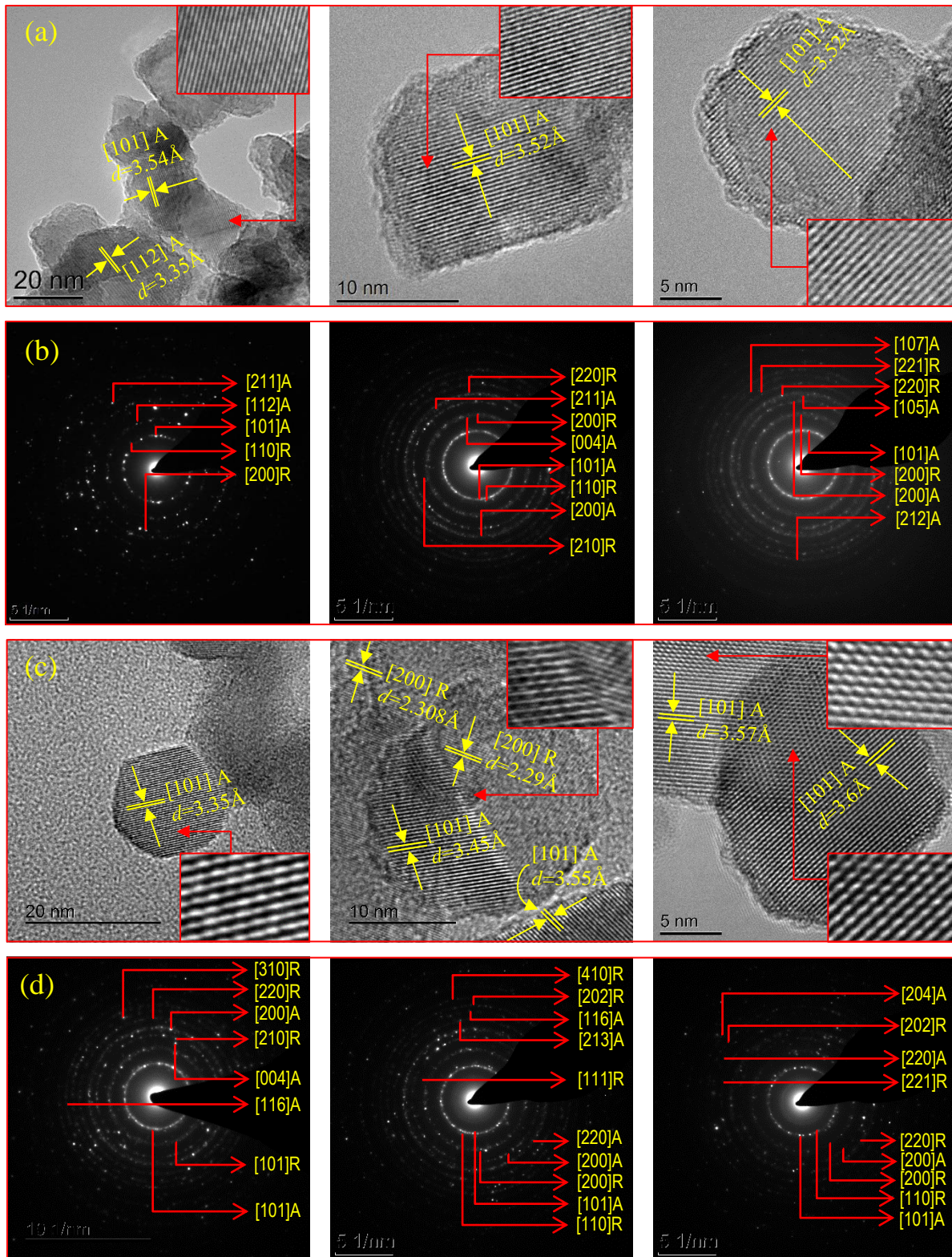
Figure 4.7 HRTEM micrograph images for TiO₂ support (a) and TiO₂/PrSO₃H catalyst (c) but SAED patterns for TiO₂ support (b) and TiO₂/PrSO₃H catalyst (d)

STEM electron energy loss spectroscopy (EELs)-maps for TiO$_2$/PrSO$_3$H catalyst were performed to obtain more information about the loading of carbon and sulphur layers on the surface of TiO$_2$ NPs. Titanium, carbon and sulphur maps were extracted from the spectrum imaging of electron energy-high loss region. Figure 4.8 demonstrates the high resolution elemental mapping of titanium, carbon and oxygen layer-by-layer distributions onto the TiO$_2$/PrSO$_3$H particles. It can be observed that the surfaces of TiO$_2$ NPs are uniformly covered by carbon and sulphur layers. These homogenous distributions of carbon and sulphur clearly confirm the surface of TiO$_2$ NPs have been functionalised by PrSO$_3$H groups. This also explains the reason for surface area reduction [Figure 4.9 (b)] and some surface roughness of particles [Figure 4.7 (c)].The STEM image further shows clear large gaps between TiO$_2$/PrSO$_3$H particles.
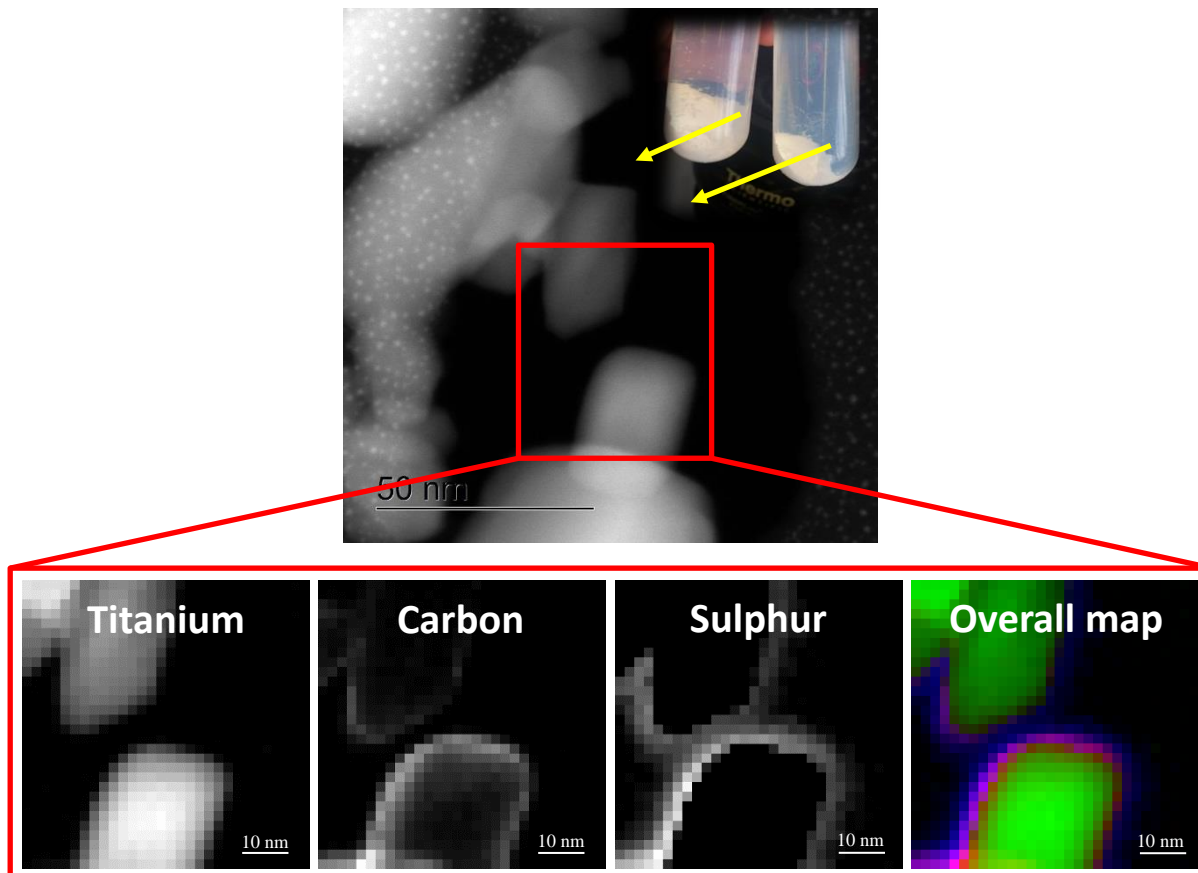
Figure 4.8 STEM image with EELs-mapping of synthesised TiO$_2$/PrSO$_3$H catalyst obtained from Titan at 300 kV illustrating the 2D elemental mapping with high quality overall map of TiO$_2$/PrSO$_3$H particles with the distribution of individual elements (Titanium in green, Carbon in violet, and Sulphur in blue).

4.2.1.2.3 N₂ porosimetry

Nitrogen adsorption–desorption isotherms and pore volume/size distributions of TiO_2 and $TiO_2/PrSO_3H$ catalyst samples are presented in Figure 4.9. The surface area was calculated from the nitrogen adsorption isotherms using the BET method, while the mean pore size and total pore volume were calculated from the desorption branch of the isotherm using the BJH methods. The adsorption isotherms for both catalysts were determined in the range P/P_o=0.05-0.2, wherein a linear relationship was maintained, which revealed that both materials are typical type IV isotherms within mesoporous structure. The differences in condensation and evaporation were attributed to the monolayer-multilayer adsorption according to the IUPAC – behaviour associated with mesoporous materials. The hysteresis loop shape for as-synthesised $TiO_2/PrSO_3H$ at relative pressure in the range of 0.75-0.985 was classified as H1-type, indicating a capillary condensation in mesoporous structure [424]. It should be noted from Figure 4.9 (inset) that the pore volume distributions in $TiO_2/PrSO_3H$ catalyst has larger mesopores with an increase of pore diameter (duplicate) compared to the initial TiO_2 NPs. The large pore size is much more preferable for minimizing diffusion limitations for long alkyl chain hydrocarbons in //FFA/TG in esterification and transesterification reactions [86, 304].
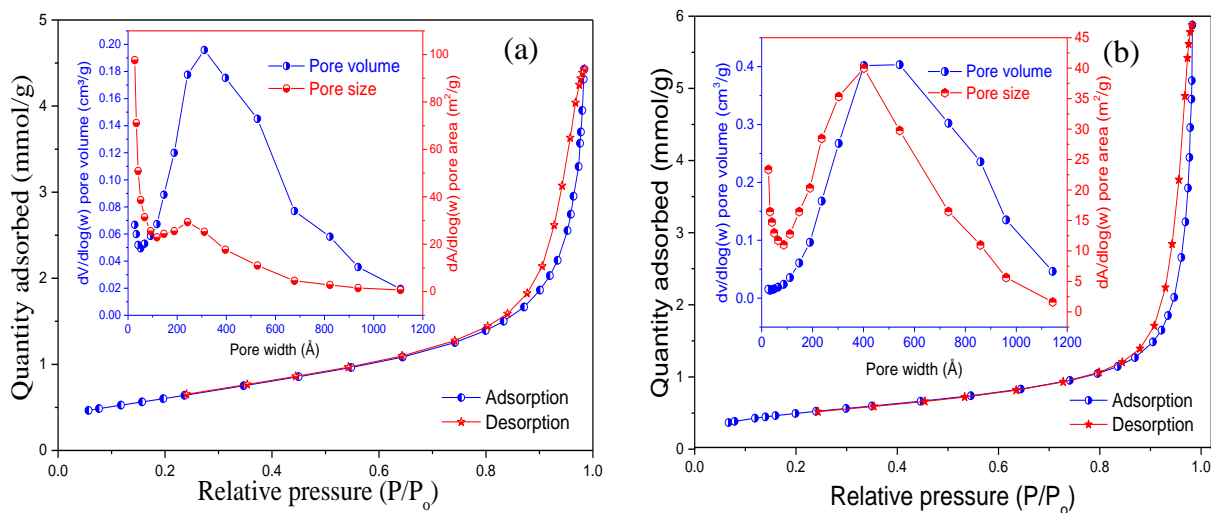
Figure 4.9 N₂ adsorption-desorption isotherms and total pore volumes with mean pore sizes (inset) for (a) TiO_2 NPs and (b) synthesised $TiO_2/PrSO_3H$ catalysts.

The detailed analyses for texture properties using N₂ adsorption-desorption isotherms, percentage of carbon and sulphur contents using CHNS analysis, as well as the percentage of sulphur using

TEM-EDS for prepared TiO$_2$/PrSO$_3$H catalyst, are summarized in Table 4.2. It was found that the loading of 1.41% of carbon and 0.28% of sulphur from PrSO$_3$H groups on the surface of TiO$_2$ NPs was accompanied by a small decrease of the BET surface area with an increase of the pore volumes and sizes.

Table 4.2 Physicochemical parameters of TiO$_2$ and TiO$_2$/PrSO$_3$H catalysts

	Texture properties [a]			CHNS analysis [b]		TEM-EDS [c]		XPS [d]			
	S$_{BET}$	V$_p$	D$_p$	C%	S%	S%	C%	S%	C%	Ti%	O%
TiO$_2$	49	0.15	12.9	--	--	--	--	--	--	1.0	2.36
TiO$_2$/PrSO$_3$H	39	0.19	24.6	5.0	1.0	1.0	5.0	1.0	4.63	1.0	6.64

[a] S$_{BET}$: BET surface area (m^2.g^{-1}) calculated over the relative pressure range 0.05–0.2, D$_p$: Mean pore size (nm) calculated by applying the BJH model from N$_2$ desorption isotherm; V$_p$: Total pore volume (cm^3.g^{-1}) was determined at P/P$_o$ =0.985. [b] C%: Carbon%, and S%: Sulphur% determined by using elemental (CHNS) analysis. [c] The atomic ratios for PrSO$_3$H loading on the surface of TiO$_2$ NPs was quantified by using TEM-EDS analysis at different TEM spots. [d] The atomic ratios of S, C, Ti and O in TiO$_2$ NPs and TiO$_2$/PrSO$_3$H catalyst was also quantified using XPS analysis.

4.2.1.2.4 XPS
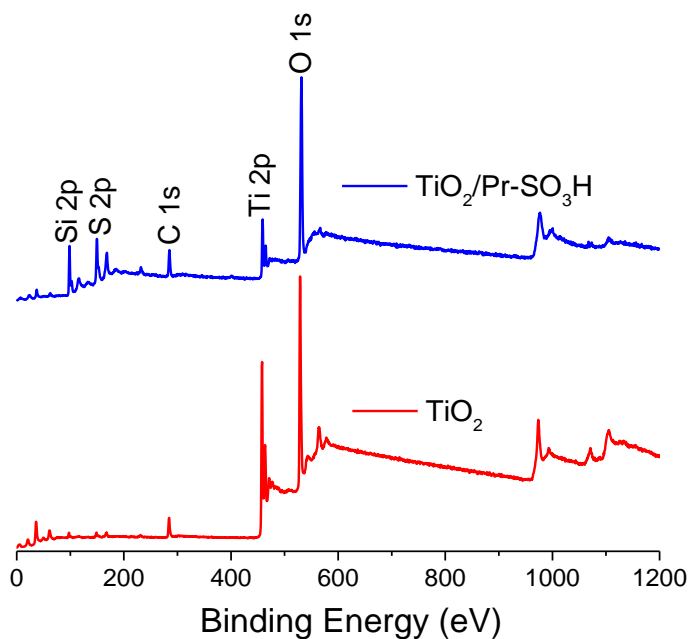
Figure 4.10 XPS survey scan of TiO$_2$ NPs and synthesised TiO$_2$/PrSO$_3$H catalyst
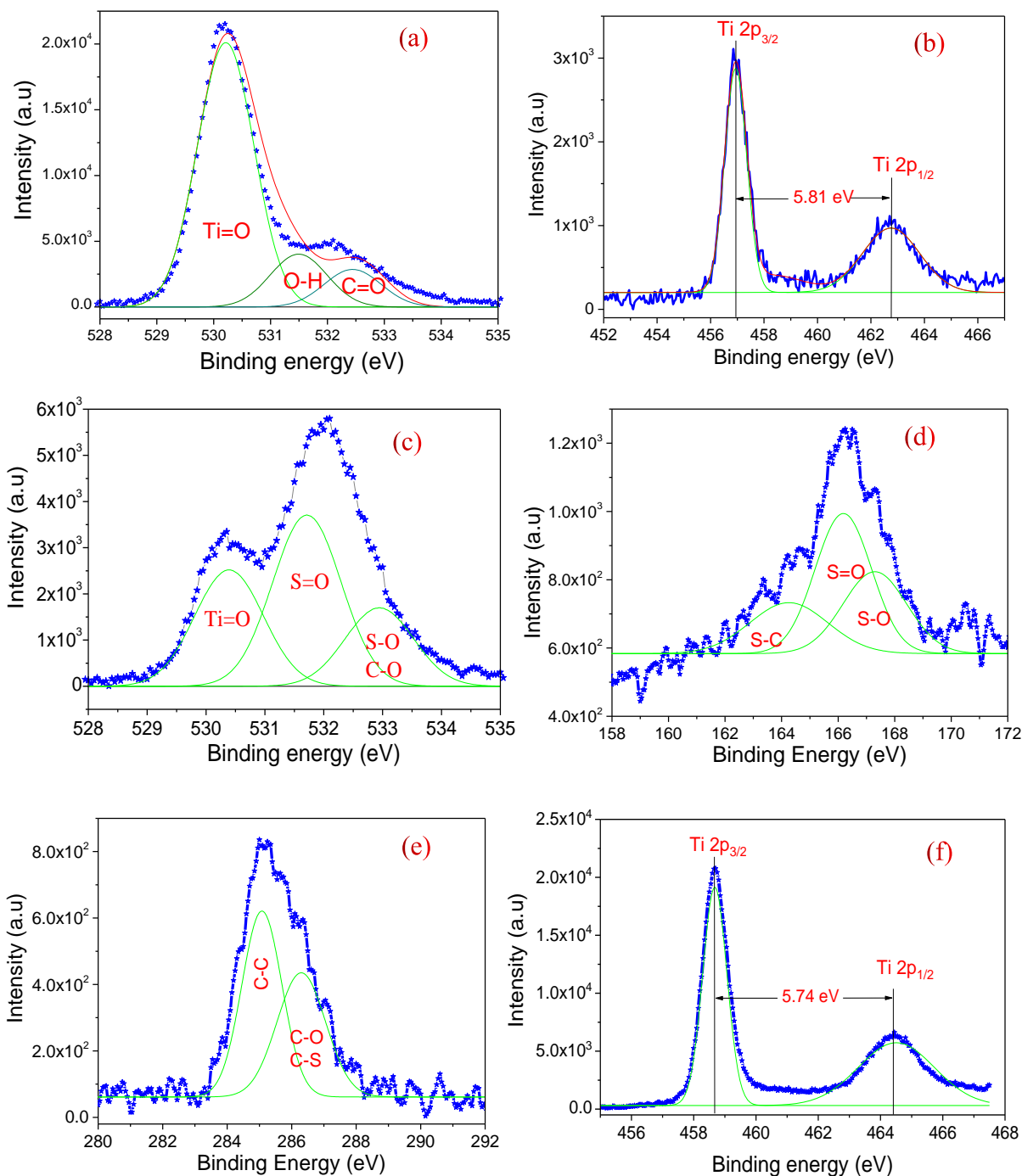
Figure 4.11 XPS spectra showing the chemical environment of (a) O 1s and (b) the de-convolution of Ti 2p peaks in TiO_2 catalyst support whilst the chemical environments of (c) O 1s, (d) S 2p & (e) C 1s and (f) the de-convolution of Ti 2p peaks in $TiO_2/PrSO_3H$ catalyst

The survey scan XPS for TiO_2 NPs and $TiO_2/PrSO_3H$ catalyst was investigated is shown in Figure 4.10. The XPS analysis provides valuable insight into the surface compositions and bonding environments for both catalysts. The detailed high resolution XPS of the O 1s and Ti 2p peaks in TiO_2 catalyst support are presented in Figure 4.11 (a) and Figure 4.11 (b), respectively. Figure 4.11 (a) shows the deconvoluted O 1s peaks of TiO_2 NPs. The spectra yielded three Gaussian peaks. The first band located at 530.2 eV with FWHM of 1.177 eV could be attributed to the Ti=O from TiO_2. The second peak centred at binding energy of 531.2 eV could be related to the C=O from absorbed CO_2 in air on the surface of the catalyst. The last peak detected at 532.52 eV is assigned to the O-H of absorbed moisture from air on the surface of the TiO_2 NPs forming [-Ti(OH)-O-Ti-O-]. This agrees with reported XPS in the literature for TiO_2 as listed in Table 4.3. Based on this, it can be inferred that the surface of TiO_2 was very active and contaminated with CO_2 and H_2O from the air [501].

Table 4.3 Comparison of de-convoluted O 1s of nano-sized TiO_2 with the reported values from the literature

	Ti=O (eV)	C=O (eV)	O-H (eV)
Present work	530.21	531.22	532.52
Sanjines, et. al [502]	530.10	531.05	532.30
Liu, et al. [503]	530.10	531.80	532.40
Ahmed, et al. [504]	530.70	531.90	532.70

The spin-orbital splitting between Ti $2p_{1/2}$ (at 462.75 eV) and Ti $2p_{3/2}$ (at 456.94 eV) is 5.81 eV (ΔEBE), as shown in figure 4.11 (b). This is significant implication is that titanium in the TiO_2 exists in a tetravalent oxidation state (Ti^{4+}) in the anatase phase of the TiO_2.

In the case of $TiO_2/PrSO_3H$ catalyst the O 1s core level spectrum [see Figure 4.11 (c)] was de-convoluted into three Gaussian peaks centred at 530.4 eV, 31.75 eV and 533 eV indicating the presence of Ti=O, S=O and S-O/C-O, respectively. However, the overlapped peaks located at 533 eV (see Figure 4.11 c) correspond to the lattice oxygen in O-C and O-S, this could be due to the binding energy (BE) of the de-convoluted O 1s peaks for O-C and O-S falling in the same energy regions which made it difficult to distinguish between the contribution of both species [505]. The S 2p spectra [see Figure 4.11 (d)] were fitted with three Gaussian peaks centred at 164.4 eV, 166.3 eV and 167.4 eV assigned to the S-C, S=O and S-O, respectively, supporting the presence of

PrSO₃H groups on the surface [505]. Moreover, the high resolution C 1s XPS spectra [Figure 4.11 (e)] included two Gaussian peaks centred at 285.1 eV and 286.4 eV which can reasonably be assigned to the C-C and C-S/C-O, respectively, in the PrSO₃H groups [506]. Figure 4.11 (f) depicts the Ti $2p_{1/2}$ - Ti $2p_{3/2}$ spin-orbit splitting at 464.4 eV and 458.7 eV, respectively, with a $\Delta EBE=5.74$ eV confirming the oxidation state of Ti in the as-prepared TiO₂/PrSO₃H is IV [507-509]. The above findings indicate the surface of TiO₂ NPs is functionalised with PrSO₃H groups

The surface atomic ratios of Ti:O, Ti:S and S:C in TiO₂/PrSO₃H catalyst were determined from the XPS data and found to be 1:6.64, 1:1 and 1:4.63, respectively. In fact, these ratios theoretically in TiO₂/PrSO₃H catalyst are supposed to be 1:5, 1:1 and 1:3 for Ti:O, Ti:C and S:C, respectively. Therefore, there was an overall increase in carbon and oxygen presumably due to surface contamination of the catalyst with CO_x and/or H_2O in the atmosphere during sample preparation for analysis. This result confirms an earlier investigation with the FT-IR spectrum for TiO₂/PrSO₃H catalyst. In addition, the percentage of sulphur to carbon atomic ratios using XPS quantitative analysis in TiO₂/PrSO₃H catalyst was 0.22. This is in agreements with the results obtained by CHNS analysis. In the case of TiO₂ NPs, the atomic concentration ratio from the XPS analysis was also found to be 1:2.36. The increase of Ti:O atomic ratio by 0.36 could have been due to the surface of TiO₂ NPs being contaminated with CO_x and/or H_2O in air which is confirmed by FT-IR and the presence of sp^2 hybridized carbon in XPS survey scan spectrum at 285 eV.

4.2.1.3 Thermal stability

Thermal stability analysis gave insights on the species evolved upon heating of the catalyst that was prepared via surface grafting (PrSO₃H). Figure 4.12 (a) shows the weight loss of TiO₂/PrSO₃H and initial TiO₂ NPs as determined by TGA under N₂ purge gas. There was a negligible weight loss from 25°C to 120°C for both samples assigned to desorption of H_2O/CO_x molecules from the surface of TiO₂. In the case of initial TiO₂ NPs, there was no further mass loss up to 900°C. In contrast, there was a gradual weight loss of about 2% from TiO₂/PrSO₃H at 210°C to 500°C; afterwards there was no further weight loss up to 900°C. This is due to the thermal decomposition of PrSO₃H species on the surface of TiO₂ NPs. This result agrees with results of the CHNS elemental analysis and is in accordance with the FT-IR results. However, the calculated weight loss of ~2% from TGA curve indicated the PrSO₃H loading was very low in comparison with the

146

initial PrSO3H loading per 1 g of TiO2 NPs. This is due to low surface of initial titania NPs. Therefore, more investigation need to be carried out in future on the high surface area titania as a catalyst support in order to provide more receptor sites per gram of TiO2. It must be noted also from the DSC results (see Figure 4.12 b) that there is only one sharp distinct endothermic peak observed at 210°C with enthalpy of -60 mJ corresponding to the decomposition of PrSO3H groups on the surface of TiO2 NPs. This is further evidence that the surface of TiO2 NPs was successfully functionalised with PrSO3H groups.
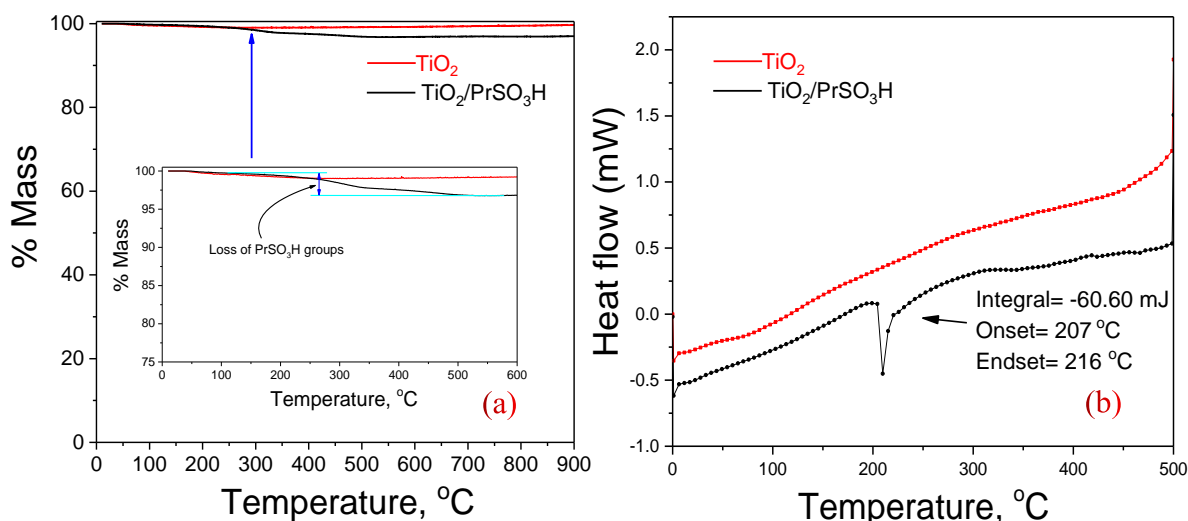
Figure 4.12 TGA (a) and DSC (b) profiles for TiO2.and TiO2/PrSO3H catalysts

4.2.1.4 Surface acidity

The ratio of Brønsted to Lewis acid sites for TiO2 NPs and TiO2/PrSO3H catalyst was found from the DRIFT spectra based on the ring vibration of pyridine in the range of 1400-1650 cm^{-1} as shown in Figure 4.13. The bands at 1445-1446 and 1607-1610 cm^{-1} were assigned to the coordinated pyridine adsorption on the Lewis acid sites in both catalysts, whereas, the peaks at 1540-1541 and 1640-1642 cm^{-1} were attributing to the strong Brønsted acid sites (absorptions of pyridinium ions) [510]. The band at 1490 cm^{-1} originated from the combination of pyridine on the Brønsted and Lewis acid sites [511, 512]. It can be also noted that the Lewis acid site (1445 cm^{-1}) proportion reduced after the pyridine titration with an increase of Brønsted acid site (1541 cm^{-1}). This resulted in an increase of the ratio of Brønsted to Lewis acid sites, which indicated the surface grafted TiO2 support with PrSO3H species generates more Brønsted than Lewis acid sites. However, the total

amount of acid loadings on the TiO_2 NPs support and $TiO_2/PrSO_3H$ catalyst were quantified using TPD-MS with n-propylamine probe as shown in Figure 4.14. The surface grafting led to an increase of the total amount of acid loading from 0.28 and 2.35 mmol/g.
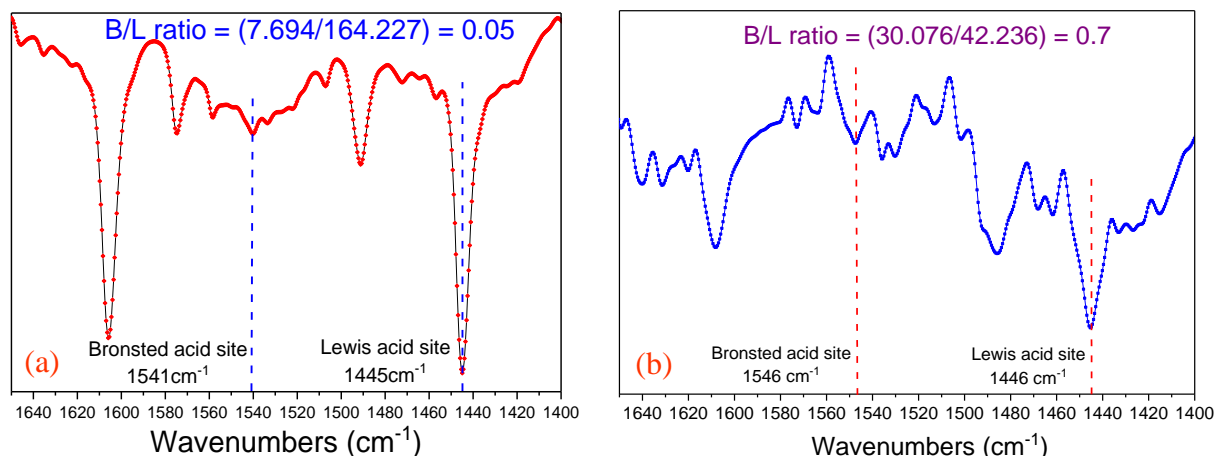
Figure 4.13 DRIFT spectra after pyridine adsorptions of (a) TiO_2 and (b) $TiO_2/PrSO_3H$ catalysts
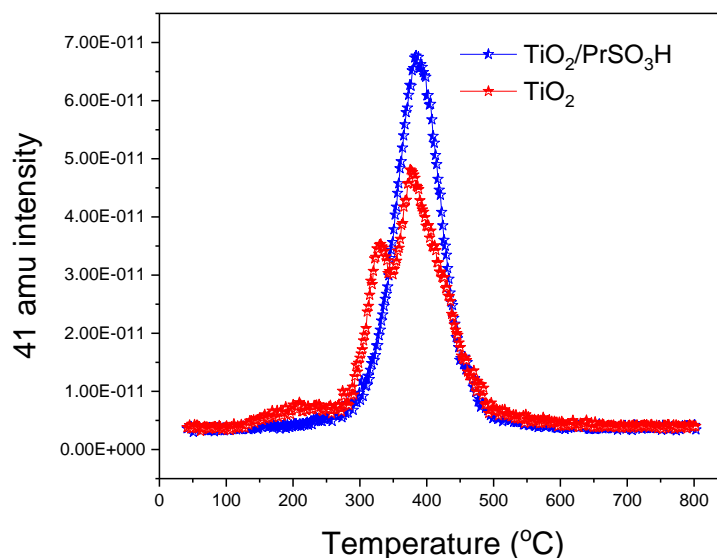
Figure 4.14 TPD-MS profiles for irreversibly adsorbed n-propylamine molecules on the surface of TiO_2 support and $TiO_2/PrSO_3H$ catalyst

Table 4.4 provides a comparison of the relative acid strength site from the current work with a published works in the literature. From Table 4.4, it can be understood that $TiO_2/PrSO_3H$ has a high acid site density compared to all other solid acid catalysts confirming the solid acid catalyst can be safely used for raw materials containing FFA.

Table 4.4 Comparison of total acid loading in $TiO_2/PrSO_3H$ with the reported values for different types of solid acid catalysts from the literature

Catalyst	Total acid amount [H$^+$]	Reference
$TiO_2/PrSO_3H$	2.35 mmol/g	Present work
Amberlyst-15	1372-4700 µmol/g	[513]
SBA-15-SO$_3$H	1.44 meq/g	[102]
SBA-15-ph-SO$_3$H	0.9 meq/g	
ZrO$_2$-SO$_3$H	2.9 mmol/g	[514]
Fe$_3$O$_4$-SBA-SO$_3$H	1.09 mmol/g	[487]
SBA-SO$_3$H	0.44-0.56 mmol/g	
Ti(SO$_4$)$_2$	1.22-3.61 mmol/g	[363]
SO$_4^=$/ZrO$_2$	0.07-0.37 mmol/g	[515]
SO$_4^=$/ZrO$_2$/TiO$_2$/Fe$_3$O$_4$	47.9-135.2 µmol/g	[516]
SO$_4^=$/TiO$_2$	793.8 µmol/g	[365]

4.2.2 Catalytic performance

The catalytic activity of TiO_2 catalyst support and $TiO_2/PrSO_3H$ solid acid catalyst for simultaneous esterification and transesterification of UCO to produce biodiesel fuel was investigated. A set of experiments were initially carried out for biodiesel production over pure TiO_2 NPs as a catalyst in order to assess true performance of surface functionalisation of TiO_2 NPs with propyl sulfonic acid; however, there were unsuccessful due to the formation of strong emulsion when the suspended catalyst-methanol was added to the UCO feedstock in the glass reactor. Consequently, the obtained biodiesel was very difficult to separate from the reaction mixtures. That is why biodiesel production over pure TiO_2 NPs as a catalyst has not been reported in the literature. The effect of different reaction times, $TiO_2/PrSO_3H$ catalyst loadings, mole ratios of methanol to oil, and reaction temperatures on the percentage of FAME yields were studied and the results are presented in Figure 4.15. The reaction time of esterification/transesterification varied between ½ and 9 h whilst other process parameters were kept constant at 1 wt% of $TiO_2/PrSO_3H$ catalyst to UCO feedstock, 6:1 methanol to oil mole ratio and 65 °C reaction temperature. It was found that the initial (trans)esterification reaction rate was very low, as shown in Figure 4.15 (a). This could possibly be due to the immiscibility of reactants (solid-liquid-liquid phases) / the initial mass transfer limitations. The FAME yield further increased but was still lower than 10% when the experiment was run for a longer time (9 h). This is because of the better miscibility of reactants (solid acid catalyst, methanol and UCO) with the time and increasing of

mass transfer. The results of different catalyst to oil loadings on the FAME yield, however, shows the yield of FAME was almost doubled [see Figure 4.15 (b)] when the (trans)esterification process was set at 9 h of reaction time, 2 wt% of catalyst to UCO, 6:1 methanol to oil mole ratio and 65 °C reaction temperature. This was attributed to the fact that the number of active sites were increasing with a rise in the catalyst concentration in the reaction system requiring a shorter time to reach the equilibrium [517]. Furthermore, the yield of FAME further increased from 14.92% to 38.7% with an increase in the catalyst loading from 2 wt% to 4.5 wt% of UCO. Increasing the catalyst concentrations will lead to an increase in the number of active sites (proton, $-SO_3H$, concentration in the interface), which enhances selectivity towards the FAME product [348].

A maximum conversion of FFA/TG into FAME is required in simultaneous esterification and transesterification reactions to obtain the highest yield of FAME in order to satisfy the EU and ASTM standards for obtained biodiesel fuel. In theory, the stoichiometric ratio for transesterification reaction requires three moles of methanol per mole of TG to obtain three moles of FAME and one mole of glycerol whilst this ratio is one to one for esterification reaction [308]. However, transesterification reaction in practice needs an excess amount of methanol in order to get a complete conversion. In order to drive the reaction towards the highest FAME yield [287], various mole ratios of methanol to UCO were used [see Figure 4.15 (c)] under the aforementioned reaction conditions. It can be noted that the highest FAME yield of 98.1% was obtained when the mole ratio of methanol to UCO was steadily increased to 15:1 whilst the other parameters were fixed. This was most probably due to a higher molar ratio of methanol to UCO leading to an increase of miscibility of reactants which shift the equilibrium to the product side and increase the probability of a methanol nucleophilic attack on the carbonyl/carboxylic acid functional groups in the FFA/TG. However, a further mole ratio of methanol to oil increase leads to a slight reduction in the FAME yield [517, 518], presumably because glycerol and FAME solubility in excess methanol can help to derive the reverse side of transesterification reaction [80].

The rate of esterification/transesterification reactions are strongly dependent on the process temperature. The effect of temperature on the FAME yield, whilst other parameters were set at 9 h reaction time, 4.5 wt% of $TiO_2/PrSO_3H$ to UCO, 15:1 molar ratio of methanol to UCO, 600 RPM agitation rate, 0.14% moisture content, and <2% of FFA content in UCO raw material, is shown in Figure 4.15 (d). It can be noted that the increase of reaction temperature from 25 °C to 60 °C led to a smooth increase in the rate of the (trans)esterification process to reach 98.3% FAME yield.
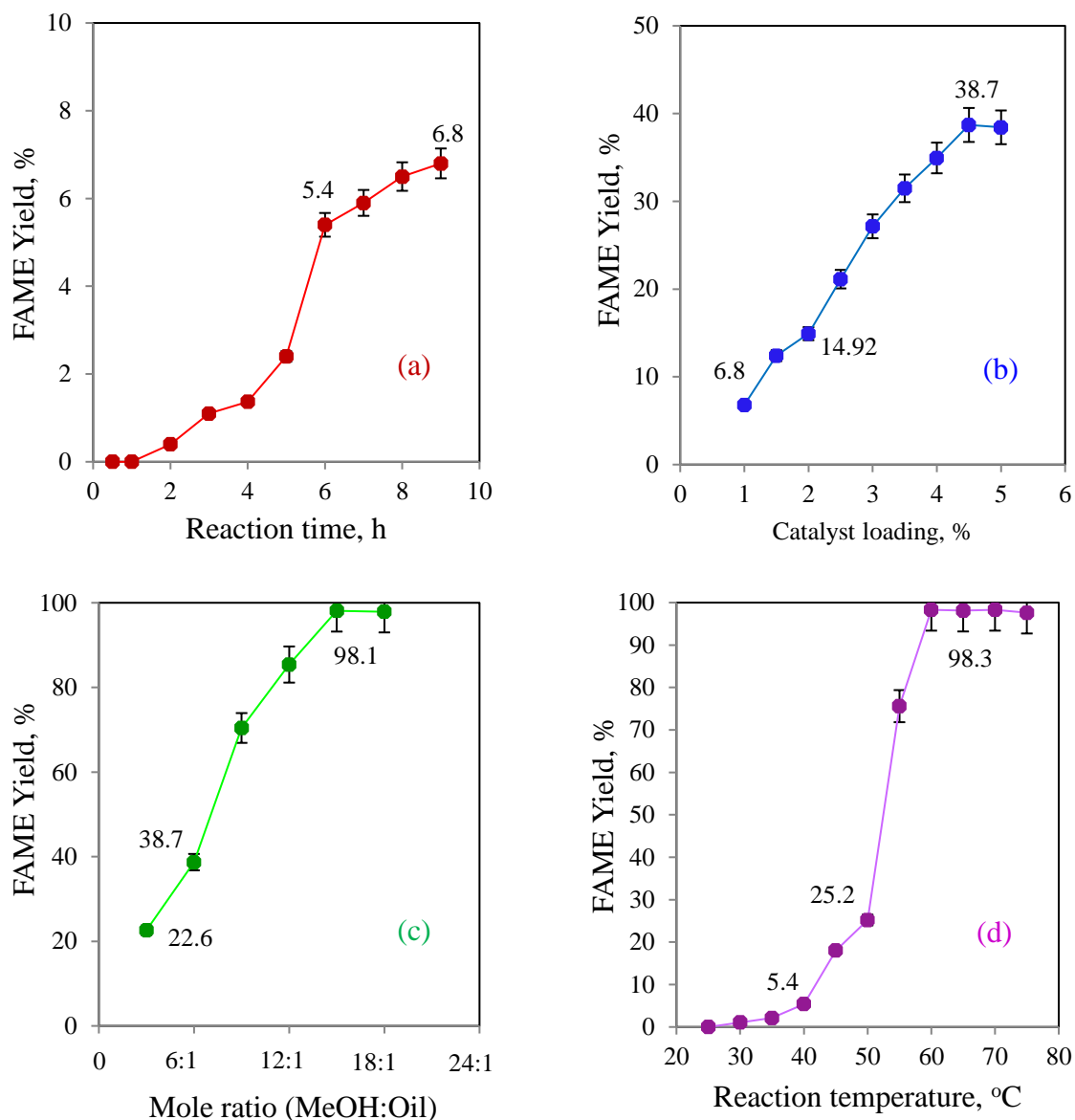
Figure 4.15 The effects of (a) reaction time, (b) $TiO_2/PrSO_3H$ catalyst loading to UCO, (c) mole ratio of methanol to UCO, and (d) reaction temperature on the percentage of FAME yield.

The reason for obtaining a high FAME yield at a higher temperature can be explained by the fact that the higher reaction temperature accelerates (1) the movement of molecules in reactants, (2) solubility of TG in methanol, (3) diffusion of TG molecules, as well as (4) generating more nucleophilic sites ($-SO_3^-$ and $–O^-$) in the reaction system which results in an increase in reaction rate. This could help to initiate the activation of carboxylic/carbonyl function groups in FFA/TG

by nucleophile [86]. Further studies on the reaction kinetic of the esterification/transesterification reaction using $TiO_2/PrSO_3H$ catalyst should be reported in the future work.

4.2.2.1 Catalytic activity and its reusability

The catalytic activity of $TiO_2/PrSO_3H$ catalyst was assessed by the addition of different percentages of oleic acid in virgin oil because the presence of FFA in the feedstock has a great influence on the deactivation of catalysts. The addition of oleic acid in virgin oil varied from 0.5% to 6% under determined optimum reaction conditions as reported in the previous section. It can be observed from Figure 4.16 (a), that the FAME yield was greatly reduced with an increase in the percentage of oleic acids in the virgin oil. This can be explained by the rate of esterification which was much faster than the transesterification [287] producing more water (by-product) in the reaction medium in a shorter time. The produced excess water in the reaction medium would probably deactivate the active sites of the catalyst. Likewise, the presence of a high concentration of oleic acid in the reaction medium leads to the rapid formation of ester and water (by-product). Produced water from the reaction as a by-product may drive the reverse reaction to re-form FFA and methanol [519, 520].
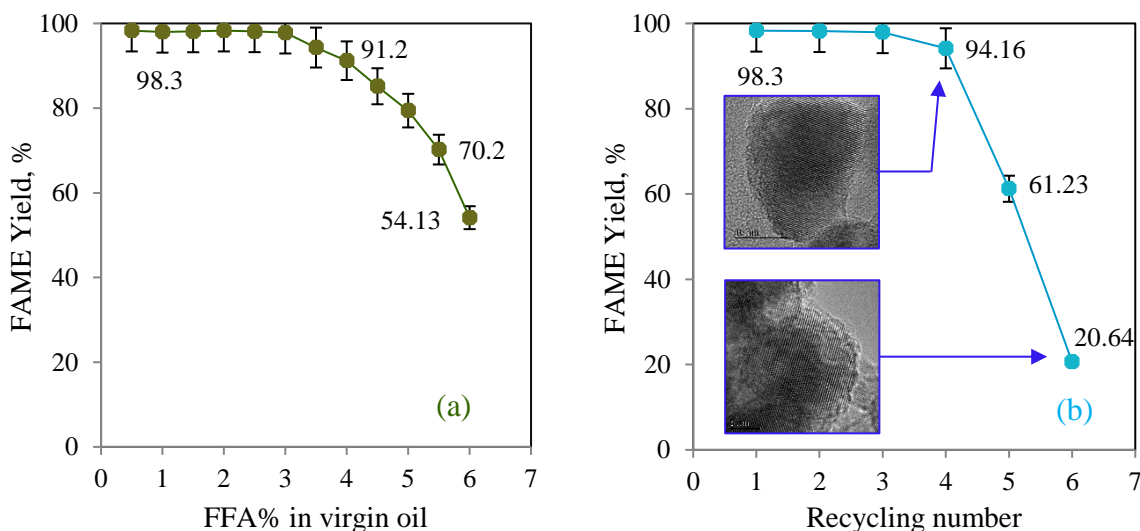
Figure 4.16 The effect of different concentration oleic acid addition in virgin oil (a) and reusability of $TiO_2/PrSO_3H$ catalyst (b) on the percentage of FAME yield.

The spent $TiO_2/PrSO_3H$ catalyst was recovered from the reaction products and by-products at the end of each run by using centrifuge (Megafuge 16R, UK) and then washed several times with 1:1

ratio of methanol to n-hexane in order to remove any remaining impurities (polar and non-polar components) on its surface. The recycled catalyst was later dried in an oven for 3 h at 110 °C to remove any moisture on the surface prior to being re-used under optimised process conditions to investigate its remaining activity.
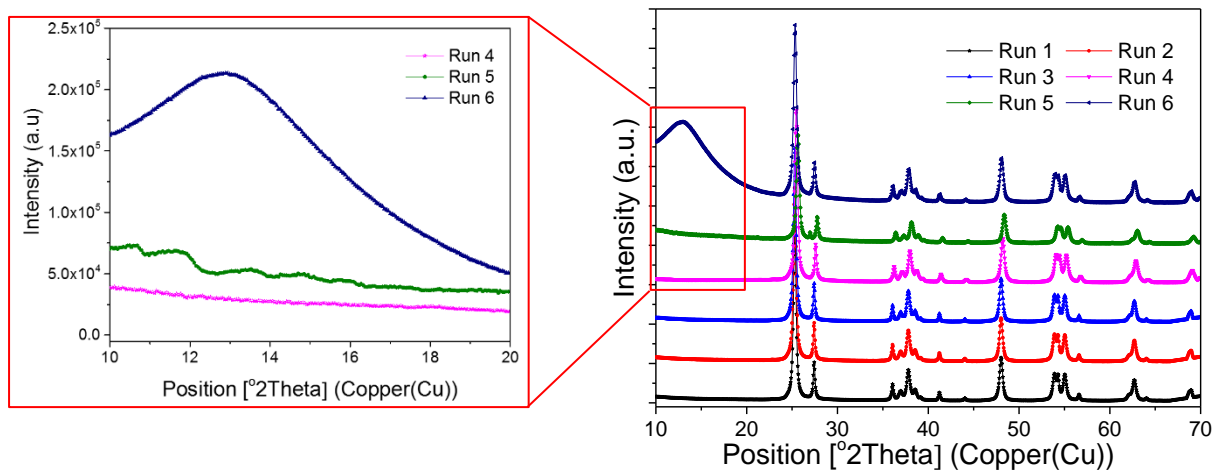
Figure 4.17 Powder XRD patterns of spent $TiO_2/PrSO_3H$ catalyst

It was found that $TiO_2/PrSO_3H$ can be re-used up to four times under optimized reaction conditions, i.e. reaction temperature of 60 °C, 4.5 wt% of $TiO_2/PrSO_3H$ catalyst to UCO, molar ratios of methanol to UCO of 15:1, 600 RPM agitation rate, 0.14% moisture, <2.0% FFA, and 9 h reaction time. However, thereafter, the yield of FAME was sharply reduced to 20.64%, as shown in Figure 4.16 (b). This obvious change in the production of FAME yield is due to the organic or carbonaceous materials on the surface of recycled catalyst causing blockage of the active sites and/or detachment (leaching) of the $PrSO_3H$ species on the surface of TiO_2 NPs [38, 318, 513, 521]. According to the XRD results shown in Figure 4.17, there was an accumulation of organic or carbonaceous materials from the surface of the prepared mesoporous solid acid catalyst after four runs. This possibly inhibited the contact between the reactants and the active sites of the catalyst [80, 384, 496, 513]. The leaching of sulfonic acid and titanium was investigated using ICP-MS after each run. It was found that the amount of titanium was not detectable in all synthesised biodiesel fuels but unfortunately the leaching of sulphur was detected in the range of 172.94 to 995.67 ppb probably due to the leaching of the active site of the solid acid catalyst. In order to fully understand the catalytic poisoning of the spent $TiO_2/PrSO_3H$ catalyst, further studies should be carried out in detail, using the XPS, TPD-MS and Hammett indicator titration.

4.2.3 Biodiesel fuel properties

The properties of obtained biodiesel are mainly dependent on the FAME compositions. Therefore, off-line GC-MS was used to analyse the final product in order to quantify FAME content of synthesised biodiesel using $TiO_2/PrSO_3H$ solid acid catalyst. The FAME compositions for obtained biodiesel are listed in Table 4.5.

Table 4.5 FAME profiles for as-prepared biodiesel from UCO

Name		% FAME
Myristic acid methyl ester	$C_{14:0}$	0.07
Palmitic acid methyl ester	$C_{16:0}$	7.86
Palmitoleic acid methyl ester	$C_{16:1}$	0.01
Stearic acid methyl ester	$C_{18:0}$	3.08
Oleic acid methyl ester	$C_{18:1}$	56.19
Linoleic acid methyl ester	$C_{18:2}$	26.74
Linolenic acid methyl ester	$C_{18:3}$	3.30
Arachidic acid methyl ester	$C_{20:0}$	0.00
Gadoleic acid methyl ester	$C_{20:1}$	1.32
Eicosadienoic acid methyl ester	$C_{21:0}$	0.10
Behenic acid methyl ester	$C_{22:0}$	0.43
Erucic acid methyl ester	$C_{22:1}$	0.64
Lignoceric acid methyl ester	$C_{24:0}$	0.12
Nervonic acid methyl ester	$C_{24:1}$	0.14

It was found from Table 4.5 that the major FAMEs are palmitic acid methyl ester, stearic acid methyl ester, oleic acid methyl ester, linoleic acid methyl ester, linolenic acid methyl ester, and gadoleic acid methyl ester. The quality of final biodiesel fuel obtained under optimum reaction conditions are summarised in Table 4.6. The key fuel properties of obtained biodiesel fuel were evaluated and the results revealed that the quality of produced biodiesel from the current study fulfilled ASTM and EU standards for biodiesel fuel quality control.

The cloud point is the temperature at which a cloud or a few crystals form in a biodiesel fuel caused by the first stage of crystallisation on cooling of the fuel. It is one of the most important properties of biodiesel, which influences its use in cold environments because of the risk of fuel injector problems, poor fuel atomisation, incomplete combustion, and deposit formation. The DSC thermogram for as-synthesised biodiesel is shown in Figure 4.18. It can be seen from the cooling DSC curve (see Figure 4.19 a) that there is only one sharp endothermic peak centred at -11 °C with

enthalpy of 67.14 mJ corresponding to the formation of crystals in biodiesel fuel. The onset temperature of crystallisation on the cooling curve at -10.57 °C represents the cloud point temperature of prepared biodiesel. In heating DSC thermogram (see Figure 4.18 b), a board exothermic peak was observed between -28 °C and 0 °C assigned to the melting of the formed crystals.

Table 4.6 Properties of UCO and obtained biodiesel over $TiO_2/PrSO_3H$ catalyst

| Property | Unit | Limits | | UCO | Synthesised biodiesel |
		ASTM D6751	EN14214		
Flash point	°C	93 min	101 min	289	171
Kinematic viscosity	mm^2/s	1.9-6.0	3.5-5.0	32. 91	4.8
Acid number	mgKOH/g	0.8 max	0.5 max	4.04	0.41
FFA	mass%	---	---	2.034	0.21
Density at 15°C	Kg/m^3	---	860-900	921	898.1
FAME content	% mass	---	96.5 min	---	98.3
Water content	ppm	---	500 max	1400	--
Linolenic acid methyl ester	% mass	---	12 max	---	3.3
Free glycerine content	% mass	0.02 max	---	---	0.154
Total glycerine content	% mass	0.24 max	0.25 max	---	0.169
Monoglyceride content	% mass	---	0.8 max	---	0.035
Diglyceride content	% mass	---	0.2 max	---	0.0
Triglyceride content	% mass	---	0.2 max	---	0.0

Thermal oxidative behaviour plays a key role in the industrial application of the biodiesel fuel [522]. The TGA thermogram for prepared biodiesel with onset and endset temperatures are shown in Figure 4.19. The onset temperature (174 °C) represent the biodiesel sample starting to decompose whilst the endset temperature (252 °C) corresponds to the completely burnt off biodiesel sample. These results indicate that the synthesised biodiesel was thermally stable in atmosphere.
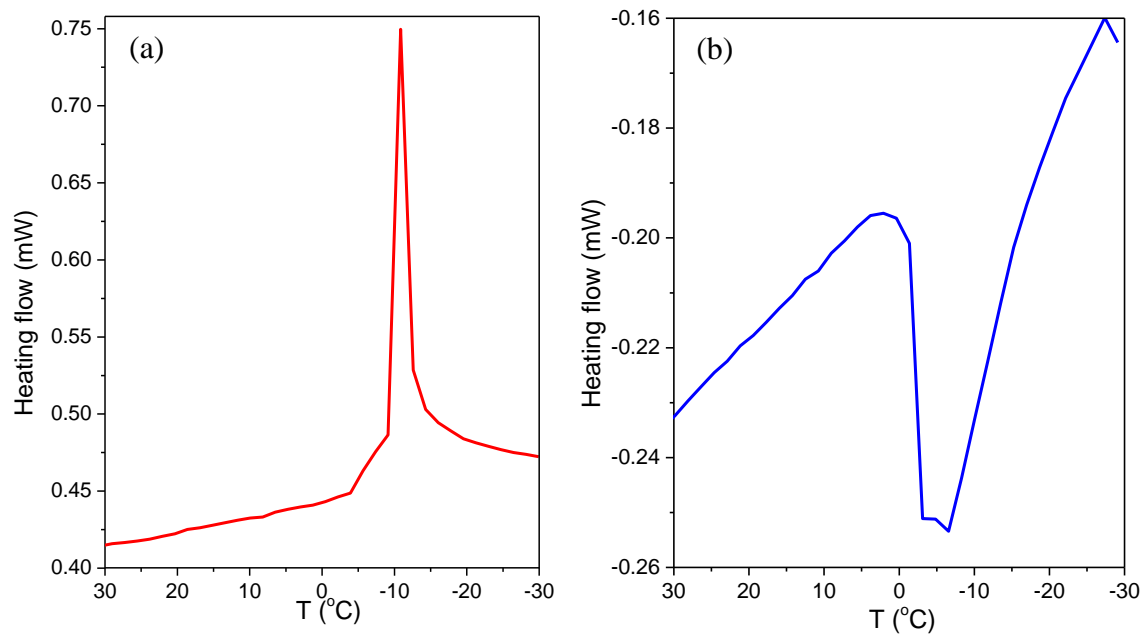
Figure 4.18 The DSC (a) cooling and (b) heating curves for obtained biodiesel
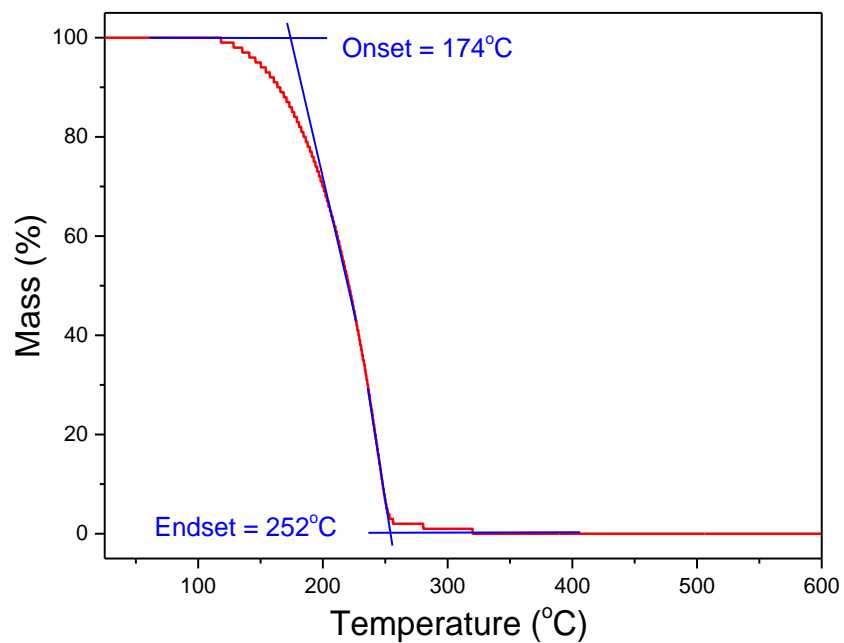
Figure 4.19 Typical TGA thermogram of obtained biodiesel in air

4.2.4 Discussion

A novel TiO$_2$/PrSO$_3$H catalyst was prepared through grafting of TiO$_2$ NPs with 1,3-propane sultone in dry toluene under reflux at 120°C for 72 h. The application of such material as a solid acid catalyst is reported for the first time for biodiesel production from UCO. The synthesised solid acid catalyst shows good catalytic activity for simultaneous esterification and transesterification of cheap feedstocks, probably due to the catalytic activity of such material according to its surface property (-SO$_3$H). It is important to mention that loading of higher density hydrophilic functional groups (-SO$_3$H) onto the surface of TiO$_2$ NPs may lead to an improvement in the hydrophilicity of TiO$_2$ NPs support and increase the accessibility of raw material (FFAs, triglycerides and methanol) in the simultaneous esterification and transesterification processes to the –SO$_3$H groups. Therefore, more investigations could be carried out in future to explore the effect of different TiO$_2$ phases (anatase, rutile and brookite) with different loadings of PrSO$_3$H species and the surface acidity/strength of TiO$_2$/PrSO$_3$H for catalytic performance. Such studies could fully utilize the potential of such catalyst on the FAME yield produced from simultaneous esterification and transesterification of UCO. The prepared solid acid catalyst was found to esterify FFA in cheap raw materials to FAME in parallel with transesterification of TG without formation of soaps. The catalyst was also found to be a non-hazardous material compared to conventional homogenous acids and it can be used in four consecutive (trans)esterification cycles with no appreciable loss in catalytic activity, which may satisfy the principle of green chemistry. Table 4.7 summarises the comparison of the results from optimised process conditions for biodiesel production from UCO/oleic acid using the solid acid catalyst in the present study with other reported solid acid catalysts in the literature. The synthesised TiO$_2$/PrSO$_3$H solid acid catalyst has found to be suitable for biodiesel production from cheap feedstock via low temperature esterification/transesterification. These results are the first demonstration of the UCO/oleic acid conversion via the use of TiO$_2$/PrSO$_3$H solid acid catalyst. Despite a low surface area compared to SBA-15-PrSO$_3$H (significantly high surface area=862 m^2/g) [523], TiO$_2$/PrSO$_3$H catalyst possesses high acid strength due to PrSO$_3$H and relative good hydrophilicity, which is making it effective in transesterification reaction.

Table 4.7 A mild process conditions for the production of biodiesel in the simultaneous esterification and transesterification from the current work compared to the some reported solid acid catalysts

	Current study	Melero et. al [80]	Fu et.al [346]	Feyzi et. al [524]
Oil/fat feedstock	UCO/Oleic acid	Crude palm oil	Rapeseed oil/Oleic acid	Sunflower oil
Methanol to oil ratio	15:1	20:1	10:1	12:1
Type of catalyst	$TiO_2/PrSO_3H$	$SBA-15-PrSO_3H$	β-Cyclodextrin-SO_3H	$CsH_3PW_{12}O_{40}/Fe-SiO_2$
Amount of catalyst, wt%	4.5	6	5.0	3
Agitation speed, RPM	600	Not reported	500	500
Time, h	9	4	12	4
Temperature, °C	60	140	60-85	60
FAME yield %	98.3	95	90.82	81
BET surface area, $m^2.g^{-1}$	38.59	666	38.2	237.5
Mean pore size Å	245.46	82	---	173.4
Average particle size, nm	23.1	Not reported	1000	38-42
Catalyst recycled number	4	2	6	Not reported

4.3 Conclusions

A novel, efficient and recyclable mesoporous $TiO_2/PrSO_3H$ solid acid catalyst with an average particle size of around 23.1 nm has been successfully synthesised as an inorganic–organic hybrid heterogeneous catalyst. This was achieved by the post-synthetic grafting of propyl sulfonic acid groups onto a mixed phase of a TiO_2 support for simultaneous esterification and transesterification of UCO containing FFA. The synthesised solid acid catalyst was characterised using FT-IR, SEM, TEM, XPS, N_2 adsorption–desorption isotherms, XRD, DSC, TGA, DRIFT-pyridine, n-propylamine TPD-MS and CHNS analysis. The percentage of loading for propyl sulfonic acid on the TiO_2 support was calculated using CHNS analysis and TGA. STEM EELs-maps shows that the $PrSO_3H$ groups decorate the surface of TiO_2 NPs layer-by-layer. The N_2 adsorption-desorption isotherms result demonstrated that surface modification reduced the surface area of TiO_2 NPs by 5% with an increase in the mean pore size and total pore volume. The XPS confirmed that the $PrSO_3H$ functional groups attached to the surface of TiO_2 NPs. The catalytic performance of $TiO_2/PrSO_3H$ on the production of the FAME (biodiesel fuel) via simultaneous esterification and transesterification reactions of UCO has been studied. The effects of different process parameters on the FAME yield showed that 98.3% of FAME can be obtained after 9 h of reaction time with 1:15 molar ratio of oil to methanol, 60 °C reaction temperature and 4.5 wt% of a catalyst loading. $TiO_2/PrSO_3H$ catalyst performance showed promising results for catalytic simultaneous esterification and transesterification of cheap raw materials for biodiesel production. The enhanced catalytic performance mainly relates to the loading of propyl sulfonic acid groups on the surface of TiO_2 NPs which increased the proportion of Brønsted acid sites, according to the DRIFT analysis. It was also found that the one-pot post-surface functionalisation strategy with hydrophilic functional groups (-SO_3H) enhanced the acid strengths of the catalyst providing more acid sites for the reactants, and improved the accessibility of methanol to the triglycerides (TG)/free fatty acids (FFAs) by increasing the pore volume/size of the catalyst. The solid acid catalyst was re-used in four consecutive runs without significant loss of catalytic efficiency. Finally, the synthesised biodiesel fuel satisfied ASTM and EN standards.

Chapter 5

Ti(SO$_4$)O catalyst

5.1 Introduction

5.2 Results and discussion

    5.2.1 Catalyst characterisations

        5.2.1.1 Crystal structure

        5.2.1.2 Surface analysis

            5.2.1.2.1 FT-IR spectroscopy

            5.2.1.2.2 XPS

            5.2.1.2.3 N$_2$ porosimetry

            5.2.1.2.4 Electron microscopy

        5.2.1.3 Thermal stability

        5.2.1.4 Surface acidity

    5.2.2 Catalytic performance

        5.2.2.1 Catalytic activity and its reusability

        5.2.2.2 Regeneration of spent catalyst

    5.2.3 Biodiesel characterisations

    5.2.4 Discussion

5.3 Conclusions

An introduction to sulphated metal oxide solid acid catalysts is presented. The effect of sulphated incorporation into the structure of TiO$_2$ NPs is covered with regard to biodiesel production from UCO. The catalytic activity of fresh, re-used and regenerated Ti(SO$_4$)O is discussed along with the physicochemical properties of produced biodiesel.

CHAPTER FIVE

5. Synthesis, characterisation and application of Ti(SO₄)O catalyst

5.1 Introduction

As discussed in previous chapters (Chapter Two and Chapter Four), solid super acid catalysts are desirable for the production of biodiesel from feedstocks containing FFA, notably UCO, amongst which sulphated metal oxides have been reported with better activities for simultaneous esterification and transesterification reactions. However, the major drawback with the sulphated metal oxide catalysts could be (i) relatively high temperature requirements, (ii) low yield, (iii) long reaction time and (iv) catalyst stability and reusability [525]. The latter could be due to the fact that, in the majority of cases, the sulphate group is placed on the surface of the catalysts (surface functionalisation), making the catalyst prone to deactivation. This chapter describes a novel method of preparing titanium sulphate oxide or titanium oxysulphate [Ti(SO₄)O] solid super acidic catalyst, where the sulphate group is chemically bonded within the structure of the catalyst with potential high stability and reusability. Characterisation and application of the developed solid super acidic catalyst for biodiesel production via simultaneous esterification and transesterification of used cooking oil (UCO) are investigated. This is prompted because there is no reported work and/or information available on the catalysts of titanium sulphate oxide Ti(SO₄)O for biodiesel production. The chemical structure, catalytic stability, morphology, particle sizes and surface area for the catalyst are determined using XRD, FT-IR spectroscopy, XPS, N_2 adsorption-desorption isotherms, SEM, TEM, and TGA/FT-IR. The effect of catalyst loading, time and temperature of reaction, methanol to UCO ratio and level of FFA in the feedstock on the biodiesel yield as well as the catalyst activity and stability during the esterification/transesterification are investigated. Additionally, the obtained biodiesel from the catalytic transesterification processes is analysed in accordance to ASTM and EN standard methods to determine characteristic fuel properties.

5.2 Results and discussion

5.2.1 Catalyst characterization

TiO_2 NPs reacts with chlorosulfonic acid (HSO_3Cl) at room temperature producing $Ti(SO_4)O$ solid super acidic catalyst (main product) and hydrochloric acid gas (by-product) as shown in Figure 5.1. At high temperature (~120 °C), chlorosulfonic acid slowly generates sulphur trioxide (SO_3) and hydrochloric acid gas [526]. The by-product (HCl) gas liberated from this reaction is corrosive, but in industry it is normally recovered either by neutralizing the off-gas with a very low concentration of sodium hydroxide as a basic scrubbing solution to produce sodium chloride salt or by diluting with water [527]. The sulphur trioxide is a very aggressive electrophilic reagent that rapidly reacts with TiO_2 NPs to form TiO_2/sulfonic acid [528]. In the presence of a reflux condenser for 2 h, the formed TiO_2/sulfonic acid is slowly converted into the sulphated titanium oxide or oxysulfate titania [$Ti(SO_4)O$].
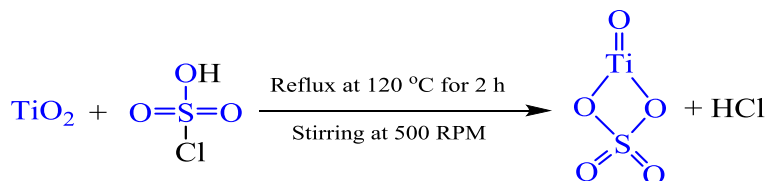
Figure 5.1 Proposed scheme showing the preparation of $Ti(SO_4)O$ solid acid catalyst

5.2.1.1 Crystal structure

The XRD patterns of base TiO_2 NPs indexed using JCPDS-ICDD confirmed 81.6% of tetragonal anatase phase (04-014-5762, TiO_2) and 18.4% of tetragonal rutile phase (01-072-4815, TiO_2). The major diffraction peaks of nano-sized TiO_2 were observed at 2θ values of 25.30°, 36.95°, 37.80°, 38.56°, 48.03°, 53.89°, 55.06°, 62.11°, 62.69° and 68.76° assigned to the [101], [103], [004], [112], [200], [105], [211], [213], [204] and [116] reflections for the anatase structure of TiO_2, respectively. The rest of the diffraction peaks were observed at 2θ values of 27.43°, 36.07°, 39.18°, 41.23°, 44.04°, 54.31°, 56.62°, 62.75°, 64.04°, 65.50° and 68.99° corresponded to the [110], [101], [200], [111], [210], [211], [220], [002], [310], [221], [301] and [112] planes for the rutile structure of TiO_2, respectively, as shown in Figure 5.2. In the case of the synthesised $Ti(SO_4)O$ catalyst, the XRD patterns indexed using JCPDS-ICDD in Figure 5.2 confirm that all diffraction peaks matched with titanium sulphate oxide or titanium oxysulfate [$Ti(SO_4)O$, 04-011-4951]. The main

diffraction peaks of Ti(SO$_4$)O were observed at 2θ values of 16.18°, 21.31°, 22.10°, 23.57°, 27.53°, and 28.13° assigned to the [200], [201], [011], [111], [211] and [301] reflections for the Ti(SO$_4$)O, respectively. It should be also noted that most of the diffraction peaks were sharp peaks indicating the high crystallinity degree of the Ti(SO$_4$)O catalyst sample. However, there are some broad peaks with low intensities at 36.80°, 45.43°, 51.89°, etc., presumably due to the amorphous degree, which could be explained by the presence of sulphate group directly bonded with the crystal structure TiO$_2$ catalyst support (see Figure 5.1). The average particle sizes of TiO$_2$ and Ti(SO$_4$)O catalysts were calculated as 28 nm and 45 nm, respectively, using Debye-Scherrer's equation.
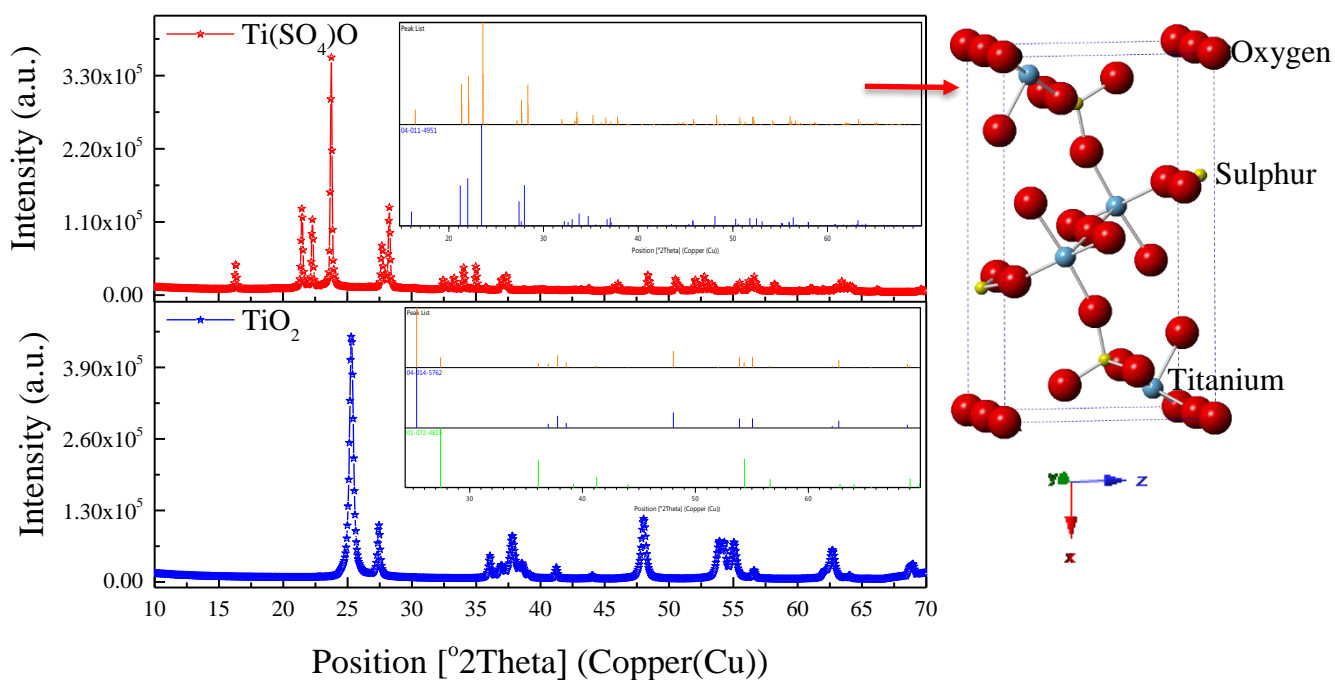
Figure 5.2 Powder D8 XRD patterns for TiO$_2$ and Ti(SO$_4$)O catalyst samples at room temperature.

5.2.1.2 Surface analysis

5.2.1.2.1 FT-IR spectroscopy

The FT-IR spectrum of the prepared Ti(SO$_4$)O solid acid catalyst shows five more band vibrations than the spectrum of TiO$_2$ NPs, suggesting sulphate group's incorporation into the structure of the TiO$_2$ molecules as shown in Figure 5.3. The sharp band in Ti(SO$_4$)O at 626.4 cm^{-1} and the broad band in TiO$_2$ at 553 cm^{-1} were assigned to the vibration stretching of Ti-O [529, 530]. Moreover,

three extra strong bands at 786.9, 915 and 1044.7 cm^{-1} in Ti(SO$_4$)O catalyst spectrum corresponded to S-O stretching vibrations in bidentate sulphate coordinated to the Ti^{4+} metal [92, 531-533]. The strong band at 1216.9 cm^{-1} referred to S=O asymmetric stretching vibration whilst the other strong band at 1132.9 cm^{-1} attributed to the S=O symmetric stretching vibration. The band at 1690.1 cm^{-1} in Ti(SO$_4$)O and at 1637.8 cm^{-1} in TiO$_2$ catalyst correspond to H-O-H symmetric vibration of absorbed water molecules on the surface of both catalysts [499, 534]. The vibration bands at 2360.8 cm^{-1} and 2352.5 cm^{-1} in TiO$_2$ and Ti(SO$_4$)O catalysts spectra, respectively, could correspond to asymmetric stretching of CO$_2$ molecules in the air, contaminating the surface of both catalysts after samples were exposed to air during the analysis [535]. The broad bands at 3045 to 3400 cm^{-1} in both catalysts were assigned to the stretching vibration of O-H functional groups from water molecules absorbed on the surface of catalysts after samples were exposed to air during the analysis [499, 534].
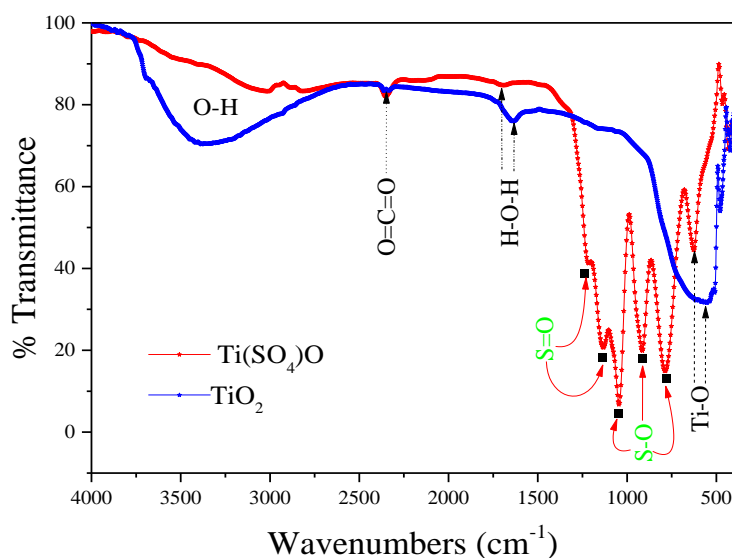
Figure 5.3 The FT-IR spectra of TiO$_2$ and synthesised Ti(SO$_4$)O catalyst samples at ambient temperature. The black dots indicate the extra absorption bands for S=O and S-O in the synthesised catalyst.

5.2.1.2.2 XPS

Figure 5.4 shows the XPS spectrum survey scan for TiO$_2$ and Ti(SO$_4$)O catalysts. In the case of TiO$_2$ NPs, the catalyst contains not only Ti (464 eV) and O (530 eV) elements but also some carbon observed at 285 eV, presumably due to the CO$_2$ contamination on the surface. The same observation was found from the FT-IR analysis. In the case of synthesised Ti(SO$_4$)O catalyst, four

significant peaks were observed at 167, 285, 457.35, and 529.95 eV, corresponding to S 2p, C 1s, Ti 2p and O 1s, respectively. The band at 167 eV is a clear evidence of sulphate group in the synthesised catalyst [Ti(SO$_4$)O].
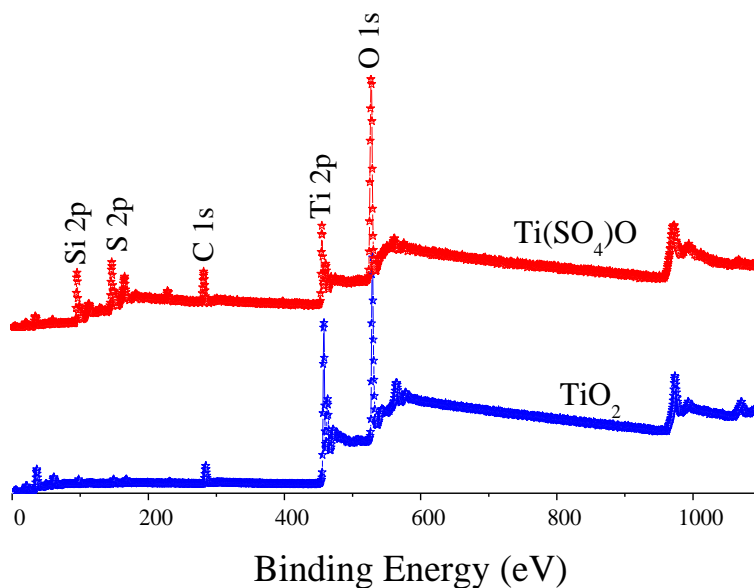
Figure 5.4 XPS survey scan of TiO$_2$ and Ti(SO$_4$)O catalyst samples. In the case of

Ti(SO$_4$)O showing an extra peak for the chemical environment at 167 eV for S 2p on the surface. The deconvoluted of O 1s spectra for Ti(SO$_4$)O catalyst was resulted in two Gaussian components as shown in Figure 5.5 (a). A broad peak located at 530.76 eV corresponds to the lattice oxygen in Ti=O and S=O, this could be due to the binding energy of the de-convoluted O 1s peaks for Ti=O and S=O falling in the same region which made it difficult to distinguish between the contribution of both species [505]. The band detected at 531.72 eV correlated to the two different oxygen species, which must be due to the presence of Ti-O and S-O bonds. Moreover, the binding energy of the Ti 2p$_{3/2}$ in Ti(SO$_4$)O, as can be seen in Figure 5.5 (b), was shifted by 2.01 eV compared to the binding energy of the Ti 2p$_{3/2}$ in TiO$_2$ [see Figure 5.5 (d)]. Furthermore, the Ti 2p$_{1/2}$ peak in Ti(SO$_4$)O located at 458.7 eV could be ascribed to Ti^{4+} oxidation state [190, 536]. The binding energy of S 2p was observed at 167 eV [see Figure 5.5 (c)], which agrees with the reported earlier values for S-O bonds in sulphate groups [190, 537-539]. This elucidates that one of the oxygen atoms in the TiO$_2$ catalyst was replaced by sulphate group as in the synthesised Ti(SO$_4$)O solid acid catalyst. The detailed high resolution XPS analysis for TiO$_2$ NPs is demonstrated in Chapter four.
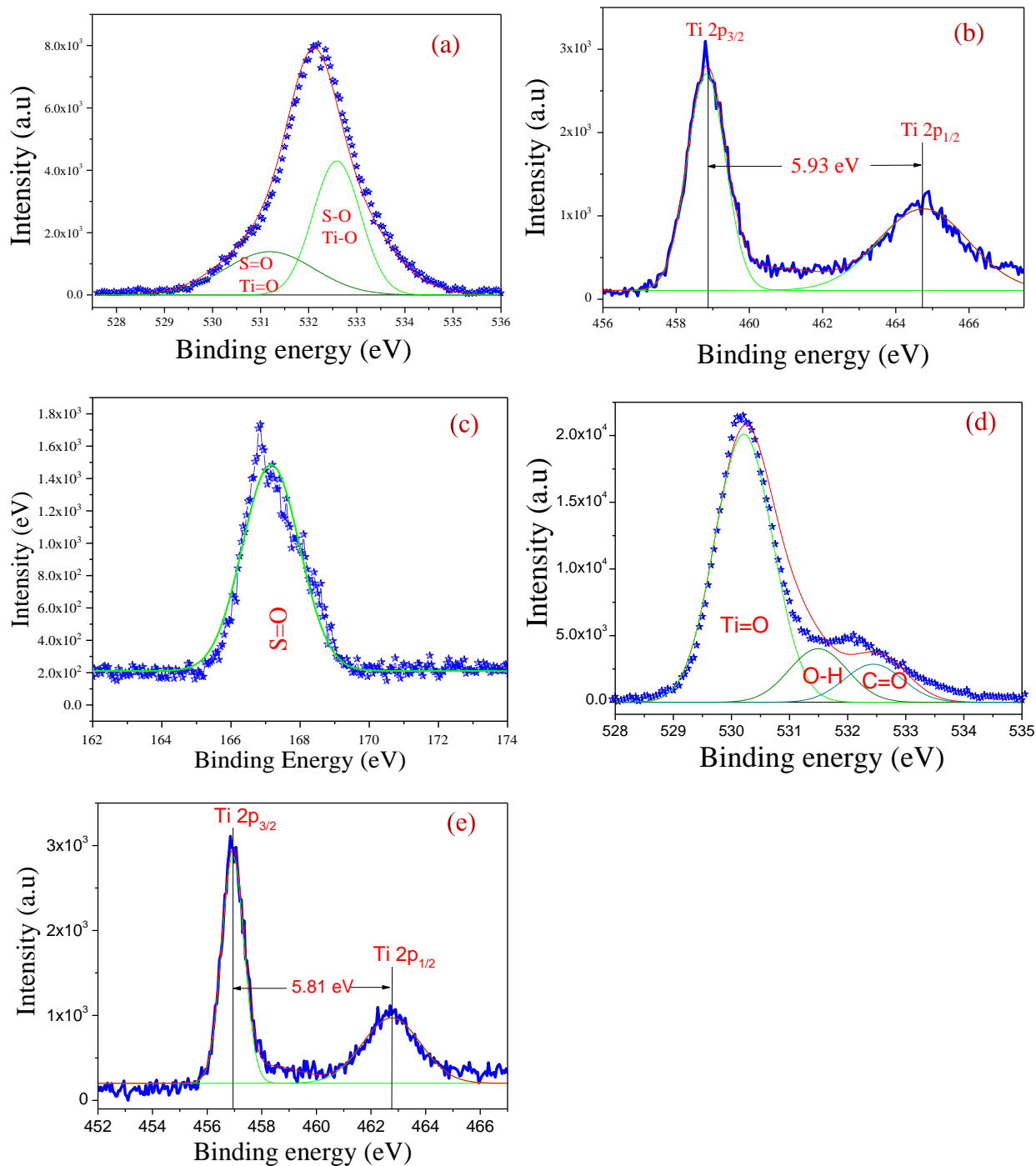
Figure 5.5 High resolution XPS showing the de-convolution of (a) O 1s, (b) Ti 2p and (c) S 2p peaks for Ti(SO₄)O while (d) and (e) the XPS for TiO₂ illustrating the chemical environments of O 1s and Ti 2p, respectively

The comparison of the elemental compositions using TEM-EDS analysis and relative surface elemental composition using XPS analysis for TiO₂ and Ti(SO₄)O catalyst samples are presented

in Table 5.1. The atomic ratio of O/Ti in TiO_2 NPs measured by TEM-EDS was 1.55:1 (see Figure 5.11) whilst this ratio was 2.35:1 by XPS. This could be due to the surface of the catalyst being contaminated with CO_2 and H_2O in air which is confirmed by FT-IR and presence of sp^2 hybridized carbon in XPS survey scan spectrum at 285 eV. The ratio of S/Ti and O/Ti in $Ti(SO_4)O$ catalyst have also been calculated from TEM-EDS and XPS analyses. According to both analyses, the atomic ratio of S/Ti was around 1:1 and for O/Ti was 5:1. Based on this result, it can be concluded that there was only one oxygen in TiO_2 replaced by sulphate group. This result is consistent with XRD analysis of $Ti(SO_4)O$.

Table 5.1 Compared atomic ratios for TiO_2 and $Ti(SO_4)O$ catalysts using XPS and TEM-EDS analyses

	Bulk atomic ratio % determined by TEM-EDS analysis		Surface atomic ratio% determined by XPS analysis	
	O:Ti	S:Ti	O:Ti	S:Ti
TiO_2	1.55:1	---	2.35:1	---
$Ti(SO_4)O$	4.45:1	0.74:1	4.8:1	1.0:1

5.2.1.2.3 N$_2$ porosimetry

In general, surface area plays a key role in effectively enhancing the activity of solid acid catalysts for esterification and transesterification processes as large surface area facilitates the reactant molecules' access to the acid sites on the solid catalyst surface. The nitrogen adsorption isotherms were used to calculate the BET surface area for both samples whilst desorption isotherms were used to calculate the average pore size and total pore volume for both samples using the BJH method. The detailed BET, average pore size and total pore volume of TiO_2 and $Ti(SO_4)O$ catalyst samples are summarised in Table 5.2. Based on these results, the loading of sulphate groups on TiO_2 has resulted in relatively no change or a bit lower BET surface area as compared to the TiO_2; this may be explained by the aggregation of the very small crystallites in synthesized catalyst with their low ordering and crystallinity [see Figure 5.7]. It was also found that the average pore size and total pore volume of $Ti(SO_4)O$ catalyst duplicated compared to TiO_2 NPs due to the macrospore voids between particles. This might be due to the effect of sulphate groups which are

incorporated into the TiO_2 structure and could perhaps account for the increase in the concentration of the structural disorder and reduction of surface area in the prepared catalyst.

Table 5.2 Summary of the properties of TiO_2 and $Ti(SO_4)O$ catalysts

Type of catalyst	BET surface area (m²/g)	BJH mean pore size (nm)	BJH total pore volume (cm³/g)
TiO_2	49	12.9	0.16
$Ti(SO_4)O$	45	22.7	0.31

The nitrogen absorption-desorption isotherms of TiO_2 and $Ti(SO_4)O$ catalysts could be classified as type IV with one hysteresis loops at a relative pressure range of 0.75-1.0 as depicted in Figure 5.6. The experimental results clearly confirmed that both samples are mesoporous (see inset from Figure 5.6) with the type of hysteresis loop H1 according to IUPAC classification witnessed for uniform pore sizes due to differences in absorption and desorption [424]. In the case of $Ti(SO_4)O$, nevertheless, the pore size distribution is inhomogeneous compared to TiO_2 NPs sample, which is more preferable for minimising diffusion limitations for long alkyl chain hydrocarbons in FFA/triglyceride (TG) [304, 390].
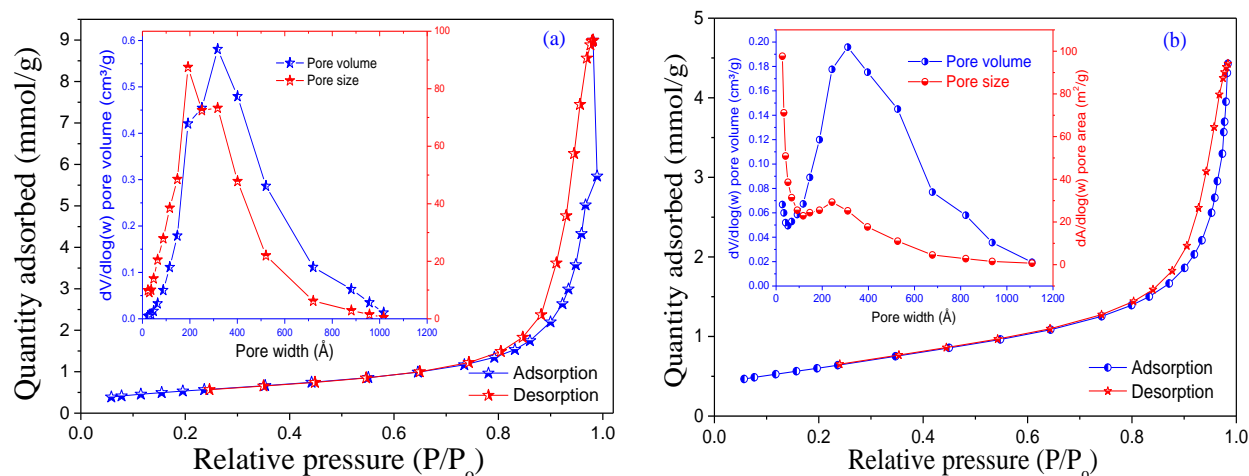
Figure 5.6 N_2 adsorption-desorption isotherms and total pore volumes with mean pore sizes (inset) for (a) synthesised $Ti(SO_4)O$ catalyst and (b) TiO_2 NPs

5.2.1.2.4 Electron microscopy

Figure 5.7 (a) and (b) shows the SEM images of TiO_2 and $Ti(SO_4)O$ samples, respectively, at 10, 50, 100 and 250 K magnifications. It can be seen clearly that the particle size and morphological
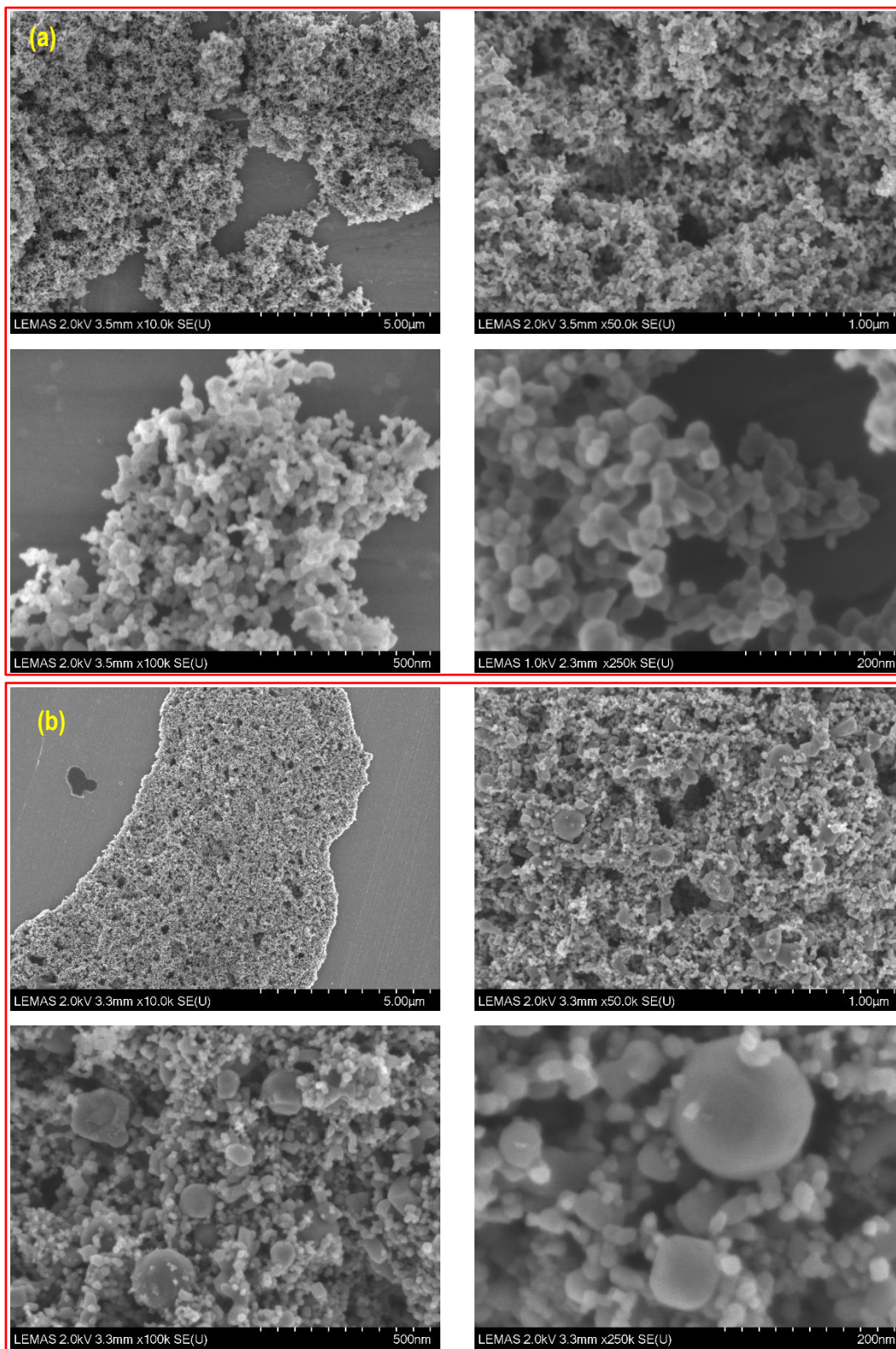
Figure 5.7 SEM micrograph images of (a) TiO_2 and (b) $Ti(SO_4)O$ catalyst samples, in case of $Ti(SO_4)O$ showing the presence of different size of particles.

features of the synthesised Ti(SO₄)O catalyst have changed compared to the TiO_2 NPs. Figure 5.7 (a) shows TiO_2 NPs have relatively uniform size particles with some agglomerates, whereas titanium sulphate oxide [Ti(SO₄)O] catalyst [see Figure 5.7 (b)] has visible signs of particle growth (enlarging the particle sizes) and shape change. This is mainly due to impregnation of sulphate species into TiO_2 structures. HR-TEM clearly confirmed the actual size of the particles, crystallographic phases and morphologies as depicted in Figure 5.8 (a) and (b) for TiO_2 and Ti(SO₄)O catalyst samples, respectively. It can be observed that the Ti(SO₄)O particles aggregate to each other forming a network, possibly due to the electrostatic attraction among SO_4^{2-} species. The number based particle size distributions of TiO_2 and Ti(SO₄)O catalysts are presented as histograms in Figure 5.8.
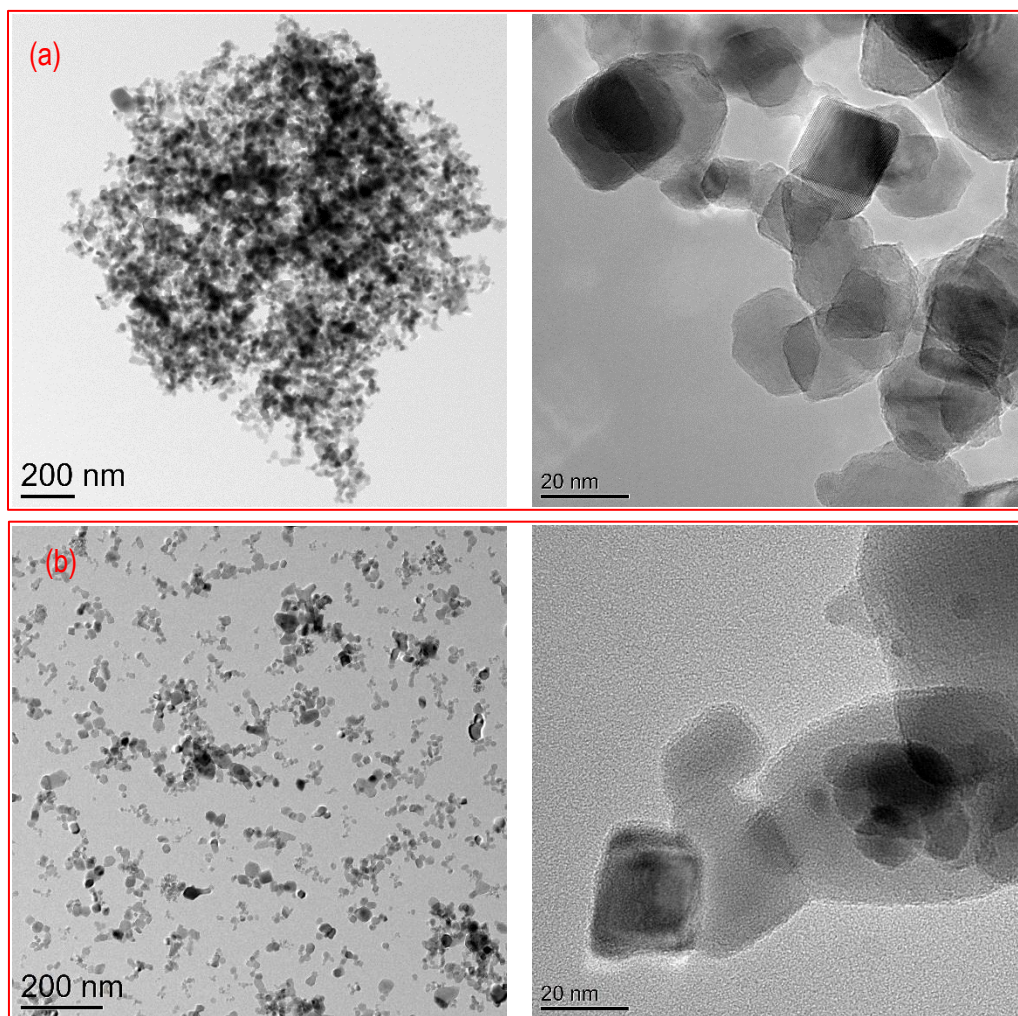
Figure 5.8 TEM images of (a) TiO_2 showing uniform size of particles having irregular morphology and (b) Ti(SO₄)O showing the presence of large particles with very fine particles.
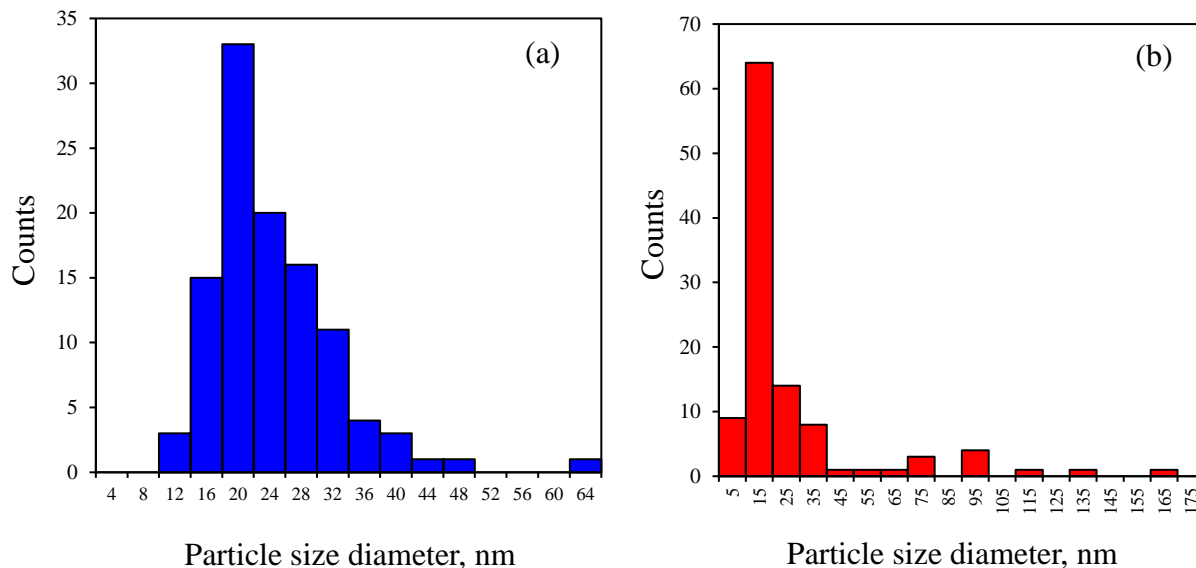
Figure 5.9 Histogram illustrating particle size distributions of TiO_2 (a) and $Ti(SO_4)O$ (b)

The synthesised $Ti(SO_4)O$ catalyst were non-uniformly distributed and with an average particle size diameter of ~25 nm (as per 108 particles in different TEM images). In contrast, the particles of TiO_2 NPs were less scattered with an average particle size diameter of ~22.34 nm, which is in agreement with data from the supplier. It is also noticeable from TEM images that most TiO_2 NPs have tetragonal morphologies.

TEM image confirms polycrystalline TiO_2 particles as depicted in Figure 5.10 (a). The visible lattice fringes with interplanar spacing of 3.518 Å correspond to [101] lattice planes of TiO_2 NPs in anatase phase, according to JCPDS-ICDD file 04-014-5762. The HR-TEM image proves that prepared $Ti(SO_4)O$ catalyst contains a small fraction of polymorphous as shown in Figure 5.10 inset (c). It was also found that these results are in agreement with XRD result for $Ti(SO_4)O$ catalyst (see Figure 5.2). The lattice fringes with interplanar spacing of 3.078 Å correspond to (301) lattice planes of $Ti(SO_4)O$ according to JCPDS-ICDD 04-011-4951. The SAED pattern of the TiO_2 NPs sample showing a set of diffused spot rings corresponding to poly-crystallinities, as shown in Figure 5.10 (b), whilst the SAED pattern of $Ti(SO_4)O$ catalyst shows brightness and spotty rings are shown in Figure 5.10 (d) assigned to the present of single to poly-crystallinities with a fraction of amorphous in the synthesised catalyst. The presence of amorphous fraction in synthesised $Ti(SO_4)O$ catalyst related to the incorporated sulphate groups into the structure of TiO_2 NPs. The details of studies of the *d*-spacing values calculated from SAED spotty rings with the

reported *d*-spacing values for TiO_2 and $Ti(SO_4)O$ in the JCPDS-ICDD card numbers 04-014-5762 (Anatase, TiO_2), 01-072-4815 (Rutile, TiO_2) and 04-011-4951 ($Ti(SO_4)O$) are presented in Table 5.3. It is noteworthy that the results of ICDD agree with *d*-spacing values obtained from XRD and SAED in this investigation. These results further confirm the successful synthesis of $Ti(SO_4)O$ catalyst using TiO_2 NPs and chlorosulfonic acid as a reagent.
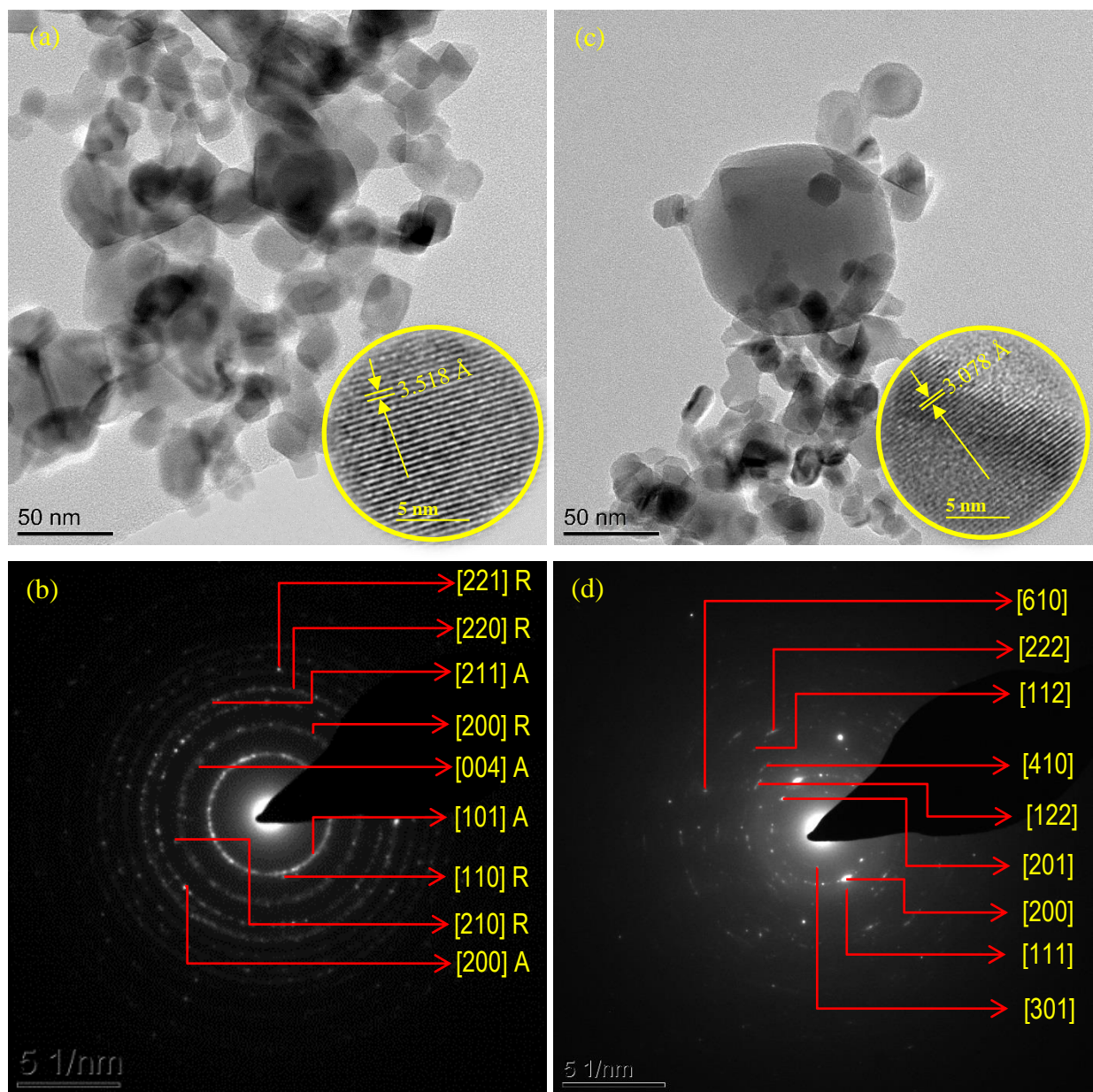
Figure 5.10 TEM images with high resolution inset for (a) TiO_2 NPs confirmed the [101] lattice planes and (c) synthesised $Ti(SO_4)O$ catalyst confirmed the [301] lattice planes; whilst images of (b and d) illustrate the SAED patterns for TiO_2 and $Ti(SO_4)O$, respectively.

Table 5.3 Comparison of *d*-spacing values from this experiment with the reported d-spacing values given in the JCPDS- ICDD reference cards

d-Spacing, Å	hkl	101	103	004	112	200	105	211	213	204
	JCPDS-ICDD	3.5165	2.4305	2.3781	2.3323	1.8923	1.6998	1.6664	1.4931	1.4807
TiO$_2$, Anatase	XRD	3.5168	2.4306	2.3780	2.3324	1.8925	1.6998	1.6665	1.4932	1.4808
	SAED	3.5476	---	2.3754	---	1.8240	---	1.6612	---	---
d-Spacing, Å	hkl	110	101	200	111	210	211	220	002	310
	JCPDS-ICDD	3.2488	2.4862	2.2972	2.1866	2.0547	1.6873	1.6244	1.4782	1.4529
TiO$_2$, Rutile	XRD	3.2485	2.4876	2.2970	2.1875	2.0545	1.6876	1.6242	1.4795	1.4528
	SAED	3.1815	---	2.2870	---	2.0997	---	1.6185	---	---
d-Spacing, Å	hkl	200	201	111	301	112	410	122	222	611
	JCPDS-ICDD	5.4743	4.1669	3.7716	3.1735	2.6447	2.4170	1.9758	1.8859	1.6616
Ti(SO$_4$)O	XRD	5.4751	4.1673	3.7714	3.1738	2.6447	2.4172	1.9757	1.8858	1.6618
	SAED	5.4795	4.1639	3.7738	3.1672	2.6317	2.4175	1.9639	1.8934	1.6656

TEM-EDS analysis of prepared Ti(SO$_4$)O catalyst showed an extra strong peak on the EDS graph at 2.15 keV, corresponding to the sulphur element. In both TEM-EDS graphs, extra peaks of C and Cu were observed due to the carbon-coated copper TEM grids used during analysis of the samples as shown in Figure 5.11.
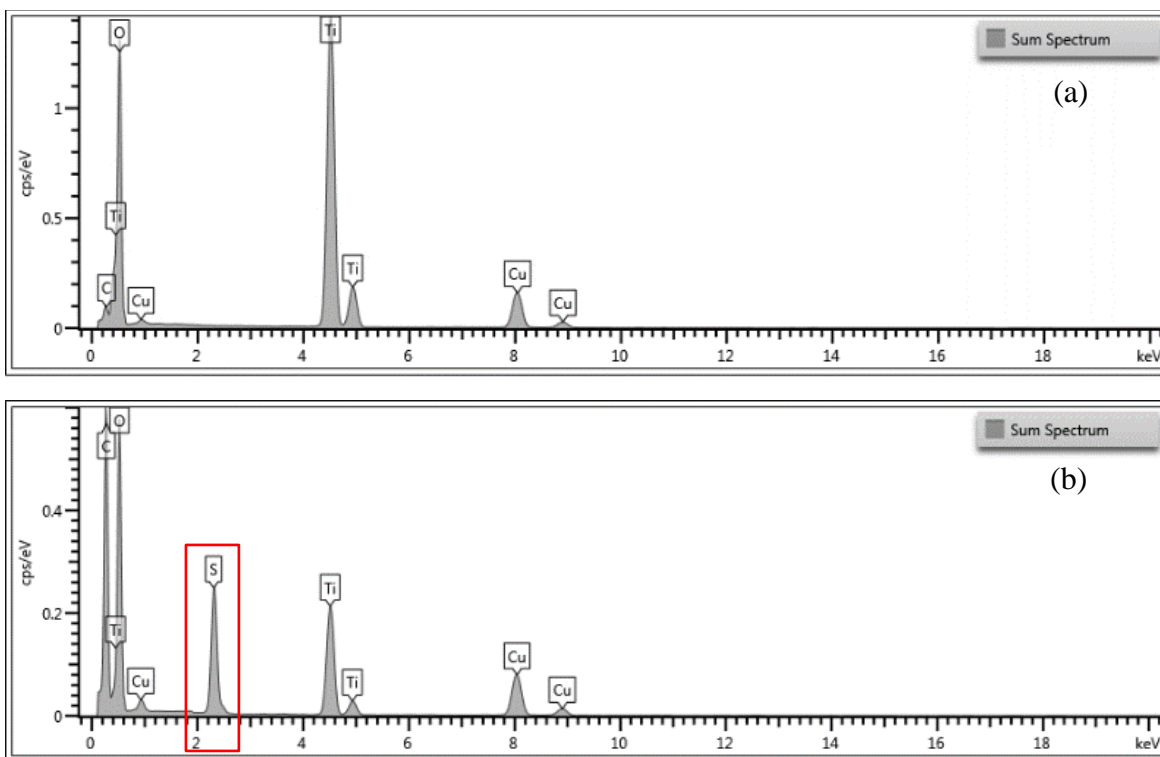
Figure 5.11 TEM-EDS for (a) TiO$_2$ NPs and (b) Ti(SO$_4$)O catalyst

Furthermore, the ratio of the intensities of titanium signal to sulphur signal was around 1:1 wt% at several different whole captured areas in TEM images for the synthesised Ti(SO₄)O. The presence of a large amount of sulphur spread over the entire area of the particles in the synthesised catalyst has been further verified by TEM EDS-mapping analysis (see Figure 5.12 b). These findings provide direct evidence that sulphur, titanium and oxygen are the main elements present in the prepared catalyst. Meanwhile, titanium and oxygen are the only elements present in the initial TiO_2 NPs, except Cu and C from TEM grids (see Figure 5.12 a).
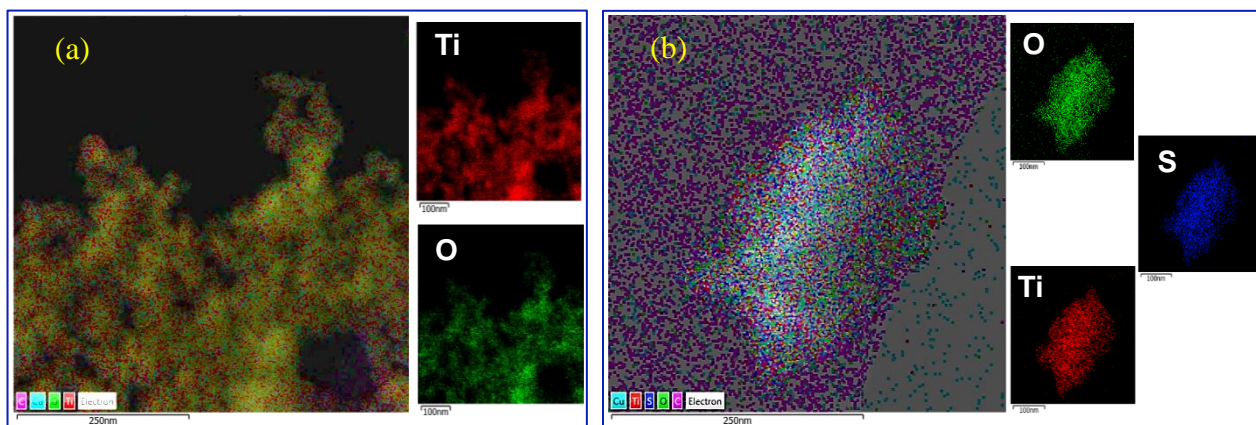
Figure 5.12 EDS-mapping for (a) TiO_2 NPs and (b) $Ti(SO_4)O$ catalyst

5.2.1.3 Thermal/oxidation stability

TGA was carried out to identify the thermal and oxidation stability of the catalyst samples during heating from 25°C to 900°C. Figure 5.13 reveals the stability of $Ti(SO_4)O$ and TiO_2 samples in nitrogen (thermal) and air (oxidative). The TGA curve of $Ti(SO_4)O$ displayed a small weight loss at 50°C to 200°C, indicating the desorption of water molecules from the surface of the catalyst (see Figure 5.13 a). One can see that the $Ti(SO_4)O$ sample has an almost negligible weight loss up to 600°C heating in both air and N_2 purge gases. These results clearly indicate that the sulphate groups are fairly stable in the structure of the prepared catalyst. The results also showed significant weight loss (about 47%) at 600°C to 800°C. In contrast, there is no further mass loss up to 900°C. This significant weight loss was due to the degradation of sulphate groups linked to the Ti atom in the $Ti(SO_4)O$ catalyst and formation of stable anatase TiO_2 [294], as can be described by the following equations:

$$Ti(SO_4)O(s) \xrightarrow{\Delta} TiO_2(s) + SO_3(g) \xrightarrow{\Delta} TiO_2(s) + SO_2(g) + \tfrac{1}{2} O_2(g)$$

174
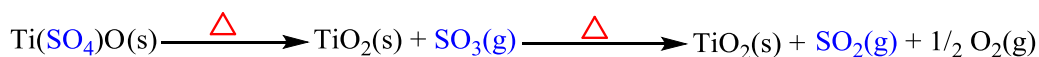
In order to confirm this, the XRD carried out at 600 °C for the Ti(SO₄)O. The diffraction peaks were observed at 2θ values of 25.74°, 37.34°, 38.10°, 38.91°, 48.37°, 54.11°, 55.48°, 62.97° and 68.85° assigned to the [101], [004], [not reported], [112], [200], [105], [211], [204] and [116] were reflected to the anatase phase of tetragonal TiO_2 (PDF-ICDD: 00-002-0406) as shown in Figure 5.14. The inset in Figure 5.14 shows the corresponding morphology and particle size for the formed anatase TiO_2 NPs from the decomposition of Ti(SO₄)O catalyst at 600 °C. On the other hand, the mass loss of the unmodified TiO_2 NPs (see Figure 5.13 b) shows that there was only one stage of weight loss from 25 to ~200°C, due to the desorption of H_2O molecules from the surface of TiO_2 nano-particles, evidence of which was observed also in absorption peaks in FT-IR spectrum at 1690.1 cm⁻¹ and 3400 cm⁻¹ (see Figure 5.3). It can be noticed also that the stability of the catalysts in nitrogen as a purge gas (inert) and air as a purge gas (oxidiser) show similar behaviour.
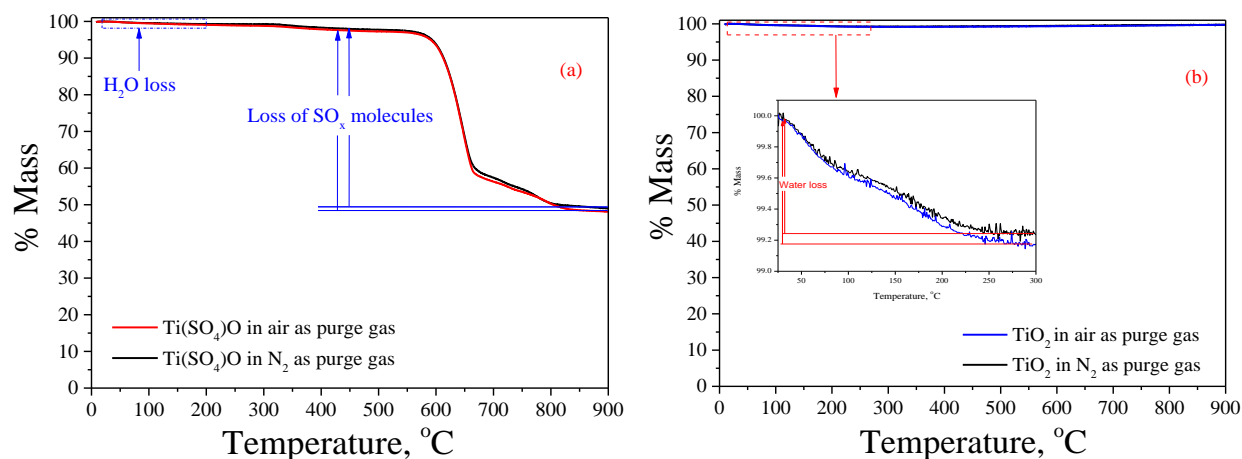
Figure 5.13 TGA profiles of (a) Ti(SO₄)O and (b) TiO_2 samples.

The 2D representation of output FT-IR spectra for evolved gases from the TGA-FTIR analysis for Ti(SO₄)O are presented in Figure 5.15. It can be observed that the main evolved gases have been identified as SO_2-loose, CO_2-loose, and H_2O-loose through spectral interpretation and comparison with database reference spectra for pure SO_2 and CO_2. In Grand-Schmidt thermographs for Ti(SO₄)O catalyst, four regions with intense peaks are observed which are: (i) bands between (3800-3900 cm⁻¹) and (1500-1700 cm⁻¹) due to O-H vibration bands from H-O-H molecule that is always present when the sample is sensitive to moisture; (ii) peaks between (3580-3780 cm⁻¹) and at (2250-2400 cm⁻¹) as well as at around (600-720 cm⁻¹) are related to O=C=O vibration bands

175

contaminated CO_2 from atmosphere; (iii) bands between at region (1080-1400 cm^{-1}) and (2460-2052 cm^{-1}) due to O=S=O vibration bands from decomposition of the catalyst; and (iv) peaks showed at low wavenumber (400-580 cm^{-1}) attributed to an intermolecular bond bending vibrations which are usually not taken into account.
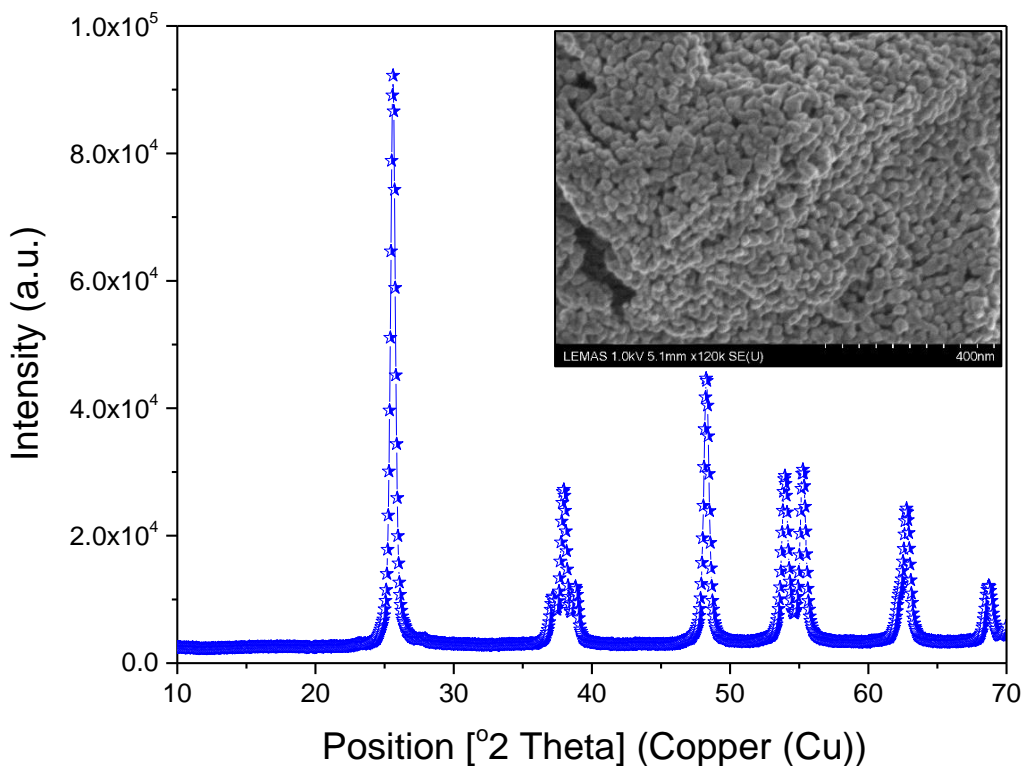
Figure 5.14 Powder XRD pattern recorded at 600 °C for Ti(SO$_4$)O catalyst

It should also be noted that there was no hydrogen sulfide gas detected during the pyrolysis of this catalyst, confirming that there was no sulfonic acid attached on the surface of TiO_2 NPs. In the case of TiO_2 NPs, there were only CO_2 and H_2O species released at various time periods. The amount of CO_2 and SO_2 evolved species versus time of TiO_2 and Ti(SO$_4$)O catalysts in air and N_2 as purge gases during pyrolysis are shown in Figure 5.16 (a & b). In both samples, the wavenumber ranges of (2150 to 2400 cm^{-1}) and (1250 to 1400 cm^{-1}) were chosen to process the chemigram profiles of CO_2 gaseous and SO_2 gaseous in both catalysts, respectively. The analysis of CO_2 chemigram profiles showed that negligible amounts of CO_2 gases are released from the pyrolysis of both catalysts; whereas, the surface of Ti(SO$_4$)O catalyst were seen to possess a higher value of contaminated CO_2 gases as compared to the surface of TiO_2 NPs, (see Figure 5.16 a).
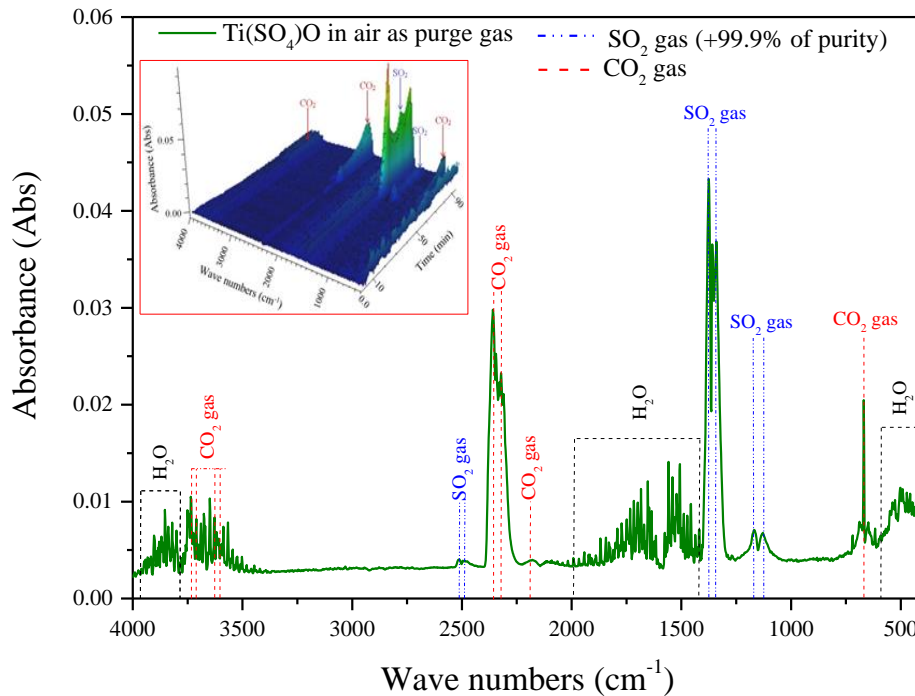
Figure 5.15 Two dimensional representation of FT-IR spectra for evolved gaseous from

the thermal decomposition of Ti(SO$_4$)O catalyst.

Meanwhile, the evolved SO$_2$ gaseous (as shown in Figure 5.16 b) in the decomposition of Ti(SO$_4$)O catalyst started at around 600 $^\circ$C of the pyrolysis process with high concentration and then the width of the peak increased with time up to the end of pyrolysis. These results further confirm that sulphate group has been incorporated into the structure of TiO$_2$ NPs for synthesised Ti(SO$_4$)O.
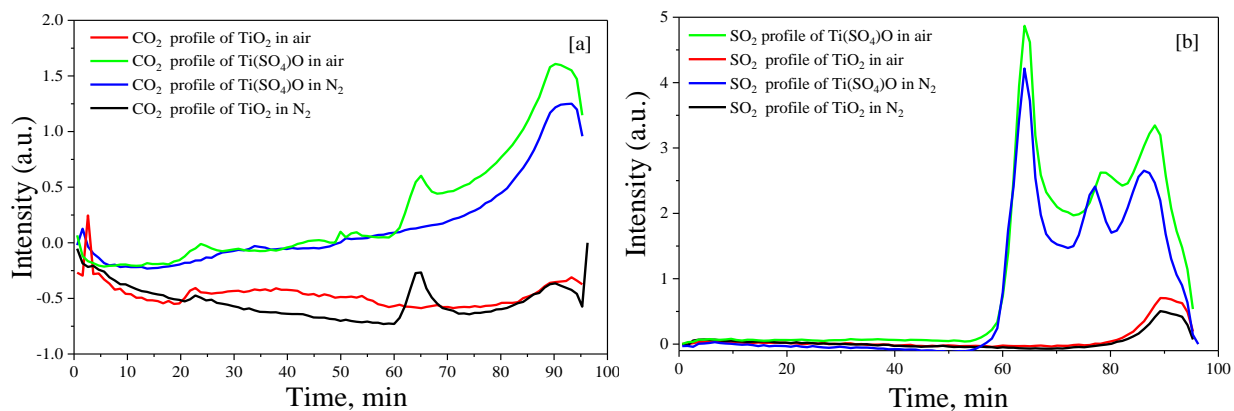
Figure 5.16 Chemigram profiles of (a) CO$_2$ and (b) SO$_2$ gases released from TiO$_2$ NPs and Ti(SO$_4$)O solid acid catalysts

177

5.2.1.4 Surface acidity

The DRIFT spectra of Ti(SO$_4$)O catalyst in comparison with TiO$_2$ NPs are displayed in Figure 5.17. The type and ratio of Brønsted to Lewis acid sites was found from the DRIFT spectra based on the ring vibrational of pyridine in the range of 1400 to 1650 cm^{-1}. The bands appeared at 1445-1448 and 1607 cm^{-1} were assigned to the coordinated pyridine adsorption on the Lewis acid sites in both catalysts, whereas, the peaks at 1541 and 1640-1642 cm^{-1} were related to the presence of Brønsted acid sites (pyridinium ions) in the solids [362, 364, 365, 510]. The reduction and peak shift of the Lewis acid site synthesised Ti(SO$_4$)O catalyst appeared at 1448 cm^{-1} and could be clearly seen in comparison with the TiO$_2$ NPs. The band at 1490 cm^{-1} is shown in both samples indicating the strong coordination of pyridine and pyridinium ions on the Brønsted and Lewis acid sites, respectively [88, 511, 512]. Furthermore, a wide band from 1600 to 1640 cm^{-1} in Ti(SO$_4$)O catalyst indicated the formation of strong Lewis acid sites than Brønsted acid sites [88, 364, 540]. The super acidity of Ti(SO$_4$)O is attributed to the presence of stronger Brønsted acid sites than the Lewis acid sites. The ratio of Brønsted to Lewis acid sites was found from their relative intensities (peak areas) of the peaks at ~1450 and ~1540 cm^{-1} [88, 362]. The ratio of Brønsted to Lewis acid sites (B/L = 1.78) in prepared Ti(SO$_4$)O was much higher compared to the initial TiO$_2$ NPs (B/L = 0.05).
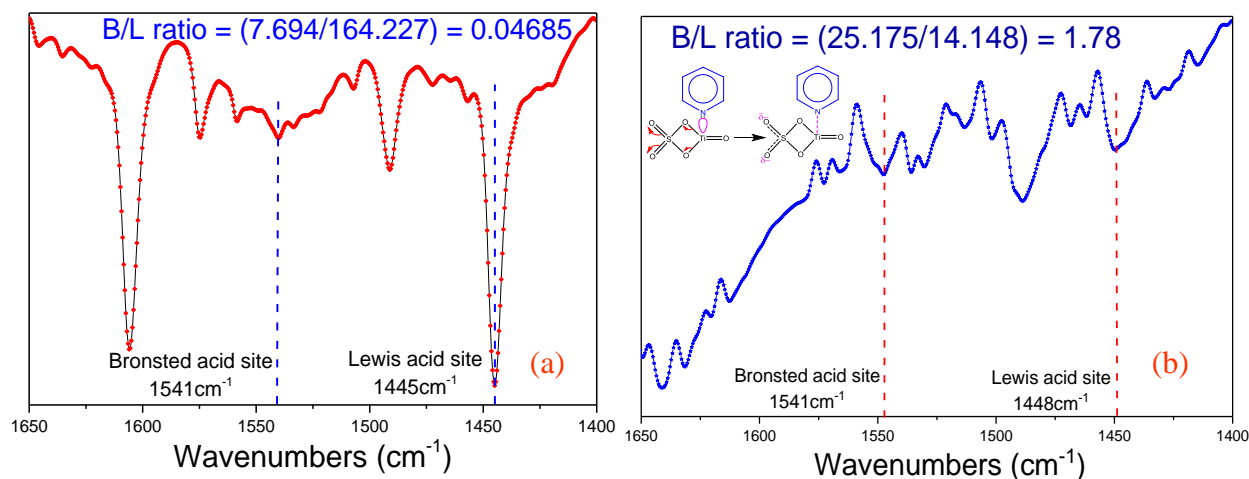
Figure 5.17 DRIFT spectra after pyridine adsorptions of (a) TiO$_2$ NPs and (b) Ti(SO$_4$)O solid acid catalyst

The quantity of acid loadings on the TiO$_2$ NPs support and Ti(SO$_4$)O catalyst were studied on the TPD-MS with n-propylamine probe. The TPD-MS profiles for both samples show

that desorption appears between 300 and 600 °C. Based on the amount of desorption as shown in Figure 5.18, it was found that the acidity of the Ti(SO$_4$)O catalyst (3.45 mmol/g) is much higher than the TiO$_2$ NPs (0.28 mmol/g).
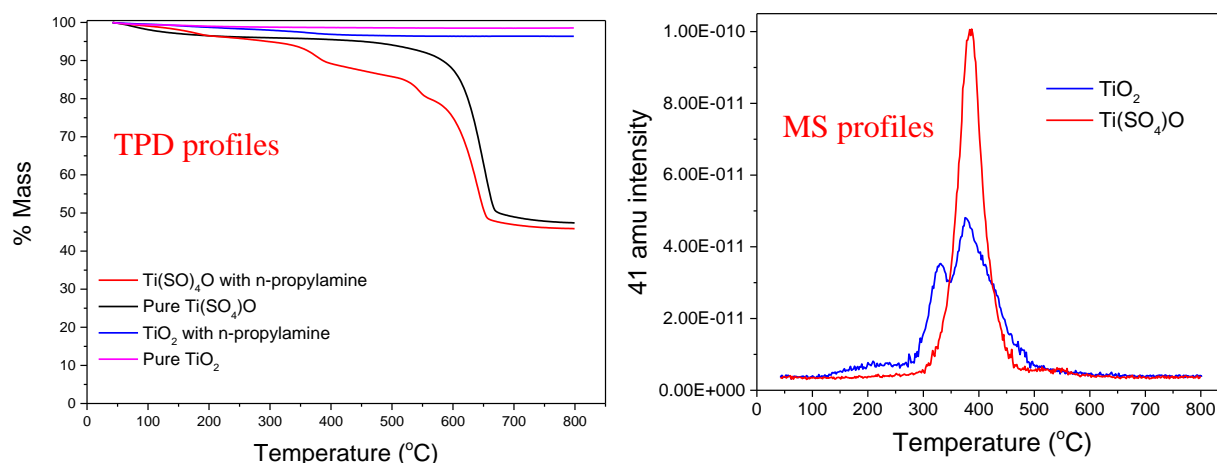
Figure 5.18 TPD-MS profiles for irreversibly adsorbed n-propylamine molecules on the surface of TiO$_2$ NPs and Ti(SO$_4$)O solid acid catalyst

The detailed total acid loading for Ti(SO$_4$)O in comparison with TiO$_2$/PrSO$_3$H and metal surface functionalised by organic and/or inorganic S-containing species reported literature is presented in Table 5.4.

Table 5.4 Comparison of total acid loading in TiO$_2$/PrSO$_3$H with the reported values for different types of solid acid catalysts from the literature

Catalyst	Total acid amount [H$^+$]	Reference
Ti(SO$_4$)O	3.45 mmol/g	Present work
TiO$_2$/PrSO$_3$H	2.35 mmol/g	Present work
Amberlyst-15	1372-4700 µmol/g	[513]
SBA-15-SO$_3$H	1.44 meq/g	[102]
SBA-15-ph-SO$_3$H	0.9 meq/g	
ZrO$_2$-SO$_3$H	2.9 mmol/g	[514]
Fe$_3$O$_4$-SBA-SO$_3$H	1.09 mmol/g	[487]
SBA-SO$_3$H	0.44-0.56 mmol/g	
Ti(SO$_4$)$_2$	1.22-3.61 mmol/g	[363]
SO$_4^=$/ZrO$_2$	0.07-0.37 mmol/g	[515]
SO$_4^=$/ZrO$_2$/TiO$_2$/Fe$_3$O$_4$	47.9-135.2 µmol/g	[516]
SO$_4^=$/TiO$_2$	793.8 µmol/g	[365]

5.2.2 Catalytic performance

The FAME yield was investigated under different catalytic process parameters, including methanol to UCO mole ratio, reaction temperature, catalyst loading, and time of esterification/transesterification, see Figure 5.19, in order to establish the optimum reaction conditions for the esterification/transesterification process of UCO to biodiesel. The esterification/transesterification of UCO with methanol using $Ti(SO_4)O$ as a solid acid catalyst is a liquid-liquid-solid reaction (three phase system) at which the mass transfer rate of reactant molecules between the UCO-methanol-catalyst phases is very slow. The conversion rate is normally found to increase with reaction time due to an increase in the miscibility of the UCO into methanol [541, 542]. The reaction time was varied between 30 to 540 min, while keeping other reaction process parameters constant at 1.0 wt% of $Ti(SO_4)O$ catalyst loading to UCO, 6:1 molar ratio of methanol to UCO, 65 °C reaction temperature, 600 RPM agitation rate, 0.14% moisture content, and 2.034 wt% free fatty acid contents in feedstock. It can be noted that the increase of reaction time from 30 min to 3 h led to the enhancement of FAME yield to 89% as shown in Figure 5.19 (a). This can be explained by the rate constants for mono-glycerides and di-glycerides conversion to glycerol and mono-glycerides being very low compared to triglycerides [543]. Additionally, a longer reaction time (after 6 h) resulted in slowly reduced production yield, possibly due to increasing the probability of pushing the reverse reaction. Similar results has been reported by Nayebzadeh [305] where a further increase in esterification reaction time resulted in a production yield decrease. The optimum ratio of $Ti(SO_4)O$ catalyst loading was determined under the other fixed reaction conditions, i.e. at 3 h reaction time, 6:1 molar ratio of methanol to UCO, 65 °C reaction temperature, 600 RPM agitation rate, 0.14 % moisture content, and 2.034 wt% free fatty acid. Figure 5.19 (b) depicts that 1.5% of $Ti(SO_4)O$ was the optimum amount in achieving the highest production yield of 92.5% under the aforementioned reaction conditions. This is due to fact that increasing the catalyst concentration in the system leads to an increase in the total number of active sites (Brønsted and Lewis acid sites), which results in a faster reaction rate to reach reaction equilibrium [544]. A plausible reaction mechanism for TG with methanol in the presence of $Ti(SO_4)O$ solid acid catalyst is depicted in Figure 5.20.

The stoichiometric ratio for transesterification reaction, theoretically, requires three moles of methanol per mole of TG but esterification reaction requires one mole of methanol per mole of FFA as shown in Figure 5.21. However, the transesterification process experimentally requires an

excess of methanol in order to push the equilibrium reaction forward direction of methyl esters as the transesterification process is a reverse reaction [287].
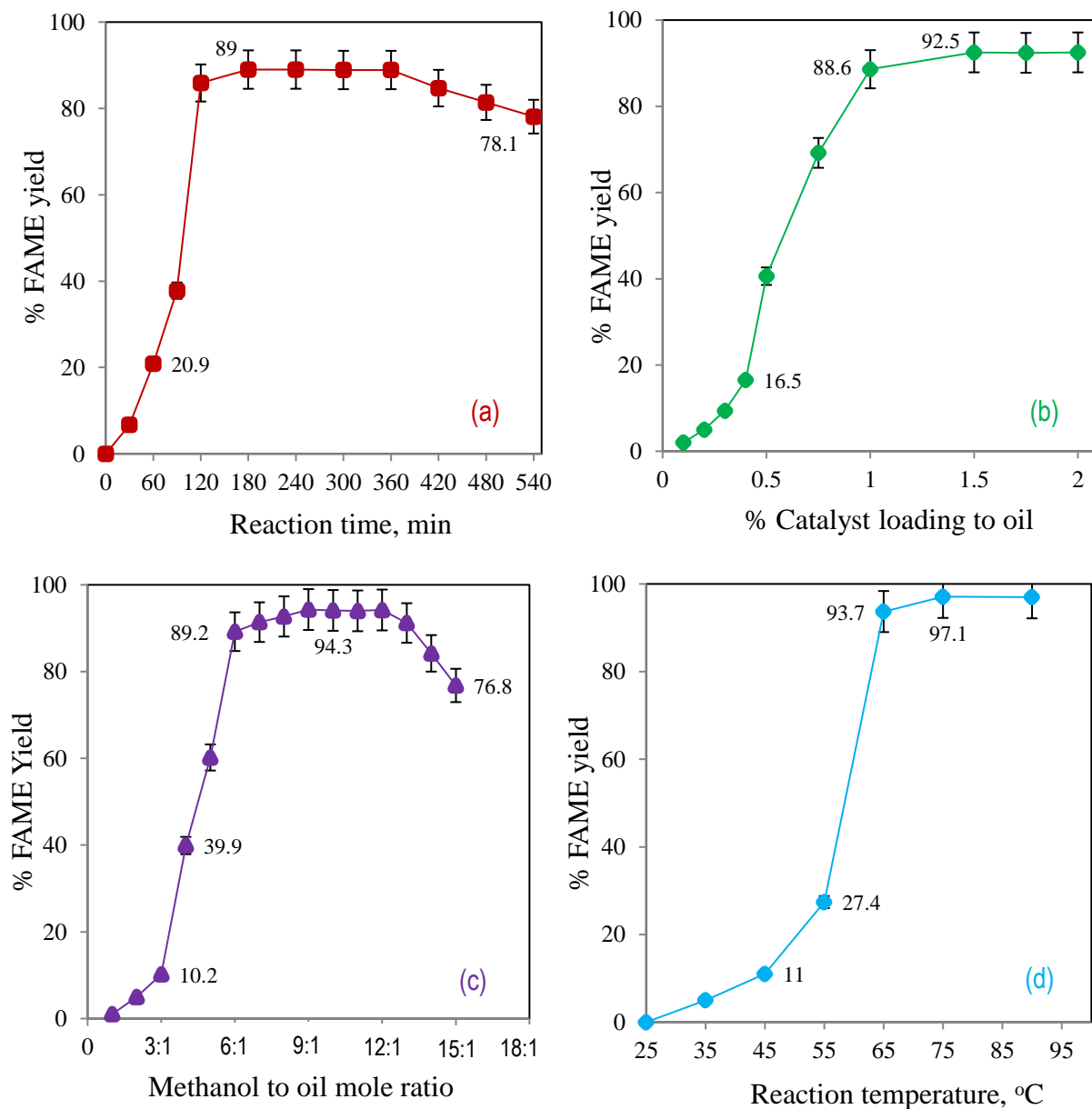
Figure 5.19 The effects of (a) reaction time, (b) Ti(SO$_4$)O catalyst loading to UCO, (c) mole ratio of methanol to UCO, and (d) reaction temperature on the percentage of FAME yield.

Maximum conversion of triglycerides into FAME is ensured by the use of excess methanol due to esterification/transesterification being a reversible reaction. Figure 5.19 (c) shows the effect of various mole ratios of methanol to UCO under the other fixed reaction process of 3 h reaction time, 1.5 wt% Ti(SO$_4$)O catalyst loading to oil, 65 °C reaction temperature, 600 RPM agitation rate,

0.14% moisture content, and 2.034 wt% FFA contents. The highest yield of 94.3% was achieved at 9:1 mole ratio of methanol to UCO.
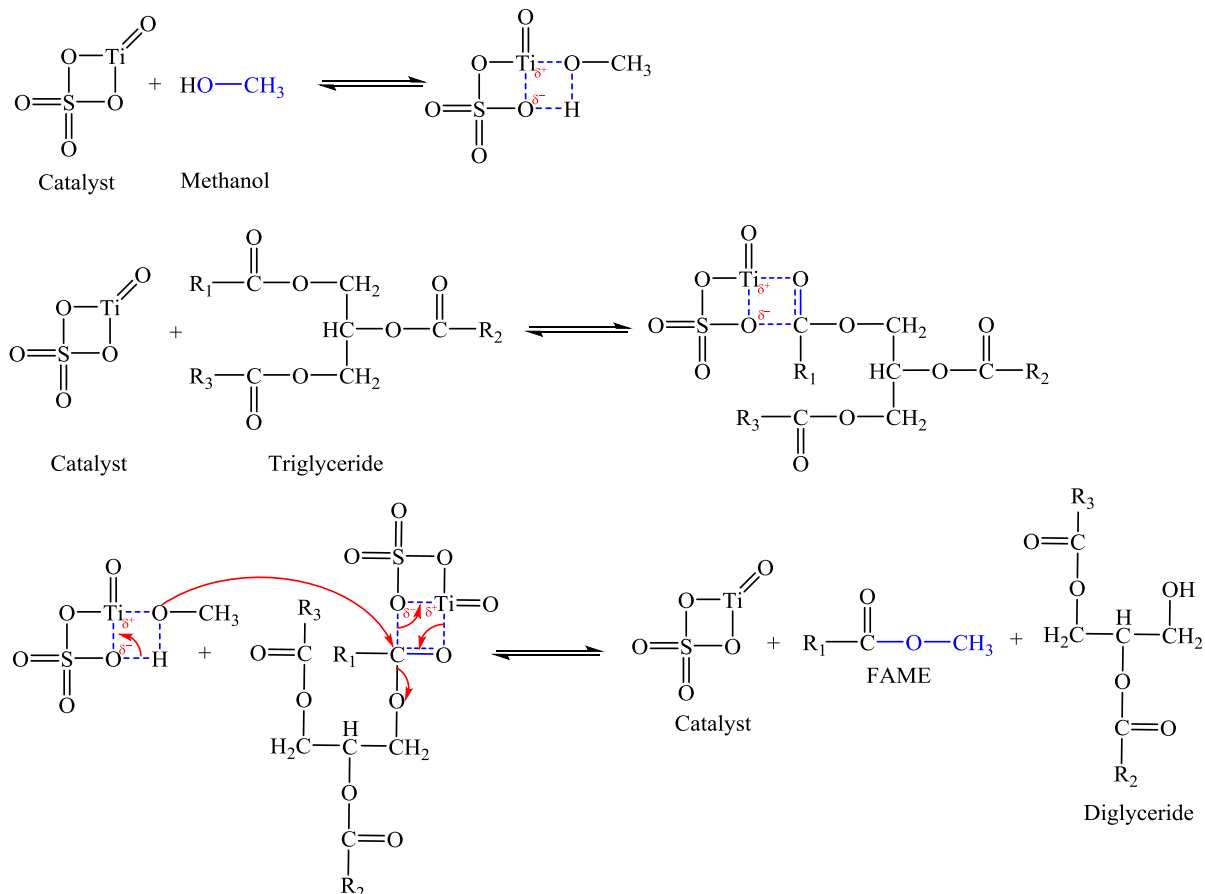
Figure 5.20 Proposed mechanism for the transesterification of UCO over Ti(SO$_4$)O catalyst

It can be noted that an increase in methanol to UCO from 1:1 to 3:1 had a slight effect on the FAME yield, while further increase of methanol from 4:1 to 9:1 raised the production yield up to the highest FAME yield. Afterwards, there was a decline in production yield with mole ratios higher than 12:1. This can be explained by an additional amount of methanol helping to drive the reversible side of reaction to re-form mono-glyceride with di-glyceride and the solubility of the by-product also being increased in the solution. Furthermore, water (by-product) is obtained during the esterification of FFAs in UCO feedstock lowering the activity of the catalyst. In addition, a large excess of methanol to oil mole ratio resulted in the flooding of the active sites which hindered the activation of remaining TG in the reaction system [348].
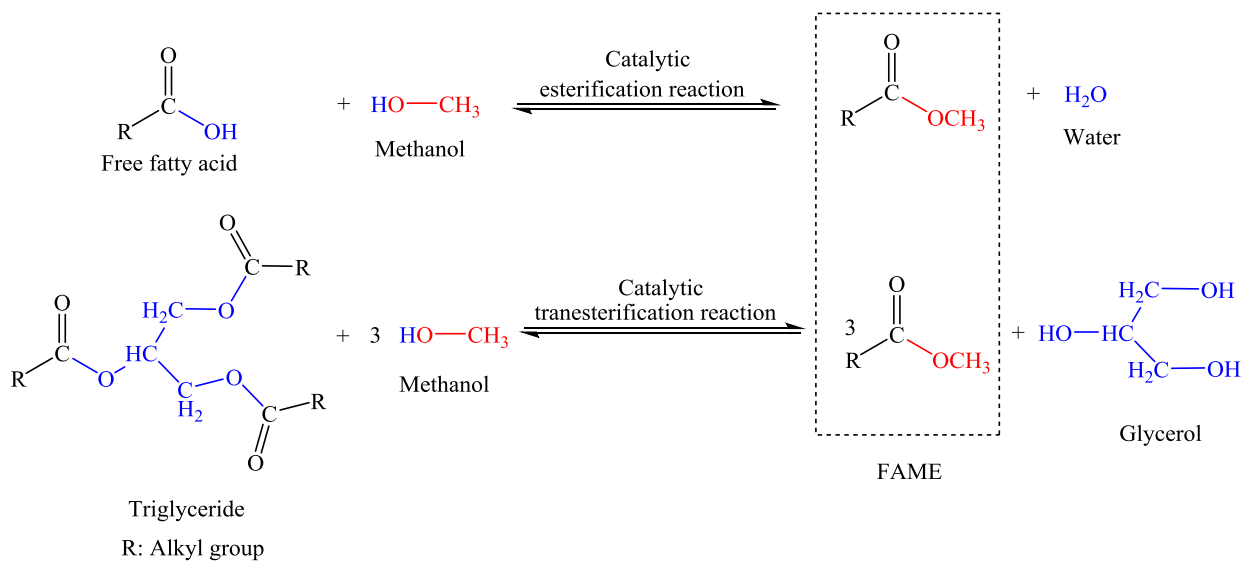
Figure 5.21 General esterification and transesterification reactions

The rate of esterification/transesterification reaction is highly affected by the reaction temperature according to Arrhenius's equation. A higher temperature also reduces the viscosities of the oils, thereby increasing the rate of the reaction. The esterification/transesterification reaction can occur at different temperatures depending on the fatty acid profiles of raw sample oils and the type of catalyst. The effect of temperature on the FAME yield using $Ti(SO_4)O$ as a solid acid catalyst was examined by varying the reaction temperatures from 25 to 90 ^{o}C while other process parameters were kept constant at 3 h reaction time, 1.5 wt% $Ti(SO_4)O$ catalyst loading, 9:1 molar ratio of methanol to UCO, 600 RPM agitation rate, 0.14% moisture content, and 2.034 wt% free fatty acid content. It was found that the yield consistently increased at higher reaction temperature as shown in Figure 5.19 (d). This can be explained by esterification/transesterification being an equilibrium process and at 25 ^{o}C reaction temperature energy is not enough to break down the ester bond in the TG molecules, whilst an increase of the reaction temperatures to 55 ^{o}C improves the FAME yield by 27.4%. A further increase of reaction temperature significantly enhances the production yield by 66.3% possibly due to the fact that the reaction temperature at 65 ^{o}C generates more nucleophilic sites in the system. Therefore with a temperature slightly higher than the boiling point of methanol, the nucleophilic attack on the carboxylic/carbonyl groups in FFA/TG is further increased. Moreover, the highest yield of FAME (97.1%) was produced at 75 ^{o}C, due to the acceleration of the mass transfer rate between the UCO-methanol-catalyst phases; higher temperature helps the activation of carboxylic/carbonyl groups in FFA/TG by protonation and the

methanol nucleophilic attack on the carboxylic/carbonyl groups [86]. In this work the optimum reaction temperature was found to be lower than previously reported work, most probably due to the high acid loadings on the TiO_2 catalyst leading to higher activity during the reaction. Further investigations on the kinetics of this reaction needs be carried out.

5.2.2.1 Catalytic activity and its reusability

The presence of FFA in the feedstock has a great influence on the poisoning of solid acid catalysts due to the formation of water from the esterification process [287]. Oleic acid was added to virgin oil to assess the effect of FFA on the catalytic activity of $Ti(SO_4)O$ as a solid acid catalyst. The amount of FFA in oil was varied from 0.5 to 7% whilst the other parameters were set constant at optimised process conditions using 3.0 h reaction time, 1.5 wt% $Ti(SO_4)O$ catalyst loading, 9:1 molar ratio of methanol to oil, 75 °C reaction temperature, 600 RPM agitation rate, and 0.14% moisture content.
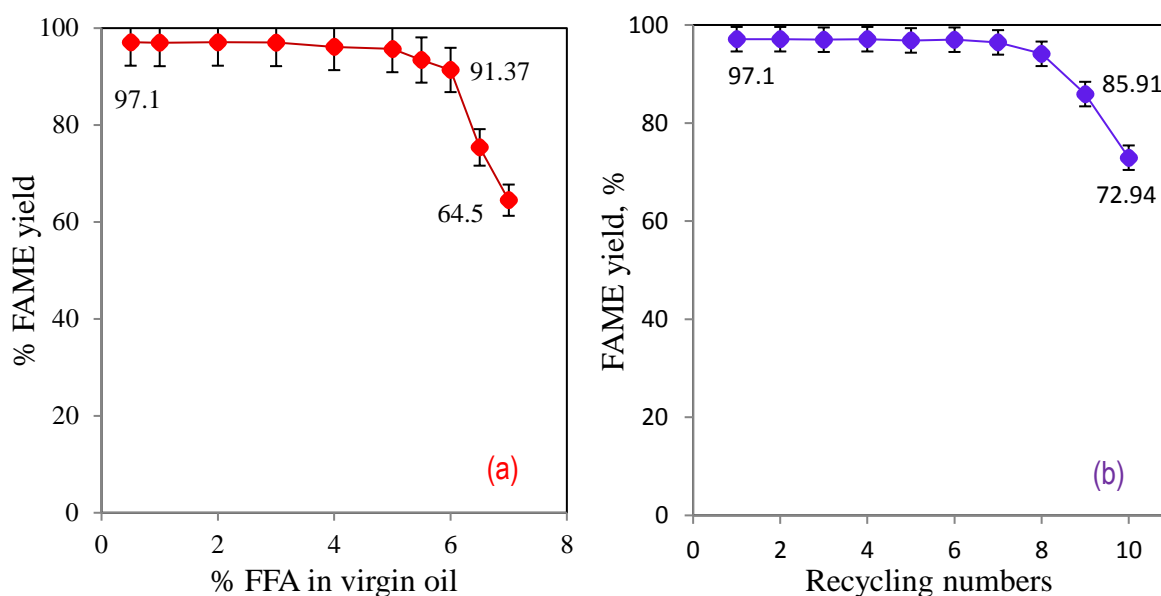
Figure 5.22 The effect of (a) FFA% and (b) reusability of $Ti(SO_4)O$ catalyst on the percentage of FAME yield.

Noticeable from Figure 5.22 (a), there is a slight decrease of yield up to 6.0 wt% FFAs in corn oil (virgin oil), then a significant decrease after 6 wt%, probably as the rapid esterification of oleic acid promotes the reverse methanolysis reaction of FAME and glycerol which demotes the transesterification process [519]. Similar conclusion was extracted from the effect of FFA (up to

4 wt%) over the TiO_2/$PrSO_3H$ solid acid catalyst. For that reason the esterification / transesterification reaction could be carried out at higher temperature over a shorter time for raw materials containing high amounts of FFA in order to achieve maximum yield of FAME [86, 287, 366]. The investigation of the effect of high temperature on the yield of raw materials containing high FFA could the subject of future studies.

The re-usability of $Ti(SO_4)O$ solid acid catalyst was also investigated to determine the catalyst life time as it can help reduce production costs for industrial purposes. The catalyst was separated from the biodiesel layer and glycerol layer (sunk to the bottom of the centrifuge tube). The recovered catalyst was then properly washed several times with 1:1 ratio of methanol to n-hexane in order to remove any remaining non-polar and polar compounds on the surface of the catalyst such as fatty acid methyl ester (FAME), glycerol, monoglycerides, diglycerides and triglycerides.
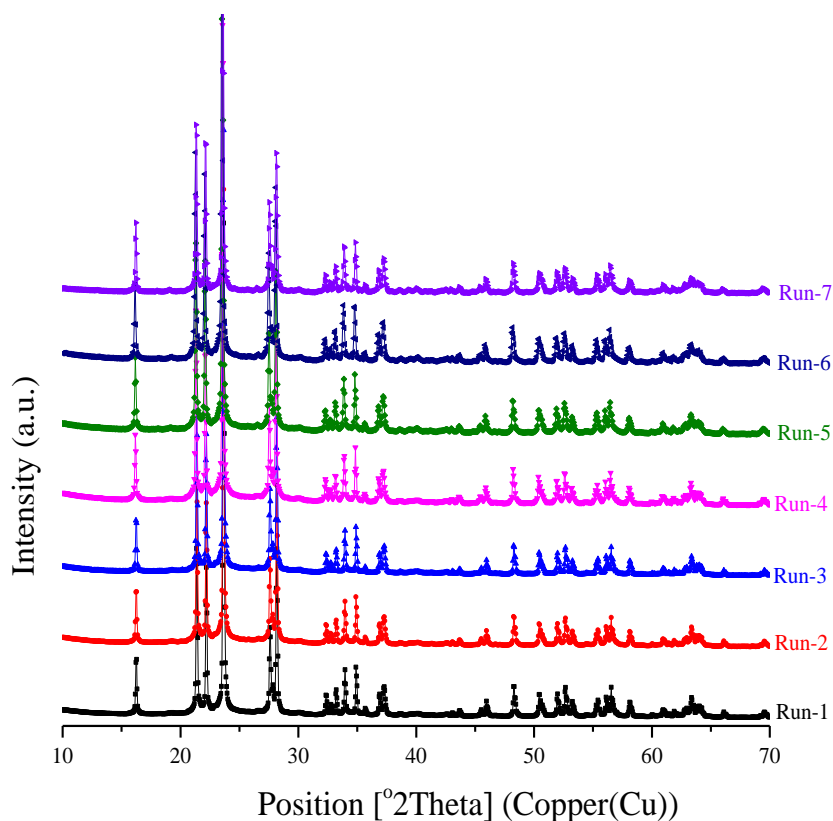
Figure 5.23 The powder XRD patterns of re-used $Ti(SO_4)O$ catalyst for run 1 to run 7

Finally, the catalyst was treated in an oven for 3 h at 110 °C to remove any moisture on the surface then the textural structure of the catalyst re-confirmed using XRD before being re-used. It was found that the $Ti(SO_4)O$ can be re-used up to 8 cycles with a slight drop in catalytic activity (see

185

Figure 5.22 b) for the esterification/transesterification reactions using the optimised parametric processes conditions (3 h reaction time, 1.5 wt% Ti(SO$_4$)O loading, 9:1 molar ratio of methanol to UCO, 75 ^{o}C reaction temperature, 600 RPM agitation rate, 0.14% moisture content, and 2.034 wt% FFA contents). The results revealed that the FAME yield significantly decreased for 9 and 10 trials by 11.19% and 24.16%, respectively (see Figure 5.22 b); this could be due to the blockage of active sites of catalyst by triglyceride (TG)/product or catalyst active sites leaching [38, 348]. The powder XRD experiments were carried out for the recycled catalyst after each run in order to investigate the catalytic deactivation and also to confirm the crystal structure of the spent catalyst. The result showed that Ti(SO$_4$)O solid acid catalyst maintained its structure after 8 runs as shown in Figures 5.23 and 5.24. The XRD patterns of recycled Ti(SO$_4$)O from run 1 to 7 shows that there was no loss of SO$_4^{2-}$ groups and/or formation of any new phases, as shown in Figure 5.23. This is an indication of the stability of the sulfate groups in Ti(SO$_4$)O catalyst and durability for the first 7 cycles in simultaneous esterification and transesterification of UCO into biodiesel.
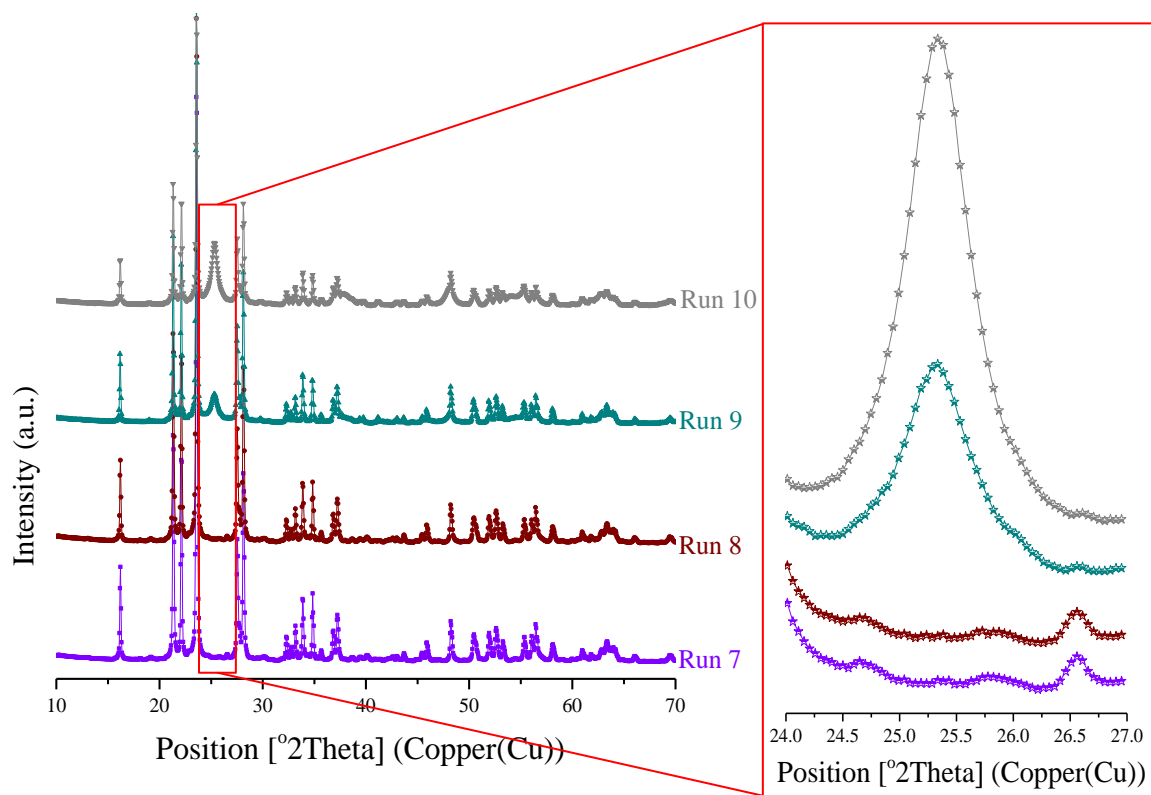
Figure 5.24 The powder XRD patterns of reused Ti(SO$_4$)O catalyst from run 7 to run 10.

Figure 5.24 shows the formation of new diffraction peak at 2θ value of 25.32° assigned to the [101] reflection for the anatase structure of TiO_2 and increase of its intensity with continued re-use of the catalyst beyond 8 runs (9% and 34.7% of anatase phase after 9 and 10 runs, respectively). The decrease in acidity of $Ti(SO_4)O$ catalyst loss of SO_4^{2-} species might affect the esterification/transesterification of FFA/TG in UCO feedstock. In contrast, some researchers reported that leaching of SO_4^{2-} species was not the main cause for the decline in the catalytic activation of different sulfonated catalysts [545, 546]. However; XRD results in this work confirmed the catalytic deactivation is caused partially by leaching of SO_4^{2-} species and formation of new phase (see Figure 5.24). The same observation was found by Zhao et al. [365] for the sulphated titania (SO_4^{2-}/TiO_2) catalyst for esterification reaction. The catalyst was recovered at the end of each run using centrifuge followed by the filtration of the fuel to eliminate remaining particles (if any). The leaching of sulphur and titanium from $Ti(SO_4)O$ catalyst was then investigated after each run by using ICP-MS. It was found that the filtrated fuel contained hardly any sulphur and titanium up to 8 runs then there were only sulphur leaching detected of 2798.14 and 2971.1 ppb for run 9 and 10, respectively. Therefore, further studies needs to be carried out to investigate the factors affecting the leaching of sulphate groups and deactivation of $Ti(SO_4)O$ catalyst.

5.2.2.2 Regeneration of spent catalyst
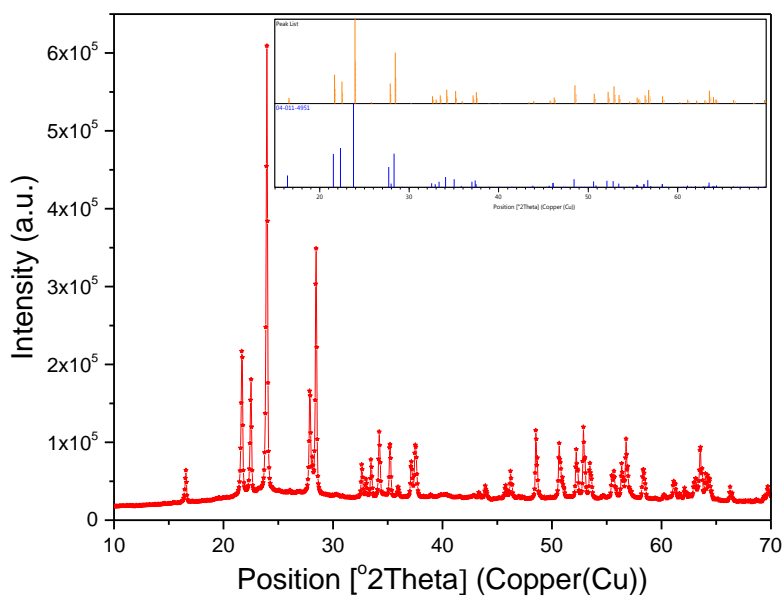
Figure 5.25 The powder XRD pattern of regenerated $Ti(SO_4)O$ catalyst

The spent catalyst recovered after 8 cycles for biodiesel production from UCO was regenerated by impregnation method, using 25 mL of 0.5 M sulfuric acid solution under 2 h reflux. The obtained gel solution was filtrated and then dried overnight in an oven at 110 ^{o}C. The XRD of regenerated Ti(SO$_4$)O catalyst is shown in Figure 5.25 and all diffraction peaks are matched with titanium sulphate oxide or titanium oxysulfate (Ti(SO$_4$)O, PDF-ICDD: 04-011-4951). Figure 5.26 presents comparison SEM images of the regenerated and spent (run 9) Ti(SO$_4$)O catalysts at different magnifications. There is not much difference in terms of morphological and particle size distributions for spent catalyst and regenerated (Ti(SO$_4$)O catalysts.
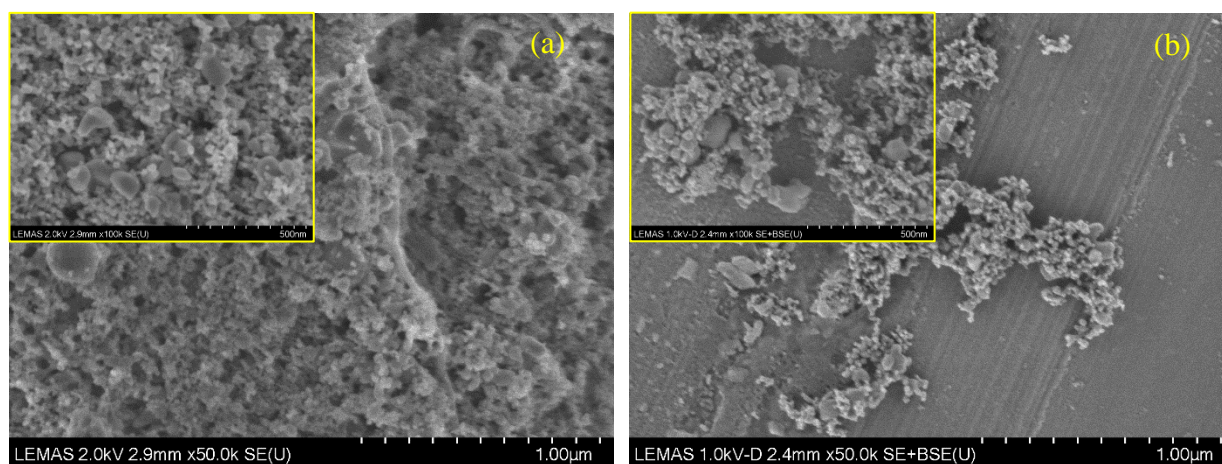
Figure 5.26 SEM images of (a) regenerated and (b) spent Ti(SO$_4$)O catalysts

The average pore size for regenerated Ti(SO$_4$)O catalyst shows a slightly larger formation compared to the fresh catalyst. This is mostly due to the rate of nucleation and growth of Ti(SO$_4$)O particles being faster in sulfuric acid solution compared to chlorosulfonic acid, which results in the formation of random size particles. The large pore size and pore volume are more preferable for minimising diffusion limitations for long alkyl chain hydrocarbons in FFA/triglyceride (TG) [304]. The detailed physical properties of regenerated catalyst are summarised in Table 5.5.

Table 5.5 The surface area, total pore volume and average pore size of regenerated Ti(SO$_4$)O

Type of catalyst	BET surface area (m^2/g)	BJH mean pore size (nm)	BJH total pore volume (cm^3/g)
Regenerated Ti(SO$_4$)O	45	28.7	0.184

One of the most important factor in the industrial catalytic process at high temperature is the thermal stability of solid acid catalysts. Figure 5.27 shows the TGA/FT-IR profile for the regenerated Ti(SO$_4$)O. In the thermogram of regenerated catalyst, two desorption peaks can be observed. The first one, in the 50 and 150 ^{o}C range, corresponded to the water molecules' desorption as can be seen clearly in 5.27 (b). Then there was almost no weight loss up to 600 ^{o}C, which indicates good thermal stability of the catalyst. A further increase of temperature to 800 ^{o}C led to decompose of the sulphate species in the regenerated catalyst, resulting in the SO$_2$ gases being emitted (see the 3D inset from Figure 5.27 b). Similar observations were reported by other researchers for SO$_4^{2-}$/TiO$_2$ catalysts [362, 371].
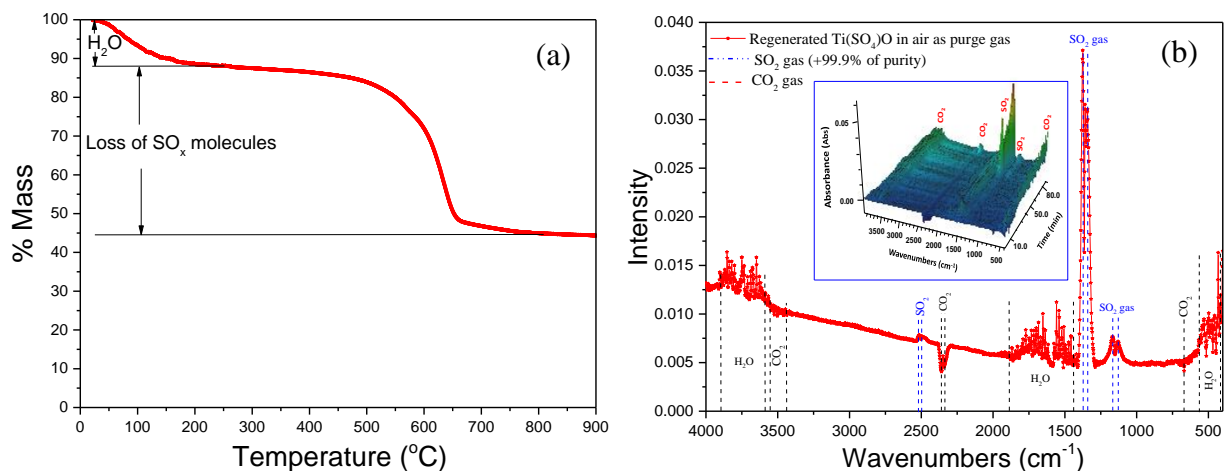
Figure 5.27 TGA profile for regenerated Ti(SO$_4$)O catalyst (a) and 2D of FT-IR spectrum for evolved gases from the thermal decomposition of regenerated Ti(SO$_4$)O catalyst (b).
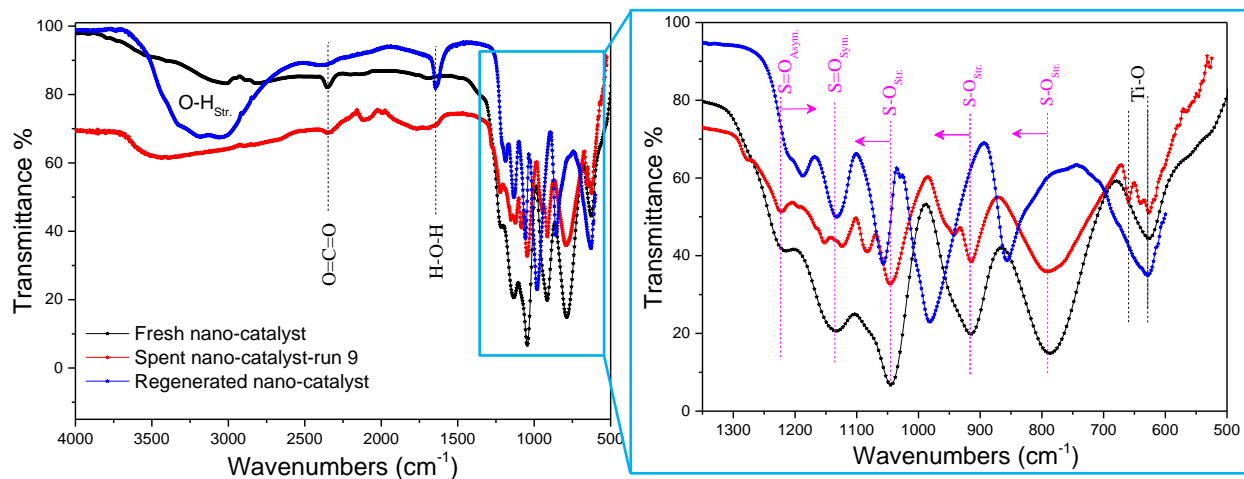
Figure 5.28 FT-IR spectra for fresh, spent and regenerated Ti(SO$_4$)O catalysts

Further analysis on the FT-IR was carried out in order to identify the functional groups in the regenerated catalyst. It was notable that the reduction of peak intensities for spent catalyst observed with a new absorption extra peak (around 2150 cm^{-1}) appeared. The surface of regenerated catalyst was highly absorbed moisture from the atmosphere as depicted in Figure 5.28. It is also worth mentioning that all corresponding peaks of S-O stretching vibration shifted to higher frequencies in the regenerated catalyst spectrum [367]. The absorption of S=O asymmetric stretching slightly shifted to lower frequency about 30 cm^{-1}. The super acidity of the catalyst is generally attributed to the presence of sulfonyl functional groups (symmetric and asymmetric) [363, 547]. The proposed structure as an acidic species for Ti(SO$_4$)O is given in Figure 5.29.
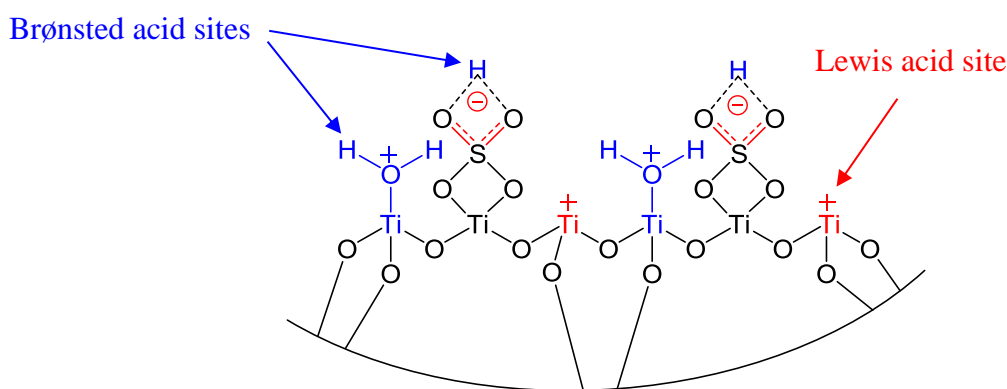
Figure 5.29 Schematic structure of acidic sites in regenerated Ti(SO$_4$)O catalyst

The regenerated catalyst was tested in the esterification/transesterification reaction of UCO under the previously determined optimum process conditions and the results are presented in Table 5.6. It can be seen that the regenerated nano-catalytic was given a reasonable catalytic activity to 5 cycles. This makes the prepared solid acid catalyst more environmentally friendly for biodiesel production from cheap feedstocks.

Table 5.6 Catalytic activity of regenerated Ti(SO$_4$)O for biodiesel production from UCO

Type of catalyst	1st run	2nd run	3rd run	4th run	5th run
% yield of FAME over regenerated Ti(SO$_4$)O	96.7	96.46	95.98	93.2	93.51

5.2.3 Biodiesel characterisations

The biodiesel produced in the esterification/transesterification processes from UCO was analysed and characterised according to ASTM and EN standards. These results are summarised in Table

5.7 and 5.8. The main components of FAME profile for obtained biodiesel were palmitic acid methyl ester, oleic acid methyl ester, linoleic acid methyl ester and linolenic acid methyl ester. The saturated and unsaturated FAME profile in produced biodiesel significantly affect the physicochemical properties of synthesised biodiesel fuel.

Table 5.7 FAME composition for obtained UCO biodiesel

FAME	Form	wt% content
Palmitic acid methyl ester	$C_{16:0}$	6.23
Stearic acid methyl ester	$C_{18:0}$	0.85
Oleic acid methyl ester	$C_{18:1}$	69.56
Linoleic acid methyl ester	$C_{18:2}$	20.41
Linolenic acid methyl ester	$C_{18:3}$	2.18
Arachidic acid methyl ester	$C_{20:0}$	0.17
Gadoleic acid methyl ester	$C_{20:1}$	0.31
Erucic acid methyl ester	$C_{21:1}$	0.16
Behenic acid methyl ester	$C_{22:0}$	0.12

It can be noted from Table 5.8 that the limits for produced biodiesel is in the range of acceptable standard specifications of biodiesel.

Table 5.8 Properties of biodiesel produced from UCO over $Ti(SO_4)O$ catalyst

Property	Unit	Limits		Synthesised biodiesel
		ASTM D6751	EN14214	
Flash point	°C	93 min	101 min	155
Kinematic viscosity	mm^2/s	1.9-6.0	3.5-5.0	4.58
Acid number	mgKOH/g	0.8 max	0.5 max	0.32
Density at 15°C	Kg/m^3	---	860-900	896.1
FAME content	% mass	---	96.5 min	97.1
Water content	ppm	---	500 max	---
Linolenic acid methyl ester	% mass	---	12 max	2.18
Free glycerine content	% mass	0.02 max	---	0.086
Total glycerine content	% mass	0.24 max	0.25 max	0.121
Monoglyceride content	% mass	---	0.8 max	0.035
Diglyceride content	% mass	---	0.2 max	0.0
Triglyceride content	% mass	---	0.2 max	0.0

Optical microscopy was carried out at different temperatures to determine the cold flow behaviours for synthesised biodiesel fuel over Ti(SO$_4$)O catalyst. Figure 5.30 illustrates the optical microscopy images for prepared biodiesel using HSM at different temperatures to detect the formed crystals. It can be observed that there were no detectable crystals during cooling the sample to -6 ^{o}C. Formation of several tiny needle-like crystals was observed below -9 °C. The nucleation of these tiny needle-like crystals increased at -15 ^{o}C whilst the size of crystals increased during further by cooling to -21 ^{o}C.
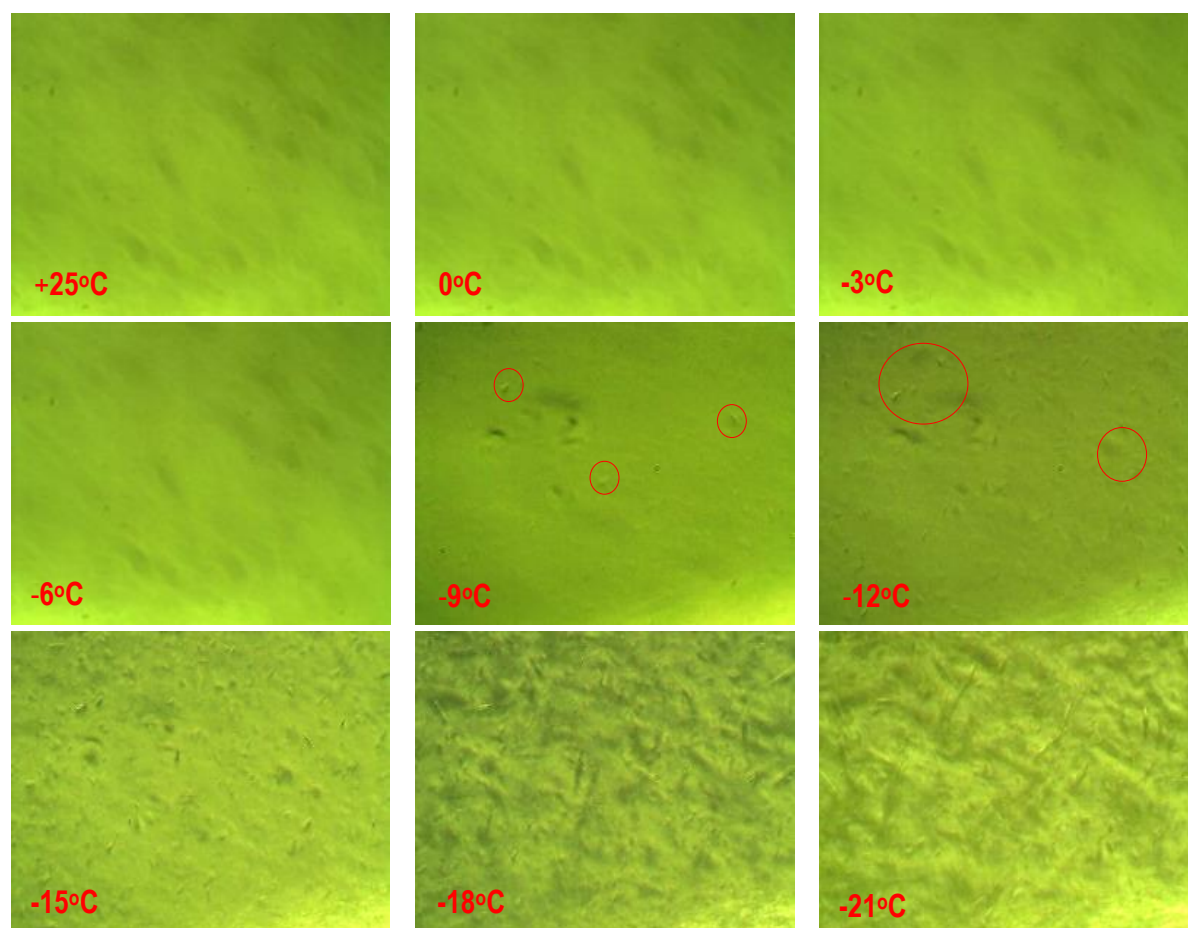
Figure 5.30 HSM images of the prepared biodiesel at different temperatures

The thermal stability of the synthesised biodiesel was performed on the TGA and the thermogram results with onset and endset temperatures are depicted in Figure 5.31. It can be noted that the prepared biodiesel is thermally stable up to 199.5 ^{o}C and then it starts decomposing until burns completely at 273 ^{o}C.
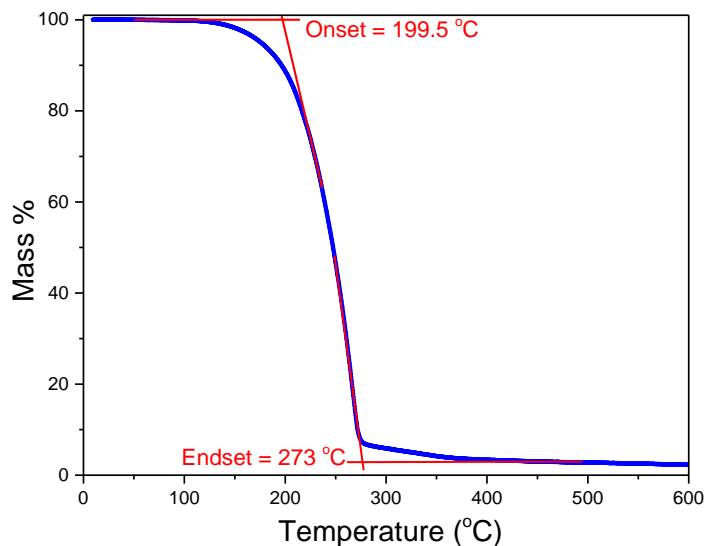
Figure 5.31 Thermal stability of synthesised biodiesel over Ti(SO$_4$)O under air purge gas

5.2.4 Discussions

The use of chlorosulfonic acid as a reagent for sulfonation of nano-sized titanium dioxide is a promising direction for loading of sulphur species into titanium dioxide. The obtained titanium sulphate oxide or titanium oxysulfate catalysts have a unique and different chemical structure than titanium dioxide (see Figure 5.2) and those from published work on sulphated metal oxides [294, 304, 361, 365]. This obvious change in the chemical structure makes the prepared Ti(SO$_4$)O catalyst more stable compared to all reported sulphated metal oxide [289, 294, 371] as in previous catalysis the sulphate species located on the surface of metal oxides which makes the molecule unstable [361, 365, 548]. The stability of synthesised Ti(SO$_4$)O catalyst is due to the formation of bidentate sulphate species inside the structure of TiO$_2$ which also leads to a higher tolerance to a high percentage of FFAs in raw material for biodiesel production. This is due to the synergic activation of bidentate sulphate species inside the structure of TiO$_2$ NPs, resulting in an increase of the Brønsted and Lewis acid sites of the catalyst. The effect of different TiO$_2$ phases (anatase, rutile and brookite) and different SO$_x$ loadings on the nano-sized TiO$_2$ on the catalytic performance could be the subject of future studies in order to better understand the influence of Brønsted and Lewis acid sites on the yield of FAME produced from simultaneous esterification and transesterification of UCO. Furthermore, there was no evidence that the presence of absorbed carbon dioxide from atmosphere had an influence on the catalytic activity of Ti(SO$_4$)O catalyst, but further investigations should be performed in future studies in order to better understand the

surface chemistry of this catalyst under different conditions. The amount of yield and optimised process conditions (e.g. catalyst loading, methanol to UCO molar ratio, reaction time, temperature, tolerance to FFA and catalyst reusability) have been significantly improved using the catalyst synthesised in this work as compared to the reported sulphated metal oxides [361, 365]. Finally, the conditions for simultaneous esterification and transesterification processes using previous solid acid catalysts compared to the current study are presented in Table 5.8. It is also important to mention that the synthesised $Ti(SO_4)O$ was much more stable than prepared $TiO_2/PrSO_3H$ solid acid catalyst. This is due to propyl sulfonic acid in $TiO_2/PrSO_3H$ catalyst located on the surface of TiO_2 NPs whilst the sulphate groups in $Ti(SO_4)O$ were within the crystalline structure of the synthesised catalyst. One of the limitation of such catalysts for usage in industry could be difficulties in separating the catalysts [49, 516]. Centrifugal techniques and ultrafiltration could be the options, however they are expensive, and difficult to scale-up. Development of magnetic catalysts could overcome these difficulties and this will be investigated in the next chapter.

Table 5.9 A comparison of reported optimum process conditions for the biodiesel production using solid acid catalyst

	Current study	Wang et al. [90]	Chen et al. [361]	
Oil/fat feedstock	UCO	UCO	Cottonseed oil	
Methanol to oil ratio	9:1	10:1	12:1	
Type of catalyst	$Ti(SO_4)O$	$SO_4^{2-}/TiO_2/La^{+3}$	SO_4^{2-}/TiO_2	SO_4^{2-}/ZrO_2
Wt of catalyst%	1.5	5	2	
Time, hr	3	1	8	
Particle size, nm	25	Not reported	Not reported	
Surface area, m^2/g	44.47	229	99.2	91.5
Temperature, ^oC	75	110	230	
FAME yield %	97.1	>90	90	80
Catalyst recycled	8	5	>4	

5.3 Conclusions

A novel solid acid catalyst [$Ti(SO_4)O$] was synthesised from impregnation of TiO_2 NPs with chlorosulfonic acid and used for the simultaneous esterification and transesterification of free fatty acids in UCO to produce biodiesel. The synthesised solid super acidic catalyst was fully characterised using different analytical techniques to differentiate the prepared $Ti(SO_4)O$ catalyst

from TiO$_2$ NPs, all confirming a 100% Ti(SO$_4$)O phase. DRIFT results confirmed the high ratio of acid sites (Brønsted to Lewis acid sites) compared to TiO$_2$ NPs and TiO$_2$/PrSO$_3$H. TPD-MS also observed the high loading of acid sites on the synthesised catalyst compared to TiO$_2$/PrSO$_3$H which is benificial for simultaneous esterification and transesterification of cheap feedstocks. The XPS results clearly confirmed that the bidentate sulphate coordinated to the Ti^{4+} metal in the catalyst product. Obtained *d*-spacing values from the experimental data of XRD peaks and the SAED pattern of produced catalyst agreed well with the *d*-spacing values from the JCPDS-ICDD card numbers [04-011-4951] for titanium sulphate oxide or titanium oxysulfate crystal structures. This confirms the sulphate groups were within the crystalline structure rather than on the surface of titania nanoparticles, which has not been previously reported in the literature. That is why the catalyst showed higher stability compared to the reported sulphated titania and TiO$_2$/PrSO$_3$H catalysts. It was found that Ti(SO$_4$)O can be used as a novel solid acid catalyst for biodiesel production from low quality and cheap feedstock such as UCO. The effect of operating process conditions such as reaction time, catalyst loading, methanol to UCO ratio, reaction temperature, FFA%, and re-usability/stability on the biodiesel yield were examined. It has been demonstrated that a 97.1% yield for the fatty acid methyl ester can be achieved using the synthetised catalyst under a reaction time of 3 h, catalyst to UCO ratio of 1.5 wt% and methanol to UCO ratio of 9:1 at 75 ^{o}C reaction temperature. Furthermore, the catalytic activity and re-usability of the Ti(SO$_4$)O for the esterification/transesterification of UCO were investigated. The solid acid catalyst was found to be most effective for the feedstock containing FFA up to ≤6 wt%. This result indicated that the novel solid acid catalyst can be used for simultaneous esterification and transesterification of UCO to biodiesel potentially reducing energy consumption in biodiesel production compared to other solid acid catalysts, including synthesised TiO$_2$/PrSO$_3$H in previous chapter. The catalyst can be re-cycled and re-used up to eight times without deactivation of the active sites, with overall superior functionality, significantly improved process conditions and higher tolerance to FFA as compared to other reported metal oxide catalysts. Moreover, XRD results confirmed that the amount of SO$_4^{2-}$ species in the solid acid catalyst slowly decreased with re-use after eight cycles under optimised conditions, but the spent catalyst can be regenerated, using sulphuric acid solution, and re-used up to 5 cycles without deactivations. Finally, the produced biodiesel was analysed according to the ASTM and EN standards and the specifications were within acceptable biodiesel limits according to the ASTM and European Norm standards.

Chapter 6

SO$_4^=$/Fe.Al.TiO$_2$ catalyst

This chapter begins with an introduction to issues of catalyst separation and its solutions. A detailed characterisation of synthesised novel magnetic solid super acid catalyst is also provided. Catalytic performance, stability and reusability are also discussed.

CHAPTER SIX

6. Synthesis, characterisation and application of SO₄⁼/Fe.Al.TiO₂ catalyst

6.1 Introduction

Solid acid catalyst design has received considerable attention and become a main feature of biodiesel production from cheap feedstocks. This is because solid acid catalysts can simultaneously perform esterification of FFAs and transesterification of triglycerides without (1) soap formation, (2) corrosion of the reactors, (3) quenching steps, and (4) neutralisation of by-products. They also allow for process intensification via continuous biodiesel production. More importantly, the potential recovery and reusability of these catalysts from the (trans)esterification reaction make them preferable for industrial biodiesel production [40, 549, 550]. Numerous synthetic routes are emerging for the preparation of solid acid catalysts for different applications [49, 101, 275, 304, 354, 356, 357, 362, 363, 366, 375, 385, 515, 516, 551-553]. Sulfated metal oxides have been recently used as typical solid super acid catalysts for the (trans)esterification process and in Chapter Five the synthesis of a novel titanium sulphate oxide [Ti(SO$_4$)O] catalyst for the (trans)esterification of used cooking oil (UCO) to form biodiesel has been reported. The addition of sulphate groups into metal oxides mainly enhance the Brønsted acidity property and catalytic activity [94, 554, 555]. However, low surface area and/or difficulty in the separation process of solid acid catalysts are the main drawbacks [487, 509, 516, 553, 556]. Some researchers have reported that the presence of magnetic properties in catalysts increases their re-usability by enabling fast recovery with little loss using external magnetic fields [49, 486, 500, 557, 558]. Magnetic properties in solid acid catalysts are an excellent approach for separating the catalyst from the reaction media but the surface of magnetic oxide materials are unstable under acidic conditions, being very sensitive compared to titania, and the particles can be easily aggregated into large clusters due to anisotropic dipolar interactions, which result in loss of their catalytic activity [559, 560]. Several methods have been introduced to overcome this issue, including a layer-by-layer coating of the surface with different metal oxides and polymers [509, 552, 553]. Therefore, it is necessary to develop a novel magnetic solid super acid material as a potential catalyst candidate that could fulfil all requirements for the industrial (trans)esterification process. In this chapter, we report, for the first time, the design of a multifunctional magnetic solid acid [$SO_4^=$/Fe-

Al-TiO$_2$] catalyst for the production of biodiesel from UCO. Characterisation and application of the designed magnetic solid acid catalyst for biodiesel production via (trans)esterification of UCO are investigated because, as yet, there is no single information available on $SO_4^=$/Fe-Al-TiO$_2$ catalyst.

6.2 Results and discussion

Figure 6.1 shows the proposed diagrammatic sketch for the designed $SO_4^=$/Fe-Al-TiO$_2$ solid acid catalyst via different methods.
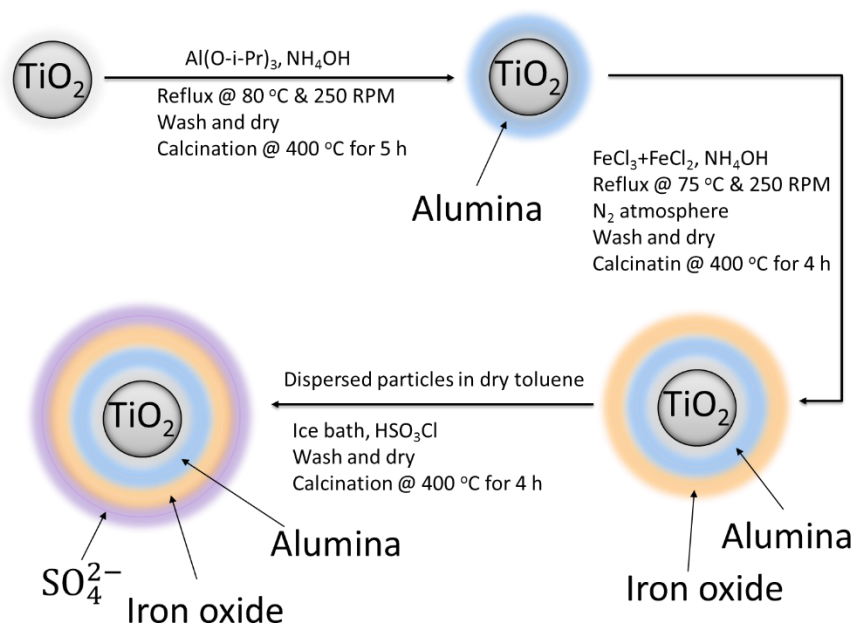
Figure 6.1 Proposed schematic diagram for synthesised SO$_4^=$/Fe-Al-TiO$_2$ catalyst

The first stage was doping of a high amount of alumina in the presence of NH$_4$OH, which can be covalently bonded to the free O-H at the surface of titania nanoparticles in order to increase the surface area of the catalyst support. This was followed by the coating/deposition of iron oxide on the surface of Al-TiO$_2$ via chemical co-precipitation of Fe^{2+} and Fe^{3+} ions in basic solution under nitrogen atmosphere in order to make the catalyst magnetic and easy separate from the reaction medium. Finally, sulphate groups was introduced to the surface of the synthesised catalyst support via impregnation method from chlorosulfonic acid. Different experiments were carried out to investigate the crystal structure, morphology, particle size distribution, acidity, magnetisation and stability of the synthesised magnetic catalyst.

6.2.1 Crystal structure

XRD was used to characterise the crystal structure of the synthesised $SO_4^=$/Fe-Al-TiO$_2$ solid super acid catalyst. The XRD patterns of the sample have been indexed and matched with JCPDS-ICDD as shown in Figure 6.2. It can be clearly seen that the main observed diffraction XRD peaks confirm the presence of rhombohedral iron oxide [rhombohedral hematite (α-Fe$_2$O$_3$), JCPDS-ICDD: 01-076-4579], rhombohedral aluminium sulphate [millosevichite, JCPDS-ICDD: 00-042-1428] and tetragonal titanium dioxide [anatase, JCPDS-ICDD: 04-006-9240; rutile, JCPDS-ICDD: 01-076-9000] in the crystal structure of $SO_4^=$/Fe-Al-TiO$_2$ catalyst. The sharp diffraction XRD peaks indicated good crystallinity of synthesised catalyst. The Rietveld refinement method for calculation of the percentages of each phase shows 48% of aluminium sulphate, 4.8% of TiO$_2$ anatase, 16.5% of TiO$_2$ rutile and 30.7% of α-Fe$_2$O$_3$ phase are present.
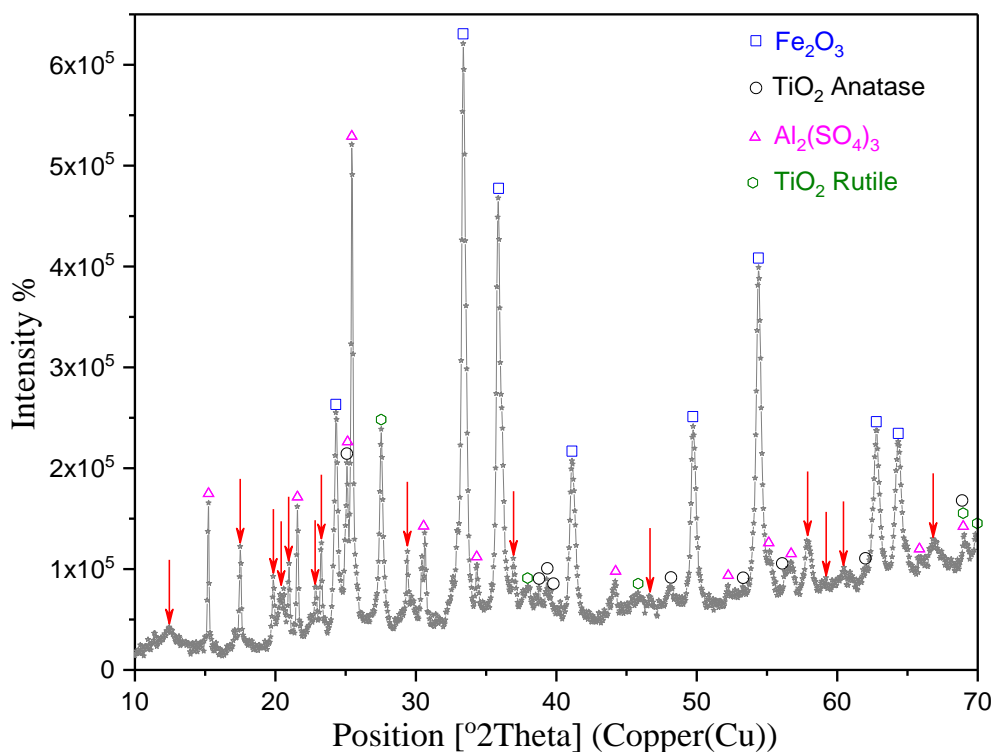
Figure 6.2 Powder XRD profile for SO$_4^=$/Fe-Al-TiO$_2$ catalyst at room temperature.

However, the XRD patterns show some unknown (non-recognisable) peaks as labelled in red arrows (see Figure 6.2). This might be due to some new phase/structure formed through the

preparation process. Furthermore, it could be some element involved in the crystal structure as dopant which would change the structure factor of the crystal giving rise to new peaks. More studies need to be carried out, using high resolution XPS, to investigate the observation/formation of extra diffraction peaks in the future work.

The crystallite sizes and d-spacing values of the 100% intensity peak for each phase from the XRD for synthesised catalyst are summarised in Table 4.2. The average crystal size was 47.33 nm.

Table 6.1 Summary of crystallite sizes and d-spacing values for $SO_4^=$/Fe-Al-TiO$_2$

Sample	XRD peak	°2θ	FWHM	d-spacing, Å	D *, nm
TiO₂	[101] A	25.0947	0.1446	3.5444	56.26
	[110] R	27.537	0.1929	3.2353	42.39
α-Fe₂O₃	104	33.3885	0.2411	2.6805	34.39
Al₂(SO₄)₃	113	25.4565	0.1446	3.4948	56.30

*D: The crystallite size of the 100% relative intensities XRD main peaks for each phases

6.2.2 Surface analysis

6.2.2.1 FT-IR spectroscopy

The FT-IR spectrum of SO_4^{2-}/Fe-Al-TiO$_2$ catalyst is depicted in Figure 6.3. The spectrum shows the characteristic bonds for SO_4^{2-} groups and M-O-M. Several strong peaks centred at 980, 1065 and 1137.5 cm^{-1} are assigned to the S-O stretching vibration in sulphates linked to metal oxides [88, 362, 364, 547]. The peaks at 1430 and 1469 cm^{-1} are attributed to the S=O asymmetric and symmetric, respectively, stretching vibration from the SO_4^{2-} groups in the chelated form (covalently bonded to metal oxides). This indicated the sulphate species present are polynuclear sulphates ($S_2O_7^{2-}$ or $S_3O_{10}^{2-}$) [371]. The formation of polynuclear complex sulphates in the synthesised catalyst could probably be due to the dimerization of chlorosulfonic acid (see Figure 6.4). The sulfonyl (S=O) groups acting as an electron withdrawing groups producing super acid sites to the synthesised catalyst. Several vibrational peaks in the region of 615 to 780 cm^{-1} are related to the Fe-O, Ti-O, Al-O and M-O-M bridging stretching [553, 561]. The peaks in the range of 2350 to 2405 cm^{-1} are related to the C=O vibrational stretching of the absorbed O=C=O from the air during the analysis.
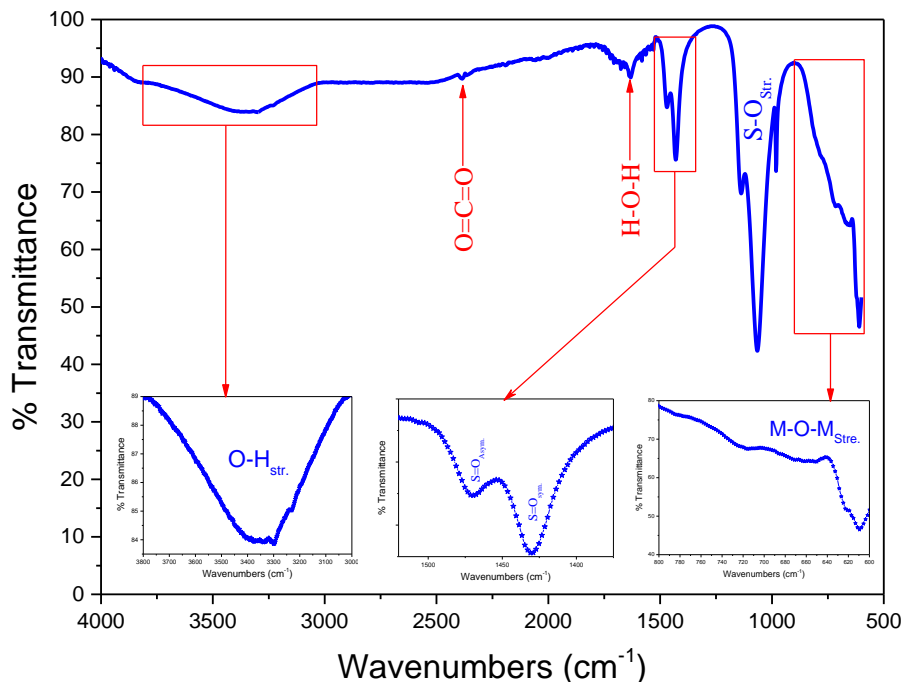
Figure 6.3 FT-IR spectrum for $SO_4^=$/Fe-Al-TiO$_2$ catalyst

The peak in the region of 1630 cm^{-1} is attributed to the vibrational bending of H-O-H molecules adsorbed on the surface of M-O-M. It is worth noting that a very broad absorption peak covered from 3050 to 3800 cm^{-1} corresponded to surface M-O-H vibrational stretching and O-H vibrational stretching of H-O-H molecules adsorbed on the surface of M-O-M [304, 364, 509, 562]. This might be due to the strong hydrophilicity of sulphate groups. The presence of O-H groups on the surface of solid acid catalysts has been reported to enhance catalytic activity [563].
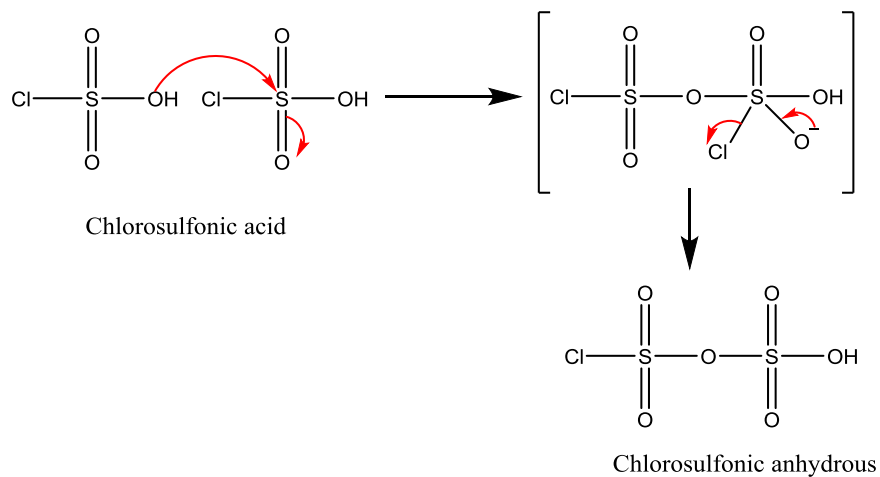
Figure 6.4 Formation of dimer chlorosulfonic anhydrous (electrophilic reagent)

6.2.2.2 Electron microscopy
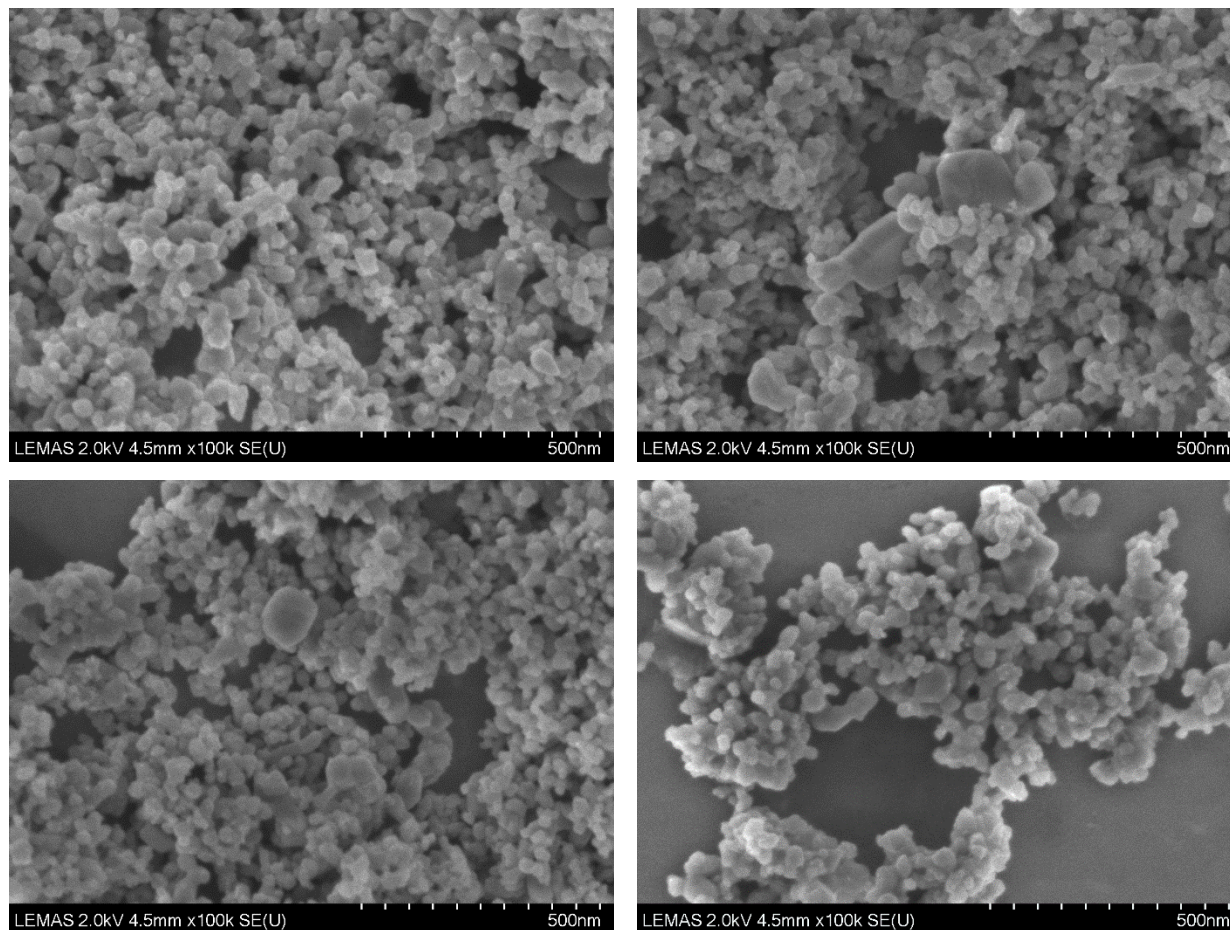
Figure 6.5 SEM micrograph images for Al-TiO$_2$ at 100 K magnification from different spots

The SEM images for synthesised alumina doped titania (Al-TiO$_2$) at magnification of 100 K are displayed in Figure 6.5. It can be clearly seen that the particle sizes enlarged with irregular morphology and size distributions. This was most probably due to the Ostwald ripening phenomenon observation from direct coalescence of TiO$_2$ NPs (resulting in particle growing in size and dimensioning numbers) and/or the incorporation of alumina into TiO$_2$ NPs. In order to get the detailed information about the aforementioned explanations, TEM for the Al-TiO$_2$ sample was carried out. The TEM images at different magnifications of synthesised Al-TiO$_2$ NPs (see Figure 6.6 (a)) show mainly tetragonal and hexagonal shapes. The remaining particles have irregular shapes. From HR-TEM, the exposure of [001] facets appear clearly in the anatase truncated octahedron crystal structure. The particle size distributions for synthesised NPs from different HR-TEM images are presented in histogram (see Figure 6.6 (b)). The average particle

size of Al-TiO$_2$ NPs was ~27.14 nm. The aggregation of Al-TiO$_2$ NPs in HR-TEM (inset Figure 6.6 a) formed a 3D mesoporous network due to the orientation attachment mechanism.
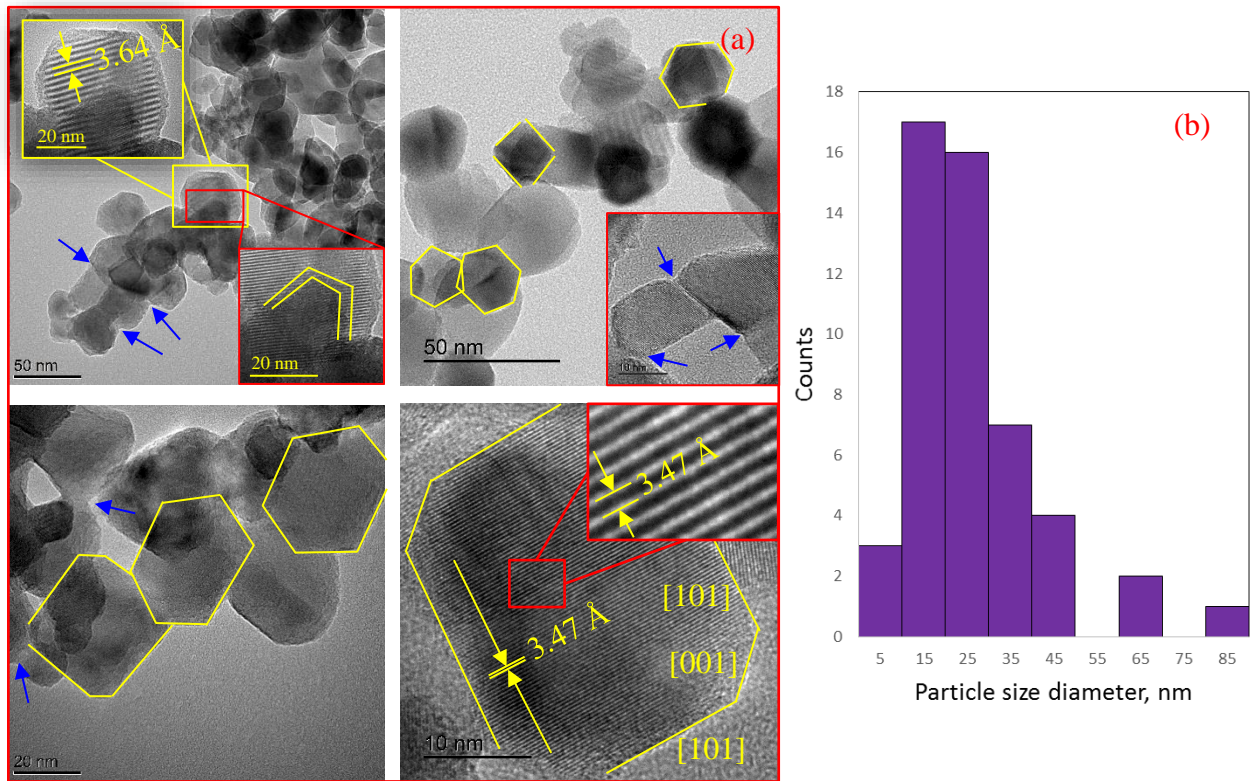
Figure 6.6 (a) TEM images at different magnifications and (b) a histogram for Al-TiO$_2$.
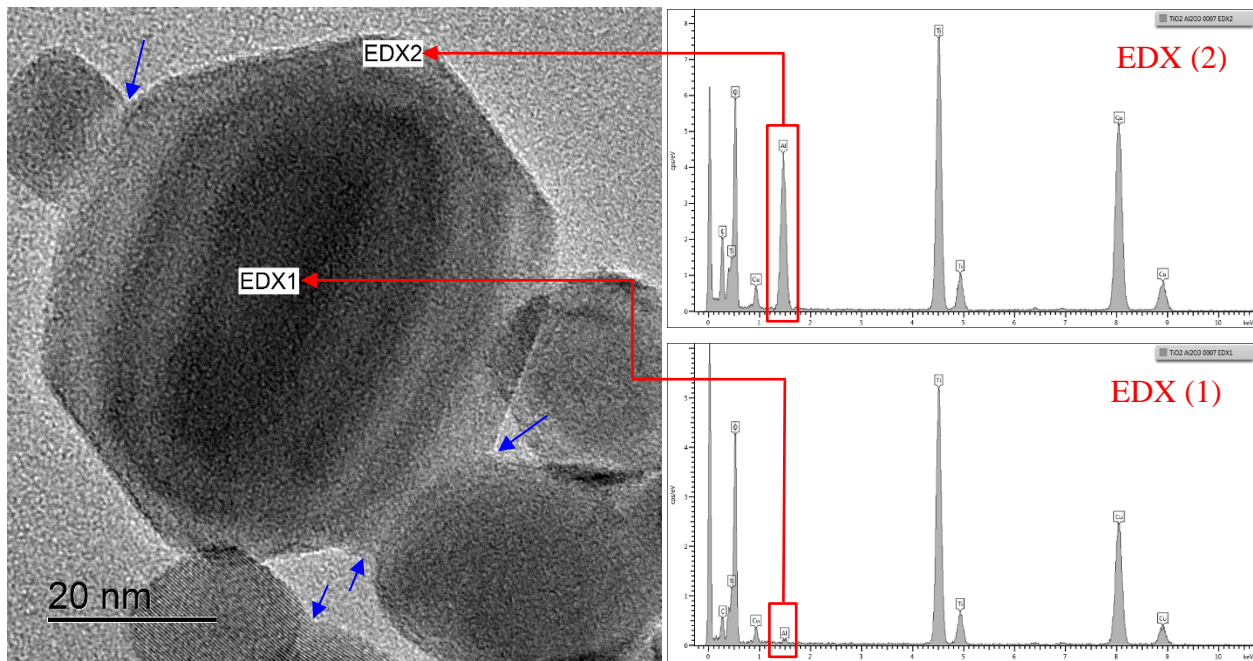
Figure 6.7 TEM-EDS spectra for a single particle shows the doping of alumina into the TiO$_2$ NPs

The TEM-EDS was carried out to identify the location of alumina in the synthesised Al-TiO$_2$ NPs. Figure 6.7 shows the EDS spectra in certain selected areas (edge and centre) for the single particle of alumina doped titania nanoparticles. The EDS (1) clearly shows the presence of alumina in the centre of the titania particle, which confirms the successful impregnation of alumina into the TiO$_2$ NPs to form a titanium aluminium oxide (Al-TiO$_2$). HR-TEM inset (see Figure 6.6 (a)) also shows the core TiO$_2$ surrounded by a layer of alumina (amorphous) ~3 nm thick.

The SEM micrograph images of synthesised Fe-Al-TiO$_2$ NPs at different magnifications from various spots of the sample are shown in Figure 6.8. There was no morphology of synthesised magnetic catalyst but it could be clearly seen the agglomeration of particles has led to form a cluster within a few microns. This was most probably because the prepared super magnetic Fe$_3$O$_4$ coated with Al-TiO$_2$ and treated at 400 ^{o}C, may be transferred to antiferromagnetic α-Fe$_2$O$_3$ in the synthesised Fe-Al-TiO$_2$ [552, 553]. In order to further confirm the formation of α-Fe$_2$O$_3$ coated Al-TiO$_2$ hybrid, TEM analysis was conducted for the synthesised sample.
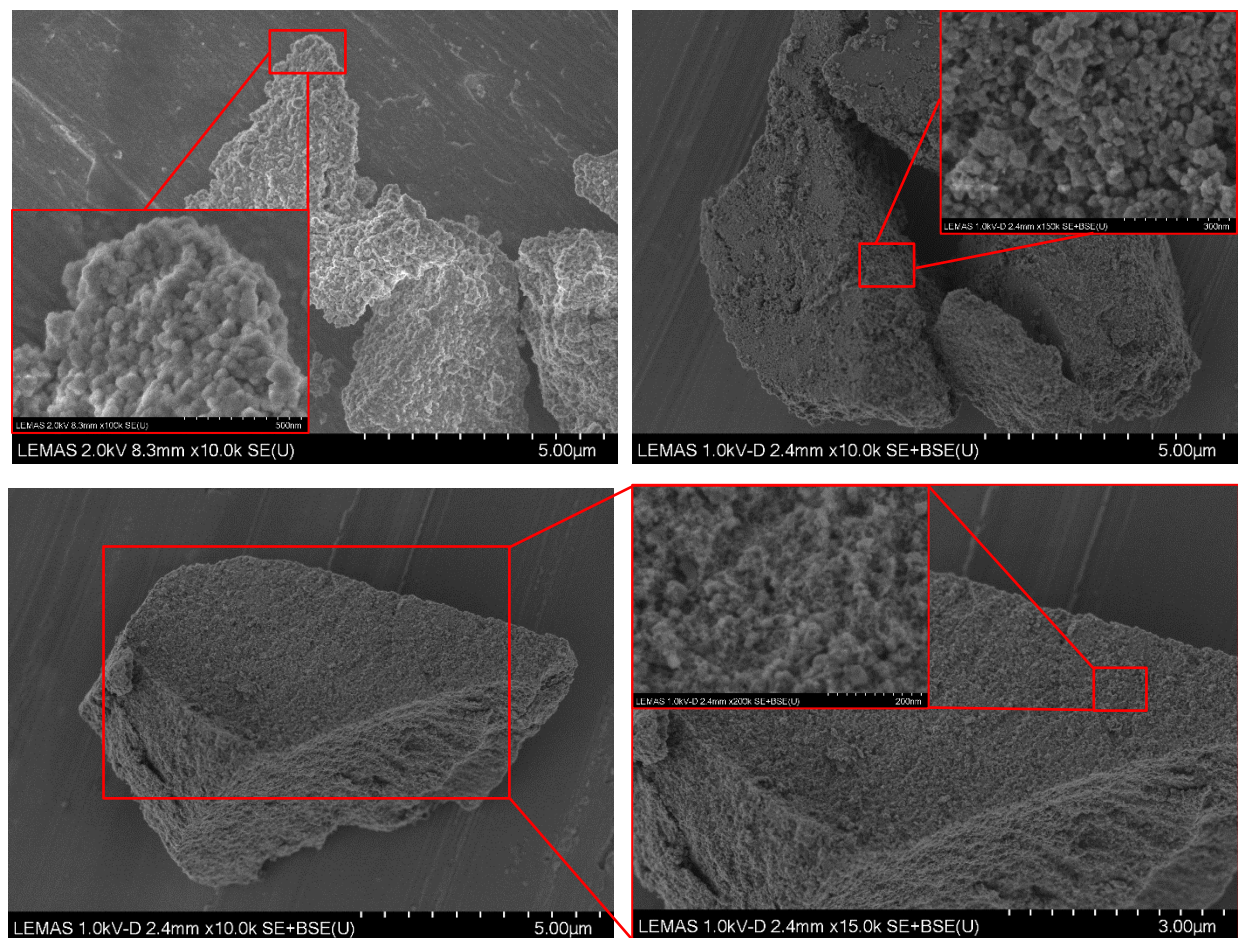
Figure 6.8 SEM micrograph images for synthesized Fe-Al-TiO$_2$ catalyst support.
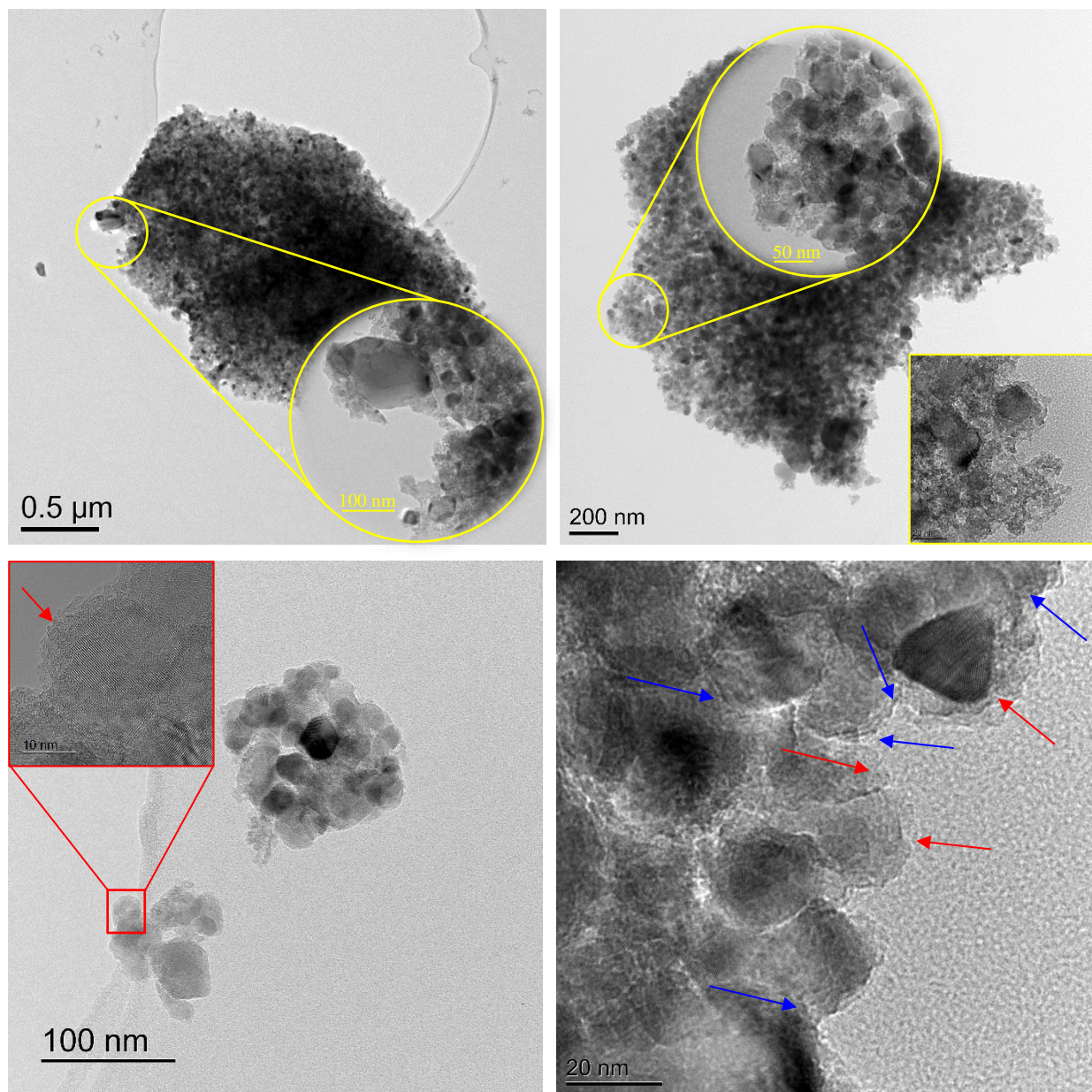
Figure 6.9 TEM images at different magnifications for synthesized Fe-Al-TiO$_2$ hybrid.

Figure 6.9 shows the TEM images at different magnifications for synthesised Fe-Al-TiO$_2$ hybrid and the inset SAED pattern corresponding to TEM image at 20 nm. The tiny iron oxide nanoparticles (smaller than Al-TiO$_2$ NPs in size) were clearly surrounded to the surface of the Al-TiO$_2$ NPs causing the change of morphologies and disordered/rough surface in most of the Fe-Al-TiO$_2$ particles. This might be due to the crystal growth (called oriented attachment mechanism) leading to the formation of new nanoparticles with irregular shapes by consuming primary nanocrystals [564]. It is also important to mention that the particles stick to each other and form a

205

large cluster due to the magnetic characteristic of Fe-Al-TiO$_2$ particles. The iron oxide NPs heterogeneously coated the surface of Al-TiO$_2$ according to the TEM-EDS and EDS-mapping. The quantification of elements for Fe-Al-TiO$_2$ hybrid was extracted from the EDS spectrum (see Figure 6.10) whilst the elemental distribution is displayed in EDS-mapping (see Figure 6.11).

Element	Wt%
O	36.94
Ti	32.60
Al	16.51
Fe	13.95
Total:	100.00
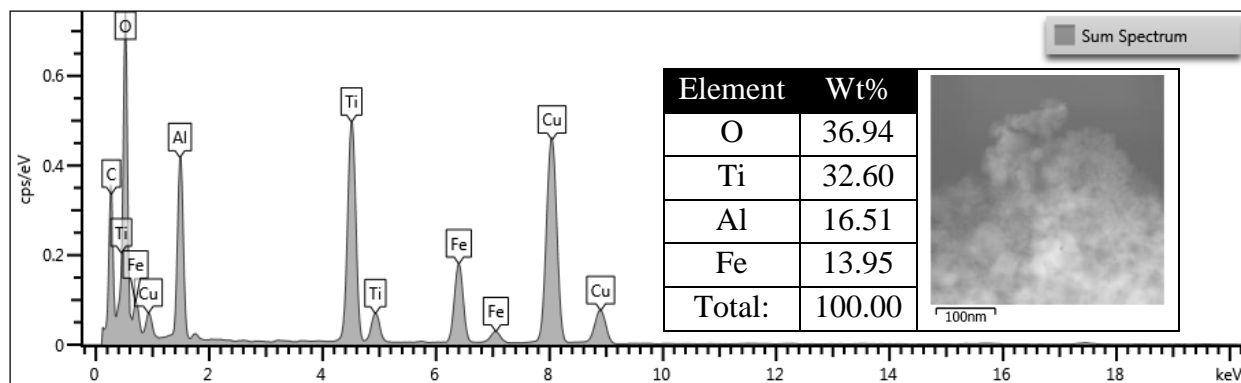
Figure 6.10 TEM-EDS for synthesised Fe-Al-TiO$_2$ hybrid (extra peaks of C and Cu were observed due to the carbon-coated copper TEM grid used during sample analysis)
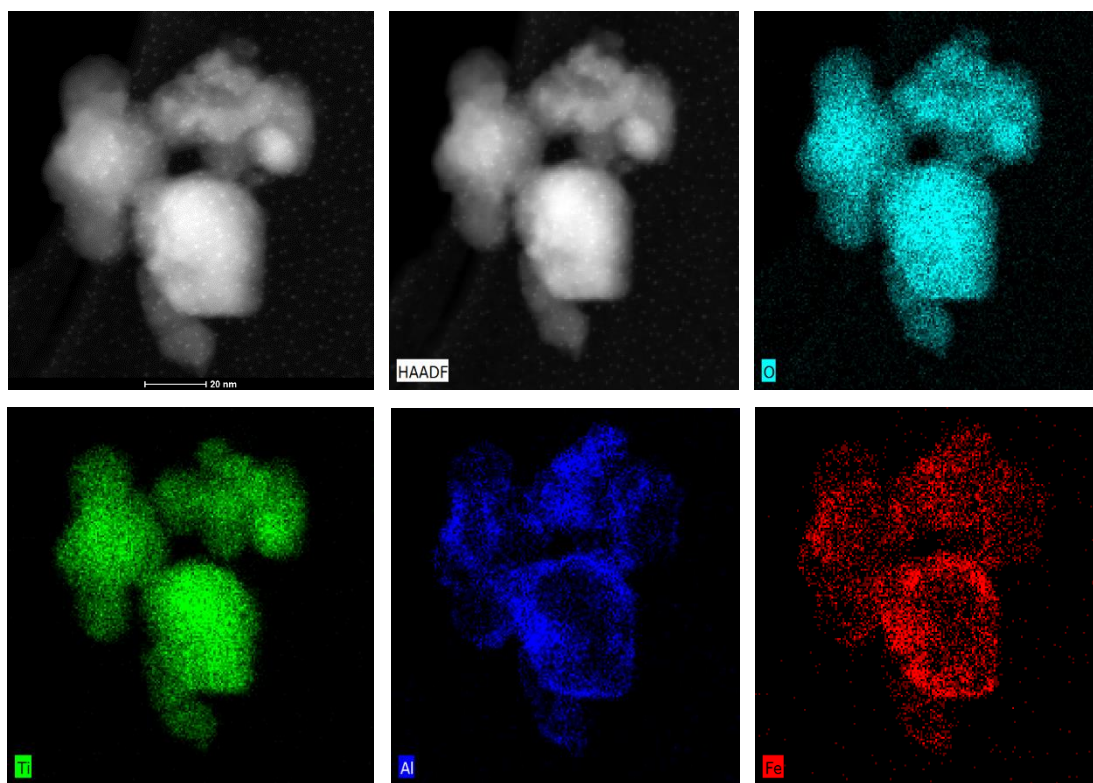
Figure 6.11 TEM EDS-mapping on Titan 300 TEM for Fe-Al-TiO$_2$ hybrid. The EDS-mapping images show the core-shells NPs with clear distributions of Al and Fe on the synthesised hybrid.

It can be clearly seen that the iron oxide particles deposition at the surface of Al-TiO$_2$ NPs via co-precipitation method was followed by calcination of the formed particles, which led to a layer-by-layer assembly (see Figure 6.11). However, the surface of iron oxide doped Al-TiO$_2$ is, as previously mentioned, very sensitive to agglomeration forming a sub- to few microns clusters (see Figure 6.12). Therefore, the surface of Fe-Al-TiO$_2$ hybrid was functionalised with sulfonic acid groups to overcome this issue, increasing the surface acidity of the synthesised Fe-Al-TiO$_2$ hybrid for biodiesel production from cheap feedstocks (see Figure 6.13).
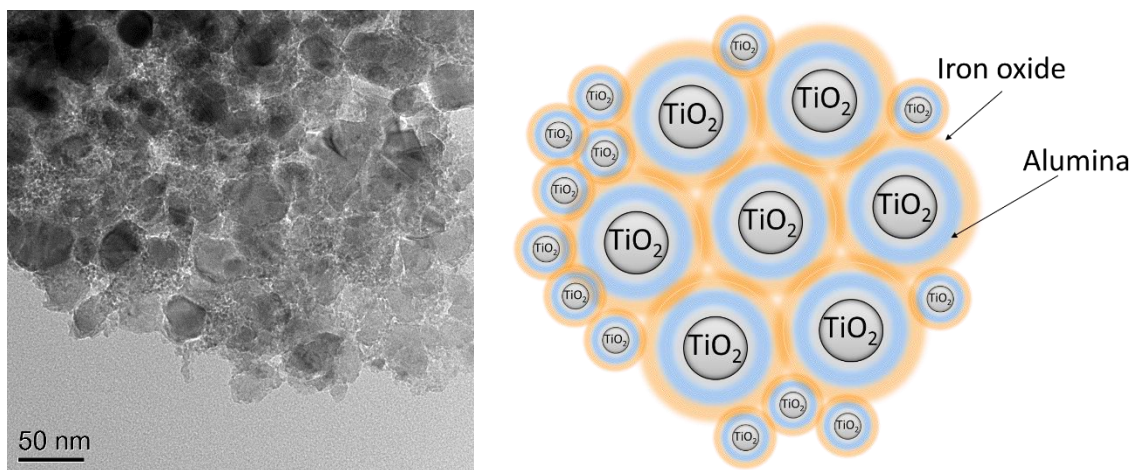
Figure 6.12 TEM image shows the agglomeration of Fe-Al-TiO$_2$ hybrid
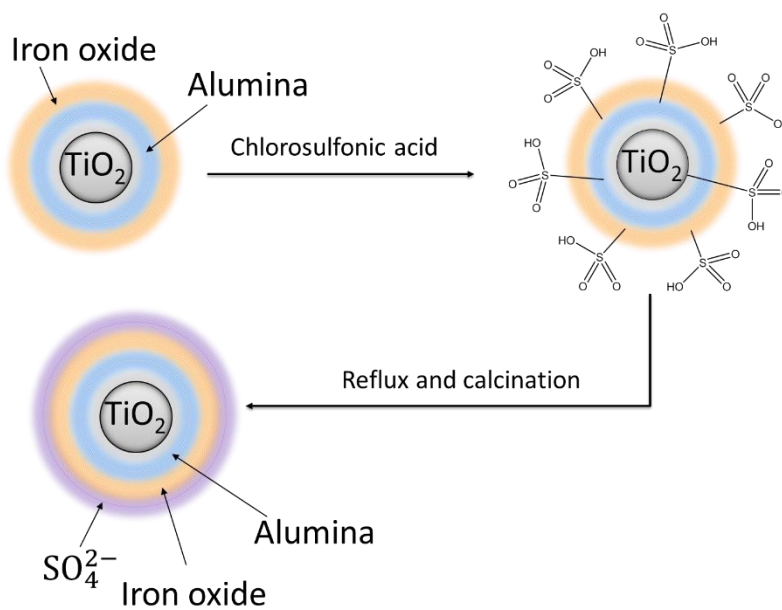
Figure 6.13 Proposed schematic surface functionalisation/doping of SO$_4^=$ into Fe-Al-TiO$_2$

In order to better understand this concept, electron microscopic (SEM and TEM) analyses of the SO_4^{2-}/Fe-Al-TiO$_2$ solid acid catalyst were undertaken. The SEM micrograph images for the solid acid catalyst are shown in Figure 6.14.
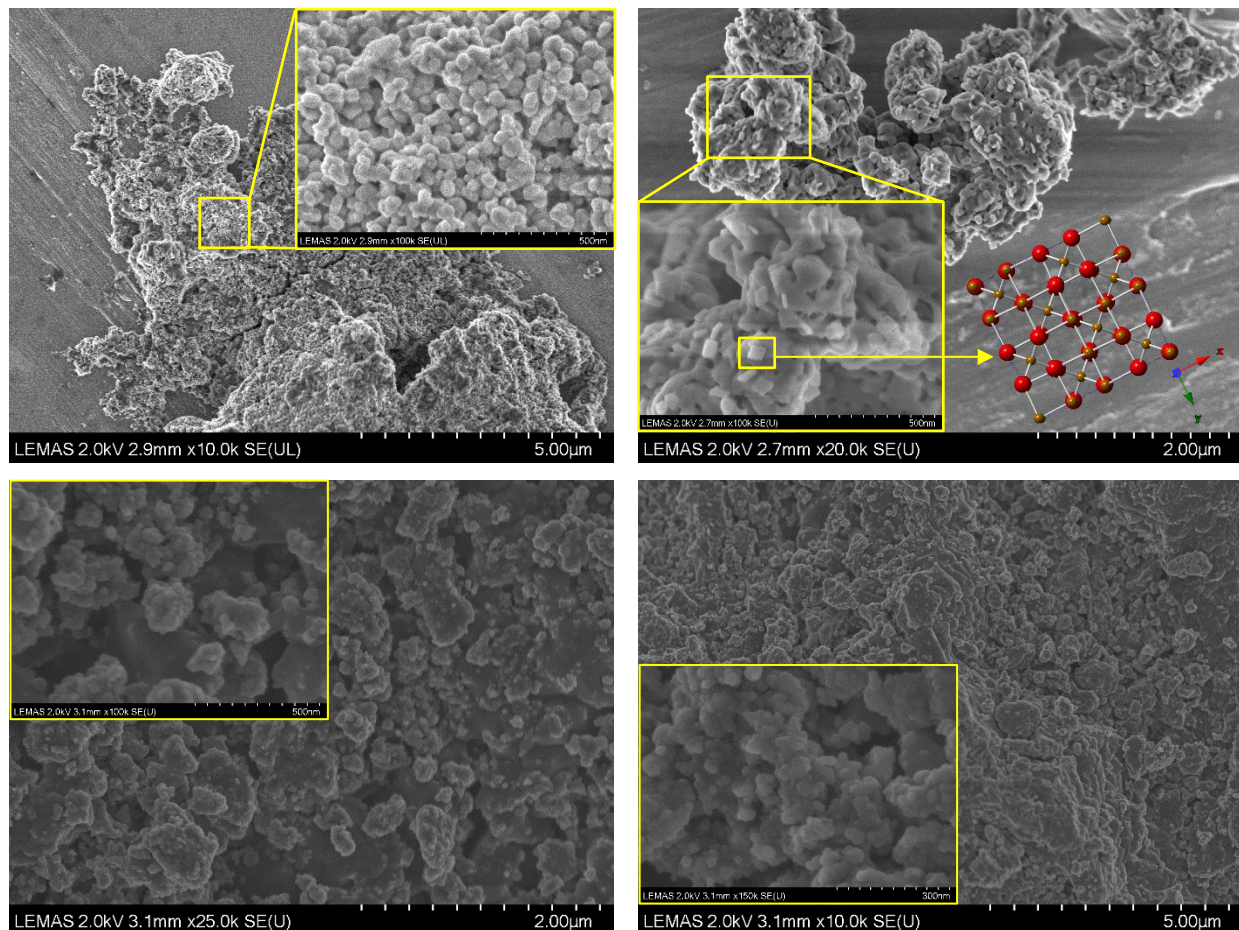
Figure 6.14 SEM images at different magnifications for SO$_4^=$/Fe-Al-TiO$_2$ catalyst

As can be seen from the SEM images, the synthesised SO_4^{2-}/Fe-Al-TiO$_2$ solid acid catalyst has different morphologies with non-uniform particle size distributions. The sulfonating of the Fe-Al-TiO$_2$ hybrid clearly changed its morphology by forming a rhombohedral crystal (agreeing with the XRD result in Figure 6.2) with the remaining other non-clear shapes due to particle agglomeration. It also reveals that larger particles with smoother surfaces formed in comparison with the Fe-Al-TiO$_2$ hybrid (see inset Figure 6.14). To get more detailed information about a new morphology presence in the synthesised SO_4^{2-}/Fe-Al-TiO$_2$ solid acid catalyst, TEM analysis was performed. The particle size distributions for prepared catalyst were clearly seen in the enlargement of catalyst as displayed in Figure 6.15.
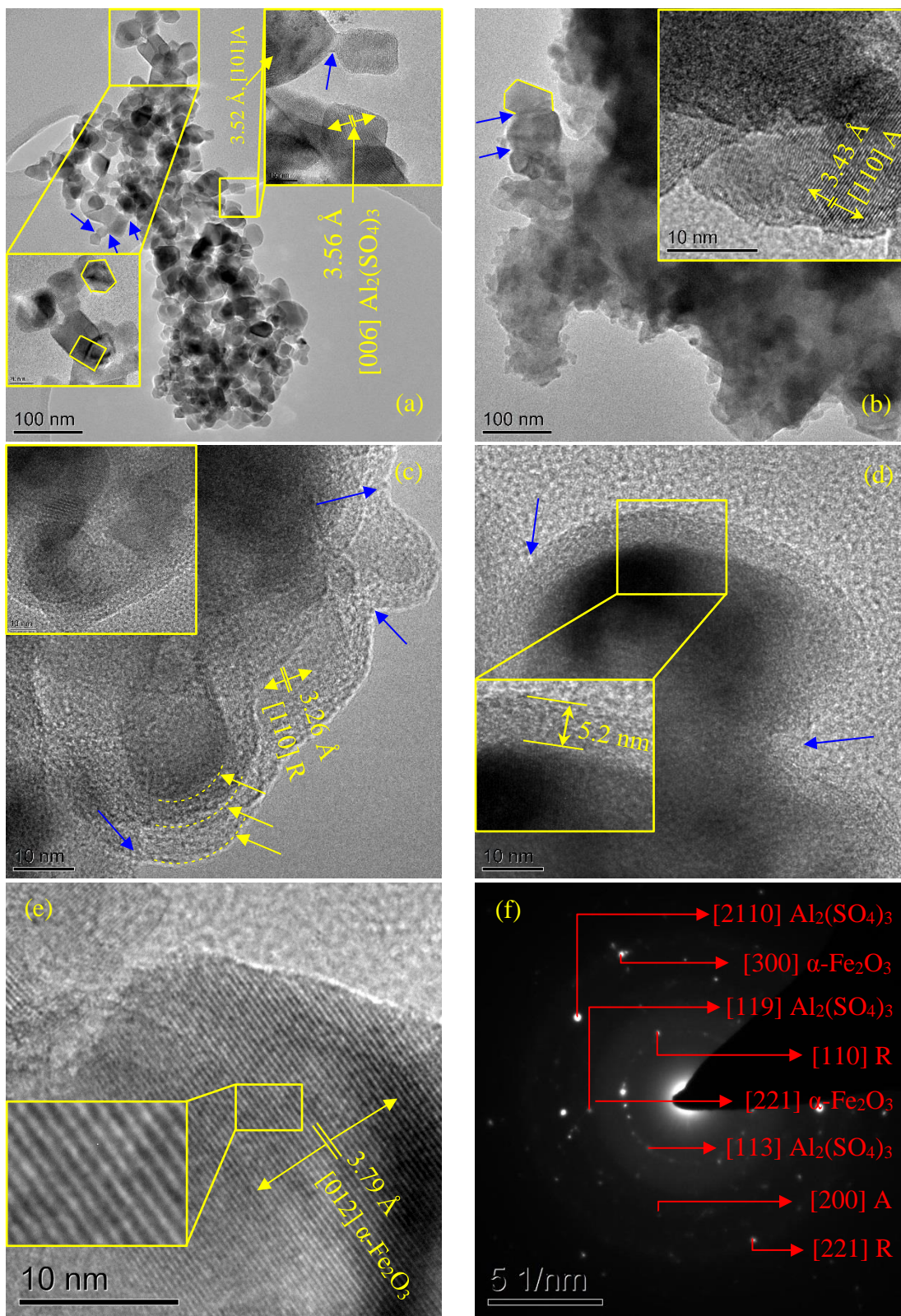
Figure 6.15 TEM images at different magnifications (a, b, c, d), HR-TEM (e) and SAED (f) for $SO_4^=$/Fe-Al-TiO$_2$ catalyst. Blue arrows represent the oriented attachment of NPs

TEM investigation revealed that the synthesised solid acid catalyst consists of different morphologies, i.e. rhombohedral, hexagonal, etc. for different crystal structures, as shown in Figure 6.15. HR-TEM (see Figure 6.15 d) shows the homogenous shell dense of the nanoparticle was ~5.2 nm, which is surrounded the main nanoparticles. Figure 6.15 (c) shows the clear layer by layer morphologies of the synthesised SO_4^{2-}/Fe-Al-TiO$_2$ magnetic solid acid catalyst. The layer by layer decoration can be clearly seen as a smooth and dense surface surrounding the main particles. Surprisingly, some small aggregates of particles were still present in the catalyst as displayed in Figure 6.15 (b). This was most probably due to the presence of large amounts of hydrophilic groups on the surface of particles. The HR-TEM images [see Figure 6.15 inset (a), inset (b), c and e] show the lattice fringes of the SO_4^{2-}/Fe-Al-TiO$_2$ catalyst. From the inset of Figure 6.15 (a), the spacing between two lattice places was 0.356 nm, assigned to the *d*-spacing value for the rhombohedral millosevichite [006] plane. Figure 6.15 inset (b) confirmed the presence of facets [110] in the tetragonal anatase TiO$_2$. The lattice fringes in figure 6.15 (c) and (e) with interplanar spacing of 0.326 and 0.379 nm, attributing to [110] and [012] lattice planes of tetragonal rutile TiO$_2$ (ICDD: 01-076-9000) and rhombohedral hematite α-Fe$_2$O$_3$ (ICDD: 01-076-4579), respectively. The SAED pattern reveals that the core-shell structure of the synthesised magnetic solid acid catalyst contain TiO$_2$ (anatase and rutile phases), α-Fe$_2$O$_3$ and Al$_2$(SO$_4$)$_3$. This result is in accordance with the results of XRD pattern. Figure 6.15 (f) shows discontinuous diffraction rings with some set of brightness spotty dots. This indicates the presence of amorphous fraction in the synthesised catalyst and most probably due to the presence of sulphate groups in the main structure. The brightness spotty dots can be indexed as [110] and [221] diffraction planes of tetragonal rutile TiO$_2$ (ICDD: 01-076-9000); [200] correspond to tetragonal anatase TiO$_2$ (ICDD: 04-006-9240); [221] and [300] assign well to that of rhombohedral hematite α-Fe$_2$O$_3$ (ICDD: 01-076-4579); and the other spotty dots [113], [119] and [2110] match well to that of rhombohedral millosevichite Al$_2$(SO$_4$)$_3$ (ICDD: 00-042-1428). It can also be seen from TEM images that some crystals collided and coalesced in the same crystal orientation during the crystal growth as indicated by blue arrows (see Figure 6.15).

The TEM-EDS confirmed that the synthesised SO_4^{2-}/Fe-Al-TiO$_2$ solid acid catalyst indicate the existence of O, S, Fe, Al and Ti elements. The overall EDS spectrum for the catalyst sample is given in Figure 6.16. This proved the presence of sulphate groups in the synthesised solid acid catalyst. The distribution of sulphur element in the synthesised SO_4^{2-}/Fe-Al-TiO$_2$ catalyst was

further confirmed by EDS-mapping. TEM EDS-mapping provided evidence of uniform decoration and good spread (dispersity) of sulphate groups on the Fe-Al-TiO$_2$ hybrid nanoparticles as shown in Figure 6.17.
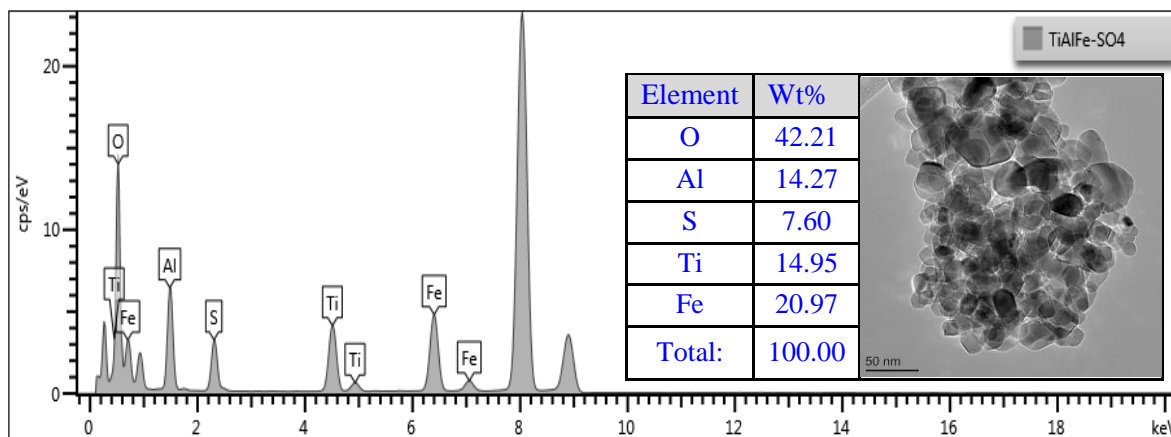
Figure 6.16 TEM-EDS for synthesised SO$_4^=$/Fe-Al-TiO$_2$ solid acid catalyst
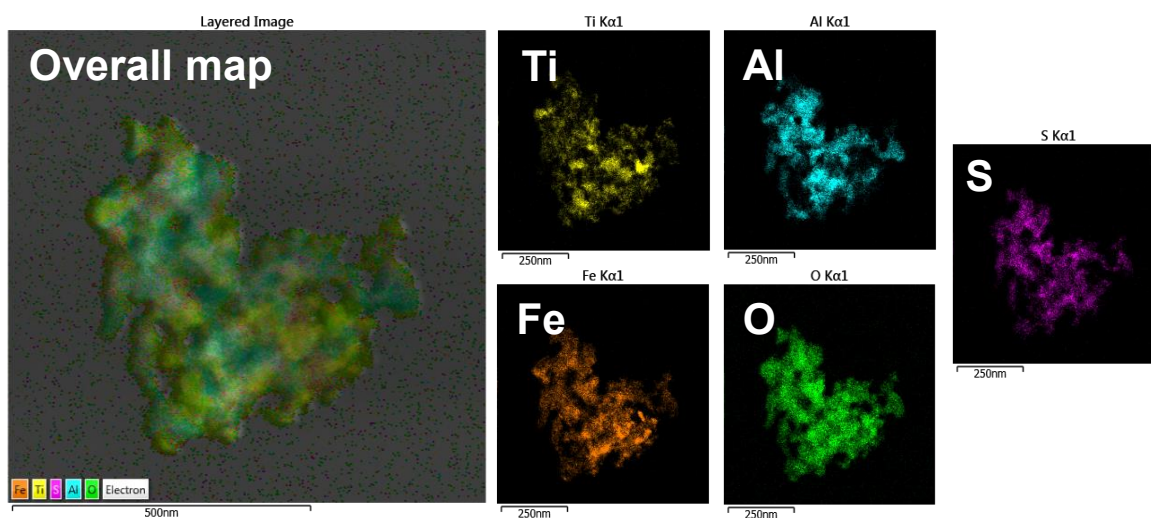
Figure 6.17 TEM EDS-mapping for synthesised SO$_4^=$/Fe-Al-TiO$_2$ solid acid catalyst. The mapping images indicate chlorosulfonic acid clearly functionalised Fe-Al-TiO$_2$ hybrid and some sulphate groups SO$_4^=$ and S$_2$O$_7^=$/ S$_3$O$_{10}^=$) located on the surface of synthesized catalyst.

6.2.2.3 Surface area and porosity

Figure 6.18 displays the nitrogen adsorption and desorption isotherms and corresponding pore size with pore volume distributions for TiO$_2$ NPs, Al-TiO$_2$, Fe-Al-TiO$_2$ and SO$_4^{2-}$/Fe-Al-TiO$_2$ catalysts. It can be seen that the adsorption isotherm of all samples were type IV, which is a characteristic of mesoporous - micro-porous materials. Furthermore, all samples exhibited one hysteresis loop

with an increase in relative pressures (P/P$_0$), resulting to the formation of capillary condensation of nitrogen within mesoporous sizes (see Figure 6.18). The observed hysteresis loops in Figure 6.18 (a, b, and d) corresponded to type I whilst the hysteresis loop in Figure 6.18 (c) assigned to type II, according to IUPAC standard [424].
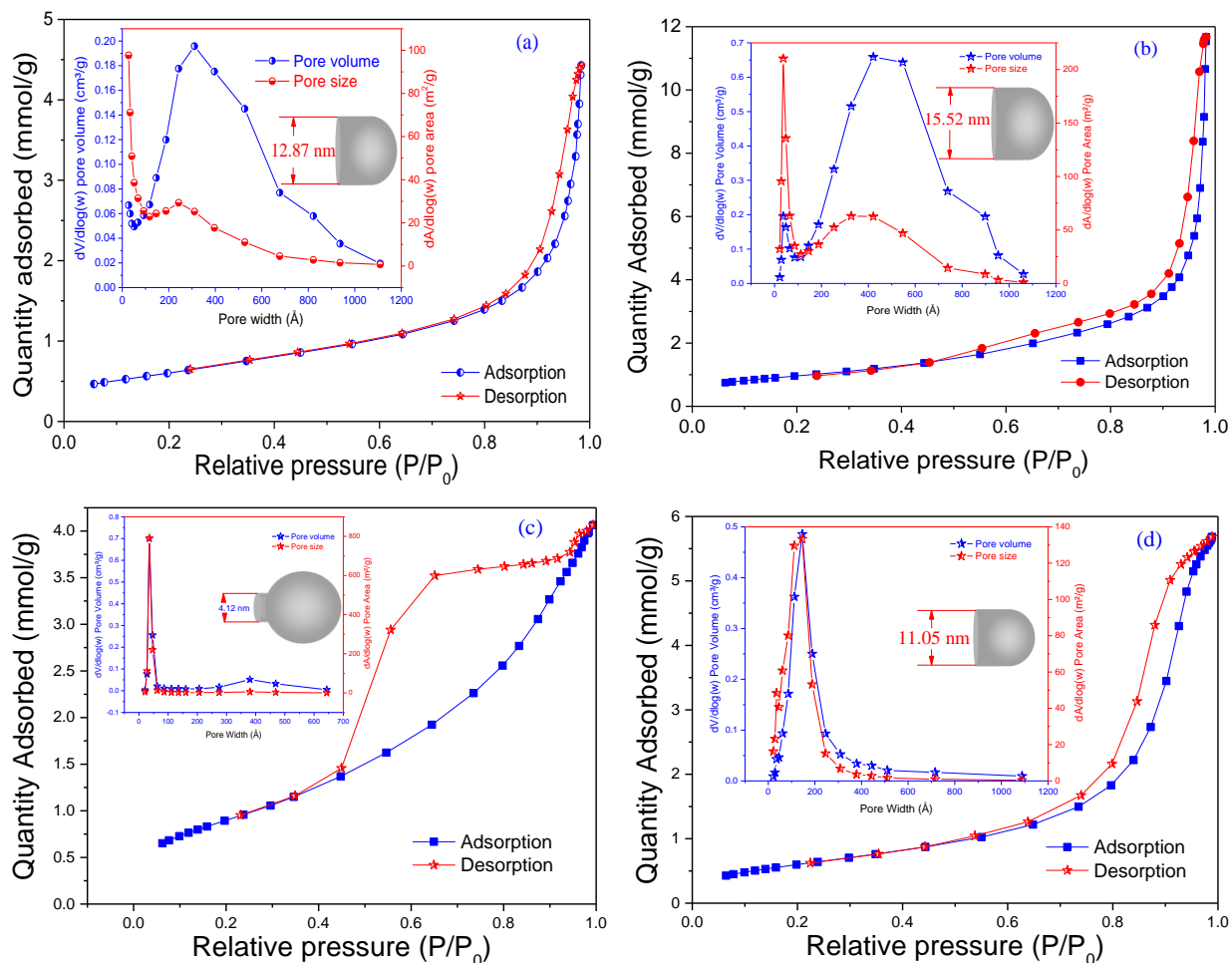
Figure 6.18 N$_2$ adsorption-desorption isotherms and total pore volumes with mean pore sizes (inset) for catalysts (a) TiO$_2$, (b) Al-TiO$_2$, (c) Fe-Al-TiO$_2$ and (d) SO$_4^=$/Fe-Al-TiO$_2$

Massive change in the sorption isotherm curve for Fe-Al-TiO$_2$ can be seen in Figure 6.18 (c). This might be because of the presence of open-blocked mesoporous in the same sample [565] and limit the number of lattice units - this arise change the solid-state chemistry of the material. The sulfonating of Fe-Al-TiO$_2$ hybrid to form SO$_4^{2-}$/Fe-Al-TiO$_2$ magnetic solid acid catalyst considerably reduced the surface area (see Table 6.2). The same observation was reported by Alaba et al. [566] for sulfonating of faujasite zeolite catalyst. The addition of iron oxide to the Al-TiO$_2$

hybrid structure led to a narrow distribution of pores centred ~ 4.12 nm (calculated from the BJH model) as shown in the inset Figure 6.18 (c). Nonetheless, the pore size distribution in other samples exhibited much broader (11-15.5 nm) as shown in insets of Figure 6.18 (a, b and d).

It is also important to mention that the doping of alumina into mixed phase of commercial titania resulted in a massive enhancement of the surface area (from 48.64 to 77.91 m^2/g). The addition of middle layer between the magnetic and titania layers is also crucial from a photocatalytic application point of view [553]. The detailed BET surface area, average pore size, total pore volume, types of adsorption isothermal and hysteresis loop from the BET and BJH analyses for TiO_2 NPs, Al-TiO_2 hybrid, Fe-Al-TiO_2 hybrid and SO_4^{2-}/Fe-Al-TiO_2 magnetic solid acid catalyst are presented in Table 6.2. All samples can be classified as mesoporous materials due to their pore size distribution being in the range from 4.1 to 15.5 nm. In the case of Fe-Al-TiO_2 hybrid, the pore size and volume reduced as can be seen in Table 6.2. This could be explained by the fact that the tiny iron oxide nano-particles surrounded Al-TiO_2 hybrid and filled the macropore voids between particles (see Figure 6.12). Moreover, the coating (addition) of iron oxide to the Al-TiO_2 hybrid compromises the crystalline structure for the obtained Fe-Al-TiO_2 hybrid [362]. These tiny iron oxide nanoparticles coated at the surface of Al-TiO_2 most probably blocked the available intrachannel spaces, which might not be allowing the large particles such as TG, to contact with active sites [487]. Furthermore, the sulfonating process of Fe-Al-TiO_2 hybrid revealed the enhancement in pore size and volumes (see Table 6.2).

Table 6.2 Summary of surface area, total pore volume and average pore size for catalysts

Type of catalyst	S_{BET}^a	D_p^b	V_p^c	Adsorption isotherm	Hysteresis loop
TiO_2 NPs	49	12.9	0.16	Type IV	Type I
Al-TiO_2	78	15.5	0.41	Type IV	Type I
Fe-Al-TiO_2	75	4.1	0.14	Type IV	Type II
SO_4^{2-}/Fe-Al-TiO_2	51	11.1	0.20	Type IV	Type I

[a] S_{BET}: BET surface area ($m^2.g^{-1}$) calculated over the relative pressure range 0.05–0.2, [b] D_p: Mean pore size (nm) calculated by applying the BJH model from N_2 desorption isotherm; [c] V_p: Total pore volume ($cm^3.g^{-1}$) was determined at P/P_o =0.983.

6.2.3 Thermal stability

The TGA profiles for TiO_2, Al-TiO_2, Fe-Al-TiO_2 and SO_4^{2-}/Fe-Al-TiO_2 catalysts can be seen in Figure 6.19. It can be clearly seen from TGA curves, that there was a slight weight loss at the beginning of heating to 150 °C for TiO_2, Al-TiO_2 and Fe-Al-TiO_2 samples, ascribing to the physisorbed water molecules at the surface of the catalysts. A further increase in temperature to 900 °C showed no more weight loss in all three samples. This indicates the stability of these catalysts. In the case of magnetic SO_4^{2-}/Fe-Al-TiO_2 catalyst, there were two weight loss regions in the TGA profile (see Figure 6.19). The first weight loss occurred when the sample was heated to 150 °C due to desorption of water molecules absorbed on the surface of the sample [516]. The second major weight loss (~25 wt%) could be clearly seen at around 633 °C continuous up to 900 °C, attributing to the decomposition of sulphate groups from the main catalyst structure. This indicated the synthesised magnetic solid acid catalyst [SO_4^{2-}/Fe-Al-TiO_2] was very stable and it could be easily used in any industrial process up to 630 °C. Other researchers claimed that sulphated metal oxides were decomposed at around 430 °C [371, 516]. It is also worth mentioning that the stability of sulphate groups in the main catalyst structure and/or at the surface of catalysts depends mainly on the calcination temperature, sulphate precursors and catalyst support.
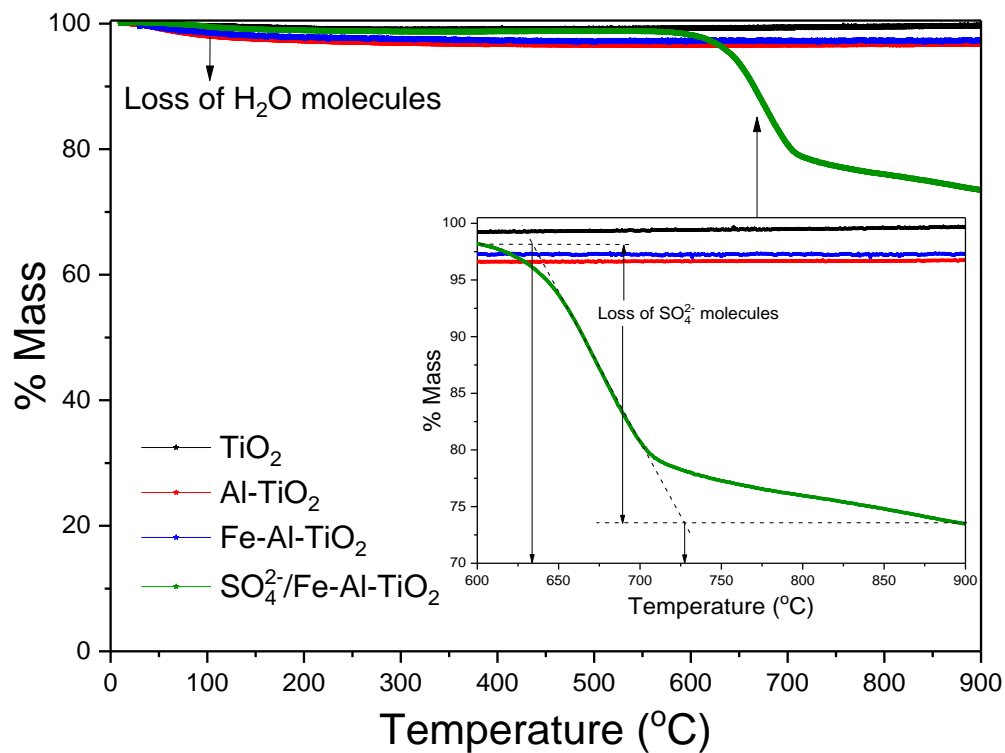
Figure 6.19 TGA profiles for TiO_2 NPs, Al-TiO_2, Fe-Al-TiO_2 and $SO_4^=$/Fe-Al-TiO_2

6.2.4 Surface acidity

DRIFT-pyridine was employed to identify the Brønsted and Lewis acid sites present in TiO_2 NPs, Al-TiO_2 hybrid, Fe-Al-TiO_2 hybrid and SO_4^{2-}/Fe-Al-TiO_2 catalyst. The type and ratio of Brønsted to Lewis acid sites was found from the DRIFT spectra based on the ring vibrational of pyridine in the range of 1400 to 1650 cm^{-1}. The DRIFT spectra for all samples are displayed in Figure 6.20. It can be clearly seen that TiO_2, Al-TiO_2 and Fe-Al-TiO_2 samples have strong Lewis acid sites compared to SO_4^{2-}/Fe-Al-TiO_2 catalyst. Whereas, Al-TiO_2 and Fe-Al-TiO_2 and SO_4^{2-}/Fe-Al-TiO_2 have stronger Brønsted acid sites compared to the initial TiO_2 NPs. The existence modes in all samples at 1445-1446 and 1610 cm^{-1} indicated the presence of coordinated pyridine adsorption on the Lewis acid sites but the modes at 1541 and 1640-1645 cm^{-1} were attributed to the presence of pyridinium ions (Brønsted acid sites) in the materials [362, 364, 365, 510]. The shifting of the stretching frequencies of the sulphate groups vibration from Al-TiO_2 and Fe-Al-TiO_2 and SO_4^{2-}/Fe-Al-TiO_2 indicates stronger interaction between the surface sulphur complex and the adsorbed pyridine molecules. This shifting increases the activity of the catalysts [547]. The mode at 1490 cm^{-1} appeared in all catalyst samples indicating the strong coordination of pyridine and pyridinium ions on the Brønsted and Lewis acid sites, respectively [512]. The ratio of Brønsted to Lewis acid (B/L) sites, extracted from the peak areas of 1541 and 1445 cm^{-1}, for all catalysts are summarised in Table 6.3.
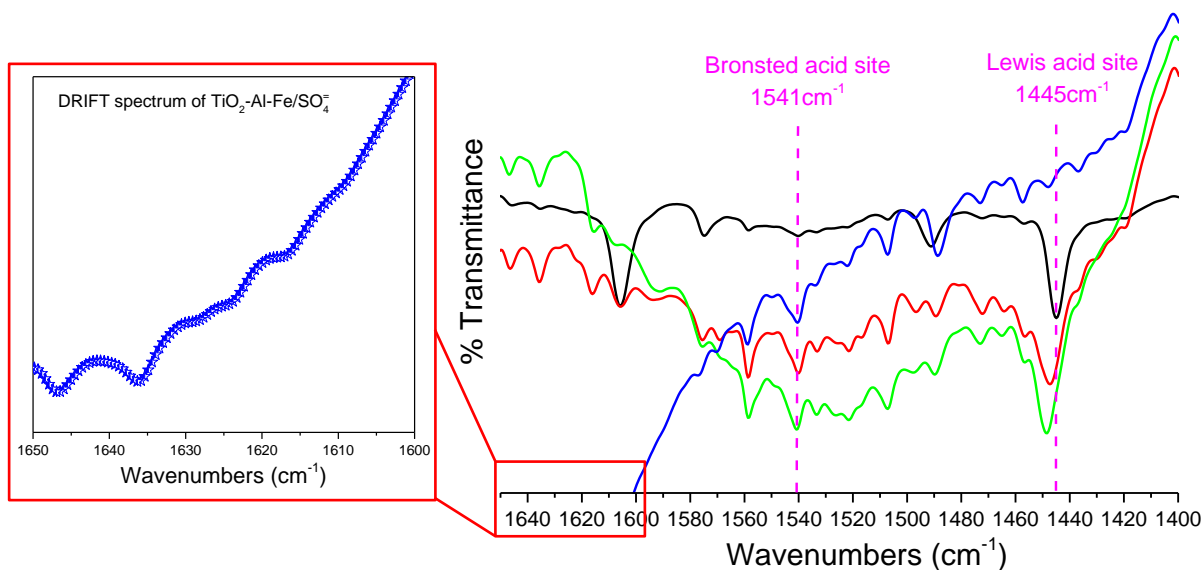
Figure 6.20 DRIFT spectra of TiO_2 (black line), Al-TiO_2 (red line), Fe-Al-TiO_2 (green line) and $SO_4^=$/Fe-Al-TiO_2 (blue line) catalysts

It is also important to mention that the Lewis acid sites in synthesised magnetic solid acid sites almost disappeared after the pyridine titration. Therefore, it might be that the catalyst possesses solely Brønsted acid sites for esterification and transesterification reactions. Detailed kinetic for esterification and transesterification of UCO using this catalyst need to be carried out in the future.

Table 6.3 Summary of B/L ratio and total acidity for all catalyst samples

	TiO$_2$	Al-TiO$_2$	Fe-Al-TiO$_2$	SO$_4^{2-}$/Fe-Al-TiO$_2$
B/L ratio	0.04685	0.3359	0.13	3.583
Total acidity, mmol/g	0.28	---	---	10.31

The quantity of total acidity loading for TiO$_2$ NPs and SO$_4^{2-}$/Fe-Al-TiO$_2$ magnetic solid acid catalysts were performed on the TPD-MS with n-propylamine probe. The results extracted from Figure 6.21 for TiO$_2$ and SO$_4^{2-}$/Fe-Al-TiO$_2$ are present in Table 6.3. It was found that the total acidity for the synthesised magnetic solid acid catalyst compared to TiO$_2$ NPs was 37 times stronger. This was mainly due to the loading of sulphate groups on the Fe-Al-TiO$_2$ hybrid as well as some of this acid loading coming from the acid sites formed by iron oxide or alumina layers [304]. An increase of the total acidity is preferable for cheap materials containing high FFA in the simultaneous esterification of FFA and transesterification of TG to form biodiesel.
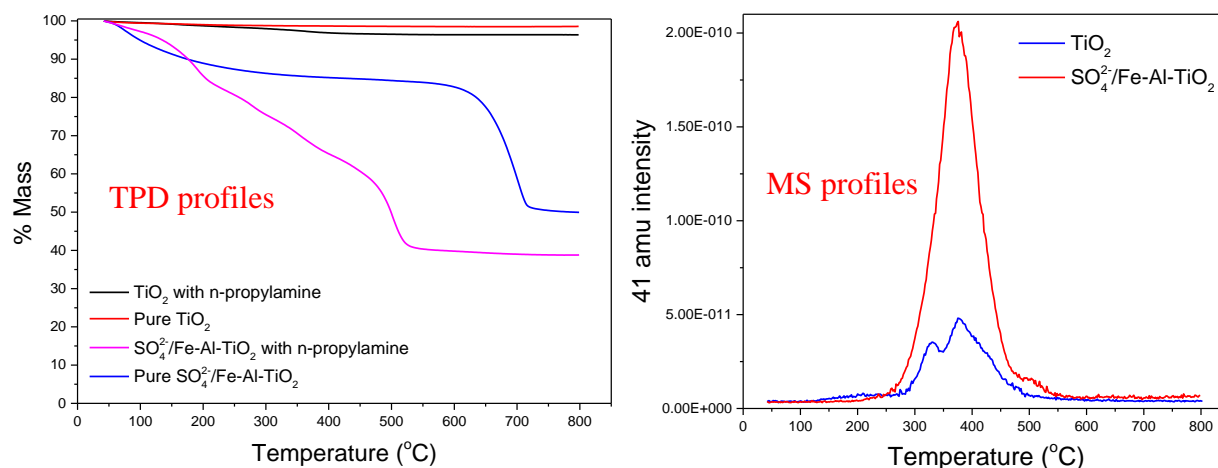
Figure 6.21 TPD-MS profiles for TiO$_2$ NPs and SO$_4^=$/Fe-Al-TiO$_2$ catalyst

6.2.5 Magnetic property

The magnetisation curve for the synthesised magnetic solid acid catalyst [SO_4^{2-}/Fe-Al-TiO$_2$] was measured at room temperature between 2 and -2 T. The obtained magnetic hysteresis loop result is presented in Figure 6.22. The magnetic field (M) versus applied magnetic field (H) curve indicates a saturation magnetisation value of the sample at 10 emu/g. The saturation magnetisation value for pure iron oxide (Fe_2O_3 and Fe_3O_4) has been reported higher in comparison with the synthesised catalyst. This is probably due to the presence of titania, alumina and surface coating with sulphate groups reducing the magnetisation property of the iron oxide in the main structure of the catalyst. Similar observation was reported for surface coating of Fe_3O_4 NPs with different surface coatings, including oleic acid, SiO_2-PrNHSO$_3$H and SiO_2-SO$_3$H [561, 567, 568]. However, the sample still shows superparamagnetic behaviour property (M_r = 0.65 emu/g and H_c = 0.0024 T are close to zero as can be seen in the inset for Figure 6.22) and sufficient for the rapid separation of catalyst from the reaction [560]. This magnetic property of the synthesised catalyst enhances resistance against deactivation of active sites due to the rapid harvest separation of the catalyst.
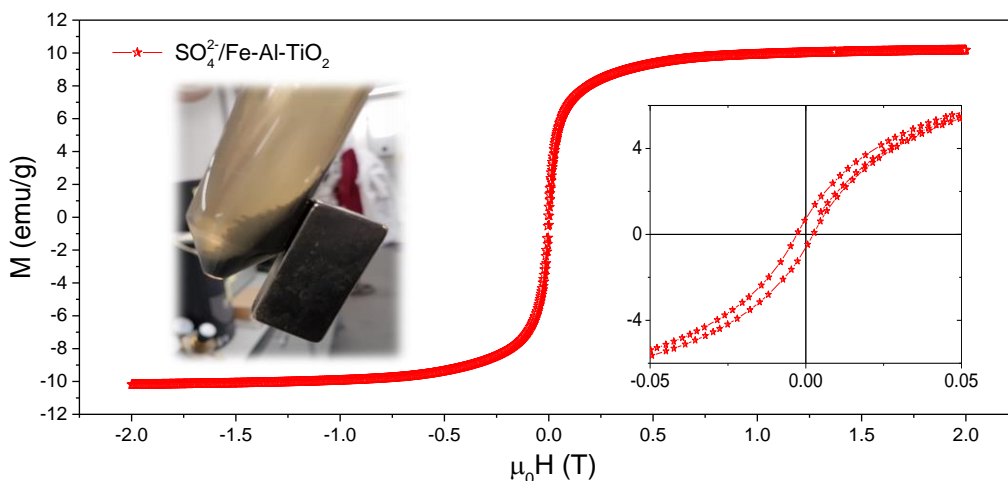
Figure 6.22 Magnetisation hysteresis loop of synthesised $SO_4^{=}$/Fe-Al-TiO$_2$ at room temperature. Right inset is the magnified field (μ_oH) from -0.05 to 0.05 Tesla whilst the left inset is the picture reveals the strong magnetic field with an external magnetic field

6.3 Catalytic performance

The synthesised magnetic solid acid catalyst [SO_4^{2-}/Fe-Al-TiO$_2$] was tested in the simultaneous esterification and transesterification of UCO to form biodiesel fuel. In order to determine the

optimum process conditions for the synthesised novel catalyst, the effect of different catalytic process parameters on the percentage of FAME yield were investigated, including methanol to UCO mole ratio, reaction temperature, catalyst loading, and time of esterification and/or transesterification as shown in Figure 6.23. Figure 6.23 (a) shows the effect of various reaction times between ½ and 5 h on the percentage of FAME under constant other process parameters at 1.5 wt% of magnetic solid acid catalyst loading to UCO, 9:1 molar ratio of methanol to UCO, 75 °C reaction temperature, 600 RPM agitation rate, 0.14% moisture content, and 2.034 wt% free fatty acid contents in feedstock (based on previous $Ti(SO_4)O$ catalyst optimum conditions). It can be seen that the yield of FAME gradually increased between ½ and 2.5 h. It was found that at the beginning of reaction a low amount of FAME formed and then increased notably up to 82.9%. This could be mainly attributed to an increase in reaction time from ½ to 2.5 h leading to high miscibility of active sites of the catalyst into FFA/TG and methanol in the reaction. The miscibility of three phases resulted in generating massive amounts of active sites in the reaction which activated the carbonyl groups in FFA/TG to form the highest conversion [289]. Thereafter, there was negligible impact on the FAME yield when the reaction time was continuously prolonged to 5 h. This indicated that the reaction reached equilibrium and the enhancement of FAME yield become very low [366, 524, 569, 570]. Therefore, the optimal reaction time for esterification and transesterification of UCO over synthesised magnetic solid acid catalyst was 2.5 h.

The amount of catalyst is considered a crucial factor on the FAME yield and needs to be optimised. In this study, the effect of different magnetic catalyst loading to UCO was studied whilst other parameters were kept constants. The amount of magnetic catalyst varied between 0.5 and 4.0 wt% as shown in Figure 6.23 (b). It can be noted that there was a significant improvement of FAME yield (12.5 to 91.21%) with the addition of catalyst loading from 0.5 to 3.0 wt%. This can be explained by there being an increase in the amount of catalyst to oil leading to an increase in the total active sites in the reaction media (mainly in the interface between TG and methanol) resulting in faster reaction rate to reach the equilibrium (shorter time required for the reaction to reach the equilibrium) [304, 569]. The total acidity of the catalyst was also sufficient in the reaction media to drive the presence of FFA in the UCO feedstock into ester. This result showed that the yield of FAME is greatly affected by the catalyst loading to UCO. When the amount of catalyst increased to 4 wt%, the FAME yield remained almost constant. This was due to sufficient amount of active sites available in the reaction occupied by the reactants [366]. Taking the cost of the catalyst into

account, the optimum catalyst loading to UCO was set at 3 wt%. It is also worth mentioning that the high activity of the synthesised magnetic catalyst must be related to the high amount of Brønsted acid sites on its framework. Stronger Brønsted acid sites compared to Lewis acid sites for the synthesised catalyst in the reaction media probably resulted in the enhancement of catalytic activity of (trans)esterification.

Both esterification and transesterification reaction are reversible, as shown in Figure 5.21 (Chapter Five), the excess of methanol is required to shift the equilibrium reaction towards the FAME (product) side. Many researchers have reported the high amount of methanol necessary to obtain a high yield of FAME [86, 360, 571]. Figure 6.23 (c) displays the effect of different mole ratios of methanol to oil under maintained while other parameters are maintained at 2.5 h reaction time, 3 wt% of catalyst loading to UCO, 75 °C reaction temperature, 600 RPM agitation rate, 0.14% moisture content, and 2.034 wt% free fatty acid contents in feedstock. It can be observed that the increment of methanol to UCO mole ratio from 1:1 to 10:1 smoothly enhanced the FAME yield to 92.1%. This was due to an increase of mole ratio of methanol to UCO leading to better miscibility of FFA/TG into methanol which shifts the equilibrium reaction towards the product side by increasing the possibility of contact between the formed active sites and FFA/TG molecules. Furthermore, a higher mole ratio of methanol to UCO feed led to less noticeable decrease of yield [365]. The drop of yield can be explained by the high amount of methanol in the reaction media causing flooding of the active sites of the catalyst which hindered contact to activate the carboxylic acid groups in FFA and the carbonyl groups in TG [86, 348]. In addition, high feed methanol to UCO ratio could possibly drive the glycerol in the reaction media as by-product with formed FAME (product) to re-form mono-glyceride, which leads to an increase in the viscosity of the reaction media [572, 573]. It can be concluded that a feed of 10:1 mole ratio of methanol to UCO is an optimum condition for activity of the synthesised magnetic solid acid catalyst.

In general, an increase of reaction temperature enhances the reaction rate and conversion efficiency. This indicates that temperature plays a key parameter in the (trans)esterification. The effect of different reaction temperatures on the FAME yield from UCO over the synthesised magnetic catalyst was also investigated under the other fixed reaction process conditions of 2.5 h reaction time, 3 wt% of catalyst loading to UCO, 10:1 methanol to oil mole ratio, 600 RPM agitation rate, 0.14% moisture content, and 2.034 wt% free fatty acid contents in feedstock. The

obtained results are presented in Figure 6.23 (d). It was found that the FAME yield gradually increased from 25 to 60 °C.
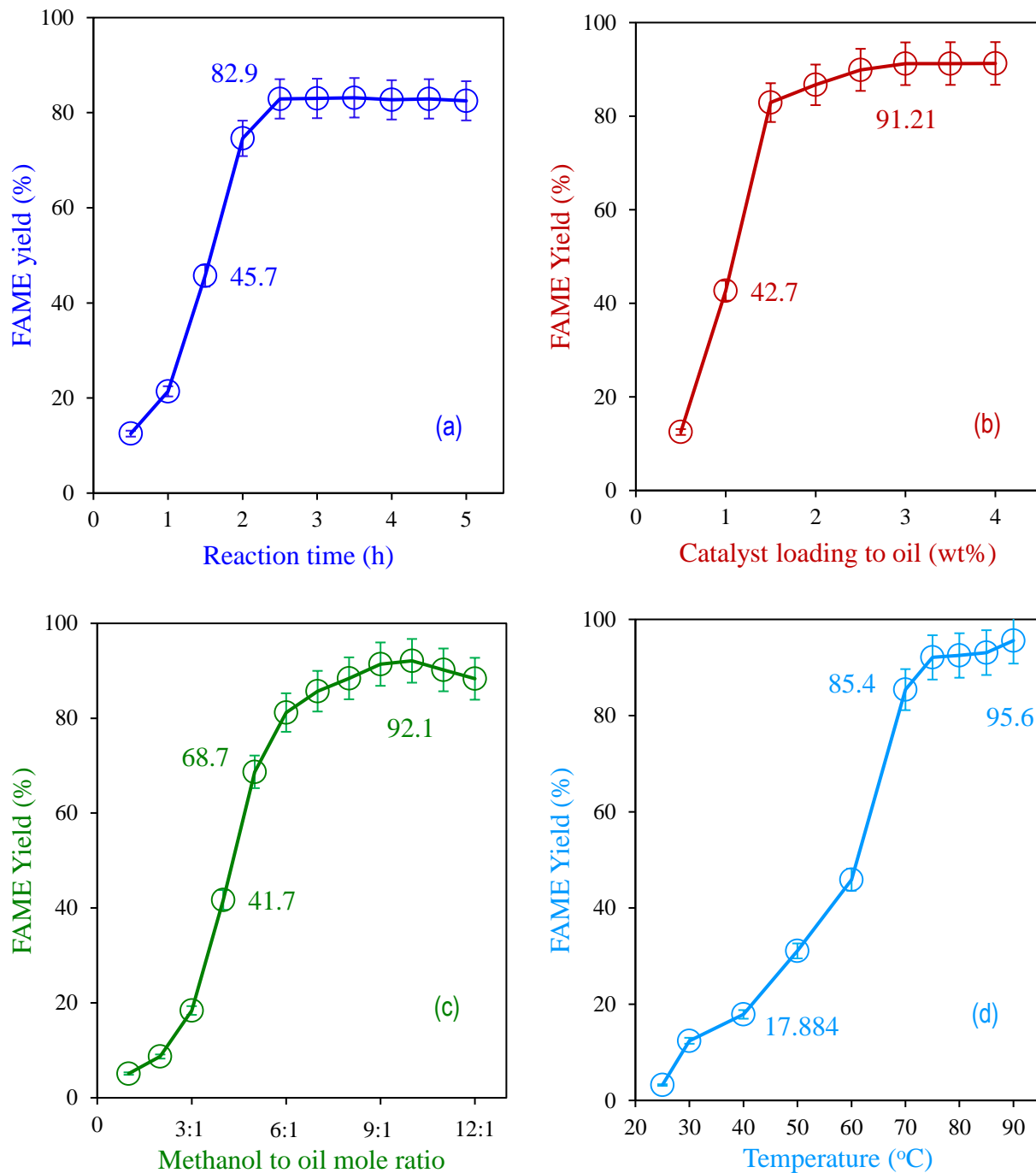
Figure 6.23 The effects of (a) reaction time, (b) magnetic solid acid catalyst loading to UCO, (c) mole ratio of methanol to UCO, and (d) reaction temperature on the percentage of FAME yield in synthesised biodiesel fuel.

This was most likely due to an increase of miscibility of three phases (solid-liquid-liquid) in the reaction media, which led to the formation of a large amount of nucleophilic sites to facilitate the carboxyl/carbonyl groups attack in the FFA/TG. This also accelerates the rate of reaction meaning a short time is needed to complete because increased kinetic energy from all reactant molecules will accelerate the mass transfer rate between solid-liquid-liquid [304]. This suggests that higher temperature is preferable for solid acid catalysts. The FAME yield improved with further rising temperatures up to 90 $^{\circ}$C because higher reaction temperature reduced the viscosity of reaction and then fastened the activation of carbonyl/carboxylic groups by methanol nucleophilic attack on the TG/FFA [569]. It is, therefore, important to carry out the (trans)esterification reaction at high temperature to achieve shorter reaction time for this magnetic catalyst. However, some researchers claimed that (trans)esterification reaction at high temperature and over a long period of time leads to FAME and glycerol decompositions to some extent [304].

6.3.1 Catalyst stability and its reusability

A catalytic stability of SO_4^{2-}/Fe-Al-TiO$_2$ magnetic solid acid catalyst was conducted under different amount of FFA in feedstock. The effect of ratios of oleic acid over virgin oil feedstock from 0.5 to 20 wt% was assessed over synthesised catalyst under the determined optimum reaction conditions (2.5 h reaction time, 3 wt% of catalyst loading to UCO, 10:1 methanol to oil mole ratio, 90 $^{\circ}$C reaction temperature and 600 RPM agitation rate) and the results are shown in Figure 6.24 (a). As can be seen, there is a slight reduction of FAME yield by 0.89% while the ratio is increased to 20 wt%. This indicates an excellent stability and tolerance of the synthesised magnetic catalyst. A possible explanation for this could be the high amount of total acidity of the catalyst.

The life time of the synthesised magnetic catalyst was also assessed in 10 consecutive runs and the results are presented in Figure 2.24 (b). The SO_4^{2-}/Fe-Al-TiO$_2$ catalyst could be very easily separated from the product and by-product layer by using an external magnetic field (less than 10 seconds). The recovered spent catalyst was then properly washed several times with 1:1 ratio of methanol to n-hexane in order to remove any remaining residue from the reaction process on the surface of the catalyst and then treated in a furnace for 2 h at 250 $^{\circ}$C followed by the confirmation of crystal structure on the XRD before being re-used (see Figure 6.25). It can be seen that there was no reduction of the FAME yield after 10 cycles under optimised reaction conditions (2.5 h reaction time, 3 wt% of catalyst loading to UCO, 10:1 methanol to oil mole ratio, 90 $^{\circ}$C reaction

temperature, 0.14% moisture content, 2.034 wt% free fatty acid contents in feedstock and 600 RPM agitation rate). On this basis the synthesised SO_4^{2-}/Fe-Al-TiO$_2$ catalyst can be considered as a good candidate for the biodiesel production in a continuous system in future work.
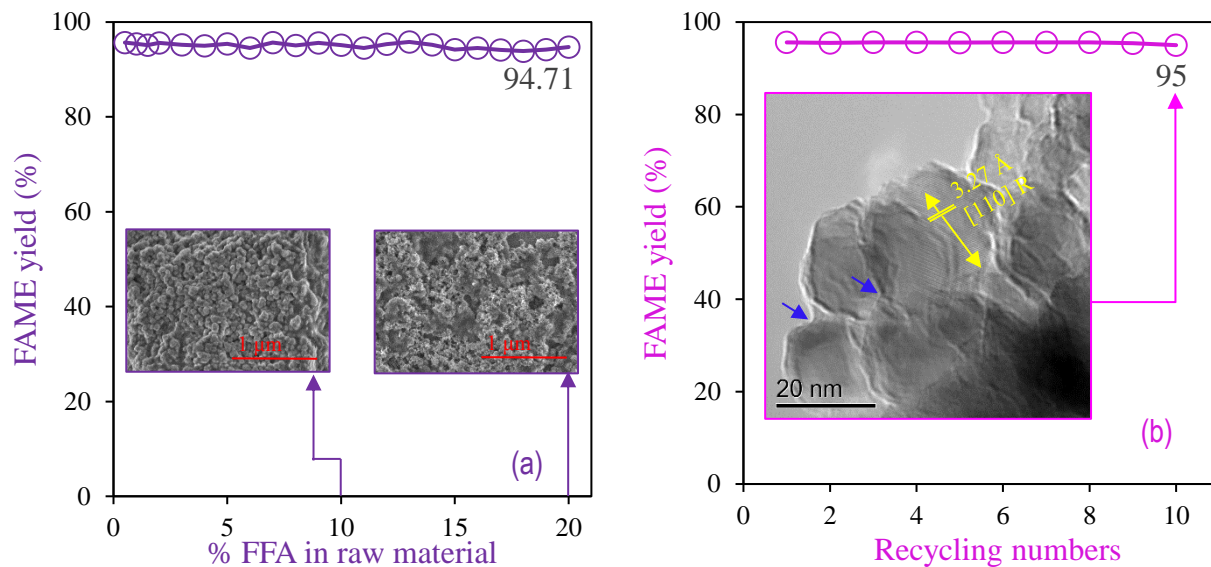
Figure 6.24 The effect of (a) FFA% and (b) reusability of magnetic solid acid catalyst on the percentage of FAME yield. The inset TEM result for the recovered spent catalyst after run 10 shows a clear [110] facets for the rutile TiO$_2$ NPs (reference code: 01-076-9000)
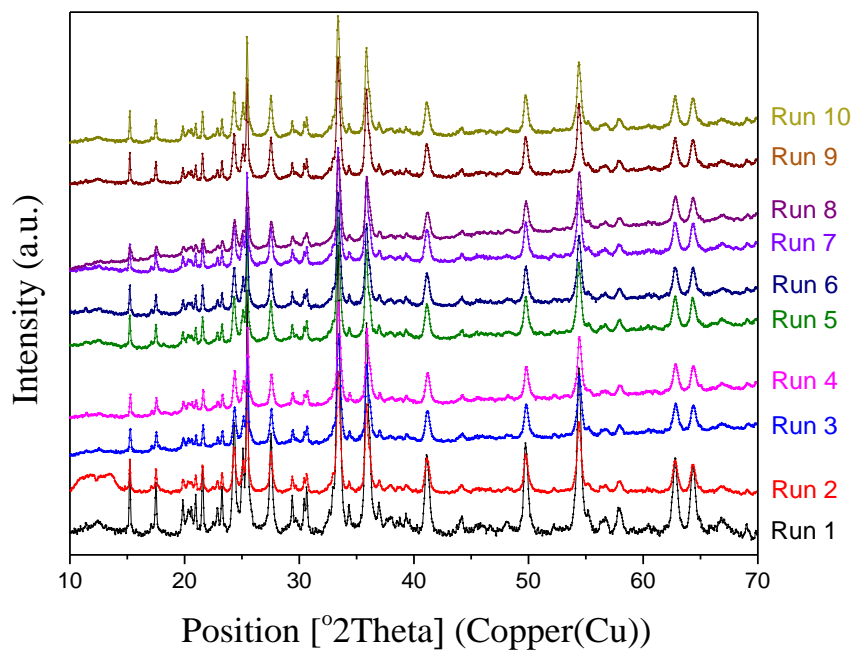
Figure 6.25 XRD patterns for the spent $SO_4^=$/Fe-Al-TiO$_2$ catalysts from run 1 to run 10

The XRD results in Figure 6.25 revealed the stability of the recovered spent catalysts apart from run 2 showing extra peaks at low diffraction angle due, possibly, to some residue from the reaction (incomplete washing of recovered catalyst). It is also important to mention that a negligible amount of sulphur was detected by ICP-MS when the synthesised biodiesel was analysed. This might be due to detachment of some sulphur groups on the surface of the catalyst. However, more investigation needs to be carried out on the recovered catalysts, i.e. surface acidity, sulphur contents, porosity and XPS analysis in future work to further understand the texture structure of the recovered magnetic catalysts.

6.3.2 Biodiesel characterisations

The prepared biodiesel from the esterification and transesterification reactions of UCO over fresh SO_4^{2-}/Fe-Al-TiO$_2$ catalyst was analysed and characterised according to ASTM and/or EN standards. The analysis of the results for obtained biodiesel is summarised in Table 6.4 whilst the characterisation results are presented in Table 6.5. From Table 6.4, it can be seen that the main chemical compositions for FAME profile are palmitic acid methyl ester, oleic acid methyl ester and linoleic acid methyl ester. The rest are trace amounts in the prepared biodiesel. The obtained results for biodiesel properties are in the range of standard acceptance according to the ASTM and EU standards.

Table 6.4 FAME profile for obtained UCO biodiesel over $SO_4^{=}$/Fe-Al-TiO$_2$ catalyst

FAME	Form	FAME content%
Myristic acid methyl ester	$C_{14:0}$	0.09
Palmitic acid methyl ester	$C_{16:0}$	5.88
Stearic acid methyl ester	$C_{18:0}$	2.05
Oleic acid methyl ester	$C_{18:1}$	64.50
Linoleic acid methyl ester	$C_{18:2}$	22.24
Linolenic acid methyl ester	$C_{18:3}$	2.14
Gadoleic acid methyl ester	$C_{20:1}$	1.42
Erucic acid methyl ester	$C_{21:1}$	1.04
Behenic acid methyl ester	$C_{22:0}$	0.42

DSC was used to detect the cloud point for synthesised biodiesel fuel from UCO over SO_4^{2-}/Fe-Al-TiO$_2$ catalyst. The DSC cooling and heating thermogram are depicted in Figure 6.26. It was found that the cooling DSC curve exhibits one sharp endothermic peak with a shoulder centred at -14.75 °C with enthalpy of 37.30 mJ attributed to the formation of the first few crystals in biodiesel fuel. The onset temperature of the nucleation of crystal on the cooling is at -11.27 °C relates to the cloud point temperature of synthesised biodiesel over the magnetic solid acid catalyst. The melting of the formed crystals was determined from the heating DSC thermogram which is a board exothermic peak observed between -23 and -4 °C.

Table 6.5 Properties of biodiesel produced from UCO over $SO_4^{=}$/Fe-Al-TiO$_2$ catalyst

Property	Unit	Limits		Synthesised biodiesel
		ASTM D6751	EN14214	
Flash point	°C	93 min	101 min	168.5
Kinematic viscosity	mm^2/s	1.9-6.0	3.5-5.0	4.61
Acid number	mgKOH/g	0.8 max	0.5 max	0.45
Density at 15°C	Kg/m^3	---	860-900	880.1
FAME content	% mass	---	96.5 min	95.6
Water content	ppm	---	500 max	---
Linolenic acid methyl ester	% mass	---	12 max	2.10
Free glycerine content	% mass	0.02 max	---	0.001
Total glycerine content	% mass	0.24 max	0.25 max	0.191
Monoglyceride content	% mass	---	0.8 max	0.073
Diglyceride content	% mass	---	0.2 max	0.043
Triglyceride content	% mass	---	0.2 max	0.074

TGA was also used to assess the thermal stability of the synthesised biodiesel over magnetic solid acid catalyst. It can be seen from Figure 6.27 that synthesised biodiesel was stable to around 144 °C and then it started decomposing completely at 226 °C. This might be due to the reason that synthesised biodiesel fuel contains high amounts of unsaturated FAME (see Table 6.4).
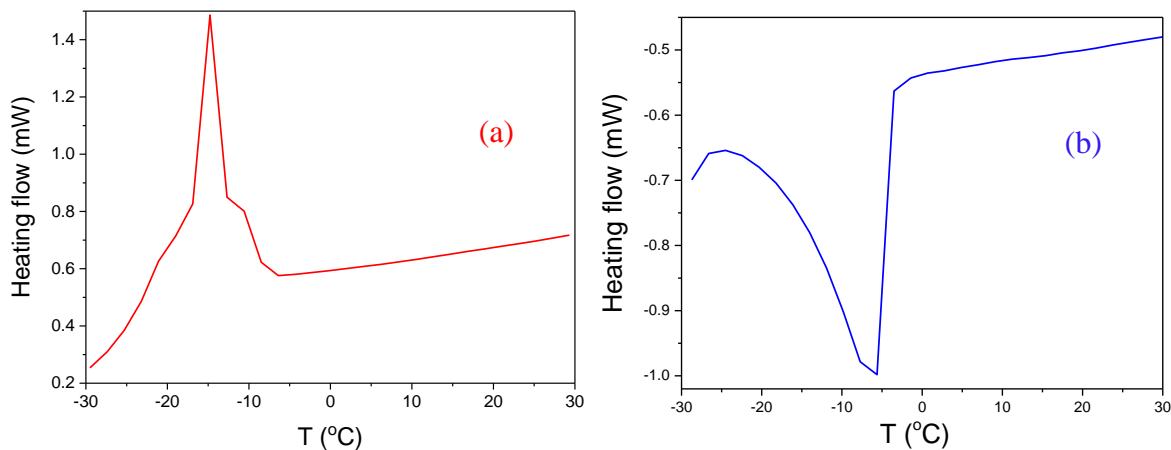
Figure 6.26 The DSC (a) cooling and (b) heating curves for synthesised biodiesel
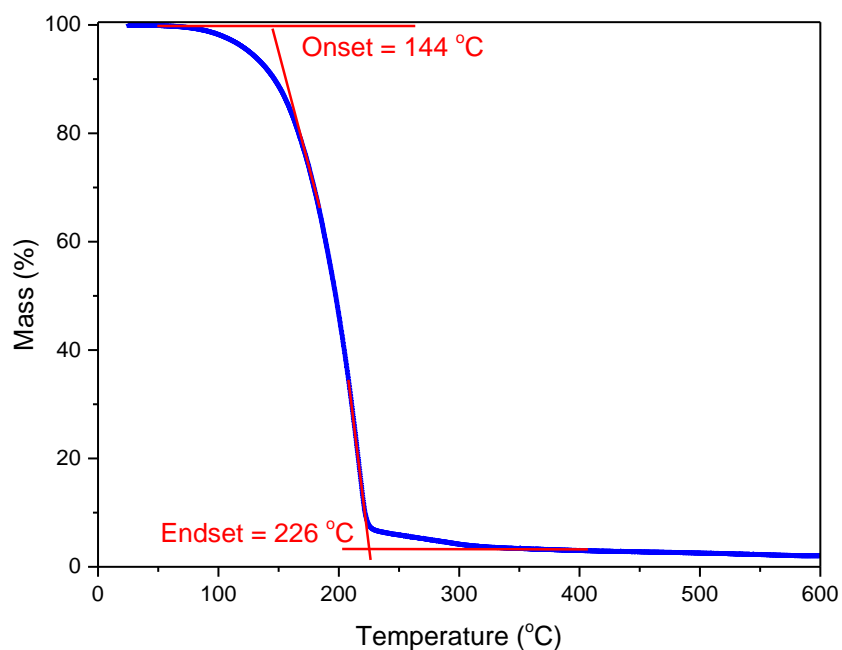
Figure 6.27 Thermal stability of synthesised biodiesel over $SO_4^=$/Fe-Al-TiO$_2$ under air purge gas

6.4 Discussions

A highly efficient, stable, super magnetic solid super acid catalyst was synthesised, for the first time, from the sulfonating of ternary metal oxides. Chlorosulfonic acid was used as a powerful and aggressive sulfonating agent. The texture of newly designed magnetic catalyst was characterised using XRD and the result matched with rhombohedral iron oxide [hematite (α-Fe$_2$O$_3$), JCPDS-ICDD: 01-076-4579], rhombohedral aluminium sulphate [millosevichite, JCPDS-ICDD: 00-042-

1428] and tetragonal titanium dioxide [anatase, JCPDS-ICDD: 04-006-9240; rutile, JCPDS-ICDD: 01-076-9000] in the crystal structure. However, some new existing diffraction peaks occurred. These could be corresponding to the dopant, new structure or phase. The detailed TEM analysis evidenced the dopant to some extend but still needs to be re-confirmed using HR-XPS.

Table 6.6 A comparison of mild process conditions for the reported solid acid catalyst with current study in the biodiesel production

	Current study	**Alhassan et al.[101]**	**Wang et al. [90]**
Oil/fat feedstock	UCO	WCO	UCO
Methanol to oil ratio	10:1	20:1	10:1
Type of catalyst	SO_4^{2-}/Fe-Al-TiO$_2$	Fe$_2$O$_3$-MnO-SO_4^{2-}/ZrO$_2$	SO_4^{2-}/TiO$_2$/La^{+3}
Wt of catalyst%	3	3	5
Time, hr	2.5	6	1
Particle size, nm	47.33	Not reported	Not reported
Surface area, m^2/g	50.58	72	229
Temperature, ºC	90	180	110
FAME yield %	95.6	96.5	>90
Catalyst recycled	10	7	5

The synthesised catalyst exhibited multifunctional properties (super acidity and super magnetism). These two properties (synergetic) in the same catalyst are favourable in simultaneous esterification and transesterification of cheap feedstocks by reducing production cost of fuel. As eliminating the pre-treatment step (reducing FFA in feedstock) and separation of catalyst are two important factors involved in the overall of production of biodiesel fuel from cheap feedstock. The synthesised magnetic catalyst showed high stability in high amounts of FFA (20 wt%) and great re-usability of to up 10 cycles without reduction of the FAME yield. ICP-MS detected negligible amount of sulphur (20.652-44.44 ppb) after analysing the fuel but there was no single piece of evidence to show the deactivation of the catalyst or reduction of FAME yield. Further studies are needed to investigate the crystal structure of the spent catalyst, i.e. using HR-XPS. It is also worth mentioning that the phase diagram of ternary metal oxides catalyst support from alumina, titania and iron oxide precursors and different SO$_x$ loadings (using different sulfonating agents), for simultaneous esterification and transesterification of feedstocks containing high FFA to obtain biodiesel fuel, could be the subject of future studies. This is because studying the phase diagram of ternary metal

oxides can identify high surface area of catalyst support allowing good dispersion of the active sites [574, 575]. The decoration of porosity for similar catalyst support systems might also merit future studies. Finally, the conditions for simultaneous esterification and transesterification processes using sulphated binary/ternary metal oxides reported in literature compared to the current study are presented in Table 6.6.

6.5 Conclusions

A magnetic solid super acid catalyst was, for the first time, synthesised and characterised using powder XRD, SEM, TEM, TEM-EDS, EDS-mapping, N_2 porosimetry, FT-IR, DRIFT pyridine, TPD-MS propyl amine, TGA, and VSM. The synthesised catalyst was active toward (trans)esterification of used cooking oil/oleic acid to form biodiesel fuel. The synthesised catalyst exhibited high acidity and magnetisation whilst DRIFT analysis confirmed the presence of stronger Brønsted acid sites compared to Lewis acid sites. Surface deposition of alumina led to increasing surface area with porosity of the initial titania. Iron oxides is used as a cheap source to magnetise the Al-doped titania hybrid. It was found that from HR-TEM, most of the particles were agglomerated to each other to form a cluster. HR-TEM also evidenced the presence of oriented attachment mechanism in the prepared Fe-Al-TiO$_2$ catalyst support. It was found that a 95.6% FAME yield from UCO feedstock can be achieved under a reaction time of 2.5 h, synthesised magnetic catalyst to UCO ratio of 3 wt% and methanol to UCO ratio of 10:1 at 90 ºC reaction temperature. The catalytic stability and re-usability of SO_4^{2-}/Fe-Al-TiO$_2$ were also investigated. The results showed that the synthesised catalyst can be used for feedstocks containing up to 20 wt% of FFA without deactivation of active sites. The recovered spent catalysts was tested for 10 successful cycles in the transesterification of UCO. This was mainly due to the fact that the catalyst can be easily separated from the reaction system using external magnetic field without losing the catalytic activity and leaching of sulphate groups. Finally, the prepared biodiesel over the magnetic catalyst would meet EU and ASTM standards.

Chapter 7

Summary and recommendations for future work

7.1   **Introduction**

7.2   **Overall conclusions**

7.3   **Recommendations for future work**

This chapter summarises the overall findings and outcomes of this project as well as providing an outlines of future work that could be performed.

CHAPTER SEVEN

7. Conclusions and recommendations for future studies

7.1 Introduction

Key parameters that should be taken into consideration for designing of solid acid catalysts in the industrial biodiesel production are their cost, long-term stability, easy recoverability after the reaction process and high surface area [576]. Titania [264] and alumina [262] have been used as a common catalyst supports in industry for different applications. Doping iron oxide and/or alumina into a commercial TiO_2 NPs offers a route for increasing the surface area and easy recovery of the designed solid acid catalyst support. This method is also reported to minimise mass transfer limitations for the catalysts in liquid phase reactions by providing better accessibility via the existence of pores [235]. Therefore, this chapter, reviews the overall conclusions drawn from the findings of the investigations for simultaneous esterification and transesterification of UCO over different synthesised catalysts performed as part of this project as well as suggesting future work and studies to further develop solid acid catalyst in the area of biodiesel production.

7.2 Conclusions

The main aim of this project was to develop a highly efficient, green, cheap, stable, easy recoverable, super acid and highly re-usable solid acid catalyst for simultaneous esterification and transesterification of cheap feedstock, i.e. UCO to form biodiesel. A variety of promising solid acid catalysts $TiO_2/PrSO_3H$, $Ti(SO_4)O$ and $SO_4^{2-}/Fe-Al-TiO_2$ have been developed in this project. Detailed characterisations, including XRD, SEM, TEM, TEM-EDS, EDS-mapping, FT-IR, DRIFT-pyridine, TPD-MS with n-propylamine, TGA/FT-IR, CHNS analysis, DSC, TGA, N_2 porosimetry, VSM and XPS, have been carried out. Every single characterisations for catalysts provided significant information in terms of physicochemical properties of the synthesised catalysts and their performances in the field of biodiesel production from UCO. The activity and stability of all synthesised catalysts have been investigated. It was found that titania grafted with propyl sulfonic acid, prepared from surface functionalisation of TiO_2 with 1,3-propane sultone (in

toluene under continuous agitation at 250 RPM reflux for 72 h), gave a high FAME yield (98.3%) from UCO feedstock under optimum process conditions of 9 h of reaction time, 1:15 molar ratio of oil to methanol, 60 °C reaction temperature and 4.5 wt% of a catalyst loading. The high catalytic activity may be related to the presence of a high amount of Brønsted acid sites. The low thermal stability and re-usability of the spent catalyst [TiO$_2$/PrSO$_3$H], however, are the main issues (catalyst poisoning) as the FAME yield dropped by ~37% after 4 consecutive cycles. This was mainly due to the blockage of the surface active sites by the deposition of a carbon layer on the surface of the catalyst as shown in XRD analysis. Based on this, it has to be mentioned that the catalytic activity of this catalyst is not good enough for industrial biodiesel application from an economic point of view. Therefore, titanium sulphate oxide or oxy-sulphate [Ti(SO$_4$)O] was developed from impregnation of TiO$_2$ NPs with chlorosulfonic acid and used as a novel solid acid catalyst for simulations esterification and transesterification of UCO to synthesise biodiesel. It has shown high catalytic performance to form 97.1 of FAME yield at optimum process conditions of 3 h of reaction time, 1.5 wt% of catalyst to UCO, 9:1 methanol to UCO mole ratio and 75 °C reaction temperature. It was also found that the spent catalyst had more tolerance of FFA (up to ≤6 wt%) in feedstock and can be re-used up to 8 cycles without deactivations. After 8 cycles, the catalyst deactivated and a series of experiments were conducted to confirm the reason for this. It was found that the sulphate groups leaching in the spent catalyst was the main factor. Therefore, the recovered spent catalyst was successfully regenerated by soaking in dilute sulfuric acid solution. The crystal structure was re-confirmed using XRD. It was found that the regenerated catalyst [XRD, ICDD 04-011-4951] can also be used for five runs without losing catalytic activity. However, the main disadvantage of such a catalyst was recovery of the spent catalyst. Ultrafiltration and high-speed centrifugal techniques are the two options for separating the catalysts from the reaction media; however they are expensive and difficult to scale-up. Therefore, a titania based super magnetic solid super acid catalyst has, for the first time, been designed to overcome these difficulties. The catalyst was synthesised via deposition of alumina to increase the surface area as well as iron oxide to introduce the magnetic property to the catalyst. The acid loading, in particular Brønsted acid sites, was impregnated into the synthesised catalyst support. It was found that the thermal stability and acidity of TiO$_2$ catalyst support was remarkably improved. Furthermore, the addition of Al and Fe into the commercial TiO$_2$ catalyst support also greatly inhibited the leaching of the sulphate groups. The synthesised SO_4^{2-}/Fe-Al-TiO$_2$ catalyst was tested

in simulations esterification and transesterification of UCO to obtain biodiesel. The results show that 95.6% of FAME yield can be obtained under optimum conditions of 2.5 h of reaction time, 3 wt% of synthesised magnetic catalyst to UCO ratio, 10:1 methanol to UCO mole ratio and 90 $^{\circ}$C reaction temperature. Surprisingly, the synthesised magnetic catalyst shows a high catalytic stability against FFA (up to 20 wt%) in feedstock and could be re-used up to 10 cycles without any deactivation or leaching of active sites. This was a remarkable improvement in comparison to other synthesised solid acid catalysts. This is probably due to the high total acidity loading and crystal structure of catalyst support. It was found that water by-product from the esterification of oleic acid had no significant impact on the deactivation or poisoning of active sites in the magnetic catalyst. Therefore, the synthesised magnetic catalyst can be used for direct esterification and transesterification of cheap feedstocks, i.e. UCO, without any pre-treatment for eliminating moistures. The detailed comparison of the optimum conditions for all solid acid catalysts are presented in Table 7.1.

Table 7.1 A comparison of mild process conditions for synthesised solid acid catalysts, in this project, in the biodiesel production

	TiO$_2$/PrSO$_3$H	Ti(SO$_4$)O	SO_4^{2-}/Fe-Al-TiO$_2$
Feedstock	UCO	UCO	UCO
Methanol to oil mole ratio	15:1	9:1	10:1
Amount of catalyst, wt%	4.5	1.5	3
Duration reaction time, h	9	3	2.5
Reaction temperature, $^{\circ}$C	60	75	90
Particle size, nm	~23	~25	~47
Surface area, m^2/g	39	45	51
Mean pore size, nm	24.6	23	11
Total pore volume, cm^3/g	0.19	0.31	0.20
B/L ratio	0.71	1.78	3.58
Total acidity loading [H$^+$], mmol/g	2.35	3.45	10.31
FAME yield, %	98.3	97.1	95.6
Catalyst recycled number	~4	~8	>10
Catalyst stability, $^{\circ}$C	210	600	633
FFA% content in virgin oil	<4	≤6	>20

The synthesised biodiesel fuels from different catalytic esterification and transesterification processes have been characterised according to EU and/or ASTM standard methods. GC-MS and

GC-FID were performed on the synthesised biodiesel to identify the purity of biodiesel fuel and quantify the FAME in biodiesel fuels. The physicochemical properties of obtained biodiesel were examined. The results revealed that biodiesel obtained over the Ti(SO$_4$)O showed better stability compared to synthesised biodiesels over other two catalysts. All the other properties are in accordance to the EU and ASTM standard limits.

7.3 Future work

This project has made progress in finding eco-friendly, non-corrosive, highly stable, highly efficient, FFA tolerant and easily separable new super magnetic solid super acid catalyst. However, further studies need to be undertaken to better understand the high catalytic performance of SO_4^{2-}/Fe-Al-TiO$_2$ catalyst. The following studies are suggested to further contribute to realising biodiesel production from cheap feedstocks using this novel magnetic catalyst:

1- Future work should primarily focus on kinetic studies for esterification and transesterification reactions.

2- An extended study should focus on the investigation of formation of some non-recognisable XRD diffraction peaks via further characterisation such as HR-XPS analysis.

3- Tests of different chain length of fatty acid composition feedstocks need to be carried out in order to better understand the effect of chain length on the catalytic performance of this type of catalyst.

4- The effect of different calcination temperatures on the catalytic performance of this magnetic catalyst needs to be fully understood.

5- Future work could also involve on developing a ternary phase diagram of metal oxides from different precursors and percentages in order to find the best ternary metal oxides ratios for the preparation of a high surface area with macro pore sizes. This could help to minimise diffusion limitation and maximise dispersion of active sites on the surface of the catalyst (high dispersions of active sites on a large surface area and high acid strength mainly decide the activity of the solid acid catalysts). An example of high surface area with tuneable porosity obtained from a preliminary study is shown in Figure 7.1. This could be an open door for a potential alternative

candidate in industrial biodiesel production from cheap feedstocks without any treatments being necessary to remove impurities or moisture.

6- Future work also needs to focus on comparing the effect of different amount for sulphate loading on ternary metal oxides on the performance in esterification and transesterification reactions for cheap feedstocks containing high FFA.

7- Finally, the performance of high dispersed active sites on the large surface area with macro pore volumes for Fe-Al-TiO$_2$ catalyst support in simultaneous esterification and transesterification of cheap feedstocks should be investigated.
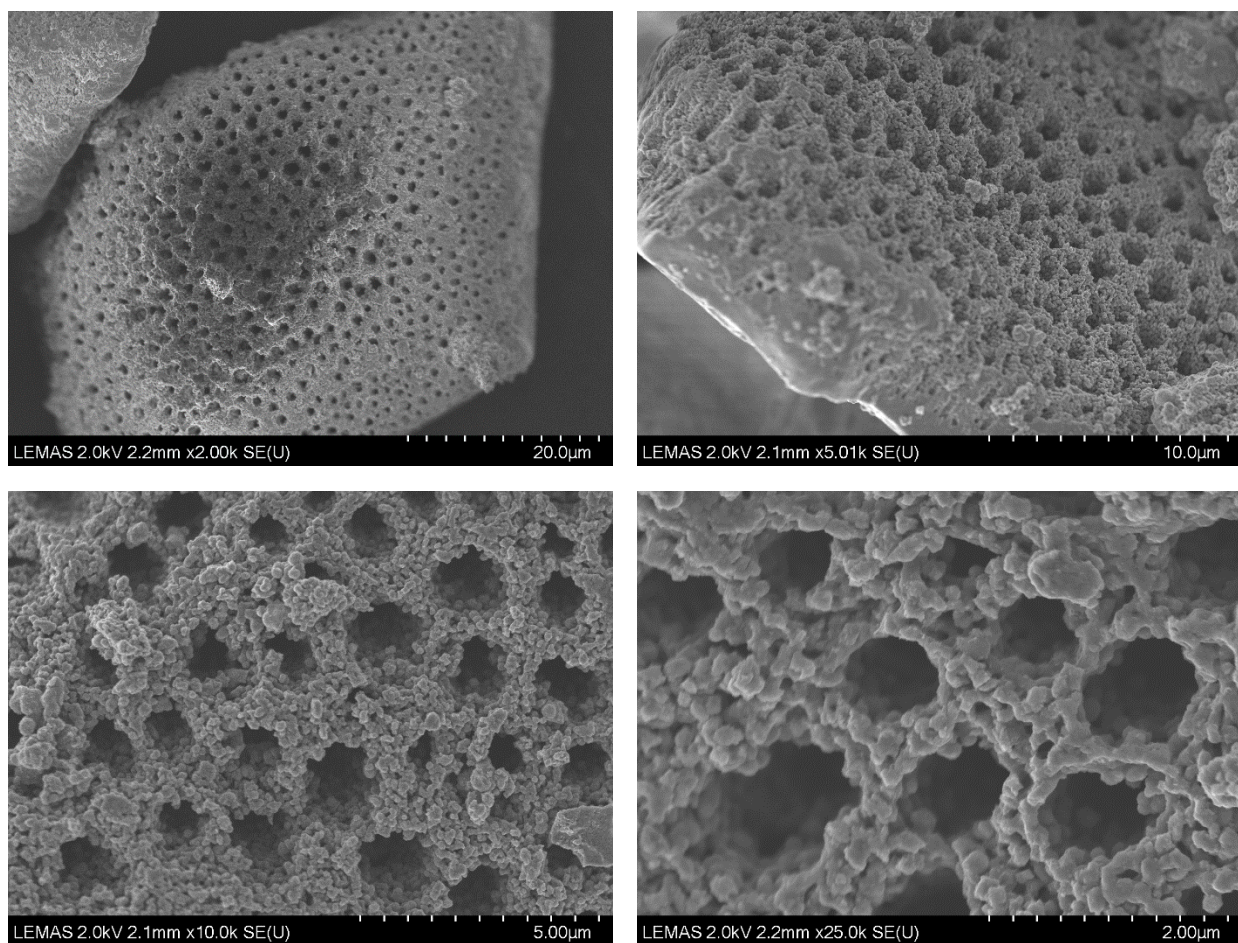
Figure 7.1 SEM images at different magnifications for one of the example of synthesised Fe-Al-TiO$_2$ catalyst support obtained from a preliminary study for Fe-Al-TiO$_2$ hybrid

References

1. Armaroli, N. and V. Balzani, *The future of energy supply: challenges and opportunities.* Angewandte Chemie International Edition, **2007**. 46(1-2): p. 52-66.
2. EIA, *International energy outlook 2016 with projections to 2040*, U.S.e. information, Editor **2016**, www.eia.gov/forecasts/ieo/pdf/0484(2016).pdf: US.
3. Atabani, A.E., A.S. Silitonga, I.A. Badruddin, T.M.I. Mahlia, H.H. Masjuki, and S. Mekhilef, *A comprehensive review on biodiesel as an alternative energy resource and its characteristics.* Renewable and Sustainable Energy Reviews, **2012**. 16(4): p. 2070-2093.
4. Bezergianni, S. and A. Dimitriadis, *Comparison between different types of renewable diesel.* Renewable and Sustainable Energy Reviews, **2013**. 21: p. 110-116.
5. Koh, M.Y. and T.I. Mohd. Ghazi, *A review of biodiesel production from Jatropha curcas L. oil.* Renewable and Sustainable Energy Reviews, **2011**. 15(5): p. 2240-2251.
6. Salvi, B.L. and N.L. Panwar, *Biodiesel resources and production technologies – A review.* Renewable and Sustainable Energy Reviews, **2012**. 16(6): p. 3680-3689.
7. Kumar, R., P. Tiwari, and S. Garg, *Alkali transesterification of linseed oil for biodiesel production.* Fuel, **2013**. 104: p. 553-560.
8. Leung, D.Y.C., X. Wu, and M.K.H. Leung, *A review on biodiesel production using catalyzed transesterification.* Applied Energy, **2010**. 87(4): p. 1083-1095.
9. Haas, M.J., A.J. McAloon, W.C. Yee, and T.A. Foglia, *A process model to estimate biodiesel production costs.* Bioresour Technol, **2006**. 97(4): p. 671-8.
10. Sinha, S., A.K. Agarwal, and S. Garg, *Biodiesel development from rice bran oil: Transesterification process optimization and fuel characterization.* Energy Conversion and Management, **2008**. 49(5): p. 1248-1257.
11. Hoekman, S.K., A. Broch, C. Robbins, E. Ceniceros, and M. Natarajan, *Review of biodiesel composition, properties, and specifications.* Renewable and Sustainable Energy Reviews, **2012**. 16(1): p. 143-169.
12. Bora, D.K. and D.C. Baruah, *Assessment of tree seed oil biodiesel: A comparative review based on biodiesel of a locally available tree seed.* Renewable and Sustainable Energy Reviews, **2012**. 16(3): p. 1616-1629.
13. Bhatti, H., M. Hanif, M. Qasim, and Ataurrehman, *Biodiesel production from waste tallow.* Fuel, **2008**. 87(13-14): p. 2961-2966.
14. Hoque, M.E., A. Singh, and Y.L. Chuan, *Biodiesel from low cost feedstocks: The effects of process parameters on the biodiesel yield.* Biomass and Bioenergy, **2011**. 35(4): p. 1582-1587.
15. Statista.com. *Global production and consumption of vegetable oils*. **2016**.
16. Silitonga, A.S., H.C. Ong, H.H. Masjuki, T.M.I. Mahlia, W.T. Chong, and T.F. Yusaf, *Production of biodiesel from Sterculia foetida and its process optimization.* Fuel, **2013**. 111: p. 478-484.
17. Madankar, C.S., S. Pradhan, and S.N. Naik, *Parametric study of reactive extraction of castor seed (Ricinus communis L.) for methyl ester production and its potential use as bio lubricant.* Industrial Crops and Products, **2013**. 43: p. 283-290.
18. Rawat, I., R. Ranjith Kumar, T. Mutanda, and F. Bux, *Biodiesel from microalgae: A critical evaluation from laboratory to large scale production.* Applied Energy, **2013**. 103: p. 444-467.
19. Gude, V.G. and G.E. Grant, *Biodiesel from waste cooking oils via direct sonication.* Applied Energy, **2013**. 109: p. 135-144.

20. Shuit, S.H., K.T. Lee, A.H. Kamaruddin, and S. Yusup, *Reactive extraction and in situ esterification of Jatropha curcas L. seeds for the production of biodiesel.* Fuel, **2010**. 89(2): p. 527-530.

21. Suganya, T., N.N. Gandhi, and S. Renganathan, *Production of algal biodiesel from marine macroalgae Enteromorpha compressa by two step process: optimization and kinetic study.* Bioresource technology, **2013**. 128: p. 392-400.

22. Cheng, J., Y. Qiu, R. Huang, W. Yang, J. Zhou, and K. Cen, *Biodiesel production from wet microalgae by using graphene oxide as solid acid catalyst.* Bioresource Technology, **2016**. 221: p. 344-349.

23. Nisar, J., R. Razaq, M. Farooq, M. Iqbal, R.A. Khan, M. Sayed, A. Shah, and I. ur Rahman, *Enhanced biodiesel production from Jatropha oil using calcined waste animal bones as catalyst.* Renewable Energy, **2017**. 101: p. 111-119.

24. Li, L., C. Zou, L. Zhou, and L. Lin, *Cucurbituril-protected $Cs_{2.5}H_{0.5}PW_{12}O_{40}$ for optimized biodiesel production from waste cooking oil.* Renewable Energy, **2017**. 107: p. 14-22.

25. de Oliveira, A.D., A.F. de Sá, M.F. Pimentel, J.G.A. Pacheco, C.F. Pereira, and M.S. Larrechi, *Comprehensive near infrared study of Jatropha oil esterification with ethanol for biodiesel production.* Spectrochimica Acta Part A: Molecular and Biomolecular Spectroscopy, **2017**. 170: p. 56-64.

26. Lin, L., Z. Cunshan, S. Vittayapadung, S. Xiangqian, and D. Mingdong, *Opportunities and challenges for biodiesel fuel.* Applied Energy, **2011**. 88(4): p. 1020-1031.

27. Huang, D., H. Zhou, and L. Lin, *Biodiesel: an Alternative to Conventional Fuel.* Energy Procedia, **2012**. 16: p. 1874-1885.

28. Europan-Biodiesel-Board, *Statistics for the EU biodiesel industry.* Available online, **2012**: p. http://www.ebb-eu.org/stats.php#.

29. European-Commission, *The promotion of the use of energy from renewable sources*, in *https://ec.europa.eu/energy/sites/ener/files/documents/1_en_act_part1_v7_1.pdf***2017**: Brussels. p. 116.

30. Joshi, R.M. and M.J. Pegg, *Flow properties of biodiesel fuel blends at low temperatures.* Fuel, **2007**. 86(1-2): p. 143-151.

31. Moser, B.R., *Biodiesel production, properties, and feedstocks.* In Vitro Cellular & Developmental Biology - Plant, **2009**. 45(3): p. 229-266.

32. Misra, R.D. and M.S. Murthy, *Blending of additives with biodiesels to improve the cold flow properties, combustion and emission performance in a compression ignition engine—A review.* Renewable and Sustainable Energy Reviews, **2011**. 15(5): p. 2413-2422.

33. Balat, M., *Potential alternatives to edible oils for biodiesel production–A review of current work.* Energy Conversion and Management, **2011**. 52(2): p. 1479-1492.

34. Keskin, A., M. Gürü, and D. Altıparmak, *Biodiesel production from tall oil with synthesized Mn and Ni based additives: Effects of the additives on fuel consumption and emissions.* Fuel, **2007**. 86(7-8): p. 1139-1143.

35. Sillanpää, M. and C. Ncibi, *A sustainable bioeconomy: The green industrial revolution*. **2017**: Springer.

36. Balat, M. and H. Balat, *Progress in biodiesel processing.* Applied energy, **2010**. 87(6): p. 1815-1835.

37. Chauhan, B.S., N. Kumar, Y. Du Jun, and K.B. Lee, *Performance and emission study of preheated Jatropha oil on medium capacity diesel engine.* Energy, **2010**. 35(6): p. 2484-2492.

38. Jitputti, J., B. Kitiyanan, P. Rangsunvigit, K. Bunyakiat, L. Attanatho, and P. Jenvanitpanjakul, *Transesterification of crude palm kernel oil and crude coconut oil by different solid catalysts.* Chemical Engineering Journal, **2006**. 116(1): p. 61-66.

39. Canakci, M. and J. Van Gerpen, *Biodiesel production via acid catalysis.* Transactions of the ASAE-American Society of Agricultural Engineers, **1999**. 42(5): p. 1203-1210.

40. Lee, A.F., J.A. Bennett, J.C. Manayil, and K. Wilson, *Heterogeneous catalysis for sustainable biodiesel production via esterification and transesterification.* Chemical Society Reviews, **2014**. 43(22): p. 7887-7916.

41. Chen, X.-R., Y.-H. Ju, and C.-Y. Mou, *Direct synthesis of mesoporous sulfated silica-zirconia catalysts with high catalytic activity for biodiesel via esterification.* The Journal of Physical Chemistry C, **2007**. 111(50): p. 18731-18737.

42. Sharma, Y. and B. Singh, *Development of biodiesel: current scenario.* Renewable and Sustainable Energy Reviews, **2009**. 13(6): p. 1646-1651.

43. O'regan, B. and M. Grfitzeli, *A low-cost, high-efficiency solar cell based on dye-sensitized.* nature, **1991**. 353(6346): p. 737-740.

44. Mills, A., R.H. Davies, and D. Worsley, *Water purification by semiconductor photocatalysis.* Chemical Society Reviews, **1993**. 22(6): p. 417-425.

45. Popov, A., A. Priezzhev, J. Lademann, and R. Myllylä, *TiO_2 nanoparticles as an effective UV-B radiation skin-protective compound in sunscreens.* Journal of Physics D: Applied Physics, **2005**. 38(15): p. 2564.

46. Patsoura, A., D.I. Kondarides, and X.E. Verykios, *Enhancement of photoinduced hydrogen production from irradiated Pt/TiO_2 suspensions with simultaneous degradation of azo-dyes.* Applied Catalysis B: Environmental, **2006**. 64(3): p. 171-179.

47. Rehan, M., X. Lai, and G.M. Kale, *Hydrothermal synthesis of titanium dioxide nanoparticles studied employing in situ energy dispersive X-ray diffraction.* CrystEngComm, **2011**. 13(11): p. 3725-3732.

48. Singh, R. and H.S. Nalwa, *Medical applications of nanoparticles in biological imaging, cell labeling, antimicrobial agents, and anticancer nanodrugs.* Journal of biomedical nanotechnology, **2011**. 7(4): p. 489-503.

49. Shen, J., Y. Zhu, X. Yang, and C. Li, *Magnetic composite microspheres with exposed {001} faceted TiO_2 shells: a highly active and selective visible-light photocatalyst.* Journal of Materials Chemistry, **2012**. 22(26): p. 13341-13347.

50. Middlemas, S., Z.Z. Fang, and P. Fan, *A new method for production of titanium dioxide pigment.* Hydrometallurgy, **2013**. 131: p. 107-113.

51. Bagheri, S., N. Muhd Julkapli, and S. Bee Abd Hamid, *Titanium dioxide as a catalyst support in heterogeneous catalysis.* The Scientific World Journal, **2014**. 2014.

52. Dai, Y., S. Shen, Z. Ma, L. Ma, Z. Sun, J. Yu, C. Wan, S. Han, D. Mao, and G. Lu, *High surface area mesoporous crystalline TiO_2: Synthesis, characterization, and application as support for making stable Au catalysts.* Journal of Nanoscience and Nanotechnology, **2017**. 17(6): p. 3772-3778.

53. Bourikas, K., M. Stylidi, D.I. Kondarides, and X.E. Verykios, *Adsorption of acid orange 7 on the surface of titanium dioxide.* Langmuir, **2005**. 21(20): p. 9222-9230.

54. Ahmed, M.H., J.A. Byrne, and T.E. Keyes, *Investigation of the inhibitory effects of TiO_2 on the β-amyloid peptide aggregation.* Materials Science and Engineering: C, **2014**. 39: p. 227-234.

55. Smith, S.J., R. Stevens, S. Liu, G. Li, A. Navrotsky, J. Boerio-Goates, and B.F. Woodfield, *Heat capacities and thermodynamic functions of TiO₂ anatase and rutile: Analysis of phase stability.* American Mineralogist, **2009**. 94(2-3): p. 236-243.

56. Dambournet, D., I. Belharouak, and K. Amine, *Tailored preparation methods of TiO₂ anatase, rutile, brookite: mechanism of formation and electrochemical properties.* Chemistry of materials, **2009**. 22(3): p. 1173-1179.

57. Liao, Y., W. Que, Q. Jia, Y. He, J. Zhang, and P. Zhong, *Controllable synthesis of brookite/anatase/rutile TiO₂ nanocomposites and single-crystalline rutile nanorods array.* Journal of Materials Chemistry, **2012**. 22(16): p. 7937-7944.

58. Mittal, V., *Surface modification of nanoparticle and natural fiber fillers*. **2015**, Singapore: John Wiley & Sons.

59. Pal, J. and T. Pal, *Faceted metal and metal oxide nanoparticles: design, fabrication and catalysis.* Nanoscale, **2015**. 7(34): p. 14159-14190.

60. Hanaor, D.A. and C.C. Sorrell, *Review of the anatase to rutile phase transformation.* Journal of Materials science, **2011**. 46(4): p. 855-874.

61. RSC, *TiO₂: Manufacture of titanium dioxide (http://www.rsc.org/learn-chemistry/resource/download/res00001267/cmp00002617/pdf):* UK.

62. Haines, J. and J. Leger, *X-ray diffraction study of TiO₂ up to 49 GPa.* Physica B: Condensed Matter, **1993**. 192(3): p. 233-237.

63. Behnajady, M., H. Eskandarloo, N. Modirshahla, and M. Shokri, *Investigation of the effect of sol–gel synthesis variables on structural and photocatalytic properties of TiO₂ nanoparticles.* Desalination, **2011**. 278(1): p. 10-17.

64. Mo, S.-D. and W. Ching, *Electronic and optical properties of three phases of titanium dioxide: Rutile, anatase, and brookite.* Physical Review B, **1995**. 51(19): p. 13023.

65. Diebold, U., *The surface science of titanium dioxide.* Surface science reports, **2003**. 48(5): p. 53-229.

66. Di Paola, A., M. Bellardita, and L. Palmisano, *Brookite, the least known TiO₂ photocatalyst.* Catalysts, **2013**. 3(1): p. 36-73.

67. Yang, S., N. Huang, Y.M. Jin, H.Q. Zhang, Y.H. Su, and H.G. Yang, *Crystal shape engineering of anatase TiO₂ and its biomedical applications.* CrystEngComm, **2015**. 17(35): p. 6617-6631.

68. Chen, X. and S.S. Mao, *Titanium dioxide nanomaterials: synthesis, properties, modifications, and applications.* Chemical reviews, **2007**. 107(7): p. 2891-2959.

69. Zhang, Q. and L. Gao, *Preparation of oxide nanocrystals with tunable morphologies by the moderate hydrothermal method: insights from rutile TiO₂.* Langmuir, **2003**. 19(3): p. 967-971.

70. Tomita, K., M. Kobayashi, V. Petrykin, S. Yin, T. Sato, M. Yoshimura, and M. Kakihana, *Hydrothermal synthesis of TiO₂ nano-particles using novel water-soluble titanium complexes.* Journal of Materials Science, **2008**. 43(7): p. 2217-2221.

71. Venkatachalam, N., M. Palanichamy, and V. Murugesan, *Sol–gel preparation and characterization of nanosize TiO₂: its photocatalytic performance.* Materials Chemistry and Physics, **2007**. 104(2): p. 454-459.

72. Moustakas, N., A. Kontos, V. Likodimos, F. Katsaros, N. Boukos, D. Tsoutsou, A. Dimoulas, G. Romanos, D. Dionysiou, and P. Falaras, *Inorganic–organic core–shell titania nanoparticles for efficient visible light activated photocatalysis.* Applied Catalysis B: Environmental, **2013**. 130: p. 14-24.

73. Liu, B., Y. Xu, J. Cui, S. Wang, and T. Wang, *Carbon nanotubes-dispersed TiO₂ nanoparticles with their enhanced photocatalytic activity.* Materials Research Bulletin, **2014**. 59(0): p. 278-282.

74. Yang, H.G., G. Liu, S.Z. Qiao, C.H. Sun, Y.G. Jin, S.C. Smith, J. Zou, H.M. Cheng, and G.Q. Lu, *Solvothermal synthesis and photoreactivity of anatase TiO₂ nanosheets with dominant {001} facets.* Journal of the American Chemical Society, **2009**. 131(11): p. 4078-4083.

75. Cao, Y., L. Zong, Q. Li, C. Li, J. Li, and J. Yang, *Solvothermal synthesis of TiO₂ nanocrystals with {001} facets using titanic acid nanobelts for superior photocatalytic activity.* Applied Surface Science, **2017**. 391: p. 311-317.

76. Rausch, N. and E. Burte, *Thin TiO₂ films prepared by low pressure chemical vapor deposition.* Journal of the Electrochemical Society, **1993**. 140(1): p. 145-149.

77. Wu, M., J. Long, A. Huang, Y. Luo, S. Feng, and R. Xu, *Microemulsion-mediated hydrothermal synthesis and characterization of nanosize rutile and anatase particles.* Langmuir, **1999**. 15(26): p. 8822-8825.

78. Abazović, N.D., L. Mirenghi, I.A. Janković, N. Bibić, D.V. Šojić, B.F. Abramović, and M.I. Čomor, *Synthesis and characterization of rutile TiO₂ nanopowders doped with iron ions.* Nanoscale research letters, **2009**. 4(6): p. 518-525.

79. Grandcolas, M. and J. Ye, *Preparation of fine, uniform nitrogen-and sulfur-modified TiO₂ nanoparticles from titania nanotubes.* Science and Technology of Advanced Materials, **2010**. 11(5): p. 055001.

80. Melero, J.A., L.F. Bautista, G. Morales, J. Iglesias, and R. Sánchez-Vázquez, *Biodiesel production from crude palm oil using sulfonic acid-modified mesostructured catalysts.* Chemical Engineering Journal, **2010**. 161(3): p. 323-331.

81. Zhao, J., M. Milanova, M.M. Warmoeskerken, and V. Dutschk, *Surface modification of TiO₂ nanoparticles with silane coupling agents.* Colloids and surfaces A: Physicochemical and engineering aspects, **2012**. 413: p. 273-279.

82. Kang, S., J. Ye, and J. Chang, *Recent advances in carbon-based sulfonated catalyst: preparation and application.* International Review of Chemical Engineering (IRECHE), **2013**. 5(2): p. 133-144.

83. Patel, A. and V. Brahmkhatri, *Kinetic study of oleic acid esterification over 12-tungstophosphoric acid catalyst anchored to different mesoporous silica supports.* Fuel processing technology, **2013**. 113: p. 141-149.

84. Toh-Ae, P., B. Junhasavasdikul, N. Lopattananon, and K. Sahakaro. *Surface modification of TiO₂ nanoparticles by grafting with silane coupling agent*. in *Advanced Materials Research*. **2014**. Trans Tech Publ.

85. Radoman, T., J. Džunuzović, K. Trifković, T. Palija, A. Marinković, B. Bugarski, and E. Dĺunuzović, *Effect of surface modified TiO₂ nanoparticles on thermal, barrier and mechanical properties of long oil alkyd resin-based coatings.* Express Polymer Letters, **2015**. 9(10).

86. Shu, Q., J. Gao, Z. Nawaz, Y. Liao, D. Wang, and J. Wang, *Synthesis of biodiesel from waste vegetable oil with large amounts of free fatty acids using a carbon-based solid acid catalyst.* Applied Energy, **2010**. 87(8): p. 2589-2596.

87. Lee, A.F. and K. Wilson, *Recent developments in heterogeneous catalysis for the sustainable production of biodiesel.* Catalysis Today, **2015**. 242: p. 3-18.

88. Noda, L.K., R.M. de Almeida, L.F.D. Probst, and N.S. Gonçalves, *Characterization of sulfated TiO₂ prepared by the sol–gel method and its catalytic activity in the n-hexane isomerization reaction.* Journal of Molecular Catalysis A: Chemical, **2005**. 225(1): p. 39-46.

89. Nishikiori, H., M. Hayashibe, and T. Fujii, *Visible light-photocatalytic activity of sulfate-doped titanium dioxide prepared by the Sol− Gel method.* Catalysts, **2013**. 3(2): p. 363-377.

90. Wang, K., J. Jiang, Z. Si, and X. Liang, *Biodiesel production from waste cooking oil catalyzed by solid acid $SO_4^{2-}/TiO_2/La^{3+}$.* Journal of Renewable and Sustainable Energy, **2013**. 5(5): p. 052001.

91. Chen, F., G. Coudurier, J. Joly, and J. Vedrine, *Superacid and catalytic properties of sulfated zirconia.* Journal of Catalysis, **1993**. 143(2): p. 616-626.

92. Morterra, C., G. Cerrato, C. Emanuel, and V. Bolis, *On the surface acidity of some sulfate-doped ZrO₂ catalysts.* Journal of Catalysis, **1993**. 142(2): p. 349-367.

93. Yadav, G.D. and J.J. Nair, *Sulfated zirconia and its modified versions as promising catalysts for industrial processes.* Microporous and mesoporous materials, **1999**. 33(1): p. 1-48.

94. Noda, L.K., R.M. de Almeida, N.S. Gonçalves, L.F.D. Probst, and O. Sala, *TiO₂ with a high sulfate content—thermogravimetric analysis, determination of acid sites by infrared spectroscopy and catalytic activity.* Catalysis today, **2003**. 85(1): p. 69-74.

95. Sun, Y., S. Ma, Y. Du, L. Yuan, S. Wang, J. Yang, F. Deng, and F.-S. Xiao, *Solvent-free preparation of nanosized sulfated zirconia with Brønsted acidic sites from a simple calcination.* The Journal of Physical Chemistry B, **2005**. 109(7): p. 2567-2572.

96. LI, G., *Surface modification and characterizations of TiO₂ nanoparticle.* Surface Review and Letters, **2009**. 16(01): p. 149-151.

97. Refaat, A., *Biodiesel production using solid metal oxide catalysts.* International Journal of Environmental Science & Technology, **2011**. 8(1): p. 203-221.

98. Cui, H., K. Dwight, S. Soled, and A. Wold, *Surface acidity and photocatalytic activity of Nb₂O₅/TiO₂ photocatalysts.* Journal of Solid State Chemistry, **1995**. 115(1): p. 187-191.

99. Cheung, T.-K. and B.C. Gates, *Activation of ethane in the presence of solid acids: Sulfated zirconia, iron- and manganese-promoted sulfated zirconia, and zeolites.* Journal of Catalysis, **1997**. 168(2): p. 522-531.

100. Ebitani, K., J. Konishi, and H. Hattori, *Skeletal isomerization of hydrocarbons over zirconium oxide promoted by platinum and sulfate ion.* Journal of Catalysis, **1991**. 130(1): p. 257-267.

101. Alhassan, F.H., U. Rashid, and Y. Taufiq-Yap, *Synthesis of waste cooking oil-based biodiesel via effectual recyclable bi-functional Fe_2O_3-MnO-SO_4^{2-}/ZrO_2 nanoparticle solid catalyst.* Fuel, **2015**. 142: p. 38-45.

102. Sani, Y.M., W.M.A.W. Daud, and A.A. Aziz, *Activity of solid acid catalysts for biodiesel production: a critical review.* Applied Catalysis A: General, **2014**. 470: p. 140-161.

103. Wang, H., J. Covarrubias, H. Prock, X. Wu, D. Wang, and S.H. Bossmann, *Acid-functionalized magnetic nanoparticle as heterogeneous catalysts for biodiesel synthesis.* The Journal of Physical Chemistry C, **2015**. 119(46): p. 26020-26028.

104. Gong, S.-w., J. Lu, H.-h. Wang, L.-j. Liu, and Q. Zhang, *Biodiesel production via esterification of oleic acid catalyzed by picolinic acid modified 12-tungstophosphoric acid.* Applied Energy, **2014**. 134: p. 283-289.

105. Lee, A.F., *Catalysing sustainable fuel and chemical synthesis.* Applied Petrochemical Research, **2014**. 4(1): p. 11-31.

106. Silitonga, A., A. Atabani, T. Mahlia, H. Masjuki, I.A. Badruddin, and S. Mekhilef, *A review on prospect of Jatropha curcas for biodiesel in Indonesia.* Renewable and Sustainable Energy Reviews, **2011**. 15(8): p. 3733-3756.

107. Meng, X., J. Yang, X. Xu, L. Zhang, Q. Nie, and M. Xian, *Biodiesel production from oleaginous microorganisms.* Renewable energy, **2009**. 34(1): p. 1-5.

108. Ahmad, A., N.M. Yasin, C. Derek, and J. Lim, *Microalgae as a sustainable energy source for biodiesel production: a review.* Renewable and Sustainable Energy Reviews, **2011**. 15(1): p. 584-593.

109. van Kasteren, J.M.N. and A.P. Nisworo, *A process model to estimate the cost of industrial scale biodiesel production from waste cooking oil by supercritical transesterification.* Resources, Conservation and Recycling, **2007**. 50(4): p. 442-458.

110. Guzatto, R., D. Defferrari, Q.B. Reiznautt, Í.R. Cadore, and D. Samios, *Transesterification double step process modification for ethyl ester biodiesel production from vegetable and waste oils.* Fuel, **2012**. 92(1): p. 197-203.

111. Joshi, H., B.R. Moser, and T. Walker, *Mixed alkyl esters from cottonseed oil: Improved biodiesel properties and blends with diesel fuel.* Journal of the American Oil Chemists' Society, **2012**. 89(1): p. 145-153.

112. Oh, P.P., H.L.N. Lau, J. Chen, M.F. Chong, and Y.M. Choo, *A review on conventional technologies and emerging process intensification (PI) methods for biodiesel production.* Renewable and Sustainable Energy Reviews, **2012**. 16(7): p. 5131-5145.

113. Atadashi, I.M., M.K. Aroua, A.R. Abdul Aziz, and N.M.N. Sulaiman, *Membrane biodiesel production and refining technology: A critical review.* Renewable and Sustainable Energy Reviews, **2011**. 15(9): p. 5051-5062.

114. Atadashi, I.M., M.K. Aroua, A.R. Abdul Aziz, and N.M.N. Sulaiman, *High quality biodiesel obtained through membrane technology.* Journal of Membrane Science, **2012**. 421-422: p. 154-164.

115. Ali, M.H., M. Mashud, M.R. Rubel, and R.H. Ahmad, *Biodiesel from Neem Oil as an Alternative Fuel for Diesel Engine.* Procedia Engineering, **2013**. 56: p. 625-630.

116. Atabani, A.E., A.S. Silitonga, H.C. Ong, T.M.I. Mahlia, H.H. Masjuki, I.A. Badruddin, and H. Fayaz, *Non-edible vegetable oils: A critical evaluation of oil extraction, fatty acid compositions, biodiesel production, characteristics, engine performance and emissions production.* Renewable and Sustainable Energy Reviews, **2013**. 18: p. 211-245.

117. Luque, R. and J.A. Melero, *Advances in biodiesel production: Processes and technologies*. **2012**: Elsevier.

118. Usta, N., B. Aydoğan, A.H. Çon, E. Uğuzdoğan, and S.G. Özkal, *Properties and quality verification of biodiesel produced from tobacco seed oil.* Energy Conversion and Management, **2011**. 52(5): p. 2031-2039.

119. Subramaniam, D., A. Murugesan, A. Avinash, and A. Kumaravel, *Bio-diesel production and its engine characteristics—An expatiate view.* Renewable and Sustainable Energy Reviews, **2013**. 22: p. 361-370.

120. Singh, S.P. and D. Singh, *Biodiesel production through the use of different sources and characterization of oils and their esters as the substitute of diesel: A review.* Renewable and Sustainable Energy Reviews, **2010**. 14(1): p. 200-216.

121. Upham, P., P. Thornley, J. Tomei, and P. Boucher, *Substitutable biodiesel feedstocks for the UK: a review of sustainability issues with reference to the UK RTFO.* Journal of Cleaner Production, **2009**. 17: p. S37-S45.

122. Cetinkaya, M. and F. Karaosmanoglu, *Optimization of base-catalyzed transesterification reaction of used cooking oil.* Energy & fuels, **2004**. 18(6): p. 1888-1895.

123. Srivastava, A. and R. Prasad, *Triglycerides-based diesel fuels.* Renewable and sustainable energy reviews, **2000**. 4(2): p. 111-133.

124. Demirbaş, A., *Biodiesel fuels from vegetable oils via catalytic and non-catalytic supercritical alcohol transesterifications and other methods: a survey.* Energy conversion and Management, **2003**. 44(13): p. 2093-2109.

125. Leung, D. and Y. Guo, *Transesterification of neat and used frying oil: optimization for biodiesel production.* Fuel Processing Technology, **2006**. 87(10): p. 883-890.

126. Romero, R., S.L. Martínez, and R. Natividad, *Biodiesel production by using heterogeneous catalysts.* Alternative Fuel, **2011**.

127. Marchetti, J.M., *A summary of the available technologies for biodiesel production based on a comparison of different feedstock's properties.* Process Safety and Environmental Protection, **2012**. 90(3): p. 157-163.

128. Demirbas, A., *Biodiesel production from vegetable oils via catalytic and non-catalytic supercritical methanol transesterification methods.* Progress in Energy and Combustion Science, **2005**. 31(5-6): p. 466-487.

129. ASTM-D6751, *Standard Specification for Biodiesel Fuel Blend Stock (B100) for Middle Distillate Fuels.* **2012**: p. 1-11.

130. EN-14214, *Automotive fuels. Fatty acid methyl esters (FAME) for diesel engines. Requirements and test methods.* **2009**: p. 1-15.

131. Wang, L.-b., H.-y. Yu, X.-h. He, and R.-y. Liu, *Influence of fatty acid composition of woody biodiesel plants on the fuel properties.* Journal of Fuel Chemistry and Technology, **2012**. 40(4): p. 397-404.

132. Sarin, R., M. Sharma, S. Sinharay, and R.K. Malhotra, *Jatropha–Palm biodiesel blends: An optimum mix for Asia.* Fuel, **2007**. 86(10-11): p. 1365-1371.

133. Yusuf, N.N.A.N., S.K. Kamarudin, and Z. Yaakub, *Overview on the current trends in biodiesel production.* Energy Conversion and Management, **2011**. 52(7): p. 2741-2751.

134. Imran, A., E.A. Bramer, K. Seshan, and G. Brem, *Catalytic flash pyrolysis of biomass using different types of zeolite and online vapor fractionation.* Energies, **2016**. 9(3): p. 187.

135. Manayil, J., A. Osatiashtiani, A. Mendoza, C. Parlett, L. Durndell, M. Isaacs, C. Michailof, E. Heracleous, A. Lappas, and A. Lee, *Impact of macroporosity on catalytic upgrading of fast pyrolysis bio‐oil by esterification over silica sulfonic acids.* ChemSusChem, **2017**.

136. Brown, R.C. and K. Wang, *Fast pyrolysis of biomass: Advances in science and technology*. Vol. 50. **2017**: Royal Society of Chemistry.

137. Maher, K.D. and D.C. Bressler, *Pyrolysis of triglyceride materials for the production of renewable fuels and chemicals.* Bioresour Technol, **2007**. 98(12): p. 2351-68.

138. Lehto, J., A. Oasmaa, Y. Solantausta, M. Kytö, and D. Chiaramonti, *Fuel oil quality and combustion of fast pyrolysis bio-oils*. **2013**: VTT Helsinki, Finland.

139. Ito, T., Y. Sakurai, Y. Kakuta, M. Sugano, and K. Hirano, *Biodiesel production from waste animal fats using pyrolysis method.* Fuel Processing Technology, **2012**. 94(1): p. 47-52.

140. Mondal, P., M. Basu, and N. Balasubramanian, *Direct use of vegetable oil and animal fat as alternative fuel in internal combustion engine.* Biofuels, Bioproducts and Biorefining, **2008**. 2(2): p. 155-174.

141. Berman, P., S. Nizri, and Z. Wiesman, *Castor oil biodiesel and its blends as alternative fuel.* Biomass and Bioenergy, **2011**. 35(7): p. 2861-2866.

142. Dufek, E., R. Butterfield, and E. Frankel, *Esterification and transesterification of 9 (10)-carboxystearic acid and its methyl esters. Kinetic studies.* Journal of the American Oil Chemists Society, **1972**. 49(5): p. 302-306.

143. Tyson, K.S., J. Bozell, R. Wallace, E. Petersen, and L. Moens, *Biomass oil analysis: research needs and recommendations*, **2004**, DTIC Document.

144. Gerpen, J.V., *Biodiesel processing and production.* Fuel Processing Technology, **2005**. 86(10): p. 1097-1107.

145. Fukuda, H., A. Kondo, and H. Noda, *Biodiesel fuel production by transesterification of oils.* Journal of bioscience and bioengineering, **2001**. 92(5): p. 405-416.

146. Lin, C.-C., *Optimization of Biodiesel Production from Waste Vegetable Oil Assisted by Co-Solvent and Microwave Using a Two-Step Process.* Journal of Sustainable Bioenergy Systems, **2013**. 03(01): p. 1-6.

147. Kattimani, V. and B. Venkatesha, *Technologies for biodiesel production from non-edible oils: A review.* Indian Journal of Energy, **2013**. 2(6): p. 129-133.

148. Freedman, B., E. Pryde, and T. Mounts, *Variables affecting the yields of fatty esters from transesterified vegetable oils.* Journal of the American Oil Chemists' Society, **1984**. 61(10): p. 1638-1643.

149. Freedman, B., R.O. Butterfield, and E.H. Pryde, *Transesterification kinetics of soybean oil 1.* Journal of the American Oil Chemists' Society, **1986**. 63(10): p. 1375-1380.

150. Ejikeme, P., I. Anyaogu, C. Ejikeme, N. Nwafor, C. Egbuonu, K. Ukogu, and J. Ibemesi, *Catalysis in biodiesel production by transesterification processes-an insight.* Journal of Chemistry, **2010**. 7(4): p. 1120-1132.

151. Lotero, E., Y. Liu, D.E. Lopez, K. Suwannakarn, D.A. Bruce, and J.G. Goodwin, *Synthesis of biodiesel via acid catalysis.* Industrial & engineering chemistry research, **2005**. 44(14): p. 5353-5363.

152. Samios, D., F. Pedrotti, A. Nicolau, Q.B. Reiznautt, D.D. Martini, and F.M. Dalcin, *A Transesterification Double Step Process — TDSP for biodiesel preparation from fatty acids triglycerides.* Fuel Processing Technology, **2009**. 90(4): p. 599-605.

153. Goff, M.J., N.S. Bauer, S. Lopes, W.R. Sutterlin, and G.J. Suppes, *Acid-catalyzed alcoholysis of soybean oil.* Journal of the American Oil Chemists' Society, **2004**. 81(4): p. 415-420.

154. Freedman, B., E. Pryde, and T. Mounts, *Variables affecting the yields of fatty esters from transesterified vegetable oils.* Journal of the American Oil Chemists Society, **1984**. 61(10): p. 1638-1643.

155. Ladner, Y., F. D'Orlyé, C. Perréard, B. Da Silva, C. Guyon, M. Tatoulian, S. Griveau, F. Bedioui, and A. Varenne, *Surface functionalization by plasma treatment and click chemistry of a new family of fluorinated polymeric materials for microfluidic chips.* Plasma Processes and Polymers, **2014**. 11(6): p. 518-523.

156. Math, M., S.P. Kumar, and S.V. Chetty, *Technologies for biodiesel production from used cooking oil—A review.* Energy for Sustainable Development, **2010**. 14(4): p. 339-345.

157. Al-Widyan, M.I. and A.O. Al-Shyoukh, *Experimental evaluation of the transesterification of waste palm oil into biodiesel.* Bioresource technology, **2002**. 85(3): p. 253-256.

158. Zhang, Y., M.A. Dube, D.D. McLean, and M. Kates, *Biodiesel production from waste cooking oil: 1. Process design and technological assessment.* Bioresour Technol, **2003**. 89(1): p. 1-16.

159. Shahid, E.M. and Y. Jamal, *Production of biodiesel: A technical review.* Renewable and Sustainable Energy Reviews, **2011**. 15(9): p. 4732-4745.

160. Huber, G.W., S. Iborra, and A. Corma, *Synthesis of transportation fuels from biomass: chemistry, catalysts, and engineering.* Chemical reviews, **2006**. 106(9): p. 4044-4098.

161. Ma, F. and M.A. Hanna, *Biodiesel production: a review[1].* Bioresource Technology, **1999**. 70(1): p. 1-15.

162. Canakci, M. and J. Van Gerpen, *Biodiesel production from oils and fats with high free fatty acids.* Transactions of the ASAE, **2001**. 44(6): p. 1429.

163. Keyes, D., *Esterification processes and equipment.* Industrial & Engineering Chemistry, **1932**. 24(10): p. 1096-1103.

164. Felizardo, P., M.J.N. Correia, I. Raposo, J.F. Mendes, R. Berkemeier, and J.M. Bordado, *Production of biodiesel from waste frying oils.* Waste management, **2006**. 26(5): p. 487-494.

165. Marris, E., *Sugar cane and ethanol: Drink the best and drive the rest.* Nature, **2006**. 444(7120): p. 670.

166. Encinar, J.M., J.F. González, and A. Rodríguez-Reinares, *Ethanolysis of used frying oil. Biodiesel preparation and characterization.* Fuel Processing Technology, **2007**. 88(5): p. 513-522.

167. Saydut, A., M.Z. Duz, C. Kaya, A.B. Kafadar, and C. Hamamci, *Transesterified sesame (Sesamum indicum L.) seed oil as a biodiesel fuel.* Bioresour Technol, **2008**. 99(14): p. 6656-60.

168. Fang, F.G.a.Z., *Biodiesel Production with Solid Catalysts.* **2011**.

169. Atapour, M., H.-R. Kariminia, and P.M. Moslehabadi, *Optimization of biodiesel production by alkali-catalyzed transesterification of used frying oil.* Process Safety and Environmental Protection, **2013**.

170. Meng, X., G. Chen, and Y. Wang, *Biodiesel production from waste cooking oil via alkali catalyst and its engine test.* Fuel Processing Technology, **2008**. 89(9): p. 851-857.

171. Kumar Tiwari, A., A. Kumar, and H. Raheman, *Biodiesel production from jatropha oil (Jatropha curcas) with high free fatty acids: An optimized process.* Biomass and Bioenergy, **2007**. 31(8): p. 569-575.

172. Rashid, U. and F. Anwar, *Production of biodiesel through base-catalyzed transesterification of safflower oil using an optimized protocol.* Energy & Fuels, **2008**. 22(2): p. 1306-1312.

173. Rashid, U. and F. Anwar, *Production of biodiesel through optimized alkaline-catalyzed transesterification of rapeseed oil.* Fuel, **2008**. 87(3): p. 265-273.

174. Rashid, U., F. Anwar, B.R. Moser, and S. Ashraf, *Production of sunflower oil methyl esters by optimized alkali-catalyzed methanolysis.* Biomass and bioenergy, **2008**. 32(12): p. 1202-1205.

175. Alenezi, R., R. Santos, S. Raymahasay, and G. Leeke, *Improved biodiesel manufacture at low temperature and short reaction time.* Renewable Energy, **2013**. 53: p. 242-248.

176. Chattopadhyay, S. and R. Sen, *Fuel properties, engine performance and environmental benefits of biodiesel produced by a green process.* Applied Energy, **2013**. 105: p. 319-326.

177. Shieh, C.-J., H.-F. Liao, and C.-C. Lee, *Optimization of lipase-catalyzed biodiesel by response surface methodology.* Bioresource Technology, **2003**. 88(2): p. 103-106.

178. Azócar, L., H.J. Heipieper, R. Muñoz, and R. Navia, *Improving fatty acid methyl ester production yield in a lipase-catalyzed process using waste frying oils as feedstock.* Journal of bioscience and bioengineering, **2010**. 109(6): p. 609-614.

179. Soumanou, M.M. and U.T. Bornscheuer, *Improvement in lipase-catalyzed synthesis of fatty acid methyl esters from sunflower oil.* Enzyme and Microbial Technology, **2003**. 33(1): p. 97-103.

180. Li, L., W. Du, D. Liu, L. Wang, and Z. Li, *Lipase-catalyzed transesterification of rapeseed oils for biodiesel production with a novel organic solvent as the reaction medium.* Journal of Molecular Catalysis B: Enzymatic, **2006**. 43(1): p. 58-62.

181. Kresnawahjuesa, O., R.J. Gorte, D. De Oliveira, and L. Lau, *A simple, inexpensive, and reliable method for measuring Brønsted-acid site densities in solid acids.* Catalysis letters, **2002**. 82(3): p. 155-160.

182. Demirbas, A., *Importance of biodiesel as transportation fuel.* Energy Policy, **2007**. 35(9): p. 4661-4670.

183. Madras, G., C. Kolluru, and R. Kumar, *Synthesis of biodiesel in supercritical fluids.* Fuel, **2004**. 83(14): p. 2029-2033.

184. He, H., T. Wang, and S. Zhu, *Continuous production of biodiesel fuel from vegetable oil using supercritical methanol process.* Fuel, **2007**. 86(3): p. 442-447.

185. Hawash, S., N. Kamal, F. Zaher, O. Kenawi, and G.E. Diwani, *Biodiesel fuel from Jatropha oil via non-catalytic supercritical methanol transesterification.* Fuel, **2009**. 88(3): p. 579-582.

186. Demirbas, A., *Biodiesel from waste cooking oil via base-catalytic and supercritical methanol transesterification.* Energy Conversion and Management, **2009**. 50(4): p. 923-927.

187. Marulanda, V.F., G. Anitescu, and L.L. Tavlarides, *Biodiesel fuels through a continuous flow process of chicken fat supercritical transesterification.* Energy & Fuels, **2009**. 24(1): p. 253-260.

188. Tan, K.T., M.M. Gui, K.T. Lee, and A.R. Mohamed, *An optimized study of methanol and ethanol in supercritical alcohol technology for biodiesel production.* The Journal of Supercritical Fluids, **2010**. 53(1): p. 82-87.

189. Lam, M.K., K.T. Lee, and A.R. Mohamed, *Homogeneous, heterogeneous and enzymatic catalysis for transesterification of high free fatty acid oil (waste cooking oil) to biodiesel: a review.* Biotechnol Adv, **2010**. 28(4): p. 500-18.

190. Chastain, J., R.C. King, and J. Moulder, *Handbook of X-ray photoelectron spectroscopy: a reference book of standard spectra for identification and interpretation of XPS data*. **1992**: Physical Electronics Division, Perkin-Elmer Corporation Eden Prairie, Minnesota.

191. Kildiran, G., S.Ö. Yücel, and S. Türkay, *In-situ alcoholysis of soybean oil.* Journal of the American Oil Chemists' Society, **1996**. 73(2): p. 225-228.

192. Siler-Marinkovic, S. and A. Tomasevic, *Transesterification of sunflower oil in situ.* Fuel, **1998**. 77(12): p. 1389-1391.

193. Georgogianni, K., M. Kontominas, P. Pomonis, D. Avlonitis, and V. Gergis, *Conventional and in situ transesterification of sunflower seed oil for the production of biodiesel.* Fuel Processing Technology, **2008**. 89(5): p. 503-509.

194. Qian, J., F. Wang, S. Liu, and Z. Yun, *In situ alkaline transesterification of cottonseed oil for production of biodiesel and nontoxic cottonseed meal.* Bioresource Technology, **2008**. 99(18): p. 9009-9012.

195. Sánchez, A., R. Maceiras, A. Cancela, and M. Rodríguez, *Influence of n-hexane on in situ transesterification of marine macroalgae.* Energies, **2012**. 5(2): p. 243-257.

196. Mootabadi, H., B. Salamatinia, S. Bhatia, and A.Z. Abdullah, *Ultrasonic-assisted biodiesel production process from palm oil using alkaline earth metal oxides as the heterogeneous catalysts.* Fuel, **2010**. 89(8): p. 1818-1825.

197. Deng, X., Z. Fang, and Y.-h. Liu, *Ultrasonic transesterification of Jatropha curcas L. oil to biodiesel by a two-step process.* Energy Conversion and Management, **2010**. 51(12): p. 2802-2807.

198. Hingu, S.M., P.R. Gogate, and V.K. Rathod, *Synthesis of biodiesel from waste cooking oil using sonochemical reactors.* Ultrason Sonochem, **2010**. 17(5): p. 827-32.

199. Talebian-Kiakalaieh, A., N.A.S. Amin, and H. Mazaheri, *A review on novel processes of biodiesel production from waste cooking oil.* Applied Energy, **2013**. 104: p. 683-710.

200. Kumar, D., G. Kumar, and C. Singh, *Fast, easy ethanolysis of coconut oil for biodiesel production assisted by ultrasonication.* Ultrasonics sonochemistry, **2010**. 17(3): p. 555-559.

201. Santos, F.F., S. Rodrigues, and F.A. Fernandes, *Optimization of the production of biodiesel from soybean oil by ultrasound assisted methanolysis.* Fuel processing technology, **2009**. 90(2): p. 312-316.

202. Thanh, L.T., K. Okitsu, Y. Sadanaga, N. Takenaka, Y. Maeda, and H. Bandow, *A two-step continuous ultrasound assisted production of biodiesel fuel from waste cooking oils: a practical and economical approach to produce high quality biodiesel fuel.* Bioresource technology, **2010**. 101(14): p. 5394-5401.

203. Thanh, L.T., K. Okitsu, Y. Sadanaga, N. Takenaka, Y. Maeda, and H. Bandow, *Ultrasound-assisted production of biodiesel fuel from vegetable oils in a small scale circulation process.* Bioresource technology, **2010**. 101(2): p. 639-645.

204. Motasemi, F. and F.N. Ani, *A review on microwave-assisted production of biodiesel.* Renewable and Sustainable Energy Reviews, **2012**. 16(7): p. 4719-4733.

205. Gole, V.L. and P.R. Gogate, *A review on intensification of synthesis of biodiesel from sustainable feed stock using sonochemical reactors.* Chemical Engineering and Processing: Process Intensification, **2012**. 53: p. 1-9.

206. Hernando, J., P. Leton, M.P. Matia, J.L. Novella, and J. Alvarez-Builla, *Biodiesel and FAME synthesis assisted by microwaves: Homogeneous batch and flow processes.* Fuel, **2007**. 86(10-11): p. 1641-1644.

207. Lertsathapornsuk, V., R. Pairintra, K. Aryusuk, and K. Krisnangkura, *Microwave assisted in continuous biodiesel production from waste frying palm oil and its performance in a 100 kW diesel generator.* Fuel Processing Technology, **2008**. 89(12): p. 1330-1336.

208. Patil, P.D., V.G. Gude, H.K. Reddy, T. Muppaneni, and S. Deng, *Biodiesel Production from Waste Cooking Oil Using Sulfuric Acid and Microwave Irradiation Processes.* Journal of Environmental Protection, **2012**. 03(01): p. 107-113.

209. Azcan, N. and A. Danisman, *Microwave assisted transesterification of rapeseed oil.* Fuel, **2008**. 87(10-11): p. 1781-1788.

210. Xi, Y. and R.J. Davis, *Influence of water on the activity and stability of activated Mg Al hydrotalcites for the transesterification of tributyrin with methanol.* Journal of Catalysis, **2008**. 254(2): p. 190-197.

211. Watkins, R.S., A.F. Lee, and K. Wilson, *Li–CaO catalysed tri-glyceride transesterification for biodiesel applications.* Green Chemistry, **2004**. 6(7): p. 335-340.

212. Narasimharao, K., D. Brown, A.F. Lee, A. Newman, P. Siril, S. Tavener, and K. Wilson, *Structure–activity relations in Cs-doped heteropolyacid catalysts for biodiesel production.* Journal of catalysis, **2007**. 248(2): p. 226-234.

213. Woodford, J.J., J.-P. Dacquin, K. Wilson, and A.F. Lee, *Better by design: nanoengineered macroporous hydrotalcites for enhanced catalytic biodiesel production.* Energy & Environmental Science, **2012**. 5(3): p. 6145-6150.

214. Hattori, H. and Y. Ono, *Solid acid catalysis: From fundamentals to applications.* **2015**: CRC Press.

215. Wilson, K. and A.F. Lee, *Rational design of heterogeneous catalysts for biodiesel synthesis.* Catalysis Science & Technology, **2012**. 2(5): p. 884-897.

216. Zhao, L., Z. Qiu, and S.M. Stagg-Williams, *Transesterification of canola oil catalyzed by nanopowder calcium oxide.* Fuel Processing Technology, **2013**. 114: p. 154-162.

217. Verziu, M., S.M. Coman, R. Richards, and V.I. Parvulescu, *Transesterification of vegetable oils over CaO catalysts.* Catalysis today, **2011**. 167(1): p. 64-70.

218. Montero, J.M., K. Wilson, and A.F. Lee, *Cs promoted triglyceride transesterification over MgO nanocatalysts.* Topics in Catalysis, **2010**. 53(11-12): p. 737-745.

219. Cantrell, D.G., L.J. Gillie, A.F. Lee, and K. Wilson, *Structure-reactivity correlations in MgAl hydrotalcite catalysts for biodiesel synthesis.* Applied Catalysis A: General, **2005**. 287(2): p. 183-190.

220. Trakarnpruk, W. and S. Porntangjitlikit, *Palm oil biodiesel synthesized with potassium loaded calcined hydrotalcite and effect of biodiesel blend on elastomer properties.* Renewable Energy, **2008**. 33(7): p. 1558-1563.

221. Gomes, J.F., J.F. Puna, L.M. Gonçalves, and J.C. Bordado, *Study on the use of MgAl hydrotalcites as solid heterogeneous catalysts for biodiesel production.* Energy, **2011**. 36(12): p. 6770-6778.

222. Silva, C.C.C., N.F. Ribeiro, M.M. Souza, and D.A. Aranda, *Biodiesel production from soybean oil and methanol using hydrotalcites as catalyst.* Fuel Processing Technology, **2010**. 91(2): p. 205-210.

223. Kaur, M. and A. Ali, *Lithium ion impregnated calcium oxide as nano catalyst for the biodiesel production from karanja and jatropha oils.* Renewable Energy, **2011**. 36(11): p. 2866-2871.

224. Liu, H., L. Su, Y. Shao, and L. Zou, *Biodiesel production catalyzed by cinder supported CaO/KF particle catalyst.* Fuel, **2012**. 97: p. 651-657.

225. Vyas, A.P., N. Subrahmanyam, and P.A. Patel, *Production of biodiesel through transesterification of Jatropha oil using KNO_3/Al_2O_3 solid catalyst.* Fuel, **2009**. 88(4): p. 625-628.

226. Umdu, E.S., M. Tuncer, and E. Seker, *Transesterification of Nannochloropsis oculata microalga's lipid to biodiesel on Al_2O_3 supported CaO and MgO catalysts.* Bioresource Technology, **2009**. 100(11): p. 2828-2831.

227. Kouzu, M., T. Kasuno, M. Tajika, Y. Sugimoto, S. Yamanaka, and J. Hidaka, *Calcium oxide as a solid base catalyst for transesterification of soybean oil and its application to biodiesel production.* Fuel, **2008**. 87(12): p. 2798-2806.

228. Granados, M.L., M.Z. Poves, D.M. Alonso, R. Mariscal, F.C. Galisteo, R. Moreno-Tost, J. Santamaría, and J. Fierro, *Biodiesel from sunflower oil by using activated calcium oxide.* Applied Catalysis B: Environmental, **2007**. 73(3): p. 317-326.

229. Huaping, Z., W. Zongbin, C. Yuanxiong, P. Zhang, D. Shijie, L. Xiaohua, and M. Zongqiang, *Preparation of biodiesel catalyzed by solid super base of calcium oxide and its refining process.* Chinese Journal of Catalysis, **2006**. 27(5): p. 391-396.

230. Venkat Reddy, C.R., R. Oshel, and J.G. Verkade, *Room-temperature conversion of soybean oil and poultry fat to biodiesel catalyzed by nanocrystalline calcium oxides.* Energy & Fuels, **2006**. 20(3): p. 1310-1314.

231. Liu, X., H. He, Y. Wang, S. Zhu, and X. Piao, *Transesterification of soybean oil to biodiesel using CaO as a solid base catalyst.* Fuel, **2008**. 87(2): p. 216-221.

232. Liu, X., H. He, Y. Wang, and S. Zhu, *Transesterification of soybean oil to biodiesel using SrO as a solid base catalyst.* Catalysis Communications, **2007**. 8(7): p. 1107-1111.

233. Koberg, M. and A. Gedanken, *Direct transesterification of castor and Jatropha seeds for FAME production by microwave and ultrasound radiation using a SrO catalyst.* BioEnergy Research, **2012**. 5(4): p. 958-968.

234. Semwal, S., A.K. Arora, R.P. Badoni, and D.K. Tuli, *Biodiesel production using heterogeneous catalysts.* Bioresource technology, **2011**. 102(3): p. 2151-2161.

235. Zabeti, M., W.M.A.W. Daud, and M.K. Aroua, *Activity of solid catalysts for biodiesel production: a review.* Fuel Processing Technology, **2009**. 90(6): p. 770-777.

236. Verziu, M., B. Cojocaru, J. Hu, R. Richards, C. Ciuculescu, P. Filip, and V.I. Parvulescu, *Sunflower and rapeseed oil transesterification to biodiesel over different nanocrystalline MgO catalysts.* Green Chemistry, **2008**. 10(4): p. 373-381.

237. Kouzu, M. and J.-s. Hidaka, *Transesterification of vegetable oil into biodiesel catalyzed by CaO: A review.* Fuel, **2012**. 93: p. 1-12.

238. Colombo, K., L. Ender, and A.A.C. Barros, *The study of biodiesel production using CaO as a heterogeneous catalytic reaction.* Egyptian Journal of Petroleum, **2016**.

239. Hattori, H., *Heterogeneous basic catalysis.* Chemical Reviews, **1995**. 95(3): p. 537-558.

240. Veljković, V.B., O.S. Stamenković, Z.B. Todorović, M.L. Lazić, and D.U. Skala, *Kinetics of sunflower oil methanolysis catalyzed by calcium oxide.* Fuel, **2009**. 88(9): p. 1554-1562.

241. Wang, L. and J. Yang, *Transesterification of soybean oil with nano-MgO or not in supercritical and subcritical methanol.* Fuel, **2007**. 86(3): p. 328-333.

242. Karmee, S.K. and A. Chadha, *Preparation of biodiesel from crude oil of Pongamia pinnata.* Bioresource technology, **2005**. 96(13): p. 1425-1429.

243. Berger, T., J. Schuh, M. Sterrer, O. Diwald, and E. Knözinger, *Lithium ion induced surface reactivity changes on MgO nanoparticles.* Journal of Catalysis, **2007**. 247(1): p. 61-67.

244. Taufiq-Yap, Y., H.V. Lee, R. Yunus, and J.C. Juan, *Transesterification of non-edible Jatropha curcas oil to biodiesel using binary Ca–Mg mixed oxide catalyst: effect of stoichiometric composition.* Chemical Engineering Journal, **2011**. 178: p. 342-347.

245. Phillipp, R. and K. Fujimoto, *FTIR spectroscopy study of carbon dioxide adsorption/desorption on magnesia/calcium oxide catalysts.* The Journal of Physical Chemistry, **1992**. 96: p. 9035-9038.

246. Alonso, D.M., R. Mariscal, M.L. Granados, and P. Maireles-Torres, *Biodiesel preparation using Li/CaO catalysts: activation process and homogeneous contribution.* Catalysis Today, **2009**. 143(1): p. 167-171.

247. Kawashima, A., K. Matsubara, and K. Honda, *Development of heterogeneous base catalysts for biodiesel production.* Bioresource technology, **2008**. 99(9): p. 3439-3443.

248. Macedo, C., F.R. Abreu, A.P. Tavares, M.B. Alves, L.F. Zara, J.C. Rubim, and P.A. Suarez, *New heterogeneous metal-oxides based catalyst for vegetable oil trans-esterification.* Journal of the Brazilian Chemical Society, **2006**. 17(7): p. 1291-1296.

249. Costantino, U., F. Marmottini, M. Nocchetti, and R. Vivani, *New synthetic routes to hydrotalcite-like compounds-characterisation and properties of the obtained materials.* European Journal of Inorganic Chemistry, **1998**. 1998(10): p. 1439-1446.

250. Zeng, H.-y., Z. Feng, X. Deng, and Y.-q. Li, *Activation of Mg–Al hydrotalcite catalysts for transesterification of rape oil.* Fuel, **2008**. 87(13): p. 3071-3076.

251. Di Cosimo, J., V. Dıez, M. Xu, E. Iglesia, and C. Apesteguıa, *Structure and surface and catalytic properties of Mg-Al basic oxides.* Journal of Catalysis, **1998**. 178(2): p. 499-510.

252. Xie, W., H. Peng, and L. Chen, *Calcined Mg–Al hydrotalcites as solid base catalysts for methanolysis of soybean oil.* Journal of Molecular Catalysis A: Chemical, **2006**. 246(1): p. 24-32.

253. Liu, Y., E. Lotero, J.G. Goodwin, and X. Mo, *Transesterification of poultry fat with methanol using Mg–Al hydrotalcite derived catalysts.* Applied Catalysis A: General, **2007**. 331: p. 138-148.

254. Debecker, D.P., E.M. Gaigneaux, and G. Busca, *Exploring, tuning, and exploiting the basicity of hydrotalcites for applications in heterogeneous catalysis.* Chemistry–A European Journal, **2009**. 15(16): p. 3920-3935.

255. Barakos, N., S. Pasias, and N. Papayannakos, *Transesterification of triglycerides in high and low quality oil feeds over an HT2 hydrotalcite catalyst.* Bioresource Technology, **2008**. 99(11): p. 5037-5042.

256. Fraile, J.M., N. García, J.A. Mayoral, E. Pires, and L. Roldán, *The influence of alkaline metals on the strong basicity of Mg–Al mixed oxides: the case of transesterification reactions.* Applied Catalysis A: General, **2009**. 364(1): p. 87-94.

257. Cross, H.E. and D. Brown, *Entrained sodium in mixed metal oxide catalysts derived from layered double hydroxides.* Catalysis Communications, **2010**. 12(3): p. 243-245.

258. Creasey, J.J., C.M. Parlett, J.C. Manayil, M.A. Isaacs, K. Wilson, and A.F. Lee, *Facile route to conformal hydrotalcite coatings over complex architectures: a hierarchically ordered nanoporous base catalyst for FAME production.* Green Chemistry, **2015**. 17(4): p. 2398-2405.

259. Shibasaki-Kitakawa, N., H. Honda, H. Kuribayashi, T. Toda, T. Fukumura, and T. Yonemoto, *Biodiesel production using anionic ion-exchange resin as heterogeneous catalyst.* Bioresource Technology, **2007**. 98(2): p. 416-421.

260. Lee, D.-W., Y.-M. Park, and K.-Y. Lee, *Heterogeneous base catalysts for transesterification in biodiesel synthesis.* Catalysis Surveys from Asia, **2009**. 13(2): p. 63-77.

261. Suppes, G.J., M.A. Dasari, E.J. Doskocil, P.J. Mankidy, and M.J. Goff, *Transesterification of soybean oil with zeolite and metal catalysts.* Applied Catalysis A: General, **2004**. 257(2): p. 213-223.

262. Kapteijn, F., A.D. Vanlangeveld, J.A. Moulijn, A. Andreini, M.A. Vuurman, A.M. Turek, J.-M. Jehng, and I.E. Wachs, *Alumina-supported manganese oxide catalysts: I. Characterization: effect of precursor and loading.* Journal of Catalysis, **1994**. 150(1): p. 94-104.

263. Tang, Y., H. Ren, F. Chang, X. Gu, and J. Zhang, *Nano KF/Al₂O₃ particles as an efficient catalyst for no-glycerol biodiesel production by coupling transesterification.* RSC Advances, **2017**. 7(10): p. 5694-5700.

264. Burch, R. and A. Flambard, *Strong metal-support interactions in nickel/titania catalysts: The importance of interfacial phenomena.* Journal of Catalysis, **1982**. 78(2): p. 389-405.

265. Gesenhues, U. and T. Rentschler, *Crystal growth and defect structure of Al³⁺-doped rutile.* Journal of Solid State Chemistry, **1999**. 143(2): p. 210-218.

266. Salinas, D., P. Araya, and S. Guerrero, *Study of potassium-supported TiO₂ catalysts for the production of biodiesel.* Applied Catalysis B: Environmental, **2012**. 117: p. 260-267.

267. Polshettiwar, V. and Á. Molnár, *Silica-supported Pd catalysts for Heck coupling reactions.* Tetrahedron, **2007**. 63(30): p. 6949-6976.

268. Abdullah, A.Z., N. Razali, and K.T. Lee, *Optimization of mesoporous K/SBA-15 catalyzed transesterification of palm oil using response surface methodology.* Fuel Processing Technology, **2009**. 90(7): p. 958-964.

269. Tangy, A., I.N. Pulidindi, and A. Gedanken, *SiO₂ beads decorated with SrO nanoparticles for biodiesel production from waste cooking oil using microwave irradiation.* Energy & Fuels, **2016**. 30(4): p. 3151-3160.

270. Yamaguchi, T., *Application of ZrO₂ as a catalyst and a catalyst support.* Catalysis Today, **1994**. 20(2): p. 199-217.

271. Omar, W.N.N.W. and N.A.S. Amin, *Biodiesel production from waste cooking oil over alkaline modified zirconia catalyst.* Fuel Processing Technology, **2011**. 92(12): p. 2397-2405.

272. Xie, W., H. Peng, and L. Chen, *Transesterification of soybean oil catalyzed by potassium loaded on alumina as a solid-base catalyst.* Applied Catalysis A: General, **2006**. 300(1): p. 67-74.

273. Kim, H.-J., B.-S. Kang, M.-J. Kim, Y.M. Park, D.-K. Kim, J.-S. Lee, and K.-Y. Lee, *Transesterification of vegetable oil to biodiesel using heterogeneous base catalyst.* Catalysis Today, **2004**. 93-95: p. 315-320.

274. Ma, H., S. Li, B. Wang, R. Wang, and S. Tian, *Transesterification of rapeseed oil for synthesizing biodiesel by K/KOH/γ-Al₂O₃ as heterogeneous base catalyst.* Journal of the American Oil Chemists' Society, **2008**. 85(3): p. 263-270.

275. Wen, Z., X. Yu, S.-T. Tu, J. Yan, and E. Dahlquist, *Biodiesel production from waste cooking oil catalyzed by TiO₂–MgO mixed oxides.* Bioresource technology, **2010**. 101(24): p. 9570-9576.

276. Mbaraka, I.K. and B.H. Shanks, *Conversion of oils and fats using advanced mesoporous heterogeneous catalysts.* Journal of the American Oil Chemists' Society, **2006**. 83(2): p. 79-91.

277. Borges, M. and L. Díaz, *Recent developments on heterogeneous catalysts for biodiesel production by oil esterification and transesterification reactions: a review.* Renewable and Sustainable Energy Reviews, **2012**. 16(5): p. 2839-2849.

278. Shumaker, J.L., C. Crofcheck, S.A. Tackett, E. Santillan-Jimenez, T. Morgan, Y. Ji, M. Crocker, and T.J. Toops, *Biodiesel synthesis using calcined layered double hydroxide catalysts.* Applied Catalysis B: Environmental, **2008**. 82(1): p. 120-130.

279. Mguni, L.L., R. Meijboom, and K. Jalama. *Biodiesel Production over nano-MgO Supported on Titania.* in *Proceedings of World Academy of Science, Engineering and Technology.* **2012**. World Academy of Science, Engineering and Technology.

280. Tantirungrotechai, J., P. Chotmongkolsap, and M. Pohmakotr, *Synthesis, characterization, and activity in transesterification of mesoporous Mg–Al mixed-metal oxides.* Microporous and Mesoporous Materials, **2010**. 128(1): p. 41-47.

281. Albuquerque, M.C., D.C. Azevedo, C.L. Cavalcante, J. Santamaría-González, J.M. Mérida-Robles, R. Moreno-Tost, E. Rodríguez-Castellón, A. Jiménez-López, and P. Maireles-Torres, *Transesterification of ethyl butyrate with methanol using MgO/CaO catalysts.* Journal of Molecular Catalysis A: Chemical, **2009**. 300(1): p. 19-24.

282. Kumar, D. and A. Ali, *Nanocrystalline K–CaO for the transesterification of a variety of feedstocks: Structure, kinetics and catalytic properties.* Biomass and Bioenergy, **2012**.

283. Luz Martínez, S., R. Romero, J.C. López, A. Romero, V.c. Sánchez Mendieta, and R. Natividad, *Preparation and characterization of CaO nanoparticles/NaX zeolite catalysts for the transesterification of sunflower oil.* Industrial & Engineering Chemistry Research, **2010**. 50(5): p. 2665-2670.

284. Vahid, B.R. and M. Haghighi, *Biodiesel production from sunflower oil over MgO/MgAl 2 O 4 nanocatalyst: Effect of fuel type on catalyst nanostructure and performance.* Energy Conversion and Management, **2017**. 134: p. 290-300.

285. Boz, N., N. Degirmenbasi, and D.M. Kalyon, *Conversion of biomass to fuel: Transesterification of vegetable oil to biodiesel using KF loaded nano-γ-alumina as catalyst.* Applied Catalysis B: Environmental, **2009**. 89(3): p. 590-596.

286. Macala, G.S., A.W. Robertson, C.L. Johnson, Z.B. Day, R.S. Lewis, M.G. White, A.V. Iretskii, and P.C. Ford, *Transesterification catalysts from iron doped hydrotalcite-like precursors: solid bases for biodiesel production.* Catalysis Letters, **2008**. 122(3-4): p. 205-209.

287. Kulkarni, M.G., R. Gopinath, L.C. Meher, and A.K. Dalai, *Solid acid catalyzed biodiesel production by simultaneous esterification and transesterification.* Green Chemistry, **2006**. 8(12): p. 1056-1062.

288. Ni, J. and F. Meunier, *Esterification of free fatty acids in sunflower oil over solid acid catalysts using batch and fixed bed-reactors.* Applied Catalysis A: General, **2007**. 333(1): p. 122-130.

289. Jacobson, K., R. Gopinath, L.C. Meher, and A.K. Dalai, *Solid acid catalyzed biodiesel production from waste cooking oil.* Applied Catalysis B: Environmental, **2008**. 85(1): p. 86-91.

290. López, D.E., J.G. Goodwin, D.A. Bruce, and S. Furuta, *Esterification and transesterification using modified-zirconia catalysts.* Applied Catalysis A: General, **2008**. 339(1): p. 76-83.

291. Peng, B.-X., Q. Shu, J.-F. Wang, G.-R. Wang, D.-Z. Wang, and M.-H. Han, *Biodiesel production from waste oil feedstocks by solid acid catalysis.* Process Safety and Environmental Protection, **2008**. 86(6): p. 441-447.

292. Suwannakarn, K., E. Lotero, K. Ngaosuwan, and J.G. Goodwin Jr, *Simultaneous free fatty acid esterification and triglyceride transesterification using a solid acid catalyst with in situ removal of water and unreacted methanol.* Industrial & Engineering Chemistry Research, **2009**. 48(6): p. 2810-2818.

293. Dhainaut, J., J.-P. Dacquin, A.F. Lee, and K. Wilson, *Hierarchical macroporous–mesoporous SBA-15 sulfonic acid catalysts for biodiesel synthesis.* Green chemistry, **2010**. 12(2): p. 296-303.

294. Shao, G.N., R. Sheikh, A. Hilonga, J.E. Lee, Y.-H. Park, and H.T. Kim, *Biodiesel production by sulfated mesoporous titania–silica catalysts synthesized by the sol–gel process from less expensive precursors.* Chemical Engineering Journal, **2013**. 215–216(0): p. 600-607.

295. Fu, X., D. Li, J. Chen, Y. Zhang, W. Huang, Y. Zhu, J. Yang, and C. Zhang, *A microalgae residue based carbon solid acid catalyst for biodiesel production.* Bioresource technology, **2013**. 146: p. 767-770.

296. da Conceição, L.R.V., L.M. Carneiro, J.D. Rivaldi, and H.F. de Castro, *Solid acid as catalyst for biodiesel production via simultaneous esterification and transesterification of macaw palm oil.* Industrial Crops and Products, **2016**. 89: p. 416-424.

297. Soltani, S., U. Rashid, S.I. Al-Resayes, and I.A. Nehdi, *Sulfonated mesoporous ZnO catalyst for methyl esters production.* Journal of Cleaner Production, **2016**.

298. Yap, C.Y., *Synthesis of solid catalyst from palm empty fruit bunch by using 4-benzenediazonium sulfonate method for production of biodiesel*, **2016**, UTAR.

299. Mahto, T.K., R. Jain, S. Chandra, D. Roy, V. Mahto, and S.K. Sahu, *Single step synthesis of sulfonic group bearing graphene oxide: A promising carbo-nano material for biodiesel production.* Journal of Environmental Chemical Engineering, **2016**. 4(3): p. 2933-2940.

300. Hara, M., *Environmentally benign production of biodiesel using heterogeneous catalysts.* ChemSusChem, **2009**. 2(2): p. 129-135.

301. Carmo, A.C., L.K. de Souza, C.E. da Costa, E. Longo, J.R. Zamian, and G.N. da Rocha Filho, *Production of biodiesel by esterification of palmitic acid over mesoporous aluminosilicate Al-MCM-41.* Fuel, **2009**. 88(3): p. 461-468.

302. Vieira, S.S., Z.M. Magriotis, I. Graça, A. Fernandes, M.F. Ribeiro, J.M.F. Lopes, S.M. Coelho, S. Nadiene Ap V, and A.A. Saczk, *Production of biodiesel using HZSM-5 zeolites modified with citric acid and SO_4^{2-}/La_2O_3.* Catalysis Today, **2017**. 279: p. 267-273.

303. Aziz, M., K. Puad, S. Triwahyono, A. Jalil, M. Khayoon, A. Atabani, Z. Ramli, Z. Majid, D. Prasetyoko, and D. Hartanto, *Transesterification of croton megalocarpus oil to biodiesel over WO_3 supported on silica mesoporous-macroparticles catalyst.* Chemical Engineering Journal, **2017**.

304. Lam, M.K., K.T. Lee, and A.R. Mohamed, *Sulfated tin oxide as solid superacid catalyst for transesterification of waste cooking oil: an optimization study.* Applied Catalysis B: Environmental, **2009**. 93(1): p. 134-139.

305. Nayebzadeh, H., N. Saghatoleslami, A. Maskooki, and B. Vahid, *Preparation of supported nanosized sulfated zirconia by strontia and assessment of its activities in the esterification of oleic acid.* Chemical and Biochemical Engineering Quarterly, **2014**. 28(3): p. 259-265.

306. Arata, K., *Organic syntheses catalyzed by superacidic metal oxides: sulfated zirconia and related compounds.* Green Chemistry, **2009**. 11(11): p. 1719-1728.

307. Li, Y., X.-D. Zhang, L. Sun, J. Zhang, and H.-P. Xu, *Fatty acid methyl ester synthesis catalyzed by solid superacid catalyst/ZrO_2–TiO_2/La^{3+}.* Applied Energy, **2010**. 87(1): p. 156-159.

308. Li, J., X. Wang, W. Zhu, and F. Cao, *$Zn_{1.2}H_{0.6}PW_{12}O_{40}$ nanotubes with double acid sites as heterogeneous catalysts for the production of biodiesel from waste cooking oil.* ChemSusChem, **2009**. 2(2): p. 177-183.

309. Toda, M., A. Takagaki, M. Okamura, J.N. Kondo, S. Hayashi, K. Domen, and M. Hara, *Green chemistry: biodiesel made with sugar catalyst.* Nature, **2005**. 438(7065): p. 178-178.

310. Guan, Q., Y. Li, Y. Chen, Y. Shi, J. Gu, B. Li, R. Miao, Q. Chen, and P. Ning, *Sulfonated multi-walled carbon nanotubes for biodiesel production through triglycerides transesterification.* RSC Advances, **2017**. 7(12): p. 7250-7258.

311. Tran, T.T.V., S. Kaiprommarat, S. Kongparakul, P. Reubroycharoen, G. Guan, M.H. Nguyen, and C. Samart, *Green biodiesel production from waste cooking oil using an environmentally benign acid catalyst.* Waste Management, **2016**. 52: p. 367-374.

312. Baig, R.N., S. Verma, M.N. Nadagouda, and R.S. Varma, *Room temperature synthesis of biodiesel using sulfonated graphitic carbon nitride.* Scientific Reports, **2016**. 6.

313. Feng, Y., B. He, Y. Cao, J. Li, M. Liu, F. Yan, and X. Liang, *Biodiesel production using cation-exchange resin as heterogeneous catalyst.* Bioresource Technology, **2010**. 101(5): p. 1518-1521.

314. Zhang, H., *Solid acid catalysts for sustainable production of biodiesel*, **2016**, University of Nottingham.

315. Fu, J., Z. Li, S. Xing, Z. Wang, C. Miao, P. Lv, and Z. Yuan, *Cation exchange resin catalysed biodiesel production from used cooking oil (UCO): Investigation of impurities effect.* Fuel, **2016**. 181: p. 1058-1065.

316. Sharma, Y.C., B. Singh, and J. Korstad, *Advancements in solid acid catalysts for ecofriendly and economically viable synthesis of biodiesel.* Biofuels, Bioproducts and Biorefining, **2011**. 5(1): p. 69-92.

317. Peterson, G. and W. Scarrah, *Rapeseed oil transesterification by heterogeneous catalysis.* Journal of the American Oil Chemists Society, **1984**. 61(10): p. 1593-1597.

318. Mo, X., E. Lotero, C. Lu, Y. Liu, and J.G. Goodwin, *A novel sulfonated carbon composite solid acid catalyst for biodiesel synthesis.* Catalysis Letters, **2008**. 123(1-2): p. 1-6.

319. Vaccari, A., *Clays and catalysis: a promising future.* Applied Clay Science, **1999**. 14(4): p. 161-198.

320. Jothiramalingam, R. and M.K. Wang, *Review of recent developments in solid acid, base, and enzyme catalysts (heterogeneous) for biodiesel production via transesterification.* Industrial & Engineering Chemistry Research, **2009**. 48(13): p. 6162-6172.

321. Harmer, M.A., W.E. Farneth, and Q. Sun, *Towards the sulfuric acid of solids.* Advanced Materials, **1998**. 10(15): p. 1255-1257.

322. Margeta, K., A. Farkas, M. Šiljeg, and N.Z. Logar, *Natural zeolites in water treatment-how effective is their use.* **2013**: INTECH Open Access Publisher.

323. Zhao, Z., *Studies on esterification reaction over aluminophosphate and silicoaluminophosphate molecular sieves.* Journal of Molecular Catalysis A: Chemical, **2001**. 168(1): p. 147-152.

324. Wu, K.-C. and Y.-W. Chen, *An efficient two-phase reaction of ethyl acetate production in modified ZSM-5 zeolites.* Applied Catalysis A: General, **2004**. 257(1): p. 33-42.

325. Shu, Q., B. Yang, H. Yuan, S. Qing, and G. Zhu, *Synthesis of biodiesel from soybean oil and methanol catalyzed by zeolite beta modified with La^{3+}.* Catalysis Communications, **2007**. 8(12): p. 2159-2165.

326. Russbueldt, B.M. and W.F. Hoelderich, *New sulfonic acid ion-exchange resins for the preesterification of different oils and fats with high content of free fatty acids.* Applied Catalysis A: General, **2009**. 362(1): p. 47-57.

327. Tesser, R., M. Di Serio, L. Casale, L. Sannino, M. Ledda, and E. Santacesaria, *Acid exchange resins deactivation in the esterification of free fatty acids.* Chemical Engineering Journal, **2010**. 161(1): p. 212-222.

328. Pan, H., H. Li, X.-F. Liu, H. Zhang, K.-L. Yang, S. Huang, and S. Yang, *Mesoporous polymeric solid acid as efficient catalyst for (trans) esterification of crude Jatropha curcas oil.* Fuel Processing Technology, **2016**. 150: p. 50-57.

329. Ma, Y., Q. Wang, X. Sun, C. Wu, and Z. Gao, *Kinetics studies of biodiesel production from waste cooking oil using $FeCl_3$-modified resin as heterogeneous catalyst.* Renewable Energy, **2017**. 107: p. 522-530.

330. López, D.E., J.G. Goodwin, and D.A. Bruce, *Transesterification of triacetin with methanol on Nafion® acid resins.* Journal of Catalysis, **2007**. 245(2): p. 381-391.

331. Kouzu, M., A. Nakagaito, and J.-s. Hidaka, *Pre-esterification of FFA in plant oil transesterified into biodiesel with the help of solid acid catalysis of sulfonated cation-exchange resin.* Applied Catalysis A: General, **2011**. 405(1): p. 36-44.

332. dos Reis, S.C., E.R. Lachter, R.S. Nascimento, J.A. Rodrigues, and M.G. Reid, *Transesterification of Brazilian vegetable oils with methanol over ion-exchange resins.* Journal of the American Oil Chemists' Society, **2005**. 82(9): p. 661-665.

333. Mizuno, N. and M. Misono, *Heterogeneous catalysis.* Chemical Reviews, **1998**. 98(1): p. 199-218.

334. Okuhara, T. and T. Nakato, *Catalysis by porous heteropoly compounds.* Catalysis Surveys from Japan, **1998**. 2(1): p. 31-44.

335. Zieba, A., L. Matachowski, E. Lalik, and A. Drelinkiewicz, *Methanolysis of castor oil catalysed by solid potassium and cesium salts of 12-tungstophosphoric acid.* Catalysis letters, **2009**. 127(1-2): p. 183.

336. Zhao, Q., H. Wang, H. Zheng, Z. Sun, W. Shi, S. Wang, X. Wang, and Z. Jiang, *Acid–base bifunctional HPA nanocatalysts promoting heterogeneous transesterification and esterification reactions.* Catalysis Science & Technology, **2013**. 3(9): p. 2204-2209.

337. Cao, F., Y. Chen, F. Zhai, J. Li, J. Wang, X. Wang, S. Wang, and W. Zhu, *Biodiesel production from high acid value waste frying oil catalyzed by superacid heteropolyacid.* Biotechnology and bioengineering, **2008**. 101(1): p. 93-100.

338. Verhoef, M.J., P.J. Kooyman, J.A. Peters, and H. Van Bekkum, *A study on the stability of MCM-41-supported heteropoly acids under liquid-and gas-phase esterification conditions.* Microporous and Mesoporous Materials, **1999**. 27(2): p. 365-371.

339. Duan, X., Y. Liu, Q. Zhao, X. Wang, and S. Li, *Water-tolerant heteropolyacid on magnetic nanoparticles as efficient catalysts for esterification of free fatty acid.* RSC Advances, **2013**. 3(33): p. 13748-13755.

340. Zhang, X., J. Li, Y. Chen, J. Wang, L. Feng, X. Wang, and F. Cao, *Heteropolyacid nanoreactor with double acid sites as a highly efficient and reusable catalyst for the transesterification of waste cooking oil.* Energy & Fuels, **2009**. 23(9): p. 4640-4646.

341. Stellwagen, D.R., F. van der Klis, D.S. van Es, K.P. de Jong, and J.H. Bitter, *Functionalized Carbon Nanofibers as Solid‐Acid Catalysts for Transesterification.* ChemSusChem, **2013**. 6(9): p. 1668-1672.

342. Shuit, S.H. and S.H. Tan, *Feasibility study of various sulphonation methods for transforming carbon nanotubes into catalysts for the esterification of palm fatty acid distillate.* Energy Conversion and Management, **2014**. 88: p. 1283-1289.

343. Zhang, D., D. Wei, Q. Li, X. Ge, X. Guo, Z. Xie, and W. Ding, *High performance catalytic distillation using CNTs-based holistic catalyst for production of high quality biodiesel.* Scientific reports, **2014**. 4.

344. Dehkhoda, A.M., A.H. West, and N. Ellis, *Biochar based solid acid catalyst for biodiesel production.* Applied Catalysis A: General, **2010**. 382(2): p. 197-204.

345. Hara, M., *Biodiesel production by amorphous carbon bearing SO₃H, COOH and phenolic OH groups, a solid Brønsted acid catalyst.* Topics in Catalysis, **2010**. 53(11-12): p. 805-810.

346. Fu, X.-b., J. Chen, X.-l. Song, Y.-m. Zhang, Y. Zhu, J. Yang, and C.-w. Zhang, *Biodiesel production using a carbon solid acid catalyst derived from β-cyclodextrin.* Journal of the American Oil Chemists' Society, **2015**. 92(4): p. 495-502.

347. Wang, C., F. Yuan, L. Liu, X. Niu, and Y. Zhu, *Transesterification of tributyrin and dehydration of fructose over a carbon‐based solid acid prepared by carbonization and sulfonation of glucose.* ChemPlusChem, **2015**. 80(11): p. 1657-1665.

348. Shu, Q., Q. Zhang, G. Xu, Z. Nawaz, D. Wang, and J. Wang, *Synthesis of biodiesel from cottonseed oil and methanol using a carbon-based solid acid catalyst.* Fuel Processing Technology, **2009**. 90(7): p. 1002-1008.

349. Ji, J., G. Zhang, H. Chen, S. Wang, G. Zhang, F. Zhang, and X. Fan, *Sulfonated graphene as water-tolerant solid acid catalyst.* Chemical Science, **2011**. 2(3): p. 484-487.

350. Sheldon, R.A., I.W. Arends, and U. Hanefeld, *Solid acids and bases as catalysts.* Green Chemistry and Catalysis, **2007**: p. 49-90.

351. Kawabata, T., M. Kato, T. Mizugaki, K. Ebitani, and K. Kaneda, *Monomeric metal aqua complexes in the interlayer space of montmorillonites as strong lewis acid catalysts for heterogeneous carbon–carbon bond‑forming reactions.* Chemistry–A European Journal, **2005**. 11(1): p. 288-297.

352. Clark, J.H., S.R. Cullen, S.J. Barlow, and T.W. Bastock, *Keynote article. Environmentally friendly chemistry using supported reagent catalysts: structure–property relationships for clayzic.* Journal of the Chemical Society, Perkin Transactions 2, **1994**(6): p. 1117-1130.

353. Kanda, L.R.S., M.L. Corazza, L. Zatta, and F. Wypych, *Kinetics evaluation of the ethyl esterification of long chain fatty acids using commercial montmorillonite K10 as catalyst.* Fuel, **2017**. 193: p. 265-274.

354. Madhuvilakku, R. and S. Piraman, *Biodiesel synthesis by TiO₂–ZnO mixed oxide nanocatalyst catalyzed palm oil transesterification process.* Bioresource technology, **2013**. 150: p. 55-59.

355. Muthu, H., V. SathyaSelvabala, T. Varathachary, D. Kirupha Selvaraj, J. Nandagopal, and S. Subramanian, *Synthesis of biodiesel from Neem oil using sulfated zirconia via tranesterification.* Brazilian Journal of Chemical Engineering, **2010**. 27(4): p. 601-608.

356. Raia, R.Z., L.S. da Silva, S.M.P. Marcucci, and P.A. Arroyo, *Biodiesel production from Jatropha curcas L. oil by simultaneous esterification and transesterification using sulphated zirconia.* Catalysis Today, **2016**.

357. Osatiashtiani, A., L.J. Durndell, J.C. Manayil, A.F. Lee, and K. Wilson, *Influence of alkyl chain length on sulfated zirconia catalysed batch and continuous esterification of carboxylic acids by light alcohols.* Green Chemistry, **2016**. 18(20): p. 5529-5535.

358. Labidi, S., M. Ben Amar, J.-P. Passarello, B. Le Neindre, and A.V. Kanaev, *Design of novel sulfated nanozirconia catalyst for biofuel synthesis.* Industrial & Engineering Chemistry Research, **2017**.

359. Chavan, S.P., P. Zubaidha, S.W. Dantale, A. Keshavaraja, A. Ramaswamy, and T. Ravindranathan, *Use of solid superacid (sulphated SnO₂) as efficient catalyst in tacile transesterification of ketoesters.* Tetrahedron letters, **1996**. 37(2): p. 233-236.

360. Furuta, S., H. Matsuhashi, and K. Arata, *Biodiesel fuel production with solid superacid catalysis in fixed bed reactor under atmospheric pressure.* Catalysis communications, **2004**. 5(12): p. 721-723.

361. Chen, H., B. Peng, D. Wang, and J. Wang, *Biodiesel production by the transesterification of cottonseed oil by solid acid catalysts.* Frontiers of Chemical Engineering in China, **2007**. 1(1): p. 11-15.

362. De Almeida, R.M., L.K. Noda, N.S. Gonçalves, S.M. Meneghetti, and M.R. Meneghetti, *Transesterification reaction of vegetable oils, using superacid sulfated TiO₂–base catalysts.* Applied Catalysis A: General, **2008**. 347(1): p. 100-105.

363. Jenie, A., D.S. Kusuma, A. Kristiani, J.A. Laksmono, and S. Tursiloadi, *Preparation and characterization of sulfated titania catalysts for the isomerisation of citronellal.* International Journal of Basic & Applied Sciences IJBAS-IJENS, **2010**. 10(06): p. 5-10.

364. Ropero-Vega, J., A. Aldana-Pérez, R. Gómez, and M. Niño-Gómez, *Sulfated titania [TiO$_2$/SO$_4$ $^{2-}$]: A very active solid acid catalyst for the esterification of free fatty acids with ethanol.* Applied Catalysis A: General, **2010**. 379(1): p. 24-29.

365. Zhao, H., P. Jiang, Y. Dong, M. Huang, and B. Liu, *A high-surface-area mesoporous sulfated nano-titania solid superacid catalyst with exposed (101) facets for esterification: facile preparation and catalytic performance.* New Journal of Chemistry, **2014**. 38(9): p. 4541-4548.

366. Li, Y., X.-D. Zhang, L. Sun, M. Xu, W.-G. Zhou, and X.-H. Liang, *Solid superacid catalyzed fatty acid methyl esters production from acid oil.* Applied Energy, **2010**. 87(7): p. 2369-2373.

367. Yang, H., R. Lu, and L. Wang, *Study of preparation and properties on solid superacid sulfated titania–silica nanomaterials.* Materials Letters, **2003**. 57(5): p. 1190-1196.

368. Embong, N.H., G.P. Maniam, and M.H.A. Rahim, *Biodiesel Preparation from Decanter Cake with Solid Acid Catalyst.* International Journal, **2014**. 5(5).

369. Nurul Hajar, E., M. Gaanty Pragas, M. Hasbi, and A. Rahim, *Biodiesel preparation from decanter cake with solid acid catalyst.* International Journal of Chemical and Environmental Engineering, **2014**. 5(5): p. 294-296.

370. Policano, M., J. Rivaldi, H. de Castro, and L. Carneiro, *Simultaneous esterification and transesterification of andiroba oil using niobium oxide-sulfate as catalyst.* International Journal of Engineering Research & Science, **2016**. 2(10): p. 175-184.

371. Smith, Y.R., K.J.A. Raj, V.R. Subramanian, and B. Viswanathan, *Sulfated Fe$_2$O$_3$–TiO$_2$ synthesized from ilmenite ore: a visible light active photocatalyst.* Colloids and Surfaces A: Physicochemical and Engineering Aspects, **2010**. 367(1): p. 140-147.

372. Raj, K., M. Prakash, R. Shanmugam, K. Krishnamurthy, and B. Viswanathan, *Surface acidic properties of sulphated Fe$_2$O$_3$-TiO$_2$.* **2011**.

373. Anuradha, S., K. Raj, V. Vijayaraghavan, and B. Viswanathan, *Sulphated Fe$_2$O$_3$-TiO$_2$ catalysed transesterification of soybean oil to biodiesel.* Indian Journal of Chemistry: Section A, **2014**. 53A: p. 1493-1499.

374. Wu, H., Y. Liu, J. Zhang, and G. Li, *In situ reactive extraction of cottonseeds with methyl acetate for biodiesel production using magnetic solid acid catalysts.* Bioresource technology, **2014**. 174: p. 182-189.

375. Guan, D., M. Fan, J. Wang, Y. Zhang, Q. Liu, and X. Jing, *Synthesis and properties of magnetic solid superacid: SO$_4$$^{2-}$/ZrO$_2$–B$_2O_3$–Fe$_3O_4$.* Materials Chemistry and Physics, **2010**. 122(1): p. 278-283.

376. Garcia, C.M., S. Teixeira, L.L. Marciniuk, and U. Schuchardt, *Transesterification of soybean oil catalyzed by sulfated zirconia.* Bioresource Technology, **2008**. 99(14): p. 6608-6613.

377. Olah, G.A., K. Laali, and O. Farooq, *Chemistry in superacids. 6. Perfluoroalkanesulfonic acid-boron perfluoroalkanesulfonates: new superacid systems for generation of carbocations and catalysts for electrophilic transformations of hydrocarbons.* The Journal of Organic Chemistry, **1984**. 49(24): p. 4591-4594.

378. Vassena, D., *Nitration of toluene and nitrotoluene with solid acids*, **2000**.

379. Melero, J.A., R. van Grieken, and G. Morales, *Advances in the synthesis and catalytic applications of organosulfonic-functionalized mesostructured materials.* Chemical reviews, **2006**. 106(9): p. 3790-3812.

380. Wan, Y., Y. Shi, and D. Zhao, *Supramolecular aggregates as templates: ordered mesoporous polymers and carbons.* Chemistry of Materials, **2007**. 20(3): p. 932-945.

381. Mbaraka, I.K., K.J. McGuire, and B.H. Shanks, *Acidic mesoporous silica for the catalytic conversion of fatty acids in beef tallow.* Industrial & engineering chemistry research, **2006**. 45(9): p. 3022-3028.

382. Wu, H., J. Zhang, Y. Liu, J. Zheng, and Q. Wei, *Biodiesel production from Jatropha oil using mesoporous molecular sieves supporting K_2SiO_3 as catalysts for transesterification.* Fuel Processing Technology, **2014**. 119: p. 114-120.

383. Soltani, S., U. Rashid, S.I. Al-Resayes, and I.A. Nehdi, *Recent progress in synthesis and surface functionalization of mesoporous acidic heterogeneous catalysts for esterification of free fatty acid feedstocks: A review.* Energy Conversion and Management, **2016**.

384. Zuo, D., J. Lane, D. Culy, M. Schultz, A. Pullar, and M. Waxman, *Sulfonic acid functionalized mesoporous SBA-15 catalysts for biodiesel production.* Applied Catalysis B: Environmental, **2013**. 129: p. 342-350.

385. Valle-Vigón, P., M. Sevilla, and A.B. Fuertes, *Sulfonated mesoporous silica–carbon composites and their use as solid acid catalysts.* Applied Surface Science, **2012**. 261: p. 574-583.

386. Wang, X., R. Liu, M.M. Waje, Z. Chen, Y. Yan, K.N. Bozhilov, and P. Feng, *Sulfonated ordered mesoporous carbon as a stable and highly active protonic acid catalyst.* Chemistry of Materials, **2007**. 19(10): p. 2395-2397.

387. Fraile, J.M., E. García-Bordejé, E. Pires, and L. Roldán, *Catalytic performance and deactivation of sulfonated hydrothermal carbon in the esterification of fatty acids: comparison with sulfonic solids of different nature.* Journal of Catalysis, **2015**. 324: p. 107-118.

388. Kuwahara, Y., T. Fujitani, and H. Yamashita, *Esterification of levulinic acid with ethanol over sulfated mesoporous zirconosilicates: Influences of the preparation conditions on the structural properties and catalytic performances.* Catalysis Today, **2014**. 237: p. 18-28.

389. Yi, Q., J. Zhang, X. Zhang, J. Feng, and W. Li, *Synthesis of SO_4^{2-}/Zr-SBA-15 catalyst for the transesterification of waste cooking oil as a bio-flotation agent in coal flotation.* Fuel, **2015**. 143: p. 390-398.

390. Dacquin, J., A. Lee, C. Pirez, and K. Wilson, *Pore-expanded SBA-15 sulfonic acid silicas for biodiesel synthesis.* Chemical Communications, **2012**. 48(2): p. 212-214.

391. Pan, H., X. Liu, H. Zhang, K. Yang, S. Huang, and S. Yang, *Multi-SO_3H functionalized mesoporous polymeric acid catalyst for biodiesel production and fructose-to-biodiesel additive conversion.* Renewable Energy, **2017**. 107: p. 245-252.

392. Dehghani, S. and M. Haghighi, *Sono-sulfated zirconia nanocatalyst supported on MCM-41 for biodiesel production from sunflower oil: Influence of ultrasound irradiation power on catalytic properties and performance.* Ultrasonics Sonochemistry, **2017**. 35: p. 142-151.

393. Shin, H.-Y., S.-H. An, R. Sheikh, Y.H. Park, and S.-Y. Bae, *Transesterification of used vegetable oils with a Cs-doped heteropolyacid catalyst in supercritical methanol.* Fuel, **2012**. 96: p. 572-578.

394. Nongbe, M.C., T. Ekou, L. Ekou, Y.K. Benjamin, E. Le Grognec, and F.-X. Felpin, *Biodiesel production from palm oil using sulfonated graphene catalyst.* Renewable Energy, **2017**.

395. Talukder, M.R., J. Wu, S. Lau, L. Cui, G. Shimin, and A. Lim, *Comparison of Novozym 435 and Amberlyst 15 as heterogeneous catalyst for production of biodiesel from palm fatty acid distillate.* Energy & Fuels, **2008**. 23(1): p. 1-4.

396. Xu, L., X. Yang, X. Yu, and Y. Guo, *Preparation of mesoporous polyoxometalate–tantalum pentoxide composite catalyst for efficient esterification of fatty acid.* Catalysis Communications, **2008**. 9(7): p. 1607-1611.

397. Yee, K.F., K.T. Lee, R. Ceccato, and A.Z. Abdullah, *Production of biodiesel from Jatropha curcas L. oil catalyzed by/ZrO 2 catalyst: effect of interaction between process variables.* Bioresource technology, **2011**. 102(5): p. 4285-4289.

398. Jiménez-Morales, I., J. Santamaría-González, P. Maireles-Torres, and A. Jiménez-López, *Calcined zirconium sulfate supported on MCM-41 silica as acid catalyst for ethanolysis of sunflower oil.* Applied Catalysis B: Environmental, **2011**. 103(1): p. 91-98.

399. Ma, L. and S. Tu, *Removal of arsenic from aqueous solution by two types of nano TiO_2 crystals.* Environmental chemistry letters, **2011**. 9(4): p. 465-472.

400. Bahnemann, D., A. Henglein, and L. Spanhel, *Detection of the intermediates of colloidal TiO_2-catalysed photoreactions.* Faraday Discussions of the Chemical Society, **1984**. 78: p. 151-163.

401. Bhongsuwan, T., D. Bhongsuwan, N. Chomchoey, and L. Boonchuay, *Effect of calcination temperature in production of magnetic nanoparticles for arsenic adsorption.* Mater. Chem. Phys, **2008**. 110(2-3): p. 426-433.

402. Massart, R., *Preparation of aqueous magnetic liquids in alkaline and acidic media.* IEEE transactions on magnetics, **1981**. 17(2): p. 1247-1248.

403. Cullity, B.D. and J.W. Weymouth, *Elements of X-ray Diffraction.* American Journal of Physics, **1957**. 25(6): p. 394-395.

404. Bragg, W.L., *The diffraction of short electromagnetic waves by a crystal.* Proceedings of the Cambridge philosophical society, **1913**. 17 - part I: p. 43-57.

405. Dinnebier, R.E., *Powder diffraction: theory and practice*. **2008**: Royal Society of Chemistry.

406. Doyle, W.M., *Principles and applications of Fourier transform infrared (FTIR) process analysis.* Process control and quality, **1992**. 2: p. 50.

407. Lahaye, L. and G. Prado, *Fundamentals of the physical-chemistry of pulverized coal combustion*. Vol. 137. **2012**: Springer Science & Business Media.

408. Pavia, D.L., G.M. Lampman, G.S. Kriz, and J.A. Vyvyan, *Introduction to spectroscopy*. **2008**: Cengage Learning.

409. Suart, B., *Infrared spectroscopy: Fundamental and applications*, **2004**, John Wiley & Sons, Ltd.

410. Hawkes, P. and J.C. Spence, *Science of microscopy*. **2008**: Springer Science & Business Media.

411. Goldstein, J., D.E. Newbury, P. Echlin, D.C. Joy, A.D. Romig Jr, C.E. Lyman, C. Fiori, and E. Lifshin, *Scanning electron microscopy and X-ray microanalysis: a text for biologists, materials scientists, and geologists*. **2012**: Springer Science & Business Media.

412. Wordpress.com, *Spotlight on Science: Scanning Electron Microscopy.* https://geologelizabeth.wordpress.com/2014/03/26/spotlight-on-science-scanning-electron-microscopy/, **2014**.

413. Reimer, L., *Scanning electron microscopy: physics of image formation and microanalysis*, **2000**, IOP Publishing.

414. Rochow, E., *An introduction to microscopy by means of light, electrons, x-ray, or ultrasound*. **2012**: Springer Science & Business Media.

415. Hk-phy.org, *Principle of TEM.* http://www.hk-phy.org/atomic_world/tem/tem02_e.html.

416. Williams, D.B. and C.B. Carter, *The transmission electron microscope*, in *Transmission electron microscopy*. **1996**, Springer. p. 3-17.

417. Condon, J.B., *Surface area and porosity determinations by physisorption: measurements and theory*. **2006**: Elsevier.

418. Lowell, S. and J.E. Shields, *Powder surface area and porosity*. Vol. 2. **2013**: Springer Science & Business Media.

419. Sing, K.S., *Reporting physisorption data for gas/solid systems with special reference to the determination of surface area and porosity (Recommendations 1984)*. Pure and applied chemistry, **1985**. 57(4): p. 603-619.

420. Micromeritics.com, *Gas adsorption theory*. http://www.micromeritics.com/Repository/Files/Gas_Adsorption_Theory_poster.pdf.

421. Langmuir, I., *The constitution and fundamental properties of solids and liquids. Part i. Solids.* Journal of the American Chemical Society, **1916**. 38(11): p. 2221-2295.

422. Brunauer, S., P.H. Emmett, and E. Teller, *Adsorption of gases in multimolecular layers.* Journal of the American chemical society, **1938**. 60(2): p. 309-319.

423. Rouquerol, F., J. Rouquerol, and K. Sing, *Adsorption by Powders and Porous Solids Academic.* New York, **1999**: p. 15.

424. Klobes, P., K. Meyer, and R.G. Munro, *Porosity and specific surface area measurements for solid materials*. Vol. Special publication 960-17. **2006**, US, Washington: US Department of Commerce, Technology Administration, National Institute of Standards and Technology. 88.

425. Rouquerol, J., F. Rouquerol, P. Llewellyn, G. Maurin, and K.S. Sing, *Adsorption by powders and porous solids: principles, methodology and applications*. **2013**: Academic press.

426. Van der Heide, P., *X-ray photoelectron spectroscopy: an introduction to principles and practices*. **2011**: John Wiley & Sons.

427. Wagner, C.D. and G. Muilenberg, *Handbook of X-ray photoelectron spectroscopy*. **1979**: Perkin-Elmer.

428. Lynch, J., *Physico-chemical analysis of industrial catalysts: a practical guide to characterisation*. **2003**: Editions Technip.

429. Walls, J. and R. Smith, *Surface science techniques.* Vacuum, **1994**. 45(6-7): p. 649-652.

430. Bruce, D.W., D. O'Hare, and R.I. Walton, *Local Structural Characterisation: Inorganic Materials Series*. **2013**: John Wiley & Sons.

431. Gabbott, P., *Principles and applications of thermal analysis*. **2008**: John Wiley & Sons.

432. Thompson, M., *CHNS elemental analysers.* AMCTB of The Royal Society of Chemistry, **2008**. 4.

433. Jin, F. and Y. Li, *A FTIR and TPD examination of the distributive properties of acid sites on ZSM-5 zeolite with pyridine as a probe molecule.* Catalysis Today, **2009**. 145(1): p. 101-107.

434. Benaliouche, F., Y. Boucheffa, P. Ayrault, S. Mignard, and P. Magnoux, *NH_3-TPD and FTIR spectroscopy of pyridine adsorption studies for characterization of Ag-and Cu-exchanged X zeolites.* Microporous and Mesoporous Materials, **2008**. 111(1): p. 80-88.

435. Parikh, S.J. and J. Chorover, *FTIR spectroscopic study of biogenic Mn-oxide formation by Pseudomonas putida GB-1.* Geomicrobiology Journal, **2005**. 22(5): p. 207-218.

436. Parikh, S.J., K.W. Goyne, A.J. Margenot, F. Mukome, and F.J. Calderón, *Soil chemical insights provided through vibrational spectroscopy.* Advances in agronomy, **2014**. 126: p. 1.

437. Khoshhesab, Z.M., *Reflectance IR spectroscopy*, in *Infrared Spectroscopy-Materials Science, Engineering and Technology*. **2012**, InTech.

438. Zaki, M.I., M.A. Hasan, F.A. Al-Sagheer, and L. Pasupulety, *In situ FTIR spectra of pyridine adsorbed on SiO_2–Al_2O_3, TiO_2, ZrO_2 and CeO_2: general considerations for the identification of acid sites on surfaces of finely divided metal oxides.* Colloids and Surfaces A: Physicochemical and Engineering Aspects, **2001**. 190(3): p. 261-274.

439. Swoboda, A. and G. Kunze, *Infrared study of pyridine adsorbed on montmorillonite surfaces.* Clays and Clay Minerals, **1966**: p. 277-88.

440. Felix, S., C. Savill-Jowitt, and D. Brown, *Base adsorption calorimetry for characterising surface acidity: a comparison between pulse flow and conventional "static" techniques.* Thermochimica acta, **2005**. 433(1): p. 59-65.

441. AZoNetwork-UK-Ltd. *Temperature-programmed desorption (TPD) for characterizing the acid sites on oxide surfaces*. **2006**.

442. Rodríguez-González, L., F. Hermes, M. Bertmer, E. Rodríguez-Castellón, A. Jiménez-López, and U. Simon, *The acid properties of H-ZSM-5 as studied by NH₃-TPD and ²⁷ Al-MAS-NMR spectroscopy.* Applied Catalysis A: General, **2007**. 328(2): p. 174-182.

443. Gorte, R., *What do we know about the acidity of solid acids?* Catalysis Letters, **1999**. 62(1): p. 1-13.

444. Pereira, C. and R. Gorte, *Method for distinguishing Brønsted-acid sites in mixtures of H-ZSM-5, HY and silica-alumina.* Applied Catalysis A: General, **1992**. 90(2): p. 145-157.

445. Stosic, D., *Acidic-basic properties of catalysts for conversion of biomass*, **2012**, Université Claude Bernard-Lyon I.

446. Darribere, C., *Evolved gas analysis-Thermal analysis*, M.-T. GmbH, Editor **2001**, Mettler Toledo (http://www.mt.com): Switzerland. p. 1-61.

447. Höhne, G.W.H., *Differential scanning calorimetry—An introduction for practitioners* W. Hemminger, Editor **1997**, Elsevier: Berlin

448. Mettler-Toledo, *Interpreting DSC curves Part 1: Dynamic measurements.* **2000**.

449. Foner, S., *Versatile and sensitive vibrating-sample magnetometer.* Review of Scientific Instruments, **1959**. 30(7): p. 548-557.

450. Jiles, D., *Introduction to magnetism and magnetic materials*. **2015**: CRC press.

451. Dodrill, B. and L.S. Cryotronics, *Magnetic media measurements with a VSM.* Lake Shore cryotronics, Inc, **2009**. 575.

452. Rosensweig, R.E., *Ferrohydrodynamics*. **2013**: Courier Corporation.

453. Freedman, B., R.O. Butterfield, and E.H. Pryde, *Transesterification kinetics of soybean oil 1.* Journal of the American Oil Chemists' Society, **1986**. 63(10): p. 1375-1380.

454. Wawrzyniak, R., W. Wasiak, and M. Frackowiak, *Determination of methyl esters in diesel oils by gas chromatography-validation of the method.* Chemical Papers-Slovak Academy of Sciences, **2005**. 59(6B): p. 449.

455. Dauqan, E.M., H.A. Sani, A. Abdullah, and Z.M. Kasim. *Fatty acids composition of four different vegetable oils (red palm olein, palm olein, corn oil and coconut oil) by gas chromatography*. in *2nd International conference on chemistry and chemical engineering, IACSIT Press, Singapore*. **2011**.

456. Chand, P., V. Reddy, J.G. Verkade, T. Wang, and D.A. Grewell, *Novel characterization method of biodiesel produced from soybean oil using thermogravimetric analysis.* An ASABE meeting presentation, paper number: 084515, **2008**: p. 1-10.

457. Holčapek, M., P. Jandera, J. Fischer, and B. Prokeš, *Analytical monitoring of the production of biodiesel by high-performance liquid chromatography with various detection methods.* Journal of chromatography A, **1999**. 858(1): p. 13-31.

458. Chattopadhyay, S., S. Das, and R. Sen, *Rapid and precise estimation of biodiesel by high performance thin layer chromatography.* Applied Energy, **2011**. 88(12): p. 5188-5192.

459. Neto, P.R.C., M.S.B. Caro, L.M. Mazzuco, and M. da Graça Nascimento, *Quantification of soybean oil ethanolysis with 1H NMR.* Journal of the American Oil Chemists' Society, **2004**. 81(12): p. 1111-1114.

460. Pinzi, S., F. Priego Capote, J. Ruiz Jiménez, M. Dorado, and M. Luque de Castro, *Flow injection analysis-based methodology for automatic on-line monitoring and quality control for biodiesel production.* Bioresource technology, **2009**. 100(1): p. 421-427.

461. Pilar Dorado, M., S. Pinzi, A. De Haro, R. Font, and J. Garcia-Olmo, *Visible and NIR Spectroscopy to assess biodiesel quality: determination of alcohol and glycerol traces.* Fuel, **2011**. 90(6): p. 2321-2325.

462. Pinzi, S., F. Alonso, J. García Olmo, and M.P. Dorado, *Near infrared reflectance spectroscopy and multivariate analysis to monitor reaction products during biodiesel production.* Fuel, **2012**. 92(1): p. 354-359.

463. EN-14103, *Fat and oil derivatives. Fatty acid methyl esters (FAME). Determination of ester and linolenic acid methyl ester contents.* **2011**: p. 18.

464. EN-14105, *Fat and oil derivatives. Fatty acid methyl esters (FAME). Determination of free and total glycerol and mono-, di-, triglyceride contents* **2011**: p. 26.

465. Ruppel, T., G. Hall, T. Huybrighs, W. Goodman, and C. Shelton, *Free and total glycerol in B100 biodiesel by gas chromatography according to methods EN 14105 and ASTM D6584.* www.perkinelmer.com, **2012**: p. 1-5.

466. Boshui, C., S. Yuqiu, F. Jianhua, W. Jiu, and W. Jiang, *Effect of cold flow improvers on flow properties of soybean biodiesel.* Biomass and Bioenergy, **2010**. 34(9): p. 1309-1313.

467. Rashid, U., F. Anwar, A. Jamil, and H.N. Bhatti, *Jatropha curcas seed oil as a viable source for biodiesel.* Pakistan Journal of Botany, **2010**. 42(1): p. 575-582.

468. EN-22719, *Methods of test for petroleum and its products. Petroleum products and lubricants. Determination of flash point. Pensky-Martens closed cup method* **1994**: p. 16.

469. ASTM-D974, *Standard test method for acid and base number by colour-indicator titration.* **2012**: p. 1-7.

470. EN-14104, *Fat and oil derivatives-fatty acid methyl esters (FAME): determination of acid value.* **2003**.

471. ASTM-D97, *Standard test method for pour point of petroleum products.* **2012**: p. 1-10.

472. Bhale, P.V., N.V. Deshpande, and S.B. Thombre, *Improving the low temperature properties of biodiesel fuel.* Renewable Energy, **2009**. 34(3): p. 794-800.

473. Quinchia, L.A., M.A. Delgado, J.M. Franco, H.A. Spikes, and C. Gallegos, *Low-temperature flow behaviour of vegetable oil-based lubricants.* Industrial Crops and Products, **2012**. 37(1): p. 383-388.

474. Rajagopal, K., C. Bindub, R.B.N. Prasadb, and A. Ahmad, *Cloud point of biodiesel and blends.* Journal of Chemical, Biological and Physical Sciences (USA): An International Peer Review E-3 Journal of Sciences: Section C: Physical Sciences. Available online at www.jcbsc.org, **2012**. 2(4): p. 1998-2003.

475. ASTM-D2500, *Standard test method for cloud point of petroleum products.* **2011**: p. 1-5.

476. ASTM-E-1131, *standard test method for composition analysis by thermogravimetry.* ASTM international, **2003**: p. 1-5.

477. Souza, F., F. Maia, S. Mazzetto, T. Nascimento, and N. de Andrade, *Oxidative stability of soybean biodiesel in mixture with antioxidants by thermogravimetry and rancimat method.* Chemical and Biochemical Engineering Quarterly, **2013**. 27(3): p. 327-334.

478. Melero, J.A., J. Iglesias, and G. Morales, *Heterogeneous acid catalysts for biodiesel production: current status and future challenges.* Green Chemistry, **2009**. 11(9): p. 1285-1308.

479. Laurent, S., D. Forge, M. Port, A. Roch, C. Robic, L. Vander Elst, and R.N. Muller, *Magnetic iron oxide nanoparticles: synthesis, stabilization, vectorization, physicochemical characterizations, and biological applications.* Chemical reviews, **2008**. 108(6): p. 2064-2110.

480. Kango, S., S. Kalia, A. Celli, J. Njuguna, Y. Habibi, and R. Kumar, *Surface modification of inorganic nanoparticles for development of organic–inorganic nanocomposites—a review.* Progress in Polymer Science, **2013**. 38(8): p. 1232-1261.

481. Díaz, I., C. Márquez-Alvarez, F. Mohino, J.n. Pérez-Pariente, and E. Sastre, *Combined alkyl and sulfonic acid functionalization of MCM-41-type silica: Part 2. Esterification of glycerol with fatty acids.* Journal of Catalysis, **2000**. 193(2): p. 295-302.

482. Yang, L., Y. Wang, G. Luo, and Y. Dai, *Functionalization of SBA-15 mesoporous silica with thiol or sulfonic acid groups under the crystallization conditions.* Microporous and mesoporous materials, **2005**. 84(1): p. 275-282.

483. Alvaro, M., A. Corma, D. Das, V. Fornés, and H. García, *"Nafion"-functionalized mesoporous MCM-41 silica shows high activity and selectivity for carboxylic acid esterification and Friedel–Crafts acylation reactions.* journal of Catalysis, **2005**. 231(1): p. 48-55.

484. Mo, X., D.E. López, K. Suwannakarn, Y. Liu, E. Lotero, J.G. Goodwin, and C. Lu, *Activation and deactivation characteristics of sulfonated carbon catalysts.* Journal of Catalysis, **2008**. 254(2): p. 332-338.

485. Melero, J.A., L.F. Bautista, J. Iglesias, G. Morales, R. Sánchez-Vázquez, and I. Suárez-Marcos, *Biodiesel production over arenesulfonic acid-modified mesostructured catalysts: optimization of reaction parameters using response surface methodology.* Topics in Catalysis, **2010**. 53(11-12): p. 795-804.

486. Sobhani, S., Z.P. Parizi, and N. Razavi, *Nano n-propylsulfonated γ-Fe$_2$O$_3$ as magnetically recyclable heterogeneous catalyst for the efficient synthesis of β-phosphonomalonates.* Applied Catalysis A: General, **2011**. 409: p. 162-166.

487. Lai, D.-m., L. Deng, Q.-x. Guo, and Y. Fu, *Hydrolysis of biomass by magnetic solid acid.* Energy & Environmental Science, **2011**. 4(9): p. 3552-3557.

488. Ahn, B.K., H. Wang, S. Robinson, T.B. Shrestha, D.L. Troyer, S.H. Bossmann, and X.S. Sun, *Ring opening of epoxidized methyl oleate using a novel acid-functionalized iron nanoparticle catalyst.* Green chemistry, **2012**. 14(1): p. 136-142.

489. Atghia, S. and S.S. Beigbaghlou, *Nanocrystalline titania-based sulfonic acid (TiO$_2$-Pr-SO$_3$H) as a new, highly efficient and recyclable solid acid catalyst for the N-Boc protection of amines at room temperature.* Journal of Organometallic Chemistry, **2013**. 745: p. 42-49.

490. Li, W.L., S.B. Tian, and F. Zhu, *Sulfonic acid functionalized nano-γ-Al$_2$O$_3$: A new, efficient, and reusable catalyst for synthesis of 3-substituted-2h-1, 4-benzothiazines.* The Scientific World Journal, **2013**. 2013.

491. Pirez, C., M.T. Reche, A. Lee, J. Manayil, V. dos-Santos, and K. Wilson, *Hydrothermal saline promoted grafting of periodic mesoporous organic sulfonic acid silicas for sustainable FAME production.* Catalysis Letters, **2015**. 145(7): p. 1483-1490.

492. Tabrizian, E., A. Amoozadeh, and S. Rahmani, *Sulfamic acid-functionalized nano-titanium dioxide as an efficient, mild and highly recyclable solid acid nanocatalyst for chemoselective oxidation of sulfides and thiols.* RSC Advances, **2016**. 6(26): p. 21854-21864.

493. Margolese, D., J. Melero, S. Christiansen, B. Chmelka, and G. Stucky, *Direct syntheses of ordered SBA-15 mesoporous silica containing sulfonic acid groups.* Chemistry of Materials, **2000**. 12(8): p. 2448-2459.

494. Basaldella, E.I., M.S. Legnoverde, I. Jiménez-Morales, E. Rodríguez-Castellón, B.O. Dalla Costa, and C.A. Querini, *Preparation, characterization and catalytic activity towards green reactions of sulfonic functionalized SBA-15.* Adsorption, **2011**. 17(3): p. 631-641.

495. Lotero, E., J.G. Goodwin Jr, D.A. Bruce, K. Suwannakarn, Y. Liu, and D.E. Lopez, *The catalysis of biodiesel synthesis.* catalysis, **2006**. 19(1): p. 41-83.

496. Melero, J.A., L.F. Bautista, J. Iglesias, G. Morales, R. Sánchez-Vázquez, K. Wilson, and A.F. Lee, *New insights in the deactivation of sulfonic modified SBA-15 catalysts for biodiesel production from low-grade oleaginous feedstock.* Applied Catalysis A: General, **2014**. 488: p. 111-118.

497. Soler-Illia, G.d.A., A. Louis, and C. Sanchez, *Synthesis and characterization of mesostructured titania-based materials through evaporation-induced self-assembly.* Chemistry of Materials, **2002**. 14(2): p. 750-759.

498. Sirsam, R. and G. Usmani, *Preparation and characterization of sulfonic acid functionalized silica and its application for the esterification of ethanol and maleic Acid.* Journal of The Institution of Engineers (India): Series E, **2016**. 97(1): p. 75-80.

499. Muthirulan, P., C.N. Devi, and M.M. Sundaram, *TiO₂ wrapped graphene as a high performance photocatalyst for acid orange 7 dye degradation under solar/UV light irradiations.* Ceramics International, **2014**. 40(4): p. 5945-5957.

500. Lu, A.H., E.e.L. Salabas, and F. Schüth, *Magnetic nanoparticles: synthesis, protection, functionalization, and application.* Angewandte Chemie International Edition, **2007**. 46(8): p. 1222-1244.

501. Kruse, N. and S. Chenakin, *XPS characterization of Au/TiO₂ catalysts: Binding energy assessment and irradiation effects.* Applied Catalysis A: General, **2011**. 391(1): p. 367-376.

502. Sanjines, R., H. Tang, H. Berger, F. Gozzo, G. Margaritondo, and F. Levy, *Electronic structure of anatase TiO₂ oxide.* Journal of Applied Physics, **1994**. 75(6): p. 2945-2951.

503. Liu, H., W. Yang, Y. Ma, Y. Cao, J. Yao, J. Zhang, and T. Hu, *Synthesis and characterization of titania prepared by using a photoassisted sol-gel method.* Langmuir, **2003**. 19(7): p. 3001-3005.

504. Ahmed, M.H., T.E. Keyes, and J.A. Byrne, *The photocatalytic inactivation effect of Ag–TiO₂ on β-amyloid peptide (1–42).* Journal of Photochemistry and Photobiology A: Chemistry, **2013**. 254: p. 1-11.

505. Barroso-Bujans, F., J. Fierro, S. Rojas, S. Sánchez-Cortes, M. Arroyo, and M. López-Manchado, *Degree of functionalization of carbon nanofibers with benzenesulfonic groups in an acid medium.* Carbon, **2007**. 45(8): p. 1669-1678.

506. Hueso, J., J. Espinós, A. Caballero, J. Cotrino, and A. González-Elipe, *XPS investigation of the reaction of carbon with NO, O₂, N₂ and H₂O plasmas.* Carbon, **2007**. 45(1): p. 89-96.

507. Chastain, J., R.C. King, and J. Moulder, *Handbook of X-ray photoelectron spectroscopy: a reference book of standard spectra for identification and interpretation of XPS data.* **1995**: Physical Electronics Eden Prairie, MN.

508. Yadav, H.M., S.V. Otari, V.B. Koli, S.S. Mali, C.K. Hong, S.H. Pawar, and S.D. Delekar, *Preparation and characterization of copper-doped anatase TiO2 nanoparticles with visible light photocatalytic antibacterial activity.* Journal of Photochemistry and Photobiology A: Chemistry, **2014**. 280: p. 32-38.

509. Wu, L., Y. Zhou, W. Nie, L. Song, and P. Chen, *Synthesis of highly monodispersed teardrop-shaped core–shell SiO2/TiO2 nanoparticles and their photocatalytic activities.* Applied Surface Science, **2015**. 351: p. 320-326.

510. Zaki, M., G. Mekhemer, N. Fouad, and A. Rabee, *Structure–acidity correlation of supported tungsten (VI)-oxo-species: FT-IR and TPD studies of adsorbed pyridine and catalytic decomposition of 2-propanol.* Applied Surface Science, **2014**. 308: p. 380-387.

511. Budarin, V.L., J.H. Clark, R. Luque, D.J. Macquarrie, A. Koutinas, and C. Webb, *Tunable mesoporous materials optimised for aqueous phase esterifications.* Green Chemistry, **2007**. 9(9): p. 992-995.

512. Tao, M., L. Xue, Z. Sun, S. Wang, X. Wang, and J. Shi, *Tailoring the synergistic Brønsted-Lewis acidic effects in heteropolyacid catalysts: applied in esterification and transesterification reactions.* Scientific reports, **2015**. 5.

513. Lopez, D.E., J.G. Goodwin, D.A. Bruce, and E. Lotero, *Transesterification of triacetin with methanol on solid acid and base catalysts.* Applied Catalysis A: General, **2005**. 295(2): p. 97-105.

514. Kolvari, E., N. Koukabi, M.M. Hosseini, M. Vahidian, and E. Ghobadi, *Nano-ZrO2 sulfuric acid: a heterogeneous solid acid nano catalyst for Biginelli reaction under solvent free conditions.* RSC Advances, **2016**. 6(9): p. 7419-7425.

515. Osatiashtiani, A., A.F. Lee, D.R. Brown, J.A. Melero, G. Morales, and K. Wilson, *Bifunctional SO_4^{2-}/ZrO2 catalysts for 5-hydroxymethylfufural (5-HMF) production from glucose.* Catalysis Science & Technology, **2014**. 4(2): p. 333-342.

516. Wang, J., P. Yang, M. Fan, W. Yu, X. Jing, M. Zhang, and X. Duan, *Preparation and characterization of novel magnetic ZrO2/TiO2/Fe3O4 solid superacid.* Materials letters, **2007**. 61(11): p. 2235-2238.

517. Li, Y., S. Lian, D. Tong, R. Song, W. Yang, Y. Fan, R. Qing, and C. Hu, *One-step production of biodiesel from Nannochloropsis sp. on solid base Mg–Zr catalyst.* Applied energy, **2011**. 88(10): p. 3313-3317.

518. Teng, G., L. Gao, G. Xiao, and H. Liu, *Transesterification of soybean oil to biodiesel over heterogeneous solid base catalyst.* Energy & Fuels, **2009**. 23(9): p. 4630-4634.

519. Rattanaphra, D., A. Harvey, and P. Srinophakun, *Simultaneous conversion of triglyceride/free fatty acid mixtures into biodiesel using sulfated zirconia.* Topics in Catalysis, **2010**. 53(11-12): p. 773-782.

520. Morales, G., L.F. Bautista, J.A. Melero, J. Iglesias, and R. Sánchez-Vázquez, *Low-grade oils and fats: effect of several impurities on biodiesel production over sulfonic acid heterogeneous catalysts.* Bioresource technology, **2011**. 102(20): p. 9571-9578.

521. Xie, W. and C. Zhang, *Propylsulfonic and arenesulfonic functionalized SBA-15 silica as an efficient and reusable catalyst for the acidolysis of soybean oil with medium-chain fatty acids.* Food Chemistry, **2016**. 211: p. 74-82.

522. Xu, Y. and M.A. Hanna, *Synthesis and characterization of hazelnut oil-based biodiesel.* Industrial crops and products, **2009**. 29(2): p. 473-479.

523. Pirez, C., J.-M. Caderon, J.-P. Dacquin, A.F. Lee, and K. Wilson, *Tunable KIT-6 mesoporous sulfonic acid catalysts for fatty acid esterification.* ACS catalysis, **2012**. 2(8): p. 1607-1614.

524. Feyzi, M., L. Nourozi, and M. Zakarianezhad, *Preparation and characterization of magnetic $CsH_2PW_{12}O_{40}/Fe–SiO_2$ nanocatalysts for biodiesel production.* Materials Research Bulletin, **2014**. 60: p. 412-420.

525. Sharma, R.V., C. Baroi, and A.K. Dalai, *Production of biodiesel from unrefined canola oil using mesoporous sulfated Ti-SBA-15 catalyst.* Catalysis Today, **2014**. 237: p. 3-12.

526. Cremlyn, R.J.W., *Chlorosulfonic Acid*. **2002**, Great Britain: Royal Society of Chemistry.

527. Chironna, R.J., *Wet scrubbing of acidic gases* http://www.s-k.com/pdf/WetScrubbing.pdf, **2011**: p. 1-4.

528. Ameta, K. and A. Penoni, *Heterogeneous catalysis: A versatile tool for the synthesis of bioactive heterocycles*. **2014**: CRC Press.

529. Beranek, R. and H. Kisch, *Tuning the optical and photoelectrochemical properties of surface-modified TiO_2.* Photochemical & Photobiological Sciences, **2008**. 7(1): p. 40-48.

530. Mali, S.S., C.A. Betty, P.N. Bhosale, and P. Patil, *Synthesis, characterization of hydrothermally grown $MWCNT–TiO_2$ photoelectrodes and their visible light absorption properties.* ECS Journal of Solid State Science and Technology, **2012**. 1(2): p. M15-M23.

531. Babou, F., G. Coudurier, and J.C. Vedrine, *Acidic properties of sulfated zirconia: an infrared spectroscopic study.* Journal of Catalysis, **1995**. 152(2): p. 341-349.

532. Sohn, J.R., S.H. Lee, P.W. Cheon, and H.W. Kim, *Acidic properties and catalytic activity of titanium sulfate supported on TiO_2.* Bulletin-Korean Chemical Society, **2004**. 25(5): p. 657-664.

533. Esteban Benito, H., T. Del Ángel Sánchez, R. García Alamilla, J. Hernández Enríquez, G. Sandoval Robles, and F. Paraguay Delgado, *Synthesis and physicochemical characterization of titanium oxide and sulfated titanium oxide obtained by thermal hydrolysis of titanium tetrachloride.* Brazilian Journal of Chemical Engineering, **2014**. 31(3): p. 737-745.

534. Thangavelu, K., R. Annamalai, and D. Arulnandhi, *Preparation and characterization of nanosized TiO_2 powder by sol-gel precipitation route.* International Journal of Emerging Technology and Advanced Engineering, **2013**. 3(1): p. 636-639.

535. Adeeva, V., J. Dehaan, J. Janchen, G. Lei, V. Schunemann, L. Vandeven, W. Sachtler, and R. Vansanten, *Acid sites in sulfated and metal-promoted zirconium dioxide catalysts.* Journal of Catalysis, **1995**. 151(2): p. 364-372.

536. Jensen, H., A. Soloviev, Z. Li, and E.G. Søgaard, *XPS and FTIR investigation of the surface properties of different prepared titania nano-powders.* Applied Surface Science, **2005**. 246(1): p. 239-249.

537. Brundle, C. and A. Carley, *XPS and UPS studies of the adsorption of small molecules on polycrystalline Ni films.* Faraday Discuss. Chem. Soc., **1975**. 60: p. 51-70.

538. Berger, F., E. Beche, R. Berjoan, D. Klein, and A. Chambaudet, *An XPS and FTIR study of SO_2 adsorption on SnO_2 surfaces.* Applied Surface Science, **1996**. 93(1): p. 9-16.

539. Hasnat, M.A., J.A. Safwan, M. Rashed, Z. Rahman, M.M. Rahman, Y. Nagao, and A.M. Asiri, *Inverse effects of supporting electrolytes on the electrocatalytic nitrate reduction activities in a Pt/ Nafion/ Pt–Cu-type reactor assembly.* RSC Advances, **2016**. 6(14): p. 11609-11617.

540. Corma, A., V. Fornes, M. Juan-Rajadell, and J.L. Nieto, *Influence of preparation conditions on the structure and catalytic properties of SO_4^{2-}/ZrO_2 superacid catalysts.* Applied Catalysis A: General, **1994**. 116(1-2): p. 151-163.

541. Yang, Z. and W. Xie, *Soybean oil transesterification over zinc oxide modified with alkali earth metals.* Fuel processing technology, **2007**. 88(6): p. 631-638.

542. Alhassan, F.H., R. Yunus, U. Rashid, K. Sirat, A. Islam, H. Lee, and Y.H. Taufiq-Yap, *Production of biodiesel from mixed waste vegetable oils using ferric hydrogen sulphate as an effective reusable heterogeneous solid acid catalyst.* Applied Catalysis A: General, **2013**. 456: p. 182-187.

543. Boocock, D.G., S.K. Konar, V. Mao, C. Lee, and S. Buligan, *Fast formation of high-purity methyl esters from vegetable oils.* Journal of the American Oil Chemists' Society, **1998**. 75(12): p. 1167-1172.

544. Liu, X., X. Piao, Y. Wang, S. Zhu, and H. He, *Calcium methoxide as a solid base catalyst for the transesterification of soybean oil to biodiesel with methanol.* Fuel, **2008**. 87(7): p. 1076-1082.

545. Yadav, G.D. and A.D. Murkute, *Preparation of a novel catalyst UDCaT-5: enhancement in activity of acid-treated zirconia—effect of treatment with chlorosulfonic acid vis-à-vis sulfuric acid.* Journal of Catalysis, **2004**. 224(1): p. 218-223.

546. Grecea, M.L., A.C. Dimian, S. Tanase, V. Subbiah, and G. Rothenberg, *Sulfated zirconia as a robust superacid catalyst for multiproduct fatty acid esterification.* Catalysis Science & Technology, **2012**. 2(7): p. 1500-1506.

547. Jin, T., T. Yamaguchi, and K. Tanabe, *Mechanism of acidity generation on sulfur-promoted metal oxides.* The Journal of Physical Chemistry, **1986**. 90(20): p. 4794-4796.

548. Varala, R., V. Narayana, S.R. Kulakarni, M. Khan, A. Alwarthan, and S.F. Adil, *Sulfated tin oxide (STO)–Structural properties and application in catalysis: A review.* Arabian Journal of Chemistry, **2016**. 9(4): p. 550-573.

549. Manayil, J.C., C.V. Inocencio, A.F. Lee, and K. Wilson, *Mesoporous sulfonic acid silicas for pyrolysis bio-oil upgrading via acetic acid esterification.* Green Chemistry, **2016**. 18(5): p. 1387-1394.

550. Guldhe, A., P. Singh, F.A. Ansari, B. Singh, and F. Bux, *Biodiesel synthesis from microalgal lipids using tungstated zirconia as a heterogeneous acid catalyst and its comparison with homogeneous acid and enzyme catalysts.* Fuel, **2017**. 187: p. 180-188.

551. Furuta, S., H. Matsuhashi, and K. Arata, *Biodiesel fuel production with solid amorphous-zirconia catalysis in fixed bed reactor.* Biomass and Bioenergy, **2006**. 30(10): p. 870-873.

552. Qin, S., W. Cai, X. Tang, and L. Yang, *Sensitively monitoring photodegradation process of organic dye molecules by surface-enhanced Raman spectroscopy based on $Fe_3O_4@SiO_2@TiO_2@Ag$ particle.* Analyst, **2014**. 139(21): p. 5509-5515.

553. Li, C., J. Tan, X. Fan, B. Zhang, H. Zhang, and Q. Zhang, *Magnetically separable one dimensional Fe_3O_4/P(MAA-DVB)/TiO_2 nanochains: preparation, characterization and photocatalytic activity.* Ceramics International, **2015**. 41(3): p. 3860-3868.

554. Zhang, H., H. Yu, A. Zheng, S. Li, W. Shen, and F. Deng, *Reactivity Enhancement of 2-Propanol Photocatalysis on SO_4^{2-}/TiO_2: Insights from Solid-State NMR Spectroscopy.* Environmental science & technology, **2008**. 42(14): p. 5316-5321.

555. Li, Z., R. Wnetrzak, W. Kwapinski, and J.J. Leahy, *Synthesis and characterization of sulfated TiO_2 nanorods and ZrO_2/TiO_2 nanocomposites for the esterification of biobased organic acid.* ACS applied materials & interfaces, **2012**. 4(9): p. 4499-4505.

556. Jiang, Y.-X., X.-M. Chen, Y.-F. Mo, and Z.-F. Tong, *Preparation and properties of Al-PILC supported SO_4^{2-}/TiO_2 superacid catalyst.* Journal of Molecular Catalysis A: Chemical, **2004**. 213(2): p. 231-234.

557. Jacinto, M.J., O.H. Santos, R.F. Jardim, R. Landers, and L.M. Rossi, *Preparation of recoverable Ru catalysts for liquid-phase oxidation and hydrogenation reactions.* Applied Catalysis A: General, **2009**. 360(2): p. 177-182.

558. Tang, S., L. Wang, Y. Zhang, S. Li, S. Tian, and B. Wang, *Study on preparation of Ca/Al/Fe3O4 magnetic composite solid catalyst and its application in biodiesel transesterification.* Fuel Processing Technology, **2012**. 95: p. 84-89.

559. Xin, T., M. Ma, H. Zhang, J. Gu, S. Wang, M. Liu, and Q. Zhang, *A facile approach for the synthesis of magnetic separable Fe_3O_4@ TiO_2, core–shell nanocomposites as highly recyclable photocatalysts.* Applied Surface Science, **2014**. 288: p. 51-59.

560. Moghanian, H., A. Mobinikhaledi, A. Blackman, and E. Sarough-Farahani, *Sulfanilic acid-functionalized silica-coated magnetite nanoparticles as an efficient, reusable and magnetically separable catalyst for the solvent-free synthesis of 1-amido-and 1-aminoalkyl-2-naphthols.* RSC Advances, **2014**. 4(54): p. 28176-28185.

561. Naeimi, H. and Z.S. Nazifi, *A highly efficient nano-Fe_3O_4 encapsulated-silica particles bearing sulfonic acid groups as a solid acid catalyst for synthesis of 1, 8-dioxo-octahydroxanthene derivatives.* Journal of Nanoparticle Research, **2013**. 15(11): p. 2026.

562. Jafar Tafreshi, M. and Z. Masoomi Khanghah, *Infrared spectroscopy studies on sol-gel prepared alumina powders.* Materials Science, **2015**. 21(1): p. 28-31.

563. Park, Y.-M., D.-W. Lee, D.-K. Kim, J.-S. Lee, and K.-Y. Lee, *The heterogeneous catalyst system for the continuous conversion of free fatty acids in used vegetable oils for the production of biodiesel.* Catalysis Today, **2008**. 131(1): p. 238-243.

564. Zhang, J., F. Huang, and Z. Lin, *Progress of nanocrystalline growth kinetics based on oriented attachment.* Nanoscale, **2010**. 2(1): p. 18-34.

565. Groen, J.C., L.A. Peffer, and J. Pérez-Ramírez, *Pore size determination in modified micro- and mesoporous materials. Pitfalls and limitations in gas adsorption data analysis.* Microporous and Mesoporous Materials, **2003**. 60(1): p. 1-17.

566. Alaba, P.A., Y.M. Sani, I.Y. Mohammed, Y.A. Abakr, and W.M.A.W. Daud, *Synthesis and characterization of sulfated hierarchical nanoporous faujasite zeolite for efficient transesterification of shea butter.* Journal of Cleaner Production, **2017**. 142: p. 1987-1993.

567. Mahdavi, M., M.B. Ahmad, M.J. Haron, F. Namvar, B. Nadi, M.Z.A. Rahman, and J. Amin, *Synthesis, surface modification and characterisation of biocompatible magnetic iron oxide nanoparticles for biomedical applications.* Molecules, **2013**. 18(7): p. 7533-7548.

568. Safari, J. and Z. Zarnegar, *Sulphamic acid-functionalized magnetic Fe_3O_4 nanoparticles as recyclable catalyst for synthesis of imidazoles under microwave irradiation.* Journal of Chemical Sciences, **2013**. 125(4): p. 835-841.

569. Zhang, Y., W.-T. Wong, and K.-F. Yung, *One-step production of biodiesel from rice bran oil catalyzed by chlorosulfonic acid modified zirconia via simultaneous esterification and transesterification.* Bioresource technology, **2013**. 147: p. 59-64.

570. Han, Y.-Z., L. Hong, X.-Q. Wang, J.-Z. Liu, J. Jiao, M. Luo, and Y.-J. Fu, *Biodiesel production from Pistacia chinensis seed oil via transesterification using recyclable magnetic cellulose-based catalyst.* Industrial Crops and Products, **2016**. 89: p. 332-338.

571. Leclercq, E., A. Finiels, and C. Moreau, *Transesterification of rapeseed oil in the presence of basic zeolites and related solid catalysts.* Journal of the American Oil Chemists' Society, **2001**. 78(11): p. 1161-1165.

572. Phan, A.N. and T.M. Phan, *Biodiesel production from waste cooking oils.* Fuel, **2008**. 87(17): p. 3490-3496.

573. Liu, Y., L. Wang, and Y. Yan, *Biodiesel synthesis combining pre-esterification with alkali catalyzed process from rapeseed oil deodorizer distillate.* Fuel Processing Technology, **2009**. 90(7): p. 857-862.

574. Zheng, N. and G.D. Stucky, *A general synthetic strategy for oxide-supported metal nanoparticle catalysts.* Journal of the American Chemical Society, **2006**. 128(44): p. 14278-14280.

575. Parlett, C.M., D.W. Bruce, N.S. Hondow, A.F. Lee, and K. Wilson, *Support-enhanced selective aerobic alcohol oxidation over Pd/mesoporous silicas.* ACS Catalysis, **2011**. 1(6): p. 636-640.

576. Cuenya, B.R., *Synthesis and catalytic properties of metal nanoparticles: Size, shape, support, composition, and oxidation state effects.* Thin Solid Films, **2010**. 518(12): p. 3127-3150.